

PROCEEDINGS OF THE 25TH NORDIC SEMINAR
ON COMPUTATIONAL MECHANICS

Lund, 25-26 October, 2012

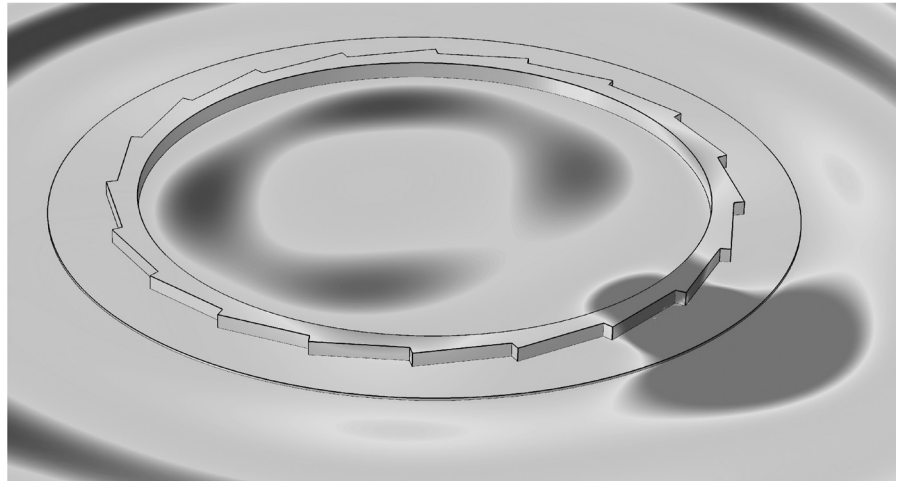
K. PERSSON, J. REVSTEDT, G. SANDBERG, and M. WALLIN (editors)



Department of Construction Sciences
Faculty of Engineering, Lund University

Proceedings of the
25TH NORDIC SEMINAR ON
COMPUTATIONAL MECHANICS
Lund, 25-26 October, 2012

K. PERSSON, J. REVSTEDT, G. SANDBERG, and M. WALLIN (editors)



ISBN 978-91-7473-456-0 ISSN 0281-6679

Copyright © 2012 by Construction Sciences, Faculty of Engineering,
Lund University, Sweden.
Printed by Media-Tryck Lund University, Lund, Sweden, October 2012.

For information, address:
Dept. of Construction Sciences, Faculty of Engineering, Lund University, Box 118,
SE-221 00 Lund, Sweden.

Homepage: www.byggvetenskaper.lth.se

Proceedings of the 25th Nordic Seminar on Computational Mechanics
K. Persson, J.Revstedt, G. Sandberg, M. Wallin (Eds.)
© Lund University, 2012

Preface

These proceedings contain the papers presented at the twenty-fifth Nordic Seminar on Computational Mechanics, held at Lund University, Lund, Sweden, 25-26 October 2012. The Nordic Seminars on Computational Mechanics represent the major activity of the Nordic Association for Computational Mechanics (NoACM). The NoACM was founded in 1988 with the objective to stimulate and promote research and practice in computational mechanics, to foster the interchange of ideas among the various fields contributing to computational mechanics, and to provide forums and meetings for dissemination of knowledge in computational mechanics. Younger researchers, including doctorate students etc., are especially encouraged to take part at these seminars. The member countries of NoACM are the Nordic countries (Denmark, Finland, Iceland, Norway and Sweden) and the Baltic countries (Estonia, Latvia and Lithuania). NoACM is a subchapter of the International Organization for Computational Mechanics (IACM) and the European Community on Computational Methods in Applied Sciences (ECCOMAS).

The responsibility for organising this year's seminar was assigned by NoACM to the Divisions of Structural Mechanics, Solid Mechanics and Fluid Mechanics at Lund University. This year's seminar contains invited lectures, a special session given in honor of Professor Niels Saabye Ottosen and more than 60 contributed presentations divided into three parallel sessions. In the present volume, all the invited lectures are placed first, followed by the contributed papers in the order of appearance.

On behalf of the organisers, sincere appreciations are extended to all contributors at the seminar, not least to the invited lectures in the Professor Ottosen session, the plenary lecturers and to the other speakers for their efforts in preparing talks and papers.

Lund, October 2012

The editors

Organising committee

MSc Ola Flodén
Associate Professor Kent Persson
MSc Peter Persson
Professor Johan Revstedt
Professor Göran Sandberg
Associate Professor Mathias Wallin

Programme Committee

Göran Sandberg, Sweden
Trond Kvamsdal, Norway
Knut Morten Okstad, Norway
Kjell Magne Mathisen, Norway
Erik Lund, Denmark
Jens Honoré Walther, Denmark
Arkadi Berezovski, Estonia (Baltic countries)
Jouni Freund, Finland
Reijo Kouhia, Finland
Ragnar Larsson, Sweden
Gunnar Tibert, Sweden

NSCM-25 secretariat

Department of Construction Sciences
Lund University
PO Box 118
S-221 00 Lund
SWEDEN
Phone: +46 46 222 7370
Fax: +46 46 222 4420
info-nscm25@listserver.lu.se
<http://nscm25.lth.se>

Thursday October 25				
08:20	Opening, Room: Stora Hörsalen			
08:30	Keynote Lecture - Ville Vuorinen, Room: Stora Hörsalen			
09:15	Coffee			
09:30	Sessions I			
	<table border="1"> <tr> <td>Computational Fluid Mechanics Room: 304</td> <td>Computational Techniques Room: Lilla Hörsalen</td> <td>Solid Mechanics I Room: Stora Hörsalen</td> </tr> </table>	Computational Fluid Mechanics Room: 304	Computational Techniques Room: Lilla Hörsalen	Solid Mechanics I Room: Stora Hörsalen
Computational Fluid Mechanics Room: 304	Computational Techniques Room: Lilla Hörsalen	Solid Mechanics I Room: Stora Hörsalen		
11:30	Keynote Lecture - Peter Hansbo, Room: Stora Hörsalen			
12:15	Lunch			
13:15	Sessions II			
	<table border="1"> <tr> <td>Finite Element Techniques Room: 304</td> <td>Structural Mechanics I Room: Lilla Hörsalen</td> <td>Session in honor of Niels S. Ottosen Room: Stora Hörsalen</td> </tr> </table>	Finite Element Techniques Room: 304	Structural Mechanics I Room: Lilla Hörsalen	Session in honor of Niels S. Ottosen Room: Stora Hörsalen
Finite Element Techniques Room: 304	Structural Mechanics I Room: Lilla Hörsalen	Session in honor of Niels S. Ottosen Room: Stora Hörsalen		
15:15	Keynote Lecture - Jesper Hattel, Room: Stora Hörsalen			
16:00	Coffee			
16:15	Sessions III			
	<table border="1"> <tr> <td>Silent Spaces Room: 304</td> <td>Optimisation Room: Lilla Hörsalen</td> <td>Constitutive Modelling Room: Stora Hörsalen</td> </tr> </table>	Silent Spaces Room: 304	Optimisation Room: Lilla Hörsalen	Constitutive Modelling Room: Stora Hörsalen
Silent Spaces Room: 304	Optimisation Room: Lilla Hörsalen	Constitutive Modelling Room: Stora Hörsalen		

Friday October 26				
09:00	Keynote Lecture - Hans Petter Langtangen, Room: Stora Hörsalen			
09:45	Coffee			
10:00	Sessions IV			
	<table border="1"> <tr> <td>Dynamics Room: 304</td> <td>Structural Mechanics II Room: Lilla Hörsalen</td> <td>Solid Mechanics II Room: Stora Hörsalen</td> </tr> </table>	Dynamics Room: 304	Structural Mechanics II Room: Lilla Hörsalen	Solid Mechanics II Room: Stora Hörsalen
Dynamics Room: 304	Structural Mechanics II Room: Lilla Hörsalen	Solid Mechanics II Room: Stora Hörsalen		
12:00	Closing			
12:15	Lunch			
13:00	Demonstration of Vibration and Acoustics Laboratory, V-Building			

Keynote Lectures	
Keynote Lecture I, Thursday 25/10, 8:30-9:15, Room: Stora Hörsalen	V. Vuorinen
Developments on flow solvers and numerical schemes for large eddy simulation of turbulent flows using Open-FOAM	
Keynote Lecture II, Thursday 25/10, 11:30-12:15, Room: Stora Hörsalen	P. Hansbo, M. G. Larson,
Tangential differential operators and finite elements for elasticity on thin curved domains	
Keynote Lecture III, Thursday 25/10, 15:15-16:00, Room: Stora Hörsalen	J. Hättel
Multiphysics modelling of manufacturing processes	
Keynote Lecture IV, Friday 26/10, 9:00-9:45, Room: Stora Hörsalen	H. P. Langtangen, M. Mortensen
Flexible software tools for computational turbulence	

Sessions I, Thursday Oct 25, 9:30-11:30	
Fluid Mechanics, Room: 304	
Computational respiratory flow dynamics for distinguishing between healthy and disease	M. Mihaescu, N. Powell, E. Gutmark, and L. Fuchs
One dimensional network models for cardiovascular applications	V. Eck, P. R. Leinan, L. R. Hellevik
Effect of dilatation on the turbulence level in compressible quasi one-dimensional steady nozzle flow	I. Grigoriev, G. Brethouwer, A. V. Johansson, S. Wallin
Large eddy simulation of a bluff body flame near lean blow off using detailed chemistry	E. Hodžic, C. Duwig, R. Z. Szász, L. Fuchs
Direct numerical simulation of constant volume auto-ignition of lean hydrogen/air mixture	R. Yu, X. s. Bai
Fluid-structure interaction of the transient evolution of cantilever beam	A. Cesur, A. Feymark
Computational Techniques, Room: Lilla Hörsalen	
Discontinuous Petrov-Galerkin finite element method for the Reissner-Mindlin plate bending model	A. H. Niemi, N. O. Collier, V. M. Calo
A high order solver for the unbounded Poisson equation	M. M. Hejlesen, J. T. Rasmussen, P. Chatelain, J. H. Walther
Effect of scale on the cellular material strength	A. Karakoç, J. Freund
A workbook for multibody systems ODE and DAE solvers	C. Andersson, C. Führer, J. Åkesson
Goal-oriented adaptivity for the Quasi-Continuum method	A. Memarhavandi, F. Larsson, K. Runesson
A conservative quaternion-based time integration algorithm for rigid body rotations with implicit constraints	M. B. Nielsen, S. Krenk
Solid Mechanics I, Room: Stora Hörsalen	
Free vibrations of non-isotropic plates with cut-outs	A. V. Lebedev, A. L. Smirnov
Wave propagation and dispersion in microstructured solids	A. Berezovski, J. Engelbrecht, M. I Berezovski
Blowup of the sensitivity of the elastic energy with respect to the uncertainties in the Poisson's ratio	O. Mali, S. Repin
Recent advances in the experimental analysis of the mechanics of sand	S. A. Hall, J. Wright
Simulation of indenter geometry effects in nanoindentation	L. Chen, A. Ahadi, J. Zhou
Stress analysis around a through crack shaped defect in a thin copper film using molecular dynamics	D. Johansson, P. Hansson, S. Melin

Sessions II, Thursday Oct 25, 13:15-15:15	
Finite Element Techniques, Room: 304	
Recovery based approach to design a posteriori error estimator in isogeometric analysis	T. Kvamsdal, M. Kumar, K. A. Johannessen, K. M. Okstad
Mortar-based isogeometric analysis applied to frictionless large deformation elastoplastic contact problems	K. M. Mathisen, K. M. Okstad, T. Kvamsdal, S. B. Raknes
Nitsche's method for discontinuous material parameters	M. Juntunen, R. Stenberg
Isogeometric FE analysis of thin plates with cracks	K. M. Okstad, T. Kvamsdal, K. A. Johannessen
Isogeometric analysis of thin structures	S. B. Raknes, Y. Bazilevs, K. M. Mathisen, T. Kvamsdal, K. M. Okstad
Isogeometric collocation method using reduced continuity order NURBS and T-splines	M. Kumar, T. Kvamsdal
Structural Mechanics I, Room: Lilla Hörsalen	
A three dimensional plasticity model for perpendicular to grain cohesive fracture in wood - an abstract	H. Danielsson, P. J. Gustafsson
Finite-element analysis of multilayered shells deformation under the load with a flat base	S. M. Bauer, L. A. Karamshina
Grouted connections with shear keys - numerical modelling with ABAQUS	R. R. Pedersen, M. B. Jørgensen, L. Damkilde, H. B. Clausen, K. Andersen
A reduced model for glass structures subjected to dynamic impact loads	M. Fröling, K. Persson, P. E. Austrell
Multiscale modeling of porous media	C. Sandström, F. Larsson
Structural modeling and analysis of a wave energy converter	A. S. Zurkinder, S. H. Lambersten, L. Damkilde
Session in honor of Niels S. Ottosen, Room: Stora Hörsalen	
On the computational homogenization of mesoscale gradient viscoplasticity	K. Runesson, M. Ekh, F. Larsson
A geometric approach in computational stability analysis	A. Fedbroff, R. Kouhia, J. Mäkinen
Meshing effects on modelling of evolving bone during distraction osteogenesis	V. LaRussa, B. Skallerud
Delamination between a unidirectional and woven composite	L. Banks-Sills, M. Gohfeld, R. Eliazi
Topology optimization based a phase-field approach and Howard's algorithm	M. Ristinmaa, M. Wallin
Thermodynamically based fictitious crack/interface model for general normal and shear loading	N. S. Ottosen, M. Ristinmaa

Sessions III, Thursday Oct 25, 16:15-17:55	
Silent Spaces, Room: 304	
Reduction of ground vibrations by landscape shaping	P. Persson, K. Persson, P. Jørstad, G. Sandberg
Reduction of models for vibration analyses of lightweight multi-storey buildings	O. Flodén, K. Persson, G. Sandberg
Finite element analysis of flanking transmission in a lightweight junction with elastic layers	J. Negreira, D. Bard, K. Persson, G. Sandberg
Finite element validation of lightweight wooden T-junction models	A. Sjöström, J. Negreira, D. Bard, G. Sandberg
Investigating acoustic fatigue using CFD and FEM on a model problem	J. Nilsson, R. Z. Szász, P. E. Austrell
Optimisation, Room: Lilla Hörsalen	
The inverse motion problem for quasi-incompressible electroelasticity	A. Ask, R. Denzer, A. Menzel, M. Ristinmaa
Stochastic model reduction applied to inverse problems	T. Garbowski, M. Putowski
Numerical modelling and optimization of all plywood sandwich panels with rib-stiffened cores	E. Labans, K. Kalnins
Thickness optimization of laminated composites using the discrete material optimization method	S. Nørgaard Sørensen, R. Sørensen, E. Lund
Design and optimization of a spring-loaded cable-driven robotic exoskeleton	L. Zhou, S. Bai, M. Skipper Andersen, J. Rasmussen
Constitutive Modelling, Room: Stora Hörsalen	
Mesoscale modeling of dislocation density gradients and microstructure evolution	H. Hallberg, M. Ristinmaa
Modeling of the cyclic behaviour of Haynes 282, including cyclic softening	R. Brommesson, M. Ekh
Comparison of the BPA model to DIC measurements of polycarbonate	J. Engqvist, M. Wallin, S. Hall, M. Ristinmaa
A constitutive model for the out-of-plane behaviour of paperboard	E. Borgqvist, M. Wallin, M. Ristinmaa
Physically based plasticity model coupled with precipitate model for IN718	M. Fisk, L. E. Lindgren

Sessions IV, Friday Oct 26, 10:00-12:00	
Dynamics, Room: 304	
Comparison of vibration suppression of flexible rotors supported by passive and controllable constraint elements during passing their critical speeds	J. Zapoměl, P. Ferfecki
Optimal brain surgeon on artificial neural networks in nonlinear structural dynamics	N. H. Christiansen, J. Hultmann Job, K. Klyver, J. Høgsbrg
A semi-analytical model for free vibrations of offshore free spanning pipelines	K. Vedeld, H. Sollund
Analytical stiffness optimization of high-precision hexapods for large optical telescope applications	B. Afzali Far, P. Lidström, K. Nilsson, A. Ardeberg
An analytical approach to solving the rigid sliding rod on the smooth walls	A. Mohammadi, M. Mohammadi
Structural Mechanics II, Room: Lilla Hörsalen	
Multi-parametric stability investigations for pressurized thin membranes	A. Eriksson
Approximate buckling model for steel-elastomer sandwich plates	O. J. Hareide, L. Brubak, E. Steen, J. Hellesland
Static redundancy factors in conceptual design	G. Tibert, L. M. Ach
Using touch and multi-touch interfaces in structural mechanics software	J. Lindemann, D. Åkesson
Finite element simulation of an excavation using diaphragm wall	A. Spetz, O. Dahlblom, P. Lindh
The influence of surface elasticity on the flexural rigidity of nanowires	P. A. T. Olsson, H. S. Park
Solid Mechanics II, Room: Stora Hörsalen	
Modelling of stress driven material dissolution	P. Ståhle, E. Hansen
Mixed methods for viscoelastic solids with weak symmetry elements	D. N. Arnold, J. J. Lee
Debonding analyses in anisotropic materials with strain-gradient effects	B. Nyvang Legarth
A non-affine micro-sphere formulation for electroactive polymers	S. Thylander, A. Menzel, M. Ristinmaa
Ductile dynamic fracture modeling using embedded strong discontinuities in CGI machining simulations	G. Ljustina, R. Larsson, M. Fagerström
Composite manufacturing modeling using porous media theory	M. Rouhi, M. Wysocki, R. Larsson

Developments on Flow Solvers and Numerical Schemes for Large Eddy Simulation of Turbulent Flows Using OpenFOAM

Ville Vuorinen

PO Box 14300, FI-00076 AALTO, Finland, ville.vuorinen@aalto.fi

Summary. During the recent years, the opensource computational fluid dynamics (CFD) toolbox OpenFOAM[®] has become highly popular in solving various problems of continuum physics with particular focus on solving conservation laws. New simulation solvers can be implemented in 'top-level' scripts with compact syntax and capability for FOAM (field operation and manipulation). OpenFOAM relies on the finite volume method (FVM). Although a sophisticated C++ architecture for discretization and parallel computing exists, OpenFOAM still lacks some standard academic algorithms for the solution of turbulent flows. Furthermore, the low order of accuracy has been and is still a limiting factor for truly high-fidelity simulations. In the present paper a brief discussion on practical implementation of Runge-Kutta based solution methods for compressible and incompressible flows is given in the OpenFOAM environment. Validation studies involving laminar and turbulent conditions with increasing level of complexity are given. The concept of scale-selective discretization (SSD) is presented for reducing numerical diffusion of any present-day numerical scheme.

Key words: Runge-Kutta, projection methods, density based solution, opensource, scale-selective discretization.

Introduction

In mathematical terms, the governing partial differential equations of laminar and turbulent fluid flow are the Navier-Stokes (NS) equations [1]. In the present work the main interest lies in developing numerical tools to simulate turbulence, i.e. chaotic swirling of fluids, in engine related applications. Here, methods called Large-Eddy Simulation (LES) and Direct Numerical Simulation (DNS) are of particular interest due to their capability of resolving the temporal and spatial structure of turbulence.

To date, one of the most popular computational fluid dynamics (CFD) methods to simulate turbulence in complex geometries is the finite volume method (FVM) which reduces to the finite difference method (FDM) on Cartesian grids [4, 2, 3]. The FVM is based on applying the Gauss' theorem on general conservation laws. Thereby, the convection and diffusion terms of form $\nabla \cdot F(x, y, z, t)$ in the NS-equations can be evaluated as volume integrals over computational cells Ω_h resulting in $\nabla \cdot F(x, y, z, t) \approx \frac{1}{\Omega_h} \int_{\Omega_h} \nabla \cdot F(x, y, z, t) d\Omega = \int_{\partial\Omega_h} F(x, y, z, t) d\mathbf{S}$ [4]. The spatial accuracy of FVM boils down to the interpolation of fluxes on the cell faces from the cell-centers.

The field of CFD could be roughly divided into academic CFD (ACFD) and industrially oriented CFD (ICFD). ACFD aims typically at high order of accuracy and high resolution in simple geometries whereas ICFD aims at robustness and fast code execution times in complex geometries. Within ACFD novel methods such as high-order compact differences or spectral elements may be employed alongside with high order Runge-Kutta time integration methods [1]. In contrast, in ICFD second order spatial and temporal accuracy is typically a standard

level of accuracy. Also some algorithmic differences can be listed between ACFD and ICFD. In incompressible flows velocity and pressure are coupled via the pressure Poisson equation. In ICFD the coupling is implemented non-linearly using e.g. the PISO method [5] whereas in ACFD projection methods, as first introduced by Chorin and Thémam [1], are typically employed. In contrast, compressible flows can be solved in principle using fully explicit methods. However, in ICFD pressure based solution strategies (i.e. leading to the solution of Poisson equation) are still employed as this approach decouples the acoustic waves from the solution with computational speedup. In contrast, in compressible ACFD studies the explicit density based Runge-Kutta methods have become accurate state-of-the-art methods at the expense of increased computational cost since acoustic waves are also resolved.

The present paper is based on our recent, ongoing work [8]-[10]. Some important steps for bridging the gap between ICFD and ACFD are presented with the aim of doing better quality LES/DNS in the future studies using the widely popular OpenFOAM toolbox. Practical programming examples of implementing the classical fourth order Runge-Kutta (RK4) methods into OpenFOAM are given. Example code of the incompressible projection method and the compressible density based method is shown. Finally, a new, novel approach to improve the diffusion properties of the present day upwind schemes on unstructured grids is presented.

Governing Equations and Solution Approaches

Incompressible Navier-Stokes Equations

The incompressible Navier-Stokes (NS) equation describes the flow of incompressible fluids and it is also known to approximate well the flow of low-speed ($Ma < 0.3$) gases. In the present study we apply the dimensional form of the NS-equations and embed the fluid density (as being a constant in incompressible flows) into the pressure. Under these assumptions, using the Einstein notation, the NS-equation reads:

$$\frac{\partial u_i}{\partial t} + \frac{\partial u_i u_j}{\partial x_j} = -\frac{\partial p}{\partial x_i} + \nu \frac{\partial^2 u_i}{\partial x_k \partial x_k}, \quad i, j, k = 1, 2, 3. \quad (1)$$

Additionally, to ensure incompressibility, the mass conservation is guaranteed by the incompressibility constraint

$$\nabla \cdot \mathbf{u} = \frac{\partial u_i}{\partial x_i} = 0. \quad (2)$$

In incompressible flows the pressure and velocity are coupled in an elliptic manner via the Poisson equation. This is seen by taking the divergence from the both sides of the equation (1) which results in the Poisson equation for the pressure i.e.

$$\frac{\partial^2 p}{\partial x_j \partial x_j} = -\frac{\partial u_i}{\partial x_j} \frac{\partial u_j}{\partial x_i}. \quad (3)$$

Thus, for a given (non-linear) convection term $C_i = \frac{\partial u_i u_j}{\partial x_j}$ one may find a pressure by solving $\frac{\partial^2 p}{\partial x_j \partial x_j} = -\frac{\partial C_i}{\partial x_i}$. The *projection methods*, as first developed by Chorin and Thémam for the case of explicit Euler time integration, are based on this principle [1]. According to the Helmholtz-Hodge decomposition of vector fields any vector field \mathbf{u} may be decomposed into two parts: a divergence free and a curl free part. For this decomposition a scalar potential p needs to be introduced so that:

$$u_i = u_i^* - \frac{\partial p}{\partial x_i}. \quad (4)$$

In the equation (4) $\frac{\partial u_i^*}{\partial x_i} \neq 0$, $\frac{\partial u_i}{\partial x_i} = 0$ and $\nabla \times \nabla p = 0$ i.e. the gradient of the scalar potential is curl-free. Hence, p is a solution of the Poisson equation with appropriate boundary conditions.

The Helmholtz-Hodge decomposition forms the mathematical basis for coupling velocity and pressure in incompressible flows.

Compressible Navier-Stokes Equations

The full NS-equations describe the conservation of mass, momentum and energy [4]. The unknowns are the density (ρ), the momentum density (ρu_i) and the energy density (ρe). The full NS-equations read:

$$\frac{\partial \rho}{\partial t} + \frac{\partial \rho u_j}{\partial x_j} = 0 \quad (5)$$

$$\frac{\partial \rho u_i}{\partial t} + \frac{\partial (\rho u_i u_j)}{\partial x_j} = \frac{\partial}{\partial x_j} (-p \delta_{ij} + \sigma_{ij}) \quad (6)$$

$$\frac{\partial \rho e}{\partial t} + \frac{\partial ((\rho e + p) u_j)}{\partial x_j} = \frac{\partial}{\partial x_j} (\sigma_{ij} u_i) + \frac{\partial}{\partial x_j} \left(\lambda \frac{\partial T}{\partial x_j} \right). \quad (7)$$

In equation (6) the viscous stress tensor is defined as

$$\sigma_{ij} = \mu \left(\frac{\partial u_i}{\partial x_j} + \frac{\partial u_j}{\partial x_i} \right) + \left(\mu_b - \frac{2}{3} \mu \right) \frac{\partial u_i}{\partial x_j} \delta_{ij}, \quad (8)$$

where μ is the dynamic viscosity and μ_b the bulk viscosity of the fluid. Often, μ_b is assumed to be zero. In our compressible solvers, we use a model for μ_b in order to capture the sharp gradients at the shock positions [11].

In equations 6-7 the pressure is explicitly coupled to the density and the temperature via the equation of state which allows usage of fully explicit RK-methods without a Poisson equation

$$p = \rho RT. \quad (9)$$

Furthermore, the internal energy of the flow is defined as the sum of thermodynamic and kinetic energies

$$e = c_v T + \frac{1}{2} \mathbf{u}^2. \quad (10)$$

Once ρ , ρu_i and ρe are known the pressure and temperature can be constructed from equation (9).

Scale-Selective Discretization

The SSD concept has particular relevance on unstructured grids where a narrow spatial discretization stencil has to be typically applied. The motivation for the SSD scheme [9] is based on the fact that very often some upwinding has to be introduced to stabilize numerical simulations via numerical diffusion. Yet, upwinding reduces the order of the method which may have an overly damping effect on the structure of the turbulent flow. The question is: why use upwinding on the whole solution when actually the numerical problems lies in the smallest scales, i.e. at wavelengths close to $2\Delta x$, only? In other words: how to limit numerical diffusion to the smallest scales of the flow? We have overcome the problem by separating the scales of the flow using a high-pass filter $HP(\dots)$. For example, a field variable u_i can be separated into smooth component $\hat{u}_i = u_i - u'_i$ and fluctuating component $u'_i = HP(u_i)$ using the filter. Thereby, e.g. a derivative of form $\frac{\partial u_i}{\partial x_j}$ can be decomposed as $\frac{\partial u_i}{\partial x_j} = \frac{\partial \hat{u}_i}{\partial x_j} + \frac{\partial u'_i}{\partial x_j}$. The SSD procedure applies a centered scheme to the first, smooth term and an upwind biased scheme to the latter, fluctuating term. As a result, on unstructured grids, the overall accuracy of the scheme stays 2nd order in contrast to falling down to 1st order. Yet, the desired diffusive nature of the scheme is implicitly

retained in the diffusive truncation error of the scheme being $\mathcal{O}(\Delta x^3)$. The SSD procedure is very useful in the so called implicit LES (ILES). In ILES turbulent dissipation is modeled via diffusive numerics i.e. an implicit filter built into the truncation error of the numerical scheme.

Code Implementation

In OpenFOAM new flow solvers can be easily implemented into a 'top-level' script. The basic idea is very simple as one essentially needs to add a `for`-loop for time stepping and the spatial discretization of the equations is provided within the software package. Thereby, solving PDEs with explicit time integration methods boils down to essentially evaluating time changes (e.g. $d\rho$) using the spatial derivatives and adding fields together. Also matrix equations can be conveniently solved at top-level. The examples below show some code syntax for incompressible and compressible RK-solvers.

Implementation of the Projection Method Using OpenFOAM®

The above described steps can be described the easiest by applying them together with the explicit Euler method which boils down to the original Chorin-Themam algorithm [1]. The projection algorithm below leads to a numerically stable formulation and corresponds to the algorithm given recently by Hirsch [4].

Step 0: Find the flux of convecting velocity (which is free of divergence) on the cell faces by taking the dot product of linearly interpolated velocity with cell face outer normal vector:

```
phi=interpolate(U)&mesh.Sf();
```

Note indeed that: U is divergence free at this point at the beginning of a time step.

Step 1: Find the change in velocity at cell centers using the convection and the diffusion terms without the pressure gradient.

```
dU = dt*(-fvc::div(phi, U) + nu*fvc::Laplacian(U));
```

Step 2: Update the velocity first at cell centroids only and then update the velocity boundary conditions

```
U = U + dU;
```

```
U.correctBoundaryConditions();
```

Step 3: Find the flux of velocity on the cell faces by taking the dot product of linearly interpolated velocity with cell face outer normal vector:

```
phi=interpolate(U)&mesh.Sf();
```

Step 4: Solve the Poisson equation for the pressure:

```
fvm::Laplacian(p) = fvc::div(phi);
```

Step 5: Project the velocity onto its divergence free component, first only at cell centers, and after that correct the boundary conditions:

```
U = U - fvc::grad(p);
```

```
U.correctBoundaryConditions();
```

In order to implement e.g. the classical RK4 algorithm the above mentioned steps are repeated four times.

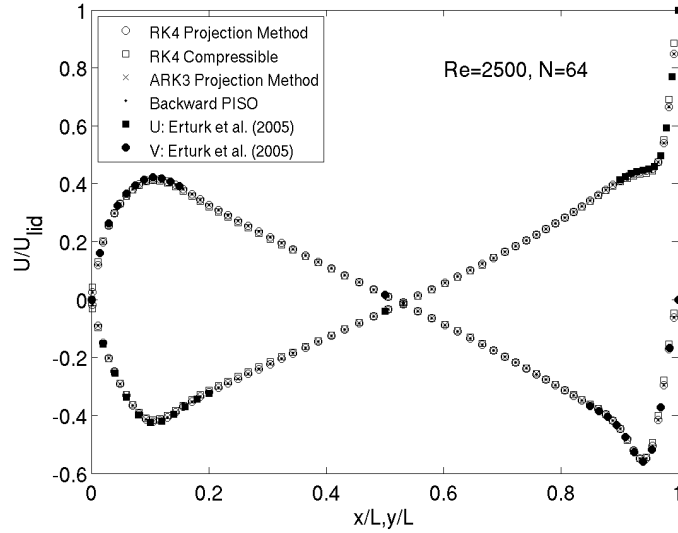


Figure 1. Velocity profiles along the horizontal and axial centerlines.

Explicit Runge-Kutta Methods for Subsonic Flows

In compressible flows, pressure is directly linked to density and temperature via the equation of state $p = \rho RT$. Hence, an explicit flow solver can be implemented without the solution of an algebraic group of equations. The general idea of solving them using OpenFOAM is basically the same as in the incompressible case. Bringing the governing full NS-equations into the δ -form and neglecting the viscous terms for simplicity, leads to the following code syntax:

```
drho = -dt*fvc::div(phi, rho);
drhoU = -dt*(fvc::div(phi, rhoU) + fvc::grad(p));
drhoE = -dt*(fvc::div(phi, rhoE + p));
```

Importantly, the code examples shown in the present paper work readily in 1d,2d and 3d cases as well as in parallel.

Some Validation Studies

Flow in a Cavity

The flow in a lid-driven cavity is a well known benchmark problem of CFD-codes [4, 6]. The setup consists of a 2D square box filled with incompressible fluid with viscosity ν . The box is enclosed by four walls of length L . The topmost wall is moving from left to right with velocity U so that a vortex forms inside the cavity. The newly implemented RK-based solvers (RK4, ARK3) for compressible and incompressible flows are all shown to be in excellent agreement with the standard PISO method and the reference data by Erturk et al. [6].

Turbulent Channel Flow

As an example of the capability of the implemented simulation codes we study the turbulent channel flow at a relatively low friction Reynolds number of $Re_\tau = 180$. Such a flow is statistically stationary due to driving gravity which maintains the flow. The grid resolution is rather fine corresponding to a DNS where all the spatial/temporal scales of the flow are resolved. An instantaneous overview of the velocity magnitude is shown in Figure 2 which shows the turbulent nature of the flow. The mean and fluctuating velocity components are plotted in Figure 3 showing the excellent match to the reference data by Moser et al. [7].

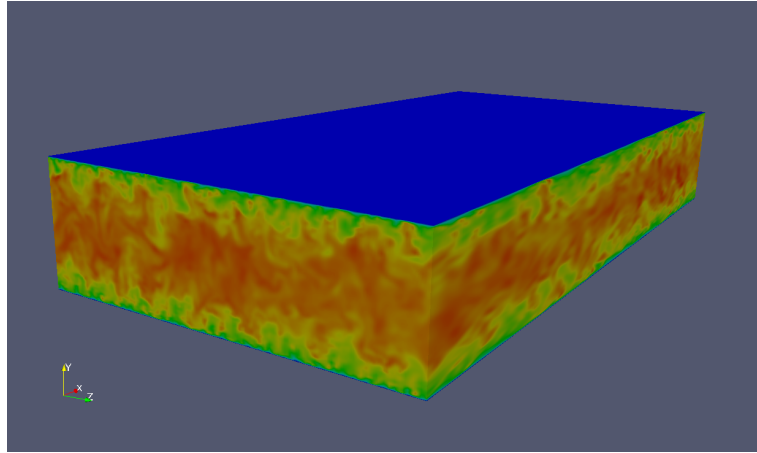


Figure 2. Visualization of the instantaneous velocity snapshot from the fully developed state for a channel flow at $Re_\tau = 590$ using the ARK3 solver.

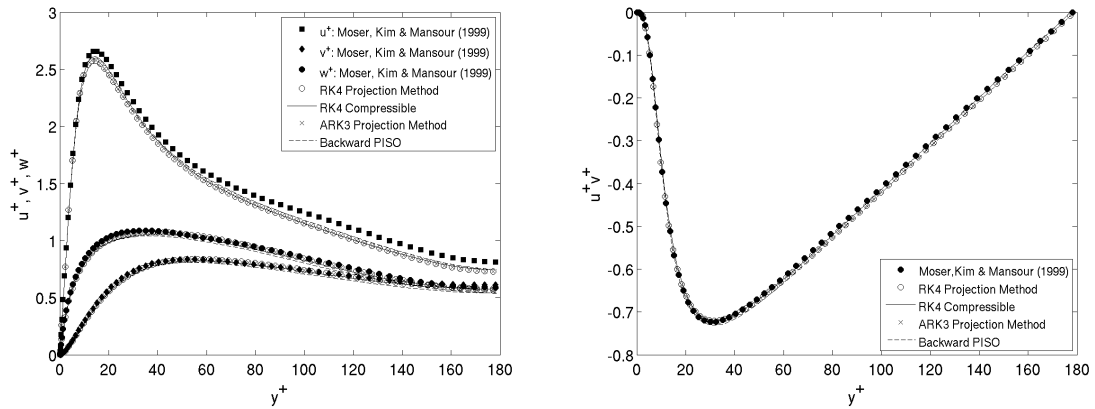


Figure 3. Reynolds stresses using the developed RK solvers and the standard PISO solver of OpenFOAM with second order backward time integration. The newly developed flow solvers perform very similarly with each other, the standard PISO algorithm and the data by Moser et al.[7]. **Top:** Diagonal components (RMS). **Bottom:** Off-diagonal component.

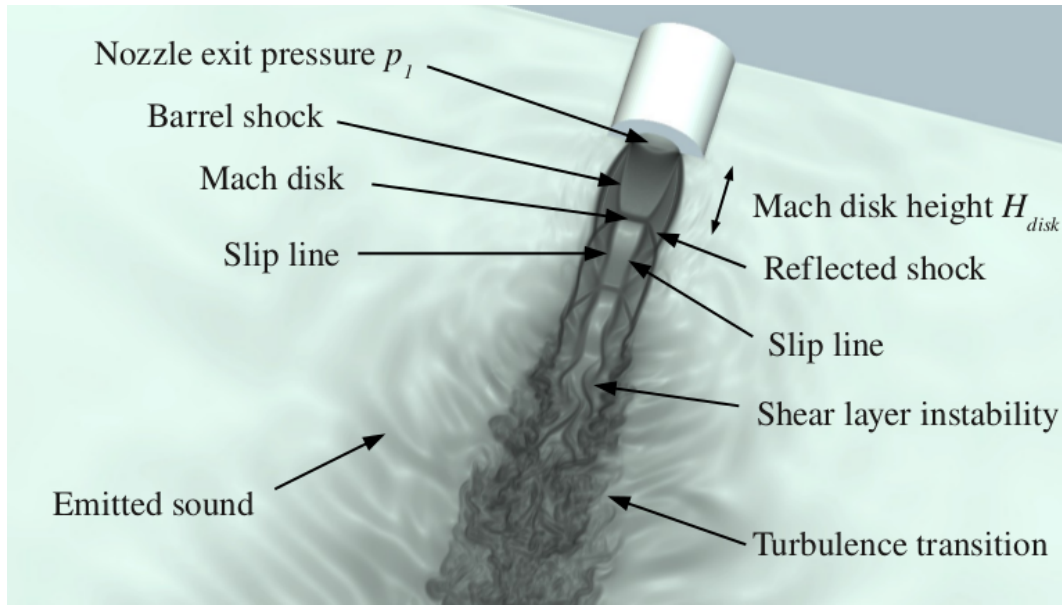


Figure 4. The classical picture on shock wave structures in underexpanded jets is reproduced by the present LES [12]. The visualization shows a close-up to the nozzle pipe exit.

Supersonic Jet

As a challenging fluid dynamical example a supersonic jet is considered. Such a jet may form e.g. when pressurized gas is released from a bottle through a nozzle hole i.e. the situation is similar to the injection of e.g. natural gas fuel into the cylinder of a gas engine. The challenge in this type of simulations is to simultaneously capture shocks and still maintain the turbulence. As seen in Figure 4 the newly developed density based RK4 solver is able to capture a complicated shock pattern involving the Mach disk, the barrel shock and a sequence of reflected shocks [12]. Furthermore we have found an excellent agreement between the shock dimensions with experimental data [10]. Simultaneously with the shocks, turbulence develops in the shear layers of the jet implying that the numerical method is not overly dissipative. The periodic motions of the transition process produce sound at distinguished frequencies as visually noted in Figure 4.

Outlook

Here a brief overview of the recent attempts to bridge the gap between academic CFD and industrial CFD was given. OpenFOAM provides a powerful syntax for solving very complicated flow problems on parallel computers with some tens of top-level code lines. The newly developed RK based solvers are able to simulate a vast number of CFD applications with increased level of flow physics and accuracy. The scale selective discretization (SSD) approach, as applied in the study, is able to non-dissipatively capture the turbulence while maintaining the numerical diffusion in the simulations in a delicate manner.

Some important challenges remain to bring the novel methods of ACFD into the ICFD codes. Perhaps the most important computational challenge for ICFD is to increase the order of spatial accuracy of the present day ICFD codes. In principle, the task sounds simple as it is more or less a question of interpolation. However, to date this has not been done in most of the existing ICFD codes due to the unstructured nature of the computational grids which complicate the task significantly. We continue our efforts and aim ultimately at Large-Eddy Simulation of combustion engines at our research group of combustion engines at the Aalto University School of Engineering. The objective involves LES in moving geometries (piston and valves), complex chemistry modeling using flamelet generated manifolds (FGM) and multiphase flow modeling

including sprays. These topics are all under current investigations.

References

- [1] Canuto C., Hussaini M.Y., Quarteroni A. and Zang T., *Spectral Methods*, ISBN 978-3-540-30727-3, Springer, (2007).
- [2] Greenshields C., Weller H., Gasparini L., and Reese J., *Implementation of Semi-Discrete, Non-Staggered Central Schemes in a Colocated, Polyhedral, Finite Volume Framework for High-Speed Viscous Flows*, Int.J.Numer.Meth.Fluids, (2009).
- [3] Vuorinen V., Hillamo H., Kaario O., Larmi M., Fuchs L., *Large Eddy Simulation of Droplet Stokes Number Effects on Turbulent Spray Shape*, Atomization and Sprays, **20**, 2, 93-114, 2010.
- [4] Hirsch C. *Numerical Computation of Internal and External Flows*, (2nd edn), Elsevier, (2007).
- [5] Ni M. and Abdou M., *A Bridge Between Projection Methods and SIMPLE Type Methods for Incompressible Navier-Stokes Equations*, Int.J.Numer.Meth.Eng., **72**, 1490-1512, (2007).
- [6] Erturk E., Corke T. and Gökçöl, *Numerical Solutions of 2-D Steady Incompressible Driven Cavity Flow at High Reynolds Numbers*, Int.J.Numer.Meth.Fluids., **72**, 1490-1512, (2007).
- [7] Moser, Kim and Mansour, *DNS of Turbulent Channel Flow up to $Re_\tau = 590$* , Physics of Fluids, **11**, 943-945, (1999).
- [8] Vuorinen V., Duwig C., Boersma B., Kaario O., and Larmi M., *Large Eddy Simulation of Highly Underexpanded Jets*, submitted to Phys.Fluids (6/2012).
- [9] Vuorinen V., Boersma B., Schlatter P., Fuchs L., and Larmi M., *A Low-Dissipative, Scale-Selective Discretization Scheme for the Navier-Stokes Equations*, submitted to Comp.&Fluids (6/2012).
- [10] Vuorinen V., Duwig C., Boersma B., Kaario O., and Larmi M., *Finite Volume Implementation of Navier-Stokes Solvers for a Variety of Flow Conditions in Open Source Environment*, submitted to Comp.&Fluids (3/2012).
- [11] Cook A. and Cabot W., *Hyperviscosity for Shock-Turbulence Interactions*, Journal of Computational Physics, **2**, 379-385, (2004).
- [12] Donaldson C.D. and Snedeker R.S., *A Study of Free Jet Impingment*. Part 1. Mean Properties of Free and Impinging Jets”, J.Fluid Mech.,**45**, 281-319, (1971).

Tangential differential operators and finite elements for elasticity on thin curved domains

Peter Hansbo¹ and Mats G. Larson²,

⁽¹⁾ Department of Mechanical Engineering Jönköping University, SE-551 11 Jönköping, Sweden
peter.hansbo@jth.hj.se ⁽²⁾ Department of Mathematics and Mathematical Statistics Umeå University, SE-90187 Umeå, Sweden

Summary. A Galerkin finite element method for the membrane elasticity problem on a meshed surface is constructed by using two-dimensional elements extended into three dimensions.

Key words: surface gradient, elasticity, membrane, finite element methods

Models of thin-shell structures are often established using differential geometry to define the ruling differential equations in two dimensions, cf., e.g., Ciarlet and Lods [1]. In the mid '90s, Delfour and Zolesio [2] instead established elasticity models on surfaces using the signed distance function, which can be used to describe the geometric properties of a surface. In particular, the intrinsic tangential derivatives were used for modeling purposes as the main differential geometric tool and the partial differential equations were established in three dimensions. A similar approach had been used earlier in a finite element setting for the numerical discretization of the Laplace-Beltrami operator on surfaces by Dziuk [4], resulting in a remarkably clean and simple implementation. For diffusion-like problems, the intrinsic approach has become the focal point of recent research on numerical solutions of problems posed on surfaces, cf., e.g., [3, 5, 7].

The purpose of this presentation is to indicate the possibilities of the intrinsic approach in finite element modeling of thin-shell structures, focusing on the simplest model, that of the membrane shell without bending stiffness, as presented in [6]. We discuss mechanical as well as numerical modeling issues and give some numerical examples.

The intrinsic approach makes use of the tangential derivative on a surface using the projector

$$\mathbf{P} = \mathbf{I} - \mathbf{n} \otimes \mathbf{n}$$

where \mathbf{n} is the normal to the surface, \mathbf{I} the identity tensor, and \otimes denotes the exterior product. The surface gradient is then written $\nabla_{\Sigma} = \mathbf{P}\nabla$ and the Laplace-Beltrami problem on a (closed) surface Σ can be formulated as seeking u such that

$$-\nabla_{\Sigma} \cdot \nabla_{\Sigma} u = f \quad \text{on } \Sigma$$

where f is a known source term. We will similarly derive the equilibrium equations on a surface as

$$-\nabla_{\Sigma} \cdot \boldsymbol{\sigma}_{\Sigma} = \mathbf{f} \quad \text{on } \Sigma$$

where $\boldsymbol{\sigma}_{\Sigma}$ is an in-plane stress tensor and \mathbf{f} is a force term. Thus the framework of [4] is immediately applicable also to elasticity, but we will also discuss more elaborate finite element models using variable normals and parametrizations.

References

- [1] P. G. Ciarlet and V. Lods: Asymptotic analysis of linearly elastic shells. I. Justification of membrane shell equations. *Archives for Rational Mechanics and Analysis*, 136 (1996), 119–161.
- [2] M. C. Delfour and J.-P. Zolésio: Tangential differential equations for dynamical thin/shallow shells. *Journal of Differential Equations*, 128 (1995), 125–167.
- [3] A. Demlow, G. Dziuk: An adaptive finite element method for the Laplace-Beltrami operator on implicitly defined surfaces. *SIAM Journal of Numerical Analysis*, 45 (2007), 421–442.
- [4] G. Dziuk: Finite elements for the Beltrami operator on arbitrary surfaces. In *Partial differential equations and calculus of variations*, volume 1357 of *Lecture Notes in Mathematics*, pages 142–155. Springer, Berlin, 1988.
- [5] C. M. Elliott, B. Stinner: Modeling and computation of two phase geometric biomembranes using surface finite elements. *Journal of Computational Physics*, 229 (2010), 6585 – 6612.
- [6] P. Hansbo, M.G. Larson: Intrinsic finite element modeling of a linear membrane shell problem, Preprint (2012).
- [7] M. A. Olshanskii, A. Reusken, J. Grande: A finite element method for elliptic equations on surfaces. *SIAM Journal of Numerical Analysis*, 47 (2009), 3339–3358.

Proceedings of the 25th Nordic Seminar on Computational Mechanics
K. Persson, J.Revstedt, G. Sandberg, M. Wallin (Eds.)
© Lund University, 2012

Multiphysics Modelling of Manufacturing Processes

J. H. Hattel¹

⁽¹⁾Department of Mechanical Engineering, Technical University of Denmark (DTU),
Kgs. Lynby, Denmark, jhat@mek.dtu.dk

During the last couple of decades the possibility of modeling multiphysics phenomena has increased dramatically, thus making numerical simulation of very complex manufacturing processes possible. These types of simulations often involve computational fluid dynamics, numerical heat transfer, computational solid mechanics and computational material science and they frequently require high computational power with calculation times varying from hours to days or even weeks. The lecture will present various examples covering different processes and application areas. Moreover, the possibility of combining process simulation with optimization will be addressed.

Flexible software tools for computational turbulence

Mikael Mortensen^{1,2}, Hans Petter Langtangen^{2,3}

⁽¹⁾Department of Mathematics, University of Oslo, mikael.mortensen@gmail.com

⁽²⁾Center for Biomedical Computing, Simula Research Laboratory

⁽³⁾Department of Informatics, University of Oslo

Summary. This article briefly describes new, flexible software tools for computing the solutions of systems of nonlinear partial differential equations in general, and various systems describing turbulent fluid flow in particular. Computational turbulence investigations need extensive software flexibility for composing models and adjusting the elements in the numerical methods. We describe how this flexibility can be met by building on the FEniCS project and utilizing the Python programming language. We also favorably assess the computational efficiency gained by this approach by comparing our codes with leading competing codes for turbulent flow.

Key words: turbulent flow, RANS models, systems of nonlinear partial differential equations, finite element methods, linearization techniques, Python, C++, FEniCS

Motivation

Most fluid flows in nature and technological devices are turbulent. With recent advances in hardware, numerical methods, and software, simulation of widely different turbulent flow phenomena has become feasible. However, choosing the right mathematical model for a given turbulent flow case is demanding. First one has to decide on the basic class of turbulent flow models: Direct Numerical Simulation (DNS), Large Eddy Simulation (LES), or Reynolds-averaged models (RANS/URANS). The RANS models come in numerous flavors of various complexity. Except for the simplest shear flow cases, it is difficult to know beforehand which type of RANS model to use, and extensive experimentation with different models is desirable.

A fundamental problem with the highly nonlinear partial differential equations that enter RANS models, is to obtain convergent and fast solution of the system of nonlinear algebraic equations to be solved at each time level. Straightforward Newton methods may easily diverge, while simple Picard schemes may lead to slow convergence. Often, a combination of Newton and Picard methods, tailored to the particular differential equations at hand, is the best way to go. Besides the chosen linearization technique of the particular differential equations, there are numerous other choices of numerical ingredients, like higher or lower order discretizations, iterative linear solvers and preconditioners, and strategies for parallelization.

The computational turbulence investigator needs, ideally, a very flexible software tool for composing the various differential equation models, linearization methods, discretizations, solvers, etc., and experimenting with various choices. Commercial CFD software, like FLUENT, offer a selection of RANS models, but is quite limited in its numerical flexibility and does not offer sophisticated RANS models such as elliptic relaxation. To meet the requirements in modern computational turbulence, we present two new software tools, `cbc.pdesys` and `cbc.cfd`, built on top of the FEniCS software. These tools provide access to a new programming technology for solving partial differential equation. Since RANS models are basically different types of highly nonlinear systems of partial differential equations, a flexible software tool for RANS modeling

will contain components that are useful far beyond computational turbulence. Essentially, we first create a sufficiently flexible tool (`cbc.pdesys`) for handling systems of partial differential equations and then we tailor this tool to the particular needs of turbulence modeling (`cbc.cfd`).

The FEniCS project

FEniCS (fenicsproject.org) can be viewed as the next generation software for programming with finite element methods. The user can write down almost any variational form in Python, using a syntax that is very close to the mathematical formulation of the problem, and flexibly choose function spaces. In particular, function spaces can easily be combined to form mixed finite elements. When executing the Python code, it will generate efficient C++ code adapted to and optimized for the finite element problem at hand and link it with finite element libraries and third-party linear algebra software, such as PETSc, Trilinos, or uBLAS. FEniCS has been tested on a wide range of different problems in computational solid and fluid mechanics as well as electromagnetics.

Our new tools

While FEniCS provides an ideal language for solving a scalar or vector partial differential equation, the Python code grows in size when the mathematical model contains a large system of equations. Much of this code is repetitive and can be made once and for all by introducing the right abstractions and data structures. We view the system of partial differential equations as a composition of subsystems. Each individual equation is identified by a name or symbol and a corresponding variational form. By combining names in a list, we can in Python easily define a subsystem of equations. A combination of such lists defines the overall system to be solved. Each subsystem is solved in a fully implicit manner, and then all the subsystems are solved by an outer iteration. The degree of implicitness is hence dictated by defining subsystems. For example, a segregated solution method views each individual partial differential equation as a subsystem.

In a simple k - ϵ model, one may split the Navier-Stokes part into a fractional step method, with one pass through the forward step, the Poisson equation, and the correction, while the k and ϵ equations may then be solved by a fully implicit formulation. The way we linearize the nonlinear k and ϵ equations also dictates the degree of implicitness. Here we have introduced a notational convenience: by adding an underscore to an unknown function we linearize that term in the sense of using the most recently computed values of the function rather than leaving it as unknown in the algebraic system. This means that through grouping names of the unknowns in lists and by adding or removing underscores, we can very flexibly control the degree of implicitness when solving large systems of partial differential equations.

Based on the subsystem composition and the associated variational forms, we can automatically generate dictionaries of various objects needed in FEniCS simulators, including function spaces and finite element functions. The Python code doing this makes heavy use of textual constructions at run-time that are turned into live code with the aid of the `eval` function.

In the presentation we will first describe the complexity of turbulence modeling for the computational investigator. Then we give a brief introduction to the FEniCS programming environment, before we present the general components of `cbc.pdesys` and the specialization `cbc.cfd` for computational turbulence. The work with these codes has also provided insight into how the finite element method works for fluid flow problems. Finally, we present an investigation of the cost of the obtained flexibility by comparing our general finite element solvers with OpenFOAM and the Stanford code CDP in large-scale, parallel simulations. The cost of the flexibility is quite low, owing to the fact that most of the CPU time is spent in linear solvers and preconditioners, and for these computations we use efficient third-party software (PETSc).

Proceedings of the 25TH NORDIC SEMINAR
COMPUTATIONAL MECHANICS, 2012

Computational Fluid Mechanics

Room: 304, Thursday 25 October, 09:30 - 11:30



Computational respiratory flow dynamics for distinguishing between healthy and disease

Mihai Mihăescu¹, Nelson Powell², Ephraim Gutmark³, and Laszlo Fuchs¹

⁽¹⁾ Royal Institute of Technology (KTH), Linné FLOW Centre, mihai@mech.kth.se

⁽²⁾ Stanford University School of Medicine, Sleep and Research Center, California, USA

⁽³⁾ University of Cincinnati, School of Aerospace Systems, Cincinnati, Ohio, USA

Summary. An upper respiratory tract simulator is proposed as a tool for quantifying the respiratory flow at the pre-treatment condition and for assessing the effect of treatment. The approach utilizes medical imaging data for extracting patient specific upper respiratory tract anatomy and Computational Fluid Dynamics (CFD) for predicting the respiratory flow. The technique is applied to a number of four patients at pre and post-treatment conditions and four healthy subjects. The analysed CFD data allow differentiating between healthy subjects and individuals with an obstructive disorder and can be useful data within the diagnosis process.

Key words: unsteady computational fluid dynamics, airway disorders, diagnosis

Introduction

Intermittent, unsteady flows through curved conduits are encountered in many human body systems including the respiratory system. The flow complexity is increased even more when constrictions are obstructing the airway. Abnormal obstructions connected to various airway disorders are found in a large number of individuals [1]. It is believed that the changes in the flow patterns associated with the obstruction are playing a role in the progress of the disorder over the time. Often, the interaction between the flow and the obstruction involves dynamic changes in the flow regime, flow separation and recirculation regions, nonlinear pressure-drop/flow rate relations, self-excited oscillations of the soft tissue, and generated noise.

Occurring at the level of the pharyngeal airway, Obstructive Sleep Apnea (OSA) is the most common obstructive airway disorder [2]. It is characterized by partial or complete narrowing of the pharyngeal airway during sleep (hypopneas and apneas), resulting in airflow cessation and oxygen de-saturation. It affects more than 12 million people in US alone. Overnight Polysomnography (PSG) is considered the gold-standard for the diagnosis of OSA. It is an expensive and time consuming process for both patient and evaluator. The OSA severity is expressed using Apnea-Hypopnea Index (AHI), which represents the total number of hypopneas and apneas occurring in one hour of sleep. A mild OSA is indicated by an AHI between 5 to 15/hour, while severe conditions are those for which AHI is greater than 30/hour. Computed Tomography (CT) or Magnetic Resonance (MR) imaging facilitated anatomical measurement of the airway, but they have little clinical utility for quantifying the functional impact of an

obstruction. These techniques cannot offer details about the effect of the airway's anatomical features on the airflow or on airway resistance.

A numerical approach based on medical imaging data and CFD is proposed to expand basic understanding of flow dynamics in 3D realistic pharyngeal airway models. It is used to characterize the flow in healthy subjects and patients with OSA before and after treatment.

Approach

The pharyngeal airway models are reconstructed from CT imaging data acquired at Stanford University Sleep and Research Center. The medical imaging software MIMICS® (Materialise, Belgium) is used with this purpose. The procedure implies grouping voxels in the Hounsfield Units ranges of interest ($\approx -1000\text{HU}$ for air) into separate masks from which, by surface triangulation, the raw 3D airway model is generated. Then, the model is exported into a remeshing software where the individual faces of the airway are demarcated and the mesh quality at the surfaces is improved. From the surface mesh one may construct an unstructured tri/tetrahedral hybrid mesh within the airway volume using an appropriate mesh generator. A finer grid density is achieved with the tetrahedral layers close to the wall surface with the aim of enhancing resolution on the complex geometrical boundary.

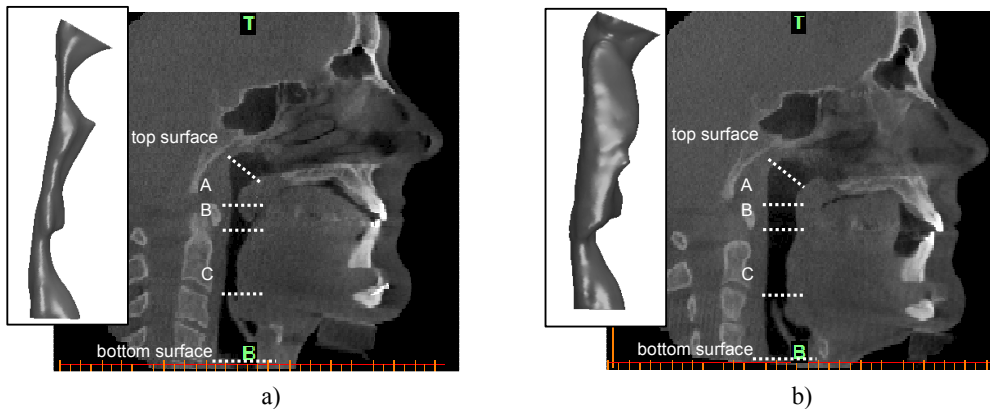


Figure 1. Pharyngeal airway before (a) and after (b) treatment (surgery). Top and bottom (base of epiglottis) surfaces of the models are marked; A - minimum cross-sectional area in the retro-palatal region at pre-treatment; B - oral-pharyngeal junction; C - epiglottis tip.

In order to solve the relatively low Reynolds number flow fields ($1800 < Re < 7000$), a more suitable formulation than the steady-state Reynolds Averaged Navier-Stokes is provided by an approach that resolves the dynamics of the flow. The approach used can be said to be locally as Large Eddy Simulation in character, capturing the airflow unsteadiness. It gives a well resolved numerical solution of the Navier-Stokes equations, since it behaves as Direct Numerical Simulation in most of the airway. Only when unresolved small scale motion develops, one has to employ a model for the effects of these un-resolved small scales. Still, it must be stressed out that the turbulence in the airway is hardly developed enough to be handled by “universal” Sub-Grid-Scale models. Such an unsteady flow simulation can predict localized rotational flow structures that may have an impact on tissue irritation as well as on the wall tissue excitation and airway wall dynamics. The validated computational approach [3] is applied for characterising the unsteady flow at pre and post-treatment conditions in four patients with OSA. Figure 1 depicts sagittal CT imaging data and the generated pharyngeal airway models before and after surgery for one of the patients. In addition, four healthy subjects are considered

as part of the study as a reference group (Controls). The unsteady flow simulations were performed under peak inspiratory and expiratory flow conditions, using a flow rate of 30 L/min. Axial velocity at the inlet plane, no-slip velocities at the wall, and flux-conserving zero-gradient condition at the outlet are imposed as boundary conditions.

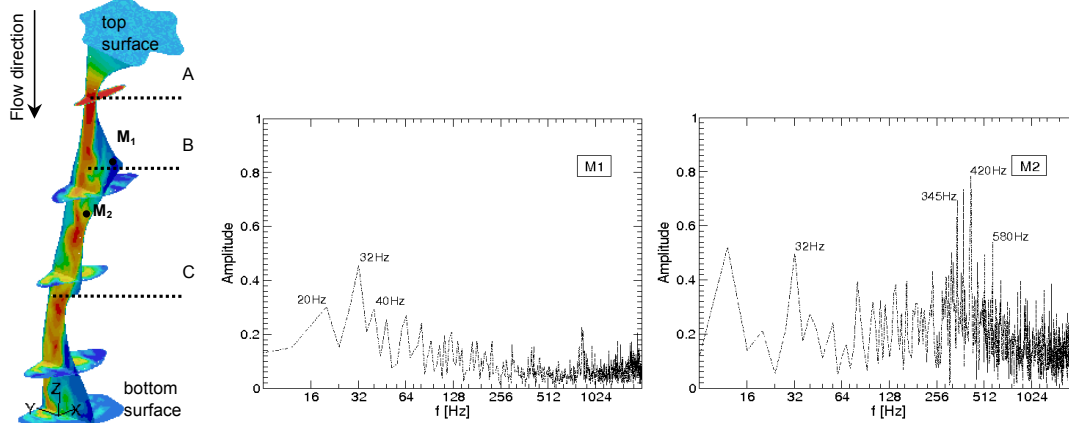


Figure 2. Pre-treatment (peak inspiratory flow condition): characteristic frequencies in the flow recirculation region (M_1) and in the jet reattachment region (M_2).

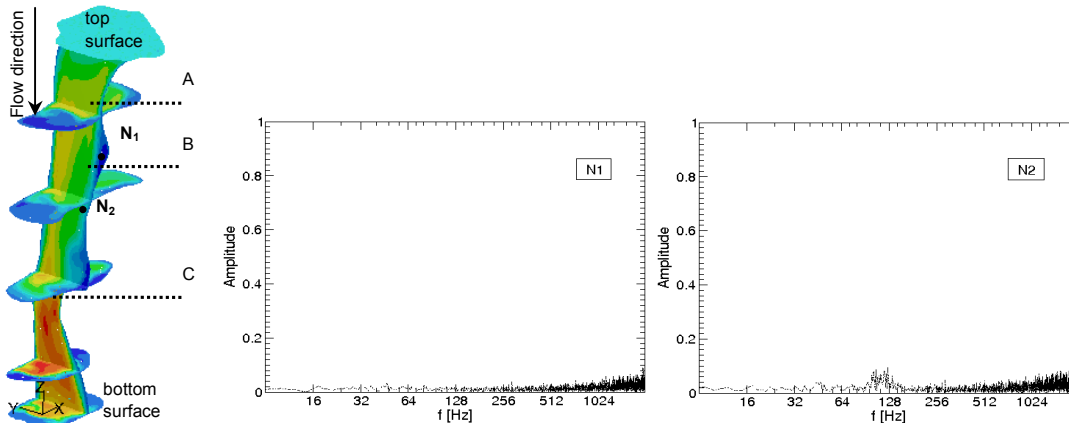


Figure 3. Post-treatment (peak inspiratory flow condition): frequencies obtained at the monitoring point locations N_1 and N_2 as shown in the far left figure.

Results and Conclusions

Axial velocity distributions along different cross-sectional planes and a longitudinal mid-plane are shown together with power spectral density plots in Figures 2 and 3 for pre and post-treatment conditions, respectively. The data obtained at the peak inspiratory flow are for the OSA patient presented in Fig. 1. At pre-treatment, flow separation occurs just downstream of the minimum cross-sectional area (Fig. 2). A recirculation flow region is observed on the airway's anterior side in the oral-pharyngeal junction (line B in Figs. 1 and 2). The initiated vortices in the jet-like shear-layers, convected by the flow are impinging on the anterior airway wall between B-C marks. Naturally, larger shear results on the airway wall in the reattachment region. In time, cumulative effect of such flow-airway wall interactions could cause tissue irritation and potential injury. Frequencies in the neighborhood of 32Hz are attributed to the

large and slow rotating recirculation bubble (monitoring point M_1), while the frequencies in the neighborhood of 400Hz (M_2) are attributed to the vortical structures impinging on the airway wall. Such flow instabilities developed during inspiration just downstream of uvula may induce soft tissue vibration and snoring. Post-surgery, the flow is streamlined with minimal separation as shown in Fig. 3. Negligible instabilities are developed in the flow field as shown in the power spectral density plots obtained at N_1 and N_2 locations. The amplitudes of the characteristic frequencies are one or two orders of magnitude lower as compared with those from the pre-treatment condition.

Clinical and CFD based data concerning four healthy adult subjects and four OSA patients at pre and post-treatment conditions are presented in Fig. 4. Despite of the low number of subjects considered, a strong correlation is observed between the CFD data (mean pharyngeal airway resistance) and the clinically obtained AHI values. A correlation coefficient (r) of 0.764 was calculated. About an order of magnitude difference between the pre (red) and the post - treatment resistances (green) is found. The post-treatment airway resistances are below or in the range of the averaged airway resistance estimated for the healthy subjects.

In conclusion, pharyngeal airflow was quantified in a number of subjects, both OSA patients and healthy individuals. The analysed data allowed differentiating between healthy and disease. Such quantitative assessment of pharyngeal airflow can contribute to a non-intrusive and inexpensive diagnosis of sleep-disordered breathing condition.

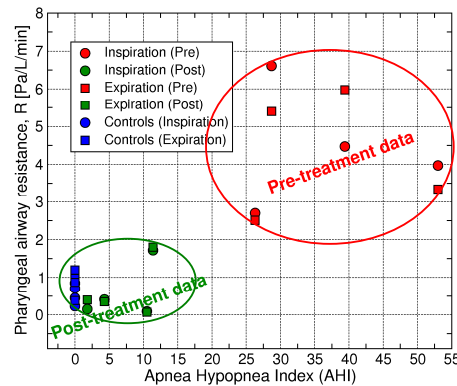


Figure 4. Predicted airway resistance and clinically measured AHI plotted for four Controls and four OSA patients at pre- and post-treatment conditions. Correlation coefficient: $r = 0.764$

Acknowledgement

The financial support from the Göran Gustafsson Stiftelse by means of “The Göran Gustafsson Young Scientist Award (UU/KTH)” conferred to Dr. Mihaescu is greatly acknowledged.

References

- [1] W.T. McNicholas, et al., Obstructive apneas during sleep in patients with seasonal allergic rhinitis. *Am. Rev. Respir. Dis.* 126: 625-628, 1982.
- [2] T. Young, et al., The occurrence of sleep-disordered breathing among middle-aged adults. *The New England J. of Med.*, 328 (17): 1230-1235, 1993.
- [3] M. Mihaescu, et al., LES of the pharyngeal airflow associated with OSA syndrome at pre and post-surgical treatment, *J. of Biomechanics*, 44(12): 2221-2228, 2011.

One dimensional network models for cardiovascular applications

Vinzenz Eck¹, Paul Roger Leinan, and Leif Rune Hellevik²

⁽¹⁾Division of Biomechanics, NTNU, Trondheim, vinzenz@eck-mail.eu

⁽²⁾Division of Biomechanics, NTNU, Trondheim, leif.r.hellevik@ntnu.no

Summary. This work presents a flexible and fast method for one dimensional flow and pressure wave simulations in arterial networks. The pressure and flow waves in the arterial system are characterized by means of cross-sectionally averaged 1D governing equations for mass and momentum, discretized with a MacCormack scheme (explicit and second order in time and space). The method was successfully validated with the simulation of the systemic arterial tree of an individual in two different life stages.

Key words: 1D simulation, computational haemodynamics, blood flow simulation, vascular network, cardiovascular systems, arterial tree, NSCM-25

Introduction

Simulation of pressure and flow waves in the arterial system by means of cross-sectionally averaged 1D governing equations for mass and momentum has been subject of many studies. In particular the influence of stenoses, aneurysms, and other vascular diseases has been investigated. Such a distributed modelling approach offers more detailed physics (pressure, flow and wall shear stress in axial direction and time) than lumped models that have no spatial dependence and thus cannot describe wave phenomena [2]. Further, a distributed approach is much less computational demanding than e.g. a 3D fluid-structure interaction approach (FSI), which is yet not feasible for larger vascular networks [1].

In this paper we present a very flexible and fast simulation model for blood flow simulations of the human systemic circulation.

Mathematics

An unclosed non-linear system for pressure (P), volume flow (Q) and cross-sectional area (A), in a compliant vessel is given by the conservation of mass and momentum (eq. 1a and 1b) [6].

$$\frac{\partial A}{\partial t} + \frac{\partial Q}{\partial z} = 0 \quad (1a)$$

$$\frac{\partial Q}{\partial t} + \frac{\partial}{\partial z} \left(2\pi \int_0^R r v^2 dr \right) + \frac{A}{\rho} \frac{\partial P}{\partial z} = -2\pi \frac{\mu}{\rho} \left[\frac{\partial v}{\partial r} \right]_{r=R} \quad (1b)$$

The walls of blood vessels have elastic properties, i.e. the cross-sectional area (A) changes due to the pressure and flow waves propagating through the vessel, which is described with the vessel compliance (C) (eq. 2). The vessel compliance is in general non-linearly dependent on the pressure and the location in the vascular tree.

$$C(z, t, P, \beta) = \frac{\partial A(P)}{\partial P} \quad (2)$$

To take the elastic properties of the vessel walls into account, i.e determine the compliance, a relation between the cross-sectional area and pressure is stated with a linear or non-linear constitutive model. A simplified constitutive model based on the Laplace-Law [3] and its compliance may be given by:

$$P = P_s + \beta(\sqrt{A} - \sqrt{A_s}), \quad (3)$$

$$C = \frac{2}{\beta} \sqrt{A_s} + \frac{2}{\beta^2} (P - P_s) \quad (4)$$

where β is a stiffness parameter, P_s is a reference pressure at the reference area A_s . Our code offers the possibility to choose between different linear and non-linear constitutive models for each vessel in the network.

Inserting the compliance (eq. 2) into the system equations (eq.1a and 1b) reduces and closes the system given by the primary variables P and Q . With introduction of a velocity profile model, the convective acceleration (second term) and viscous forces (fourth term) in the 1D momentum balance (1b), can be approximated. Here assumed shape profiles are applied, where in general, a function $\phi(r)$ is defined such that:

$$v(z, r, t) = \phi(r)v_z(z, t), \quad (5)$$

where $v_x(x, t)$ is the mean (cross sectional) axial velocity and $\phi(r)$ is a shape function. For e.g. a power law profile, $\phi(r)$ is assumed to be [5]:

$$\phi(r) = \frac{\gamma + 2}{\gamma} \left(1 - \left(\frac{r}{R}\right)^\gamma\right), \quad (6)$$

where R is the radius of the vessel, and γ determines the bluntness of the velocity profile. The closed system of governing equation can be written as followed:

$$\frac{\partial P}{\partial t} + \frac{1}{C} \frac{\partial Q}{\partial z} = 0, \quad (7a)$$

$$\frac{\partial Q}{\partial t} + \delta \frac{\partial}{\partial z} \left(\frac{Q^2}{A}\right) + \frac{A}{\rho} \frac{\partial P}{\partial z} = -2\pi(\gamma + 2) \frac{\mu}{\rho} \frac{Q}{A} \quad (7b)$$

where $\delta = \frac{(\gamma+2)}{(\gamma+1)}$.

Rearranged in matrix form, the system of governing equations becomes:

$$\frac{\partial \mathbf{u}}{\partial t} + \mathbf{M}(\mathbf{u}) \frac{\partial \mathbf{u}}{\partial z} = \mathbf{b}(\mathbf{u}) \quad \text{with} \quad \mathbf{u} = \begin{bmatrix} P \\ Q \end{bmatrix}, \quad (8)$$

where

$$\mathbf{M} = \begin{bmatrix} 0 & \frac{1}{C} \\ C(c^2 - \delta v_z^2) & 2\delta v_z \end{bmatrix}, \quad \mathbf{b} = \begin{bmatrix} 0 \\ -2\pi(\gamma + 2) \frac{\mu}{\rho} v_z \end{bmatrix}, \quad c^2 = \frac{A}{\rho C}. \quad (9)$$

The equation system (eq. 8) can be transformed into a system of decoupled characteristic variables $\mathbf{w} = [w_1, w_2]$ (eq. 10) using the eigenvalue matrix $\mathbf{\Lambda}$ and the left \mathbf{L} and right \mathbf{R} eigenvector matrices of the system matrix \mathbf{M} [3]. The characteristic variables w_1 and w_2 represent the forward and backward propagating information respectively.

$$\frac{\partial \mathbf{w}}{\partial t} + \mathbf{\Lambda} \frac{\partial \mathbf{w}}{\partial z} = \mathbf{Lb} \quad (10)$$

The characteristic variables are used to impose boundary conditions and for solving network bifurcations. Applying the boundary values with Riemann variables yields in prescribing either forward or backward directed pressure or flow waves. In contrast, setting the flow or pressure at the boundary directly, prescribes the total waves (forward and backward), i.e. a part of the solution, the backward contribution would be prescribed, as well. In addition, it is possible to apply different in-ward and out-ward directed conditions at a boundary without interference. E.g. prescribed inflow combined with a reflection coefficient for the backwards Riemann variables.

Numerical methodology

The implementation of our code is based on Python for the framework and overall structure. Further are C and Fortran used for all algorithms which require fast numerical calculations. The code is strictly kept object-oriented, to achieve more transparency and flexibility.

A vascular network consist of a ramified network of blood vessels. Each vessel is defined as individual object. The connection between vessels is described with the mother-daughter relation, i.e. each vessel can be a 'mother'-vessel of maximum two 'daughter'-vessels. Blood vessels branch only into two smaller daughter vessels, which is emulated with the mother-daughter relation as the maximum amount of daughters is fixed to two; a left and right daughter. With this topology, less information is required to describe the network connections compared to e.g. a node-description where each vessel has a start and end node. In addition, the network can be seen and handled as binary tree. During the solver procedure and other calculations, the network is traversed by means of a binary tree.

The numerical speed $c_{num} = \Delta x / \Delta t$ is bounded through the CFL-condition (resulting in a small time-step), to capture the physics of wave phenomena, nevertheless regarding the type of numerical scheme; explicit or implicit [4]. As the system matrices change each time step due to the non-linearity and the elastic wall properties, the explicit scheme is the more convenient choice, regarding computational speed and implementation of the system matrices. Therefore an explicit time-stepping scheme is applied, which allows also the modularisation of the solver procedure. In addition, are calculations efficient to parallelise, as the solution of each time-step depends only on the solution of the previous one.

The network shows three different type of numerical problems which need to be solved; 1D discretized vessels, boundary conditions and bifurcations. To solve the non-linear system of governing equations of a vessel segment the explicit McKormack scheme is applied. The two step method (predictor and corrector step) is second order in space and time. Each predictor and corrector step, boundary grid points of each vessel are determined either by boundary conditions or connections. The boundary conditions are imposed by Riemann variables from which the correct pressure and flow values are determined. At network bifurcations six equations are solved with a Newton iteration scheme; the conservation of mass and conservation of total pressure, for the boundary nodes and three equations to ensure, new values do not change the Riemann variables leaving the vessels.

As the time iteration scheme is explicit, all three numerical problems can be solved at each step independently. Thus a vascular network can be defined as accumulation of numerical objects with individual solver methods of three different types; vessels, boundary conditions and connections. Each numerical object of a vascular network is initialized as specialized class instance of a superior vessel-, boundary- and connection-class respectively. During the solver procedure, the defined numerical objects are solved by traversing the binary tree of the network, from the root node to the ends, twice per time step (once for the predictor and once for the corrector step). As the numerical objects can be solved independently, the process is very suitable for parallel computing. By traversing the tree from inside to the outside it is possible to start solving e.g the next predictor step of the root vessel, while the last numerical objects of the previous corrector step are still calculated.

Results

For validation of our model the systemic arterial tree of a human in two life stages, corresponding to a young and old individual, is simulated. The results (fig. 1) illustrate the change of pressure waves in the ascending aorta by variations of the compliance. Especially the pathology of systolic hypertension of the old individual, i.e. drastic increase of the systolic pressure (maximum) due to stiffer arteries, is represented by our model outstanding. In addition, show the pressure waves characteristic patterns, similar to those found comparative clinical studies.

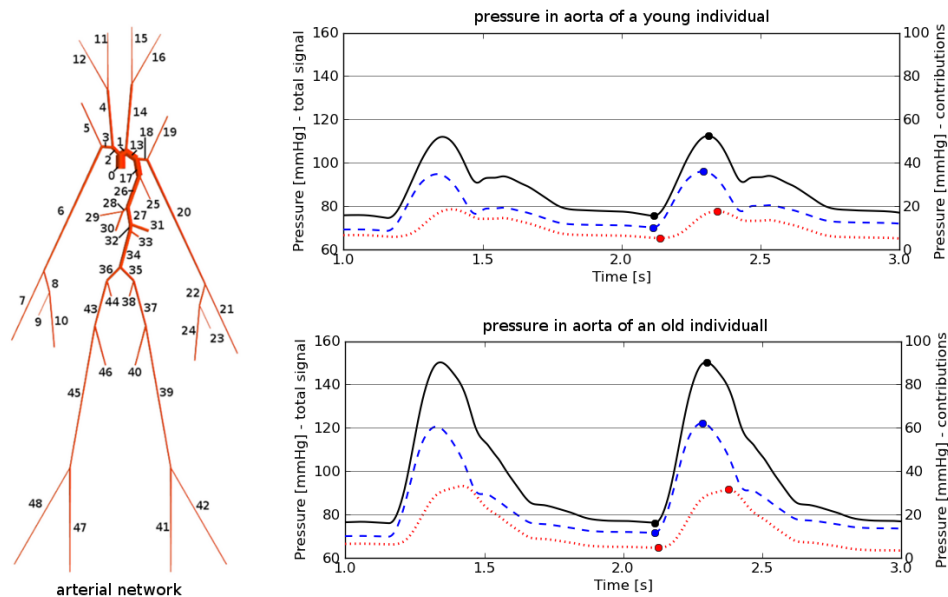


Figure 1. Left: vascular network of the arterial tree consisting of 49 vessels. Right: pressure waves in the ascending aorta (vessel number 0) of a young individual (top) and old individual (bottom); straight line: total pressure, dashed line: forward contribution, dotted line: backward contribution

Conclusion

The results obtained let us conclude that our distributed 1D model, which creates an individual solver procedure with specific numerical objects for a given vascular network, is able to predict qualitative physiologic pressure and flow patterns of the systemic circulation.

List of References

References

- [1] L. Formaggia and A. Quarteroni and A. Veneziani (Eds.). *Cardiovascular Mathematics - Modelling and simulation of the circulatory system*, Springer Berlin, Heidelberg, 2009
- [2] Y. Shi, P. Lawford and R. Hose. Review of Zero-D and 1-D Models of Blood Flow in the Cardiovascular System *BioMedical Engineering OnLine*, 2011
- [3] S.J. Sherwin and V. Franke and J. Peiro and K. Parker. One-dimensional modelling of a vascular network in space-time variables *Journal of Engineering Mathematics*, Springer, 2003
- [4] C. Hirsch. Numerical Computation of Internal and External Flows *Butterworth-Heinemann*, 2007
- [5] T.J.R. Hughes and J. Lubliner. On the one-dimensional theory of blood flow in the larger vessels *Mathematical Biosciences*, 1973
- [6] A.C. L. Barnard and W.A. Hunt and W.P. Timlake and E. Varley. A Theory of Fluid Flow in Compliant Tubes *Biophysical Journal*, 1966

Effect of dilatation on the turbulence level in compressible quasi one-dimensional steady nozzle flow .

I. Grigoriev¹, G. Brethouwer¹, A. V. Johansson¹, S. Wallin^{1,2}

⁽¹⁾KTH Mechanics, Osquars backe 18, SE-10044 Stockholm, igor@mech.kth.se

⁽²⁾FOI Swedish Defence Research Agency, SE-17290 Stockholm, stefan.wallin@foi.se

Summary. An explicit algebraic Reynolds-stress model (EARSM) was developed for compressible turbulent flow. In this work it is applied to the modelling of steady quasi one-dimensional nozzle flow. The results obtained indicate that dilatation works analogously to the streamwise shear-strain leading to the amplification of turbulent kinetic energy level, the dilatation being prevailing in supersonic regime. Due to turbulent kinetic energy the transition from subsonic to supersonic regime and vice versa takes place at smaller A_{inlet}/A_{throat} .

Key words: EARSM, $k - \omega$ model, compressible turbulence, nozzle flow

Outline

One of the primary issues in the investigation of compressible turbulent flows is a pressure strain-rate correlation used. The main problem is to appropriately account for mean dilatation effect in the model. It is especially important in systems with zero spanwise shear-strain, the main practical example is flow through the nozzle, where mean dilatation and streamwise shear are the only possible turbulence-driving factors. And here the question arises, which of the two factors will dominate in particular regime of the flow. Combined with the approach based on an explicit algebraic Reynolds-stress model [1], the modelling of compressible turbulence appears very attractive method, being both clear physically and not much demanding computationally. Here we use EARSM with renewed consideration of mean dilatation effects. The nozzle flow, besides being a good example to examine the effect of dilatation on the turbulence level, is an important engineering facility to accelerate subsonic flow to supersonic speed and to decelerate supersonic flow to subsonic speed, in both cases the sonic regime is achieved in the throat [2]. It's of practical importance to predict the influence of turbulence on required geometrical parameters to arrive at the operational regime of the nozzle.

The non-diagonal components of Reynolds-stress tensor R_{ij} , associated with spanwise shear, are zero, and diagonal are:

$$R_{xx} = k \left(\beta_1 \mathcal{J} + \frac{\beta_2}{3} + \frac{2}{3} \right), \quad R_{yy} = k \left(-\beta_1 \mathcal{J} + \frac{\beta_2}{3} + \frac{2}{3} \right),$$

$$\beta_1 = -\frac{6}{5N}, \quad \beta_2 = -\frac{3}{5} \frac{\mathcal{D}}{N}, \quad N^2 - c' N - \frac{27}{5} \mathcal{J}^2 - \frac{9}{20} \mathcal{D}^2 = 0, \quad (1)$$

$$\mathcal{J} = \frac{\tau}{2} (\partial_x U - \partial_y V), \quad \mathcal{D} = \tau (\partial_x U + \partial_y V) = -\tau U \frac{\partial_x \bar{\rho}}{\bar{\rho}}, \quad \tau = \frac{k}{\varepsilon},$$

where $c' = 9/4(c_1 - 1)$ and c_1 is Rotta's constant.

The application of $k - \omega$ model for the steady case reads:

$$\begin{aligned} \bar{\rho} U \partial_x U &= -\partial_x p - \partial_x R_{xx} + \mu \partial_x \left(\partial_x U - \frac{1}{3} \frac{\partial_x \bar{\rho}}{\bar{\rho}} \right), \quad p/\rho^\gamma = const, \\ U \partial_x k &= \underbrace{\varepsilon \left(\frac{\mathcal{D}^2 + 12 \mathcal{J}^2}{5 N} - \frac{2}{3} \mathcal{D} \right)}_{P_k} - \varepsilon + \partial_x \left(\left(\mu + \frac{\mu_t}{\sigma_k} \right) \partial_x k \right), \\ U \partial_x \omega &= \alpha \frac{\omega}{k} P_k - \beta \omega^2 + \frac{1}{\bar{\rho}} \partial_x \left(\left(\mu + \frac{\mu_t}{\sigma_\omega} \right) \partial_x \omega \right), \quad \omega = \frac{\varepsilon}{\beta_s k}, \quad \mu_t = -\frac{\beta_1 k \tau}{2}, \end{aligned} \quad (2)$$

where μ_t is turbulent viscosity and α, β, β_s are modelling parameters. This system is treated here with a simple solver, second derivatives are evaluated implementing quickly converging procedure.

Results

As seen in figure 1. (for the flow going from subsonic to supersonic regime with $M = 1$ at $x = 0.5$) for high-enough turbulent time-scale τ the turbulence can be amplified due to streamwise shear, competing with negative effect of dilatation, even in the absence of spanwise shear.

Similarly, in figure 2. the corresponding results are shown for the transition from supersonic to subsonic regime ($M = 1$ at $x = 0.5$). But in this case for the turbulence growth to occur we need much more less values of τ , because here the dilatation production is positive too.

The production of kinetic energy due to dilatation in comparison to production governed by streamwise strain is negligible in subsonic region and is overwhelming in supersonic, a sharp transition coincides with common transonic regime $0.8 < M < 1.2$.

To initiate a flow to transcend $M = 1$ point at the throat, we have to impose a large enough area ratio of the inlet and the throat. The examination of turbulence action on the flow shows, that it makes the necessary value A_{inlet}/A_{throat} smaller.

The model extends in a straightforward way to the more realistic two-dimensional rectangular nozzle geometry, which can be computed by the same solver. In particular this may be interesting in view of analysis of interplay and competition of shear-strain and dilatation. We are going to perform it in further investigations.

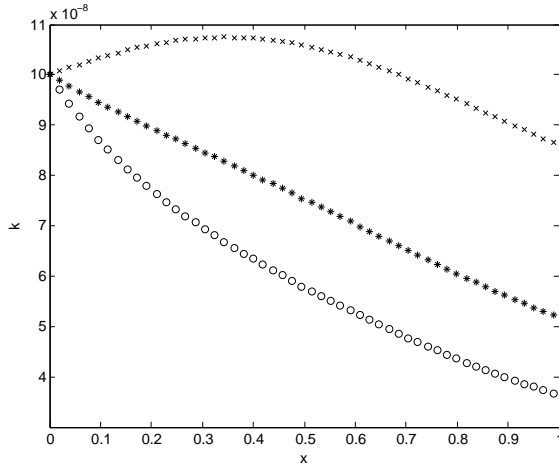


Figure 1. Turbulent kinetic energy under transition from $M=0.6$ to $M=1.48$: $\tau \partial_x U = 5.5$ - crosses, $\tau \partial_x U = 1$ - asterisks, $\tau \partial_x U = 0.55$ - circles

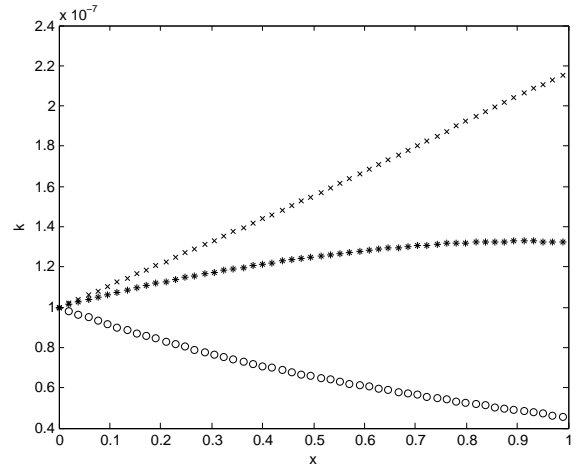


Figure 2. Turbulent kinetic energy under transition from $M=1.6$ to $M=0.56$: $\tau \partial_x U = 2.7$ - crosses, $\tau \partial_x U = 1$ - asterisks, $\tau \partial_x U = 0.27$ - circles

References

- [1] S. Wallin, A.V. Johansson. An explicit algebraic Reynolds stress model for incompressible and compressible turbulent flows. *Journal of Fluid Mechanics*, 403:89–132, 2000.
- [2] J.D.Anderson. *Modern Compressible Flow: With Historical Perspective*. Mc Graw Hill, International Edition, 2004.

Large Eddy Simulation of a bluff body flame near lean blow off using detailed chemistry

Erdzan Hodzic¹, Christophe Duwig¹, Robert-Zoltán Szász¹ and Laszlo Fuchs¹

⁽¹⁾Division of Fluid Mechanics, Department of Energy Sciences, Lund University, Box 118, 221 00 Lund, Sweden
Erdzan.Hodzic@energy.lth.se

Summary. A lean premixed flame near lean blow off was simulated with Large Eddy Simulation (LES) and finite rate chemistry. The goal is to predict lean blow-off and understand flame stabilization. The results are compared to corresponding laser diagnostics showing that the LES tool captures accurately the recirculation zone and flame location. Further, the snapshots are examined evidencing two regions in the flame and the influence of surrounding air entrainment. The results show that it is possible to study the dynamics of blow-out phenomena by examining the 3D results which successfully characterizes the flame.

Key words: Large Eddy Simulation, Premixed combustion, lean blow off

Introduction

In order to reduce harmful emissions, the current trend in the design of industrial combustors is to operate under fuel lean and premixed conditions near the blow-out limit [1]. Peak temperature in the combustion device is reduced together with NO_x emissions but instabilities, flashback or flame blow off might occur. Indeed the very fuel lean conditions enabling low emissions often result in flames that are very sensitive to perturbations. Therefore, a key issue for viability of industrial devices is flame stabilization and flame holding. A possibility for flame stabilization is to anchor the flame in a recirculation zone, where hot gases are trapped in the wake of a body to ignite fresh gases. The body creates a recirculation zone (RZ), bringing burnt hot gases towards the fresh gases and thereby maintain the combustion at rather lean condition [2]. The contact between hot (burnt) gases and incoming fresh (unburnt) gases delimits the flame front. Successful stabilization implies capturing sufficient amount of hot gases in the RZ and maintaining the high temperature during operation. If these two conditions are not fulfilled, lean blow off (LBO) occurs with decreasing temperature in the RZ until the flame is not sustained. Considering a wake behind a cone, Kariuki et al. [2] exemplified the LBO sequence by decreasing the fuel supply, varying the equivalence ratio from 0.64 to 0.63. Figure 1 shows the corresponding response followed by high-speed laser diagnostics. The response is originally slow and with relatively small variations of the OH field but evolves to a rapid decrease of OH signal just before (few milliseconds) LBO. This behavior highlights the complex nature of turbulent combustion in general and LBO in particular.

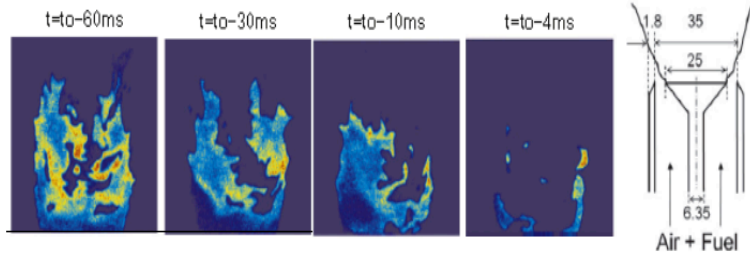


Figure 1. Left: example of LBO in a bluff body stabilized flame captured by time resolved OH-PLIF [2]. The flame responds to a decrease of equivalence ratio from 0.64 to 0.63. The time t_0 denotes the LBO. Right: schematic of the bluff body [2] – dimensions are in mm.

Despite more than 60 years of research, turbulent combustion still poses considerable challenges for the community [3]. The interaction between turbulent structures and chemical reactions features a multi-scale non-linear problem. Far from LBO (hence well established flame), laboratory scale experiments often fall in the flamelet regime and have led to numerous studies and successful modeling activities [3-4]. However, this regime is not always relevant to industrial combustion devices, which commonly operate in the distributed combustion regime or close to LBO. Under these conditions, the scale separation between the flow and the flame is not valid and requires a coupled treatment with time dependent flow governing equations supplemented by finite rate chemistry. The following sections present the modeling approach and the burner geometry before discussing the results.

Modeling approach

Since LBO and flames near LBO exhibit significant time dependent behavior, we based the modelling on Large Eddy Simulation (LES). In addition, to the filtered continuity and Navier-Stokes equations, we resolve one filtered transport equation per chemical specie of interest and the filtered enthalpy equation. The reaction term in the filtered scalar equations requires closure and based on experience, we chose Implicit LES (ILES), also referred sometimes as Monotonically Integrated LES - MILES. When applied to the heat release the corresponding ILES expression can be simplified to:

$$\overline{\dot{w}_j(Y_i, T)} = \dot{w}_j(\tilde{Y}_i, \tilde{T}). \quad (1)$$

where j is the index of the reaction in the species j -equation which depends on temperature and all other species i . The rate is obtained from an Arrhenius expression. We should highlight here that relation (1) would fail in the RANS framework but is valid for laminar flow simulation and direct numerical simulation (DNS). LES being an intermediate between RANS and DNS, the validity of (1) would depend on the relative grid resolution and on the subgrid physics. In fact, using a typical LES-grid (i.e. far from DNS), relation (1) may approximate reasonably well the reaction rate as reviewed in [5]. Incorporating combustion chemistry into LES involves finding a suitable reaction mechanism and solving the filtered species equations. For methane combustion, comprehensive chemical kinetics mechanisms can potentially involve hundreds of species and thousands of reactions. A pragmatic choice consists of selecting a skeletal mechanism, including some features of the finite rate chemistry considering only 20 species [6].

The ILES was performed using a LES solver based upon the OpenFOAM object-oriented library [7] and features a reacting low Mach number formulation. The spatial discretisation uses an unstructured FV method, [7], based on Gauss theorem. The reconstruction of convective fluxes by central differencing gives second order accuracy in space and second order accurate backward discretisation is used in time. The convective terms in the scalar equations are treated using a Total Variation Diminishing scheme maintaining high resolution and second order accuracy while preserving boundedness. Time stepping is done implicitly; the pressure-velocity coupling is done with the PISO method. The present settings are well in line with previous works and the reader is referred to [5] for more details.

Presentation of the computational case

We consider a lean flame near LBO investigated by Kariuki et al [2], referred as case A1. The burner geometry consists of a conical flame holder shown in Figure 1. For the case A1, the fuel/air mixture matches a fuel/air equivalence ratio of 0.75 and is supplied at the bottom of the burner and guided to issue around the bluff body. The fuel/air supply features an annular jet surrounding the flame and RZ. The grid includes 1.5M polyhedral cells, 90% of them being cubes (in the flow) while the rest are prism and polyhedron featuring the wall and refinement layers around the walls. A maximum Courant-Fredrich-Levy number of 0.3 is enforced corresponding to a physical time step $\Delta t \sim 10^{-6}$ s. The experimental data (PIV and PLIF images) are taken from [2].

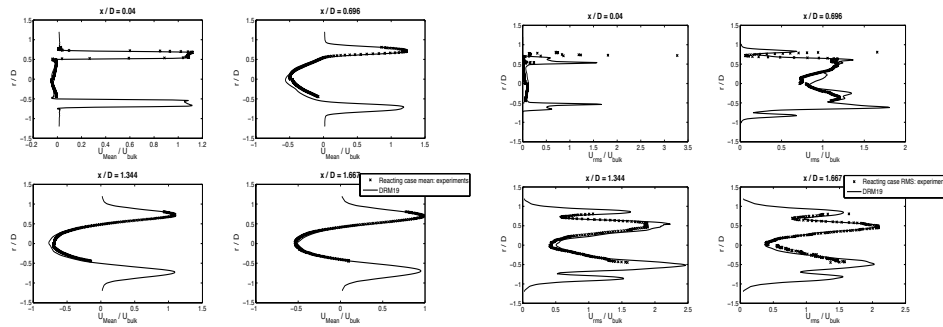


Figure 2. Axial velocity field along radial lines downstream of the bluff body – LES and PIV data. Mean and RMS fields are presented at $X/D=0.04, 0.696, 1.344$ and 1.667 .

Results and discussion

Mean flow field

The mean and RMS velocity profiles normalized by the bulk velocity from LES are compared to PIV data in Figure 2 at four different downstream locations. Very good agreement is found for the average and RMS values. Recirculation zone development is also seen and the highest RMS:s are as expected at the shear layer location.

Snapshots and flame dynamics

Snapshots of the flame front are shown in Figure 3 where OH-LES and OH-PLIF images are compared to each other. Furthermore, the temperature and CH₂O field are also shown. Both OH-LES and OH-PLIF show similar flame pattern with bands of high OH values and sharp decrease delimiting the flame location. The 3D OH level image shows the flame front and the impact of the negative radial velocity causing large scale wrinkling on the top of the flame front. This negative radial velocity causes the entrainment of air into the recirculation zone.

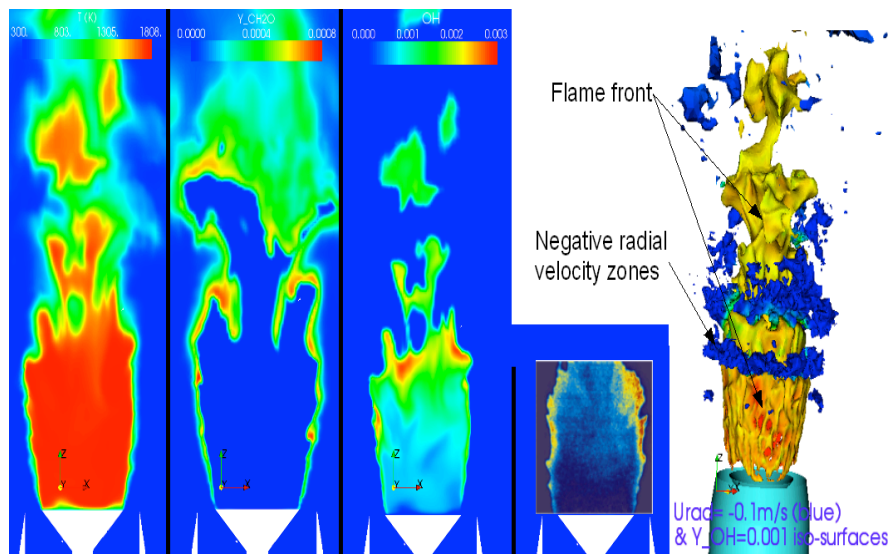


Figure 3. Snapshots of the flame front; from left to right: temperature field (LES), CH₂O field (LES), OH field (LES), OH signal (PLIF) [2], 3D OH level (LES).

References

- [1] Lefevbre, A.H., The role of fuel preparation in low-emission combustion. *J. Eng. Gas Turb. Power*, 117:617–654, 1995.
- [2] Kariuli et al., Measurements in turbulent premixed bluff body flames close to blow-off, *Combustion and Flame*, 159:2589-2607, 2012.
- [3] R.W. Bilger, S.B. Pope, K.N.C. Bray, *J.F. Driscoll Proc. Combust. Inst.* 30:21-42, 2005.
- [4] T. Poinot and D. Veynante, *Theoretical and Numerical Combustion*, RT Edwards, Philadelphia, USA, 2001.
- [5] Duwig C., Nogenmyr K-J., Chan CK., Dunn M.J., *Comb. Theory Mod.*, 15-4:537-568, 2011
- [6] Kazakov A, Frenklach M., *Reduced Reaction Sets based on GRI-Mech 1.2*, <http://www.me.berkeley.edu/drm/>, 1994
- [7] Weller H.G., Tabor G., Jasak H. & Fureby C., *A Tensorial Approach to CFD using Object Oriented Techniques*, *Comp. in Physics*, 12:629, 1997

Direct numerical simulation of constant volume auto-ignition of lean hydrogen/air mixture

Rixin Yu¹, Xue-song Bai¹

⁽¹⁾ Division of Fluid Mechanics, Lund University, Sweden, rixin.yu@energy.lth.se, xue-song.bai@energy.lth.se

Summary. This paper reports on three-dimensional (3D) and two-dimensional (2D) direct numerical simulations (DNS) of a constant-volume auto-ignition of a lean H₂/air mixture with temperature stratification. The combined propagation of spontaneous ignition front and deflagration front is identified in 3D configuration. The difference between 2D- and 3D-DNS is investigated by comparing the evolutions of global combustion parameters such as the averaged heat release rate, total reaction front area and the averaged displacement speed of the reaction front. The extra space dimension is found to lead an overall delay but more rapid bulk ignition.

Key words: 2D/3D DNS, Reacting flow, Auto-Ignition, HCCI

Introduction

In past decade homogenous charge compression ignition (HCCI) engines have attracted great attention from the engine industry and the combustion research community owing to its promise of high efficiency and low emission. A realistic HCCI combustion occurs in a turbulent environment with certain level inhomogeneity in temperature and sometimes fuel concentration. The reaction front of HCCI combustion is different from the classical flames. Depending on the temperature gradient, the reaction front may propagate as a premixed flame or as an ignition wave [1]. Understanding the fundamental structures of HCCI reaction fronts is important for developing control method of HCCI combustion.

Previous studies of HCCI process rely on performing two-dimensional (2D) direct numerical simulations (DNS) of the ignition of a thermally stratified turbulent H₂/air mixture in a periodical rectangular domain[2, 3]. The 2D-DNS studies have provided useful insight into the physics of HCCI combustion; however, the lack of one spatial dimension casts doubt on the previous conclusions.

With the recent development in an efficient DNS solver for reacting flow [4], we present in this work a combined 2D/3D-DNS study of lean H₂/air auto-ignition similar to the 2D-DNS work in [2]. The emphasis is on the similarity and difference between 2D and 3D simulation of auto-ignition problem.

Numerical methods and running conditions

An in-house DNS solver for reacting flow with detailed chemistry and transport properties is used. The solver relies on the low Mach number assumption to allow large time steps for speeding up computation. The temporal integration is performed using the 2nd order symmetrical Strang splitting algorithm [5] with one full time step of chemistry calculation placed in between of two half-step calculations of the diffusion and convection. The diffusion integration is further split into multiple sub-steps of integrations. The chemistry is computed with an accurate stiff solve DVODE [6]. The spatial discretion is a mixed 6th order center difference and 5th order WENO scheme [7]. The spatial/temporal accuracy has been verified with grid/time-step dependency tests. The code is written in a vector form enabling simulations from 1D to 3D [4].

The 3D case is an extension of the 2D setup in [2]. The computational domain is a 4.1 mm³ periodical cube described by a 512³ grid. The H₂/air mechanism in [8] is used. The initial mixture has an equivalence ratio $\Phi=0.1$, mean temperature of $T_0=1070$ K and pressure of $P_0=41$ atm. The initial turbulence field is generated using the Passot-Pouquet spectrum [9]. The turbulence integral scale is 1 mm and the integral velocity is $u_0=0.5$ m/s. For the initial temperature field, the integral scale is 1.32 mm and the rms is $T'_0=15$ K. Based on the above condition the homogenous ignition delay time is $\tau_0=3.3$ ms and the maximum heat release rate is $HR_0=2.94 \times 10^{10}$ J/m³/s. The computational time step is set to 1 μ s. Two additional 2D-DNS runs are also performed with the same setup except the grid: one with a 512² grid, another with a 1024² grid, comparable to [2].

Results and discussions

Fig.1 shows multiple disconnected reaction fronts in the domain, created most likely by spontaneous auto-ignition of local hot spots. The growth of the already ignited spots due to the combined propagations of deflagration and ignition fronts, together with the new front surface from ignition, leads to a rapid increase in the total front surface area. It is seen that at early ignition (2.4 ms) most of the reaction front propagates as a slow deflagration wave, with small portion of the reaction front propagating as the fast ignition wave, e.g. around the sharp tip region of the ignited spots. Later the fraction of ignition front within the total reaction front becomes larger, at 2.9 ms the area of the fast ignition fronts are comparable to that of the slow deflagration fronts, suggesting that the averaged front speed is increasing.

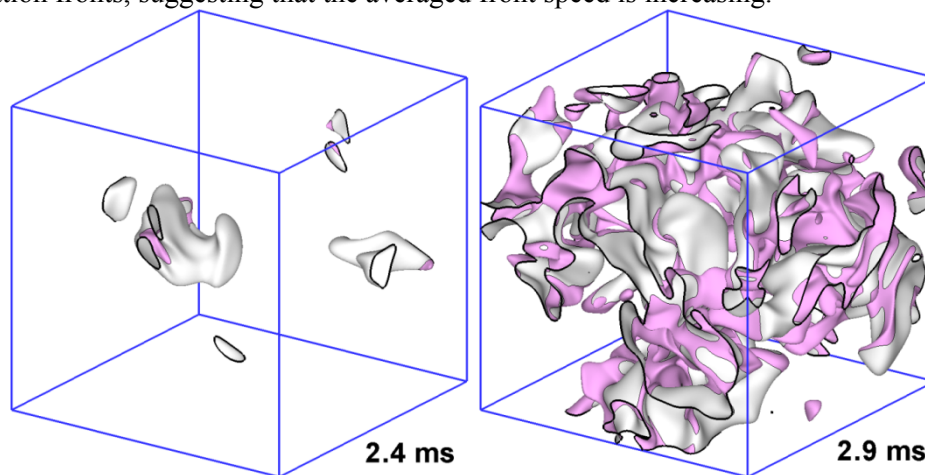


Fig. 1. The 3D instantaneous front surfaces at 2.4 and 2.9 ms. The grey shadow denotes the slow deflagration front while purple shadow represents the fast spontaneous ignition front.

Fig. 2 shows the pressure trace and the normalized heat release rate from the 3D/2D-DNS. The main ignition events in all cases (peak heat release rate) can be found around 3.05 ms. The peak values of the normalized heat release from two 2D cases are around 0.33, comparable to 0.34 in [2]. However the 3D DNS shows a delayed ignition but more rapid heat release (0.40 in the normalized peak value, 15% higher than in 2D), as also shown by the pressure traces.

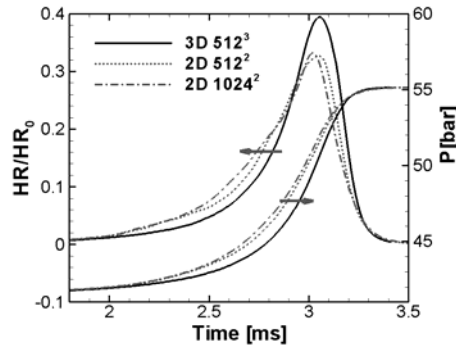


Fig. 2. Pressure and the normalized heat release rate (HR/HR_0) from 3D/2D DNS cases.

Fig. 3 shows that compared with 2D, 3D-DNS predicts a slower increase of the front area during early ignition. Later, the reaction front area increases more rapidly in 3D; it reaches a higher maximum value at 3.05 ms (can be expected from Fig.3). At this instance the heat release rate reaches peak, however the averaged front speed (S_d^*) in 3D is not higher than the 2D one. The higher peak heat release rate in 3D than in 2D is achieved through a larger total front area.

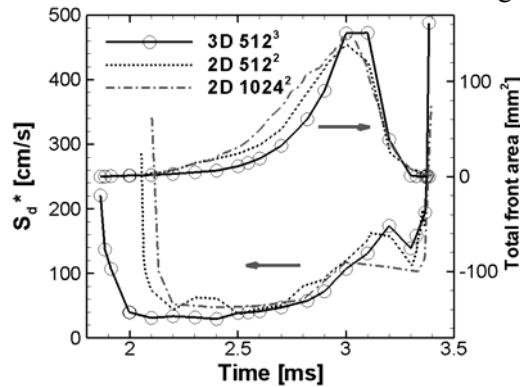


Fig.3. Averaged front displacement speed (S_d^*) and total reaction front area from all DNS cases.

Fig. 4.a shows that the 3D-DNS predicts a much faster temperature field mixing (quicker drop in the rms temperature T') during the early evolution than the 2D-DNS, which results in the observed 3D rapid heat release at the later ignition of the bulk mixture. Assuming no density variation and negligible reaction during the early period, the evolution equation of T' shows that the T' decay is just decided by the mean temperature gradient square, which is plotted in fig.4.b to start the same but increase faster and reach to a higher value in 3D. From the evolution equation of mean temperature gradient square it is further seen that its production rate is determined by a multiplication of three terms involving the mean strain rate, the mean temperature square itself and a normalized term. The last term has been found evolving similarly under all cases. Fig. 4.c shows the 3D strain rate starts from an higher initial value (1.5 time of the 2D one) and also has an early increase raise compared to the monotonically decrease

in 2D. The 1.5 time of initial strain rate in 3D than in 2D is the consequence of one extra space dimension, for the 3D initial turbulence field to maintain the same values of both the time and length scales as in 2D. The early rising of 3D strain rate is also due to one extra dimension, since the strain rate production is through a strain-self-amplification term, which is positive in 3D while zero in 2D [10].

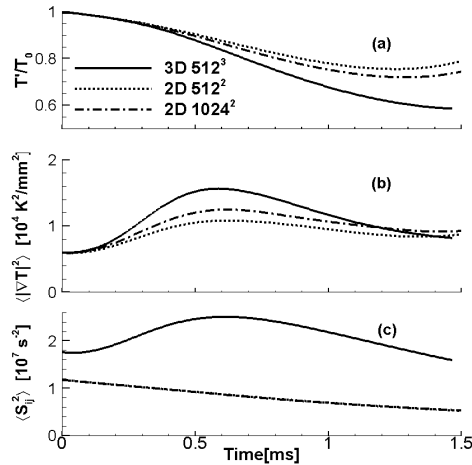


Fig. 4. Normalized rms temperature (T'/T'_0 , a), mean temperature gradient square ($\langle |\nabla T|^2 \rangle$, b), and square of the velocity strain rate ($\langle S_{ij}^2 \rangle$, c), during early ignition time from all DNS cases.

References

- [1] Y.B. Zeldovich, Regime Classification of an Exothermic Reaction with Nonuniform Initial Conditions. *Combustion and Flame*, 39(2): 211-214,1980.
- [2] J.H. Chen, et al., Direct numerical simulation of ignition front propagation in a constant volume with temperature inhomogeneities - I. Fundamental analysis and diagnostics. *Combustion and Flame*, 145(1-2): 128-144,2006.
- [3] E.R. Hawkes, et al., Direct numerical simulation of ignition front propagation in a constant volume with temperature inhomogeneities - II. Parametric study. *Combustion and Flame*, 145(1-2): 145-159,2006.
- [4] R.X. Yu, et al., An improved high-order scheme for DNS of low Mach number turbulent reacting flows based on stiff chemistry solver. *Journal of Computational Physics*, 231(16): 5504-5521,2012.
- [5] G. Strang, On the Construction and Comparison of Difference Schemes *SIAM Journal on Numerical Analysis*, 5(3): 11,1968.
- [6] P.N. Brown, et al., Vode - a Variable-Coefficient Ode Solver. *Siam Journal on Scientific and Statistical Computing*, 10(5): 1038-1051,1989.
- [7] G.S. Jiang, et al., Efficient implementation of weighted ENO schemes. *Journal of Computational Physics*, 126(1): 202-228,1996.
- [8] J. Li, et al., An updated comprehensive kinetic model of hydrogen combustion. *International Journal of Chemical Kinetics*, 36(10): 566-575,2004.
- [9] J.O. Hinze, *Turbulence*. 2d ed., McGraw-Hill, 1975.
- [10] P. Sagaut, et al., *Homogeneous turbulence dynamics*. Cambridge University Press, 2008.

Fluid-Structure Interaction of the Transient Evolution of a Cantilever Beam

Alper Cesur¹, Andreas Feymark²

⁽¹⁾Department of Energy Sciences and Division of Fluid Mechanics, Lund University,
alper.cesur@energy.lth.se

⁽²⁾Department of Shipping and Marine Technology, Chalmers University of
Technology, andreas.feymark@chalmers.se

Summary. This paper comprises the study of transient dynamics of a cantilever beam in a fluid-structure interaction context. The investigation is focused on the dynamical response of a cantilever exposed to fluid flow at $Re=50000$, where the implicitly coupling method serves as the key function in the study.

Key words: CFD/CSD, FV, FEM, Dynamics

Introduction

Fluid-Structure Interaction (FSI) is a multiphysics problem where a fluid and solid domain interact via their mutual interface at the boundary between the fluid flow and solid structure. Aero- and hydroelasticity are typical important areas for fluid-structure interaction problems, where the former considers engineering problems as, e.g., aerodynamic flutter on aeroplane wings whereas the latter involves the analysis and prediction of e.g. wave-induced vibrations, such as whipping and slamming, propeller singing, signature levels from submarines etc. Other FSI related engineering problems are encountered within the biomedical industry. Here, ongoing study is established in order to understand and treat human diseases, e.g. the investigation of back-pressure in veins in the upper part of the body, which may lead to collapse of the veins etc. A typical FSI problem can computationally be formulated either using the *monolithic* or *partitioned* approach, where the former solves the fluid- and the solid equations simultaneously, [1], and the latter utilizes a sequential technique, [2]. The monolithic approach is considered to be more stable and accurate, however expensive in computational time whereas the partitioned approach is considered to be more flexible.

The aim of this study is to investigate the behaviour and the features of a parallelized partitioned coupling method capable of producing accurate and reliable predictions of FSI related problems. This study also comprises the development of an interface between two different open source codes OpenFOAM, [3], for fluid dynamics and OOFEM, [4], for structural dynamics.

Numerical method and Computational Setup

Finite Volume for Fluid flow

The fluid under consideration is isothermal, incompressible and Newtonian. The flow is governed by the time-dependent, three-dimensional conservation equations of mass and momentum for a linear viscous fluid, extended to handle moving grids, e.g.,

$$\partial_t(\mathbf{v}) + \nabla \cdot (\mathbf{v} \otimes (\mathbf{v} - \mathbf{v}_m)) = -\nabla p + \nabla \cdot \boldsymbol{\tau}, \quad \nabla \cdot \mathbf{v} = 0, \quad (1)$$

where \mathbf{v} is the velocity, \mathbf{v}_m the grid velocity, p the pressure, $\boldsymbol{\tau} = 2\nu\boldsymbol{\varepsilon}$ is the viscous stress tensor, $\boldsymbol{\varepsilon} = \frac{1}{2}(\nabla\mathbf{v} + \nabla\mathbf{v}^T)$ the rate-of-strain tensor and ν the viscosity.

The system of governing equations in Eq. (1) are discretized using an unstructured collocated Finite Volume (FV) method in which the discretization uses Gauss theorem together with a multi-step time-integration method, [5]. Furthermore, here Implicit Large Eddy Simulation (ILES), which effectively filters the system of governing equations over the grid using an anisotropic kernel defined by the tessellation of the computational domain into a set of non-overlapping finite volumes, [6], has served as the turbulence model.

Finite Element for Structure

The counterpart to Eq. (1) for solid dynamics reads

$$\int_v \rho \delta \mathbf{u}^T \ddot{\mathbf{u}} dv + \int_v \hat{\mathbf{E}}^T \mathbf{S} dv - \int_v \delta \mathbf{u}^T \mathbf{t} ds - \int_v \delta \mathbf{u}^T \mathbf{b} dv = 0, \quad (2)$$

and describes the balance relation of linear momentum for a continuous body in the Total Lagrangian context based on the virtual work expression. This formulation naturally leads to deformations described in terms of the Green strain tensor, \mathbf{E} , corresponding to the conjugate second Piola-Kirchhoff stress tensor, \mathbf{S} . The discretization has been conducted in OOFEM using the Nonlinear Finite Element Method (NLFEM), which allows for large deformations and small strains. The solution procedure is performed by utilizing implicit time integration for the dynamic problem, where the nonlinear Newmark algorithm, [7] has functioned in conjunction with Newton-Raphson iteration scheme to achieve numerical convergence and accuracy of the solution.

Problem Setup

The computations have been performed for the case of confined flow past a beam in a rectangular channel with quadratic cross-section at a Reynolds number of 50000, based on bulk velocity and beam hydraulic diameter (D). The dimensions of the computational domain, shaped as a rectangular cuboid, are $9D$, $9D$, and $30D$, in the x -, y - and z -direction, respectively. The beam has the dimensions $1D$, $1D$ and $5D$, where $1D = 0.02$ m, and is horizontally centred $9D$ from the inlet. The flow is in the z -direction with a freestream velocity of 2.875 m/s and the beam has no restrictions in its motional degrees of freedom, whatsoever.

At the inlet, a Dirichlet condition is used for the velocity and Neumann condition for the pressure. At the outlet, Neumann conditions are used for the velocity, and a Dirichlet condition for the pressure. At the top and sides, slip conditions have been posed whereas a Dirichlet condition was used for the bottom of the fluid domain. Moreover, the flexible beam was consolidated with no-slip condition. The flow is predicted using ILES on a grid with $4 \cdot 10^5$ cells.

The Coupling

The focus of the coupling method in question lies on creating an interface, between the fluid- and structural solver, which is accurate and stable enough to be able to handle relevant FSI problems occurring in real life applications. The procedure has been facilitated by making sure that the two solvers communicate the solution information as a single executable and by restricting the interface topology to have the same number of nodes and faces. This yields an exactly matching interface surface with a predetermined tolerance, where no interpolation routine is needed. Furthermore, the coupling methodology itself relies on an *implicit*, [8], algorithm of the partitioned solution procedure of the system of equations. Another choice would be to perform the coupling conditions *explicitly*, [9]. Nevertheless, due to improved numerical stability and accuracy, better energy and momentum conservation, the ability to use larger time steps, and also, the nature of the problem itself made implicit partitioned solution procedure the choice for the conducted simulations in this study. Furthermore, the data transfer in-between the two solvers, which is not trivial in parallel communication, has been addressed using Portable, Extensible Toolkit for Scientific Computation (PETSc), [10].

Results and Conclusions

The FSI simulations results illustrated in Figure 1 are for a case where the coupling tolerance between fluid and structure surface meshes is 10^{-8} , the fluid to structure density ratio is 0.2, and the Poisson number and Young's modulus are 0.3 and 0.03 GPa, respectively.

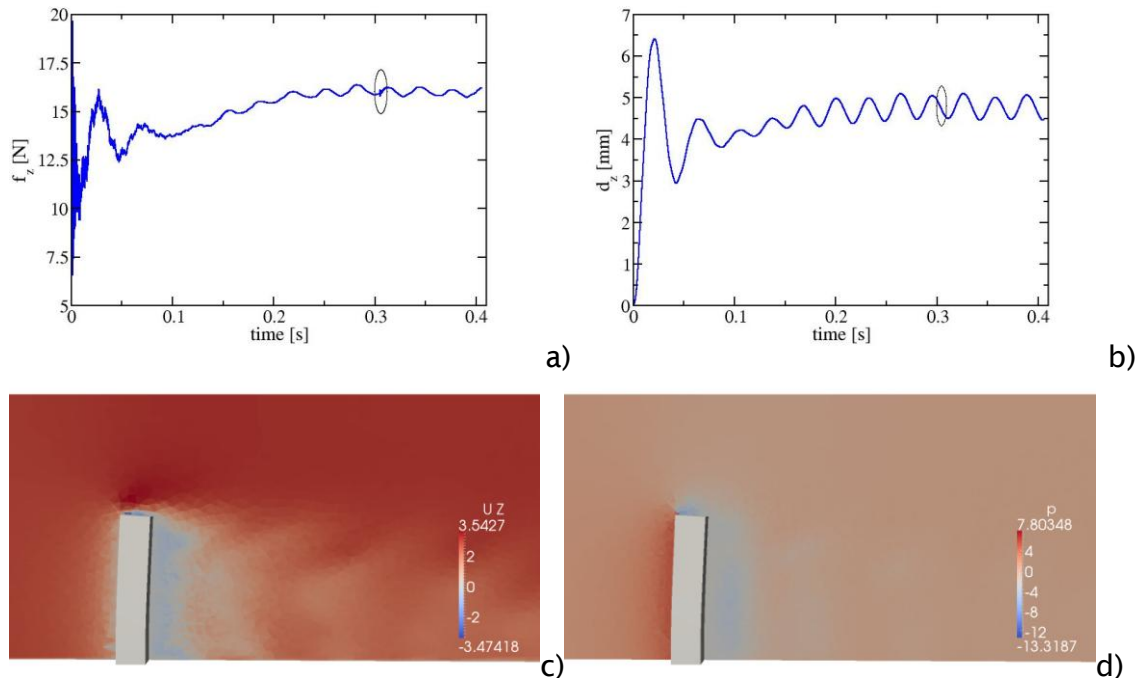


Figure 1: a) Maximum structural forces. b) Maximum structural displacement. c) Velocity in z-direction at $t = 0.304$ s d) Pressure field at $t = 0.304$ s.

At the top part of Figure 1 the dynamical response in terms of structural force and structural displacement in the flow direction is presented for the cantilever beam. As can be seen, the structure achieves quite large deformations initially where the fluid flow is not yet fully developed. Nevertheless, as the fluid flow becomes fully developed this trend transitions gradually to a stable pattern with average deformation around 4.5 mm, where a constant maximum to minimum amplitude of displacement is perceived. The same pattern can be observed for the forces, however, with rather stronger transient fluctuations. It should be noted that the first 10 data points of the structural forces have been removed in Figure 1 due to heavy fluctuations.

At the bottom right of Figure 1, the pressure distribution in the fluid field at time, $t = 0.304$ s, around the cantilever is shown, with an almost constant pressure on the upstream and downstream side. This behaviour can be associated to the counterpart of the almost constant wavelength character of the structural force. Furthermore, the velocity field at the bottom left in Figure 1 illustrates that the maximum velocity occurs at the top of the cantilever and then decreases in a pulsating manner further in the wake, indicating an oscillatory and undamped behaviour of the cantilever dynamics.

References

- [1] Andrew T. Barker, Xiao-Chuan Cai. *Scalable parallel methods for monolithic coupling in fluid-structure interaction with application to blood flow modelling*. Preprint submitted to Journal of Computational Physics, 2009.
- [2] Hermann G. Matthies, Jan Steindorf. *Partitioned strong coupling algorithms for fluid-structure interaction*. Computers and Structures, 81, 805-812, 2003.
- [3] Weller, H. G., Tabor G., Jasak, H., and Fureby, C., *A Tensorial Approach to Computational Continuum Mechanics Using Object Oriented Techniques*, Computers in Physics, Vol. 12, No.6, pp. 620-531, 1998.
- [4] B. Patzák and Z. Bittnar., *Design of Object Oriented Finite Element Code*, Advances in Engineering Software, Vol.32, No.10-11, pp. 759-767, 2001.
- [5] Lambert, J. D., *Computational Methods in Ordinary Differential Equations*, 1st ed., John Wiley & Sons Inc, New York, 1973.
- [6] Grinstein, F. F., Margolin, L., and Rider, B. *Implicit Large Eddy Simulation: Computing Turbulent Fluid Dynamics*, 1st ed., Cambridge University Press, Cambridge, England, UK, 2007.
- [7] Newmark, N. M. *A method of computation for structural dynamics*, Journal of the Engineering Mechanics Division, ASCE, 85, EM3, 67-94, 1959.
- [8] E. Longatte, V. Verreman, M. Souli. *Time marching for simulation of fluid-structure interaction problems*, Journal of Fluids and Structures, Vol. 25, pp. 95-111, 2009.
- [9] Cui Peng, Han Jinglong. *Prediction of flutter characteristics for a transport wing with wingtip devices*, Aerospace Science and Technology, 2011.
- [10] Balay, S., Brown, J., Buschelman, K., Gropp, W. D., Kaushik, D., Knepley, M. G., Curfman-McInnes, L., Smith, B. F., and Zhang, H., <http://www.mcs.anl.gov/petsc>, 2011.

Proceedings of the 25TH NORDIC SEMINAR
COMPUTATIONAL MECHANICS, 2012

Computational Techniques

Room: Lilla Hörsalen, Thursday 25 October, 09:30 - 11:30



Discontinuous Petrov-Galerkin Finite Element Method for the Reissner-Mindlin Plate Bending Model

Antti H. Niemi¹, Nathaniel O. Collier², and Victor M. Calo²

⁽¹⁾Aalto University, Espoo, Finland, antti.h.niemi@aalto.fi

⁽²⁾King Abdullah University of Science and Technology, Thuwal, Saudi Arabia

Summary. We apply the discontinuous Petrov-Galerkin (DPG) finite element method to the Reissner-Mindlin model of plate bending. We show that the hybrid variational formulation underlying the DPG method is well-posed (stable) with a thickness-dependent constant in a norm encompassing the L_2 -norms of the bending moment, shear force, transverse deflection and the rotation vector. We then construct a numerical solution scheme based on quadrilateral scalar and vector finite elements of degree p . We show that for affine meshes the discretization inherits the stability of the continuous formulation provided that the optimal test functions are approximated by polynomials of degree $p + 3$. We prove a theoretical error estimate in terms of the mesh size h and polynomial degree p and demonstrate numerical convergence on affine as well as non-affine mesh sequences.

Key words: plate bending; finite element method; discontinuous Petrov-Galerkin; discrete stability;

Introduction

Displacement-based finite elements are the most widely used tools for computing the deformations and stresses of elastic bodies under external loads. However, in the modeling of thin-walled structures, the basic formulation leads to so-called locking, or numerical over-stiffness, unless special techniques (reduced integration, nonconforming elements) are applied. Another difficulty related to the displacement based formulations is stress recovery. It is well known that the accuracy of the stress field derived from the displacement field can be much lower than that of the displacement field. Therefore special recovery techniques are often applied to improve the accuracy of stress approximations. Practical finite element design relies heavily on heuristics, intuition and engineering expertise which makes numerical analysis of the formulations very difficult. This is because the various physical and geometrical assumptions do not have obvious interpretations in the functional analytic setting required for mathematical error analysis.

Mixed formulations where stresses are declared as independent unknowns are attractive because they often avoid the problem of locking by construction and allow direct approximation of the quantities of interest. However, in contrast to pure displacement formulations, mixed finite element methods do not inherit stability from the continuous formulation, but the stability of the discretization must be independently verified for each choice of finite element spaces. The recently introduced discontinuous Petrov-Galerkin (DPG) variational framework provides means for automatic computation of test functions that guarantee discrete stability for any choice of trial functions, see [1, 2]. In this work, we will present a numerical analysis of the framework when applied to the Reissner-Mindlin model of plate bending.

Reissner-Mindlin Plate Model

The model for bending of a plate corresponds to a system of partial differential equations

$$\begin{aligned} \gamma^{-1}t^2\mathbf{V} - \nabla w + \boldsymbol{\psi} &= \mathbf{0}, & \mathcal{C}^{-1}\mathbf{M} - \nabla^S \boldsymbol{\psi} &= \mathbf{0} \\ -\nabla \cdot \mathbf{V} &= p, & -\nabla \cdot \mathbf{M} - \mathbf{V} &= \mathbf{0} \end{aligned} \quad \text{on } \Omega \quad (1)$$

where Ω is taken to be a convex polygonal domain in \mathbb{R}^2 representing the middle surface of a plate. We take $L = \text{diam}(\Omega)$ as the length unit and assume that the plate thickness t is small as compared with unity, that is the plate is thin. The deformation of the plate is described in terms of the transverse deflection w and the rotation vector $\boldsymbol{\psi}$. The first row in (1) relates them to the shear force vector \mathbf{V} and the bending moment tensor \mathbf{M} . In these constitutive laws \mathcal{C}^{-1} is a two-dimensional ‘‘compliance tensor’’ (we assume homogeneous isotropic material), and γ is the shear correction factor used in plate theory. The second row in (1) then constitutes the basic laws of static equilibrium.

The DPG approximation of the model is based on the ultra-weak hybrid form of (1). This is associated to a partitioning of Ω to elements and is obtained by integration by parts. We are able to show in [3] that this variational form is well-posed and can be used to construct finite element approximations with a best-approximation property in a norm encompassing the $L_2(\Omega)$ -norms of $w, \boldsymbol{\psi}, \mathbf{V}, \mathbf{M}$.

Results

Some illustrative results are shown in Table 1 for a model problem with a softly clamped square plate under uniform loading. The computational domain Ω is partitioned into a uniform $N \times N$ mesh and the main unknowns $w, \boldsymbol{\psi}, \mathbf{V}, \mathbf{M}$ are represented as bilinear functions on each element. The results show the convergence of the deflection w and the bending moment $-M_{11}$ at the center of a plate as the number of elements is increased. For comparison, we show also the values obtained with the bilinear element based on the standard energy principle and selective reduced integration (SRI). The results show that on a very coarse mesh DPG gives much better results, but the difference between the methods diminishes as the mesh is refined.

Table 1. Clamped Square Plate Under Uniform Loading.

Convergence of the Central Deflection							
Mesh	2×2		8×8		32×32		
t	DPG	SRI	DPG	SRI	DPG	SRI	True
0.05	1.609	0.067	1.345	1.314	1.329	1.326	1.329
0.01	1.560	0.003	1.288	1.253	1.268	1.267	1.268
0.001	1.559	0.000	1.285	1.251	1.265	1.264	1.265
0.0001	1.559	0.000	1.285	1.251	1.265	1.264	1.265

Convergence of the Central Moment							
Mesh	2×2		8×8		32×32		
t	DPG	SRI	DPG	SRI	DPG	SRI	True
0.05	2.926	0.000	2.356	2.334	2.304	2.302	2.301
0.01	2.927	0.000	2.349	2.331	2.294	2.293	2.291
0.001	2.927	0.000	2.348	2.331	2.293	2.293	2.291
0.0001	2.927	0.000	2.348	2.331	2.293	2.293	2.291

References

- [1] L. Demkowicz, J. Gopalakrishnan: A class of discontinuous Petrov-Galerkin methods. Part II: Optimal test functions. *Numerical Methods for Partial Differential Equations*, 27 (2010), 70–105
- [2] A.H. Niemi, J. Bramwell, L. Demkowicz: Discontinuous Petrov-Galerkin method with optimal test functions for thin-body problems in solid mechanics. *Computer Methods in Applied Mechanics and Engineering*, 200 (2011), 1291-1300
- [3] V.M. Calo, N.O. Collier, A.H. Niemi: Analysis of the Discontinuous Petrov-Galerkin Method with Optimal Test Functions for the Reissner-Mindlin Plate Bending Model. *Submitted*.

A high order solver for the unbounded Poisson equation

Mads M. Hejlesen¹, Johannes T. Rasmussen¹, Philippe Chatelain², and Jens H. Walther^{1,3}

⁽¹⁾Department of Mechanical Engineering, Technical University of Denmark, Building 403, DK-2800 Kgs. Lyngby, Denmark, mmhej@mek.dtu.dk, jtra@mek.dtu.dk, jhw@mek.dtu.dk

⁽²⁾Institute of Mechanics, Materials and Civil Engineering, Université catholique de Louvain, B-1348, Belgium, philippe.chatelain@uclouvain.be

⁽³⁾Computational Science and Engineering Laboratory, ETH Zürich, Universitätsstrasse 6, CH-8092 Zürich, Switzerland, walther@mavt.ethz.ch

Summary. This work improves upon Hockney and Eastwood's Fourier-based algorithm for the unbounded Poisson equation to formally achieve arbitrary high order of convergence without any additional computational cost. We assess the methodology on the kinematic relations between the velocity and vorticity fields.

Key words: Poisson solver, unbounded domain, numerical integration, particle-mesh methods

Introduction

The solution of the Poisson equation on an unbounded domain is essential in many physical problems and appear among others in the field of fluid dynamics, molecular dynamics, and astrophysics. The Poisson equation often describes the energy or potential of a physical system, and is either directly or indirectly governing for the dynamics of the system.

We find the Green's function solution to the Poisson equation through an integral formulation carried out in a discrete sense by convolving the field with an integration kernel. In order to achieve free-space boundary conditions the domain must be extended to twice the size, to avoid the periodicity of the discrete convolution operator. Hockney and Eastwood [1] showed that it is possible to impose free-space boundary conditions by zero-padding the right-hand side density field and convolving this with a free-space integration kernel of equal size.

The convolution of the density field and the integral kernels is inherently based on a mid-point numerical quadrature and is therefore limited to a second order convergence as shown by Rasmussen [2]. In the present work the Greens function based Poisson solver is extended to achieve a high order of convergence of the convolution integral for a continuous field by formulating regularised integration kernels. These are derived based on the work of Beale and Majda [3] and Winckelmans and Leonard [4] who used Gaussian and algebraic smoothing to achieve high order regularised integration kernels for mesh-free vortex methods.

Vorticity-velocity equations and Fourier-based convolution for their solution

In fluid mechanics, kinematics relates the vorticity ω and the velocity \mathbf{u} fields. By defining a solenoidal vector potential (ψ : $\nabla \cdot \psi = 0$) referred to as the stream function, the velocity field can be calculated from the vorticity field by the three kinematic relations

$$\omega \equiv \nabla \times \mathbf{u}, \quad \mathbf{u} \equiv \nabla \times \psi, \quad \nabla^2 \psi = -\omega. \quad (1)$$

The latter relation constitutes the well known Poisson equation which can be solved on the unbounded domain \mathbb{R}^d using a Green's function approach, yielding

$$\psi = G * \omega \quad \text{or} \quad \mathbf{u} = \nabla \times (G * \omega). \quad (2)$$

G is the Green's functions for which $\nabla^2 G(\mathbf{x}) = -\delta(\mathbf{x} - \boldsymbol{\xi})$ and $*$ denotes the discrete linear convolution operator. Linear convolution is obtained by zero-padding the vorticity field to twice the domain size and applying the discrete cyclic convolution operator to the now zero-padded vorticity field and the integration kernel of equal size.

The convolution is performed efficiently in Fourier space whereas the linearity of the problem also enables the curl of the stream function to be carried out in Fourier space to calculate the velocity directly.

$$\widehat{\psi} = \widehat{G} \widehat{\omega} \quad \text{or} \quad \widehat{\mathbf{u}} = \iota \mathbf{k} \times \widehat{\psi} = \iota \mathbf{k} \times \widehat{G} \widehat{\omega} \quad (3)$$

Here $\widehat{\cdot}$ denotes the Fourier transform, ι is the imaginary unit and $\mathbf{k} = \{k_x, k_y, k_z\}$ is the wavenumber corresponding to the Fourier coefficients.

High order methods: Regularised integration kernels

As the Greens function is constructed from a delta function the resulting integration kernel G is singular at $|\mathbf{x}| = 0$. The singularity of the integration kernels is impossible to represent discretely and one is forced to replace the singularity with a finite value which introduces additional errors to the integration and thereby restricts the method to a limited order of accuracy.

In the present work, we remove the singularity and achieve higher order by using smoothing functions. Effectively, a smoothed version of the right-hand side of the Poisson equation is considered

$$\omega_\epsilon = \zeta_\epsilon * \omega \quad (4)$$

where ζ_ϵ is a filter function with a smoothing radius ϵ . For conservation properties we have $\int_{\mathbb{R}^d} \zeta_\epsilon(\mathbf{x}) d\mathbf{x} = 1$.

The convolution of this smoothed source term with the Green's function can be written as

$$\psi_\epsilon = G * (\zeta_\epsilon * \omega) = (G * \zeta_\epsilon) * \omega = G_\epsilon * \omega. \quad (5)$$

where G_ϵ is the mollified Green's function. For a given filter function ζ_ϵ , it is straightforward to derive the G_ϵ from $\nabla^2 G_\epsilon(\mathbf{x}) = -\zeta_\epsilon(\mathbf{x} - \boldsymbol{\xi})$.

The order of accuracy of the smoothed solution is now determined by the number of vanishing moments of the smoothing function ζ_ϵ . An m -order accurate radially-symmetric filter will satisfy $0^\beta = \int \rho^\beta \zeta_\epsilon(\rho) d\rho$ where $\beta = \{0, 2, \dots, m-2\}$.

Because we use a family of radially-symmetric kernels, the odd moments will be satisfied automatically whereas in order to obtain an m -order integration kernels the smoothing function ζ_ϵ must satisfy $m/2$ equations. Using a Gaussian kernel the smoothing function is constructed by

$$\zeta_\epsilon(\rho) = P_m(\rho) \exp(\rho^2/2) \quad \text{where} \quad P_m(\rho) = a_1 + a_2 \rho^2 + a_3 \rho^4 + \dots + a_{m/2} \rho^{m-2} \quad (6)$$

is an even polynomial of order $m-2$ that supplies the $m/2$ degrees of freedom. The coefficients $a_1, a_2, \dots, a_{m/2}$ can be calculated by solving the system of equations consisting of the $m/2$ equations for the m moments. Alternatively, one can follow Chatelain and Leonard [5] and apply successive extrapolations to $\zeta_\epsilon(\rho)$ where an $m+1$ order scheme can be built from an m -order scheme with

$$P_{m+2} = \left(1 + \frac{d}{m} - \frac{1}{m} \rho\right) P_m + \frac{2}{m} \rho \frac{\partial P_m}{\partial \rho}. \quad (7)$$

For the Gaussian smoothing function of the regularised Greens function kernel G_ϵ takes the general form

$$G_\epsilon(|\mathbf{x}|) = \begin{cases} \frac{1}{2\pi} \left(\log(|\mathbf{x}|) - Q_m \left(\frac{|\mathbf{x}|}{\epsilon} \right) \exp \left(\frac{-|\mathbf{x}|^2}{2\epsilon^2} \right) + E_1 \left(\frac{|\mathbf{x}|^2}{2\epsilon^2} \right) \right) & \text{in 2D} \\ -\frac{1}{4\pi|\mathbf{x}|} \left(\frac{1}{\sqrt{2\pi}} R_m \left(\frac{|\mathbf{x}|}{\epsilon} \right) \exp \left(\frac{-|\mathbf{x}|^2}{2\epsilon^2} \right) + \operatorname{erf} \left(\frac{|\mathbf{x}|}{\sqrt{2}\epsilon} \right) \right) & \text{in 3D} \end{cases} \quad (8)$$

where $E_1(z)$ is the first exponential integral function, $\operatorname{erf}(z)$ is the regular error function and the polynomials Q_m and R_m for $m = 4, 6, 8, 10$ are

$$Q_4(\rho) = 1 - \frac{1}{2}\rho^2 \quad R_4(\rho) = -2\rho + \rho^3 \quad (9)$$

$$Q_6(\rho) = 1 - \rho^2 + \frac{1}{8}\rho^4 \quad R_6(\rho) = -2\rho + \frac{9}{4}\rho^3 - \frac{1}{4}\rho^5 \quad (10)$$

$$Q_8(\rho) = 1 - \frac{3}{2}\rho^2 + \frac{3}{8}\rho^4 - \frac{1}{48}\rho^6 \quad R_8(\rho) = -2\rho + \frac{89}{24}\rho^3 - \frac{20}{24}\rho^5 + \frac{1}{24}\rho^7 \quad (11)$$

$$Q_{10}(\rho) = 1 - 2\rho^2 + \frac{3}{4}\rho^4 - \frac{1}{12}\rho^6 + \frac{1}{384}\rho^8 \quad R_{10}(\rho) = -2\rho + \frac{1027}{192}\rho^3 - \frac{349}{192}\rho^5 + \frac{35}{192}\rho^7 - \frac{1}{192}\rho^9 \quad (12)$$

The finite centre value of the regularised Green's function $G_\epsilon(\mathbf{0})$ is given by

$$G_\epsilon(0) = \lim_{x \rightarrow 0} (G_\epsilon) = \begin{cases} \frac{1}{2\pi} \left(\frac{\gamma}{2} + \log(\sqrt{2}\epsilon) + Q_m(0) \right) & \text{in 2D} \\ \frac{\sqrt{2}}{8\pi^{3/2}} \left(\frac{R_m \left(\frac{|\mathbf{x}|}{\epsilon} \right)}{|\mathbf{x}|} \right)_{x=0} + \frac{\sqrt{2}}{4\pi^{3/2}\epsilon} & \text{in 3D} \end{cases} \quad (13)$$

Here the centre value of the 2D mollified Green's function is derived using a infinite series expansion of $E_1(z)$ [6].

Validation

To investigate the convergence of the free-space Poisson solver, the test function i.e. the vorticity distribution, must be enclosed within the computational domain. This is achieved by using a compact vortex blob to form a vorticity patch in 2D and a torus shaped vortex ring in 3D. We propose the use of a bump function distribution with an infinite number of continuous derivatives to avoid limitations of the convergence rate. The bump function is defined as

$$f(\rho) = \begin{cases} \exp \left(-\frac{c}{1-\rho^2} \right) & \text{for } |\rho| < 1 \\ 0 & \text{for } |\rho| \geq 1 \end{cases} \quad (14)$$

where $c = 20$ is an arbitrary positive constant. Using centred polar (r, θ) and cylindrical (r, θ, z) coordinates for the 2D and 3D case, respectively, the stream functions are defined as

$$\psi = f \left(\frac{r}{R} \right) \quad \text{in 2D} \quad \psi = f \left(\frac{\sqrt{(r-R)^2 + z^2}}{R} \right) e_\theta \quad \text{in 3D} \quad (15)$$

where R is the radius of the centre of the vorticity patch and e_θ is the azimuthal normal vector. The initial vorticity field and the resulting velocity field are found analytically by Eq. (1).

The root-mean-squared (rms) error of the 2D and 3D test cases are shown in Fig. 1 for the regularised integration kernels G_ϵ with $m = 4, 6, 8, 10$. As seen, the 2D and the 3D convergence is virtually identical and the convergence rate corresponds to the respective design of the integration kernels. The same convergence rate is observed with the maximum error (not shown).

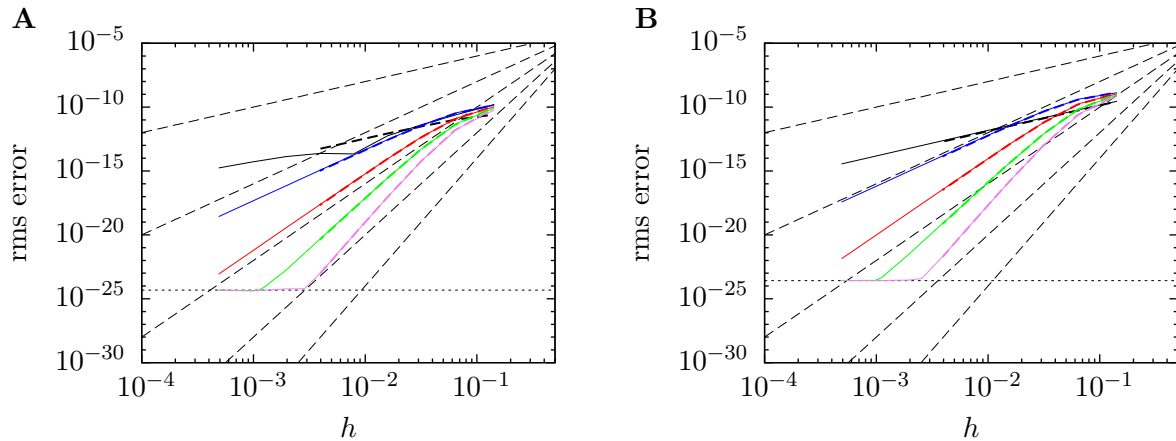


Figure 1. The rms error of the resulting stream function (A) and velocity field (B). (----): from top h^2 , h^4 , h^6 , h^8 , h^{10} ; (.....): round off error; Integration kernels: (—): non-regularised; (—): $m = 4$; (—): $m = 6$; (—): $m = 8$; (—): $m = 10$. Full line: 2D; Bold dashed line: 3D.

Conclusion

A convolution integral method was presented for calculating the solution to the Poisson equation of a continuous field in an unbounded domain to an arbitrary high order of convergence. The smoothing method applied in mesh-free vortex methods to produce vortex blobs was combined with the FFT-based Poisson solver of particle-mesh methods to achieve a high rate of convergence at a low computational cost.

References

- [1] R. W. Hockney and J. W. Eastwood. *Computer Simulation Using Particles*. 2nd Edition, Institute of Physics Publishing, Bristol, PA, USA, 1988.
- [2] J. T. Rasmussen. *Particle methods in bluff body aerodynamics*, Ph.D. thesis, Technical University of Denmark (October 2011).
- [3] J. T. Beale and A. Majda. High order accurate vortex methods with explicit velocity kernels *J. Comput. Phys.*, 58 (1985) 188–208.
- [4] G. S. Winckelmans and A. Leonard. Contribution to vortex particle methods for the computation of three-dimensional incompressible unsteady flows *J. Comput. Phys.*, 109 (1993) 247–273.
- [5] P. Chatelain and A. Leonard. Isotropic compact interpolation schemes for particle methods *J. Comput. Phys.*, 227 (2008) 3244–3259.
- [6] M. Abramowitz and I. A. Stegun. *Handbook of Mathematical Functions With Formulas, Graphs and Mathematical Tables*, National Bureau of Standards. Applied Mathematics Series. 55, 1972.

Effect of scale on the cellular material strength

A. Karakoç¹ and J. Freund²

⁽¹⁾Researcher, Aalto University FI-00076 Aalto Finland, alp.karakoc@aalto.fi

⁽²⁾Senior lecturer, Aalto University FI-00076 Aalto Finland, jouni.freund@aalto.fi

Summary. This article presents the relationship between the scale and strength of the cellular materials. Specimens with irregular hexagonal cell geometries are tested for different sizes and the results are expressed in terms of the mean values and standard deviations of the critical external stress defining the cellular material strength. As a result of the study, it is deduced that the increase in scale inversely influences the strength of tested cellular materials.

Key words: Scale, strength, critical external stress, cellular material.

Introduction

A cellular material is considered as an aggregate of cells and their surrounding walls. When such material is subjected to the external stresses to a stress of increasing magnitude, it is likely to experience failure on a cell wall at some point [1]. The stress at which the weakest cell wall fails refers to the cellular material strength. According to [2, 3], the strength in this sense depends on the size of the cellular material. The phenomenon, called as the scale effect in the literature, cannot be predicted through a deterministic model [4]. Despite the importance of the phenomenon in the structural applications, relatively little attention has been paid on prediction of strength in statistical sense and the effect of scale on the predictions.

The aim of the present study is to explain the effect of scale on the cellular material strength in terms of the mean value and standard deviation of the critical external stress. The material element of the study has a planar hexagonal cellular structure points of which are given random offsets from their regular positions, which brings a non-deterministic element into the model.

Methodology

Material element

The material element of the strength simulation experiment is a planar hexagonal cellular structure of figure 1. The independent variables of the experiment are the measure of geometrical irregularity α and the number of cells n in the material element. The regularity of the material is described by a one parameter model, in which $\alpha = 0$ and $\alpha > 0$ correspond to the regular and irregular material geometries, respectively. To be precise, the cell vertex points are randomly picked from the lists of uniformly distributed points over the disks of radius

$\Delta h = \alpha h^0$, the centre coordinates of which are equal to the vertex coordinates of the regular cellular material having cell wall length h^0 .

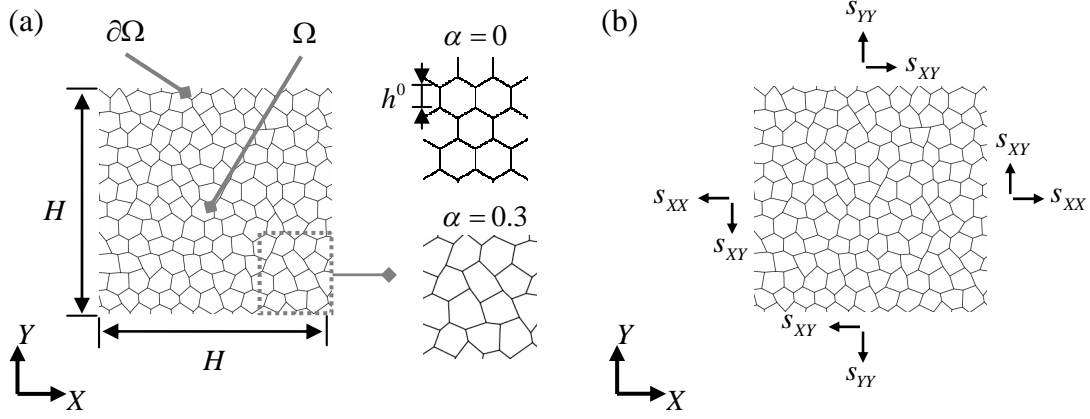


Figure 1. Material element: (a) solution domain Ω , boundary domain $\partial\Omega$ and illustration of regular and irregular cell geometries, (b) external stresses acting on $\partial\Omega$.

Micromechanical model

In the micromechanical model, the cell walls of figure 1 are modelled as elastic Bernoulli beams. The material inside the cells is taken to be soft compared to that of the walls, thus its influence on the mechanical response is neglected.

Strength criterion

The failure mechanism is taken to be bending so that a beam fails when the magnitude of its bending moment M_j exceeds the given critical value M_{cr} . Under linearity assumption, the critical external stress tensor \mathbf{s}_{cr} resulting in the first element to fail is obtained by scaling

$$\mathbf{s}_{cr} = \frac{M_{cr}}{\max |M_j|} \mathbf{s}, \quad (1)$$

in which the maximum is taken over the cell walls in Ω and \mathbf{s} is the external stress tensor. The value obtained in this manner describes the strength in direction \mathbf{s} of the stress space.

Experiments

A simulation experiment is designed similar to a physical one: in order to study the population characteristics, such as strength of an irregular cellular material, experiment is repeated on a random sample, and the failure initiation statistics is estimated based on the results of the sample. In the current experiments, the sample size is 20 and populations used were characterized by $\alpha = 0.3$ and $n \in \{40, 160, 360\}$. A large value of α is used to obtain a clearly non-deterministic material behaviour. The loadings applied to the specimen correspond consists of $10 \times 10 \times 10$ directions of the (three dimensional) stress space.

The dependent variable in these experiments is the critical external stress value of failure initiation \mathbf{s}_{cr} which is obtained through expression (1). Material parameters of the model are assumed to satisfy the condition $E_s I / E_s A h^2 \ll 1$ so that the bending effect is significant [5].

Results and discussions

The mean values and standard deviations of the critical external stresses, which determine the cellular material strength, are listed in table 1 for selected loading cases (I), (II) and (III) corresponding to uni-axial tensions along X -, Y -axes and pure shear, respectively.

Table 1. Mean value and standard deviation of critical external stress as function of loading direction and number of cells.

Loading case	n	$\mu(s_{cr}/s)$	$\sigma(s_{cr}/s)$
(I)	40	2.28	0.48
	160	1.88	0.17
	360	1.76	0.12
(II)	40	2.18	0.32
	160	1.89	0.14
	360	1.79	0.13
(III)	40	1.17	0.16
	160	1.00	0.07
	360	0.94	0.06

The results of table 1 indicate a clear relationship between the scale and strength of the cellular materials. A clearer picture is obtained by repeating the calculation for more directions of the stress space. The outcome gives the failure initiation probability of the hexagonal cell material sample of certain size under the known stress e.g. the strength of the material in statistical sense.

Acknowledgments

The authors gratefully acknowledge the financial support of Multidisciplinary Institute of Digitalisation and Energy through Energy Efficient Wood Processing and Machining Project (E-wood) at Aalto University and the Ministry of Education of Finland through the National Graduate School in Engineering Mechanics.

References

- [1] D.W. Green, Wood: Strength and stiffness, *Encyclopedia of Materials: Science and Technology*, 9732-9736, 2001.
- [2] M.R. Gurvich, Strength/size effect for anisotropic brittle materials under a random stress state, *Composites Science and Technology*, 59: 1701-1711, 1999.
- [3] W. Weibull, A statistical theory of the strength of materials. *Ingeniorsvetenskaps akademien Handlingar*, 151: 1-29, 1939.
- [4] A. Tabiei, J. Sun, Analytical simulation of strength size effect in composite materials, *Composites Part B: Engineering*, 31: 133-139, 2000.
- [5] A. Karakoç, J. Freund, A statistical failure initiation model for honeycomb materials, *Composite Structures*, 2012, doi: 10.1016/j.compstruct.2012.07.001

A Workbench for Multibody Systems ODE and DAE Solvers

Christian Andersson^{1,3}, Claus Führer¹, Johan Åkesson^{2,3}

⁽¹⁾Centre for Mathematical Sciences, Lund University, Sweden, [chria, claus]@maths.lth.se

⁽²⁾Department of Automatic Control, Lund University, Sweden, johan.akesson@control.lth.se

⁽³⁾Modelon AB, Sweden

Summary. A workbench, ASSIMULO, is presented. ASSIMULO is a simulation package connecting a variety of different codes for solving ordinary differential equations, among them special purpose multi-body solvers. The intention of this talk is to describe on one hand the special design of ASSIMULO and its suitability for multibody systems simulations. On the other hand, we want to emphasize a complete workflow from multibody systems modeling software to a simulation tool by a newly defined standard.

Key words: Assimulo, Multibody systems, ODEs, DAEs

Introduction

During the last three decades, a vast variety of methods to numerically solve ordinary differential equations (ODEs) and differential algebraic equations (DAEs) has been developed and investigated. Few of them met industrial standards and even less are available within industrial multibody simulation software. Multibody Systems (MBS) offer a challenging class [5] of applications for these methods, since the resulting system equations are in the unconstrained case ODEs which are often stiff or highly oscillatory. In the constrained case the equations are DAEs of index-3 or less. Friction and impact in the MBS model introduce discontinuities into these equations while coupling to discrete controllers and hardware-in-the-loop components couple these equations to additional time discrete descriptions. Many of the developed numerical methods have promising qualities for these types of problems, but rarely got the chance to be tested on large scale problems. One reason is the closed software concept of most of the leading multibody system simulation tools or interface concepts with a high threshold to overcome. Thus, these ideas never left the academic environment with their perhaps complex but dimensionally low scale test problems. In this talk we will present a workbench, ASSIMULO [4], which allows easy and direct incorporation of new methods for solving ODEs or DAEs written in FORTRAN, C, Python or even MATLAB and which indirectly interfaces to multibody programs such as Dymola [1] and Simpack [2], via a standardized interface, the *functional mock-up interface* [3].

The Functional Mock-up Interface (FMI)

The Functional Mock-up Interface (FMI) defines a standard for model exchange with a small set of functions for model interaction while at the same time it provides the necessary means for simulation of complex hybrid dynamic models. The FMI is a result of the ITEA2 project MODELISAR where the idea is that a modeling and / or simulation environment generates a

dynamic library or source files, written in *C*, which then can be exchanged between different tools and connected to other models.

FMI 1.0 was released in January 2010 and has received a significant amount of attention among vendors. There are currently 28 tools that support or plan to support the FMI. Example of tools includes the commercial products Dymola and Simpack as well as the open-source platform JModelica.org [8].

Assimulo

ASSIMULO is a workbench for solving ordinary differential equations formulated as first or second order explicit ordinary differential equations, (1) and implicit ordinary differential equations (differential–algebraic equations, DAEs), (2).

$$\dot{y} = f(t, y), \quad y(t_0) = y_0 \quad (1)$$

$$F(t, y, \dot{y}) = 0, \quad y(t_0) = y_0, \quad \dot{y}(t_0) = \dot{y}_0. \quad (2)$$

ASSIMULO is written in the high-level programming language Python and combines a variety of different solvers written in FORTRAN, *C* and even Python via a common high-level interface. ASSIMULO consists of mainly two parts, problem definitions and solvers. The problem definitions are not only limited to, for instance the *right-hand-side* of the problem, but they may also contain event functions in order to support hybrid systems with state, step and time events. Additionally, a problem definition can specify options related to the problem such as which states are actually algebraic variables. The idea is to keep information related to a problem separate from the solver. For instance, the tolerances, which are important quantities to control the solver, are attributes of the solver class rather and are kept separate from the problem description.

The solvers interfaced to ASSIMULO consist of a variety of different codes. The codes include explicit and implicit Runge–Kutta methods, Rosenbrock–Wanner methods, multistep methods of Adams and BDF type, Newmark and HHT- α methods. It is planned to include even extrapolation methods for DAEs. Some methods come with a continuous solution representation which enables root-finding for event detection to correctly handle hybrid systems.

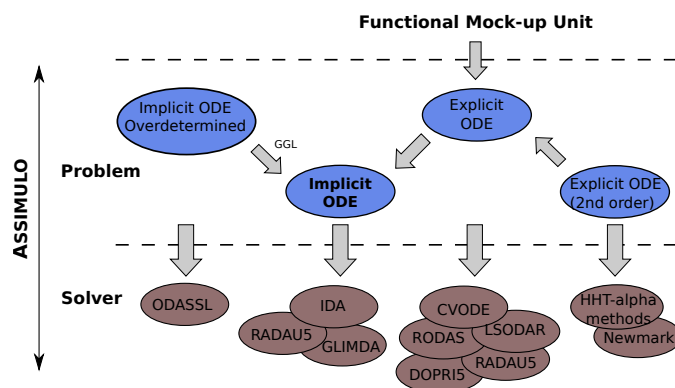


Figure 1. Connection between the different problem formulations and the different solvers available in ASSIMULO. The connection of the Functional Mock-up Interface to ASSIMULO is also shown.

The solver and problem classes are related to each other corresponding to Figure 1. The most universal solver class handles implicit ODEs. Explicit ODEs are thus transformed to their implicit counterpart (residual formulation), when solved with an implicit solver. Correspondingly overdetermined mechanical DAEs [6] are in this case transformed to fully determined DAEs by

using a GGL-stabilization technique [7]. Also, mechanical problems given as second order ODEs are automatically transcribed to implicit ODEs, when exposed to a solver of that class.

Example

For racing applications, finding the maximal performance of the car is crucial. One method to quickly estimate the impact on performance of a change to the vehicle setup is to solve for the steady state limits under different driving conditions. Identifying a set of critical points along a race track and calculating the maximum achievable speed for each point can give a good indication on how the change will affect the lap time.

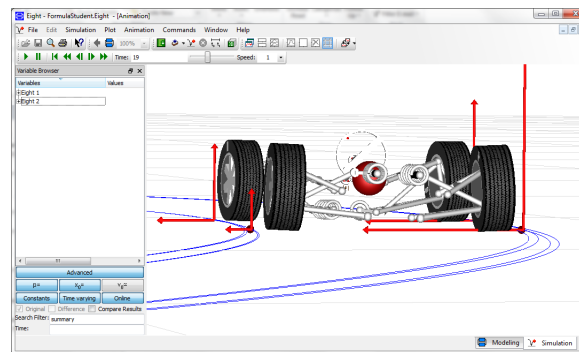


Figure 2. Dymola model of a student formula race car with 47 states.

In this example, a race car is modeled in Dymola, Figure 2, and exported to an FMI compliant model. The latter is then imported into Python, by means of the JModelica.org platform, and made available for simulation using the integrators in ASSIMULO. The result of a simulation is

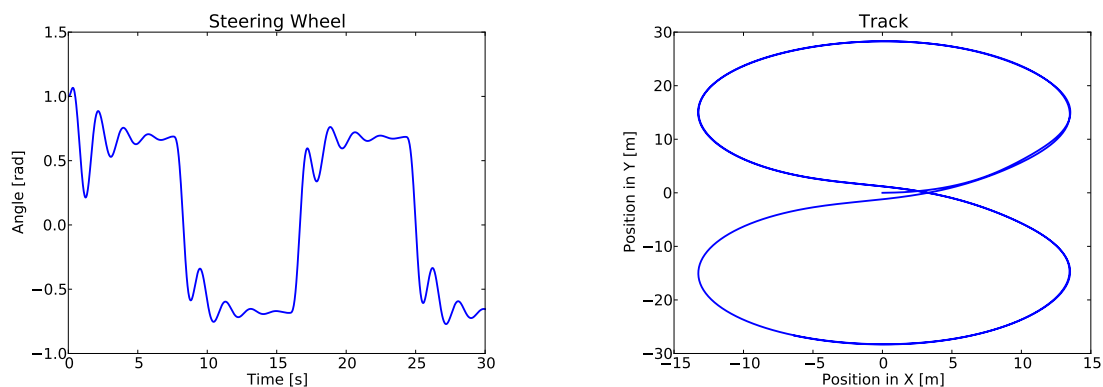


Figure 3. Results from a simulation of the race car driving on an eight shaped course. The left figure shows the angle of the steering wheel while the right figure shows the position of the race car. The model was generated as an FMU from Dymola and simulated in ASSIMULO using the solver CVODE.

shown in Figure 3.

This demonstrates the potential of the presented concept to connect industrial models from acknowledged multibody software to a wide range of ODE and DAE integrators.

Acknowledgments

The first author gratefully acknowledges the financial support from the Lund Center for Control of Complex Systems, LCCC, funded by the Swedish Research Council.

References

- [1] Dymola - multi-engineering modeling and simulation. Dassault Systèmes. <http://www.dymola.com/>.
- [2] Simpack - multi-body simulation software. SIMPACK AG. <http://www.simpack.com/>.
- [3] Functional mock-up interface for model exchange. Interface specification, MODELISAR, January 2010.
- [4] Christian Andersson, Claus Führer, Johan Åkesson, and Magnus Gäfvert. Assimulo. <http://www.assimulo.org>.
- [5] M. Arnold, B. Burgermeister, C. Führer, G. Hippmann, and G. Rill. Numerical methods in vehicle system dynamics: state of the art and current developments. *Vehicle System Dynamics*, 49(7):1159–1207, 2011.
- [6] Edda Eich-Soelner and Claus Führer. *Numerical Methods in Multibody Dynamics*. European Consortium for Mathematics in Industry (ECMI). Teubner, 1998.
- [7] C.W. Gear, B. Leimkuhler, and G.K. Gupta. Automatic integration of euler-lagrange equations with constraints. *Journal of Computational and Applied Mathematics*, 12-13(0):77 – 90, 1985.
- [8] Johan Åkesson, Karl-Erik Årzén, Magnus Gäfvert, Tove Bergdahl, and Hubertus Tummescheit. Modeling and optimization with Optimica and JModelica.org—languages and tools for solving large-scale dynamic optimization problem. *Computers and Chemical Engineering*, 34(11):1737–1749, November 2010.

Goal-oriented adaptivity for the Quasi-Continuum method

Arash Memarnahavandi¹, Fredrik Larsson¹, and Kenneth Runesson¹

⁽¹⁾Chalmers University of Technology, SE41296 Göteborg,
arashm@chalmers.se fredrik.larsson@chalmers.se kenneth.runesson@chalmers.se

Summary. A goal-oriented algorithm for error control in quantities of interest is developed for the Quasi-Continuum method, accounting for both discretization and quadrature. The procedure has been applied on the molecular statics problem pertinent to the homogenization of a graphene monolayer with sparse defects.

Key words: Quasi-Continuum, Goal-oriented adaptivity

Introduction

Mechanical properties of materials result from different mechanisms on vastly separated length scales. In order to consider virtual materials (not physically manufactured), or in order to predict complex behavior, on a higher length scale when the physics is better understood on a lower scale, homogenization (coarse-graining) is an important tool. The homogenization of atomistic systems can be used to derive continuum properties of materials, thus replacing the need for empirical continuum models. When there is a large separation of scales, i.e. when the length scales of the sought continuum solution by far exceeds the atomistic length scale, computational homogenization can be adopted, cf. [1]. Using this approach, the continuum stress-strain response can be obtained implicitly by considering a representative unit lattice (RUL). In the case of scale-mixing, i.e. when the continuum scale and the atomistic scale needs be resolved concurrently in the spatial domain, one popular method is the Quasi-Continuum (QC) method, cf. [2, 3]. It allows for coarse-graining of atomistic response in terms of interpolation on a "finite-element-type" mesh. The QC method is an approximation of the atomistic problem, which can thus be combined with a homogenization technique.

In this contribution we establish the macro-scale response using atomistic-to-continuum homogenization of a molecular statics problem (0 Kelvin temperature). In particular, we are interested in computing the representative response for different imperfections in a lattice. To this end, we wish to consider relatively large lattices on the atomistic scale. In order to facilitate such an analysis, we proceed along the lines of, e.g., [4] and devise a goal-oriented adaptive QC procedure for solving the atomistic problem inside the RUL. Within the goal-oriented framework it becomes natural to consider the macro scale (continuum) stress as the goal-quantity for which the error is quantified and controlled.

The model problem

We consider the discrete problem of relaxing all atoms $i \in \mathcal{I}$ inside a window, while all atoms in the surrounding (Cauchy-Born) frame \mathcal{CB} are prescribed according to a macroscopic (continuum) deformation gradient $\bar{\mathbf{F}}$, cf. figure 1. The potential energy of the system is defined by suitable inter-atomic potentials as $V(\{\mathbf{x}_i\})$. The molecular statics problem can be defined by

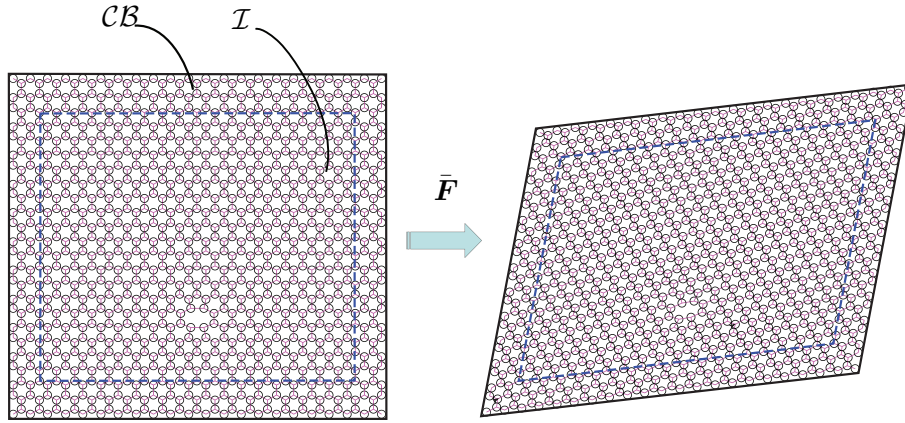


Figure 1. Illustration of the representative unit lattice containing a defect, with interior relaxed atoms (\mathcal{I}) inside a Cuchy-Born frame (\mathcal{CB}) with assumed homogeneous deformation.

the stationarity of the potential energy w.r.t. the unconstrained atom positions $\{\mathbf{x}_i\}_{i \in \mathcal{I}}$. The resulting strong form of the problem thus reads

$$\mathbf{f}_i = \mathbf{0} \quad \forall i \in \mathcal{I}, \quad \mathbf{x}_i = \bar{\mathbf{F}} \cdot \mathbf{X}_i \quad \forall i \in \mathcal{CB}, \quad (1)$$

where $\mathbf{f}_i := dV/d\mathbf{x}_i$ and \mathbf{X}_i is the reference positions of atom i . For a given solution, the macroscale continuum stress can be evaluated as

$$\bar{\mathbf{P}} = \frac{1}{|\Omega_{\square}|} \sum_{i \in \mathcal{CB}} \mathbf{f}_i \otimes \mathbf{X}_i, \quad (2)$$

where $|\Omega_{\square}|$ represents the reference volume occupied by the RUL.

We state the nonlinear problem in matrix notation as

$$\underline{f}(\underline{x}) = \underline{0}, \quad (3)$$

where \underline{f} and \underline{x} are the collected tensors \mathbf{f}_i and \mathbf{x}_i , respectively, for all atoms $i \in \mathcal{I}$.

The Quasi-Continuum method

The QC method is introduced in two steps. First, we consider the restriction of atom displacements in terms of the "representative atoms" as a model reduction, i.e., we describe the positions of all atoms in terms of discrete weights and the placements of certain so-called representative atoms. In short, the approximation can be described as the model reduction

$$\underline{x}_S = \underline{S} \underline{x}^R \quad \rightarrow \quad \underline{f}^R := \underline{S}^T \underline{f}(\underline{x}_S) = \underline{0}, \quad (4)$$

where \underline{x}_S is the placements of all the atoms, \underline{x}^R are the position of the representative atoms, \underline{S} is the typical model reduction matrix and \underline{f}^R represents the reduced forces.

More specifically, the model reduction matrix \underline{S} is typically built up by considering a linear interpolation of all atoms within an "element" being the region which vertices are the representative atoms. Based on this approximation, while accounting for the exact summation of all the bond-energies, we are able to compute goal-oriented error estimators in a straight-forward fashion based on an adjoint (dual) problem pertaining to the chosen output of interest. This computable error estimator pertains to a discretization error in the finite element method.

The second step in the QC method is that of quadrature. For large QC elements, i.e. for a large amount of atoms whose placements are governed by the same representative atoms, the

bond energy and its derivatives are typically computed using an appropriate discrete quadrature. In this presentation, we shall discuss different approximations where atoms inside a radius r from each representative atom is considered; namely force-based and energy-based cluster approximations. This approximation generates a model error (in addition to the discretization error discussed above) by introducing the approximation $\underline{f}(\underline{y}) \approx \underline{f}^{(r)}(\underline{y})$ for any vector \underline{y} . In summary, the approximate problem is stated as

$$\underline{f}^{\text{R},(r)} := \underline{S}^{\text{T}} \underline{f}^{(r)}(\underline{x}_{\mathcal{S},(r)}) = \underline{0}, \quad (5)$$

from which the approximate solution $\underline{x}_{\mathcal{S},(r)} = \underline{S} \underline{x}_{(R)}^{\text{R}}$ can be solved for.

A posteriori error estimation

Using the goal-oriented error estimation technique, cf. [6], the error in a quantity of interest can be estimated as

$$Q(\underline{x}) - Q(\underline{x}_{\mathcal{S},(r)}) \approx (\underline{x}^*)^{\text{T}} \underline{R}_{\mathcal{S}} + (\underline{x}^*)^{\text{T}} \underline{R}_{(r)} \quad (6)$$

where \underline{x}^* is the dual solution, and the discretization and model residuals are

$$\underline{R}_{\mathcal{S}} = -\underline{f}^{(r)}, \quad \underline{R}_{(r)} = \underline{f}^{(r)} - \underline{f}, \quad (7)$$

respectively. The derivation of the estimator relies on linearization of the problem as well as the quantity of interest together with the formulation of the dual problem, stated as

$$\underline{K}^{\text{T}} \underline{x}^* = \frac{\text{d}Q}{\text{d}\underline{x}}, \quad (8)$$

where $\underline{K} := \text{d}f/\text{d}\underline{x}$.

In this contribution, we consider the macroscale stress $\bar{\mathbf{P}}$ as the quantity of interest and compute approximate error estimators. In addition to computing the dual problem approximately, we also introduce an hierarchical approach, whereby we restrict the residuals to a refined QC-reduction

$$\underline{R}_{\mathcal{S}}, \underline{R}_{(r)} \rightarrow \left(\tilde{\underline{S}}\right)^{\text{T}} \underline{R}_{\mathcal{S}}, \left(\tilde{\underline{S}}\right)^{\text{T}} \underline{R}_{(r)} \quad (9)$$

(pertaining to the enriched approximation $\underline{x} \approx \tilde{\underline{S}} \tilde{\underline{x}}$). Finally, the model residual $\underline{R}_{(r)}$ is evaluated approximately by comparing to the forces computed for larger radii of the cluster approximation, i.e. $\underline{f} \approx \underline{f}^{(r+\Delta r)}$.

We remark that the error estimator is well suited for individual adaptation of the discretization (S) and quadrature (r), thus allowing for efficient overall error control.

Numerical investigations

As a model problem, we consider a mono-layer of graphene. The homogenization of the macroscale membrane forces, including initial relaxation, is considered for defective graphene lattices. The 0 Kelvin condition is considered by omitting lattice vibration and the Carbon-Carbon energy bonds are modeled via the Tersoff-Brenner potential, cf. [5], which involves next-nearest neighbor couplings. Preliminary results for adaptive QC-discretization, considering the discretization error pertinent to the model reduction, are presented in figure 2.

Future developments

Future developments include periodic boundary conditions on the RUL and the extension of the method to 3D material systems such as, e.g., crystalline metal.

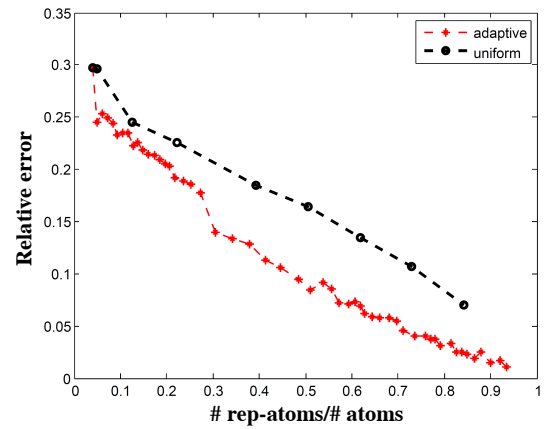
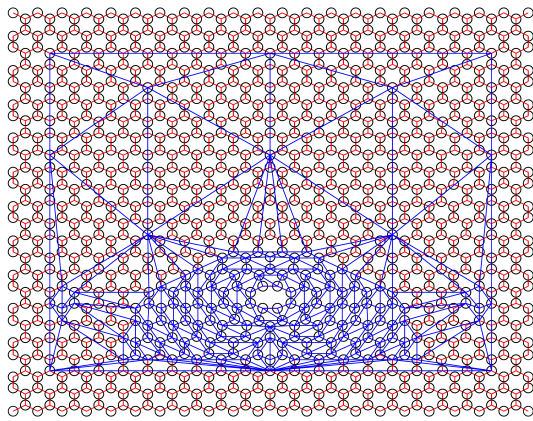


Figure 2. Example of an adaptive Quasi-Continuum mesh (left) and the convergence of the error in the macroscale stress (the quantity of interest) for uniform and adaptive mesh refinement (right).

References

- [1] R. Larsson and K. Samadikhah. Atomistic continuum modeling of graphene membranes. *Computational Material Science*, 50: 1744–1753, 2011.
- [2] R. Miller and E. Tadmor. The quasicontinuum method: Overview, applications, and current directions. *Journal of Computer-Aided Design*, 9: 203–239, 2002.
- [3] J. Knap and M. Ortiz. An analysis of the the quasicontinuum method. *Journal of the Mechanics and Physics of Solids*, 49: 1899–1923, 2001.
- [4] S. Prudhomme, P. Baumann and J. Oden. Error control for molecular statics problems. *International Journal for Multiscale Computational Engineering*, 4, 647–662, 2006.
- [5] D. Brenner. Empirical potential for hydrocarbons for use in simulating chemical vapor deposition of diamond films. *Physical Review B*, 42: 9458–9471, 1990.
- [6] F. Larsson and K. Runesson. Modeling and discretization errors in hyperelasto-(visco-)plasticity with a view to hierarchical modeling. *Computer Methods in Applied Mechanics and Engineering*, 193, 5283–5300, 2004.

A conservative quaternion-based time integration algorithm for rigid body rotations with implicit constraints

Martin Bjerre Nielsen and Steen Krenk

Department of Mechanical Engineering, Technical University of Denmark, Kgs. Lyngby, Denmark, e-mail: mbni@mek.dtu.dk

Summary. A conservative time integration algorithm for rigid body rotations is presented in a purely algebraic form in terms of the four quaternion components and the four conjugate momentum variables via Hamilton's equations. The introduction of an extended mass matrix leads to a symmetric set of eight state-space equations where constraints are embedded without explicit use of Lagrange multipliers. The algorithm is developed by forming a finite increment of the Hamiltonian, which defines the proper selection of increments and mean values that leads to conservation of energy and momentum. The accuracy and conservation properties are illustrated by examples.

Key words: finite rotations, quaternion parameters, conservative integration

Introduction

Time-integration of rigid body motion is of interest in numerous applications in engineering. Conservative integration procedures derived from an integrated form of the equations of motion are particularly attractive since they can be designed to provide energy and momentum conserving schemes, see e.g. [1] or [2]. However, the integration of finite rotations is complicated by the fact that they do not obey simple vector addition rules.

In this paper, a conservative time-integration algorithm for rigid body rotations is presented in terms of the four-component unit quaternions as this allows for a purely algebraic format without singularities. The governing equations are derived from the finite increment of the Hamiltonian in terms of the quaternion parameters and their four-component conjugate momentum vector yielding a symmetric set of eight state-space equations similar to [3]. However, the present formulation illustrates that the Lagrange multiplier - initially introduced in connection with the quaternion normalization constraint - can be eliminated by introduction of a projection operator in front of the load potential gradient. Furthermore, the formulation makes use of an extended mass matrix and role of the auxiliary inertia parameter is identified as an enforcing multiplier on the normalization constraint.

Equations of rigid body motion

Unit quaternions or Euler parameters are characterized as a four component quantity composed by a scalar part q_0 and a vector part \mathbf{q} in the form

$$\mathbf{q}^T = [q_0, \mathbf{q}^T]. \quad (1)$$

Only three independent parameters are required for describing three-dimensional rotations, and thus the four quaternion parameters are redundant and satisfy the normalization constraint

$$\mathbf{q}^T \mathbf{q} - 1 = 0. \quad (2)$$

A particularly attractive feature of the quaternion representation of rotations is that the angular velocity is a bi-linear form in terms of the quaternion \mathbf{q} and its time-derivative $\dot{\mathbf{q}}$, hence the kinetic energy can be expressed in the bi-quadratic format

$$\mathcal{T} = \frac{1}{2} \boldsymbol{\Omega}^T \mathbf{J} \boldsymbol{\Omega} = \frac{1}{2} \dot{\mathbf{q}}^T \mathbf{M}(\mathbf{q}, \mathbf{q}) \dot{\mathbf{q}}, \quad (3)$$

Here, an augmented inertia matrix $\mathbf{J} = \text{diag}[J_0, \mathbf{J}]$ is introduced with the auxiliary parameter $J_0 > 0$. This leads to a non-singular 4×4 mass matrix $\mathbf{M}(\mathbf{q}, \mathbf{q}) = 4 \mathbf{Q}(\mathbf{q}) \mathbf{J} \mathbf{Q}(\mathbf{q})^T$ where $\mathbf{Q}(\mathbf{q})$ denotes the orthogonal 4×4 matrix associated with quaternion pre-multiplication with \mathbf{q} . Several proposals for a specific value of J_0 based on physical reasoning have been given in the literature, e.g. [3]. However, the following examples demonstrate its role as a multiplier on the normalization constraint (2) rather than a physical parameter.

The conjugate four-component momentum vector follows as the partial derivative of the kinetic energy \mathcal{T} with respect to $\dot{\mathbf{q}}$ as

$$\mathbf{p} = \frac{\partial \mathcal{T}}{\partial \dot{\mathbf{q}}^T} = \mathbf{M}(\mathbf{q}, \mathbf{q}) \dot{\mathbf{q}}, \quad (4)$$

and is easily shown to satisfy the following orthogonality constraint

$$\mathbf{q}^T \mathbf{p} = 0. \quad (5)$$

This can be used to prove the alternative representations of the kinetic energy

$$\mathcal{T} = \frac{1}{2} \mathbf{p}^T \mathbf{M}^{-1}(\mathbf{q}, \mathbf{q}) \mathbf{p} = \frac{1}{2} \mathbf{q}^T \mathbf{M}^{-1}(\mathbf{p}, \mathbf{p}) \mathbf{q}, \quad (6)$$

where the roles of \mathbf{q} and \mathbf{p} can be interchanged without changing the value of the total product.

Hamilton's equations is a convenient starting point for deriving the equations of motion for rigid body rotations and can be expressed as the two first-order differential equations

$$\dot{\mathbf{q}} = \frac{\partial \mathcal{H}}{\partial \mathbf{p}^T}, \quad \dot{\mathbf{p}} = -\frac{\partial \mathcal{H}}{\partial \mathbf{q}^T}. \quad (7)$$

In the present formulation it is advantageous to use an augmented form of the Hamiltonian, where the normalization constraint (2) initially is included via a Lagrange multiplier λ

$$\mathcal{H} = \mathcal{T}(\mathbf{q}, \mathbf{p}) + \mathcal{V}(\mathbf{q}) + \lambda(\mathbf{q}^T \mathbf{q} - 1), \quad (8)$$

and where it is assumed that the external forces can be derived from a potential $\mathcal{V}(\mathbf{q})$.

The equations of motion then follow by differentiation of (8) using either of the bi-quadratic expressions for the kinetic energy (6). Hereby the kinematic and dynamic equations of motion are obtained as

$$\dot{\mathbf{q}} = \mathbf{M}^{-1}(\mathbf{q}, \mathbf{q}) \mathbf{p} \quad (9a)$$

$$\dot{\mathbf{p}} = -\mathbf{M}^{-1}(\mathbf{p}, \mathbf{p}) \mathbf{q} - \partial \mathcal{V} / \partial \mathbf{q}^T - 2\lambda \mathbf{q}. \quad (9b)$$

In addition, differentiation with respect to the Lagrange multiplier gives the normalization constraint (2).

A crucial step in the present formulation is that the Lagrange multiplier can be eliminated by using the time-derivative of the orthogonality condition (5) given by

$$\mathbf{q}^T \dot{\mathbf{p}} + \mathbf{p}^T \dot{\mathbf{q}} = -\mathbf{q}^T (\partial \mathcal{V} / \partial \mathbf{q}^T + 2\lambda \mathbf{q}) = 0. \quad (10)$$

This determines the Lagrange multiplier and substitution into the dynamic equation (9b) yields

$$\dot{\mathbf{p}} = -\mathbf{M}^{-1}(\mathbf{p}, \mathbf{p}) \mathbf{q} - \left(\mathbf{I} - \frac{\mathbf{q} \mathbf{q}^T}{\mathbf{q}^T \mathbf{q}} \right) \frac{\partial \mathcal{V}}{\partial \mathbf{q}^T}. \quad (11)$$

It is seen that the effect of eliminating the Lagrange multiplier essentially corresponds to introducing a projection operator in front of the external potential gradient that eliminates any component proportional to \mathbf{q} . Hereby the time-derivative of the orthogonality constraint (5) is satisfied for any external potential \mathcal{V} . In addition, it is easily verified that the time-derivative of the normalization constraint (2) is contained in the kinematic equation (9a) by pre-multiplication with \mathbf{q}^T and utilization of the orthogonality condition (5).

An energy and momentum conserving time-integration algorithm can be obtained by deriving the discretized form of the equations of motion via the finite increment of the augmented Hamiltonian over the time interval Δt . The kinetic energy (6) is a symmetric quadratic form, and thus the increment can be expressed as twice the product of the increment of the first factor and the mean value of the other factor. The potential gradient is introduced via its finite derivative $\partial\mathcal{V}^*/\partial\mathbf{q}$, and the Lagrange multiplier is eliminated by using the incremental form of (5) analogous to the equivalent continuous system. This ensures, that the two original time-dependent constraint conditions are contained in the discrete equations of motion via their increments, and thus, if the constraints are satisfied initially, they will also be satisfied at any later time step without recourse to Lagrange multipliers.

Examples

The accuracy and conservation properties are illustrated by considering two examples: First a freely rotating box is considered. The geometry and parameters are given in [2], and the motion is initiated as unstable rotation around its intermediate axis of inertia with a small perturbation.

The local components of the angular velocity are illustrated in Fig. 2. Initially the box rotates around the global x_3 -axis. At time $t = t_1$ the box tips over approaching a preliminary state with rotation about the initial rotation axis turned upside down, and at time t_3 the box returns to its initial configuration. This behavior is repeated in a periodic manner. While the kinetic energy, the global components of the angular momentum and the magnitude of the local angular momentum are conserved within a relative error of 10^{-12} , the algorithm exhibits a second-order period error. This can be evaluated as the difference between two turning points in

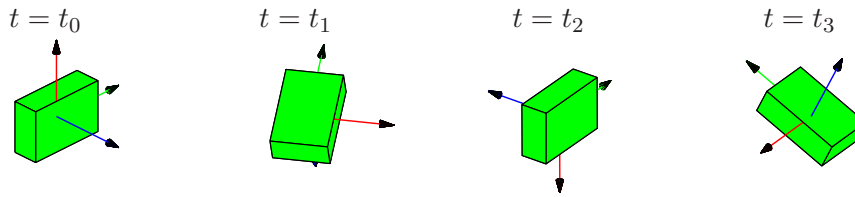


Figure 1. Motion of box at selected time steps, $\Delta t = 0.01$.

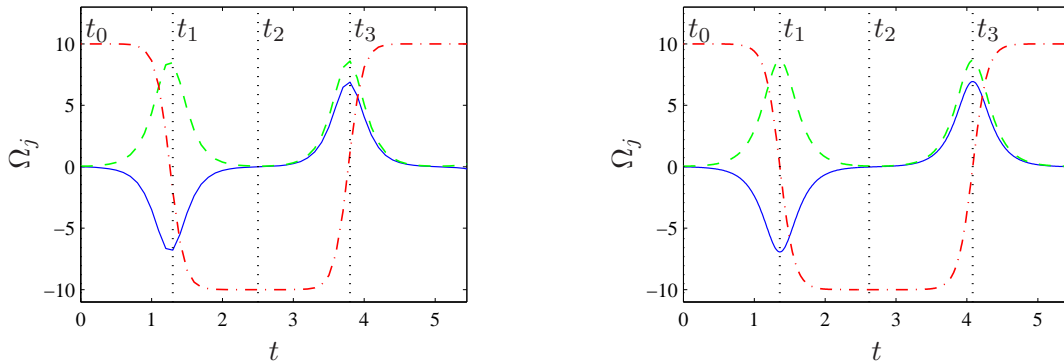


Figure 2. Local angular velocity components Ω_1 (—), Ω_2 (---), Ω_3 (-.-). (a) $\Delta t = 0.1$, (b) $\Delta t = 0.01$.

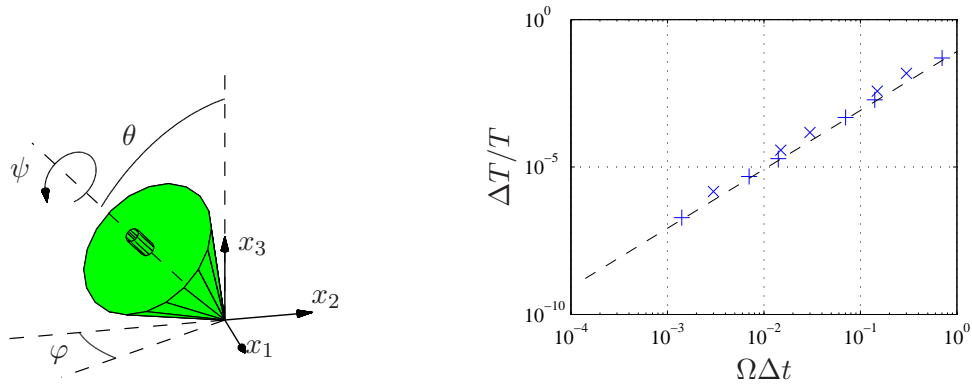


Figure 3. (a) Configuration of rotating top. (b) Relative period error. Precessing top (+), Fast top (\times), $(\Omega\Delta t)^2/12$ (---).

Fig. 2(a) and 2(b) corresponding to a shortening in time scale of approximately 8% when using $\Delta t = 0.1$. Furthermore, simulations illustrate that the error on the normalization constraint (2) decreases roughly in proportion to the increase in J_0 , while the orthogonality constraint (5) is satisfied within the numerical accuracy irrespective of value of J_0 .

The second example considers the motion of a top in a gravitational field with one point fixed. The motion is characterized in terms of the nutation angle θ , the precession angle φ and the spin angle ψ as illustrated in Fig. 3(a). The dimensions correspond to the ones used in [3], and two types of initial conditions have been applied: A fast top, i.e. $2\mathcal{V}/\mathcal{T} < 0.05$, and a purely precessing top, see e.g. [4]. For both cases the energy and the spatial component l_3 of the angular momentum are conserved within the iteration tolerance when the projection operator is included in front of the gradient of the gravitational potential in (11), and the second-order convergence is still retained in the presence of an external potential as illustrated in Fig. 3(b).

Conclusions

An energy and momentum conserving time-integration algorithm for rigid body rotations has been presented in terms of the four quaternions parameters and their conjugate momentum variables. It is illustrated that the two constraint conditions associated with the redundant parametrization are embedded in the equations of motions and do not require special attention apart from a projection of the external potential gradient. Furthermore, the role of the auxiliary inertia parameter has been revealed as a weighting factor on the normalization constraint and should be chosen large compared to the physical moments of inertia in order to ensure accurate satisfaction of the constraint condition.

References

- [1] J.C. Simo, K.K. Wong. Unconditionally stable algorithms for rigid body dynamics that exactly preserve energy and momentum, *International Journal for Numerical Methods in Engineering*, 31:19–52, 1991.
- [2] S. Krenk. A vector format for conservative time integration of rotations, In *Multibody Dynamics 2007, ECCOMAS Thematic Conference*, Milan, Italy, 1–12, 2007.
- [3] P. Betsch, R. Siebert. Rigid body dynamics in terms of quaternions: Hamiltonian formulation and conserving numerical integration, *International Journal for Numerical Methods in Engineering*, 79:444–473, 2009.
- [4] H. Goldstein, C. Poole, J. Safko. *Classical Mechanics*, 3rd ed., Addison Wesley, San Francisco, 2001.

Proceedings of the 25TH NORDIC SEMINAR
COMPUTATIONAL MECHANICS, 2012

Solid Mechanics I

Room: Stora Hörsalen, Thursday 25 October, 09:30 - 11:30



Free vibrations of non-isotropic plates with cut-outs

Alexandr V. Lebedev and Andrei L. Smirnov

St. Petersburg State University, Russia 198904, University Ave. 28,
privater@mail.ru, a.l.smirnov@mail.ru

Summary. The research refers to free vibrations off non-homogeneous (weakened with holes) isotropic and non-isotropic elastic thin plates. The purpose of the study is to examine the effect of shape, area, position, number and proportions of the holes, ratio of the plate sides and boundary conditions on free vibrations of plates. The plates are considered to be thin enough to apply 2D Kirchhoff-Love theory. Mathematically vibration problems for membranes and plates with cutouts are reduced to solution of the eigenvalue problems for nonsimply connected domains, which are solved in the research with analytic (when possible), asymptotic and numerical methods.

Key words: plate vibrations, plates with, cut-outs

Square plate

We start our study with a square plate weakened with a central square hole. Let the plate side length be a and the hole side length be d , $w(x, y)$ denotes the plate deflection. In [1] the formula for free vibration frequencies for simply supported rectangular plate with a rectangular hole has been reported. The deflection was represented in the form

$$w(x, y) = f \sin(\alpha x) \sin(\beta y) \quad (1)$$

, where $\alpha = m\pi/a$, $\beta = n\pi/b$. Then Rayleigh-Ritz method was applied to get the following formula for natural frequencies

$$\omega^2 = \frac{D(s(S - S_1) - c/(4\alpha\beta)(2\rho + m_1m_2) + 2(1 - \mu)\alpha\beta\rho}{\gamma h(S - S_1 - 1/(4\alpha\beta)(2\rho + m_1m_2)}, \quad (2)$$

where $c = (\alpha^2 + \beta^2)^2$, $S = ab$ — the plate area, $S_1 = (x_2 - x_1)(y_2 - y_1)$ — the hole area, $m_1 = \sin 2\alpha x_1 - \sin 2\alpha x_2$, $m_2 = \sin 2\alpha y_1 - \sin 2\alpha y_2$, $\rho = m_1(y_2 - y_1)\beta + m_2(x_2 - x_1)\alpha$, D — the plate cylindrical stiffness, γ — the plate density, h — the plate thickness. x_1, x_2, y_1, y_2 — the coordinates of the hole vertices. It is easy to check that for a homogeneous plate one gets the classical formula for natural frequencies of a rectangular plate [2].

It appears that this formula well agrees with numerical results for rectangular plates, but for some cases badly agrees with numerical results for a square plate. In Fig.1 we plot the values for several low free frequencies obtained with formula (1) (dashed lines) and by FEM (solid lines) vs the hole size. For homogeneous square plate with symmetric boundary conditions the free frequencies are double. The hole makes some frequencies to split and some not. It depends on the wave number of the vibration mode. The frequencies split when both wave numbers are both either different odd or different even numbers. In this case formula (1) works especially badly since the one term representation of the deflection (1) is insufficient.

It may be proved that for small hole area the dependence of free frequencies on the hole side length is

$$\omega = \omega_0 + \omega_1 d^2 + \omega_2 d^4 + \dots ,$$

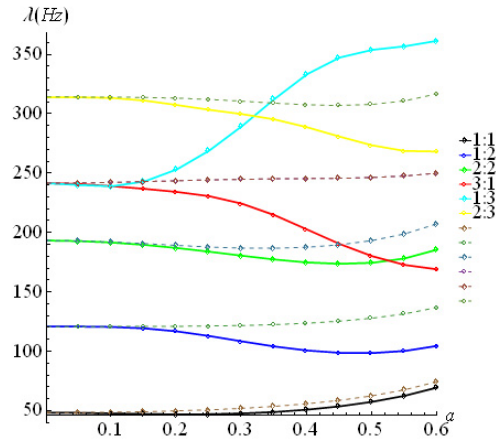


Figure 1. Free frequencies of a free supported square plate vs hole size

where $\omega_1 = \pm\Lambda \neq 0$, if $n \neq m$ and n, m are both even or odd.

Rectangular plate

For rectangular plate we study the effect of the hole ratio and multiple cut-outs on free frequencies. Consider the simply supported rectangular plate with the side length ratio 2:1, the hole area is constant $S_1 = 0.0625$, the hole side ratio $a/b = \sqrt{1 + \varepsilon^2}$, where $\varepsilon = 0$ for the square hole and $\varepsilon < 0$ for the hole stretched on the y -direction. The results are plotted in Fig.2 The

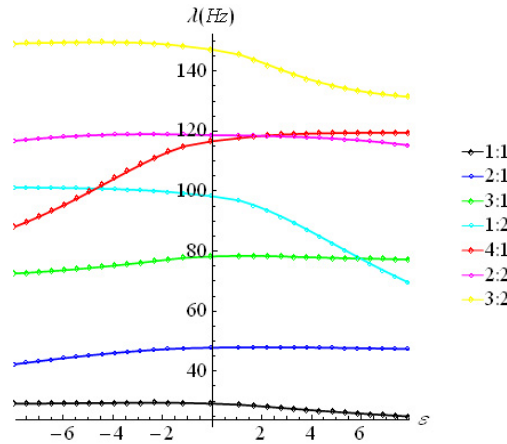


Figure 2. Free frequencies of a free supported rectangular plate vs hole ratio

hole ratio effects the most significantly on the higher frequencies when the difference between vibration mode numbers is large.

For the multiple cut outs the effect of the hole numbers is complex. We consider the case when the total holes area is constant. Consider simply supported plate with the side ratio 2:1. For that for small total area the value of the fundamental frequency converges to some constant value when the number of holes increases. That is valid for holes set either in x (solid lines) or y (dashed lines) directions. For larger holes area the free frequency decreases significantly with the number of holes in x directions since the cut outs for large hole numbers practically cut the plate. The new “edge” becomes weakly supported that makes the frequency goes down.

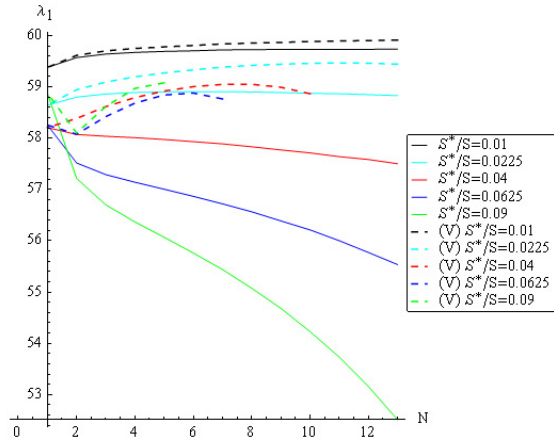


Figure 3. Free frequencies of a free supported rectangular plate vs hole numbers

Circular plate

For circular plate we study the effect of the hole area size and multiple cut-outs on free frequencies. Consider the clamped circular plate with the radius R and the central circular hole with area S^* . In this case the analytical solution may be obtained in Bessel functions. The effect of the hole size on four lower frequencies obtained analytically (red dots) [5] and with FEM (solid lines) is presented in Fig.4. For large values of the hole area all frequencies increase with the hole

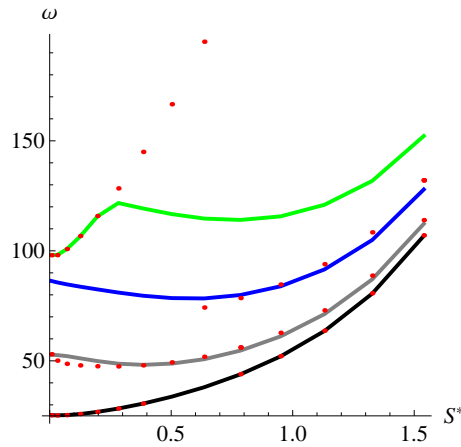


Figure 4. Free frequencies of a clamped circular plate vs hole size

area. It means that the loss of the plate mass plays more important role than the loss on the plate stiffness. But for small values of the hole area some frequencies slightly decrease. There is no significant difference (at least for the lower frequencies) between the results obtained for the circular, elliptic or multiple holes of same total area, if the area is relatively small. However the split of the initially double frequencies happens.

Elliptic plate

For free frequencies of the homogenous elliptic plate the approximate formula was obtained in [3]. The problem can be solved using Mathieu functions [4]. Here we study the effect of the hole area size and the shape of the hole and discuss only the results for the clamped elliptic plate with the central circular hole of radius r . Since the elliptic plate with the circular hole is not symmetric system all of the frequencies are simple. However for the large values of the hole size

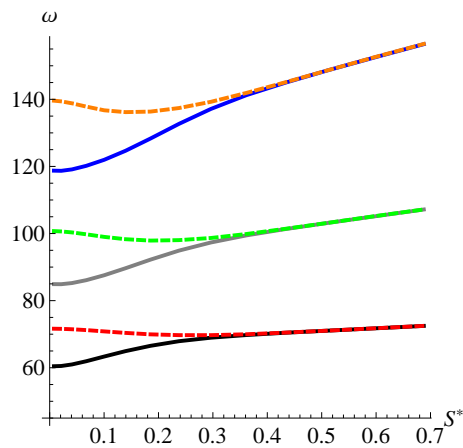


Figure 5. Free frequencies of a clamped elliptic plate vs hole size

the coupled frequencies merge. Before that the odd frequencies decrease and the even increase with the hole area. For elliptic plate with central elliptic hole, the frequencies grow faster when the hole and the plate ellipses are coaxial.

Conclusions

The most important and interesting is the effect of the area of a hole on natural frequencies and modes of free vibrations. It appeared that the natural frequencies may either increase or decrease with the hole area since the cutout affects both the stiffness and the mass of a plate. Special attention is devoted to frequencies those are doubled for homogeneous plates, for example, frequencies of the square plates with similar boundary conditions on all edges. Depending on the wave numbers frequencies may split (or may not) as the hole area increases. For small cutout area the asymptotic formula for natural frequencies has been obtained and the asymptotic results have been compared with the results of numerical analysis. The values of the natural frequencies appear to be very sensitive to proportion of the hole and plate. The change of the ratio may cause the switch of the vibration modes. For elliptic plates, stretching the plate and the hole along different axes makes frequency to go up faster, then stretching the plate and the hole along one axis.

References

- [1] I.N. Preobrazhensky, *Buckling and vibrations of plates and shells with the holes*. M.: Mashinostroyeniye, 1981 (in Russian).
- [2] J.N. Reddy. *Theory and analysis of elastic plates and shells*. CRC Press, Taylor and Francis, 2007.
- [3] L. Collatz, *Numerische Behandlung Von Differentialgleichungen*. Springer Verlag; Second Edition, 1955.
- [4] V.A. Kovalev. Dynamics of Multilayered Thermoviscoelastic Plates. *Izv. Saratov. Univ. Mat. Mekh. Inform*, 9:4(1):61–78, 2009 (in Russian).
- [5] C.G. Chizhevsky. *Analysis of circular and annular plates*. Mashinostroyeniye, 1977 (in Russian).

Wave propagation and dispersion in microstructured solids

Arkadi Berezovski¹, Jüri Engelbrecht¹, and Mihhail Berezovski^{1,2}

⁽¹⁾Centre for Nonlinear Studies, Institute of Cybernetics at Tallinn University of Technology, Akadeemia tee 21, 12618 Tallinn, Estonia, Arkadi.Berezovski@cs.ioc.ee

⁽²⁾Department of Mathematical Sciences, Worcester Polytechnic Institute, 100 Institute Rd, Worcester, MA, 01609, USA, mberezovski@wpi.edu

Summary. A series of numerical simulations is carried on in order to understand the accuracy of dispersive wave models for microstructured solids. The computations are performed by means of the finite-volume numerical scheme, which belongs to the class of wave-propagation algorithms. The dispersion effects are analyzed in materials with different internal structures: microstructure described by micromorphic theory, regular laminates, laminates with substructures, etc., for a large range of material parameters and wavelengths.

Key words: microstructured solids, wave dispersion, numerical simulation

Introduction

Microstructural effects are observed in wave propagation in solids when the wavelength of a travelling signal becomes comparable with the scale of material heterogeneities. A vivid example of the influence of microstructure on wave propagation is the wave dispersion that profoundly alters both the shape and the velocity of propagating waves. The most recognizable signature of the wave dispersion is that the phase and group velocities of propagating waves differ from each other. The dispersive effects of wave propagation in microstructured solids become non-negligible for sufficiently high frequencies.

Wave propagation in heterogeneous solids has been a subject of considerable research for many years. However, micro-structural details are rarely taken into account in large-scale structural dynamics or dynamic impact simulations. The reason is the enormous complexity of wave phenomena in highly heterogeneous media. There exist two alternative approaches to the description of microstructural effects on wave propagation in solids. The first one is focused on the determining so-called effective properties of a material. It is expected that these averaged or smoothed properties reflect in some global sense the response of specimens of the material to external loads. Another approach to involve microstructural effects into the description of wave propagation is provided by higher order or generalized theories of elastic continua. These theories have been proposed in 1960s [1, 2], and later clarified, classified, and extended [3]. The well-established framework for higher grade and higher order theories is, however, accompanied by too many usually undetermined phenomenological coefficients. Nevertheless, dispersive wave equations in solid mechanics are based either on a homogenization procedure or on a generalized continuum theory.

Dispersive wave models

Wave propagation in a homogeneous medium is a well known phenomenon in mechanics. The corresponding one-dimensional wave equation is a classical example of hyperbolic partial differ-

ential equations in textbooks

$$u_{tt} = c^2 u_{xx}, \quad (1)$$

where u is the displacement, c is the elastic wave speed and subscripts denote derivatives. The wave equation (1) possesses no dispersion. Considering a harmonic wave

$$u(x, t) = \hat{u} \exp[i(kx - \omega t)] \quad (2)$$

with wave number k and frequency ω , we obtain the dispersion relation

$$\omega^2 = c^2 k^2. \quad (3)$$

It is easy to see that here the group velocity $\partial\omega/\partial k$ is equal to the phase velocity c , which means that no dispersion is present.

To describe wave propagation in heterogeneous materials reflecting dispersion effects, several modifications of the wave equation are proposed. The simplest generalization of the wave equation is the linear version of the Boussinesq equation for elastic crystals (cf. [4])

$$u_{tt} = c^2 u_{xx} + c^2 l^2 A_{11} u_{xxxx}, \quad (4)$$

where l is an internal length parameter and A_{11} is a dimensionless coefficient. The dispersion relation is obtained by using again the harmonic wave solution (2)

$$\omega^2 = c^2 k^2 - c^2 l^2 A_{11} k^4. \quad (5)$$

This dispersion relation is nonlinear, which means that phase and group velocities are different. Another generalization of the wave equation is the Love-Rayleigh equation for rods accounting for lateral inertia (cf. [5], p.428)

$$u_{tt} = c^2 u_{xx} + l^2 A_{12} u_{xxtt}, \quad (6)$$

where A_{12} is again a dimensionless constant. The corresponding nonlinear dispersion equation has the form

$$\omega^2 = c^2 k^2 - l^2 A_{12} \omega^2 k^2. \quad (7)$$

A more general equation combining the two dispersion models gives

$$u_{tt} = c^2 u_{xx} + c^2 l^2 A_{11} u_{xxxx} + l^2 A_{12} u_{xxtt}. \quad (8)$$

Similar model proposed by Engelbrecht and Pastrone [6] introduces additionally a contribution of microstructure on slowing down of the propagation velocity c_A^2

$$u_{tt} = (c^2 - c_A^2) u_{xx} + c^2 l^2 A_{11} u_{xxxx} + l^2 A_{12} u_{xxtt}. \quad (9)$$

Accordingly, it has the dispersion relation in the form

$$\omega^2 = (c^2 - c_A^2) k^2 - c^2 l^2 A_{11} k^4 - l^2 A_{12} \omega^2 k^2. \quad (10)$$

Due to three additional terms combined, the last model has larger dispersion properties.

In its turn, the Maxwell-Rayleigh model of anomalous dispersion [4] introduces in consideration the four-order time derivative

$$u_{tt} = c^2 u_{xx} + \frac{l^2 A_{22}}{c^2} (u_{tt} - c^2 u_{xx})_{tt}. \quad (11)$$

Four-order time derivatives are included also in the "causal" model for the dispersive wave propagation proposed by Metrikine [7]

$$u_{tt} = c^2 u_{xx} - c^2 l^2 A_{11} u_{xxxx} + l^2 A_{12} u_{xxtt} - \frac{l^2}{c^2} A_{22} u_{tttt}, \quad (12)$$

and in the model based on the Mindlin theory of microstructure [8], which can be represented in the form

$$u_{tt} = (c^2 - c_A^2) u_{xx} + l^2 P (u_{tt} - c^2 u_{xx})_{xx} + \frac{l^2}{c^2} Q (u_{tt} - c^2 u_{xx})_{tt}. \quad (13)$$

Here P and Q are dimensionless constants. It is clear that corresponding dispersive relations are nonlinear.

As it is shown recently [9], the last two models for dispersive wave propagation can be unified as follows

$$u_{tt} = (c^2 - c_A^2) u_{xx} + l^2 P (u_{tt} - c^2 u_{xx})_{xx} + \frac{l^2}{c^2} Q (u_{tt} - c^2 u_{xx})_{tt} + c^2 l^2 R u_{xxxx}. \quad (14)$$

It is clear that the unified model (14) generalizes both approaches (12) and (13).

Numerical simulations

In order to understand the accuracy of the dispersive models, a series of numerical simulations is carried on. The computations are performed by means of the finite-volume numerical scheme, which belongs to the class of wave-propagation algorithms [10]. Details of the numerical scheme can be found in [11]. The dispersion effects of 1D waves are demonstrated in materials with different internal structures: microstructure described by micromorphic theory, regular laminates, laminates with substructures, etc.

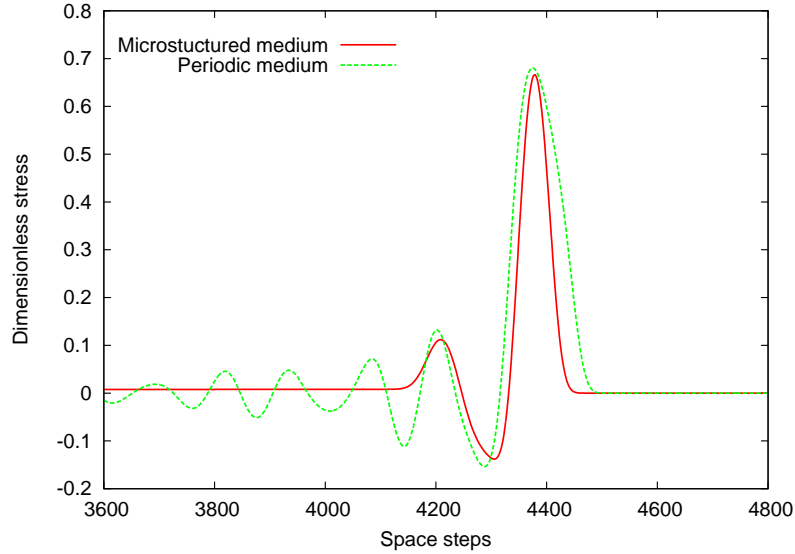


Figure 1. Deformed shape of an initially Gaussian stress pulse in periodic and microstructured solids.

One of the important problems is to compare the results obtained by means of various models. As an example, the comparison of a direct numerical simulation of a Gaussian stress pulse propagation along the elastic bar containing an inhomogeneous part constructed by periodically alternating layers and a computation based on the Mindlin-type microstructure model (14) is shown in Fig.1.

As one can see, the effect of microstructure in the model manifests itself only locally, whereas the dispersion in the periodic laminate is non-local due to consecutive reflections. In principle, the localization of the microstructure influence is expected, since the presence of the microstructure is invisible in the absence of loading.

In order to get matching results, one should critically revise the free energy function in the micromorphic theory for adequate modelling of interaction forces between macro- and microstructures. In the considered case, the pulse length is 5 times longer than the inhomogeneity size. This particular case was chosen because it clearly shows the synergy of the two microstructure models unified in [9]. The matching results are obtained by modifying the coupling between macro- and microstructures including also the dependence on gradients of the internal variables. The correlation between models is analyzed in detail for a large range of material parameters and wavelengths.

The research was supported by the EU through the European Regional Development Fund and by the Estonian Science Foundation (grant No. 8702).

References

- [1] R.D. Mindlin. Microstructure in linear elasticity. *Archive for Rational Mechanics and Analysis*, 16:51–78,1964.
- [2] A.C. Eringen and E.S. Suhubi. Nonlinear theory of simple microelastic solids I & II. *International Journal of Engineering Science*, 2:189–203,389–404,1964.
- [3] S. Forest. Micromorphic approach for gradient elasticity, viscoplasticity and damage. *Journal of Engineering Mechanics*, 135:117–131,2009.
- [4] G.A. Maugin. On some generalizations of Boussinesq and KdV systems. *Proceedings of the Estonian Academy of Sciences. Physics. Mathematics*, 44:40–55,1995.
- [5] A.E.H. Love. *Mathematical Theory of Elasticity*. Dover, New York, 1944.
- [6] J. Engelbrecht and F. Pastrone. Waves in microstructured solids with nonlinearities in microscale. *Proceedings of the Estonian Academy of Sciences. Physics. Mathematics*, 52:12–20,2003).
- [7] A.V. Metrikine. On causality of the gradient elasticity models. *Journal of Sound and Vibration*, 297:727–742,2006.
- [8] J. Engelbrecht, A. Berezovsk, F. Pastrone, M. Braun. Waves in microstructured materials and dispersion. *Philosophical Magazine*, 85:4127–4141,2005.
- [9] A. Berezovski, J. Engelbrecht, and M. Berezovski. Waves in microstructured solids: a unified viewpoint of modeling. *Acta Mechanica*, 220:349–363,2011.
- [10] A. Berezovski. Thermodynamic interpretation of finite volume algorithms. *Journal of Structural Mechanics (Rakenteiden Mekaniikka)*, 44/3,156–171,2011.
- [11] M. Berezovski, A. Berezovski and J. Engelbrecht. Waves in materials with microstructure: numerical simulation. *Proceedings of the Estonian Academy of Sciences*, 59/2, 99–107,2010.

Blowup of the sensitivity of the elastic energy with respect to the uncertainties in the Poisson's ratio

O. Mali¹ and S. Repin^{1,2}

⁽¹⁾University of Jyväskylä, Department of Mathematical of Information Technology, Mattilanniemi 1, Agora (4th floor), 40014 JY, Finland, olli.mali@jyu.fi, serepin@jyu.fi

⁽²⁾Steklov Institute, St. Petersburg department, RAS, 27 Fontanka, 191023, St. Petersburg, Russia, repin@pdmi.ras.ru

Summary. This paper describes the phenomena of the sensitivity blowup of the elastic energy with respect to the uncertain Poisson's ratio on the incompressibility limit. Moreover, we present two classes of boundary conditions for which the behavior of the elastic energy increment on the incompressibility limit is significantly different. The main tools to derive the results are the so called functional a posteriori error estimates.

Key words: incompletely known data, Poisson's ratio, linear elasticity

Introduction

In real life simulations, the material data is often generated by measurements or the material itself is not homogeneous as in, e.g., geomechanics, and exact parameters are difficult to define. This motivates us to study the errors generated by incompletely known data.

We consider the linear elasticity model defined by equations

$$-\operatorname{div} \boldsymbol{\sigma} = \mathbf{f}, \quad \text{in } \Omega \subset \mathbb{R}^d \quad (1)$$

$$\boldsymbol{\sigma} = \mathbf{L}\boldsymbol{\epsilon}(\mathbf{u}), \quad \text{in } \Omega \quad (2)$$

$$\boldsymbol{\epsilon}(\mathbf{u}) = \frac{1}{2} (\operatorname{grad} \mathbf{u} + (\operatorname{grad} \mathbf{u})^T), \quad \text{in } \Omega \quad (3)$$

$$\mathbf{u} = \mathbf{g}, \quad \text{on } \Gamma_D \quad (4)$$

where in the constitutive relation (2) the elasticity tensor \mathbf{L} is not completely known. In the case of isotropic material, \mathbf{L} can be expressed with the help of two material parameters (Lame constants):

$$\mathbf{L}\boldsymbol{\epsilon}(\mathbf{u}) = \lambda \operatorname{div} \mathbf{u} \mathbf{I} + 2\mu \boldsymbol{\epsilon}(\mathbf{u}).$$

Another pair of material parameters often used in engineering is the Young's modulus E and the Poisson's ratio ν , which present λ and μ in the form

$$\lambda = \frac{E\nu}{(1+\nu)(1-2\nu)}, \quad \mu = \frac{E}{2(1+\nu)}.$$

In our study, we are concerned on the incompletely known Poisson's ratio $\nu \in [0, \frac{1}{2})$. In particular, we are interested on the behavior on the incompressibility limit $\nu \rightarrow \frac{1}{2}$. For simplicity, we assume that $\mathbf{f} = \mathbf{0}$ and the elastic energy is

$$\mathcal{E}^\nu(\mathbf{w}) := \frac{1}{2} \int_{\Omega} \mathbf{L}^\nu \boldsymbol{\epsilon}(\mathbf{w}) : \boldsymbol{\epsilon}(\mathbf{w}) \, dx.$$

We use the superscript ν to denote the dependence of various quantities on the Poisson's ratio. The set of admissible displacements for the problem (2)–(4) is

$$V_g := \{\mathbf{w} \in H^1(\Omega, \mathbb{R}^d) \mid \mathbf{u} = \mathbf{g}, \text{ on } \Gamma_D\},$$

where the boundary conditions are satisfied in the sense of traces. The variational form of the problem is to find $\mathbf{u}^\nu \in V_g$ such that

$$\mathcal{E}^\nu(\mathbf{u}^\nu) = \min_{\mathbf{w} \in V_g} \mathcal{E}^\nu(\mathbf{w}).$$

Lower estimate of the energy increment

Our main goal is to estimate energy sensitivity with respect to the ν and to show that for some classes of linear elasticity problems exact solutions are extremely sensitive with respect to the small variations of ν . We compare the energies of two solutions \mathbf{u}^ν and $\mathbf{u}^{\nu+\delta}$, which are generated by problems, where Poisson's ratios are ν and $\nu + \delta$, respectively. The quantity of interest is the energy increment, i.e.,

$$\Delta_\delta^\nu \mathcal{E} := \frac{\mathcal{E}^{\nu+\delta}(\mathbf{u}^{\nu+\delta}) - \mathcal{E}^\nu(\mathbf{u}^\nu)}{\delta}$$

and its normalized counterpart

$$\frac{\Delta_\delta^\nu \mathcal{E}}{\mathcal{E}^\nu}.$$

In the following theorem, we present a lower bound for the normalized energy increment.

Theorem 1 *Let $\mathbf{u}_g \in V$ be a function with the minimal divergence norm, i.e.,*

$$\|\operatorname{div} \mathbf{u}_g\| = \min_{\mathbf{u} \in V_g} \|\operatorname{div} \mathbf{u}\|.$$

Then, for sufficiently small positive δ ,

$$\Delta_\delta^\nu \mathcal{E} \geq \frac{1}{2} C_1^\nu \|\operatorname{div} \mathbf{u}_g\|^2 - C_2^\nu \|\boldsymbol{\epsilon}(\mathbf{u}_g)\|^2.$$

Since the right hand side does not depend on δ , we can pass to the limit, $\delta \rightarrow 0$,

$$\frac{\partial \mathcal{E}^\nu}{\partial \nu} \geq \frac{1}{2} C_1^\nu \|\operatorname{div} \mathbf{u}_g\|^2 - C_2^\nu \|\boldsymbol{\epsilon}(\mathbf{u}_g)\|^2,$$

where

$$C_1^\nu := \frac{4(1 + 2\nu^2)}{(5 + 2\nu)(1 + \nu)(1 - 2\nu)^2}$$

$$C_2^\nu := \frac{1}{(1 + \nu)^2} \left(1 + \frac{(1 + 2\nu^2)(1 - 2\nu)}{d(2 + \nu + 2\nu^2)} \right).$$

Proof of Theorem 1 can be found from [2]. It exploits functional a posteriori error estimates, which are widely discussed in [3, 4] and references therein. We note that if $\|\operatorname{div} \mathbf{u}_g\| = 0$, the elastic energy is bounded for all $\nu \in [0, \frac{1}{2})$. Indeed,

$$\mathcal{E}^\nu(\mathbf{u}^\nu) \leq \mathcal{E}^\nu(\mathbf{u}_g) = \frac{1}{1 + \nu} \left(\frac{\nu}{1 - 2\nu} \|\operatorname{div} \mathbf{u}_g\|^2 + \|\boldsymbol{\epsilon}(\mathbf{u}_g)\|^2 \right).$$

Since $\|\operatorname{div} \mathbf{u}_g\| = 0$, we find that

$$\mathcal{E}^\nu(\mathbf{u}^\nu) \leq \mathcal{E}^\nu(\mathbf{u}_g) = \frac{1}{1 + \nu} \|\boldsymbol{\epsilon}(\mathbf{u}_g)\|^2.$$

Concluding remarks

Theorem 1 indicates that if $\|\operatorname{div} u_g\| > 0$, the sensitivity of the energy with respect to the Poisson's ratio tends to infinity on the incompressibility limit. It is important to realize that this observation is relevant already before the asymptotic limit. The uncertainty of the Poisson's ratio may generate an accuracy limit for the solution that makes it impossible to obtain results by desired engineering accuracy. We want to emphasize that the accuracy limit generated by the incompletely known data is not related to any numerical method (it is another topic to devise numerical methods that are able to produce high quality approximations for nearly incompressible materials, see, e.g., [1]), but is a fundamental property of the problem itself.

References

- [1] R. Kouhia and R. Stenberg. A linear nonconforming finite element method for nearly incompressible elasticity and stokes flow. *Computer Methods in Applied Mechanics and Engineering*, 124(3):195–212,1995.
- [2] O. Mali and S.Repin, *Blowup of the energy increment caused by uncertainty of the Poisson' ratio in elasticity problems*, Russian J. Numer. Anal. Math. Modelling 26, no. 4, pp. 413-425, 2011.
- [3] P. Neittaanmäki and S. Repin: *Reliable Methods for Computer Simulation, Error Control and A Posteriori Estimates*, Elsevier, 2004.
- [4] S. Repin, *A Posteriori Estimates for Partial Differential Equations*, Walter de Gruyter, 2008.

Recent advances in the experimental analysis of the mechanics of sand

Stephen A. Hall¹ and Jonathan Wright²

⁽¹⁾ Division of Solid Mechanics, Lund University and European Spallation Source AB,
P.O. Box 118, SE-221 00 Lund, Sweden, Stephen.Hall@solid.lth.se

⁽²⁾ European Synchrotron Radiation Source, 6 Rue Jules Horowitz, 38000 Grenoble, France,
wright@esrf.fr

Summary. New experimental tools are now enabling analysis of the fundamental mechanics of granular media at the key controlling scale, i.e., that of the grains. X-ray tomography imaging during loading, linked with volumetric image analysis, already permits analysis of continuum strain and porosity fields, individual grains kinematics and the structural organisation of the contacting grains. New developments are now leading towards the detection and, eventually, quantification of force transfer through real 3D granular materials, such as sand. These different approaches and example results are presented including original results on intra-granular strain measurement.

Key words: granular media, experimental mechanics, x-ray tomography, image analysis, x-ray diffraction

Introduction

Granular materials, such as sand, are complex systems in which relatively simple building blocks (i.e., contacting particles - sand grains) interact collectively to produce structural evolution over a range of different spatial and temporal scales from contacting-particle interactions to intermediate (meso-) scale communication and structure formation (e.g., localised deformation such as shear bands) to longer-range pattern formation. These kinematic effects are associated with the build-up of stress and possible relaxation via structural reorganisation and particle damage. Accurate simulation of the mechanical behaviour of granular systems is, thus, non-trivial and remains a quite open challenge. However, many standard (and not-so standard) modelling approaches exist, but there is also a need for experimental data, at the appropriate scales, to identify and characterise the important mechanisms controlling the material responses, to provide ground truth and to identify model input parameters. Unfortunately, traditional experimental methods fall short of providing the necessary data for these ambitious modelling approaches, as they provide information relating to the macro-scale, “averaged” response and no details on internal structure evolution or deformation mechanisms, e.g., shear-band development, individual grain kinematics and force-transmitting contact distributions.

An overview of different recent experimental analyses will be presented that provide extended insight into the mechanics of granular media (specifically sand) over a range of scales; from the sample-scale down to that of the grains and grain-contacts and further down to the internal deformation of the grains themselves. The techniques used are “full-field” approaches involving in-situ x-ray micro-tomography, 3D-volumetric digital image analysis/correlation and grain tracking, in-situ 3D x-ray diffraction and in-situ, spatially-resolved neutron diffraction. These approaches permit characterisation of phenomena including dilation, grain rotation and grain-contact evolution associated with strain localisation plus new data and analyses that are now providing new insight into inter-granular force transfer mechanisms.

Full-field measurement of strain localisation, dilation and grain kinematics

In experimental analysis of sand, x-ray tomography has been used since the early 1980s to reveal localisation patterning and answer key questions on concepts of “critical state”; see [2] for a review. In these early studies the image resolution possible was such that the studied sands had to be considered as continua in both the imaging sense - grains were not seen individually and a volume average of grains and porosity was given at each voxel (the 3D version of pixels) - and the mechanics sense - any discrete or strongly-discontinuous deformation was blurred out by the spatial resolution. Such approaches provided good insight into emergent structures associated with deformation, e.g., localisation patterns (if accompanied by a sufficient density change), but less into the underlying mechanisms.

X-ray tomography has advanced steadily, since its advent in the 1970s, such that now micro-tomography and sub-micron tomography is possible using both synchrotron and laboratory facilities. For sands, whose grain-sizes are in the range of 100s μm (and bigger) micro-tomography with resolutions of μm to 10s μm^3 scale now allows sand to be studied as a discrete material, i.e., one made up of individual, discrete particles. For example, [7] presented micro tomography images of sand grains inside a shear band, showing organised structures that had only previously been observed in 2D thin sections. In work by [5][6][1] x-ray micro-tomography imaging performed during triaxial compression tests on samples containing about 50 000 to 100 000 grains of sand, imaged with voxel sizes of around $14 \times 14 \times 14 \mu m^3$, permitted clear identification of individual grains (with, in the order of, 5000 voxels per grain). Analysis of these data using 4D digital image analysis and correlation techniques (including both continuum and discrete 3D-volumetric Digital Image Correlation, DIC) allowed extraction of quantitative measures of deformation phenomena and structural evolution such as porosity evolution, grain-contact network development, tensor strain fields and individual grain kinematics.

Force transfer analysis

In recent years there has been much discussion of force transmission in granular media and, in particular the development of “force chains” and their importance in controlling the mechanics at the larger scale (e.g., [9]). Force chains can be thought of as spatially continuous lines of forces between contacting grains, by which the boundary forces are transmitted through granular masses. These have been observed in experiments using photoelastic materials (e.g., [3]) and in discrete element method (DEM) simulations (e.g., [9]). The buckling of such force-chains has been cited as a key mechanism associated with localised deformation and failure of granular bodies (e.g., [7]). To understand such micro-scale mechanisms in granular materials requires the ability to measure (i) the kinematics (particle displacements and rotations) (ii) the force distribution through the granular assembly. Whilst insight into both can be gained from DEM simulations, these are just models and can, therefore, only help in the absence of real experimental data. Photoelasticity experiments can be also very insightful, but, whilst “real”, are highly simplified. For real granular materials (i.e., sands in this case), the first challenge, of characterising full grain kinematics, can now be addressed as described above. The second challenge, i.e., measuring force distributions in real (3D) materials remains open, but new work is heading towards this possibility, as described below.

Whilst, forces cannot be measured, they might be inferred from strains. In physics, various techniques, exploiting x-ray or neutron diffraction, have been proposed to measure crystal lattice strains that might be related to the forces acting on them. [4] demonstrated the use of neutron diffraction measurements over a small volume of grains in a larger sample; this could be extended for spatial mapping in a “continuum” type analysis. Other techniques exist that might permit grain-resolved grain-strain measurements, namely three-dimensional x-ray diffraction (3DXRD) ([8]). First results of 3DXRD applied to granular materials were presented by [4], but challenges associated with the geologic deformation history of real sand led to a new set of experiments

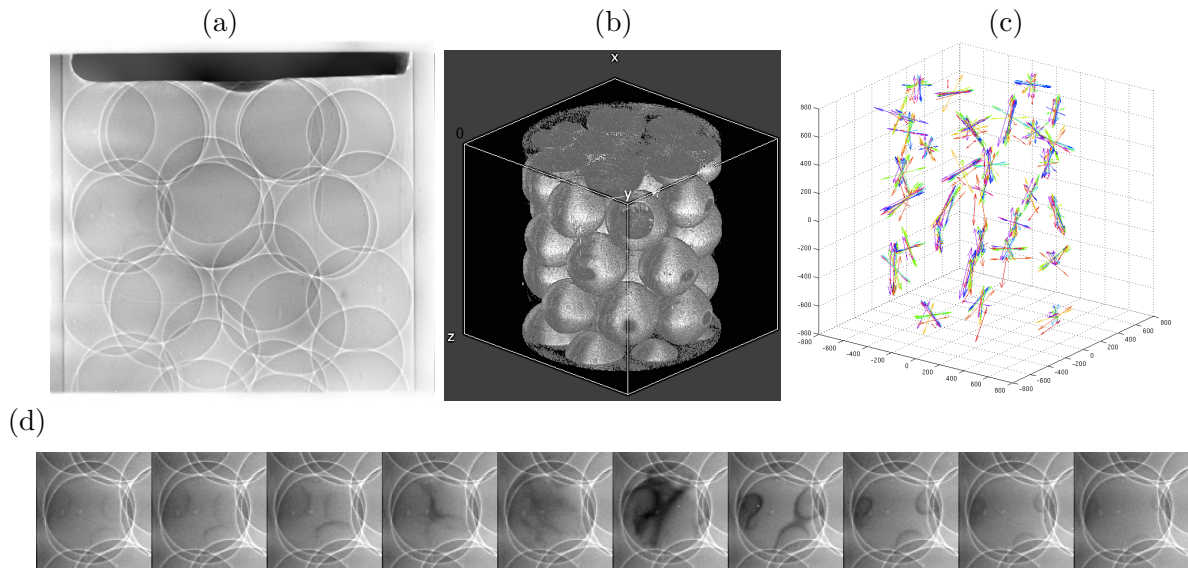


Figure 1. Preliminary results from combined 3DXRD and x-ray tomography measurements of an ‘ideal’ sand under 1D compression: (a) Radiography image through the upper fifth of the sample; (b) volume rendering of the 3D tomography image at one stage of loading; (c) Principal strain vectors for 12 loading stages up to 70 N and 3 unloading stages back to 28 N plotted at the grain centre-of-mass positions at each load step for the grains in (b); (d) Zoom into a region of radiography images through the sample, under a compressive load, showing the contacting grains and heterogeneous strain field signature - the image sequence is taken at 0.01° interval sample rotations about an angle where ‘extinction’ due to Bragg diffraction was observed (grain size is about $400 \mu\text{m}$ and in total there were 95 grains, sample diameter was 1.5 mm and height 5.21 mm)

using a ‘perfect’ sand made from carefully eroded 1 mm cubes of single crystal quartz. These experiments, carried out recently on beamline ID11 at the ESRF in Grenoble, France, involved loading of about 100 such grains in 1D (oedometric) compression with 3DXRD and x-ray tomography measurements performed at different stages of compression. Data analysis is still underway, but first results are shown in Figure 1.

The results in Figure 1 present images of the perfect grains and 3DXRD-derived grain-averaged principal strain vectors for different stages during loading and unloading. The strain plot indicates some consistency in the strain orientations over different load steps, but with some ‘flips’ in direction. Currently work is underway to refine this strain analysis and also to determine the grain-contact network to investigate how the grain-strains relate to the potential force transfer pathways; this will lead to inferences on the force transfer paths and contact-forces by inverse analysis. In addition, experimental developments are underway to assess the validity of the approach whereby an average strain tensor per grain is determined by 3DXRD; due to the granular nature of the material and the grain packing with small contact points between adjacent grains, the strain field inside the constituent loaded grains can not be homogeneous. In fact, measurements performed during the experiments demonstrated that the manufactured grains are perfect single crystals with uniform diffraction, and thus uniform crystal structure, over their volume in their unloaded state. However, as load was applied, the transmission of forces across grain contacts led to inhomogeneous strain fields in the grains, which could be observed as a change in the crystal lattice spacings, and thus of diffraction angles, through the grains; see Figure 1. In particular, these results show the variations in deformation are focussed, unsurprisingly, on the contact points between the grains. The challenge now is to extend the measurement technique to assess the strains associated with these intra-granular variations in diffraction.

Conclusions

With the new experimental tools available, it is now possible to probe the fundamental mechanics of granular media at the key controlling scale, i.e., that of the grains. In particular x-ray tomography imaging during loading, linked with volumetric image analysis, permits analysis of continuum strain and porosity fields, individual grains kinematics and the structural organisation of the contacting grains. Furthermore, new developments are opening up the possibility to fill in the final piece of the puzzle, i.e., detection and, eventually, quantification of the force transfer through real 3D granular materials. Such results will provide a quite complete picture of the granular mechanics and be the real experiment counterpart of the massive number of DEM simulations currently being performed (and thus provide much needed calibration and ground-truth for such approaches).

List of references

References

- [1] Andò, E., Hall, S.A., Viggiani, G., Desrues, J. and Bésuelle, P., Grain scale experimental investigation of localised deformation in sand: a discrete particle tracking approach, *Acta Geotechnica*, 7: 1-13, 2012.
- [2] Desrues, J. Tracking strain localization in geomaterials using computerized tomography, in *X-ray CT For Geomaterials: Soils, Concrete, Rocks*, eds. Otani, J. Otani, J. and Obara, Y., Balkema, p. 15-41, 2004.
- [3] Drescher, A. and De Josselin de Jong, G., Photoelastic verification of a mechanical model for the flow of a granular material, *J. Mech. Phys. Solids* 20:337-351, 1972.
- [4] Hall, S.A., Wright, J., Pirling, T., Andò, E., Hughes, D.J. and Viggiani, G., Can intergranular force transmission be identified in sand? First results of spatially-resolved neutron and x-ray diffraction, *Granular Matter* 13: 251-254, 2011.
- [5] Hall, S.A., Bornert M., Desrues J., Pannier Y., Lenoir N., Viggiani, G., Bésuelle, P., Discrete and Continuum analysis of localised deformation in sand using X-ray micro CT and Volumetric Digital Image Correlation, *Géotechnique*, 60: 315-322, 2010.
- [6] Hall, S.A., Lenoir, N., Viggiani, G., Bésuelle, P. and Desrues, J., Characterisation of the evolving grain-scale structure in a sand deforming under triaxial compression, in *Advances in Computed Tomography for Geomaterials, GeoX 2010*. Ed. Khalid .A. Alshibi and Allen H. Reed, Wiley & Sons, Hoboken, NJ, p. 34-42, 2010b.
- [7] Oda, M., Takemura, T. and Takahashi, M., Microstructure in shear band observed by microfocus X-ray computed tomography, *Géotechnique*, 54: 539-542, 2004.
- [8] Poulsen, H.F., *Three-dimensional X-ray diffraction microscopy: mapping polycrystals and their dynamics*, Springer, 2008.
- [9] Tordesillas, A. and Muthuswamy, M., On the modeling of confined buckling of force chains, *J. Mech. Phys. Solids* 57: 706-727, 2009.

Simulation of indenter geometry effects in nanoindentation

Ling Chen, Aylin Ahadi, and Jinming Zhou

Department of Mechanical Engineering, Lund University, Box 118, 221 00 Lund, Sweden,
ling.chen@iprod.lth.se

Summary. The elastic-plastic behaviour as the response to indenter geometry, such as tip radius and angle, are simulated in the study. The hardness and the Young modulus of the material are determined combining both analytical and numerical methods and their dependence on the tip radius and angle is investigated.

Key words: nanoindentation, indenter geometry, hardness, Young's modulus, FE-simulations

Introduction

Nanoindentation has been developed extensively over the last decades and is capable of very precise measurements of load and depth at small scales, such as thin films and coating technology. The classical analytical models used to extract mechanical properties, such as hardness and elastic modulus often have limitation and thus little consideration on effects of tip size, blunting effect, pile-up and sink-in phenomena as shown in Ref. [1-3]. Over the years, a number of methods have been developed to determine the actual indenter geometry. Area-function calibration method was proposed by Ref. [1]. Determining the indenter tip shape by imaging the impressions left by large indentations using transmission electron microscopy and scanning electron microscopy was suggested by Ref. [2]. However, such methods are difficult to use and may not be valid for very shallow indentations because of elastic recovery effects. The purpose of this work is to investigate indenter geometric effects on elastic-plastic behavior with use of finite element (FE) method, in particular focus on the variation of indenter tip radii and indenter angles. A comparison is made between the mechanical properties results obtained using two different ways of calculating the contact area of indentation.

Theory of nanoindentation

The nanoindentation is a type of indentation test with a very low load and it is described in the ISO 14577-1. During the nanoindentation test the indentation depth is typically less than 0.2 μm , and the indentation force does not exceed 2 N. Typical load-displacement curve produced during the process is showed in figure 1.

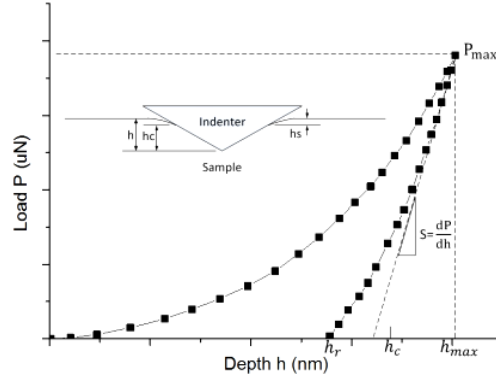


Figure 1. Typical load-displacement curves during nanoindentation of plastic-elastic material.

From the load-displacement curve, several essential parameters can be determined for further characterization of mechanical properties of test material. These include: the maximum depth of indenter h_{max} , the maximum indentation load P_{max} , the contact depth at the maximum indentation load h_c and the contact stiffness $S=dP/dh$. Mechanical properties, such as hardness (H_{IT}) and Young's modulus (E_{IT}) can be derived, see Ref. [1]. The hardness H_{IT} is described as:

$$H_{IT} = P_{max} / A_p(h_c) \quad (1)$$

where $A_p(h_c)$ is the contact area at the contact depth h_c . The Young's modulus E_{IT} can be derived from the following equations:

$$E_{IT} = \frac{1 - \nu_s^2}{1/E_r - (1 - \nu_i^2)/E_i} \quad E_r = \left(\frac{\pi}{4}\right)^{1/2} \left(\frac{1}{A_p(h_c)}\right)^{1/2} \left(\frac{dP}{dh}\right)_{unloading} \quad (2)$$

where E_r is the reduced modulus, accounting for elastic deformation in the indenter and $(dP/dh)_{unloading}$ is the experimentally measured initial unloading stiffness. The projected contact area often varies with the type of the indenter used. The most common indenters are the spherical, the Vickers and the Berkovich indenters. The contact area A_p is determined from the area function, $A_p(h_c)$, which expresses the projected area of the indenter in terms of the contact depth.

$$A_p = \begin{cases} \pi h_c(2R - h_c) & \text{for } h_c \leq (h-d) \\ 24.5(h_c + d)^2 & \text{for } h_c > (h-d) \end{cases}, \quad h_c = h_{max} - \varepsilon \frac{dP}{dh}, \quad h = \frac{R}{\sin \theta} - R \sin \theta, \quad d = \frac{R}{\sin \theta} - R \quad (3)$$

R , in the equations above, is the tip radius and $\theta=70.3^\circ$. The contact depth, h_c , between the indenter and the test piece, is showed in the figure 1b. ε is a geometrical constant. Obviously, correct determination of the projected contact area $A_p(h_c)$ is a crucial factor in calculation of the hardness from (1) and the Young's modulus from (2).

Model and results

The material model used for the test specimen is a Von Mises plasticity with isotropic hardening. Copper with mechanical properties of: elastic modulus $E_s = 140 \text{ GPa}$, yield stress $\sigma_y = 1.3 \text{ GPa}$ and Poisson's ratio $\nu_s = 0.343$, is chosen since copper is a single face material with simple structure. A diamond indenter is assumed in the simulation. The advantage of the simulation is that the indenter contact depth can be obtained by directly measuring the deformed specimen. With this approach, the effect of both elastic deformation of material and tip radius to

the indenter contact depth was considered. Figure 2 shows the sink-in and pile-up of the specimen surface, from which the depth of sink-in h_s and the contact depth h_c can be determined. The second approach to determine h_c by using (3), in which the maximum depth h_{max} and the stiffness $S=(dP/dh)$ are obtained from each force-displacement curves obtained from FE simulation. These values are denoted by $h_{c,FEM}$.

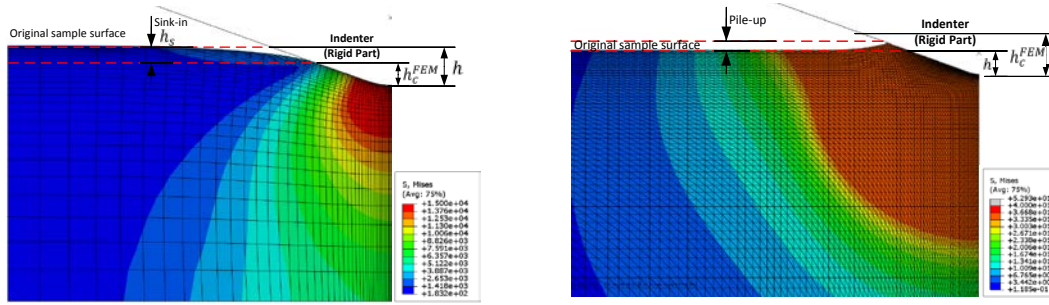


Figure 2. (a) Sink-in and (b) Pile-up effects in nanoindentation.

Ideal sharp indenters do not exist. Due to the small scale of the indentations, tip radius may become an important issue if it becomes too severe. Simulation of six load-displacement curves which represent the six indenter tip radius varied from 20 nm to 400 nm, were performed. In order to study the geometrical influence of the angle of the indenter, the angle was varied. The angle values of 68° and 70.3° correspond to the Vickers and Berkovich indenter respectively. Table 2 is the summary of the indenter contact depth for different indenter tip radii and angles measured with two different approaches.

Due to machining differences during manufacturing, the indenter tip always has a certain degree of radius or curvature. When the indentation depth is small, most of the contact occurs in the uppermost spherical depth range, and real contact area is quite different from that of the ideal indenter. Therefore, the area function needs to be calibrated for a specific range of indentation depths for nanoindentation to obtain an accurate and simple geometrical representation.

Table 1. Measured $h_{c(FEM)}$ and calculated h_c at different indenter radii and angles.

R (nm)	$h_{c(FEM)}$ (nm)	h_c (nm)	h_s (nm)	Angle($^\circ$)	$h_{c(FEM)}$ (nm)	h_c (nm)	h_s (nm)
20	22.52	23.88	7.48	45	25.54	27.11	4.46
40	21.97	23.59	8.03	50	24.86	26.82	5.14
70	21.51	23.46	8.49	60	23.72	25.77	6.28
100	21.43	22.88	8.57	68	23.35	25.65	6.65
200	20.28	21.98	9.72	70.3	22.37	24.38	7.63
400	18.68	21.04	11.32	75	21.55	23.89	8.45

Table 2 indicates that the contact depths decrease with the increase of tip radius. The values of the contact depth $h_{c(FEM)}$ obtained from FEM are about 10 % lower compared to the values of h_c calculated analytically from equation (3). The determined values for the maximum force, the values for the contact area and stiffness are then used to evaluate the hardness H_{IT} from (1), the reduced Young's modulus E_r from (2) and finally the Young's modulus E_{IT} from (2). Detailed calculations are presented in Ref. [4]. The variation of the hardness and the Young's modulus with the tip radius of the indenter is presented in the figure 3, whereas the variation with the

increased angle is seen in figure 4. These results are in agreement with the results for the hardness obtained by [5]. The Young modulus is an intrinsic material parameter and should not vary. However, it is difficult of calculate the projected contact area correctly are associated with the "pile-up" or "sink-in" of the material on the edges of the indent. None of the two analytical methods take into account these effects.

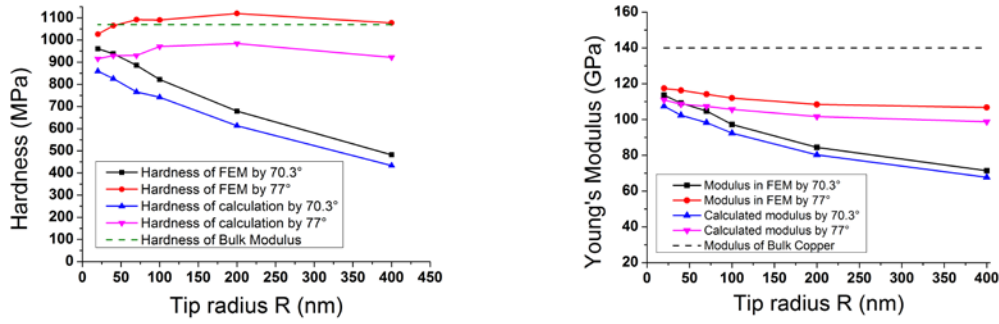


Figure 3. Effect of the tip radius on a) hardness and b) Young's Modulus.

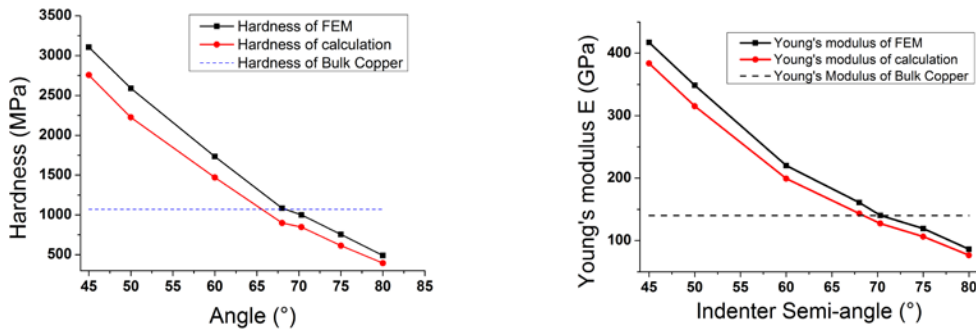


Figure 4. Effect of the angle on a) hardness and b) Young's Modulus

References

- [1] W. C Oliver and G. M. Pharr, An Improved Technique for Determining Hardness and Elastic-Modulus Using Load and Displacement Sensing Indentation Experiments, *Journal of Materials Research*, 7:1564-1583, 1992.
- [2] K. McElhaney, J. Vlassak, and W. Nix, Determination of indenter tip geometry and indentation contact area for depth-sensing indentation experiments, *Journal of Materials Research*, 13:1300-1306, 1998.
- [3] J.A., Knapp, D.M. Follstaedt, S.M. Myers, J.C. Friedmann, Finite-element modelling of nanoindentation. *Journal of Applied Physics*, 85(3):1460-1474, 1999.
- [4] C. Ling, A. Ahadi, J. Zhou, and J-E Ståhl, Characterisation of mechanical properties of machined surface by nanoindentation — Part 1: Simulation of indenter geometry effects, SPS12, Sweden, 2012.
- [5] L. Calabri, L., N. Pugno, and S. Valeri, AFM nanoindentation: tip shape and tip radius of curvature effect on the hardness measurement. *Journal of Physics-Condensed Matter*, 20(47):6127-6132, 2008.

Stress analysis around a through crack shaped defect in a thin copper film using molecular dynamics

Dan Johansson¹, Per Hansson², and Solveig Melin³

(1,2,3) Division of Mechanics, Department of Mechanical Engineering, Lund University, P.O. Box 118, 22100 Lund, Sweden, Dan.Johansson@mek.lth.se, Per.Hansson@mek.lth.se, Solveig.Melin@mek.lth.se

Summary. A small rectangular strip of FCC Cu, containing a through crack on the nano-scale subjected to loading under displacement control, is simulated using molecular dynamics. The geometry is chosen to mimic that of a thin film between two stiff layers and therefore the height of the strip is much smaller than the width. A plain strain situation is modeled by applying periodic boundary conditions in the direction of the crack front. The Lennard-Jones pair potential is used for the inter-atomic forces. The centrally placed crack is created by removing a few atoms inside the specimen. The crack is loaded perpendicular to the crack plane and comparisons with traditional linear elastic fracture mechanics concepts are made. The ultimate goal is to find a limit in model size beneath which linear elastic fracture mechanics loses their meaning.

Key words: Molecular dynamics simulations, Thin strip, Stress intensity, Fracture mechanics

Introduction

Considering thin metallic layers, one difficulty lies in finding proper dimensioning rules that are scientifically based and commonly accepted among designers. One challenge lies in the prediction of sudden failure of the layer induced by mechanical loading. One critical failure mode is cracking. Even if the crack is small, of the length of a few nanometers only, it might jeopardize the functionality of the coating and, eventually, extend to cause complete collapse of the component. Such unexpected events are, of course, necessary to understand and be able to predict. In this work, a thin strip of Cu, with height of only a few nanometers and holding a centrally placed crack loaded perpendicular to the crack plane through displacement control will be considered by molecular dynamics (MD) simulations using an in-house code. The results will be compared to traditional linear elastic fracture mechanics (LEFM) solutions to judge the impact of size of the geometry.

Problem specification

A thin strip of Cu, holding a centrally placed crack shape defect of length $2a$ along the x -direction according to Fig. 1 is studied. The defect is loaded perpendicular to the crack plane under displacement control. Coordinate directions (x, y, z) are shown in Figure 1.

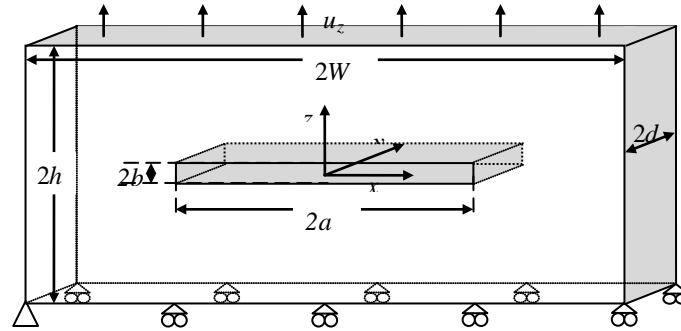


Figure.1. Model configuration. The crack is initially rectangular of size $2a \times 2b$.

The atomic arrangement in the strip is built from FCC Cu unit cells with lattice constant a_0 . The height of the strip in the z -direction is $2h$, the width in the x -direction $2W$ and the thickness $2d$. The basic model comprises six unit cells in the y -direction so that $2d = 6a_0$. By imposing periodic boundary conditions in the y -direction, a state of plane strain is reached.

A crack is not naturally atomistically sharp and here the crack is introduced by removing a strip of height two unit cells along the crack line, giving a rectangular crack shape with length $2a$ and height $2b = 2a_0$.

Simulation procedure

Because of its computational simplicity, in this paper the Lennard-Jones 12-6 pair potential ϕ is employed, cf. [1,2] and the stresses is calculated according to [3].

Each molecular dynamics simulation comprises three phases; problem setup, relaxation and loading. During the problem setup phase all specific simulation parameters are imposed. The present choice stems from [4,5]. The atomic arrangement is generated, atoms are removed to form the crack defect and the boundary conditions are imposed at the bottom atomic layer.

In the second phase, the relaxation phase, the chosen temperature is assigned. This is done by multiplying the velocity of each atom with a scaling factor at a certain interval. During the relaxation phase the strip in terms of size and volume moves towards a steady state, where the internal stress components only oscillate slightly around zero so that the relation between potential and kinetic energies keeps constant to a chosen magnitude. Further, during the relaxation, the atoms in atomic layer two to six have the same acceleration in the z -direction and the atoms in the top six atomic layers have the same acceleration in the z -direction.

After remaining at steady state for a few thousand time steps, the loading phase is entered and the six top atom layers are given a constant velocity in positive z direction causing the displacement, and, hence, the simulations are displacement controlled. In this phase, the atoms in atomic layer two to six are not allowed to move in the z -direction.

During all simulation steps, the atoms in the bottom layer are not allowed to move in the z -direction.

Results and Discussion

In Figure 2 the stresses σ_{zz} and σ_{zx} for the largest strip, which has 40 free unit cells in the z-direction. Figure 2a and Figure 2c show the results from the MD simulation and Figure 2b and Figure 2d are the LEFM solutions for an infinitely sharp crack in a displacement control loaded finite strip as taken from [6]. The stresses in Figure 2b and Figure 2d are shown with the exclusion of an area of height $2a_0$ around the crack, marked by a line, in similarity to Figure 2a and Figure 2c from the MD simulation. Note that the length scales differ between the plots of the MD and LEFM results, and in Figure 2a and Figure 2c the areas for which the linear elastic solutions in Figure 2b and Figure 2d are presented, are framed. Also note that for the MD simulation, the entire height of the strip, $2h$, is displayed.

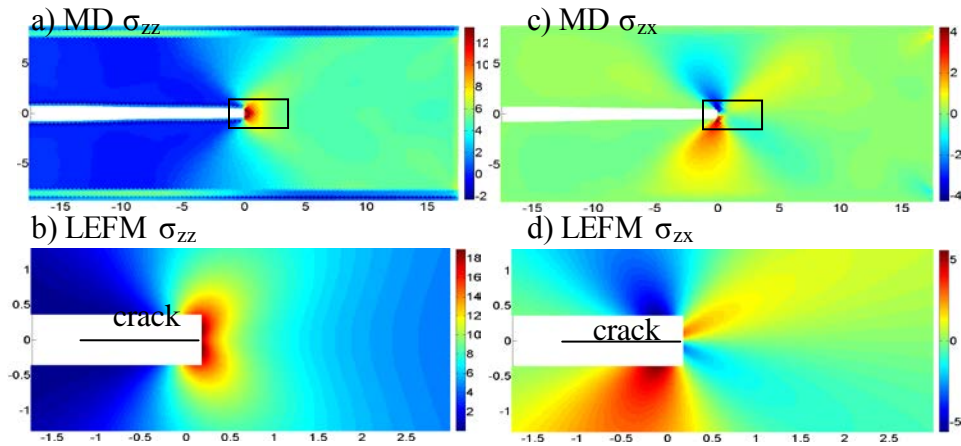


Figure.2. σ_{zz} and σ_{zx} for the right half of the largest simulation. Abscissa and ordinate are given in [nm]. The bars are in [GPa] a) and c): MD simulations. b) and d): LEFM solutions.

When the stresses from the simulations were compared it could be observed that the thicker the film, the higher the stresses and the larger the high stress distribution area. Also, stresses in the z-direction were, far away from the crack tip, higher for thinner films. That result agreed with an observation done for simulations without a crack which showed that thinner films have a stiffer elastic response than thicker films, which can be seen in Figure 3.

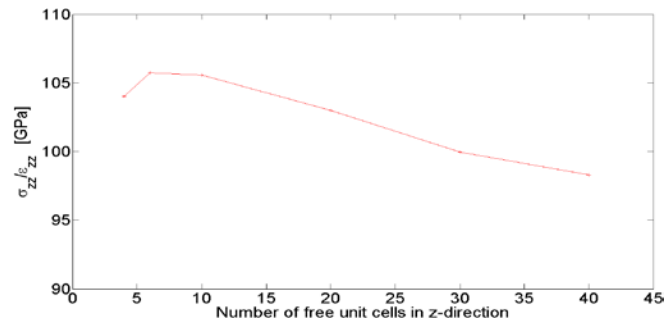


Figure.3. Elastic response to strip height.

Another observation that was done is that the agreement between the simulations and the LEFM solutions concerning the stress distribution areas is better for large simulations, which can be seen in Figure 4.

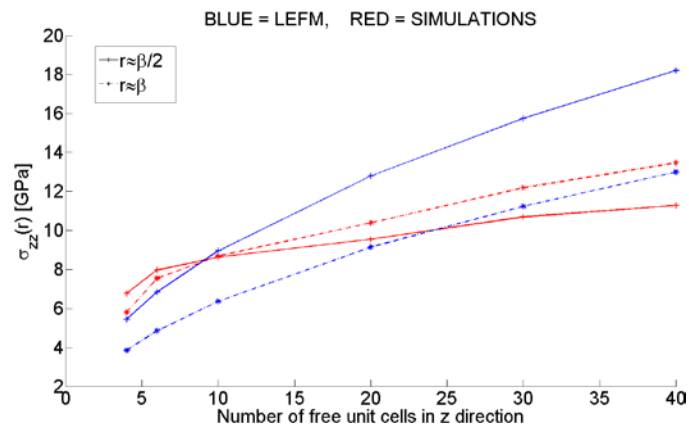


Fig.4. σ_{zz} for the two atoms closest to the crack tip to the number of free unit cells.

Conclusions

Molecular dynamics simulations have shown that cracked layers of small enough size react differently than macroscopic components upon loading. In this investigation, displacement controlled loading of cracked layers of Cu, with layer thicknesses less than a nanometer, were considered. The stress fields obtained from the MD simulations were compared to LEFM continuum solutions close to the crack front.

The stress fields as determined from MD and LEFM continuum solutions were, shown to increasingly deviate as the layer thickness decreased. Even so, the general appearances of the stress distributions were kept. The influence from boundaries increased markedly as the layer thickness decreased. Hence, LEFM will give a good approximation but due to boundary effects the LEFM result will only be able to describe the general shapes of the stress fields and give an idea of the stress magnitudes for the atoms that are very near the crack tip.

References

- [1] J.E. Jones: On the Determination of Molecular Fields, Proc. R. Soc. Lond. A Vol. 106 (1924), p. 463-477
- [2] D.C. Rapaport: The Art of Molecular Dynamics (Cambridge University Press, UK 2004).
- [3] M. Zhou: A new look at the atomic level virial stress: on continuum-molecular system equivalence, Proc. R. Soc. Lond. A Vol 459 (2003), p. 2347-2392
- [4] G. Ziegenhain, A. Hartmaier and H.M. Urbassek: Pair vs many-body potentials: Influence on elastic and plastic behavior in nanoindentation of fcc metals, J. Mech Phys. Solids Vol. 57, 1514-1526, (2009)
- [5] D.R. Askeland: The Science and Engineering of Materials (Chapman & Hall, UK/China 1996).
- [6] M. Isida: Effect of width and length on stress intensity factors of internally cracked plates under various boundary conditions, Int. J. Fract. Mech. 7 (1971) p 301.

Proceedings of the 25TH NORDIC SEMINAR
COMPUTATIONAL MECHANICS, 2012

Finite Element Techniques

Room: 304, Thursday 25 October, 13:15 - 15:15



Nitsche's method for discontinuous material parameters

Mika Juntunen and Rolf Stenberg

Aalto University School of Science,
Department of Mathematics and Systems Analysis,
P.O. Box 11100, FI-00076 Aalto, Finland
mojuntun@gmail.com, rolf.stenberg@aalto.fi

Summary. In Nitsche's method the continuity of the solution and the flux are enforced weakly. Unfortunately, if the material parameters are discontinuous, the conventional straightforward enforcing produces oscillating fluxes. In this work we show how to derive Nitsche's method through stabilized Lagrange multiplier method. This constructive derivation automatically gives the correct weighting for the enforcing terms for discontinuous material parameters. Lastly the results are tested numerically.

Key words: Nitsche's method, Lagrange multipliers, finite element method, FEM, domain decomposition

Introduction

One of the advantages of the Nitsche's method is the simplicity of joining non-matching meshes. It is often easiest to divide the domain along material edges which leads to a situation where the material parameters are discontinuous over the subdomain interfaces. If the jump in the material parameters is moderate, the method as it was described in, e.g., [2] readily applies. However, large discontinuities may lead into poor results if Nitsche's method is applied in a straightforward matter, see [1, 4] and the references there in. Some of the problems are avoided by finding a suitable material parameter dependent ratio for the fluxes, see [1, 6], and using this as the mean flux over the interface. In this article we show a constructive derivation of Nitsche's method for a problem where the material parameters have large discontinuities. The derivation takes advantage of the fact that Nitsche's method can be derived through stabilized Lagrange multiplier method [5].

Model problem

Consider a domain $\Omega \subset \mathbb{R}^2$ with piecewise smooth boundary $\partial\Omega$. Assume the domain is divided into two non-overlapping subdomains Ω_1 and Ω_2 . The subdomains cover the whole domain, that is, $\Omega = \Omega_1 \cup \Omega_2$ and they share a boundary $\Gamma = \partial\Omega_1 \cap \partial\Omega_2$. We solve the Poisson problem such that

$$-\nabla \cdot k_i \nabla u_i = f \quad \text{in } \Omega_i, \quad i = 1, 2, \quad (1)$$

$$u_i = 0 \quad \text{on } \partial\Omega, \quad (2)$$

$$u_1 - u_2 = 0 \quad \text{on } \Gamma, \quad (3)$$

$$k_1 \frac{\partial u_1}{\partial n_1} + k_2 \frac{\partial u_2}{\partial n_2} = 0 \quad \text{on } \Gamma, \quad (4)$$

in which $k_i : \mathbb{R}^2 \rightarrow \mathbb{R}$, $0 < k_{\min} < k_i < k_{\max}$, $i = 1, 2$ are the material parameters, $f \in L^2(\Omega)$ is the load function, $k_i \frac{\partial u_i}{\partial n_i} = k_i \nabla u_i \cdot \vec{n}_i$, and \vec{n}_1 and \vec{n}_2 denote the outer normals of the subdomains.

For simplicity, assume the material parameters k_i are element-wise constants.

Let the subdomains be divided into a set of non-overlapping elements denoted by \mathcal{T}_1^h and \mathcal{T}_2^h , in which h denotes the maximum diameter of elements. These meshes induce meshes also for the boundary Γ denoted by \mathcal{G}_1^h and \mathcal{G}_2^h . In what follows we will also need the intersection mesh on boundary Γ denoted by \mathcal{G}_I^h . This mesh is created with vertexes of both \mathcal{G}_1^h and \mathcal{G}_2^h and it is such that each element in \mathcal{G}_I^h overlaps with only one element in both \mathcal{G}_1^h and \mathcal{G}_2^h . In addition to the intersection mesh, we define a mesh on the boundary Γ that is independent of meshes \mathcal{G}_1^h and \mathcal{G}_2^h . This mesh is denoted with \mathcal{G}^H in which H denotes the diameter of the elements.

Let the finite element subspaces be

$$V_i^h = \{v \in H^{3/2+\epsilon}(\Omega_i) : v|_K \in \mathcal{P}^k(K) \forall K \in \mathcal{T}_i^h\}, \quad i = 1, 2, \quad (5)$$

in which \mathcal{P}^k denotes the polynomials of order k and $\epsilon > 0$. In addition, we denote a pair of finite dimensional functions by $v^h \in V^h = V_1^h \times V_2^h$. For the Lagrange multiplier methods we also need the space

$$\Lambda^H = \{v \in L^2(\Gamma) : v|_E \in \mathcal{P}^l(E) \forall E \in \mathcal{G}^H\}. \quad (6)$$

Stabilized Lagrange multiplier method

Next we recall the stabilized Lagrange multiplier method [5]. Constructing finite dimensional spaces for the standard Lagrange multiplier method can be difficult but in the stabilized version the spaces can be chosen freely.

The stabilized bilinear form is

$$\begin{aligned} \mathcal{A}^h(u^h, \lambda^H; v, \mu) = & \sum_{i=1}^2 (k_i \nabla u_i^h, \nabla v_i)_{\Omega_i} - (\lambda^H, \llbracket v \rrbracket)_{\Gamma} - (\llbracket u^h \rrbracket, \mu)_{\Gamma} \\ & - \sum_{i=1}^2 \sum_{E \in \mathcal{G}_i^h} \frac{h_i}{\gamma k_i} \left(k_i \frac{\partial u_i^h}{\partial n} - \lambda^H, k_i \frac{\partial v_i}{\partial n} - \mu \right)_E, \quad (7) \end{aligned}$$

in which $\gamma > 0$ is a stability parameter and h_i denotes the local element size of the element $E \in \mathcal{G}_i^h$. Above $\llbracket v \rrbracket = v_1 - v_2$ denotes the jump and to match this definition we also define $\vec{n} = \vec{n}_1 = -\vec{n}_2$. The stabilized problem is: Find $(u^h, \lambda^H) \in V^h \times \Lambda^H$ such that

$$\mathcal{A}^h(u^h, \lambda^H; v, \mu) = \sum_{i=1}^2 (f, v_i)_{\Omega_i} \quad \forall (v, \mu) \in V^h \times \Lambda^H. \quad (8)$$

Nitsche's method

In this section we derive Nitsche's method associated with the stabilized Lagrange multiplier method. The idea is to solve the Lagrange multiplier analytically and then substitute the value back to the equation. The advantage of this derivation becomes evident when we take into account the local mesh size and the discontinuity of the material parameters k_i .

Since the choice of finite element spaces is very flexible in the stabilized method, we can state the problem as: Find $(u^h, \theta) \in V^h \times L^2(\Gamma)$ in (8) for all $(v, \mu) \in V^h \times L^2(\Gamma)$. Now, testing with $(0, \mu) \in V^h \times L^2(\Gamma)$ and solving for θ gives

$$(\theta, \mu)_{\Gamma} = \sum_{E \in \mathcal{G}_I^h} \left(\left\{ \left\{ k \frac{\partial u^h}{\partial n} \right\} \right\} - \frac{\gamma k_1 k_2}{k_2 h_1 + k_1 h_2} \llbracket u^h \rrbracket, \mu \right)_E,$$

in which we have defined a weighted average

$$\left\{ \left\{ k \frac{\partial v^h}{\partial n} \right\} \right\} = \frac{k_2 h_1}{k_2 h_1 + k_1 h_2} k_1 \frac{\partial v_1^h}{\partial n} + \frac{k_1 h_2}{k_2 h_1 + k_1 h_2} k_2 \frac{\partial v_2^h}{\partial n}. \quad (9)$$

Since this holds for all $\mu \in L^2(\Gamma)$, we get

$$\theta = \theta(u^h) = \left\{ \left\{ k \frac{\partial u^h}{\partial n} \right\} \right\} - \frac{\gamma k_1 k_2}{k_2 h_1 + k_1 h_2} \llbracket u^h \rrbracket \quad (10)$$

on every $E \in \mathcal{G}_I^h$. This function $\theta : V^h \rightarrow L^2(\Gamma)$ gives the Lagrange multiplier associated with any function $v \in V^h$. Nitsche's method is just the stabilized Lagrange multiplier method with $\lambda = \theta(u^h)$ and $\mu = \theta(v)$ as the Lagrange multiplier and associated test function. In other words, Nitsche's method is: Find $u^h \in V^h$ such that

$$\mathcal{B}^h(u^h, v) := \mathcal{A}^h(u^h, \theta(u^h); v, \theta(v)) = \sum_{i=1}^2 (f, v_i)_{\Omega_i} \quad \forall v \in V^h. \quad (11)$$

The bilinear form, although it seems complicated at first, simplifies to

$$\begin{aligned} \mathcal{B}^h(u^h, v) &= \sum_{i=1}^2 (k_i \nabla u_i^h, \nabla v_i)_{\Omega_i} + \sum_{E \in \mathcal{G}_I^h} \left[- \left(\left\{ \left\{ k \frac{\partial u^h}{\partial n} \right\} \right\}, \llbracket v \rrbracket \right)_E - \left(\left\{ \left\{ k \frac{\partial v}{\partial n} \right\} \right\}, \llbracket u^h \rrbracket \right)_E \right. \\ &\quad \left. + \frac{\gamma k_1 k_2}{k_2 h_1 + k_1 h_2} (\llbracket u^h \rrbracket, \llbracket v \rrbracket)_E - \frac{\gamma^{-1} h_1 h_2}{k_2 h_1 + k_1 h_2} \left(\left[\left[k \frac{\partial u^h}{\partial n} \right] \right], \left[\left[k \frac{\partial v}{\partial n} \right] \right] \right)_E \right], \end{aligned} \quad (12)$$

in which

$$\left[\left[k \frac{\partial u}{\partial n} \right] \right] = k_1 \frac{\partial u_1}{\partial n} - k_2 \frac{\partial u_2}{\partial n} = k_1 \frac{\partial u_1}{\partial n_1} + k_2 \frac{\partial u_2}{\partial n_2}.$$

Observe that this form is similar to the usual Nitsche bilinear form [3]. Essentially the only difference is that the coefficient are weighted with local parameters k_i in (12). For example, suppose that $k = k_1 = k_2$ and $h = h_1 = h_2$. Then the weighted average (9) becomes regular average value and the other coefficients simplify to

$$\frac{k_1 k_2}{k_2 h_1 + k_1 h_2} = \frac{1}{2} \frac{k}{h} \quad \text{and} \quad \frac{h_1 h_2}{k_2 h_1 + k_1 h_2} = \frac{h}{k},$$

which are exactly the values in the usual Nitsche's method.

Error estimates

Since the proposed method is equivalent to the stabilized Lagrange multiplier method, the stability and a priori results are inherited from the stabilized Lagrange multiplier. However, these results are easy to derive directly for the proposed method too. The interesting part is the a posteriori estimate. Taking the material parameters carefully into account yields slightly modified a posteriori estimates, compared to e.g. [2]. In the case of discontinuous material parameters the conventional estimate tends to over-refine the mesh near the interface. The new estimate, on the other hand, refines the mesh near the boundary only on the side that has more error, not on both sides. See Figure 2 for an example of this.

Numerical example

The model problem is the same as (1)–(4) with $\Omega = (0, 2) \times (0, 1) \subset \mathbb{R}^2$. The domain is divided into $\Omega_1 = (0, 1) \times (0, 1)$ and $\Omega_2 = (1, 2) \times (0, 1)$. The model parameters are such that there is a large discontinuity over the interface: $k_1 = 1 \cdot 10^3$ and $k_2 = 1 \cdot 10^{-3}$. The load functional is $f = 1$ in $(0, 2) \times (0.25, 1)$ and zero elsewhere.

Figure 1 shows the exact flux in the x-direction and the numerical approximations given with the conventional and the proposed Nitsche's method using linear elements. The figure shows that the conventional method has oscillatory flux where as the proposed method gives a smooth flux.

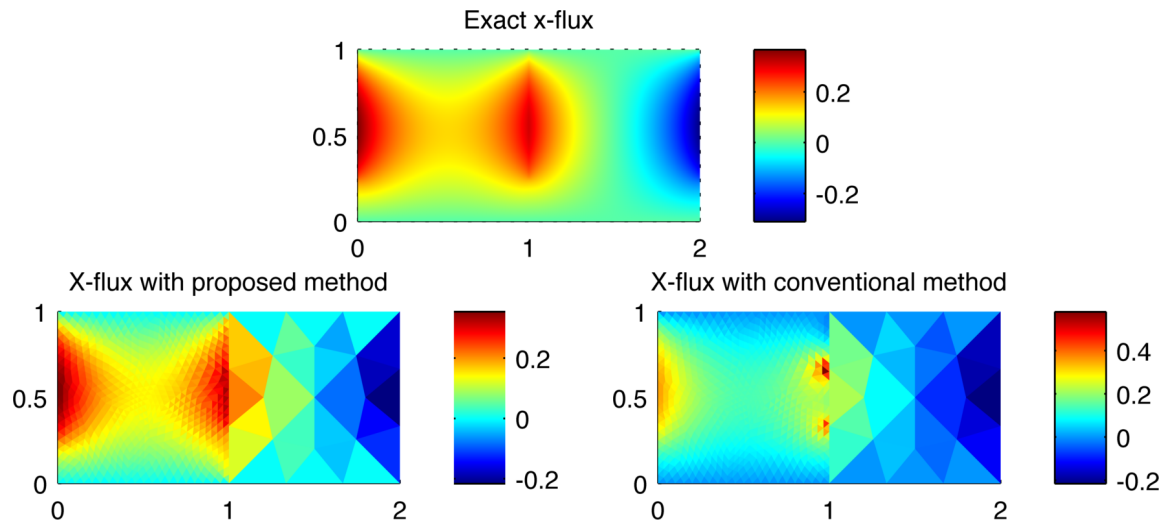


Figure 1. Flux in x-direction; top: exact, bottom left: proposed, bottom right: conventional.

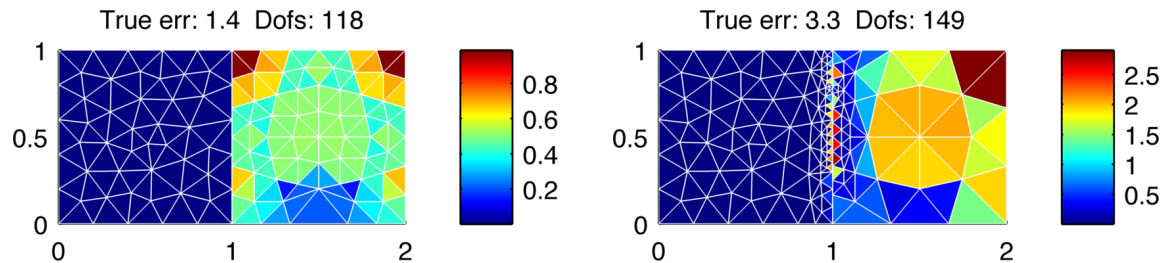


Figure 2. Adaptive refinement applied to the model problem; left: proposed, right: conventional method.

References

- [1] Chandrasekhar Annavarapu, Martin Hautefeuille, and John E. Dolbow. A robust nitsche's formulation for interface problems. *Computer Methods in Applied Mechanics and Engineering*, 225-228:44–54, 2012.
- [2] Roland Becker, Peter Hansbo, and Rolf Stenberg. A finite element method for domain decomposition with non-matching grids. *M2AN Math. Model. Numer. Anal.*, 37(2):209–225, 2003.
- [3] Mika Juntunen and Rolf Stenberg. Nitsche's method for general boundary conditions. *Math. Comp.*, 78(267):1353–1374, 2009.
- [4] Tod A. Laursen, Michael A. Puso, and Jessica Sanders. Mortar contact formulations for deformable-deformable contact: past contributions and new extensions for enriched and embedded interface formulations. *Comput. Methods Appl. Mech. Engrg.*, 205/208:3–15, 2012.
- [5] Rolf Stenberg. On some techniques for approximating boundary conditions in the finite element method. *J. Comput. Appl. Math.*, 63(1-3):139–148, 1995. International Symposium on Mathematical Modelling and Computational Methods Modelling 94 (Prague, 1994).
- [6] Rolf Stenberg. Mortaring by a method of J. A. Nitsche. In *Computational mechanics (Buenos Aires, 1998)*, pages CD-ROM file. Centro Internac. Métodos Numér. Ing., Barcelona, 1998.

Recovery based approach to design a posteriori error estimator in isogeometric analysis

Trond Kvamsdal¹, Mukesh Kumar¹, Kjetil Andre Johannessen¹, Knut Morten Okstad²

¹Department of Mathematical Sciences, Norwegian University of Science and Technology, Alfred Getz vei 1, N-7491 Trondheim, Norway

²Department of Applied Mathematics, SINTEF ICT, N-7465 Trondheim, Norway
{Trond.Kvamsdal, Mukesh.Kumar, kjetijo}@math.ntnu.no, Knut.Morten.Okstad@sintef.no

Summary. In this article, we investigate an approach for a posteriori error estimation based on recovery of an improved stress (gradient) field in isogeometric analysis (IGA). We design a local recovery procedure of smoothing of stress (gradient) components over small patches of elements in isogeometric analysis framework that fulfills the criteria of stress (gradient) recovery operator set out by Ainsworth and Craig in [1]. Further the recovery technique is used in the computation of the Zienkiewicz-Zhu error estimator [2] to demonstrate accurate estimation of the exact error attainable. Numerical test are performed to illustrate the effectivity of the error estimators in the energy norm.

Key words: Isogeometric analysis, NURBS, LR B-splines, error estimation, stress recovery.

Introduction

Isogeometric analysis (IGA) has been introduced in [3] as an innovative numerical methodology for the discretization of Partial Differential Equations (PDEs), which is based on developments in the modeling of complex geometries using Computer Aided Design (CAD). Non-uniform rational B-splines (NURBS) are the dominant geometric representation format for CAD. The construction of NURBS are based on a tensor product structure and, as a consequence, knot insertion is a global operation. Adaptive local refinement has become one of the key issues in isogeometric analysis. To solve this remedy several local refinement strategies has been proposed using an alternative to NURBS, e.g., T-splines, LR B-splines, PHT-splines, and Hierarchical B-splines. While to apply a local refinement strategy to solve PDEs problem in adaptive isogeometric analysis the *a posteriori error estimator* is required. This is the subject of current work.

This work is motivated from the Superconvergent Patch Recovery (SPR) of [4]. Here we design a local recovery procedure of smoothing of stress (gradient) components over small patches of elements in isogeometric analysis framework that fulfills the criteria of stress (gradient) recovery operator set out by Ainsworth and Craig in [1]. The implementation of this recovery technique is simple and cost effective. Further the recovery technique is used in the computation of the Zienkiewicz-Zhu error estimator [2] and numerical test are performed to illustrate the effectivity of the error estimators in the energy norm.

Isogeometric analysis

Let $\Omega \subset \mathbb{R}^d$, $d \in \mathbb{Z}^+$ be an open, bounded and connected Lipschitz domain with boundary $\partial\Omega = \partial\Omega_D \cup \partial\Omega_N$. Let \mathbf{n} denote the outer unit normal vector to $\partial\Omega$, and let $\mathbf{f} \in (L^2(\Omega))^d$ and $\mathbf{g} \in (L^2(\partial\Omega_N))^d$ be given functions. Find $\mathbf{u} : \bar{\Omega} \rightarrow \mathbb{R}^d$ such that

$$\mathbf{L}\mathbf{u} \equiv \mathbb{D}^T \mathbf{C} \mathbb{D}\mathbf{u} = \mathbf{f} \quad \text{in } \Omega, \quad \mathbf{G}\mathbf{u} = \mathbf{g} \quad \text{on } \partial\Omega, \quad (1)$$

where \mathbf{L} is a second order elliptic partial differential operator and \mathbf{G} is a linear operator that describe the boundary conditions. The typical examples of this model problem are the scalar diffusion problem and the linearized elasticity problem, where \mathbf{u} is the displacement vector and $\boldsymbol{\sigma}(\mathbf{u}) = \mathbf{C}\mathbb{D}\mathbf{u}$ is the stress tensor (or flux).

The variational form of the model problem (1) can be written as follows: Find $\mathbf{u} \in \mathbf{V}_D$:

$$a(\mathbf{u}, \mathbf{v}) = \ell(\mathbf{v}) \quad \forall \mathbf{v} \in \mathbf{V}_0, \quad (2)$$

where $\ell(\mathbf{v}) = (\mathbf{f}, \mathbf{v})_\Omega + (\mathbf{g}, \mathbf{v})_{\partial\Omega_N}$, the space $\mathbf{V}_0 \subset (H_0^1(\Omega))^d$ contains test functions which vanish at the Dirichlet boundary and we set $\mathbf{V}_D \subset (H^1(\Omega))^d$ consists of functions which fulfill the Dirichlet boundary conditions on $\partial\Omega_D$.

The NURBS space on Ω is defined as the span of the push forward of the basis function $\mathbf{R}_{\mathbf{k},\mathbf{p}}$

$$\mathcal{V}^h = \text{span}\{\hat{R}_{\mathbf{k},\mathbf{p}} = R_{\mathbf{k},\mathbf{p}} \circ \mathbf{F}^{-1}, \mathbf{k} = 1, \dots, \mathbf{n}\} \subset H^1(\Omega). \quad (3)$$

The numerical solution of (2) is sought in the finite dimensional discrete NURBS space $\mathbf{V}^h = (\mathcal{V}^h)^d \subset (H^1(\Omega))^d$. We define

$$\mathbf{V}_0^h = \{\mathbf{v} \in \mathbf{V}^h : \mathbf{v}|_{\Gamma_D} = 0\} \quad \text{and} \quad \mathbf{V}_D^h = \{\mathbf{v} \in \mathbf{V}^h : \mathbf{v}|_{\Gamma_D} = \mathbf{g}\} \subset (\mathcal{V}^h)^d \cap (H_{\partial\Omega_D}^1)^d. \quad (4)$$

The discrete formulation of (2) reads as: find $\mathbf{u}_h \in \mathbf{V}_D^h$ such that

$$a(\mathbf{u}_h, \mathbf{v}_h) = \ell(\mathbf{v}_h) \quad \forall \mathbf{v}_h \in \mathbf{V}_0^h. \quad (5)$$

The discrete solution \mathbf{u}_h in (5), for $\mathbf{x} \in \bar{\Omega}$, is represented as

$$\mathbf{u}_h(\mathbf{x}) = \sum_{\mathbf{k}=1}^{\mathbf{n}} \hat{\mathbf{u}}_{\mathbf{k}} \hat{R}_{\mathbf{k},\mathbf{p}}(\mathbf{x}) = \mathbf{R}\hat{\mathbf{u}} \quad (\text{say}), \quad (6)$$

where the real valued coefficients $\hat{\mathbf{u}}_{\mathbf{k}}$ are referred to as *control variables* or *degrees of freedom* (DOF) and \mathbf{R} is the matrix crossponding to the functions $\{\hat{R}_{\mathbf{k},\mathbf{p}}\}_{\mathbf{k}=1}^{\mathbf{n}}$. The directly computed consistent, stresses (or gradients, fluxes) is obtain from (6) using the stress-displacement relation as

$$\boldsymbol{\sigma}_h = \mathbf{C}\mathbb{D}\mathbf{u}_h = \mathbf{C}\mathbb{D}\mathbf{R}\hat{\mathbf{u}} = \mathbf{S}\hat{\mathbf{u}} \quad (\text{say}). \quad (7)$$

The computed stresses (or gradients, fluxes) $\boldsymbol{\sigma}_h$ in (7) involve the differentiation of the displacement \mathbf{u}_h or the functions $\{\hat{R}_{\mathbf{k},\mathbf{p}}\}_{\mathbf{k}=1}^{\mathbf{n}}$ with respect to the differential matrix \mathbb{D} . Thus the computed solution is less smooth than the exact one.

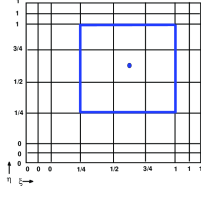
Stress recovery procedure

In this section, inspired by the original SPR method [4] and its main idea of existence of some points with high accuracy, i.e., superconvergent points, we explain a local smoothing procedure for the improved stresses field components, σ_{α}^* , expressed as

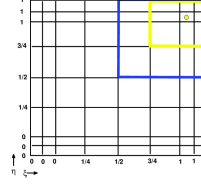
$$\sigma_{\alpha}^* = \mathcal{P}(\mathbf{x})a_{\alpha} \quad (8)$$

where \mathcal{P} is a matrix of polynomial terms in the Cartesian coordinates, $\mathbf{x} = \{x, y\}^T$ and a_{α} are the unknown coefficients. The coefficients a_{α} are then determined from a least square fit of the field σ_{α}^* to the values of computed σ_{α}^h at optimal sampling points within the elements in the element patch as shown in Fig. 1, i.e., we minimize the following

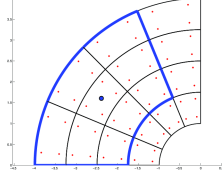
$$\mathcal{F}(a_{\alpha}) = \sum_{i=1}^{n_{sp}^{el}} (\sigma_{\alpha,i}^* - \sigma_{\alpha,i}^h)^T (\sigma_{\alpha,i}^* - \sigma_{\alpha,i}^h) \quad (9)$$



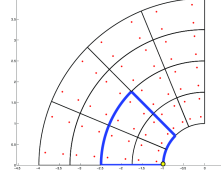
(a) Index/parametric space



(b) Index/parametric space



(c) Physical space



(d) Physical space

Figure 1. Element patch formation for bi-quadratic NURBS: normal case (left) and special case (right)

The stationary condition for $\mathcal{F}(\mathcal{P}_\alpha)$, gives

$$\frac{\partial \mathcal{F}}{\partial a_\alpha} = 0 \Rightarrow \mathbf{A}a_\alpha = \mathbf{B} \Rightarrow a_\alpha = \mathbf{A}^{-1}\mathbf{B}, \quad (10)$$

with

$$\mathbf{A} = \sum_{i=1}^{n_{sp}^{el}} \mathcal{P}_i^T(\mathbf{x}_i)\mathcal{P}_i(\mathbf{x}_i) \quad \text{and} \quad \mathbf{B} = \sum_{i=1}^{n_{sp}^{el}} \mathcal{P}_i^T(\mathbf{x}_i)\sigma_{\alpha,i}^h$$

In order to construct a global recovered field, we follow Blacker and Belytschko [5] for conjoin the polynomial expansion. Adopting this approach the control variable \mathbf{P}_α of global recovered stress $\sigma_\alpha^* = \mathbf{R}\mathbf{P}_\alpha$ are obtain by Greville projection as interpolation of these recovered values by

$$\mathbf{R}(\tau_k)\mathbf{P}_\alpha = \sigma_{\alpha,e}^*(\tau_k) \quad (11)$$

Error measure and effectivity index

The energy norm for the model problem is defined as

$$\|e\|^2 = \int_{\Omega} (\sigma - \sigma_h)^T \mathbf{C}^{-1}(\sigma - \sigma_h) d\Omega, \quad (12)$$

where \mathbf{C} , e.g., elasticity matrix, is given by the source problem. Using Zienkiewicz and Zhu [2] error estimator the approximate energy norm is defined as

$$\eta^2 = \int_{\Omega} (\sigma_h^* - \sigma_h)^T \mathbf{C}^{-1}(\sigma_h^* - \sigma_h) d\Omega, \quad (13)$$

where σ_h^* is the recovered gradient obtained using recovery techniques in isogeometric analysis. In practice, these error norms are calculated over each knot elements and summed up as

$$\eta^2 = \sum_{i \in I} \eta_i^2, \quad \text{with} \quad \eta_i^2 = \int_{\Omega_i} (\sigma_h^* - \sigma_h)^T \mathbf{C}^{-1}(\sigma_h^* - \sigma_h) d\Omega_i. \quad (14)$$

To measure the quality and accuracy of an error estimator, the effectivity index is defined as

$$\theta^* = \frac{\|\eta\|}{\|e\|} \quad \theta^{el} = \frac{\|\bar{e}^{el}\|}{\|e^{el}\|} \quad (\text{at element level}). \quad (15)$$

While the distribution of θ^{el} , d is defined by

$$d = \theta^{el} - 1, \quad \text{if} \quad \theta^{el} \geq 1, \quad \text{and} \quad d = 1 - \frac{1}{\theta^{el}}, \quad \text{if} \quad \theta^{el} < 1.$$

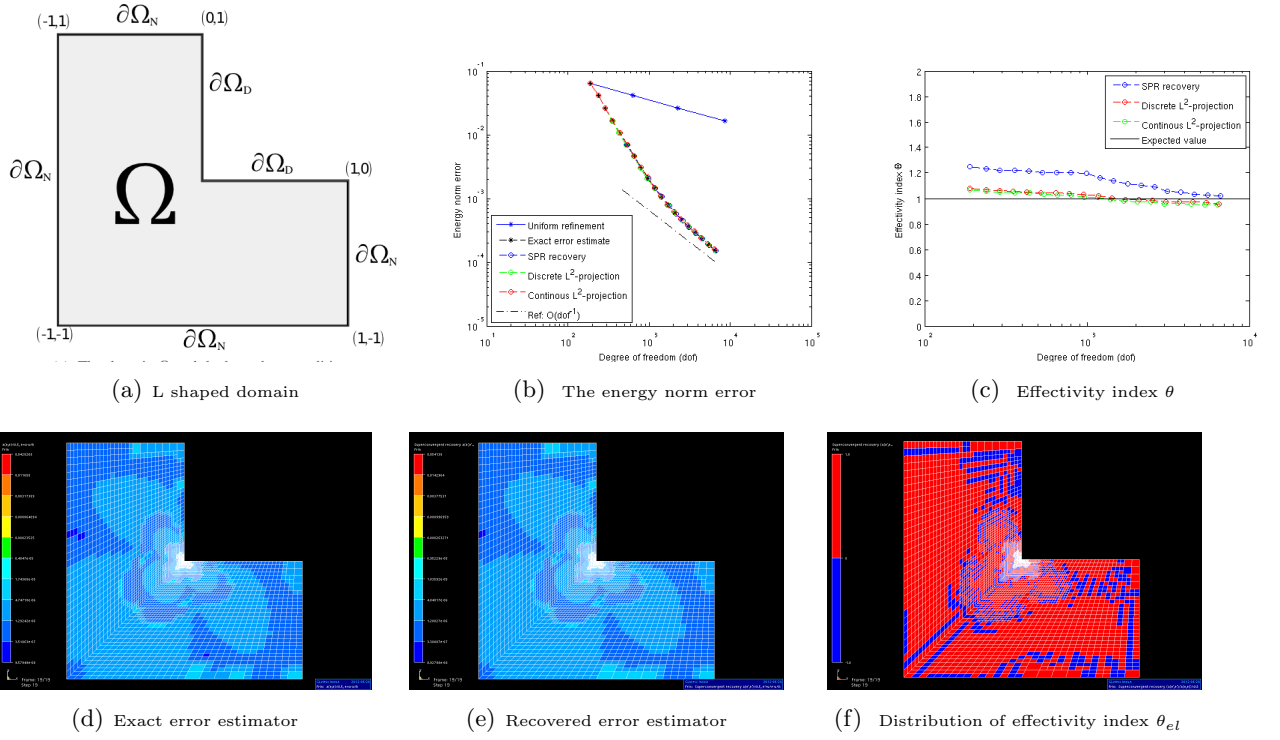


Figure 2. Adaptive LR B-spline refinement at Last Step

Numerical results

We consider the model elliptic problem on L-shaped domain $\Omega = [-1, 1]^2 \setminus [0, 1]^2$ with appropriate boundary condition as shown in Fig. 2(a), i.e.

$$\nabla^2 u = 0 \text{ in } \Omega, \quad u = 0 \text{ on } \partial\Omega_D \text{ and } \frac{\partial u}{\partial n} = g \text{ on } \partial\Omega_N,$$

where g is based on the exact solution u given by $u(r, \theta) = r^{2/3} \sin\left(\frac{2\theta + \pi}{3}\right)$. We perform adaptive refinement using LR B-spline refinement algorithm taking with a posteriori error estimator based on present SPR recovery technique. The numerical results shown in Fig. 2 demonstrate the effectiveness of proposed a posteriori error estimator in isogeometric analysis.

References

- [1] M. Ainsworth, A. Craig, A posteriori error estimators in the finite element method, *Numerische Mathematik*, 60:429–463, 1992.
- [2] O. C. Zienkiewicz and J. Z. Zhu, A simple error estimator and adaptive procedure for practical engineering analysis, *Internat. J. Numer. Methods Engrg.*, 24(2):337–357, 1987.
- [3] T.J.R. Hughes, J.A. Cottrell, Y. Bazilevs, Isogeometric analysis: CAD, finite elements, NURBS, exact geometry, and mesh refinement, *Comput. Methods Appl. Mech. Engrg.*, 194:4135–4195, 2005.
- [4] O. C. Zienkiewicz, J. Z. Zhu, The superconvergent patch recovery and a posteriori error estimates. I. The recovery technique, *Internat. J. Numer. Methods Engrg.*, 33(7):1331–1364, 1992.
- [5] T. Blacker, T. Belytschko, Superconvergent patch recovery with equilibrium and conjoint interpolant enhancements, *Internat. J. Numer. Methods Engrg.*, 37(3):517–536, 1994.

Mortar-based isogeometric analysis applied to frictionless large deformation elastoplastic contact problems

Kjell Magne Mathisen¹, Knut Morten Okstad², Trond Kvamsdal² and Siv Bente Raknes¹

⁽¹⁾Department of Structural Engineering, Norwegian University of Science and Technology, NTNU, NO-7491 Trondheim, Norway, kjell.mathisen@ntnu.no, siv.bente.raknes@ntnu.no

⁽²⁾SINTEF ICT - Department of Applied Mathematics, NO-7034 Trondheim, Norway, knut.morten.okstad@sintef.no, trond.kvamsdal@sintef.no

Summary. This paper focuses on the application of isogeometric analysis to model frictionless large deformation elastoplastic contact between deformable bodies and rigid surfaces that may be represented by analytical functions. The contact constraints are satisfied exactly with the augmented Lagrangian method, and treated with a mortar-based approach combined with a simplified integration method to avoid segmentation of the contact surfaces. The spatial discretization of the deformable body is performed with arbitrary order NURBS and C^0 -continuous Lagrange polynomial elements. The numerical examples demonstrate that isogeometric surface discretization delivers more accurate and robust predictions of the response compared to Lagrange discretizations.

Key words: isogeometric analysis, NURBS, large deformation plasticity, contact mechanics, mortar method

Introduction

Large deformation elastoplastic contact problems involve geometrical, material and contact non-linearity, which need to be solved simultaneously. Non-smooth C^0 -continuous finite element discretization techniques still constitute the most widely used approach in solving computational contact problems. In order to improve the performance of contact algorithms, various smoothing techniques have been proposed based on e.g. Hermite C^1 , Bézier and NURBS discretization of the contact surface. Although surface smoothing improves the evolution of the contact pressure, these approaches in general do not preserve consistency between volume and surface discretization. Within the framework of isogeometric analysis, which was introduced by Hughes *et al.* [1], smooth surface discretization can be achieved by representing the contact geometry by a NURBS surface that is directly inherited from the NURBS discretization of the volume.

The robustness of contact computations also depends on an accurate and smooth description of not only the contact geometry but also the contact pressure. It is well-known that node-to-surface (NTS) contact formulations is affected by several pathologies, and has been shown not to satisfy the contact patch test, which implies that mesh refinement do not necessarily increase the accuracy of the contact pressure. Several improvements to the NTS (or knot-to-surface, KTS, for isogeometric analysis) have been proposed, but they either do not satisfy the contact patch test or cause LBB-instability. However, the more recent mortar-based approaches constitute a method of consistently treating the global and local contact interaction, satisfying both the patch test and LBB-stability, albeit at a higher computational cost.

The penalty (PL) method is the simplest and apparently the most widely used approach for solving contact problems. It leads to a purely displacement formulation where the constraints

are enforced approximately. Furthermore, illconditioning may appear as the penalty parameter is increased in order to improve the satisfaction of the contact constraints. To avoid the drawbacks of the PL method, the augmented Lagrangian (AL) method may be adopted. There are two solution schemes commonly used in the context of the AL method. The so-called Uzawa method, which combines the AL regularization with a first-order update of the Lagrange multipliers [2]. Alternatively, a Newton-like solution scheme can be applied to solve the saddle-point problem simultaneously for the displacements and Lagrange multipliers as proposed by Alart and Curnier [3]. In view of the ascertained drawbacks of a non-mortar approach, we apply a mortar-based approach to satisfy the contact constraints combined with the latter version of the AL method, which is characterized by a remarkable degree of robustness and yields an asymptotic quadratic convergence rate in the Newton iterations. For comparison purposes, we have also implemented the PL method and C^0 -continuous Lagrange polynomial elements. In this paper mortar-based isogeometric analysis as formulated by De Lorenzis *et al.* [4] is extended to model large deformation elastoplastic contact problems.

Large deformation contact problem

This section gives a summary of the contact variables and the contact constraints within a continuum formulation of large deformation frictionless contact between two bodies. More details can be found in the monograph of Wriggers [2].

In this study finite deformation quasi-static frictionless contact problems will be considered in a purely mechanical setting. Consider two bodies \mathcal{B}^i , where the subscript $i = \{s, m\}$ denotes the slave (non-mortar) and master (mortar) bodies, respectively. The relation between the initial (reference) configuration \mathbf{X}^i , the displacement \mathbf{u}^i and the current configuration \mathbf{x}^i of a generic point of each body is given by

$$\mathbf{x}^i = \mathbf{X}^i + \mathbf{u}^i \quad (1)$$

For modelling of contact between the two bodies \mathcal{B}^s and \mathcal{B}^m , the contact interface denoted $\Gamma_c := \Gamma_c^s = \Gamma_c^m$ is pulled back to $\Gamma_{c0} := \Gamma_{c0}^s \neq \Gamma_{c0}^m$, where Γ_c^i and Γ_{c0}^i denote the contact boundary in the current and in the reference configuration of body \mathcal{B}^i , respectively. In the present formulation all contact integrals will be evaluated on Γ_{c0}^s . Defining $g_N = (\mathbf{x}^s - \mathbf{x}^m) \cdot \mathbf{n}^m$ to be the normal gap, λ_N the normal contact traction defined as the normal component of the interface Piola traction $\mathbf{t} := \mathbf{t}^m = -\mathbf{t}^s = \lambda_N \mathbf{n}^m$; the Kuhn-Tucker conditions for impenetrability on Γ_{c0} are

$$g_N \geq 0, \quad \lambda_N = \mathbf{t} \cdot \mathbf{n}^m \leq 0 \quad \text{and} \quad g_N \lambda_N = 0 \quad (2)$$

The frictionless contact problem between deformable elastic bodies can be formulated as a constrained minimization problem [2].

$$\min_{\mathbf{u}} \Pi(\mathbf{u}) \quad \text{subject to} \quad g_N \geq 0 \quad \text{on} \quad \Gamma_c \quad (3)$$

where $\Pi(\mathbf{u})$ is the potential energy.

In the PL method the contact constraints are enforced approximately

$$\lambda_N = \varepsilon_N \langle g_N \rangle_- \quad \text{where} \quad \langle g_N \rangle_- = \begin{cases} g_N, & g_N \leq 0 \\ 0, & g_N > 0 \end{cases} \quad (4)$$

where $\varepsilon_N > 0$ is the penalty parameter. Applying the above penalty regularization the constrained minimization problem may be transformed into an unconstrained minimization problem

$$\min_{\mathbf{u}} \Pi^{PL}(\mathbf{u}) \quad (5)$$

where the potential energy $\Pi(\mathbf{u})$ has been augmented by the following contact contribution to the virtual work

$$\delta \Pi_c^{PL} = \int_{\Gamma_{c0}} t_n \delta g_N d\Gamma \quad (6)$$

δg_N denotes the variation of the normal gap.

For the solution of the constrained minimization problem we have adopted the AL method as formulated by Alart and Curnier [3]. In the AL method, a dual field of Lagrange multipliers λ_N is defined on the contact surface Γ_c , and the AL functional \mathcal{L} is constructed as

$$\mathcal{L}(\mathbf{u}, \lambda_N) = \Pi(\mathbf{u}) + \int_{\Gamma_{c0}} l_n(g_N, \lambda_N) d\Gamma, \quad l_n(g_N, \lambda_N) = \begin{cases} (\lambda_N + \frac{\varepsilon_N}{2} g_N) g_N, & \hat{\lambda}_N \leq 0 \\ -\frac{1}{2\varepsilon_N} \lambda_N^2, & \hat{\lambda}_N > 0 \end{cases} \quad (7)$$

Here, $\varepsilon_N > 0$ is an arbitrary penalty parameter while the AL multiplier $\hat{\lambda}_N = \lambda_N + \varepsilon_N g_N$ is used to discriminate between contact ($\hat{\lambda}_N \leq 0$) and separation ($\hat{\lambda}_N > 0$). The main advantage of the AL method over the PL method and the Lagrange multiplier alternatives is that l_N and \mathcal{L} are C^1 -differentiable. Hence, the contact problem may now be reformulated as an unconstrained saddle-point problem

$$\min_{\mathbf{u}} \max_{\lambda_N} \mathcal{L}(\mathbf{u}, \lambda_N) \quad (8)$$

and the necessary condition of the saddle point takes the form

$$\delta \mathcal{L}(\mathbf{u}, \lambda_N) = \delta \Pi(\mathbf{u}) + \int_{\Gamma_{c0}} \left[\hat{\lambda}_N^{\text{eff}} \delta g_N + C_N \delta \lambda_N \right] d\Gamma = 0 \quad (9)$$

where the following notation has been introduced [4]

$$\hat{\lambda}_N^{\text{eff}} = \frac{\partial l_N}{\partial g_N} = \begin{cases} \hat{\lambda}_N, & \hat{\lambda}_N \leq 0 \\ 0, & \hat{\lambda}_N > 0 \end{cases}, \quad C_N = \frac{\partial l_N}{\partial \lambda_N} = \begin{cases} g_N, & \hat{\lambda}_N \leq 0 \\ -\frac{\lambda_N}{\varepsilon_N}, & \hat{\lambda}_N > 0 \end{cases} \quad (10)$$

The AL multiplier $\hat{\lambda}_N^{\text{eff}}$ is the state dependent normal contact traction, whereas C_N defines the constraints that are active depending on the contact state. Due to the C^1 -differentiability of \mathcal{L} , continuity of both $\hat{\lambda}_N^{\text{eff}}$ and C_N is preserved as the contact state changes from contact to separation, hence upon discretization the resulting equations can be efficiently solved with Newton's method. Also note that in contrast to the PL method, for the AL method the contact constraints are enforced exactly regardless of the value of the penalty parameter, which can be kept conveniently low to improve the convergence behavior.

Numerical results

A large deformation 2D example is considered to demonstrate that isogeometric surface discretization deliver more accurate and robust predictions of the response compared to Lagrange discretization. A rigid cylinder is pressed vertically into an elastic slab ($\nu = -0.075$) and then moved in the horizontal direction ($u = 2$). A standard compressible neo-Hookean hyperelastic material behavior is assumed for the slab, with material parameters $E = 1$ and $\nu = 0.3$. The rectangular slab that is fixed vertically at the bottom has width 3.0 and height 1.0, while the radius of the rigid cylinder is 0.5. A similar problem has also been studied by De Lorenzis *et al.* [5]. However, they consider the cylinder being elastic ($E = 1000$ and $\nu = 0.3$), account for friction ($\mu = 0.3$) and employed the PL method. Therefore, we cannot expect full compliance with the results obtained in [5]. The slab is analyzed using quadratic and cubic NURBS as basis functions, and compared with standard quadratic and cubic Lagrange elements. All NURBS and Lagrange discretizations includes 49 basis functions in the horizontal and 25 in the vertical direction, respectively.

The results in terms of Mises stress for the cubic NURBS mesh and strain energy for NURBS and Lagrange discretizations of varying order are presented in Figure 1. The plot of the strain energy demonstrate the remarkable smoothness obtained with the NURBS discretizations, while in contrast the Lagrange solutions are stiffer and experience oscillations. The obtained results stems from the higher degree of smoothness which is achieved by representing the contact geometry by a NURBS surface that is directly inherited from the NURBS discretization of the volume.

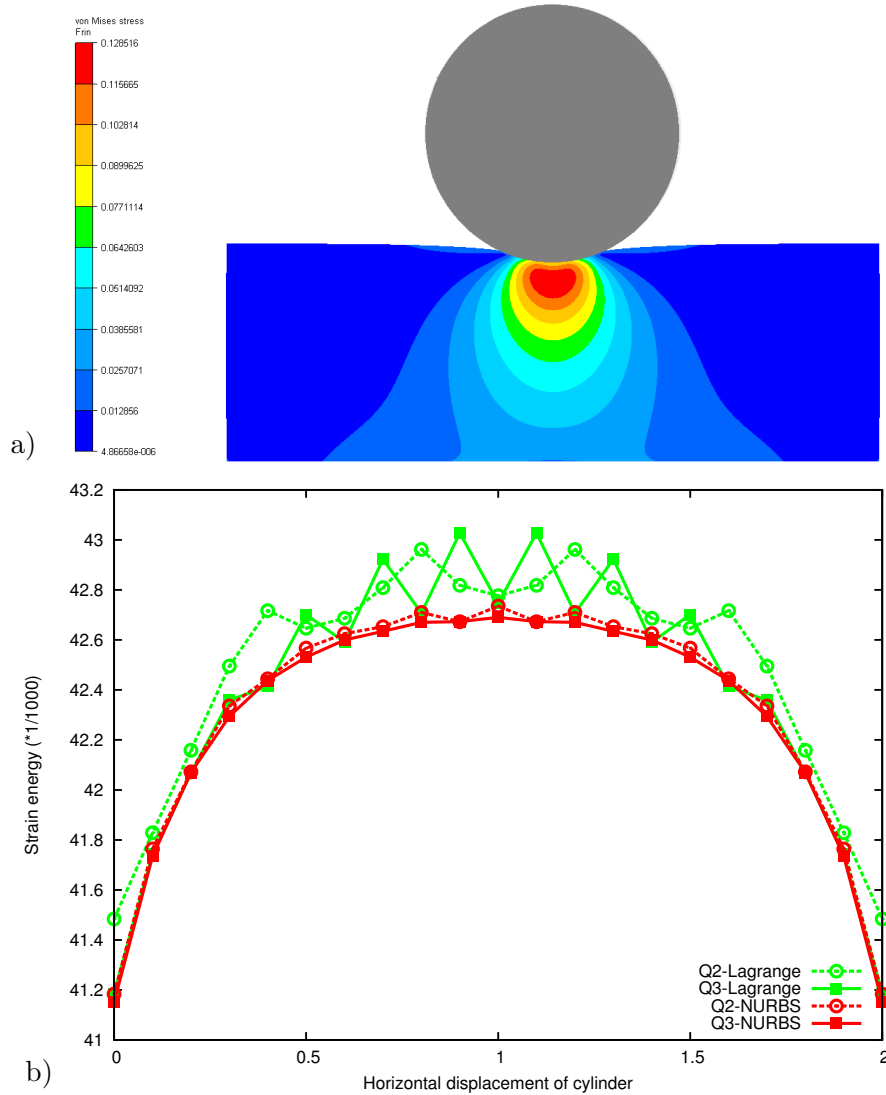


Figure 1. Ironing problem: a) Deformed configuration with Mises stress for cubic order NURBS discretization. b) Strain energy for quadratic and cubic order NURBS and Lagrange discretizations.

References

- [1] T.J.R. Hughes, J.A. Cottrell and Y. Bazilevs. Isogeometric analysis: CAD, finite elements, NURBS, exact geometry and mesh refinement. *Computer Methods in Applied Mechanics and Engineering*, 194:4135–4195, 2005.
- [2] P. Wriggers. *Computational contact mechanics*. Springer, Berlin, Germany, 2006.
- [3] P. Alart and A. Curnier. A mixed formulation for frictional contact problems prone to Newton like solution methods. *Computer Methods in Applied Mechanics and Engineering*, 92:353–375, 1991.
- [4] L.De. Lorenzis, P. Wriggers and G. Zavarise. A mortar formulation for 3D large deformation contact using NURBS-based isogeometric analysis and the augmented Lagrangian method. *Computational Mechanics*, 49:1–20, 2012.
- [5] L.De. Lorenzis, P. Wriggers and G. Zavarise. A large deformation frictional contact formulation using NURBS-based isogeometric analysis. *International Journal for Numerical Methods in Engineering*, 87:1278–1300, 2011.

Isogeometric FE analysis of thin plates with cracks

Knut Morten Okstad¹, Trond Kvamsdal^{1,2}, and Kjetil Andre Johannessen²

⁽¹⁾SINTEF ICT, Department of Applied Mathematics, Strindveien 4, NO-7465 Trondheim, Trond.Kvamsdal@sintef.no, Knut.Morten.Okstad@sintef.no

⁽²⁾Norwegian University of Science and Technology, Department of Mathematical Sciences, Richard Birkelands vei 1a, NO-7491 Trondheim, kjetijo@math.ntnu.no@ntnu.no

Summary. The fourth order Kirchhoff-Love thin plate theory is characterized by requiring C^1 continuous transversal displacements w . This is a challenge for traditional finite elements (FE) methods and has typically been circumvented by introducing rotational degrees of freedom, that adds complexity to the FE-formulation. However, the isogeometric FE approach is well suited to handle problems of higher regularity as the B-spline or NURBS typically facilitate C^{p-1} regularity. Thus, isogeometric elements with $p \geq 2$ may solve Kirchhoff-Love thin plate problems with only transversal displacements. The extension to LR B-splines makes it straight forward to also model plates with cracks, as it enables the representation of internal discontinuities in the geometry and solution field through the introduction of internal mesh lines. In this study we use LR B-splines to conduct an isogeometric analysis of a thin plate with an internal crack.

Key words: Thin plates, C^1 finite elements, Isogeometry, LR B-splines, discontinuity

Introduction

The maritime and offshore structures are often characterized by being thin-walled, i.e. that the thickness of structural elements like plates and shell are small compared to the in-plane size of the element. A plate is a plane structural element whereas shell is non-planar, i.e. plates may be considered a special (or simplified) type of shells.

For small deformations of plates we may use linear plate theories where we have decoupled the in-plane (membrane) and out-of-plane (transversal) deformation modes. Kirchhoff-Love theory is the common approach to solve thin plate problems involving pure transversal deformations. It may be considered as the natural 2D extension of the Euler-Bernoulli 1D beam theory. It may also be looked upon as a reduced order model, i.e., a 2D theory for representing 3D elastic continua with one dimension (the thickness direction) much smaller than the two others.

Through the isogeometric FE analysis concept [1], using splines as basis functions instead of the traditional Lagrange polynomials, the Kirchhoff-Love equations can efficiently be solved numerically with FEM without the introduction of rotational degrees of freedom, since the inter-element continuity is of order $p - 1$ for elements of order p . However, if the plate has a discontinuity caused by cracks, such features can not be represented with a regular spline basis due to their tensorial character, without dividing the plate into several patches with the added complexity of retaining (at least) C^1 continuity across the patch interfaces. Instead, we may then use the recently proposed Locally Refined B-splines (LR B-splines) [2], which enables the introduction of internal discontinuities in the geometry and solution field along internal mesh lines of arbitrary length.

The mathematical formulation

The Kirchhoff-Love hypothesis implies that the 3D displacement field has the form:

$$u_\alpha(x_1, x_2, x_3) = u_\alpha(x_1, x_2, 0) - x_3 \frac{\partial w(x_1, x_2, 0)}{\partial x_\alpha}; \quad \alpha = 1, 2 \quad (1)$$

$$u_3(x_1, x_2, x_3) = w(x_1, x_2, 0) \quad (2)$$

Herein, we will only address transversal loaded thin plates with small deformations and therefore we only need to determine the transversal displacement of the mid-surface $w := w(x_1, x_2, 0)$.

The governing equation for a homogeneous isotropic Kirchhoff-Love thin plate of constant stiffness D only subjected to a transverse load q , is the following biharmonic partial differential equation (PDE):

$$D\nabla^4 w = q \quad \text{in } \Omega \quad (3)$$

$$w = \bar{w} \quad \text{on } \partial\Omega_w \quad (4)$$

$$\frac{\partial w}{\partial n} = \bar{\theta} \quad \text{on } \partial\Omega_\theta \quad (5)$$

where n denotes the outer normal for the plate boundary, and \bar{w} is some prescribed deflection along the boundary $\partial\Omega_w$ and $\bar{\theta}$ some prescribed normal rotation along the boundary $\partial\Omega_\theta$, with $\partial\Omega = \partial\Omega_w \cup \partial\Omega_\theta$ and $\partial\Omega_w \cap \partial\Omega_\theta = \emptyset$. The biharmonic operator $\nabla^4 = \nabla^2 \nabla^2$ is given by

$$\nabla^4 \equiv \frac{\partial^4}{\partial x^4} + 2 \frac{\partial^4}{\partial x^2 \partial y^2} + \frac{\partial^4}{\partial y^4} \quad (6)$$

The corresponding finite element formulation is as follows: Find $w_h \in \mathcal{W}_h \subset \mathcal{W}$ such that

$$a(w_h, v_h) = l(v_h) \quad \forall v_h \in \mathcal{V}_h \subset \mathcal{V} \quad (7)$$

where the bilinear form $a(\cdot, \cdot)$ and the linear form $l(\cdot)$ is given by:

$$a(w_h, v_h) = (D\nabla^2 w_h, \nabla^2 v_h)_\Omega \quad (8)$$

$$l(v_h) = (q, v_h)_\Omega \quad (9)$$

and the inner product $(\cdot, \cdot)_\Omega$ is defined as

$$(u, v)_\Omega = \int_\Omega u \cdot v \, dV \quad (10)$$

Proper function spaces for the trial- and test displacements w and v are as follows:

$$\mathcal{W} = \left\{ w \in H^2(\Omega) \mid w = \bar{w} \text{ on } \partial\Omega_w \text{ and } \frac{\partial w}{\partial n} = \bar{\theta} \text{ on } \partial\Omega_\theta \right\} \quad (11)$$

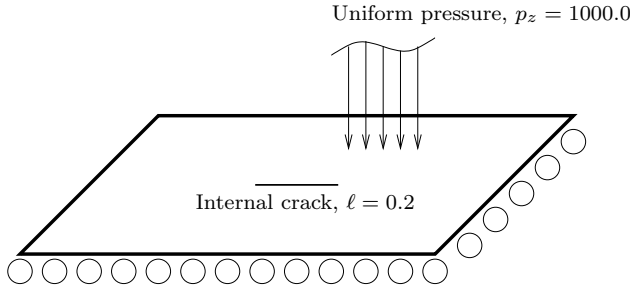
$$\mathcal{V} = \left\{ v \in H^2(\Omega) \mid v = 0 \text{ on } \partial\Omega_w \text{ and } \frac{\partial v}{\partial n} = 0 \text{ on } \partial\Omega_\theta \right\} \quad (12)$$

In the isogeometric FE method using LR B-splines we use the notation \mathcal{S}_p^r for our splines space, where p and r denote the polynomial order and regularity, respectively, in both parameter directions. Proper function spaces for respectively the FE trial displacements w_h and the FE test displacements v_h to achieve compatible FE spaces are then as follows:

$$\mathcal{W}_h(\Omega) = \{ w_h \in \mathcal{W}(\Omega) \mid w_h(F^{-1}(x_1, x_2)) \in \mathcal{S}_p^r(\xi, \eta) \} \quad (13)$$

$$\mathcal{V}_h(\Omega) = \{ v_h \in \mathcal{V}(\Omega) \mid v_h(F^{-1}(x_1, x_2)) \in \mathcal{S}_p^r(\xi, \eta) \} \quad (14)$$

where the coordinate mapping F is assumed to be an onto and invertible mapping between the parameter domain \square and the true domain Ω i.e. for any $(x_1, x_2) \in \Omega$ there exist $(\xi^*, \eta^*) \in \square$ such that $(x_1, x_2) = F(\xi^*, \eta^*)$.



Geometry: Length and width: 1.0
 Thickness: $t = 0.01$

Material: $E = 2.1 \times 10^{11}$
 $\nu = 0.3$
 $D = \frac{Et^3}{12(1-\nu)}$

Figure 1. Simply supported rectangular plate with internal crack and uniform pressure load.

Numerical example

Figure 1 shows a simply supported rectangular plate with an internal crack, subjected to a uniform pressure load. The crack is modelled by enforcing the multiplicity p of the mesh lines along the crack, as depicted in Figure 2 for the case $p = 2$, such that the geometry (and solution) here becomes C^{-1} continuous. This introduces a singularity in the solution at each crack tip.

To catch these singularities in the FE solution, it is necessary to focus the degrees of freedom around the crack tip. This is most effectively done through some adaptive refinement scheme, where we refine the mesh based on a computed error estimate. Herein, we use the energy norm error $\|e_*\| = \sqrt{a(w_* - w_h, w_* - w_h)}$, where w_* represents an enhanced solution obtained by a global L2-projection of the FE bending moments, $m_h^{\alpha\beta}$ onto the C^{p-1} continuous basis of the primary solution, w_h .

In Figure 3 we plot the convergence of the energy norm error for four different simulations; two uniform refinements with quadratic and cubic basis functions, respectively, and two adaptive refinements with the same basis. We here clearly see that through adaptive refinement, the LR B-spline basis is able to reproduce the theoretical convergence rate governed by the polynomial

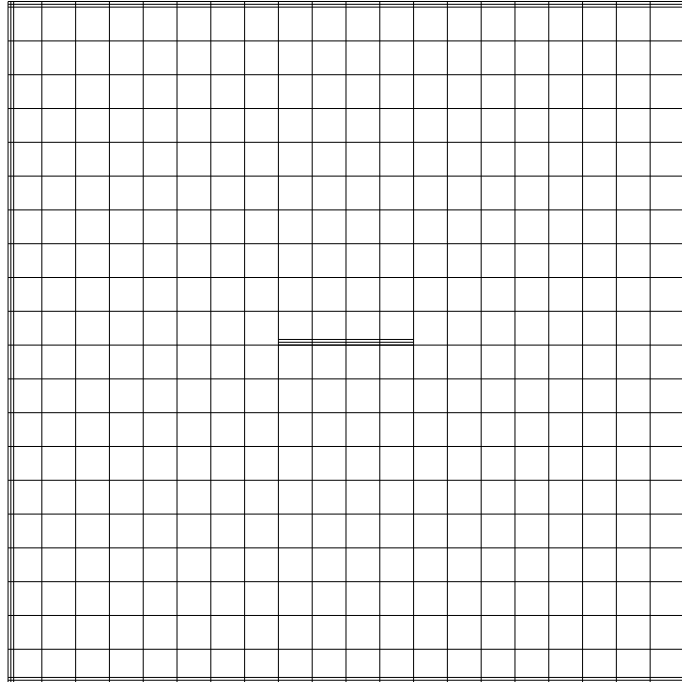


Figure 2. Initial mesh for the Quadratic ($p = 2$) case illustrating the multiplicity along the crack and external boundaries.

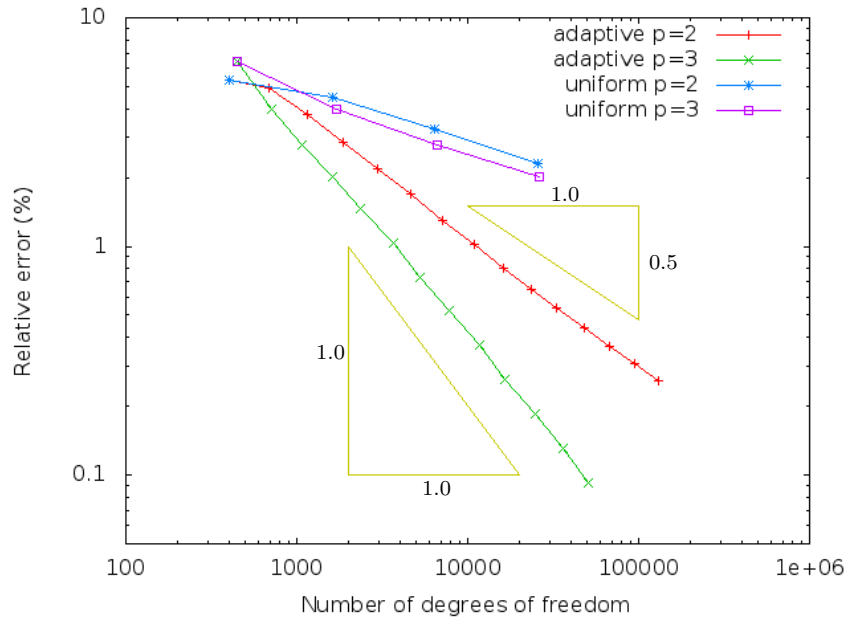


Figure 3. Convergence of the global relative error for two adaptive simulations and two uniform refinement simulations, using quadratic ($p = 2$) and cubic ($p = 3$) LR B-spline elements.

order (illustrated by the two triangles in the plot), whereas the uniform refinement completely fails to do so. The distribution of the error around the crack on the initial and 5th adaptively refined mesh is shown in Figure 4 for the quadratic case.

References

- [1] T. J. R. Hughes, J. A. Cottrell, and Y. Bazilevs. Isogeometric Analysis: CAD, Finite Elements, NURBS, Exact Geometry and Mesh Refinement. *Computer Methods in Applied Mechanics and Engineering*, 194:4135–4195, 2005.
- [2] K. A. Johannessen, T. Kvamsdal, and T. Dokken. Isogeometric Analysis using LR B-splines. *Computer Methods in Applied Mechanics and Engineering*, (in review 2012).

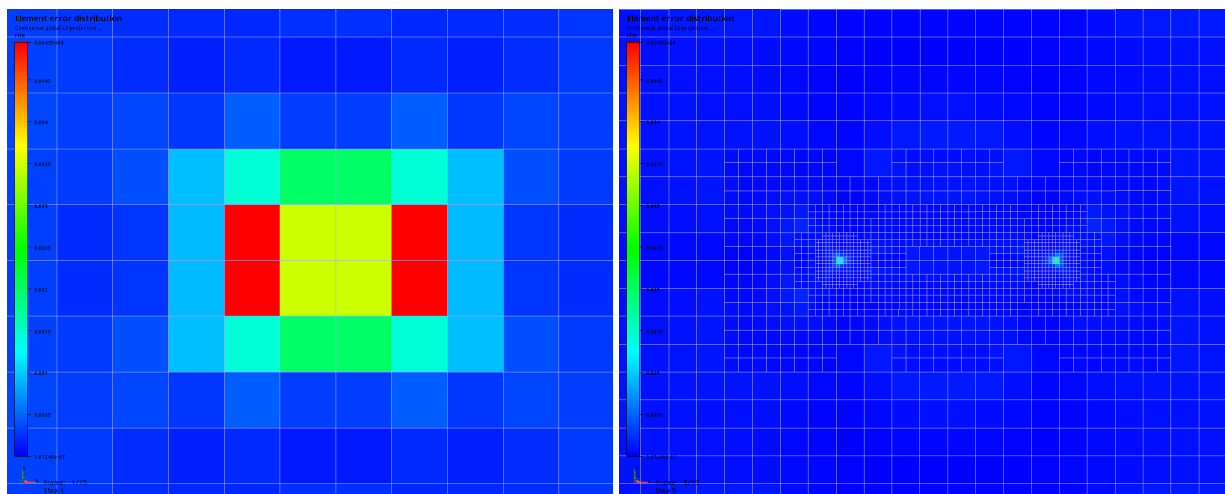


Figure 4. Error distribution around the crack for the initial (left) and 5th (right) adaptively refined mesh for the quadratic ($p = 2$) case.

Isogeometric analysis of thin structures

S.B. Raknes¹, Y. Bazilevs², K.M. Mathisen¹, T. Kvamsdal³, K.M Okstad⁴

⁽¹⁾Norwegian University of Science and Technology, Department of Structural Engineering, Richard Birkelandsvei 1A, N-7491 Trondheim, siv.bente.raknes@ntnu.no, kjell.mathisen@ntnu.no

⁽²⁾University of California San Diego, Department of Structural Engineering, 9500 Gilman Drive, La Jolla, CA 92093-0085, yuri@ucsd.edu

⁽³⁾Norwegian University of Science and Technology, Department of Mathematical Sciences, Alfred Getz' vei 1, N-7034 Trondheim, trond.kvamsdal@math.ntnu.no

⁽⁴⁾SINTEF ICT, Department of Applied Mathematics, Strindveien 4, N-7034 Trondheim, knut.morten.okstad@sintef.no

Summary. In this paper we introduce a large deformation thin beam in a dynamic non-linear setting. The beam is described by Euler-Bernoulli theory using only transversal degrees of freedom. Not using additional rotational degrees of freedom is possible as we parametrize by NURBS (Non Uniform Rational B-Spline) elements.

Key words: Isogeometric analysis, NURBS, Euler-Bernoulli, large displacements, dynamic, non-linear.

Large-deformation 3D Euler-Bernoulli beam

We have developed isogeometric finite elements for simulating Euler-Bernoulli beams with curved geometry in a dynamic non-linear setting. We have modelled a flexible Euler-Bernoulli beam as a curve in 3D with a constant arbitrary cross section that remain plane and normal to the mid curve during deformation. The beam is parametrized by NURBS in the length direction only, as we pre-integrate over the cross sectional area. The beam is modelled to account for bending and axial deformation.

Only translational degrees of freedom are used in our calculations. For the thin Euler-Bernoulli beam we will have second derivatives in the variational formulation, meaning that we need at least C^1 continuity between the elements. Using NURBS as basis functions we obtain C^{p-1} continuity across element boundaries [1], see Figure 1. Thus, using isogeometric elements with order $p \geq 2$, we may solve Euler-Bernoulli thin beam problems with only transversal displacements, and no rotational degrees of freedom.

Kinematics

We describe the beam by its reference configuration \mathbf{X} and current configuration \mathbf{x} . The displacement is given by $\mathbf{u} = \mathbf{x} - \mathbf{X}$ and the deformation gradient by $\mathbf{F} = \frac{d\mathbf{x}}{d\mathbf{X}}$. We introduce a local curvilinear coordinate system with tangent $\mathbf{x}_{,\xi_1}(\xi_1)$, binormal $\mathbf{b}(\xi_1)$ and normal $\mathbf{n}(\xi_1)$, as shown in Figure 2. Similarly for the reference configuration. ξ_1 represents the length direction, ξ_2 and ξ_3 the cross section. In 3D the beam is described by

$$\mathbf{x}^{3D}(\xi_1, \xi_2, \xi_3) = \mathbf{x}(\xi_1) + \phi_1(\xi_2, \xi_3)\mathbf{b}(\xi_1) + \phi_2(\xi_2, \xi_3)\mathbf{n}(\xi_1).$$

$\mathbf{x}(\xi_1)$ represents the mid curve of the beam, while $\phi_1(\xi_2, \xi_3)$ and $\phi_2(\xi_2, \xi_3)$ gives the position on the cross section in the directions of the binormal and the normal.

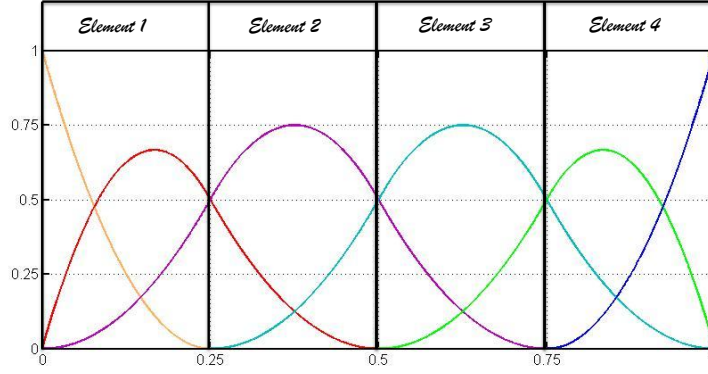


Figure 1. Quadratic B-spline basis functions for knot vector $\mathcal{H} = \{0, 0, 0, 0.25, 0.5, 0.75, 1, 1, 1\}$.

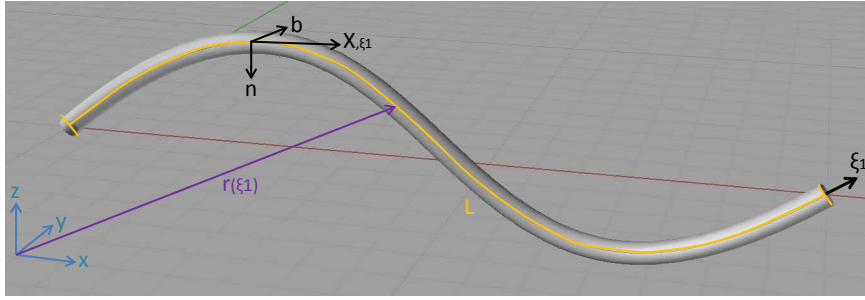


Figure 2. Sketch of the beam

Strain measure

We use the Green-Lagrange strain tensor given by

$$\mathbf{E} = \frac{1}{2}(\mathbf{F}^T \mathbf{F} - \mathbf{I}) = \mathbf{E}_{\alpha\beta} \mathbf{G}^\alpha \otimes \mathbf{G}^\beta$$

where

$$\mathbf{E}_{\alpha\beta} = \frac{1}{2}(\mathbf{g}_\alpha \mathbf{g}_\beta - \mathbf{G}_\alpha \mathbf{G}_\beta) = \frac{1}{2}(\mathbf{x}_{,\xi_\alpha}^{3D} \cdot \mathbf{x}_{,\xi_\beta}^{3D} - \mathbf{X}_{,\xi_\alpha}^{3D} \cdot \mathbf{X}_{,\xi_\beta}^{3D}).$$

\mathbf{G}^α are the reference contravariant basis vectors. For thin beams $\alpha, \beta = 1$ and we only have the term \mathbf{E}_{11} . After some calculations we can represent the dimensionless $\bar{\mathbf{E}}_{11} = \mathbf{E}_{11} \|\mathbf{G}^1\|^2$ by a term ϵ , that is the strain due to membrane action, and a term κ , that is the change in curvature due to bending; $\bar{\mathbf{E}}_{11} = \epsilon + \phi_2 \kappa$.

Constitutive equation

We use the second Piola-Kirchhoff stress tensor, \mathbf{S} , and introduce a linear constitutive law on the dimensionless stress-strain relation; $\bar{\mathbf{S}}_{11} = E_c \bar{\mathbf{E}}_{11}$. E_c is Young's modulus.

Equilibrium of virtual work

The equilibrium of virtual work, $\delta W = \delta W^{ext} + \delta W^{int} = 0$, is given by

$$\begin{aligned} \delta W^{ext} &= \int_V \delta \mathbf{x} \cdot \left(\frac{\partial^2 \mathbf{x}}{\partial t^2} - \mathbf{f}^b \right) \rho dV = \int_L \delta \mathbf{x} \cdot \left(\frac{\partial^2 \mathbf{x}}{\partial t^2} - \mathbf{f}^b \right) \rho A dL, \\ \delta W^{int} &= \int_V \bar{\mathbf{S}} : \delta \bar{\mathbf{E}} dV = \int_L (E_c A \epsilon) : \delta \epsilon + (E_c I \kappa) : \delta \kappa dL. \end{aligned}$$

V is the volume, A the cross sectional area, L the length, ρ the density per unit length and \mathbf{f}^b the body forces per unit mass.

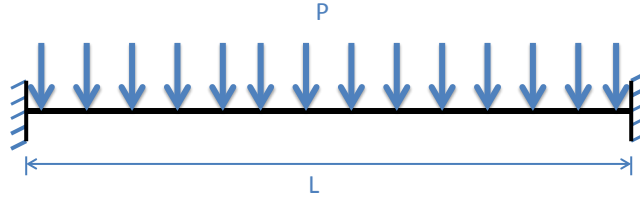


Figure 3. Beam fixed at both ends and subjected to uniformly distributed transverse loading.

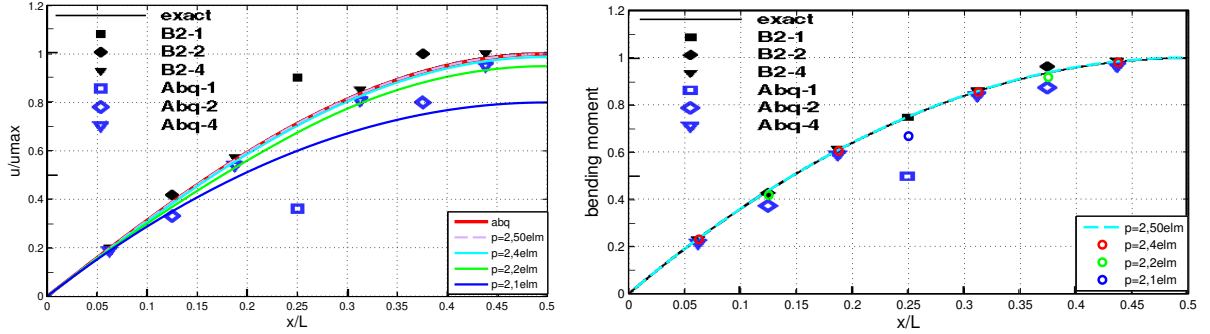


Figure 4. Displacement and bending moment of beam subjected to uniformly distributed transverse quasi-static loading. Results are compared to Abaqus [3] and an rotation-free formulation by Flores and Oñate [2].

Solving the equations of motion

Next we state the equations of motion, perform the time integration and solve for the unknown displacements by applying Newmark formulas, Newton iterations and the Generalized α -method. Doing so we need to calculate the tangent stiffness matrix;

$$\mathbf{K}_{ij} = \frac{\partial^2 W^{int}}{\partial u_i \partial u_j} = \int_L (E_c A \epsilon_{,i} \cdot \epsilon_{,j} + E_c A \epsilon_{,ij} \cdot \epsilon + E_c I \kappa_{,i} \cdot \kappa_{,j} + E_c I \kappa \cdot \kappa_{,ij}) dL.$$

Numerical examples

Beam subjected to uniformly distributed transverse quasi-static loading

We have considered a simply supported beam pinned at both ends and exposed to a uniformly distributed load, $P = 1N$, as shown in Figure 3. The bending stiffness is set to $EI = 426600Nm^2$ and the axial stiffness to $EA = 32MN$. The length of the beam is $L = 10m$. Both quadratic and cubic elements are tested. Our results are compared to the Euler-Bernoulli beam element in Abaqus [3], as well as to a rotation-free finite element formulation by Flores and Oñate [2]. Figure 4 shows that for $p = 2$ our NURBS based formulation gives more accurate displacements than both Abaqus and those presented in [2]. Regarding the bending moment, our element performs better than Abaqus. Using four elements we obtain the exact solution. However, for $p = 3$, as shown in Figure 5, we get excellent results both for displacement and bending moment when modelling half the beam with only one element.

Beam subjected to uniformly distributed transverse dynamic loading

We have considered the same beam configuration (Figure 3) in a dynamic setting with $P(t) = (2 \cdot 10^5 N) \cdot t$. In this example, the bending stiffness is set to $EI = 2.2 \cdot 10^6 Nm^2$ and the axial stiffness to $EA = 2.2 \cdot 10^6 N$. The length of the beam is now $L = 20m$. We have used the density $\rho = 0.3kg/m^3$ and a constant time step $dt = 10^{-4}s$. Cubic elements are tested and compared to the Euler-Bernoulli $B33$ element in Abaqus. Figure 6 shows that we get excellent results for all

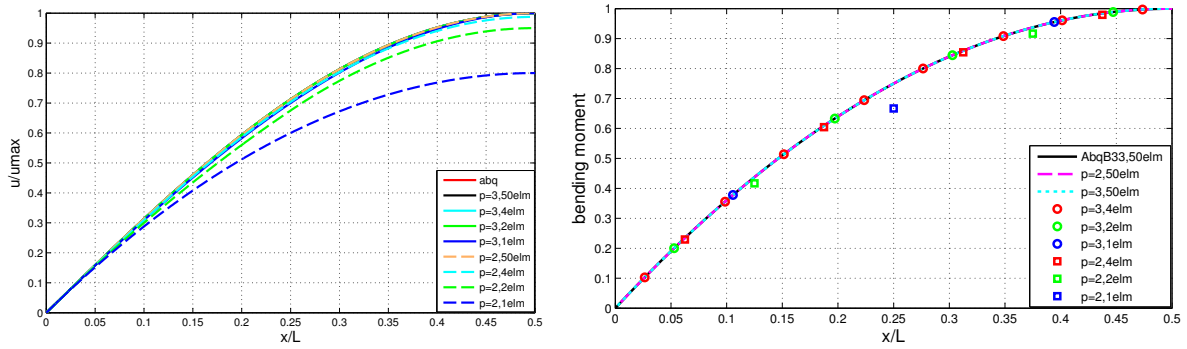


Figure 5. Displacement and bending moment of beam subjected to uniformly distributed transverse loading.

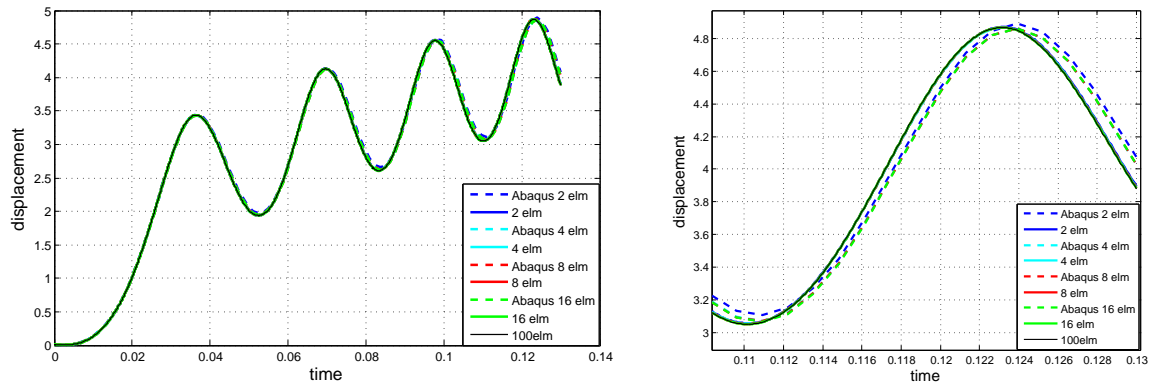


Figure 6. Beam subjected to uniformly distributed transverse loading; dynamic response in mid point.

numbers of elements. Zooming in on the last part of the simulation, we observe that our results are better than results from Abaqus.

References

- [1] J. A. Cottrell, T. J. R. Hughes and Y. Bazilevs. Isogeometric Analysis: CAD, Finite Elements, NURBS, Exact Geometry and Mesh Refinement. *Computer Methods in Applied Mechanics and Engineering*, 194:4135-4195,2005.
- [2] F. G Flores and E. Oñate. Rotation-free finite element for the non-linear analysis of beams and axisymmetric shells. *Computer Methods in Applied Mechanics and Engineering* 195(41-43):5297-5315,2006.
- [3] Abaqus 6.11. *Abaqus Theory Manual*, section 3.5.3 Euler-Bernoulli beam elements.

Isogeometric collocation method using reduced continuity order NURBS and T-splines

Mukesh Kumar, Trond Kvamsdal

Department of Mathematical Sciences, Norwegian University of Science and Technology, Alfred Getz vei 1, N-7491 Trondheim, Norway
Mukesh.Kumar@math.ntnu.no, Trond.Kvamsdal@math.ntnu.no

Summary. The authors in [1] initiate the study of collocation method in isogeometric analysis. The idea is to connect the superior accuracy and smoothness of NURBS basis functions with the low computational cost of collocation. The purpose of this paper is two-fold. First, a reduced continuity order NURBS based isogeometric orthogonal collocation method is given. Second, we propose a T-spline based collocation method using a particular class of T-splines of reduced continuity order on T-meshes [2]. The numerical results are reported to illustrate the potential of these methodologies.

Key words: Isogeometric analysis, Non-uniform rational B-spline, T-splines, Collocation methods.

Introduction

Isogeometric analysis (IGA) has been introduced in [3] as an innovative numerical methodology for the analysis of PDE's problem, allowing for an exact description of CAD type geometries. Non-uniform rational B-splines (NURBS) are a standard in Computer Aided Design (CAD) community and the basis function used to define the geometry can be systematically enriched by h -, p -, or k -refinement without altering the geometry or its parametrization. However the use of high degree basis functions as k -refinement, raises the issue of an efficient implementation. In [1], the authors initiate the study of an efficient NURBS based collocation method in isogeometric analysis. They established the theoretical framework in 1D that allows to select the Greville abscissae and second order Demko abscissae as a collocation points in the method. The purpose of this article is two fold. First, an isogeometric orthogonal collocation method using reduced continuity order NURBS basis collocating on mapped Gaussian points is given. This method is the extension of [4] in isogeometric analysis and shows optimal order accuracy of solution in L^∞ -norm, i.e., fourth order in bi-cubic NURBS case. As T-spline seems to be an alternative to break the tensor product structure of NURBS in geometrical modeling. Second, we propose a T-spline based collocation method using a particular class of T-splines, namely the one of reduced regularity, i.e., for T-splines of degree p and regularity $\alpha = p - 1 - \lfloor p/2 \rfloor$, see [2].

Isogeometric collocation method

Consider the following boundary value problem

$$\mathcal{L}u = f \text{ in } \Omega, \quad \mathcal{G}u = g \text{ on } \partial\Omega, \quad (1)$$

where the solution $u : \Omega \rightarrow \mathbb{R}$, \mathcal{L} represents a scalar differential operator, $\mathcal{G}u : \partial\Omega \rightarrow \mathbb{R}^r$ is a vector operator representing boundary conditions, and f, g are given data.

Then the isogeometric collocation approximation of (1) reads: find $u_h \in \mathcal{V}_\alpha^p$ (NURBS or T-splines space of degree $p - 1$ and regularity α) such that

$$\mathcal{L}u_h(\tau_v) = f(\tau_v) \quad \forall v \in \mathcal{I}_\mathcal{L}, \quad \mathcal{G}u_h(\tau_v) = g(\tau_v) \quad \forall v \in \mathcal{I}_\mathcal{G}, \quad (2)$$

where \mathbf{F} is the geometrical mapping and $\tau_v = \mathbf{F}(\hat{\tau}_v)$, for all $v \in \mathcal{I}$ with finite set of points $\{\hat{\tau}_v\}_{v \in \mathcal{I}}$ in the parametric space $\hat{\Omega} = [0, 1]^2$, which is divided into two distinct sets \mathcal{I}_L and \mathcal{I}_G , such that $\mathcal{I} = \mathcal{I}_L \cup \mathcal{I}_G$, and

$$v \in \mathcal{I}_L \Rightarrow \hat{\tau}_v \in \partial\hat{\Omega}, \quad \#\mathcal{I}_L + r \cdot \#\mathcal{I}_G = \dim \mathcal{V}_\alpha^p,$$

where $\#$ indicates the cardinality of a set. The choice of collocation points is crucial for the stability and good behavior of the discrete problem (2).

NURBS based isogeometric orthogonal collocation method

Assume $\Xi_d = \{0 = \zeta_{1,d}, \zeta_{2,d}, \dots, \zeta_{m_d,d} = 1\}$, $d = 1, 2$ as an ordered vector of knots without repetitions in parametric space $\hat{\Omega} = [0, 1]^2$. Now we define k -Gauss points $\{\hat{\zeta}_{ij,d}\}_{j=1}^k$ in each intervals $[\zeta_{i,d}, \zeta_{i+1,d}]$ by

$$\hat{\zeta}_{ij,d} = \frac{(\zeta_{i,d} + \zeta_{i+1,d}) + \rho_{ij}(\zeta_{i+1,d} - \zeta_{i,d})}{2}, \quad i = 1, \dots, m_d - 1, \quad j = 1, \dots, k, \quad (3)$$

where ρ_{ij} are the roots of orthogonal polynomial of degree k in each interval $[\zeta_{i,d}, \zeta_{i+1,d}]$. Now, on combining the boundary points $\zeta_{1,d} = 0, \zeta_{m_d,d} = 1, d = 1, 2$ with $(m_d - 1)k$ Gaussian points, we define the set of collocation points:

$$\hat{\gamma}_d = \{\gamma_{1,d}, \dots, \gamma_{n_d,d}\} := \{0 = \zeta_{1,d}, \underbrace{\hat{\zeta}_{11,d}, \dots, \hat{\zeta}_{1k,d}}_{k \text{ terms}}, \dots, \underbrace{\hat{\zeta}_{m_d-1,1,d}, \dots, \hat{\zeta}_{m_d-1,k,d}}_{k \text{ terms}}, \zeta_{m_d,d} = 1\}.$$

It should be noted that all the Gaussian points $\hat{\zeta}_{ij,d} \in (0, 1)$ and $\dim(\hat{\gamma}_d) = n_d = (m_d - 1)k + 2$.

Now we evaluate the collocation points $\tau_{ij} \in \Omega$, by tensor product structure as

$$\tau_{i,j} = \mathbf{F}(\hat{\tau}_{ij}), \quad \hat{\tau}_{ij} = (\gamma_{i,1}, \gamma_{j,2}), \quad \text{for } i = 1, \dots, n_1, \quad j = 1, \dots, n_2. \quad (4)$$

Then, the isogeometric orthogonal collocation approximation reads: find $u_h \in \mathcal{V}_{m-1}^{m+k}$:

$$\begin{cases} \mathcal{L}u_h(\tau_{ij}) = f(\tau_{ij}), & i = 2, \dots, n_1 - 1, \quad j = 2, \dots, n_2 - 1, \\ \mathcal{G}u_h(\tau_{ij}) = g(\tau_{ij}), & (i, j) \in \{1, n_1\} \times \{1, \dots, n_2\} \cup \{1, \dots, n_1\} \times \{1, n_2\}. \end{cases} \quad (5)$$

We wish to remark that collocation at Gaussian points shows optimal order convergence in comparison to collocation at Greville abscissae for $\mathcal{V}_{m-1}^{m+k} \subset C^{m-1}(\Omega)$.

T-spline based isogeometric collocation method

In T-spline based collocation method, we consider the collocation points as the Greville abscissae obtain from local knot vectors of each anchors of T-meshes. An example, in bi-cubic case, let $\Xi_s^a := \{s_{a1}, s_{a2}, s_{a3}, s_{a4}, s_{a5}\}$ and $\Xi_t^a := \{t_{a1}, t_{a2}, t_{a3}, t_{a4}, t_{a5}\}$ be the local knot vector associated with the anchor $a \in \mathcal{U}$ of T-mesh. Then its Greville abscissae points are given by

$$\bar{\xi}_a = (s_{a2} + s_{a3} + s_{a4})/3, \quad \bar{\eta}_a = (t_{a2} + t_{a3} + t_{a4})/3.$$

Using this we define the collocation points $\tau_k \in \Omega$ by

$$\tau_k = \mathbf{F}(\hat{\tau}_k), \quad \hat{\tau}_k = (\bar{\xi}_k, \bar{\eta}_k) \in \hat{\Omega}, \quad k = 1, \dots, \mathcal{N}.$$

Let $\mathcal{G}_{\partial\Omega}$ be the set of $(2n + 2m)$ Greville abscissae points on the boundary associated with each anchors $\{a = (i, j) \in \mathcal{U} | (i, j) \in \{1, n\} \times \{1, \dots, m\} \cup \{1, \dots, n\} \times \{1, m\}\}$ and let $\mathcal{G}_{\Omega \setminus \partial\Omega}$ be the set of $\mathcal{N} - (2n + 2m)$ Greville abscissae points within the domain Ω .

Then the isogeometric collocation approximation for T-splines space reads: find $u_T \in \mathcal{V}_T$ such that

$$Lu_T(\tau_k) = f(\tau_k) \quad k \in \mathcal{G}_{\Omega \setminus \partial\Omega}, \quad Bu_T(\tau_k) = g(\tau_k) \quad k \in \mathcal{G}_{\partial\Omega}. \quad (6)$$

Some particular T-meshes

In this section we explore the possibility of employing Greville abscissae as collocation points in (6) for some T-meshes of practical interest as shown in Fig. 1(a). Now we consider a T-spline interpolation problem with Greville abscissae, defined by $u_T(\tau_k) = f(\tau_k) \quad \forall \tau_k \in \mathcal{K}$, where f is any given smooth function. The growth of conditioning number of interpolation matrix is reported in Fig. 1(b). This shows that Greville abscissae can provide a stability to collocation formulation (6) on these types of particular T-meshes.

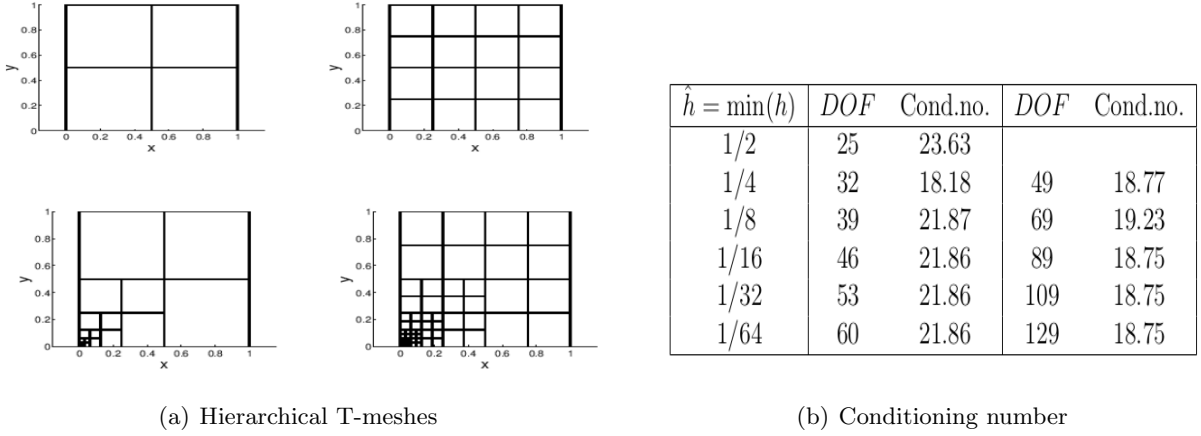


Figure 1. Sequences of Hierarchical T-meshes and growth of conditioning number w.r.t. mesh size \hat{h} .

A counter example on general T-meshes

First of all, a general question arises: Can the Greville abscissae on T-meshes always provide a stability to collocation formulation? The answer is negative as shown in Fig. 2(a). The T-spline blending functions associated with anchors (3,4) and (4,5) are given by

$$B^{(3,4)}(s, t) := N[0 \ 0 \ 1/2 \ 1/2 \ 1](s)N[0 \ 1/2 \ 1/2 \ 1 \ 1](t),$$

$$B^{(4,5)}(s, t) := N[0 \ 0 \ 1/2 \ 1/2 \ 1](s)N[0 \ 1/2 \ 1/2 \ 1 \ 1](t).$$

By calculating the Greville abscissae for both anchors it comes equal to $(1/3, 2/3)$. This gives instability to collocation formulation on general T-meshes. To overcome this problem we consider a particular class of T-splines with reduced regularity (on regular T-meshes), i.e., for T-splines of degree p and regularity $\alpha = p - 1 - \lfloor p/2 \rfloor$, for more details see [2].

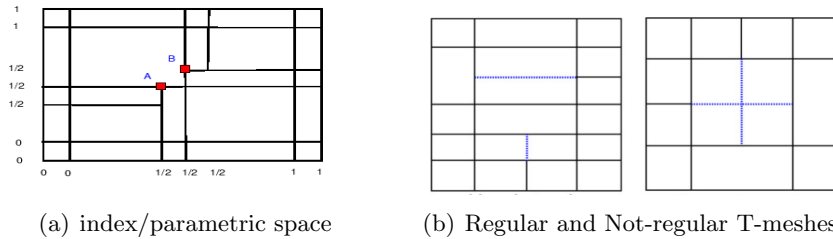


Figure 2. A counter example of Greville abscissae on T-mesh, and regular and not-regular T-meshes.

Numerical results

First, we consider an elliptic problem on a quarter of an annulus, Fig. 3(a)

$$-\Delta u + u = f \quad \forall x \in \Omega, \quad \text{with bc's } u|_{\partial\Omega} = 0, \quad (7)$$

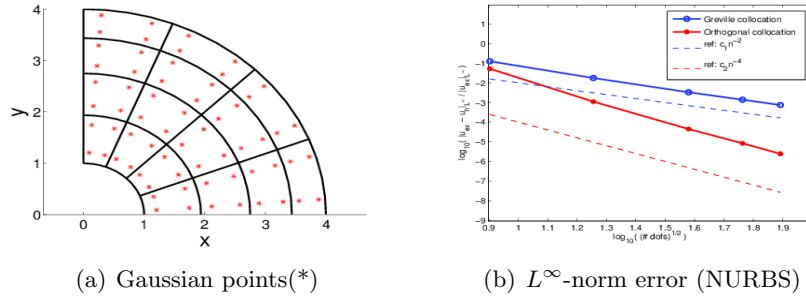


Figure 3. Numerical results using C^1 bi-cubic NURBS for problem (7).

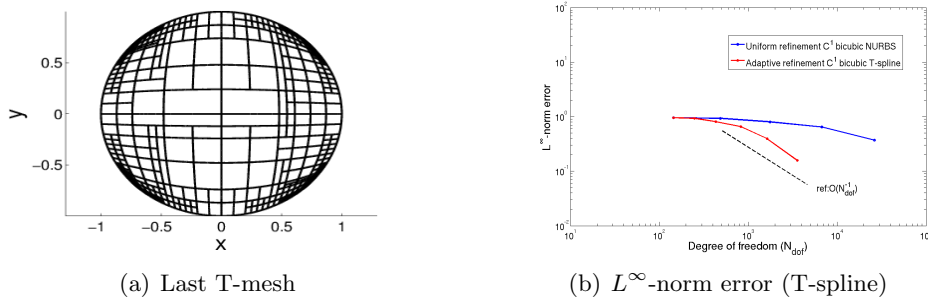


Figure 4. Numerical results using C^1 bi-cubic T-spline for problem (8) with $\varepsilon = 0.01$

with f is chosen such that $u = (x^2 + y^2 - 1)(x^2 + y^2 - 16) \sin(x) \sin(y)$. Here we consider C^1 bi-cubic NURBS space in isogeometric orthogonal collocation method (5) to solve the problem (7). It can be seen from the Fig. 3(b) that the orthogonal collocation method shows optimal order of convergence, i.e., fourth order in comparison to second order method of [1].

Second, consider a singularly perturbed reaction diffusion problem on unit disk $\Omega = \{(r, \theta) : r < 1\}$, defined as

$$-\varepsilon^2 \Delta u + u = 1 \quad \forall x \in \Omega, \quad \text{with bc's } u|_{\partial\Omega} = 0, \quad (8)$$

with exact solution $u(r, \theta) = u(r) = 1 - \frac{I_0(r/\varepsilon)}{I_0(1/\varepsilon)}$, where $I_0(r)$ is the modified Bessel function of order zeros. We consider the C^1 bi-cubic T-spline space in (6) to solve the problem (8) and adaptive refinement results in comparison to uniform refinement with C^1 bi-cubic NURBS is shown in Fig. 4(b).

References

- [1] F. Auricchio, L. Beirao da Veiga, T. J. R. Hughes, A. Reali and G. Sangalli, Isogeometric collocation methods. *Math. Models Methods Appl. Sci.*, 20(11):2075–2107, 2010.
- [2] A. Buffa, D. Cho, M. Kumar, Characterization of T-splines with reduced continuity order on T-meshes, *Comput. Methods Appl. Mech. Engrg.*, 201-204:112–126, 2012.
- [3] T.J.R. Hughes, J.A. Cottrell, Y. Bazilevs, Isogeometric analysis: CAD, finite elements, NURBS, exact geomerty, and mesh refinement, *Comput. Methods Appl. Mech. Engrg.*, 194:4135–4195, 2005.
- [4] C. de Boor, B. Swartz, Collocation at Gaussian points, *SIAM J. Numer. Anal.*, 10:582-606, 1973.

Proceedings of the 25TH NORDIC SEMINAR
COMPUTATIONAL MECHANICS, 2012

Structural Mechanics I

Room: Lilla Hörsalen, Thursday 25 October, 13:15 - 15:15



A three dimensional plasticity model for perpendicular to grain cohesive fracture in wood - an abstract

Henrik Danielsson and Per Johan Gustafsson

Division of Structural Mechanics, Lund University, P.O. Box 118, SE-221 00, Lund, Sweden
henrik.danielsson@construction.lth.se
per-johan.gustafsson@construction.lth.se

Summary. A three dimensional cohesive zone model for perpendicular to grain fracture analysis of wood is presented. The material model is derived within the framework of plasticity theory and implemented for numerical calculations by the finite element method. The criterion used for strain instability and localization to a fracture plane is according to the orthotropic Tsai-Wu criterion accounting for all six stress components. The subsequent softening performance is governed by the three out-of-fracture plane stress and plastic deformation components. The material model is applied to analysis of end-notched beams and beams with a hole. Numerical results relating to beam strength and fracture course are presented and compared to results of experimental tests.

Key words: wood, cohesive zone modeling, plasticity theory, orthotropy

Introduction

A three dimensional cohesive zone model for perpendicular to grain fracture analysis of wood is presented. This type of failure, initiated by perpendicular to grain tensile stress and shear stress, is a major concern in timber engineering and a relatively common cause for structural damage. Wood has strongly anisotropic properties, with material strength and stiffness being much lower perpendicular than parallel to grain. Wood further has anisotropic properties also in the plane perpendicular to grain. The presented material model is derived within the framework of plasticity theory and accounts for orthotropic properties since distinction is made concerning material strength and stiffness in all three material principal directions and also concerning fracture energy for the different modes of deformation.

Material model

A three dimensional macro scale continuum representation is used considering cylindrical orthotropy where distinction is made between the material longitudinal, radial and tangential directions. The material is assumed to be homogeneous, meaning that knots and other defects are disregarded. Small strain assumptions and additive decomposition of elastic and plastic strains are used. The cohesive zone model is applied to a thin predefined potential crack plane, within which a fracture process zone may initiate and evolve. This plane is here assumed to be oriented as the global xz -plane and the global x -direction is further assumed to coincide with the material longitudinal direction. The bulk material is modeled as a linearly elastic orthotropic material.

The Tsai-Wu criterion [5] is often proposed as a suitable failure criterion for wood since it includes orthotropic strength properties and allows for different tensile and compressive strengths.

It is here used as criterion for initiation of yielding, i.e. the formation of a fracture process zone and initiation of softening. An initial yield function F is hence defined according to

$$F(\boldsymbol{\sigma}) = \boldsymbol{\sigma}^T \mathbf{q} + \boldsymbol{\sigma}^T \mathbf{P} \boldsymbol{\sigma} - 1, \quad (1)$$

where $\boldsymbol{\sigma}$ is the stress and where \mathbf{q} and \mathbf{P} are given by the material strengths properties. The post softening initiation performance is assumed to be governed by the three out-of-fracture plane stress and plastic deformation components. As softening has initiated, the yield function is changed accordingly and the updated yield function f defined as

$$f(\boldsymbol{\sigma}, K) = \sigma_{yy}^2 F_{yy} + \tau_{xy}^2 F_{xy} + \tau_{yz}^2 F_{yz} - K, \quad (2)$$

where F_{yy} , F_{xy} and F_{yz} are fictitious material strength parameters and K is a softening parameter. An associated plastic flow rule is adopted. Since the yield function f only depends on the three out-of-fracture plane stress components, plastic strains are obtained only in these three directions corresponding to the fracture mechanics modes of deformation I, II and III. The softening parameter K is a function of the internal variable δ_{eff} and the following softening law is adopted

$$K = \begin{cases} \exp(\ln(c)\delta_{eff}^m) & \text{for } \delta_{eff} \leq 1 \\ 0 & \text{for } \delta_{eff} > 1 \end{cases}, \quad (3)$$

where m is a model parameter determining the shape of the softening curve and where c should be a small, but nonzero, number. The evolution law for the internal variable is defined as

$$\dot{\delta}_{eff} = \sqrt{\left(\frac{\dot{\delta}_{yy}}{A_{yy}}\right)^2 + \left(\frac{\dot{\delta}_{xy}}{A_{xy}}\right)^2 + \left(\frac{\dot{\delta}_{yz}}{A_{yz}}\right)^2}, \quad (4)$$

where the incremental plastic deformations $\dot{\delta}_{yy} = h\dot{\varepsilon}_{yy}^p$, $\dot{\delta}_{xy} = h\dot{\gamma}_{xy}^p$ and $\dot{\delta}_{yz} = h\dot{\gamma}_{yz}^p$ by assuming constant strain over the small out-of-plane height h of the predefined potential crack plane. A_{yy} , A_{xy} and A_{yz} are scaling parameters of dimension length, defined such that the work required for complete separation in any of the three modes of deformation equals the corresponding fracture energy.

Numerical implementation

The material model is implemented for finite element analysis in MATLAB using supplementary routines from the toolbox CALFEM. The highly nonlinear global response, often including snap-back, is solved in an incremental-iterative fashion using an arc-length type of path following method, see e.g. [1]. The constraint equation used to determine the increments in displacement and load is based on an energy dissipation approach presented in [6]. The stress is determined by numerical integration of the constitutive relations according to the fully implicit (Backward Euler) return method, see e.g. [4].

Application examples

End notched beam

End notched beams are commonly used in beam-to-beam or beam-to-column connections in timber structures. The analysis presented here deals with strength and fracture course for beams of different sizes and with different orientations of the material principal directions, i.e. with different growth ring patterns. Geometry, boundary conditions, loading and finite element mesh is presented in figure 1. Experimental tests with corresponding setup are presented in [3]. The nominal shear stress vs. displacement and considered growth ring patterns (with wide horizontal lines indicating the locations of the crack planes) are presented in figure 2.

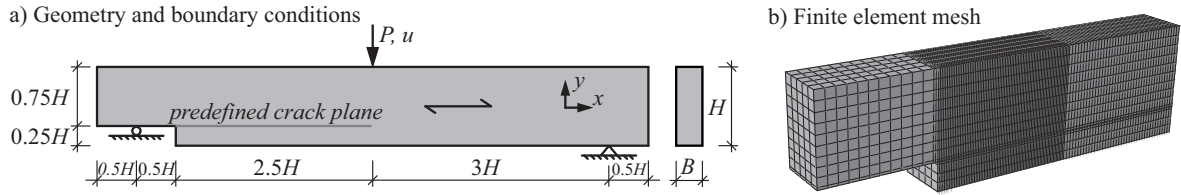


Figure 1. End notch beam geometry, boundary conditions, loading (a) and finite element mesh (b).

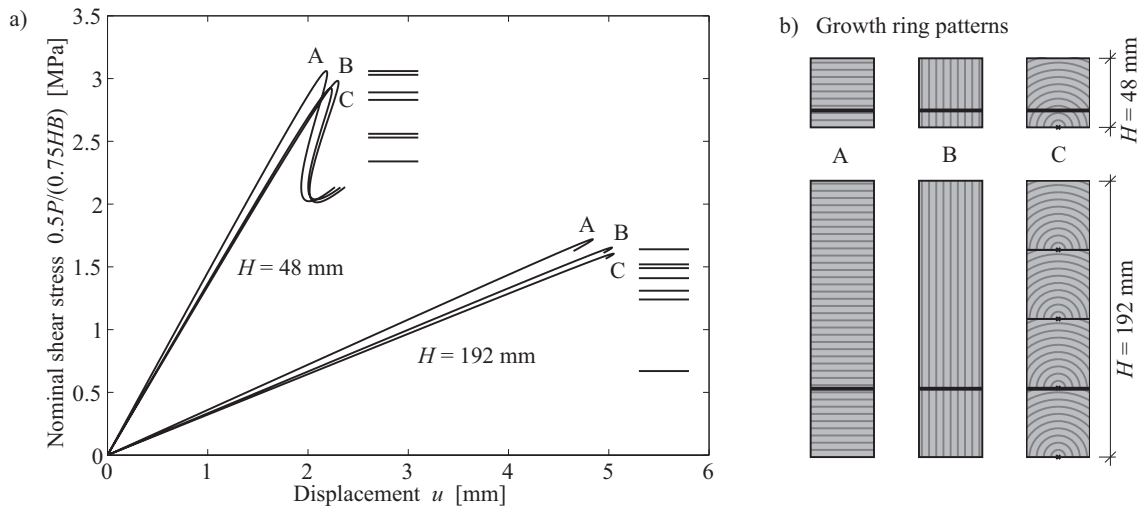


Figure 2. Nominal shear stress vs. displacement (a) for end notched beams with three types of growth ring patterns (b). Horizontal lines in (a) represent maximum load for 7+7 individual experimental tests with equal geometry and loading presented in [3].

Beam with a hole

Numerical analyses of glulam beams with a hole have also been carried out. The numerical results have been compared to results of experimental tests, in general showing a fairly good agreement both with respect to beam depth influence and general fracture behavior. A parameter study related to influence of growth ring pattern, beam width and different types of initial cracks have also been performed. The results indicate that all these parameter may influence the nominal beams strength to a significant extent.

An example of analysis of a glulam beam with a hole is presented; with geometry, boundary conditions, loading and finite element mesh according to figure 3. The beam has a cross section of $H \times B = 180 \times 115 \text{ mm}^2$ and contains a quadratic hole of side length 60 mm which is placed in the upper part of the beam. Numerical results in terms of nominal shear stress vs. displacement is presented in figure 4 together with results of four individual experimental tests of a beam with equal geometry and loading presented in [2]. Illustrations of the extension of the fracture process zones on both sides of the hole are presented in figure 5; for maximum load and for the last point of the snap-back part of the load vs. displacement path in figure 4.

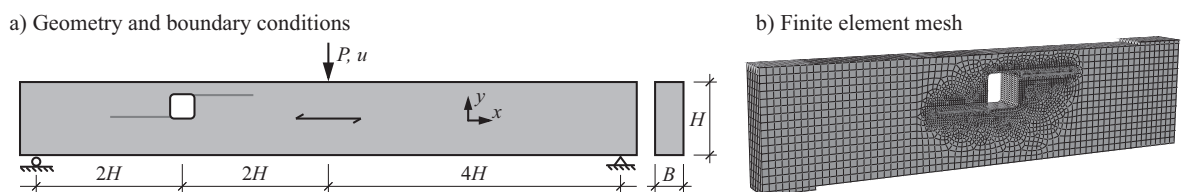


Figure 3. Geometry, boundary conditions, loading (a) and finite element mesh (b) for analysis of a beam with a hole.

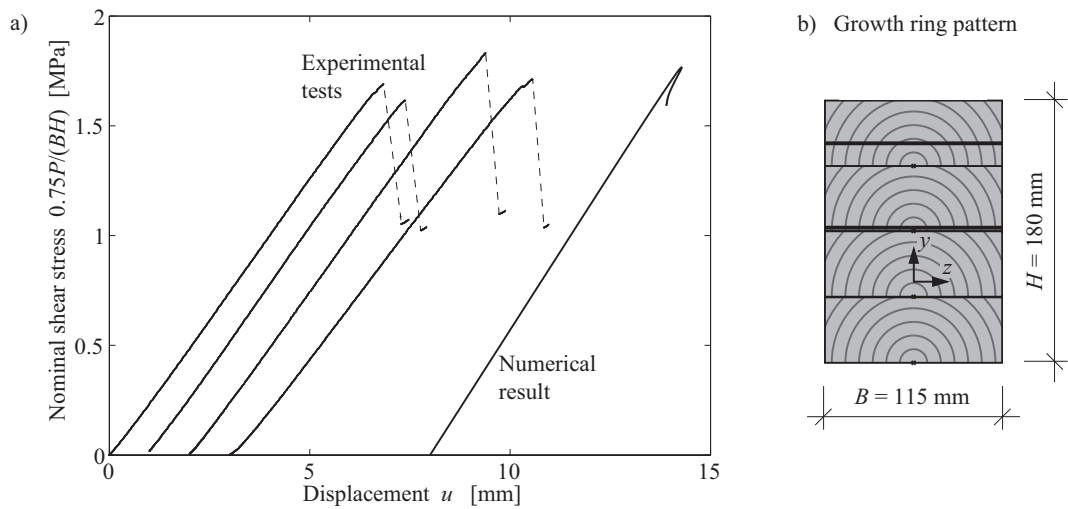


Figure 4. Nominal shear stress vs. displacement (a) for a beam with a hole and growth ring pattern (b).

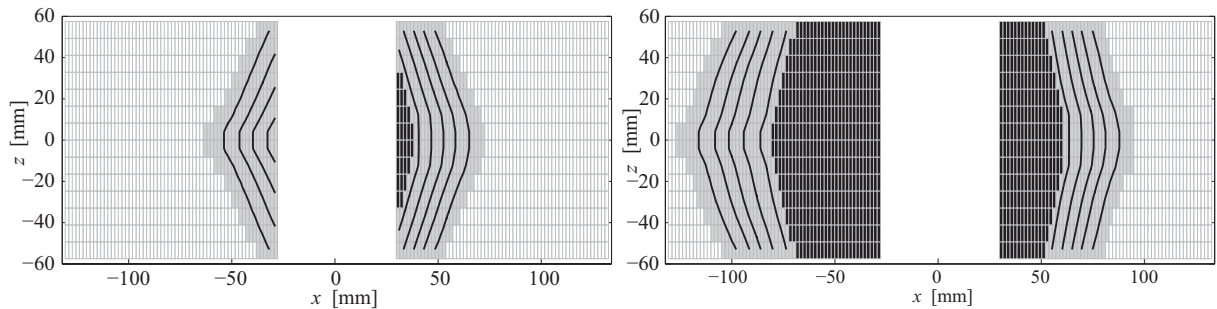


Figure 5. Extensions of fracture process zones at maximum load (left) and at the last point of the snap-back part of the load vs. displacement path (right): black elements represent traction-free crack, grey elements represent fracture process zone and isolines represent δ_{eff} values of 0.1, 0.3, 0.5, 0.7 and 0.9.

References

- [1] M.A. Crisfield. *Non-linear finite element analysis of solids and structures*. Volume 1, John Wiley & Sons Ltd, Chichester, England, 1991.
- [2] H. Danielsson and P.J. Gustafsson. A probabilistic fracture mechanics method and strength analysis of glulam beams with holes. *European Journal of Wood and Wood Products*, 69:407-419, 2011.
- [3] P.J. Gustafsson and B. Enquist. *Träbalks hållfasthet vid rätvinklig urtagning*. Report TVSM-7042, Division of Structural Mechanics, Lund University, Sweden, 1988.
- [4] N.S. Ottosen and M. Ristinmaa. *The mechanics of constitutive modeling*. Elsevier, Great Britain, 2005.
- [5] S.W. Tsai and E.M. Wu. A general theory of the strength of anisotropic materials. *Journal of Composite Materials*, 5:58-80, 1971.
- [6] C.V. Verhoosel, J.J.C. Remmers, M.A. Gutiérrez. A dissipation based arc-length method for robust simulation of brittle and ductile failure. *International Journal for Numerical Methods in Engineering*, 77:1290-321, 2009.

Finite-Element analysis of multilayered shells deformation under the load with a flat base

S. M. Bauer¹, L. A. Karamshina¹

⁽¹⁾Department of Theoretical and Applied Mechanics, St. Petersburg State University, Russia, 198504, St. Petersburg, University ave. 28, e-mail: s_bauer@mail.ru, l_karamshina@mail.ru

Summary. A finite-element model of two thin transversely-isotropic conjoined spherical shells with different radii of curvature and biomechanical properties under internal pressure and external load with a flat base are presented. Shell with the smaller radius splits into several layers of different thickness and elastic properties. The external load is applied to the shell of a smaller radius. The comparison of results obtained before and after the removal of shell layers is analyzed. The proposed finite-element model simulates the measurements of intraocular pressure (IOP) using Goldmann's applanation tonometer (GAT) and Maklakov's applanation tonometer (MAT) (weight 5 g and 10 g) and suitable for global analysis of cornea deformations before and after refractive surgery.

Key words: intraocular pressure measurements, Goldmann's tonometer, Maklakov's tonometer, multilayer shells, refractive surgery, LASIK, PRK.

Introduction

The problem of the stress-strain state of soft and close to soft shells under the load with a flat base is important for the analysis of the data associated with the measurements of essential feature in ophthalmology – intraocular pressure (IOP). IOP plays an important role in diagnostic of a number of eye diseases and the development of effective methods for their treatment.

Applanation tonometry estimates intraocular pressure (IOP) by quantifying the force needed to create a defined amount of deformation of the cornea (Goldmann's tonometer) or by estimating the diameter of the circular contact area of the cornea and flat tonometer of defined load (Maklakov's tonometer). See figure 1.

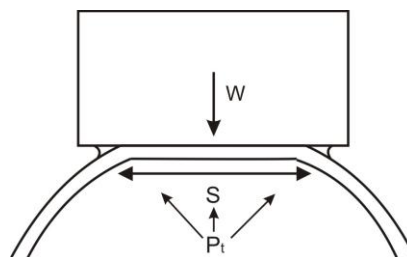


Figure1. The cornea under the load with a flat base.

It is known, that refractive surgery significantly changes the thickness and curvature of the cornea. At the present time it is recognized that cornea thickness and curvature significantly affect the IOP readings [1-6]. Standardization of IOP measurements and examination of the effect of different parameters of the eyeball onto the value of intraocular pressure are among urgent questions today.

The changes in IOP readings after refractive surgery can't be described by the theory of soft shells. In order to analyze the effect of decreasing of the corneal thickness in the central zone on the IOP readings obtained by Goldmann's and Maklakov's tonometers after refractive surgery the following model problem is considered.

Problem statement

The eye shell is modeled as conjectured spherical shells with different diameters and elastic properties (see figure 2). It is assumed that before loading the composite shell is filled by incompressible liquid with real pressure p (the true intraocular pressure). The cornea is modeled by a spherical segment with smaller radius which divided into four layers (see figure 3) that represent epithelium (L_1), Boymen's membrane (L_2), stroma (L_3), Descemet's membrane (L_4) consequently. The sclera is modeled as monolayer spherical segment with the bigger radius (L_5).

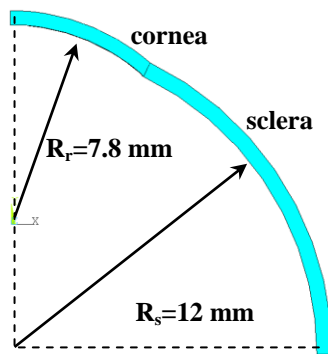


Figure 2. The cornea is modeled by conjectured shells

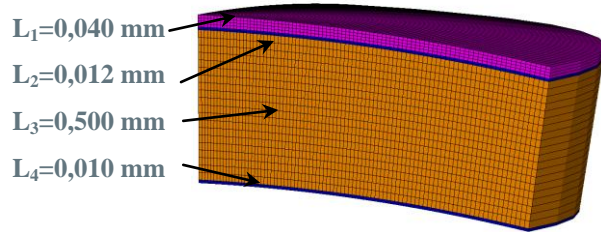


Figure 3. The cornea is divided into four layers

In figure 4 the layers of the cornea (L_6), which are exposed to a laser beam in the refractive surgery LASIK and PRK are shown.

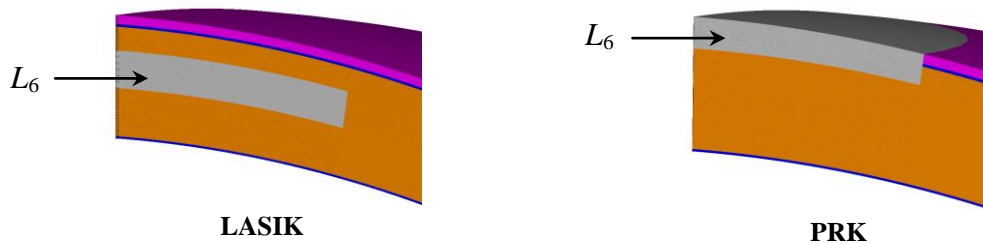


Figure 4. The cornea after refractive surgery: LASIK and PRK.

According to experimental data [6] sclera and cornea can be considered as transversally-isotropic shells, therefore, on elastic coefficients the following conditions [7] are imposed:

$$|\nu_i'| < (E_i'/E_i)^{1/2}, \quad -1 < \nu_i < 1 - 2(\nu_i')^2(E_i/E_i'), \quad (E_i > 0, E_i' > 0), \quad i = 1, \dots, 5. \quad (1)$$

Here E_i and E_i' are elastic moduli under tension and compression on the surface of isotropy

and in the normal to this surface direction; ν_i and ν'_i are Poisson ratios. Transverse moduli for the surface of isotropy are defined by the following relation $G_i = E_i / 2(1 + \nu_i)$.

Average values of the elastic moduli for the whole cornea in the tangential direction E and in the normal direction E' are determined from [8]:

$$E = \frac{(1 - \nu^2)}{\sum_{i=1}^n h_i} \left[\sum_{i=1}^n \frac{E_i h_i \nu_i}{1 - \nu_i^2} \right], \quad E' = \frac{(1 - \nu'^2)}{\sum_{i=1}^n h_i} \left[\sum_{i=1}^n \frac{E'_i h_i \nu'_i}{1 - \nu_i'^2} \right], \quad i = 1, \dots, 4, \quad (2)$$

where ν , ν' are averaged Poisson ratios,

$$\nu = \sum_{i=1}^n \frac{E_i h_i \nu_i}{1 - \nu_i^2} \bigg/ \sum_{i=1}^n \frac{E_i h_i}{1 - \nu_i^2}, \quad \nu' = \sum_{i=1}^n \frac{E'_i h_i \nu'_i}{1 - \nu_i'^2} \bigg/ \sum_{i=1}^n \frac{E'_i h_i}{1 - \nu_i'^2}. \quad (3)$$

Relations (1) and (2) allow us to estimate the effect of a multilayer structure of the cornea on average parameters of the whole cornea (thickness, elastic moduli and Poisson ratios), therefore, to estimate the change of the parameters of IOP.

In the measurement of intraocular pressure by Maklakov's method the tonometer with flat foundation (weight 10 g) is placed on cornea. Under the influence of this load cornea is deformed and the diameter of the contact area is registered.

Goldman's method is based on the measuring of the force that must be applied to a fixed central region of cornea. Flattened area should have a diameter of 3.06 mm, since for this contact area the force of 0.1 g applied to the tonometer corresponds to IOP equal to 1 mm Hg, therefore, force (in grams) is multiplied by ten and sets to be equal to IOP.

Measurement of IOP by Maklakov's and Goldmann's tonometers are modeled by contact problems in program package ANSYS. At the first step the intraocular pressure is applied, next the force $F = m \text{ g}$ is applied. In the first problem the force applied to the cornea was equal to 10 grams (0.1 H) and the contact area was estimated. In the second problem the force varied so that the contact area was equal to 3.06 mm.

Numerical analysis

In order to estimate the influence of multilayer structure of cornea on changes of intraocular pressure during measurements only elastic parameters of the cornea layers were varied, while the thickness and elastic modulus of sclera remained constant. For each series of calculation was carried out comparison of results obtained for multilayered shell and one-layered shell with average elastic modulus.

Calculations showed that in case of the IOP measurement by the use of Maklakov's tonometer the contact area of the cornea and tonometer for the multilayer model appears bigger than for single-layer model with averaged elastic coefficients (2, 3). In the case of the measuring of IOP by Goldmann's tonometer the value of the force that must be applied to the tonometer in order to obtain the contact area of the tonometer and shell was equal to 3.06 mm, appears lower for multilayer model. Thus, it was shown that multilayer corneal model gives a more accurate estimation of the true IOP.

After LASIK surgery an additional layer (flap) is created. In order to estimate the influence of this layer on the IOP readings obtained after LASIK, cornea was modeled with five layers, while after PRK cornea was modeled with four layers. It was assumed that the change in corneal thickness in both cases occurs on one value h .

Conclusions

The calculations have shown that the heterogeneity of the cornea in the thickness direction provides more closely adjacent values of the true and tonometric IOP. After refractive surgery the bending stiffness of the cornea reduces, and, consequently, reduces the IOP readings obtained by Goldmann's and Maklakov's applanation tonometers. The changes of IOP readings obtained by Maklakov's tonometer are imperceptible. The IOP readings obtained by Goldmann's tonometer after refractive surgery depend strongly on the depth of laser impact (ablation).

The result of calculations showed that IOP readings obtained after LASIK are lower than the IOP readings obtained after PRK. It could be explained by the appearance of additional layer after LASIK. The increase of layers number reduces the bending stiffness of the cornea, and as a consequence, reduces the data of IOP obtained by Goldmann's and Maklakov's tonometers.

References

- [1] M. J. Doughty , M.L. Zaman. Human corneal thickness and its impact on intraocular pressure measures: a review and meta-analysis approach. *Surv Ophthalmology*, 44 (5): 367-408, 2000.
- [2] S.M. Bauer, A.B. Kachanov, B.N. Semenov, I. Sliesoraityte. The effect of cornea thickness on measurements of IOP by applanation methods. *Ocular biomechanics*, Moscow, 119-124, 2007.
- [3] O.I. Lebedev, A.E. Yavorskii. The impact of refractive surgery on the level of intraocular pressure readings in myopic patients. *Russian Ophthalmological Journal*, 2: 23-25, 2008.
- [4] S.E. Avetisov, I.A. Novikov, I.A. Bubnova, A.A. Antonov. The Investigation of biomedical properties of cornea after refractive surgery, *IV Russian ophthalmology forum 5-7. 10.2011*, Moscow: 22-25, 2011.
- [5] E.P. Tarutta, V.P. Elichev, T.Y. Larina, Controlling intraocular pressure after keratorefractive operations. *Ocular biomechanics*, Moscow: 120-122, 2004.
- [6] E.N. Iomdina, Mechanical properties of tissues of the human eye. *Modern Problems of Biomechanics*, Moscow State University, 11: 183-200, 2006.
- [7] V.A. Rodionova, B.F. Titaev, K.F. Chenyh. *Applied theory of plates and shells*, Saint-Petersburg State University, 1996.
- [8] E.I. Grigolyuk, P.P. Chulkov. *Stability and oscillations of three-layered shells*. Moscow: Mashinostroenie, 1973.

Grouted Connections with Shear Keys - Numerical Modelling with ABAQUS

R.R. Pedersen¹, M.B. Jørgensen¹, L. Damkilde¹, H.B. Clausen² and K. Andersen³

⁽¹⁾Aalborg University, Niels Bohrs Vej 8 DK-6700 Esbjerg, rrp@civil.aau.dk

⁽²⁾ Rambøll Offshore Wind, Hannemanns Allé 53, DK-2300 Copenhagen, hbc@ramboll.dk

⁽³⁾ Rambøll Offshore Wind, Adgangsvejen 3, DK-6700 Esbjerg, kxa@ramboll.dk

Summary. This paper presents a finite element model in the software package ABAQUS in which a reliable analysis of grouted pile-to-sleeve connections with shear keys is the particular purpose. The model is calibrated to experimental results and a consistent set of input parameters is estimated so that different structural problems can be reproduced successfully.

Key words: Finite element method, ABAQUS, Plasticity, Damage, Grouted Connections, Shear Keys.

Introduction

The grouted pile-to-sleeve connection shown in Figure 1 has been used in oil & gas structures for decades. In these structures the grouted connections mainly transfer axial compressive forces and the diameter of the connections is relatively small. However, today grouted connections

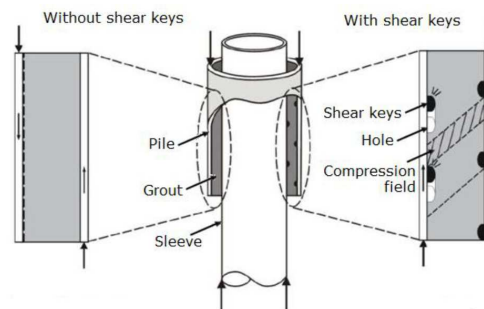


Figure 1. A grouted connection with and without shear keys.

with much larger diameters are used between mono piles and wind turbine towers. Additionally, these connections are exposed to significant cyclic bending moments next to the axial forces. The first grouted connections of this type were designed based on the same design rules as used for offshore oil & gas installations. Consequently, sliding damage was observed in many of these connections and a revised design practice was necessary. Therefore, Det Norske Veritas (DNV) reviewed the design practice for calculating the axial load capacity of grouted connections with large diameters and without shear keys. DNV concluded that the existing design practice was invalid and inaccurate. A joint industry project (JIP) phase 1 was established with the primary goal to update and improve the design recommendations for grouted connections with large diameters. Plain cylindrical shaped grouted connections without shear keys can no longer be recommended and a new design methodology for conical shaped grouted connections is given

in DNV-OS-J101 (2011). During the JIP phase 2 a design procedure for cylindrical shaped grouted connections with shear keys subjected to cyclic dynamic loading has been developed and will be included in the coming DNV-OS-J101. The conclusions and results from the JIP projects can be found in a publication from DNV [5]. A clear statement from the JIP report regarding modelling of grouted connections with shear keys: *Presently, there is no finite element analysis method/programme readily available to the industry that can be used for reliable analysis of the ultimate capacity of these connections.* Therefore, the aim of this study is to examine if ABAQUS can be used to simulate the failure process of a grouted connection with shear keys. However, a numerical model in ABAQUS is only attractive for the industry if the model

- includes the physical mechanisms behind the mechanical properties of the grouted connection
- is robust i.e. no severe convergence problems
- is objective with respect to finite element size
- includes unique model parameters

Numerical model in ABAQUS

We have applied the Concrete Damaged Plasticity model available in ABAQUS, where the flow potential G is similar to a Drucker-Prager hyperbolic function

$$G = \sqrt{(\epsilon \sigma_{c0} \tan \psi)^2 + \bar{q}^2} - \bar{p} \tan \psi, \quad (1)$$

where \bar{p} is the hydrostatic pressure and \bar{q} is the equivalent Von Mises stress both expressed in the effective stress space. The dilatation angle ψ , the eccentricity parameter ϵ and the initial compression strength σ_{c0} define the shape of G in the $p - q$ plane. The Lubliner yield criteria [6] is used

$$F = \frac{1}{1 - \alpha} (\bar{q} - 3\alpha\bar{p} + \beta \langle \bar{\sigma}_{p,\max} \rangle + \gamma \langle -\bar{\sigma}_{p,\max} \rangle) - \sigma_c(\epsilon_c^{\text{pl}}), \quad (2)$$

where the scale parameter α depends on the initial material strengths, whereas β is controlled by both the initial strengths and the current stress state, which depends on the equivalent plastic strain and the damage level ω . The factor γ depends on the shape parameter K_c , where $K_c = 1$ implies that the yield surface F is similar to a Drucker-Prager yield surface. The maximum principal stress in the effective stress space is denoted $\bar{\sigma}_{p,\max}$. The Concrete Damaged Plasticity model in ABAQUS adopts the concept of isotropic damaged elasticity in combination with isotropic tensile and compressive plasticity to represent the inelastic behaviour of concrete. Furthermore, it is assumed that tensile cracking and compressive crushing are the main failure mechanisms. Therefore, we need to input at integration point level the curves $\sigma_c(\epsilon_c^{\text{pl}})$ and $\sigma_t(\epsilon_t^{\text{pl}})$, where ϵ_c^{pl} and ϵ_t^{pl} are the inelastic strain in compression and tension, respectively. Additionally, we define the damage curves $\omega_t(\epsilon_t^{\text{pl}})$ and $\omega_c(\epsilon_c^{\text{pl}})$. The model is regularized by visco-plasticity with the relaxation time μ as input. The regularization ensures more stable convergence and objective results with respect to the finite element size. A successful model is able to capture the correct force-displacement response as well as a realistic damage pattern (failure mode). This requires a careful input of the 4 material curves and the relaxation time, which is the main challenge of the material model in ABAQUS. In this calibration process we found inspiration in [3]. We have been able to define a unique set of input curves and model parameters so the same material model can be used to reproduce experimental observations from different structural problems. Finally, we have defined friction between grout and steel with a friction parameter $\mu_f = 0.4$ and the main input parameters are presented in Table 1.

Table 1. Model parameters defined in the ABAQUS material model.

E	ν	σ_{c0}	σ_{t0}	ψ	ϵ	$\frac{\sigma_{b0}}{\sigma_{c0}}$	K_c	μ	μ_f
[MPa]	[-]	[MPa]	[MPa]	[°]	[-]	[-]	[-]	[s]	[-]
55000	0.19	150	7	38	1.0	1.12	0.666	0.001	0.4

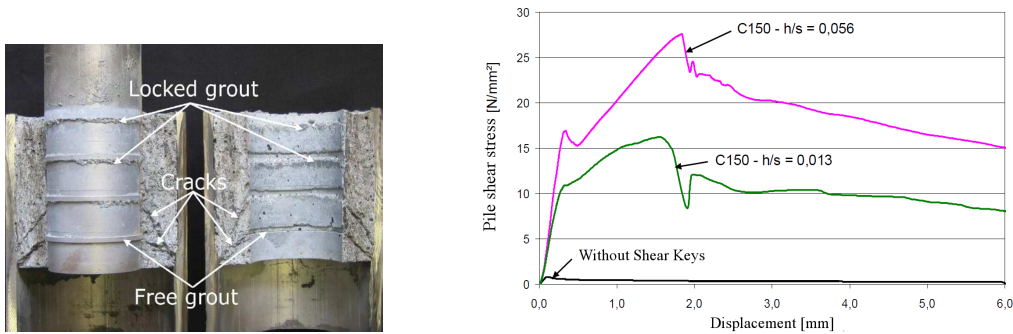


Figure 2. Scaled axial compression test from [1], where the cracks and typical force-displacement curves are shown. A compression strength $\sigma_{c0} = 150$ MPa is used and h is the height of the shear key and s is the spacing distance between the shear keys.

Results

In order to calibrate the model i.e. define a set of model parameters, adjust the inelastic strain-stress and the inelastic strain-damage input curves we have done preliminary simulations with plain grout in different structural set-ups: uni-axial tension, uni-axial compression, three-point bending and compared to experimental results from the literature. Next we have studied the experimental and numerical work on grouted connections from [7, 1, 2] among others. Here we present the numerical results from ABAQUS, where the experiments from Steffen Anders [1] are considered. Figure 2 shows the results from uni-axial compression tests [1], where the influence of the shear key and the shear key spacing on the capacity of the grouted connection is highlighted. The first sudden decrease in capacity is related to a slip between grout and steel material which initiates the first tensile cracks between the shear keys on pile and sleeve, see Figure 2 (left). The second sudden decrease in capacity is caused by the further slips and compressive damage. The numerical results from an axi-symmetric model in ABAQUS is presented in Figure 3. We have marked 5 points on the stress-deformation plot and the corresponding damage plots are presented in Figure 4. The numerical results ($h/s = 0.056$) correspond well with the experimental results in the displacement range [0-1.5] mm, where the first capacity decrease due to tensile cracking (point 1-2) is captured. In order to fit the next decrease (point 3) it is necessary to include yielding of the steel material. This is also in agreement with the conclusions from [2]. The confinement of the grout material is decreased when the steel material yields due to hoop stresses. Consequently, the grout material fails in compression and when a full crushing zone is established, see Figure 4 (left), the second sudden decrease is observed.

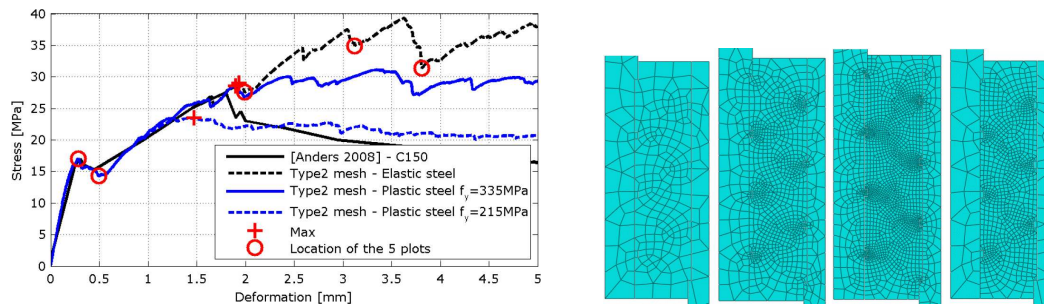


Figure 3. Numerical results from ABAQUS, where the results are compared to the experiments from [1]. The depicted element discretizations are tested and Type 2 mesh refers to the last mesh, where the grout and steel elements are non-conforming.

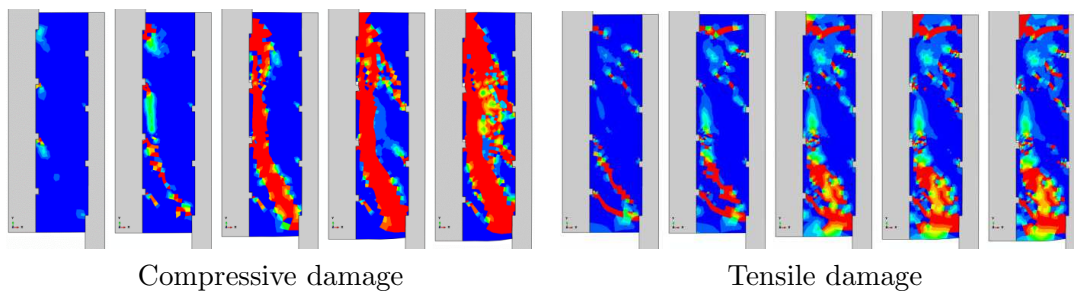


Figure 4. Numerical results from an axi-symmetric model in ABAQUS, where the evolutions of compressive and tensile damage are shown for the 5 steps highlighted in Figure 3.

Concluding remarks

The Concrete Damaged Plasticity model from ABAQUS is adopted to simulate the failure process of a grouted connection with shear keys exposed to uni-axial compression. We conclude that the simulations are successful and that the model can be used to further analysis of structural problems with grouted connections.

References

- [1] S. Anders Betontechnologische einflüsse auf das tragverhalten von grouted joints. *PhD-Thesis*, Leibniz University Hannover, Germany, (2007)
- [2] W. Aritenang, A.S. Elnashai, P.J. Dowling and B.C. Carroll Failure mechanisms of weld-beaded grouted pile/sleeve connections. *Marine Structures*, **3**, 391–417, (1990)
- [3] T. Jankowiak and T. Lodygowski Identification of Parameters of concrete damage plasticity constitutive model. *Foundation of Civil and Enviromental Engineering*, **6**, 53–69, (2005)
- [4] J.H. Ling, A.B.A. Rahman, I.S. Ibrahim and Z.A. Hamid Behaviour of grouted pipe splice under incremental tensile load. *Construction and Building Materials*, **33**, 90–98, (2012)
- [5] I. Lotsberg, A. Serednicki, H. Bertnes and A. Lervik Design of grouted connections for monopile offshore structures results from two joint industry projects. *Stahlbau*, **81**, Heft 9, 695–704, (2012)
- [6] L. Lubliner, J. Oliver, S. Oller and E. Oñate A plastic damage model for concrete. *Int. J. Solids Structures*, **25**, 299–326, (1989)
- [7] P. Schaumann, F. Wilke and S. Lochte-Holtgreven Fatigue performance of grouted joints for offshore wind energy converters in deeper waters. *Proceedings of the Twentieth International Offshore and Polar Engineering (ISOPE) Conference*, Beijing, China, 2010.

A reduced model for glass structures subjected to dynamic impact loads

Maria Fröling, Kent Persson, and Per-Erik Austrell

Dept. of Construction Sciences, Lund University, P.O. Box 118, SE-221 00 Lund, Sweden,
Maria.Froling@construction.lth.se, Kent.Persson@construction.lth.se,
Per_Erik.Austrell@construction.lth.se

Summary. A reduced model for determining the maximum principal stress of a glass pane subjected to dynamic impact load is developed. The aim is to integrate the model into a glass design program for strength design of glass structures. The model performs well for clamped glass panes of modest sized in-plane glass dimensions. Further model development is required in order for the method to deal with for instance varying glass pane dimensions and boundary conditions.

Key words: glass, strength design, dynamic impact load

Introduction

When performing strength design of glass structures, dynamic impact load is one of the load cases which might be included in the analysis. Since glass is a brittle material, it is sensitive to impact load and it is necessary to accurately determine the stress distribution in the glass due to this load case. At present strength design of glass structures may be performed by means of experimental tests. The European and Swedish standard SS-EN-12600, [1], is available to classify glass for impact strength. However, when performing strength design of glass structures, the properties of the system may be different from those prescribed in the standard. It is possible to apply the impact load according to the standard to a glass structure, but the process is time consuming when considering parameter variation in strength design. An alternative is to use finite element simulations. Among others Persson and Doepker (2009), [2], performed a finite element analysis of the test arrangement that is described by the standard. It was proven that the finite element simulations yield results close to experimental results for standard parameter values. Further analyses showed that the results are sensitive to parameter variations, which implies that it is important to consider the actual conditions for the structure under consideration when performing strength design. However, finite element modeling could be advanced and time consuming. In this work, the aim is to develop a reduced model for strength design of glass structures subjected to dynamic impact load. The resulting model is to be integrated into a glass design computer program which allows fast and accurate strength design of glass structures.

A pendulum impact test for classifying glass for impact strength

The experimental test arrangement used to classify glass for impact strength, [1], consists of a glass pane held within a steel frame and an impactor consisting of a weight encased in a tire. During the test, the tire is swung in a pendulum motion into the glass pane. The dimensions of the frame are standardized, as well as the weight of the impactor. For use in this work, the impactor drop height is set to 1200 mm.

A reduced model for glass panes subjected to dynamic impact loads

A finite element model of the glass pane was made in Matlab. The two-dimensional geometry of the pane is displayed in Figure 1.

The area A is the contact area between the impactor and the glass. In the finite element model, a pressure load which represents the contact force distribution between the impactor and the glass was applied to this area. In order to increase the computational efficiency, a solid-shell element developed in [3] and whose efficiency when applied to glass structures was demonstrated in [4], was used. The model was used to determine the maximum principal stress of the glass pane. As a boundary condition, the frame was set as clamped.

The contact force between impactor and glass is $F = k_g u_{max}$, where k_g is the generalized stiffness of the glass and u_{max} is the maximum displacement of the glass as determined by a two-degree-of-freedom model of the system.

The material parameters were chosen in accordance with the dynamic finite element model of Persson and Doepker (2009), [2].

In order to determine k_g and u_{max} , a standard two-degree-of-freedom model was used to model the system, [5]. A sketch of the model is displayed in Figure 2.

k denotes stiffness and m denotes mass of the glass, g , and impactor, i , respectively. u_1 and u_2 are the displacements of the glass and the impactor and $\dot{u}_2(0)$ is the initial velocity of the impactor. m_i was known, [1], whereas the other mass and the stiffnesses were to be determined.

k_i was determined by means of ABAQUS/CAE through a static application of the impactor onto a rigid surface. From a linear approximation of the force-displacement relation for the impactor, k_i was obtained as the slope.

k_g and m_g could be determined by means of the finite element model in Matlab. A unit force $F = 1$ was applied to A . The resulting solution of the system gave a distribution of displacements, $\mathbf{u}(x, y)$. Following Chopra (2007), [5],

$$\mathbf{u}(x, y) = \Psi(x, y)z, \quad (1)$$

where $\Psi(x, y)$ is the shape function and z is the generalized coordinate which here was chosen as the maximum value of $\mathbf{u}(x, y)$. $\Psi(x, y)$ is the fundamental mode of vibration of the glass. It can be shown that

$$m_g = \Psi^T \mathbf{M} \Psi = \frac{\mathbf{u}^T \mathbf{M} \mathbf{u}}{z^2}, k_g = \Psi^T \mathbf{K} \Psi = \frac{\mathbf{u}^T \mathbf{K} \mathbf{u}}{z^2}, \quad (2)$$

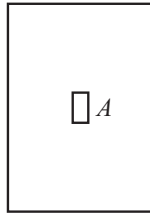


Figure 1. Two-dimensional geometry of glass pane.

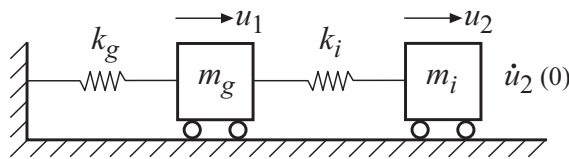


Figure 2. Two-degree-of-freedom model for pendulum impact test.

where \mathbf{M} is the mass matrix and \mathbf{K} is the stiffness matrix. A system of equations could be set up for the two-degree-of-freedom model, and a solution for free vibration of the system could be obtained using standard methods, [5]. The solution provided a time series of values for u_1 and u_2 . The maximum (absolute) value of u_1 is corresponding to u_{max} .

Test example

As a test example of the modeling framework described in the previous section, a glass pane of the dimensions corresponding to the standard SS-EN-12600 was chosen, [1]. The glass thickness t_g was set to 10 mm. The mass of the impactor was also chosen according to the standard, [1]. In Persson and Doepker (2009), [2], $\dot{u}_2(0)$ for a drop height of 1200 mm is given and this value is stated in Table 1.

The parameter values for the two-degree-of-freedom model are displayed in Table 1.

A is the estimated area of the glass which is in contact with the impactor at the moment of maximum value of the displacements in the corresponding dynamic finite element simulation, [2].

The solution of the two-degree-of-freedom model provided $u_{max} = 0.03$ m. A graph showing the displacements versus time is given in Figure 3. For comparison, the results for the displacement of the center of the glass from the dynamic finite element simulation, [2], are provided. All displacements have been multiplied by -1.

The resulting value of the maximum principal stress, σ_{max} , normalized by the corresponding quantity determined by means of a dynamic finite element computation, [2], $\sigma_{max,dyn}$, is presented in the first row of Table 2. The difference between the model results is around 1 %.

Table 1. Parameter values for two-degree-of-freedom model.

k_i (kN/m)	k_g (kN/m)	m_g (kg)	$\dot{u}_2(0)$ (m/s)	A (m ²)
400	586	1.17	-4.85	0.2×0.18

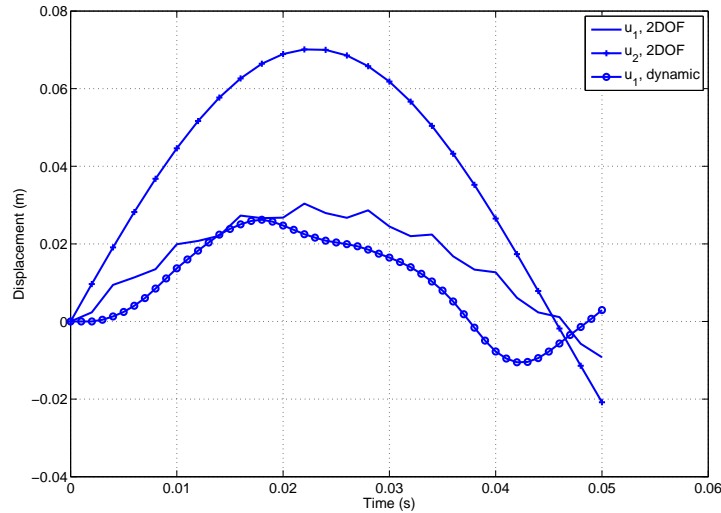


Figure 3. Displacements versus time for two-degree-of-freedom model.

Table 2. Normalized maximum principal stress for different glass dimensions.

Glass dimensions (mm ²)	$\sigma_{max}/\sigma_{max,dyn}$
1950 × 887	1.01
1000 × 1000	0.96
2000 × 2000	1.37

Varying the glass pane dimensions

In order to test whether the current model is valid for different glass pane dimensions, the test case of the previous section was analyzed, but for varying glass pane dimensions. The normalized test results are presented in Table 2.

The difference in model results is acceptable, which means less than 5 %, for the smaller glass panes. When the dimensions of the glass pane reach $2 \times 2 \text{ m}^2$, this difference is greater.

Conclusions and future work

A reduced model for determining the maximum principal stress of a glass pane subjected to dynamic impact load has been developed. The model has been calibrated to results from Persson and Doepker (2009), [2]. For smaller glass pane dimensions, the results of the reduced model are good. When increasing the glass pane dimensions, it is necessary to further develop the model in order to yield satisfactory results. Apparently it is not enough to represent the behavior of glass pane by the fundamental mode of vibration, but higher modes of vibration have to be included in the analysis. In the end, the reduced model framework is to be integrated into a glass design program with the aim to perform strength design of glass structures. The model has to be flexible enough to deal with variations in for instance glass dimensions and boundary conditions.

References

- [1] SS-EN-12600. *Glass in Building-Pendulum Test-Impact Test Method and Classification for Flat Glass*. Swedish Standards Institute, March 2003.
- [2] K. Persson and B. Doepker. Glass panes subjected to dynamic impact loads. *Proceedings of the XXIV A.T.I.V. Conference*, July 9-10, Parma, Italy, 2009.
- [3] R.P.R. Cardoso, J.W. Yoon, M. Mahardika, S. Choudry, R.J. Alves de Sousa and R.A. Fontes Valente. Enhanced assumed strain (EAS) and assumed natural strain (ANS) methods for one-point quadrature solid-shell elements. *International Journal for Numerical Methods in Engineering*, 75:156–187, 2008.
- [4] M. Fröling and K. Persson. Computational methods for laminated glass. Accepted for publication in *Journal of Engineering Mechanics*. doi:10.1061/(ASCE)EM.1943-7889.0000527.
- [5] A.K. Chopra. *Dynamics of Structures-Theory and Applications to Earthquake Engineering*. Pearson Prentice Hall, Upper Saddle River, New Jersey, 2007.

Multiscale Modeling of Porous Media

Carl Sandström* and Fredrik Larsson

*Department of Applied Mechanics
Chalmers University of technology
SE-412 96 Göteborg, Sweden
e-mail: carl.sandstrom@chalmers.se

Summary. Homogenization of a Stokes flow in an open pore system is studied. The homogenization results in a Darcy flow on the macroscale. On the heterogeneous subscale, a (possibly nonlinear) Stokes flow problem is formulated on a Representative Volume Element (RVE). As periodicity on both the velocity and pressure fields on the subscale satisfies the macrohomogeneity condition and due to the difficulties involved in generating periodic meshes, especially in 3D, a method to impose weak periodicity on the RVE is proposed.

Key words: Porous Media, FE², Computational Homogenization, Weak Periodicity.

Introduction

Porous materials are present in many natural as well as engineered structures such as sandstone which can contain oil, different kinds of filters and fiber networks during manufacturing of composite materials to name a few. On the subscale, the material has a strongly heterogeneous composition consisting of both a solid and a fluid phase, while on the macroscale the material is often modeled as homogeneous using an averaged constitutive relation (e.g. Porous Media Theory, cf. [1]). Due to the complexity of the substructure in this kind of materials, it is difficult to make an accurate model on the macroscopic level, thus exploring the possibilities of a multiscale approach is a natural step, see e.g. [2].

By separation of scales, it turns out that a Darcy flow is present on the macroscale, which is solved using the Finite Element Method. However, instead of using a conventional constitutive relation associating the seepage velocity to the pressure gradient, another Finite Element problem is solved in each Gausspoint in order to produce the velocity given the pressure gradient. The problem solved in each Gausspoint is referred to as the subscale problem which consists of a Stokes flow that is solved for on a Representative Volume Element (RVE)[3]. The RVE is a geometrical representation of the substructure of the porous medium and must be large enough to be representative to the material yet small enough to be computationally efficient. The solution to the subscale problem is homogenized and the result determines the material response on the macroscale. It can be shown that by imposing periodicity on the RVE, the macrohomogeneity condition is satisfied which means that the macroscale and the subscale are equivalent in terms of energy. The pertinent homogenization procedure is a generalization of classic homogenization, following along the lines in [4]. This work introduces a method for imposing periodicity in a weak sense, thus, the need for a periodic mesh is void.

Fully resolved Stokes flow

Consider a fully resolved domain Ω consisting of an topologically periodic open pore system Ω^F and solid obstacles which are assumed to be rigid. The boundary Γ^F is the part of $\Gamma := \partial\Omega$ which intersects the boundary of Ω^F , i.e. the part of Γ where fluid can enter or exit the domain. Furthermore, the boundary Γ^{int} is introduced as the part of $\partial\Omega^F$ which is contained inside Ω , i.e. the boundaries of the obstacles in the porous domain. A Stokes flow on Ω can be derived by minimizing the potential function $\Phi(\mathbf{v} \otimes \nabla)$ which is defined such that $\frac{\partial\Phi(\mathbf{v} \otimes \nabla)}{\partial\mathbf{v} \otimes \nabla} = \boldsymbol{\sigma}^v$ where $\boldsymbol{\sigma}^v$ is the deviatoric part of the Cauchy stress. The minimization problem can be given as

$$\inf_{\mathbf{v} \in \mathcal{V}} \sup_{p \in \mathcal{P}} \left\{ \int_{\Omega^F} \Phi(\mathbf{v} \otimes \nabla) dV - \int_{\Omega^F} p(\nabla \cdot \mathbf{v}) dV - \int_{\Gamma_P^F} \hat{\mathbf{t}} \cdot \mathbf{v} dS \right\} \quad (1)$$

where

$$\mathcal{V} = \{[\mathbf{v} \in H^1(\Omega^F)]^3 : \mathbf{v} = 0 \text{ on } \Gamma^{\text{int}}, \mathbf{v} = \hat{v}_n \mathbf{n} \text{ on } \Gamma_V^F\} \quad (2a)$$

$$\mathcal{P} = \{p \in L_2(\Omega^F)\} \quad (2b)$$

and \mathbf{v} is the fluid velocity, p is the pressure and $\hat{\mathbf{t}}$ is the traction defined as $\hat{\mathbf{t}} = \hat{p} \mathbf{n}$ where \hat{p} is the prescribed pressure along the boundary Γ_P^F and Γ_V^F is the part of the boundary where the velocity is prescribed. It should be noted that the pressure p is the Lagrange multiplier pertinent to the incompressibility condition. We proceed by splitting the domain into a finite number n domains $\Omega_{\square,i}$ such that $\Omega = \cup \Omega_{\square,i}$ and such that each subdomain retains geometric periodicity. We can now rewrite the first two terms in Equation 1 as the sum of each subdomain. Note that up to this point, the velocity \mathbf{v} and p are continuous on the whole domain Ω .

$$\inf_{\mathbf{v} \in \mathcal{V}} \sup_{p \in \mathcal{P}} \sum_{i=1}^n \left\{ \int_{\Omega_{\square,i}^F} \Phi(\mathbf{v} \otimes \nabla) dV - \int_{\Omega_{\square,i}^F} p(\nabla \cdot \mathbf{v}) dV \right\} - \int_{\Gamma_P^F} \hat{\mathbf{t}} \cdot \mathbf{v} dS \quad (3)$$

At this point, we split the pressure p into a smooth macroscale part p^M and a fluctuating subscale part p^S such that $p = p^M + p^S$. Using Gauss's theorem on the resulting macroscale pressure part, we get

$$\inf_{\mathbf{v} \in \mathcal{V}} \sup_{\substack{p^M \in \mathcal{P}^M \\ p^S \in \mathcal{P}^S}} \sum_{i=1}^n \left\{ \int_{\Omega_{\square,i}^F} \Phi(\mathbf{v} \otimes \nabla) dV - \int_{\Omega_{\square,i}^F} p^S(\nabla \cdot \mathbf{v}) dV + \int_{\Omega_{\square,i}^F} \nabla p^M \cdot \mathbf{v} dV \right\} - \int_{\Gamma_P^F} \mathbf{n} \cdot \mathbf{v} p^M dS \quad (4)$$

where \mathbf{n} is the outward pointing normal to Γ^F . By removing the assumption on continuity on \mathbf{v} and p over the internal boundaries, reaction forces arise and the macrohomogeneity condition can be stated as

$$\int_{\Gamma_{\square}^F} \mathbf{t}^S \cdot \mathbf{v} dS = 0$$

where $\mathbf{t}^S = (\boldsymbol{\sigma}^v - p^S \mathbf{I}) \cdot \mathbf{n}$ is the traction on the boundary. The condition is fulfilled by imposing periodicity on \mathbf{v} and p^S on the boundary Γ_{\square}^F . Due to the difficulties involved in generating periodic meshes, the periodicity is imposed in a weak sense. We now proceed by splitting the boundary Γ_{\square} into two parts; one Γ_{\square}^{F+} which has a normal in the positive x or y direction and one Γ_{\square}^{F-} which has a normal in the negative x or y direction. Moreover, we introduce the jump operator $[[\bullet]]$ such that $[[f]] = f|_{\Gamma_{\square}^{F+}} - f|_{\Gamma_{\square}^{F-}}$ and add the periodicity constraints $[[\mathbf{v}]] = \mathbf{0}$ and

$[[p^S]] = 0$. The additional conditions give rise to the Lagrange multipliers β and γ . Thus, Equation 4 is rewritten as

$$\inf_{\substack{\mathbf{v} \in \mathcal{V}_\square \\ p^M \in \mathcal{P}^M \\ p^S \in \mathcal{P}_\square^S \\ \beta \in \mathcal{B}_\square}} \sup_{\gamma \in \mathcal{G}_\square} \inf_{\sum_{i=1}^n} \left\{ \int_{\Omega_{\square,i}^F} \Phi(\mathbf{v} \otimes \nabla) - p^S(\nabla \cdot \mathbf{v}) + \nabla p^M \cdot \mathbf{v} dV - \int_{\Gamma_{\square,i}^{F+}} [[\mathbf{v}]] \cdot \beta + [[p^S]] \cdot \gamma dS \right\} - \int_{\Gamma_V^F} \mathbf{n} \cdot \mathbf{v} p^M dS$$

We can now produce the respective macroscale and subscale equations by varying the pertinent quantities. By varying the macroscale pressure p^M and introducing the macroscale quantity $\bar{p} \in \mathcal{P}^M = \{\bar{p} \in H^1(\Omega), \bar{p} = \hat{p} \text{ on } \Gamma_P\}$ such that $\nabla \bar{p} = \nabla p^M$, the macroscale equation is given as

$$\int_{\Omega} \bar{\mathbf{w}} \cdot \nabla \delta \bar{p} dV = \int_{\Gamma} \bar{\mathbf{w}} \cdot \mathbf{n} \delta \bar{p} dS \quad \forall \delta \bar{p} \in \mathcal{P}^{M,0}$$

where seepage $\bar{\mathbf{w}}$ is defined as $\bar{\mathbf{w}} = \phi \langle \mathbf{v} \rangle_\square$, ϕ is the porosity and the operator $\langle \bullet \rangle_\square$ is the averaging operator defined as

$$\langle f \rangle_\square = \frac{1}{|\Omega_\square^F|} \int_{\Omega_\square^F} f dV$$

and the function space $\mathcal{P}^{M,0}$ is the linear counterpart of \mathcal{P}^M

By varying the subscale quantities \mathbf{v} , p^S , β and γ , the weak form of the subscale equation is given as

$$\begin{aligned} \int_{\Omega_{\square,i}^F} \boldsymbol{\sigma}^v(\mathbf{v} \otimes \nabla) : [\delta \mathbf{v} \otimes \nabla] dV - \int_{\Omega_{\square,i}^F} [\delta \mathbf{v} \cdot \nabla] p^S dV - \int_{\Gamma_{\square,i}^F} [[\delta \mathbf{v}]] \cdot \beta dS &= - \int_{\Omega_{\square,i}^F} \nabla p^M \cdot \delta \mathbf{v} dV \\ - \int_{\Omega_{\square,i}^F} [\mathbf{v} \cdot \nabla] \delta p^S dV - \int_{\Gamma_{\square,i}^F} [[\delta p^S]] \gamma dV &= 0 \\ - \int_{\Gamma_{\square,i}^F} [[\mathbf{v}]] \cdot \delta \beta dV &= 0 \\ - \int_{\Gamma_{\square,i}^F} [[p^S]] \delta \gamma dV &= 0 \end{aligned}$$

Here, the solution spaces \mathcal{V}_\square , \mathcal{P}_\square^S , \mathcal{B}_\square and \mathcal{G}_\square govern the approximation and the testfunctions are chosen as $\delta \mathbf{v} \in \mathcal{V}_\square^0$, $\delta p^S \in \mathcal{P}_\square^{S,0}$, $\delta \beta \in \mathcal{B}_\square$ and $\delta \gamma \in \mathcal{G}_\square$ respectively. In particular, we follow along the lines of [5] and introduce global polynomials for \mathcal{B}_\square and \mathcal{G}_\square .

Numerical example

The numerical example presented in this section illustrates how weak periodic boundary conditions is imposed on a unit cell with a circular obstacle which is slightly moved to the left in order to create a non-periodic mesh. Note that by assuming periodicity, the subscale properties are independent of the position of the RVE. A pressure gradient $p^M = [-1 \ 0]$ is applied. In this example, the Lagrange multipliers are approximated by a polynomial of degree 4. The resulting shapes of the Lagrange multiplier functions β and γ can be seen in Figure 1 together with the velocity field and pressure field.

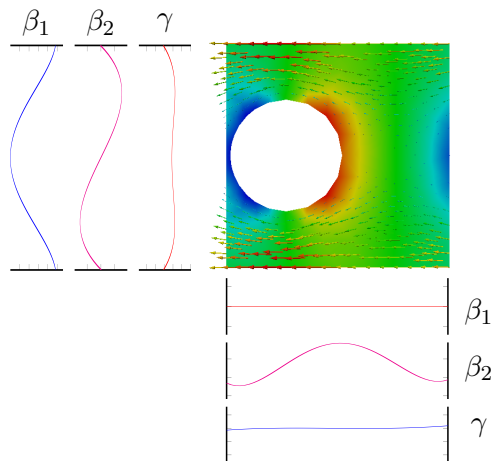


Figure 1. Weak periodicity is imposed on an RVE by Lagrange multipliers approximated as polynomials of degree 4.

Conclusions and outlook

It has been shown that imposing periodicity in a weak form on an RVE is possible and that the solution convergence towards strong periodicity by increasing the number of degrees of freedom of the approximations on the pertinent Lagrange multipliers.

As for future work, a method for a priori determination of the number of degrees of freedom on the approximation of the Lagrange multipliers is desired in order to rid the need for frequent convergence studies. As a main goal is to couple permeability and deformation, a transition to 3D is of the essence.

References

- [1] R. de Boer, *Trends in Continuum Mechanics of Porous Media*. 2005.
- [2] E. Sánchez-Palencia, *Non-homogeneous media and vibration theory*. Springer-Verlag, 1980.
- [3] T. I. Zohdi and P. Wriggers, *An introduction to computational micromechanics*. Springer-Verlag, 2008.
- [4] F. Larsson, K. Runesson, and F. Su, “Variationally consistent computational homogenization of transient heat flow,” *International Journal for Numerical Methods in Engineering*, 2009.
- [5] P. Heintz and P. Hansbo, “Stabilized Lagrange multiplier methods for bilateral elastic contact with friction,” *Computer Methods in Applied Mechanics and Engineering*, vol. 195, pp. 4323–4333, July 2006.

Structural modeling and analysis of a wave energy converter

Andrew S. Zurkinden¹, Søren H. Lambersten¹, and Lars Damkilde¹

⁽¹⁾Aalborg University, Department of Civil Engineering, Sohngårdsholmsvej 57, 9000 Aalborg, Denmark, az@civil.aau.dk, shl@civil.aau.dk, lda@civil.aau.dk

Summary. A fatigue analysis is being carried out for a wave energy converter subjected to ocean wave loads. The device is a bottom fixed structure, located in a shallow water environment. Interest is focused on the local stress response of a structural detail and a subsequent calculation of its fatigue life by using the rainflow counting approach. The wave energy converter is characterized by its ability to enter in a storm protection mode which - whenever extreme conditions occur - will drastically reduce the exposure to wave loads. The predicted fatigue life is calculated for two different control cases. Finally the question will be answered which control strategy is more favorable regarding the trade off between fatigue damage reduction and power production on the wave energy device.

Key words: Structural modeling, fatigue damage calculation, control strategies.

Introduction

The present study is concerned with the structural design of the Wavestar device which is currently being deployed in Hanstholm, at the Danish Westcoast. The Wavestar Hanstholm WEC is a grid connected prototype with two floats each equipped with a generator. The prototype has been in operation since 2007 with a total installed capacity of 110 kW. The electrical energy produced by the two generators was 22.8 MWh in the period from May 2010 to April 2012. A number of studies have been carried out during the last two years focusing on the numerical modeling and the control of the device Ref. [1]. In [2] it was found that the effect of non-linear buoyancy forces have a influence on the dynamics of the device for waves with a steepness factor larger than 0.05. In order to account for non-linearities in the load calculation the only practical option is a non-linear time domain motion analysis. On the other hand solutions based on time series which account for non-linear effects are expensive to implement and may require long computational time. However, the emphasis in the present paper is more given on the structural modeling rather than on an advanced hydrodynamical model. The hydrodynamical and structural analysis are thus performed separately. The hydrodynamic analysis was conducted previously based on diffracting panel elements over the wetted surface of the hemisphere-shaped float by applying the Boundary Element Method (BEM). Rigid body motions were computed by a linearized time domain model and are then used as boundary conditions in the structural model. In the structural model the device is modeled as a flexible body consisting of shell elements. Stress concentrations are assumed to occur in the connections joints. A transient structural analysis is carried out in order to determine the dynamic response of the system subjected to the time-varying control load calculated by the hydrodynamic analysis.

Hydrodynamical model - rigid body assumption

The rigid body motions were previously analyzed by the following integro-differential equation, Ref.[3].

$$(M + a^\infty)\ddot{\phi}(t) + \int_0^t K(t - \tau)\dot{\phi}(\tau)d\tau + C\phi(t) = M_{Ex}(t) + M_c(t) \quad (1)$$

where $\phi(t)$ represents the angular rotation of the body around the bearing point A, see Fig. 1. M is the inertia coefficient of the rigid body motion; a^∞ represents the added mass at infinite high wave frequencies; the next term is the convolution of the radiation memory function $K(t)$ with the angular velocity $\dot{\phi}(\tau)$ and C represents the buoyancy coefficient. $M_{Ex}(t)$ is the wave excitation moment. The last term $M_c(t)$ can be interpreted as any non-linear external force such as viscous forces, mooring forces or feedback forces from a wave energy power take-off system. In our case, a linear passively damped energy conversion system has been assumed which consists of a damping coefficient c multiplied with the angular velocity $\dot{\phi}$. The equation of motion is solved applying an explicit 4th order Runge-Kutta time integration scheme with a constant time stepping. The control force $F_c(t) = M_c(t)/x(t)$ is plotted in Fig. 2 in function of three different damping coefficients $c_{1,2,3}$ for an incident irregular wave train, (Jonswap: $H_{m0} = 1.5m$, $T_p = 4.5s$). By comparing the control force with the instantaneous power in Fig. 3, it can be concluded that the optimum control parameter c may vary by considering the accumulated damage in the structural detail, i.e. where the cylinder is connected to the structure.

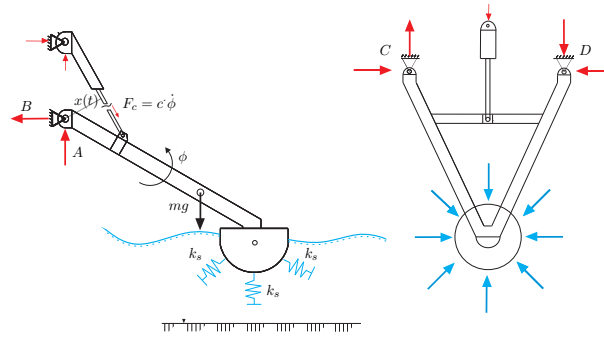


Figure 1. Equivalent beam model, multidirectional wave loading

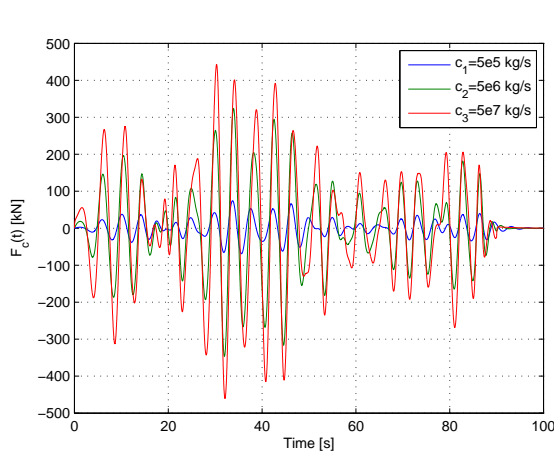


Figure 2. Control force $F_c(t)$.

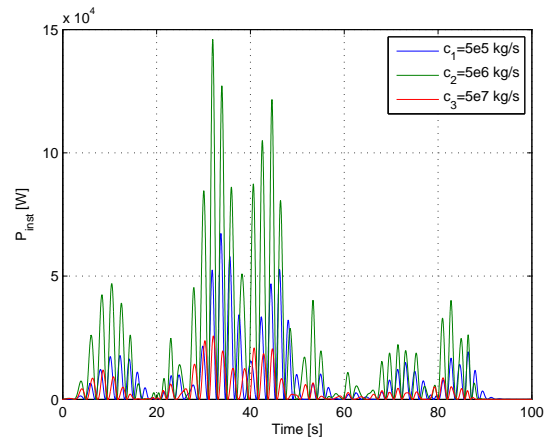


Figure 3. Instantaneous power $P_{inst} = F_c(t) \cdot \dot{\phi}(t) \cdot x(t)$.

Structural model - flexible body

In a next step, the focus is given on the development of a global structural model which is used to approximate the overall displacement and stress distribution in the arm under the given load pattern. In order to account for inertial forces in the deformable body and at a latter stage of the project for non-linear effects, the authors have decided to work out a transient structural analysis for the given problem. The general equation of motion for the structural model is given as follows:

$$\mathbf{M}\ddot{\mathbf{U}} + \mathbf{C}\dot{\mathbf{U}} + (\mathbf{K} + k_s)\mathbf{U} = \mathbf{F} \quad (2)$$

where \mathbf{M} , \mathbf{C} , and \mathbf{K} are the global mass, damping and stiffness matrices. \mathbf{F} is the vector of externally applied loads and \mathbf{U} , $\dot{\mathbf{U}}$, and $\ddot{\mathbf{U}}$ are the displacement, velocity and acceleration vectors of the finite element assemblage. k_s is a spring stiffness term which represents the support at the end of the arm due to the presence of the water. The spring can only transfer pressure loads, traction forces are omitted. Non-linear effects such as the non-linear buoyancy force may be included by updating the stiffness coefficient k_s at each time step. For the present case a constant value of 192 kN/m has been assumed which is equal to the water plane area of the float ($d=5.0$ m) times the density of the water ($1000\text{kg}/\text{m}^3$).

ANSYS shell model

A detailed ANSYS shell model of the arm has been elaborated and is shown in Figure 4. Four-noded shell elements were used to represent the global stiffness model. The shell structure consists of 16887 elements, 16714 nodes and 96941 unknown variables. The modulus of elasticity of steel was assumed to be $205\text{ kN}/\text{mm}^2$. The structure is supported at two sections by a simply supported boundary condition which allows a free rotation in the three directions. At the end of the structure an external spring element is attached which allows longitudinal pressure forces. The structure is subjected to a time-varying load $F_c(t)$ shown in Figure 2 and is attached at the connection between the arm and the cylinder. Results of the stress distribution in the welded connection will be presented in the next paragraph.

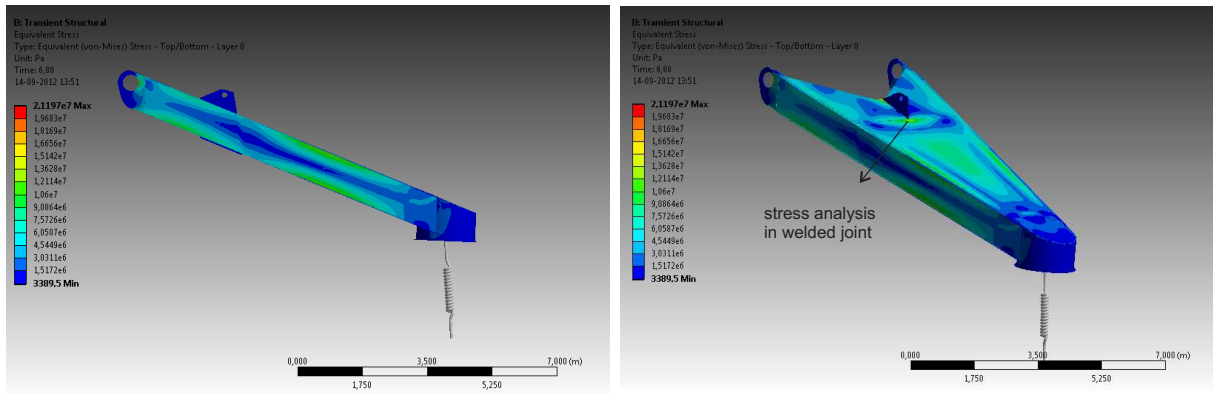


Figure 4. Shell model, von Mises stress distribution assuming a stiffness coefficient of $k_s = 192\text{kN}/\text{m}$ for a significant wave height: $H_{m0} = 1.5\text{m}$ and a peak period of $T_p = 4.5\text{s}$, assuming irregular waves (Jonswap, $\gamma = 3.3$).

Results

The accumulated damage in the structural detail was calculated based on a rainflow counting algorithm Ref. [4] and the given time series of the von Mises stresses, Fig. 5. At this moment

the simulation time was limited to 100 s. The damage ratios for the three different damping coefficients are shown in Table 1.

Table 1. Average power production, accumulated damage for the calculated time series for three different damping coefficients.

$c_{1,2,3}$:	$5e^5$	$5e^6$	$5e^7$	[kg/s]
D_i :	$6.58 \cdot 10^{-8}$	$1.217 \cdot 10^{-6}$	$7.6 \cdot 10^{-5}$	[-]

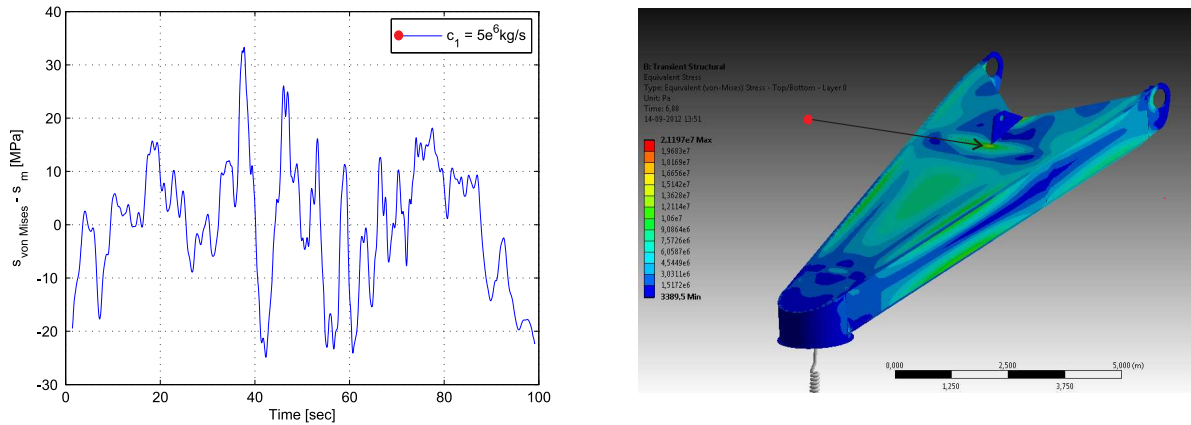


Figure 5. Time series of stresses for $c_1 = 5 \cdot 10^5 \text{ kg/s}$ at the structural detail.

Conclusion

A structural analysis of a wave energy converter has been carried out by a detailed finite element model. The hydrodynamic loads were computed based on the diffraction theory and a rigid body assumption. The separation of the hydrodynamic and structural models is justified, considering the high eigenmodes of the flexible structure compared to the relatively low peak frequencies encountered in a typical sea state. In order to analyze the effect of more advanced control strategies it was suggested to perform a transient analysis in order to account for time dependent control parameters. Short-term damage calculations have shown that the fatigue life of the analyzed welded section is considerably increased for a less aggressive control strategy

References

- [1] Hansen, R.H., Kramer, M.M. Modelling and Control of the Wavestar Prototype. *Proc. 9th European Wave and Tidal Energy Conference, EWTEC 2011.*
- [2] Zurkinden, A.S., Kramer, M.M., Sichani, M.T., Alves M. Comparison between numerical modeling and experimental testing of a point absorber WEC. *Proc. of the ASME 31st Int. Conf. on Ocean, Offshore and Arctic Engineering, OMAE 2012.*
- [3] Newman, J.N. Marine Hydrodynamics. *The MIT Press Cambridge, Massachusetts.*
- [4] WAFO group Matlab Toolbox for Analysis of random waves and loads. *Lund University, Faculty of Engineering, Mathematical Statistics.*

Proceedings of the 25TH NORDIC SEMINAR
COMPUTATIONAL MECHANICS, 2012

Session in Honor of Niels S. Ottosen

Room: Stora Hörsalen, Thursday 25 October, 13:15 - 15:15



On the Computational Homogenization of Mesoscale Gradient Viscoplasticity

Kenneth Runesson, Magnus Ekh, and Fredrik Larsson¹

⁽¹⁾Department of Applied Mechanics, Chalmers University of Technology, keru@chalmers.se

Summary. Computational homogenization is considered for a class of gradient-enhanced dissipative mesoscale material models relevant for the modeling of size-dependent macroscale material response. The adopted homogenization assumptions result in the classical equilibrium equation for a local continuum on the macroscale, while the internal variables "live" on the mesoscale only. The macroscale stress and ATS-tensor in a given time-increment are derived via stationarity conditions of an incremental pseudo-potential, which represents an extension of the situation for a local continuum model. Bingham viscoplasticity with gradient-enhanced hardening is chosen as the prototype model problem for the numerical examples.

Key words: computational homogenization, gradient-enhanced viscoplasticity, pseudo-potential

Introduction

A large class of higher order continuum models, which can be used to represent the macroscale response while the subscale features are incorporated in an approximate way, emerge after some sort of (implicit or explicit) homogenization argument. Starting from a standard continuum formulation on the mesoscale (the next lower scale in the material), a well-established approach is to introduce, as a model assumption, higher order "strain-like" quantities as part of a Taylor series expansion of the macroscale displacement field. In the simplest case of linear expansion, the classical first order homogenization models are obtained. The fluctuation field, which is added to capture the fine-scale features, is implicitly accounted for only via the homogenization. Typical proponents for this type of reasoning are the 2nd order homogenization model in [2] and the micropolar model in [3]. Via this procedure, loosely speaking, a standard continuum description on the subscale level translates to a generalized continuum on the macroscale. The important fact is that the resulting macroscale problem becomes quite complex, both from modeling (higher order boundary conditions) and numerical (higher regularity conditions) points of view.

A quite different approach to the modeling of (in particular) polycrystals is to incorporate a "higher order" model on the mesoscale, viz. gradient effects within and between the grains. A variety of phenomenological model concepts that involve gradient effects are then at our disposal. One class of models employ gradients of internal variables in the free energy density. A recent account on gradient-extended standard dissipative solids is given in [5]. For a polycrystal, it is possible to impose further restrictions along the grain boundaries by formally introduce "inter-grain boundary conditions", e.g. [4]. Obviously, a phenomenological model of the grain boundary "resistance" to deformation represents some sort of a priori homogenization of micro-effects (below the mesolevel) in terms of dislocation gradients, etc. When applied to the polycrystal, it is desirable that (first order) homogenization will lead to a standard continuum format on the macroscale, involving the macroscale stress as the only relevant homogenized "flux" variable, whereas possible microstresses are confined to the mesoscale and are automatically "suppressed" on the macroscale as part of the homogenization.

Theory and method

In this contribution we apply a fairly general setting of variationally consistent homogenization to the chosen class of non-standard continuum models on the mesoscale. The chosen setting is that of the "Variational Multiscale Method", originally proposed in [1] in a quite different context, and it is based on a Variationally Consistent Macrohomogeneity Condition, VCMC (that generalizes the well-known Hill-Mandel condition to a large class of time-dependent and multi-field problems, cf. [6]). Via the VCMC, the appropriate homogenized (macroscale) problem is derived.

We consider a (sub)class of gradient-enhanced dissipative materials in the time-continuous and the time-discrete formats. In particular, we establish the semi-dual format in terms of a "micro-stress energy" (obtained after partial Legendre transformation of the free energy). The resulting generalized saddle-point problem, based on an incremental pseudo-potential, represents the "workhorse" for evaluation of bounds on the macroscale stress (stiffness). The "canonical format" of the SVE-problem (SVE = Statistical Volume Element) for a single realization is established via the assumption of weakly enforced micro(anti)periodicity of displacement fluctuations and microtractions. Dirichlet and Neumann boundary conditions are considered as the two extreme types in the chosen semi-dual variational setting. Finally, energetic bounds are established for a single SVE.

Bingham viscoplasticity, cf. [7], complemented with gradient-enhanced hardening is chosen as a prototype model for individual grains in a polycrystal, and the pertinent nested iteration algorithm for solving the SVE-problem for different combinations of boundary conditions is outlined. Finally, computational results illustrate the various theoretical findings and predictions.

References

- [1] T.J.R. Hughes, Multi-scale phenomena: Green's functions, the Dirichlet-to-Neumann formulation, subgrid scale models, bubbles and the origins of stabilized methods. *Comput. Meth. Appl. Mech. Engrg.* 127:387-401, 1995.
- [2] V. Kouznetsova, M.G.D. Geers and W.A.M. Brekelmanns, Multi-scale constitutive modeling of heterogeneous materials with a gradient-enhanced computational homogenization scheme. *Int. J. Numer. Meth. Engrg.* 54:1235-1260, 2002.
- [3] R. Larsson and S. Diebels, A second order homogenization procedure for multiscale analysis based on micropolar kinematics. *Int. J. Numer. Meth. Engrg.* 69:2485-2512, 2007.
- [4] M. Ekh, M. Grymer, K. Runesson and T. Svedberg, Gradient crystal plasticity as part of the computational modeling of polycrystals. *Int. J. Numer. Meth. Engrg.* 72:197-220, 2007.
- [5] C. Miehe, A multi-field incremental variational framework for gradient-extended standard dissipative solids. *J. Mech. Phys. Solids* 59:898-923, 2011.
- [6] F. Larsson, K. Runesson and F. Su, Variationally consistent computational homogenization of transient heat flow. *Int. J. Numer. Meth. Engrg.* 81: 1659-1686, 2010.
- [7] N.S. Ottosen and M. Ristinmaa. *The Mechanics of Constitutive Modeling*. Elsevier, 2005.

A geometric approach in computational stability analysis

Alexis Fedoroff¹, Reijo Kouhia², and Jari Mäkinen²

⁽¹⁾Aalto University, Department of Civil and Structural Engineering
P.O. Box 12100, 00760 Aalto, Finland, alexis.fedoroff@aalto.fi

⁽²⁾Tampere University of Technology, Department of Mechanics and Design
P.O. Box 589, 33101 Tampere, Finland, reijo.kouhia@tut.fi, jari.m.makinen@tut.fi

Summary. In this paper a geometric approach, in which the eigenvector is considered as a locally smooth function defined on the criticality manifold, is proposed. Special emphasis is given to the question whether the eigenmode resulted from a standard linear stability eigenvalue analysis is a relevant one. Preliminary results for evaluating computable a priori error bounds on the eigenvalue and especially on the eigenvector will be presented.

Key words: non-linear eigenvalue problem, critical point, critical eigenmode, criticality manifold

Introduction

In practical engineering analysis critical loads are usually determined by linearized stability eigenvalue analysis, where the linearization is performed at the initial undeformed state. According to the knowledge of the authors, accuracy of the computed solution has not been addressed in the literature and especially the question, whether the computed critical mode is a relevant one, has not been discussed in the literature.

A proper stability analysis of a buckling sensitive structure should include determination of the critical loads and its imperfection sensitivity. Computation of critical points on an equilibrium path requires solution of a non-linear eigenvalue problem, for which solution several techniques exist. Imperfection sensitivity analyses have been primarily focused on application of Koiter's initial post-buckling theory.

Determination of the critical point requires the solution of a non-linear eigenvalue problem. However, if the pre-buckling displacements are negligible, it is *usually sufficient* to solve the linearized eigenvalue problem, where the linearization is performed with respect to the undeformed configuration. However, as it will be shown in this paper, the linearity of the primary equilibrium path is *not sufficient* to guarantee small error in the computed critical load and especially the eigenmode.

The non-linear stability eigenvalue problem constitutes of solving the equilibrium equations simultaneously with the criticality condition. First appearance of this idea seems to be from 1973 by Keener and Keller [1]. In their approach the criticality condition is augmented as an eigenvalue equation, such approach has been used also in Refs. [2, 3, 4, 5, 6]. Another approach uses a scalar equation indicating the criticality [7, 8] or expansion to a higher order polynomial eigenvalue problem [9].

Stability eigenvalue problem

The problem of finding a critical point along an equilibrium path can be stated as: find the critical values of \mathbf{q} , λ and the corresponding eigenvector ϕ such that

$$\mathbf{f}'(\mathbf{q}, \lambda)\phi = \mathbf{0} \quad \text{and} \quad \mathbf{f}(\mathbf{q}, \lambda) = \mathbf{0}. \quad (1)$$

where \mathbf{f} is a vector defining the equilibrium equations and \mathbf{f}' denotes the Gateaux derivative (jacobian matrix) with respect to the state variables \mathbf{q} , i.e. the stiffness matrix. At the critical point the equilibrium equation (1)₂ has to be satisfied at the same time with the criticality condition (1)₁, which states the zero stiffness in the direction of the critical eigenmode ϕ . Such a system is considered in Refs. [10, 3].

The equilibrium equation (1)₁ constitutes the balance of internal forces \mathbf{r} and external loads \mathbf{p} , which is usually parametrized by a single variable λ , the load parameter, defining the intensity of the load vector: $\mathbf{f}(\mathbf{q}, \lambda) \equiv \mathbf{r}(\mathbf{q}) - \lambda\mathbf{p}_r(\mathbf{q})$. If the loads does not dependent on deformations, like in dead-weight loading, the reference load vector \mathbf{p}_r is independent of the displacement field \mathbf{q} .

Alternatively, the non-linear eigenvalue problem can be approximated by a polynomial eigenvalue problem. Assuming an equilibrium state $(\mathbf{q}_*, \lambda_*)$ with a regular tangent matrix, a Taylor expansion of criticality condition (1)₁ results in

$$\left(\mathbf{K}_* + \Delta\lambda\dot{\mathbf{K}}_* + \frac{1}{2}(\Delta\lambda)^2\ddot{\mathbf{K}}_* + \dots \right) \phi = \mathbf{0}, \quad (2)$$

where $\Delta\lambda = \lambda - \lambda_*$ and the superimposed dot denotes the differentiation with respect to the load parameter λ . Expanding the displacement vector $\mathbf{q} = \mathbf{q}_* + \Delta\mathbf{q} = \mathbf{q}_* + \Delta\lambda\mathbf{q}_1 + \frac{1}{2}(\Delta\lambda)^2\mathbf{q}_2 + \dots$ the matrices in (2) are

$$\mathbf{K}_* = \mathbf{f}'_*, \quad \dot{\mathbf{K}}_* = \mathbf{f}''_*\mathbf{q}_1 + \dot{\mathbf{f}}'_*, \quad \ddot{\mathbf{K}}_* = \mathbf{f}''_*\mathbf{q}_2 + \mathbf{f}'''_*\mathbf{q}_1\mathbf{q}_1 + \ddot{\mathbf{f}}'_*\mathbf{q}_1 + \ddot{\mathbf{f}}'_*, \quad (3)$$

where $\mathbf{f}'_* = \mathbf{f}'(\mathbf{q}_*, \lambda_*)$ etc. Displacement vectors \mathbf{q}_i can be solved from linear systems as

$$\mathbf{K}_*\mathbf{q}_1 = -\dot{\mathbf{f}}'_*, \quad \mathbf{K}_*\mathbf{q}_2 = -\left[\mathbf{f}''_*\mathbf{q}_1\mathbf{q}_1 + 2\dot{\mathbf{f}}'_*\mathbf{q}_1 + \ddot{\mathbf{f}}'_* \right]. \quad (4)$$

It is worthwhile to notice that the coefficient matrix to solve $\mathbf{q}_1, \mathbf{q}_2, \dots$ is the same for all cases.

In the classical linear stability analysis the reference state is the undeformed stress free configuration. Assuming dead weight loading, the term $\dot{\mathbf{f}}'_*$ and its higher order derivatives with respect to the load parameter will vanish. For the linear stability eigenvalue problem the matrices are simply the following:

$$\mathbf{K}_0 = \mathbf{f}'(\mathbf{0}, 0), \quad \dot{\mathbf{K}}_0 = \mathbf{f}''(\mathbf{0}, 0)\mathbf{q}_1, \quad (5)$$

where $\mathbf{K}_0\mathbf{q}_1 = \mathbf{p}_r$. Therefore the strains are linear functions of the displacements \mathbf{q}_1 and the geometric stiffness matrix $\dot{\mathbf{K}}$ is a linear function of the displacements \mathbf{q}_1 .

In this paper the main emphasis is a study of the possible error in the eigenmode of the standard linearized eigenvalue analysis as compared to the fully non-linear eigenvalue problem (1).

Example

In figure 1 a simple three d.o.f model is shown. It represents a truss structure that is initially plane with a loading constricted to that plane. The plane is the one orthogonal to \mathbf{e}_1 going through the point A , which is always restricted to that plane. Two different buckling modes, or combinations of them are possible: as a rigid bar, such that the segments $A'B'$ and $B'C'$ remain

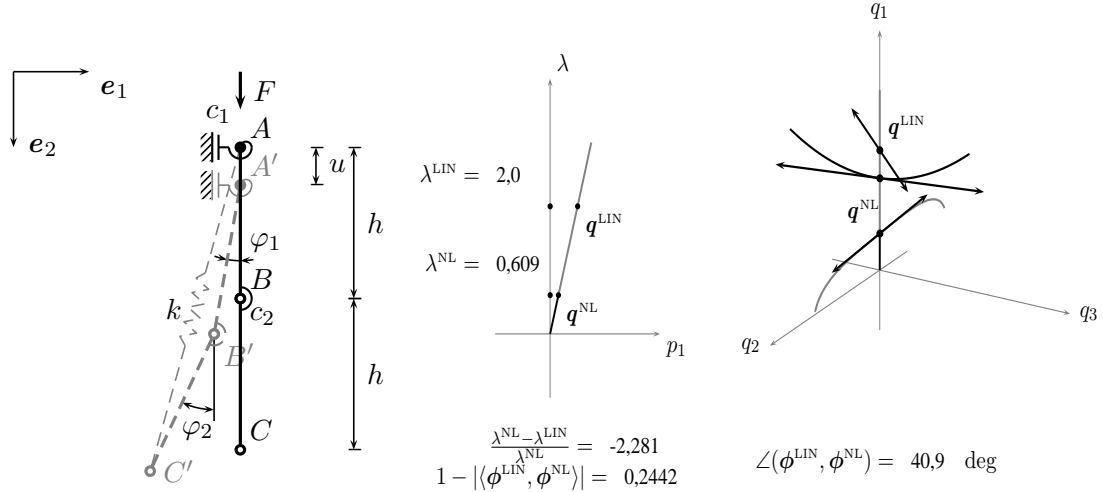


Figure 1. A simple buckling model and the post-buckling equilibrium paths.

in line, or as Euler column buckling such as the nodes A' and C' remain in the original plane while the “column” consisting of the rigid segments AB and BC “bends” at B' .

The point A' is connected to the rigid frame via a “torsional” linear spring with coefficient c_1 whereas the relative angle of $A'B'$ with respect to $B'C'$ is controlled by a “flexural” linear spring with coefficient c_2 . The nodes A' and C' are connected with a axial linear spring of coefficient k . The non-dimensional state variables are defined as: $q_1 := u / (2h)$, $q_2 := (\varphi_2 + \varphi_1) / 2$ and $q_3 := (\varphi_2 - \varphi_1) / 2$ as well as the constants $\eta_1 := c_1 / (k(2h)^2)$, $\eta_2 := 4c_2 / (k(2h)^2)$ and $\lambda := F / (k2h)$.

Classical state space presentation. Fig. 1 shows the equilibrium paths projected on the hyperplanes $\{q_2 = 0, q_3 = 0\}$ and $\{\lambda = 0\}$. The example has been calculated for a particular case where the ratio of η_2 to η_1 is 20, meaning that the “torsional rigidity” c_1 of the upper chord of the truss is only 1/5 of the “flexural rigidity” c_2 of the compressed vertical member.

Looking at the secondary equilibrium paths, it can be seen that at the lower positive critical point given by the non-linear eigenproblem, the eigenmode is pointing almost in the direction of q_2 , i.e. $\varphi_1 \approx \varphi_2$, suggesting a rigid bar buckling mode. On the other hand the higher positive critical point given by the non-linear eigenproblem suggests, by pointing almost at q_3 , a euler column buckling mode ($\varphi_1 \approx -\varphi_2$).

The result given by the linearized eigenproblem seems to point in the direction such that $q_2 \approx q_3$, which means that $\varphi_2 \approx 0$. Physically this eigenmode is rather unexpected considering the values that have been given to the spring constants.

Presentation using the criticality manifold. Fig. 2 shows the primary jacobian path \mathcal{J}_1 embedded in the ambient $\mathbb{R}^{3 \times 3}$ space of symmetric square matrices. However, since the jacobian matrix evaluated at the primary path of equilibrium is block diagonal and that the block related to the primary state variable q_1 is assumed to be non-singular (it is actually constant in this case), the positive definiteness can be investigated from the block related to the secondary state variables q_2 and q_3 . Due to the symmetry of the matrices, it is easy to draw the criticality manifold and the primary jacobian paths projected on the space spanned by $\{\mathbf{e}_2 \otimes \mathbf{e}_2, \mathbf{e}_3 \otimes \mathbf{e}_3, \mathbf{e}_2 \otimes \mathbf{e}_3\}$.

From fig. 2 it is easy to see that although the primary equilibrium path \mathcal{E}_1 is linear, the primary jacobian path \mathcal{J}_1 is far from being linear. One can further notice that both the non-linear jacobian path \mathcal{J}_1 and the tangent space $T_0\mathcal{J}_1$ are fully contained in the plane $\{[\mathbf{K}]_{23} = -\eta_1\}$

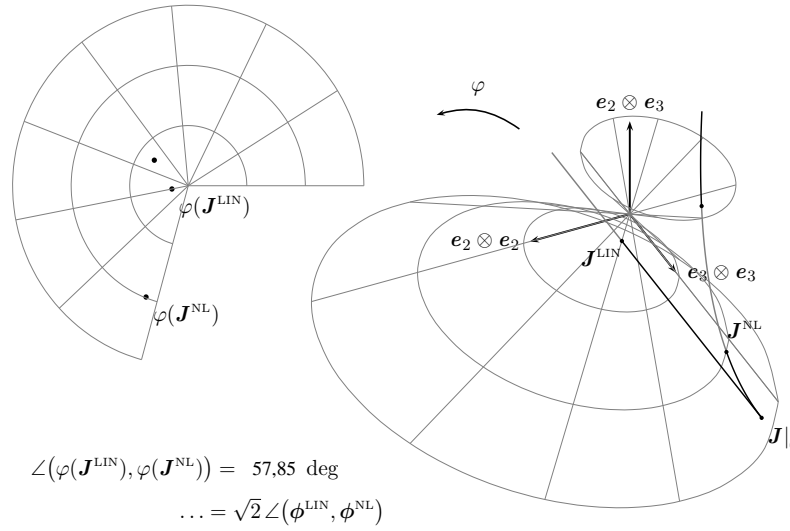


Figure 2. Jacobian path and criticality manifold with parameter values $\eta_1 = 0.1$ and $\eta_2 = 2.0$

and that the tangent space is parallel to the vector $\mathbf{e}_3 \otimes \mathbf{e}_3$ in the matrix space. The latter statement implies that there is only one intersection between the criticality manifold and the tangent space.

References

- [1] J.P. Keener and H.B. Keller. Perturbed bifurcation theory. *Archive for Rational Mechanics and Analysis*, 50:159–175, 1973.
- [2] J.P. Keener. Perturbed bifurcation theory at multiple eigenvalues. *Archive for Rational Mechanics and Analysis*, 56:348–366, 1974.
- [3] P. Wriggers and J.C. Simo. A general procedure for the direct computation of turning and bifurcation problems. *International Journal for Numerical Methods in Engineering*, 30:155–176, 1990.
- [4] A. Cardona and A. Huespe. Evaluation of simple bifurcation points and post-critical path in large finite rotation problems. *Computer Methods in Applied Mechanics and Engineering*, 175(1–2):137–156, 1999.
- [5] A. Ibrahimbegović and M. Al Mikdad. Quadratically convergent direct calculation of critical points for 3d structures undergoing finite rotations. *Computer Methods in Applied Mechanics and Engineering*, 189:107–120, 2000.
- [6] J. Mäkinen, R. Kouhia, A. Fedoroff, and H. Marjamäki. Direct computation of critical equilibrium states for spatial beams and frames. *International Journal for Numerical Methods in Engineering*, 89(2):135–153, 2012.
- [7] J.P. Abbot. An efficient algorithm for the determination of certain bifurcation points. *Journal Computational and Applied Mathematics*, 4:19–27, 1987.
- [8] J.-M. Battini, C. Pacoste, and A. Eriksson. Improved minimal augmentation procedure for the direct computation of critical points. *Computer Methods in Applied Mechanics and Engineering*, 192(16–18):2169–2185, 2003.
- [9] J. Huitfeldt. Nonlinear eigenvalue problems - prediction of bifurcation points and branch switching. Technical Report 17, Department of Computer Sciences, Chalmers University of technology, 1991.
- [10] R. Seydel. Numerical computation of branch points in nonlinear equations. *Numerische Mathematik*, 33:339–352, 1979.

Meshing effects on modelling of evolving bone during distraction osteogenesis

Valentina LaRussa¹ and Bjørn Skallerud¹

⁽¹⁾Department of Structural Engineering, Norwegian Univ Science and Techn, N-7491, Trondheim, Norway. e-mail: bjorn.skallerud@ntnu.no

Summary. This article presents a simple method to reduce inaccuracies in stiffness values due to finite element size when computing global stiffness of bone regenerate during leg-lengthening (distraction osteogenesis).

Key words: microCT, microFEM, mesh dependency, inaccuracies, stiffness estimates, bone modelling

Introduction

Distraction osteogenesis is a technique used to elongate parts of the skeleton in order to achieve longer limbs or repair major bone trauma. An external frame is attached to the limb, with pre-tensioned wires through the bone distal and proximal to the bone non-union, is employed. Axial rods are then screwed apart about one mm a day, pushing the two bone segments apart, until the intended limb length is obtained. This process may take several weeks. Then the frame is kept in place some more weeks for stability while the bone is consolidating (evolving into stiffer and more mature bone). Finally the frame is removed. An important clinical question is: when is it safe to remove the frame without risking fracture of the newly developed bone callus? A promising method to answer this question is to combine μ CT recordings and μ -finite element modeling. The CT scans provide bone density values that are strongly correlated to Young's moduli and strength. With this, a heterogeneous solid finite element model, where each solid element has a site-specific stiffness, is obtained. This FE model can be used to estimate the global axial/bending/torsion-stiffness of the newly generated bone part. However, the finite element models derived from μ CT data can become huge, and there is still a challenge to obtain simulation results within reasonable computer times. One remedy for this is to use a mesh that is coarser than the one that naturally is obtained from the μ CT scans. A μ CT scan with e.g. 20 μ m resolution yields solid elements with extensions of the same magnitude. This is a detailed mesh that captures the micro-architecture and stiffness distribution. Using a 20 μ m solid finite element based mesh on a typical bone re-generate leads to the order of $30 \cdot 10^9$ finite elements, whereas coarsening to a 200 micrometer sized solid element reduces this to about 30 million

finite elements. This may, however, lead to loss of micro-architectural information and accuracy of predictions. The present study addresses the inaccuracy of coarsened meshes. The bone regenerate material used is from rabbit tibia[1].

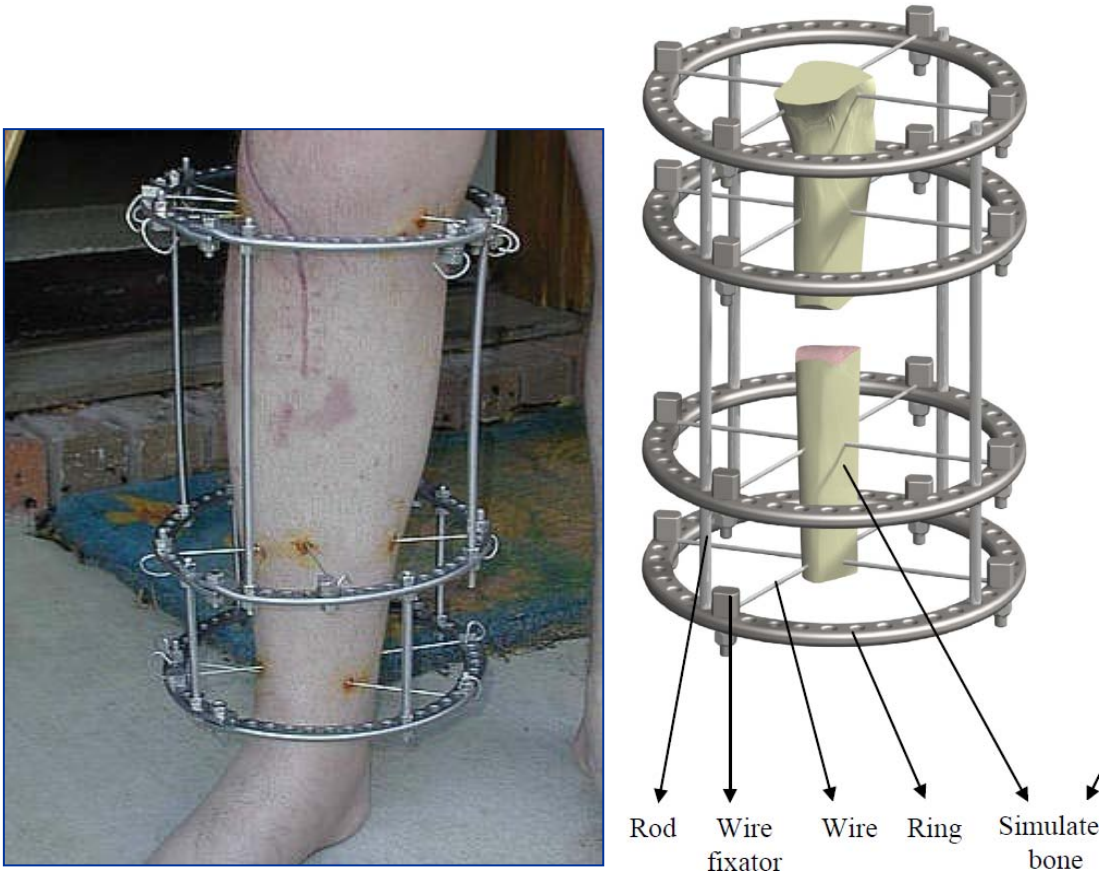


Figure 1. Ilizarov frame used in distraction osteogenesis.

Methods

μ CT scanning with resolution 20 micrometer for rabbit tibia was carried out 35 days after surgery, corresponding to end of the consolidation phase [1]. Five cubical volumes of interest (VOI) of size 3mm were extracted from the μ CT data at central part of the callus (see right part of Figure 2) [2]. The VOIs were discretised with finite elements of extension $h=40, 60, 80, 100, 120, 200 \mu\text{m}$. Also a few models were generated with $h=20 \mu\text{m}$. Then the VOIs were subjected to nominal axial compression in three orthogonal directions separately (Fig. 2 B-D), in addition a shear loading case was simulated (Fig. 2 E) [2]. ABAQUS was employed, with C3D8 solid elements.

The pixel value corresponding to each voxel was employed to find a grey value ranging from 0 to 1. Value 0 corresponds to no density and zero stiffness, 1 corresponds to fully mineralized bone with a Young's modulus representative for healthy mature tibial cortical bone. The elasticity assignment to each element was according to the following relationship:

$$E_{\text{voxel element}} = E_{\text{tissue}} \cdot \left(\frac{\text{pixelvalue}}{\text{highest_pixelvalue}} \right)^\gamma$$

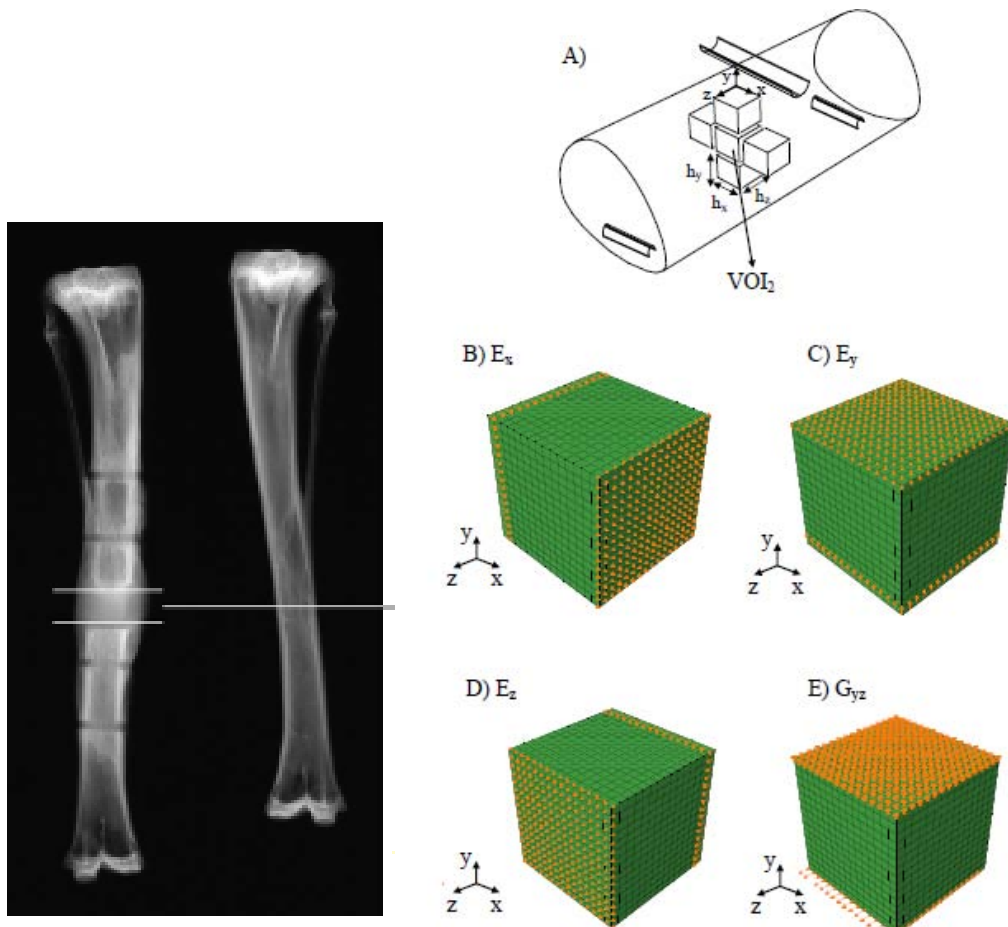


Figure 2. Distracted rabbit tibia, volumes of interest and boundary conditions for simulations.

E_{tissue} is not found from the CT scans, and must be determined in order to do quantitative stiffness assessments of the callus. In the present study, focusing on the effects of finite element size, the E_{tissue} is a common parameter to all simulations. Hence, normalizing a nominal stiffness corresponding to one mesh with the stiffness obtained from another mesh, E_{tissue} cancels and has no effect on the mesh study. Herein, we present normalized stiffness as function of mesh refinement. The exponent γ is introduced as a mesh sensitive parameter. We assume that the finest mesh ($h=20 \mu\text{m}$) captures all details of micro-architecture and density distribution. Hence, the exponent is set to 1 in this case. First, all simulations are run with $\gamma=1$. Then γ is adjusted in order to make the nominal stiffness independent of the mesh. A similar approach has been employed for trabecular bone in [3] and [4].

One side of the cube was fixed, the opposite side was subjected to a nominal displacement. The resulting total reaction force was divided by nominal surface area in order to obtain nominal stress. Displacement was divided by nominal length to get nominal strain. The slope of stress-strain curve then provided a nominal stiffness, i.e. Young's modulus.

Results

Figure 3 shows one example of how the nominal Young's moduli evolve for the five VOIs in one bone sample as function of finite element size. We note that the stiffness varies a lot

between the different VOIs, showing heterogeneity. Also, the nominal stiffness increases as the mesh is getting coarser. In order to find an exponent γ that gives the same stiffness when $h=200$ micrometer as for the “gold standard” stiffness corresponding to $h=20$ micrometer, an optimization on the square error between stiffnesses for the two meshes was carried out. The result is $\gamma=1.1$. In Figure 3, the use of exponent 1.1 for mesh 200 micrometer is depicted by the stars. A dotted line from stiffness for $h=20$ to $h=200$ is plotted in order to show the improvement in nominal stiffness prediction using $\gamma=1.1$ (compared to using $\gamma=1$, the fully drawn lines). Similar results are obtained for loading in the other (x, y, and shear) directions. An interesting result is that in shear, the optimal exponent takes value 1.2. This indicates that coarsening of the mesh has a more detrimental effect in shear compared to axial loadings.

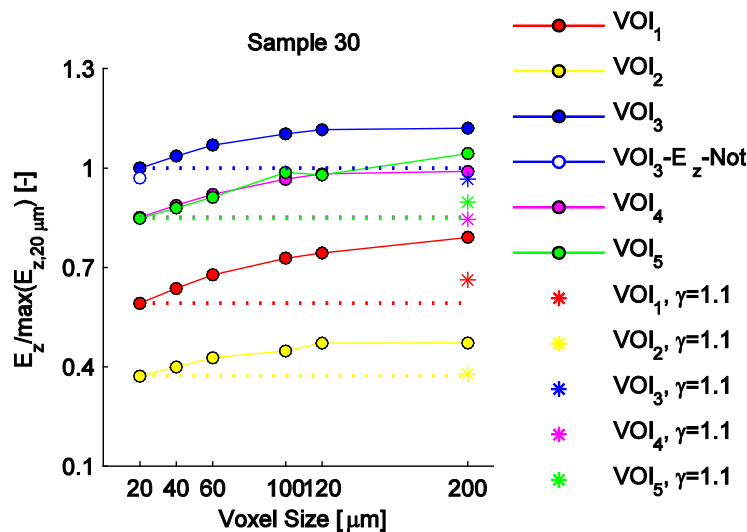


Figure 3. Influence of finite element size on nominal normalised axial stiffness.

Conclusion

A method to determine nominal stiffnesses of callus tissue that reduces the inaccuracy of mesh coarsening is presented. With this, feasible finite element models of complete bone re-generate parts can be generated, that accounts for loss of micro-architecture and density distributions. With the development of more powerful computer power this will not be necessary, and μ FEM from μ CT can be utilised directly with the maximum resolution provided by the μ CT scanners.

References

- [1] Aleksyniene R, Thomsen JS, Eckhardt H, Bundgaard KG, Lind M, and Hvid I. Three-dimensional microstructural properties of regenerated mineralized tissue after PTH treatment in a rabbit tibial lengthening. *J Musculoskelet, Neuronal Interact.*, vol 9, 268-277, 2009.
- [2] LaRussa V. *Biomechanical aspects of distraction osteogenesis*. PhD Thesis, Norwegian Univ Science and Techn, Trondheim, Norway, 2012.
- [3] Homminga J, McCready BR, Weinans H, and Huiskes R. Introduction and evaluation of a grey value voxel conversion technique. *J Biomechanics*, vol 34, 513-517, 2001.
- [4] MacNeil JA and Boyd SK. Bone strength at the distal radius can be estimated from high-resolution peripheral quantitative computed tomography. *Bone*, vol 42, 1203-1213, 2008.

Delamination between a unidirectional and woven composite

Leslie Banks-Sills^{1,2}, Maya Gohfeld¹, and Rami Eliazi¹

⁽¹⁾School of Mechanical Engineering, Tel Aviv University, Ramat Aviv, Israel, banks@eng.tau.ac.il

⁽²⁾Division of Solid Mechanics, Lund University, Lund, Sweden

Summary. A delamination between a unidirectional fiber reinforced carbon/epoxy material with the fibers in the 90° -direction and a balanced weave with fibers in the $0^\circ/90^\circ$ directions is considered (see Fig. 1). The first term of the asymptotic solution for the stress and displacement fields is found. These expressions are used to extend two methods for determining the stress intensity factors: displacement extrapolation and the interaction energy or M -integral. The methods are employed in conjunction with finite element calculations. The energy release rate and phase angles are also obtained. Sample solutions are presented.

Key words: delamination, stress intensity factors, M -integral

Introduction

The problem of a delamination within a multi-directional laminate is of central importance and has been receiving much attention. It is necessary to be able to predict the propagation of such damage within structures. Tests using Brazilian disk specimens have been carried out and presented in [1, 2] for the $0^\circ/90^\circ$ and $+45^\circ/-45^\circ$ interfaces. In order to analyze the test specimens, asymptotic fields were found previously and the displacement extrapolation and M -integral methods were extended for those cases. In this study, the required analytical and numerical methods are developed for the interface between a unidirectional fiber reinforced carbon/epoxy material with the fibers in the 90° -direction and a balanced weave with fibers in the $0^\circ/90^\circ$ directions as shown in Fig. 1). These tools will be used in the future to carry out tests on this interface in order to obtain its fracture toughness.

Asymptotic solutions

The first term of the asymptotic solution is determined by means of the Stroh [3] and Lekhnitskii [4] formalisms. It is found that there are two singular solutions, one in which the singularity is square-root, oscillatory, and one in which it is square-root. For both cases, the displacement field \mathbf{u} and stress function ϕ for each material are found. The in-plane and out-of-plane fields

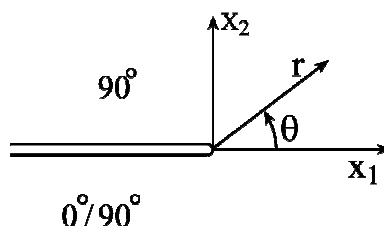


Figure 1. Delamination front coordinates.

decouple. Note that the upper material is transversely isotropic with the symmetry plane $x_3 = 0$ (see Fig. 1). It has five independent mechanical properties. The lower material is tetragonal with six independent mechanical properties.

The in-plane stress field is given by

$$\sigma_{\alpha\beta}^{(k)} = \frac{1}{\sqrt{2\pi r}} \left[\Re (K r^{i\varepsilon}) {}_k\Sigma_{\alpha\beta}^{(1)}(\theta) + \Im (K r^{i\varepsilon}) {}_k\Sigma_{\alpha\beta}^{(2)}(\theta) \right]; \quad (1)$$

whereas, the out-of-plane stress field is found as

$$\sigma_{\alpha 3}^{(k)} = \frac{K_{III}}{\sqrt{2\pi r}} {}_k\Sigma_{\alpha 3}^{(III)}(\theta). \quad (2)$$

In eqs. (1) and (2) $\alpha, \beta = 1, 2$, and $k = 1, 2$ denotes the upper and lower materials, respectively. The symbols \Re and \Im denote the real and imaginary part of the quantity in parentheses, respectively. The oscillatory parameter ε is given by

$$\varepsilon = \frac{1}{\pi} \tanh^{-1} \beta = \frac{1}{2\pi} \ln \frac{1 + \beta}{1 - \beta}. \quad (3)$$

The expression for β may be found from the Barnett-Lotte tensors as

$$0 \leq \beta = \left\{ -\frac{1}{2} \text{tr}(\check{\mathbf{S}}^2) \right\}^{\frac{1}{2}} < 1. \quad (4)$$

The 3×3 matrix

$$\check{\mathbf{S}} = \mathbf{D}^{-1} \mathbf{W}, \quad (5)$$

$$\mathbf{D} = \mathbf{L}_1^{-1} + \mathbf{L}_2^{-1}, \quad (6)$$

$$\mathbf{W} = \mathbf{S}_1 \mathbf{L}_1^{-1} - \mathbf{S}_2 \mathbf{L}_2^{-1} \quad (7)$$

and $\text{tr}(\cdot)$ is the trace of the matrix in parentheses. The tensors \mathbf{S}_k and \mathbf{L}_k ($k = 1, 2$ represents the upper and lower materials, respectively), known as the Barnett-Lothe tensors, are real and related to the matrices \mathbf{A} and \mathbf{B} by

$$-\mathbf{A}_k \mathbf{B}_k^{-1} = \mathbf{S}_k \mathbf{L}_k^{-1} + i \mathbf{L}_k^{-1}, \quad (8)$$

where there is no summation on k and $i = \sqrt{-1}$. The 3×3 matrices \mathbf{A} and \mathbf{B} are dependent on the mechanical properties of the materials. The crack tip, polar coordinates r and θ are shown in Fig. 1. The complex stress intensity factor in eq. (1) is given by

$$K = K_1 + iK_2 \quad (9)$$

where K_1 and K_2 are real and, respectively, the modes 1 and 2 stress intensity factors; K_{III} is the mode III stress intensity factor. The nondimensional functions ${}_k\Sigma_{\alpha\beta}^{(1)}(\theta)$, ${}_k\Sigma_{\alpha\beta}^{(2)}(\theta)$ and ${}_k\Sigma_{\alpha\beta}^{(III)}(\theta)$ depend on the coordinate θ and the mechanical properties; they are associated with modes 1, 2 and III, respectively.

It is possible to show that the tractions along the interface may be related to the stress intensity factors as

$$\left(\sigma_{22} + i \sqrt{\frac{D_{11}}{D_{22}}} \sigma_{12} \right) \Big|_{\theta=0} = \frac{K r^{i\varepsilon}}{\sqrt{2\pi r}}, \quad \sigma_{32} \Big|_{\theta=0} = \frac{K_{III}}{\sqrt{2\pi r}}. \quad (10)$$

General expressions for the in-plane displacement field may be written as

$$u_{\alpha}^{(k)} = \frac{1}{(1 + 4\varepsilon^2) H_k \cosh \pi \varepsilon} \sqrt{\frac{r}{2\pi}} \left[\Re (K r^{i\varepsilon}) {}_kU_{\alpha}^{(1)}(\theta) + \Im (K r^{i\varepsilon}) {}_kU_{\alpha}^{(2)}(\theta) \right]; \quad (11)$$

whereas, the out-of-plane displacement is given by

$$u_3^{(k)} = \frac{2}{\tilde{H}_k} \sqrt{\frac{r}{2\pi}} K_{III} U_3^{(III)}(\theta) . \quad (12)$$

In eqs. (11) and (12), H_k and \tilde{H}_k have units of stress, ${}_k U_\alpha^{(1)}(\theta)$, ${}_k U_\alpha^{(2)}(\theta)$ and ${}_k U_\alpha^{(III)}(\theta)$ are nondimensional functions of θ and the mechanical properties and associated, respectively, with modes 1, 2 and III.

The displacement jump across the crack faces near the crack tip is found as

$$\Delta u_2 + i \sqrt{\frac{D_{22}}{D_{11}}} \Delta u_1 = \frac{2D_{22}}{(1 + 2i\varepsilon) \cosh \pi\varepsilon} \sqrt{\frac{r}{2\pi}} K r^{i\varepsilon} , \quad \Delta u_3 = 2D_{33} \sqrt{\frac{r}{2\pi}} K_{III} \quad (13)$$

where D_{11} , D_{22} and D_{33} are diagonal elements of the matrix \mathbf{D} in eq. (6). In addition

$$\Delta u_i = u_i(r, \theta = \pi) - u_i(r, \theta = -\pi) . \quad (14)$$

Other interfaces have been studied in the past. This is the first time in which a woven composite has been considered.

Methods for extracting stress intensity factors

Stress intensity factors are calculated by two methods. First of all, finite element analyses are carried out to determine the displacement field. Then the displacement extrapolation method and the three-dimensional, interaction energy or M -integral are used to determine the K -values along the crack front. These methods utilize the asymptotic solutions presented in the previous section.

Sample problems

Several sample problems are solved for the interface considered in the study. Path independence of the M -integral, as well as solution convergence are examined.

Conclusions

An interface delamination between a unidirectional fiber reinforced carbon/epoxy material with the fibers in the 90°-direction and a balanced weave with fibers in the 0°/90° directions is considered. Two methods for calculating stress intensity factors are used with results produced for several problems. These methods will be used in the future to analyze test results.

References

- [1] L. Banks-Sills, V. Boniface and R. Eliasi. Development of a methodology for determination of interface fracture toughness of laminate composites—the 0°/90° pair. *International Journal of Solids and Structures*, 42:663–680,2005.
- [2] L. Banks-Sills, Y. Freed, R. Eliasi and V. Fourman. Fracture toughness of the +45°/–45° interface of a laminate composite. *International Journal of Fracture*, 141:195–210,2006 .
- [3] A.N. Stroh. Dislocations and cracks in anisotropic elasticity. *Philosophical Magazine*, 3:625–646, 1958.
- [4] Lekhnitskii, S.G.: Theory of Elasticity of an Anisotropic Body, Holden-Day, San Francisco, translated by P. Fern, 1950, in Russian; 1963, in English.

Topology optimization based on a phase-field approach and Howard's algorithm.

Matti Ristinmaa¹, Mathias Wallin²

⁽¹⁾Solid Mechanics, Lund University, Box 118, SE-22100 Lund, matti.ristinmaa@solid.lth.se

⁽²⁾Solid Mechanics, Lund University, Box 118, SE-22100 Lund, mathias.wallin@solid.lth.se

Summary. The topology optimization problem is formulated in a phase-field approach. The solution procedure is based on the Allen-Cahn diffusion model. The functional defining the minimization problem includes a gradient term which introduces cost for boundaries and thereby regularizing the problem. To avoid non-physical densities obstacles are introduced. It is shown that the problem can be stated as a variational inequality or a max-min problem. The numerical solution procedure are based on the finite element method and Howard's algorithm.

Key words: Topology optimization, Allen-Cahn, phase-field

Introduction

It is well-known that the classical SIMP (Simple Isotropic Material Penalization) scheme lacks a solution but when used together with the finite element method a solution is obtained since a length scale enters via the finite element discretization. Evidently, this solution is severely mesh dependent and thus difficult to use. To overcome the mesh dependence, several strategies for regularizing the problem have been proposed. Methods for regularizing the formulation have historically been based on constraining the gradient of the density or via filtering techniques.

In the present paper we explore the phase-field approach for solving the maximum stiffness problem. The objective functional consist of costs for compliance, for gradients and for diffuse designs. The numerical algorithm for finding the optimal design is based on a steepest decent algorithm which corresponds to the Allen-Cahn model. Upper and lower bounds on the density are strictly enforced via a penalty function that includes barriers at the limits.

The barrier function imposing infinite penalty for densities exceeding the chosen limits gives rise to a non-smooth problem. This class of problems, normally referred to as obstacle problems, occur frequently in financial mathematics.

Problem formulation

The problem considered is that of finding a design $\rho : \Omega \rightarrow [-1, 1]$ that maximizes the stiffness of an elastic structure within the design domain, $\Omega \in \mathbb{R}^{n_{dim}}$. Void material is characterized by $\rho = -1$ whereas material is defined by $\rho = 1$. The total amount of material available for the design is given by $V_o = \int_{\Omega} \rho dV$. As an alternative to maximizing the stiffness, we choose to minimize the compliance, C . The constitutive law for the elastic response is given by $\sigma = \mathbf{D} : \varepsilon$ where the stiffness tensor, \mathbf{D} scales with the material density, i.e. $\mathbf{D}(\rho) = g(\rho)\mathbf{D}_0$. Moreover, a distinct design is sought and therefore a penalization of diffuse designs is introduced. The penalization is given by $\psi = \psi(\rho)$ which satisfies $\psi(-1) = \psi(1) = 0$, i.e. no penalization is imposed for void material and full material. A penalized stiffness problem will require a length scale to be introduced and therefore also a cost for interfaces between material and non-material

is introduced. The cost for interfaces is taken to be proportional to the square of the gradient of the density leading to

$$\Phi(\rho) = \int_{\Omega} \left(\frac{1}{\epsilon} \psi(\rho) + \frac{\epsilon}{2} \nabla \rho \cdot \nabla \rho \right) dV \quad (1)$$

In conclusion the following objective functional is obtained,

$$E(\rho, \mathbf{u}) = \Phi(\rho) + \eta C(\rho, \mathbf{u}) \quad (2)$$

where ϵ and η are numerical parameters that control the width of the interface separating the two phases and the weight of the compliance to the objective functional, respectively. To minimise (2), we make use of a steepest descent approach. The field equations associated with the solution of (2) is solved using the finite element method. Since the penalty function ψ will include obstacles the problem can be formulated as a max-min problem. Here we choose the Howard's policy iteration scheme for solving the max-min problem. The details of the solution procedure can be found in [1].

Numerical example

The talk will be closed by demonstrating the optimization procedure for some test cases. Below the evolution of the algorithm is shown for a classical Michell type structure.

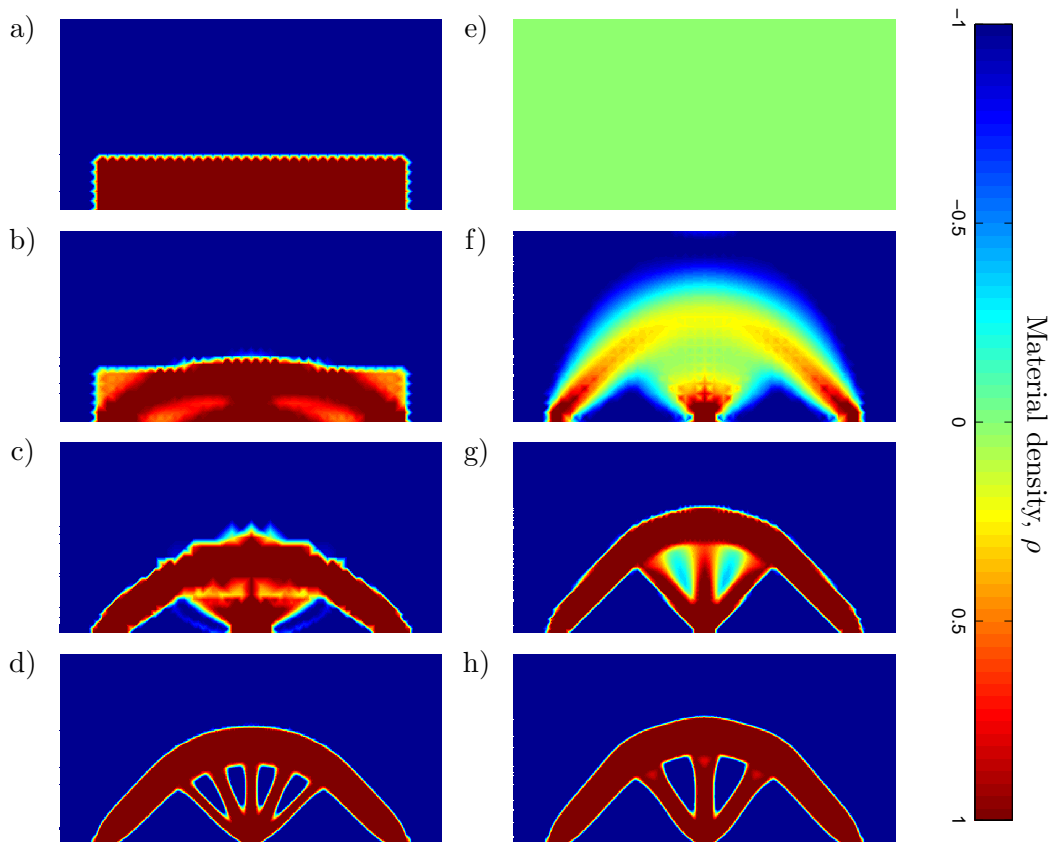


Figure 1. The evolution of the design for two initial designs using the same amount of material

References

- [1] M. Wallin and M. Ristinmaa Howard's algorithm in a phase-field topology optimization approach *International Journal for Numerical Methods in Engineering*, Accepted for publication.

Thermodynamically based Fictitious Crack/Interface Model for General Normal and Shear Loading

Niels Saabye Ottosen and Matti Ristinmaa

Division of Solid Mechanics, Lund University, Box 118, 22100 Lund, Sweden

Summary. A crack model that considers general normal and shear loading is proposed. It involves elasticity, plasticity and damage and it is thermodynamically based. An essential feature of the model is its consistency with the concepts behind the fictitious crack model.

Key words: Fictitious Crack model, thermodynamics, damage

Introduction

The fictitious crack model proposed by Hillerborg et. al (1976) was formulated for uniaxial loading. Before crack initiation, no crack opening w occurs and the $\sigma - w$ relation therefore exhibits a stiffness at unloading that, initially, is infinitely large.

A number of formulations have been proposed that generalize the fictitious crack/interface model to combined normal and shear loading and as, a prominent example, we mention the formulation given by Carol et al. (1997). Some of these models provide predictions that are in good agreement with experimental data obtained for complex load paths; often the experimental data of Hassanzadeh (1990) are used as a reference. However, all these proposals have the common feature that a certain crack opening occurs before crack initiation and this implies a stiffness at unloading that initially is finite and not infinitely large as inherently required by the concept of a fictitious crack. Even though this crack opening before crack initiation can be made small, it is in contradiction with the intrinsic concepts of a fictitious crack. The reason that this aspect normally is accepted, is that it facilitates the constitutive modeling significantly as classic topics from plasticity and damage mechanics can be adopted directly.

Here, we present a constitutive formulation that is in complete accordance with the concepts of a fictitious crack model. The formulation is thermodynamically based and it combines elasticity, plasticity and damage; in addition, it is formulated for finite deformations in the general 3D situation. For the same set of parameters, model predictions are compared with various experimental data for concrete and a close agreement is achieved.

Proceedings of the 25TH NORDIC SEMINAR
COMPUTATIONAL MECHANICS, 2012

Silent Spaces

Room: 304, Thursday 25 October, 16:15 - 17:55



Reduction of ground vibrations by landscape shaping

Peter Persson¹, Kent Persson¹, Per Jørstad¹ and Göran Sandberg¹

⁽¹⁾Division of Structural Mechanics, Lund University, Box 118, 221 00 Lund, Sweden,
peter.persson@construction.lth.se

Summary. This extended abstract presents a numerical study on reduction of vibrations in ground by landscape shaping. The vibrations, induced by traffic, were investigated by means of the finite element method with steady-state analyses. It was concluded from the analyses that if more valleys than hills are applied in the shaped landscape, amplification may occur. When using continuous hills, the hills seem to capture and guide waves in the direction of the hill. Locally this could reduce vibrations of significant importance but also guide the waves towards the evaluation points. Applying the constraints given within the numerical example, vibration reduction of more than 20 % was seen.

Keywords: vibration reduction, landscape shaping, soil dynamics, finite element method

Introduction

In this paper, vibration reduction at a high-tech facility, MAX IV, will serve as a numerical example, see Figure 1 for an architectural sketch. A new storage ring is needed to improve research possibilities. The research fields are e.g. material science and medicine. The storage ring is controlled by a large number of magnets that are distributed along the ring. Since the quality of the measurements is dependent on the vibration levels of the magnets, very low vibration levels at the magnet foundations are required. A mean vertical vibration level less than 20-30 nm during one second in the frequency span 5-100 Hz is desirable. The goal of this study is to investigate the reduction of traffic-induced vibrations by applying different shapes to an initially flat landscape. The aim is to evaluate the influence of landscape shaping to minimize the vibration levels in the MAX IV facility, especially at the magnet foundations.

The dynamic behaviour of the MAX IV facility and its surrounding landscape were analysed by means of the finite element (FE) method in a report, see [1]. It was concluded from the analyses that the material parameters of the soil have a significant influence on the vibration levels in the facility and more reliable material parameters are needed for the finite element analysis to achieve more precise results. A comparison between measurements at the construction site of the facility and results from the finite element model were carried out in [2]. It was concluded that the measurements and the calculations correlated fairly well. The FE-model was also improved in terms of accuracy and computational cost. Reduction of ground vibrations at MAX IV considering traffic-induced vibrations was investigated in [3]. To evaluate the traffic load from the nearby highway, green-field in-situ measurements were

performed. In the previous work it was concluded that frequencies over 20 Hz in the traffic load have negligible influence on the vibration levels at the magnet foundations. It was also concluded that the stiffness and damping of the soil have a large influence on the vibration levels.

At large construction sites, large amounts of soil will be excavated in order to smooth the surface before the construction starts. These masses of soil may instead be useful at the construction site in order to construct a shaped landscape with hills and valleys. The idea was originally suggested by the Division of Structural Mechanics at Lund University and implemented by the architects in the MAX IV project as it is an aesthetically desirable solution. The efficiency of landscape shaping on reducing ground vibrations was investigated with two-dimensional (2D) as well as three-dimensional (3D) parametric studies by varying the shapes in the landscape.



Figure 1. Shaped landscape at MAX IV. Left: Architectural sketch by Fojab and Snøhetta. Right: Aerial photograph of construction site by Perry Nordeng.

Material properties

In the numerical example, MAX IV, the area between the highway and the facility consists of 14 m layer of soil, Low Baltic clay till, and bedrock consisting of shale. Since the materials are exposed to loads with low magnitude and the wave lengths are long compared to local variations, the pre-consolidated clay till as well as the shale were modelled as linear elastic isotropic materials. The material parameters, determined by geotechnical consultants in the MAX IV project, are shown in Table 1. The loss factor includes material damping and other attenuation effects, such as varying topology of the soil as well as the bedrock.

Table 1. Material properties.

Property	Clay till	Shale
Depth	14 m	-
Young's modulus	476 MPa	8809 MPa
Density	2125 kg/m ³	2600 kg/m ³
Poisson's ratio	0.48	0.40
Loss factor	0.14	0.10

FE-model and numerical study

Steady-state analyses were performed considering traffic load from the nearby highway, regarded as the main external vibration source. Geometric and material constraints, determined by the MAX IV project, were applied. The steady-state analyses consider a frequency span of

5-20 Hz. Plain strain conditions were applied for the 2D FE-models. The 2D models ended up at 29,960 elements using 120,714 degrees of freedom (dofs) and the 3D model ended up at 518,400 elements using 1,093,358 dofs. To evaluate the traffic load from the nearby highway, green-field in-situ measurements were performed. The load was applied as a vertical point load in a node in the middle of the top surface of the models. The shapes were applied at a zone of 80 m, starting 10 m from the excitation point and ending 10 m from the evaluation point, see Figure 2. Due to the scattering of the propagating waves in 3D, the displacements were evaluated along a straight line, 100 m from the excitation point.

A constant curvature of the arcs that create the shapes was set as a constraint with a maximum slope of 30 degrees. The number of arcs that were used to create the shapes, always stretching over the same zone, was varied between 1-6 arcs. The maximum height/depth of the shaped hills and valleys was also varied. Three different principal shape configurations were investigated in the 3D analyses. The initial configuration of shapes corresponds to the shapes applied for the two-dimensional model, i.e. the arcs in the 2D were extruded. The second main configuration considers rotated extruded arcs, rotated 45 degrees in the horizontal plane. The difference to the previous version is that the incident surface waves will impinge with a different incident angle. The third main configuration was considered a checkered pattern of hills and/or valleys. This version resembles the architectural sketch in Figure 1. The vertical displacements were evaluated in terms of the root mean square value (RMS-value) of the magnitude of the complex amplitude.

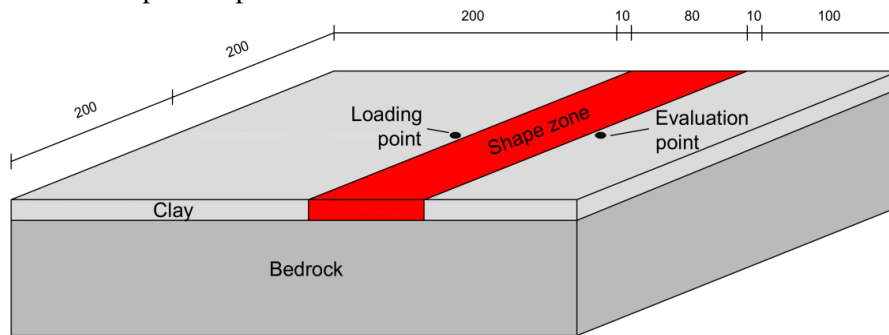


Figure 2. Location of loading point and evaluation point.

Results and conclusions

The numerical investigation showed that in general, shaped landscape generated a significant reduction of the vertical displacements at the evaluation points. However, for a negative volume change of soil, i.e. applying more valleys than hills amplification may occur, especially seen when only valleys were applied. However, only one deep valley will behave as a wave barrier and lead to reduction. Considering only hills, a few larger sized hills are more efficient than several smaller sized hills, stretching over the same zone. With smaller sized hills, the best solution is to apply hills exclusively.

The two best performing shapes from the 2D analyses and the corresponding 3D analyses (straight shapes) are altering hills and valleys with two arcs, showing a vibration reduction of approximately 25 %. Continuous hills may capture and guide waves in the direction of the hill. This effect depends on the angle of the incident wave. By rotating the hills in the horizontal plane, local vibration reduction of up to 50 % was obtained. However, hills directed towards the evaluation point may also guide waves and thus generate amplification. A checkered pattern of

hills and valleys behaves in the same manner as continuous hills, i.e. waves follow the paths of neighbouring hills. Applying only hills in the checkered pattern may create a straight path between the hills that guide the waves to the evaluation point and thus generate amplification. A checkered pattern of both hills and valleys with a fine defined pattern, see Figure 3, is the best performing checkered pattern showing vibration reduction of approximately 20 %.

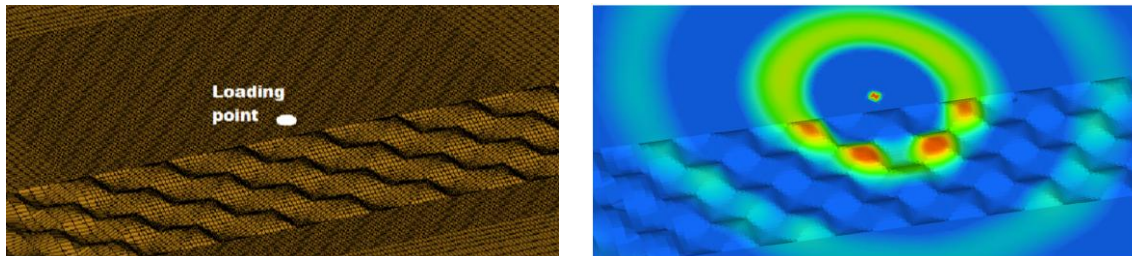


Figure 3. FE-model of 3D checkered shapes. Left: FE-mesh and loading point. Right: Visualisation of the vertical displacements.

Further work

The horizontal displacements may also be considered in order to draw more general conclusions regarding the efficiency of a shaped landscape in the sense of vibration reduction. The geometrical and mechanical constraints could be neglected to generate results and conclusions that are more applicable to other projects, i.e. the parametric studies could be extended to include more parameters. Different types of loading could also be considered, e.g. simulating the traffic load as a moving transient load. Use of materials with more defined material properties in the hills, could possibly be of significant importance. The 3D architectural landscape design suggested for MAX IV could also be investigated with FE-analyses.

Acknowledgement

The Silent Spaces project, a part of the EU program Interreg IVA, is gratefully acknowledged for the financial support.

References

- [1] Persson P., Analysis of Vibrations in High-Tech Facility, Report TVSM-5164, Division of Structural Mechanics, Lund University, 2010.
- [2] Persson P., Persson K., Analysis of Dynamic Soil-Structure Interaction at High-Tech Facility, Proceedings of NSCM-23: the 23rd Nordic Seminar on Computational Mechanics, Stockholm, 2010.
- [3] Persson P., Persson K., Sandberg G., Reduction of traffic-induced vibrations at high-tech facility using trenches, Proceedings of NSCM-24: the 24rd Nordic Seminar on Computational Mechanics, Helsinki, 2011.

Reduction of models for vibration analyses of lightweight multi-storey buildings

Ola Flodén¹, Kent Persson¹ and Göran Sandberg¹

⁽¹⁾Division of Structural Mechanics, Lund University, Box 118, 221 00 Lund,
ola.floden@construction.lth.se

Summary. This paper presents an investigation of various model reduction techniques applied to wooden floor and wall structures intended to be assembled into large building models. A finite element model of a floor structure, previously compared to experimental studies, was used as a test case for the analyses. The model was reduced using three different techniques; Guyan reduction, component mode synthesis and structural elements. The reduced models were compared by performing both eigenvalue and steady-state analyses and conclusions were made about the accuracy of the reduction techniques.

Key words: model reduction, finite element method, vibrations, buildings, multi-storey, lightweight, wood

Introduction

Application of wood as a construction material when building multi-storey buildings has advantages such as light weight, sustainability and low energy consumption during the construction and lifecycle of the building [1]. However, compared to heavy structures, it is a greater challenge to build lightweight structures without noise and disturbing vibrations between storeys and rooms due to e.g. footsteps, vibrating machines or external sources like railways and roads.

The studies presented in this paper are part of a larger project where the aim is to create finite element (FE) models for low-frequency vibration analyses of multi-storey wood buildings, valid for general load-cases. The modelling is performed in a modular manner, where detailed models of floor and wall structures are assembled into global models of complete buildings. When assembling the models, the number of degrees of freedom (dofs) quickly increases to exceed the limits of computer capacity, at least in a reasonable amount of time. The question then arises of how the FE-models can be reduced in size while still being able to represent the dynamic characteristics of the structures with sufficient accuracy.

The objective of the analyses in this paper is to evaluate methods for model reduction of FE-models of floor and wall structures and to investigate the influence of reducing the computational cost on the dynamic response of the models in terms of eigenfrequencies, eigenmodes and vibration transmission. The studies were performed using an FE-model of a wooden floor structure as reference model and were restricted to the low-frequency range, 0-100 Hz.

Model reduction

There are many methods for reduction of the linear equation of motion available in literature. The methods involve either a condensation of dofs, a transformation to generalised coordinates or a combination of both. Condensations may be done by e.g. Guyan reduction [2] or dynamic reduction [3]. The generalised coordinates are the amplitudes of some Ritz vectors, which may be determined in different manners. In component mode synthesis (CMS) [4], a method frequently

used in structural dynamics, the vectors are the eigenmodes of the system. In the last years, methods of model reduction from the area of control theory have been applied to problems in structural mechanics. These methods can be divided into two main categories, methods based on Krylov subspaces and balanced truncation.

Koutsovasilis and Beitelschmidt [5] compared several reduction methods for an eigenvalue analysis of an elastic rod and concluded that Krylov methods perform well compared to methods originating from structural mechanics. Witteveen [6] compared CMS to the methods from control theory for a simple beam structure and found that the methods from control theory are sensitive to off-tuning of the system by introducing a spring at one of the input/output dofs. The situation of off-tuned systems is the case in this study, where models of floor and wall structures are supposed to connect to other models in assemblies of complete buildings. Also, Guyan reduction and CMS are the two methods of model reduction implemented in commercial FE software and therefore these two methods are investigated in this paper together with a third approach using structural finite elements. With structural elements, the constraints are imposed on the analytic models of structural components instead of imposing constraints on the dynamics of the discretised system, as is the case for the other methods mentioned.

Analyses

Flodén and Ejenstam [7] developed a 3D solid FE-model of a wooden floor-wall structure and compared the eigenfrequencies and eigenmodes to measurements on a full-scale experimental structure. The eigenfrequencies of the FE-model showed good agreement to measurements below 100 Hz and the first eigenmodes were of good resemblance. The comparison of different reduction methods presented in this paper uses a reference model developed from the FE-model in [7]. A number of interface nodes were added at the boundary with both displacement and rotational dofs in order to fulfil compatibility in the connection to other floor and wall models.

Reduced models were created by Guyan reduction, CMS with various numbers of retained eigenmodes and structural elements. Two different analyses were performed to compare the accuracy of the reduced models; an eigenvalue analysis and a steady-state analysis.

The eigenvalue analysis was performed in order to obtain both eigenfrequencies and eigenmodes of the models. The eigenfrequencies were compared by studying the relative error of the frequencies compared to the reference model and the eigenmodes were compared by using the modal assurance criterion (MAC).

The steady-state analysis was made to study the vibration transmission. The floor models were placed on top of three wall panels, one at each end of the floor and one in the middle. A load was applied to the wall panel on one end and the amplitudes measured at the wall panel on the other end. A frequency sweep was performed up to 100 Hz and in each step, an RMS-value was calculated of the displacement magnitudes in all nodes of the receiver wall panel.

Results

Eigenvalue analysis

Table 1 shows the number of dofs and computation time needed for the eigenvalue analyses. The analyses were performed on a personal computer with an Intel Xeon W3530 CPU of 2.80 GHz and enough RAM memory to fit the eigenvalue analyses. It can be observed that the computation time of CMS with 1000 retained eigenmodes is almost twice as long as for structural elements even though the latter model contains far more dofs. This is a consequence of the fully populated matrices obtained from model reduction with CMS in contrast to the banded FE matrices.

The relative error of the eigenfrequencies below 100 Hz from the reduced models compared to the reference model is shown in Figure 1. With Guyan reduction, only the first eigenfrequencies are of good accuracy and the error is 30 % at the eight eigenfrequency. The error of CMS is

Table 1. Size of the models and computation time of the eigenvalue analysis.

Model	dofs	Time [s]
Reference model	632820	434.0
Structural elements	24762	7.0
Guyan reduction	1038	1.6
CMS, 10 retained eigenmodes	1048	1.7
CMS, 50 retained eigenmodes	1088	3.0
CMS, 100 retained eigenmodes	1138	3.2
CMS, 500 retained eigenmodes	1538	6.2
CMS, 1000 retained eigenmodes	2038	12.0

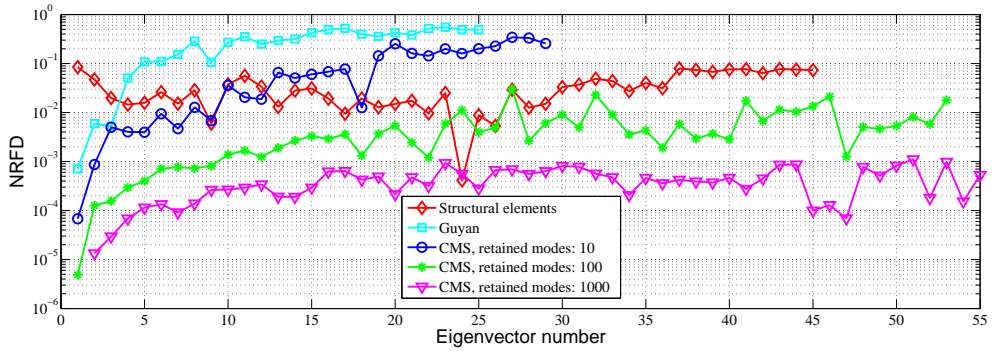


Figure 1. Normalised relative frequency differences for eigenfrequencies below 100 Hz.

reduced by increasing the number of retained eigenmodes and with 1000 retained eigenmodes the error is below 0.1 % for all eigenfrequencies. The structural elements model produces errors below 10 % for the 45 eigenfrequencies below 100 Hz and an average error below 4 %.

Corresponding observations were made from the comparison of eigenmodes; Guyan reduction only modelled a few eigenmodes with good accuracy, while CMS with 1000 retained eigenmodes resulted in very good correlation in the whole frequency range. With structural elements, only a few eigenmodes were modelled with very good accuracy, but there was also a relatively good correlation to the reference model at the higher frequencies.

Steady-state analysis

Figure 2 shows the RMS-values of the displacements at the receiver wall panel from the analyses of the different models. Below 40 Hz, all the reduction methods display vibration levels close to the reference model. Above 40 Hz, the accuracy of Guyan reduction is poor. By using CMS with 10 retained eigenmodes, good accuracy is obtained up to 65 Hz, while 1000 retained eigenmodes produces accurate results in the whole frequency range. The structural elements model behaves very similar to the reference model, but with relatively large errors at particular frequencies, indicating that some deformation patterns of the structure are affected by the constraints imposed in the structural finite elements.

Conclusions

- As expected, the accuracy of Guyan reduction was poor due to its static nature. Acceptable results were obtained only at the lower frequencies in both the eigenvalue and steady-state

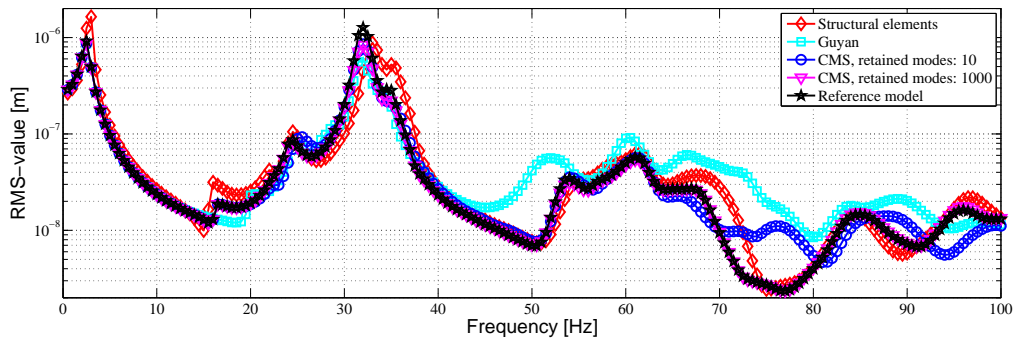


Figure 2. RMS-values of the receiver wall displacements for each excitation frequency.

analysis.

- With CMS, there is a straightforward trade-off between accuracy and computational cost. By including up to 100 retained eigenmodes, the accuracy increases quite rapidly. Thereafter, the convergence is slower. With 1000 retained eigenmodes, there was a good accuracy both in eigenfrequencies and eigenmodes as well as in the steady-state analysis. However, the computation time is quite large compared to structural elements due to the fully populated matrices.
- There is not a unique way of creating a model with structural elements and it is therefore more difficult to draw general conclusions. The model behaved similar to the reference model in the whole frequency range, but with relatively large errors at particular frequencies. An optimisation of the model may lead to more accurate results.

Acknowledgements

This research is supported by Silent Spaces, a part of the EU program Interreg IV A.

References

- [1] L. Gustavsson et al. Carbon Dioxide Balance of Wood Substitution: Comparing Concrete- and Wood-Framed Buildings. *Mitigation and Adaptation Strategies for Global Change*, 11:667–691,2006.
- [2] R.J. Guyan. Reduction of Stiffness and Mass Matrices. *AIAA Journal*, 3:380,1965.
- [3] A.Y.T. Leung. An Accurate Method of Dynamic Condensation in Structural Analysis. *International Journal for Numerical Methods in Engineering*, 12:1705–1715,1978.
- [4] R.R. Craig and M. Bampton. Coupling of substructures in dynamic analysis. *AIAA Journal*, 6:1313–1319,1968.
- [5] P. Koutsovasilis and M. Beitelshmidt. Comparison of model reduction techniques for large mechanical systems. *Multibody System Dynamics*, 20(2):111–128,2008.
- [6] W. Witteveen. Comparison of CMS, Krylov and Balanced Truncation Based Model Reduction from a Mechanical Application Engineer’s Perspective. *Proceedings of the 30th IMAC, A Conference on Structural Dynamics*, Volume 2:319–331,2012.
- [7] O. Flodén and J. Ejenstam. *Vibration Analyses of a Wooden Floor-Wall Structure – Experimental and Finite Element Studies*. Division of Structural Mechanics, Lund University, Sweden, 2011.

Finite element analysis of flanking transmission in a lightweight junction with elastic layers

Juan Negreira¹, Delphine Bard¹, Kent Persson¹ and Göran Sandberg¹

⁽¹⁾ Department of Construction Sciences, Divisions of Engineering Acoustics and Structural Mechanics, Lund Tekniska Högskola, BOX 118, 22100 Lund, Sweden.
juan.negreira_montero@construction.lth.se

Summary. In this paper, a flanking transmission investigation when introducing a rubber foam material in a lightweight junction is presented. Specifically, the variation in the transfer function when varying the placement of the elastomer within the junction was studied for several types of floors and ceilings by means of the finite element method.

Key words: Lightweight, junction, elastomer, finite element, flanking transmission.

Introduction

When the Swedish construction code in 1994 allowed wooden multi-storey buildings, this type of lightweight structures became popular due to low cost and ease of construction [1]. A drawback in those buildings is disturbing vibrations and noise propagating in the construction, especially through the junctions. To reduce noise and vibration through the junctions, rubber foam materials may be introduced between walls, floors and ceilings [1], especially in between prefabricated building elements, [2]. In this study, the properties of a junction when introducing a rubber foam material - Sylodyn[®] - in between were investigated by means of the finite element method using the commercial software Abaqus[®]. The flanking transmission was specifically analysed. Several types of floors and ceilings as well as different placements and properties of the Sylodyn have been studied.

Problem description

In this investigation, a standard volume of a room (3.6x6x3 m) was considered. In Figure 1 the drawings from Lindbäck's Bygg's project Brunnby Park in Upplands Väsby are shown. This lightweight structure using volume modules was chosen due to its widespread use in Sweden and also because of a feasible future comparison between finite element simulations and in-situ measurements which have already been performed.

Two different setups were analysed as shown in Figure 2 (hereafter denoted as case A and case B respectively). In both case A and B, the beams comprising the floor and the ceiling were considered to be placed along the shorter dimension, i.e. widthwise. Furthermore, for case A, the variation on the flanking transmission was also investigated when considering the beams along the lengthwise direction. A parameter study varying the material properties for the Sylodyn was carried out, and finally, an analysis of the same junction without Sylodyn was performed.

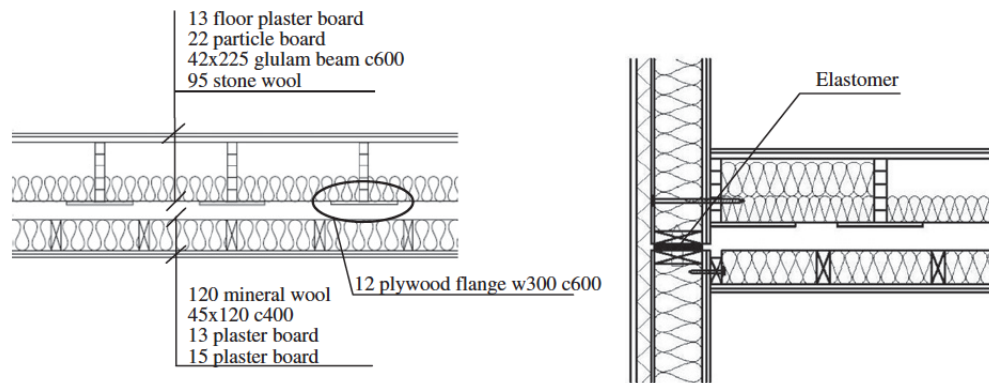


Figure 1. Modular building system drawings. Separate floor and ceiling (left) and facade junction (right)

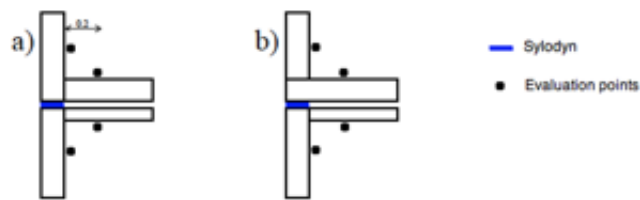


Figure 2. Different placements for the Sylodyn studied

Finite element model

Modelling a junction is a very complicated task as it must be able to capture all phenomena occurring in reality. This first investigation aims, by studying the relative differences between the modelled results; to gain knowledge on the behaviour of the structure, enabling to eventually create a more refined model which could correlate experimental and simulation results.

In this first approach, massive wood was considered all over the whole model with exception of the Sylodyn. This simplification will not disrupt the relative differences between the different cases studied. Furthermore, only negligible vibrations are transmitted through the insulation. Hence, in order to reduce calculation time, the insulation was excluded and taken into account by increasing the damping of the other materials.

The elastomer used in the studied structure to reduce the noise and vibration transmission was Sylodyn NE, a mixed cellular polyurethane dampening material developed by Getzner Werkstoffe GmbH. It is shaped as 100x100x25 squared blocks. The distance c/c (centre-to-centre) between two blocks was set to 400 mm. A linear elastic material model was applied since the quasi-static tests shown in [3] depict a fairly linear behaviour within the recommended operative range. As the structure will only be exposed to loads and displacements with low magnitude, all non-linear behaviour was neglected and the wood was also modelled as linear elastic. The properties of the materials considered were provided by the manufacturers.

All parts were individually created and assembled considering full coupling between them. This creates stiff connections, as it is believed to be the case in the real structure. Only 8-nodes brick elements were used (solid C3D8R elements for wood and the hybrid elements C3D8RH for Sylodyn) giving a FE-model with approximately 2 million degrees of freedom.

A 5 N harmonic concentrated force at the middle of the floor was considered and a frequency sweep was carried out from 10 to 100 Hz in steps of 1 Hz. Fixed boundary conditions were applied at the top and bottom of the walls. The model (for case A) can be seen in Figure 3. The blocks of Sylodyn are shown in grey, the floor in blue, the ceiling in red, the inner walls (apartment separating walls) in yellow and the outer (facade) walls in green.

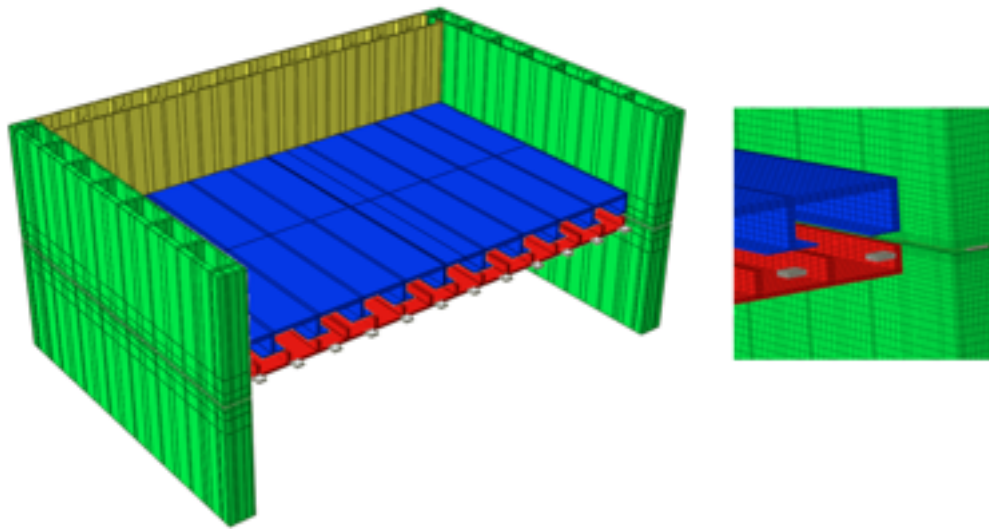


Figure 3. Case A with beams oriented widthwise

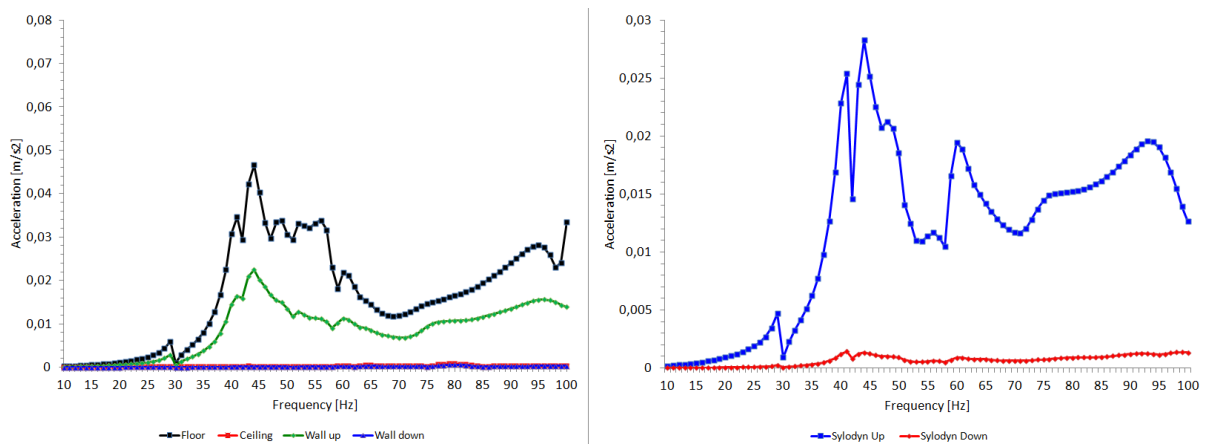


Figure 4. Case A widthwise. Acceleration magnitudes evaluated on the floor, ceiling, upper and bottom walls (left) and acceleration magnitudes evaluated on top and bottom of the Sylodyn (right)

Results

The following results show the performance of the junctions regarding the flanking transmission as plots of acceleration versus frequency. Furthermore, the vertical transmission from the source, located on the middle of the floor, to the ceiling underneath through the long side of the room was investigated. Although more calculations were done, just the results corresponding to case A widthwise as well as the ones for the junction without Sylodyn are hereafter presented.

The frequency dependent acceleration was evaluated at 6 nodes along the floor, walls and ceiling, all placed 0.2 m from the junction (see Figure 2). An average acceleration for the 6 nodes was calculated and plotted for the different elements composing the junction. Likewise, the acceleration magnitudes were also evaluated on top and bottom of the Sylodyn blocks.

As seen in Figure 4, for case A widthwise; the maximum acceleration magnitudes occur between 35 and 60 Hz. One can also identify that Sylodyn dampens nearly all vibrations, as the acceleration levels evaluated on the ceiling and the wall underneath are very low.

The performance of the junction without Sylodyn was also investigated (wood-wood connections all over). The comparative results are shown in Figure 5. It is apparent that the acceleration magnitudes evaluated at the bottom room without the Sylodyn are much higher, which indicates the advantages of using the Sylodyn as a vibration insulator in the junction.

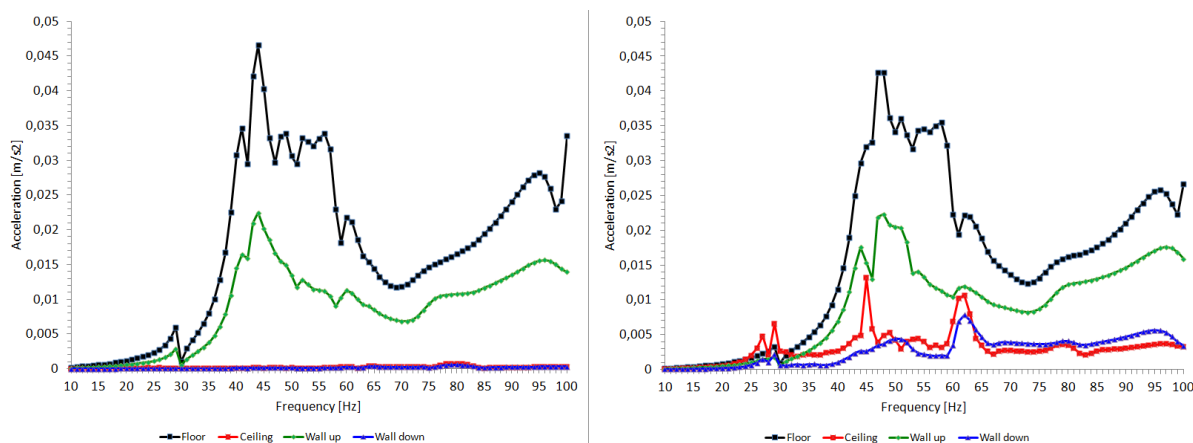


Figure 5. Comparison between the acceleration magnitudes for the junction with Syldyn (left) and without Syldyn (right). Case A with widthwise beams. The acceleration was evaluated on the floor, ceiling and both wall in the upper and lower level

Conclusions

An investigation regarding the flanking transmission when introducing Syldyn in a lightweight junction was carried out. It was shown for all cases studied, regardless of the orientation of the load bearing beams in the floor and ceiling or the placement of the Syldyn, that the reduction of acceleration magnitudes within the blocks of Syldyn is very effective. In addition, the performance of a junction with Syldyn was compared to the same junction without Syldyn. It was observed that the vibrations transmitted are much higher in the latter than in the former case. Hence, using Syldyn for this type of junction was proved to be advantageous.

Calculations not shown in this abstract portrayed through a parameter study that a variation in the modulus of elasticity of the Syldyn does not greatly influence the vibration transmission through the junction. Likewise, it was seen that case B may perform better than case A, although a more extensive study is needed in order to confirm this fact.

It was also shown that the linear elastic material model may not be accurate for the Syldyn as its behaviour does not resemble the real one (in reality not all vibrations are dampened out). Dynamic measurements to get frequency-dependent properties are being performed.

An insight into the performance of this specific type of junction (although many on the market are similar) regarding flanking transmission has been gained. Ultimately, this will allow the creation of more refined models in order to correlate both experimental and simulation results, which could be used as a prediction tool during the design phase of the structures.

Acknowledgments

This research was funded by the Silent Spaces project, a part of the EU program Interreg IV.

References

- [1] J. Forssén et al. Acoustics in wooden buildings. State of the art 2008. Vinnova Project 2007-01653. *SP Technical Research Institute of Sweden Report 2008:16*. Stockholm (2008).
- [2] F. Ljunggren, A. Ågren (2011), *Potential solutions to improved sound performance of volume based lightweight multi-storey timber buildings*, *Applied Acoustics*; 72:231-240.
- [3] Getzner Werkstoffe GmbH (2004). *Data sheet of the Syldyn NE*.
- [4] K.J. Bathe, *Finite Element Procedures*, Prentice Hall, New York, United States (1996).

Finite element validation of lightweight wooden T-junction models

Anders Sjöström¹, Juan Negreira¹, Delphine Bard¹, and Göran Sandberg

⁽¹⁾Division of Engineering Acoustics, Department of Construction Sciences, Lund University, Box 118, SE-22100, anders.sjostrom@construction.lth.se

Summary. The finite element software ABAQUS was utilized to model the behavior of two types of wooden junctions. The models were validated using measurements of mock-ups. The mode shapes of the models and the measured mock-ups were compared using the Modal Assurance Criteria. The attenuation in the models was also studied.

Key words: FEM, ABAQUS, T-junctions, MAC, validation

Introduction

Using lightweight materials, more specifically, timber materials, in buildings can be both cost effective and time saving when constructing multistorey buildings. However, the use of such materials is often the cause of complaints related to sound transmission and vibration particularly in the low frequency region. In order to reliably predict the acoustic performance of lightweight multi-storey buildings, knowledge on the behavior of the different types of junctions present in the structure is needed. In this paper a finite element model of two types of junctions typically found in lightweight wooden floors is validated using measured values from measurements performed on mock-ups of the joints further studies on this type of joints can be found in [1],[2],[3],[4],[5],[6],[7],[8],[9],[10]. The influence of the use of adhesives in addition to screws on the performance of the joints is also investigated. A comparison between measurements and simulations was carried out.

The Mock-ups

The junctions in the experimental part of this work were made out of timber and chipboard and were suspended from soft rubber strings. They are divided into two types: A single continuous plate of chipboard attached to a wooden beam, and two sheets of chipboard attached to a wooden beam leaving a small gap between the plates. The dimensions of the single plate are 1.2m×0.6m with a thickness of 22mm and the dimensions of the dual plates are 0.6m×0.6m each and with a thickness of 22mm. The plates were attached to the beam using screws. A schematic of the two types of junctions can be seen in Figure 1. The same structures were built a second time, but this time glue was applied around the screws on the contact surfaces, summing up a total number of 4 mockups.

Finite Element Model

The model was implemented in the commercial FEM package ABAQUS. All the individual parts of the structure were modeled and assembled in the finite element model in order to re-

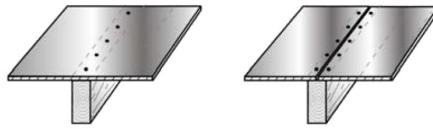


Figure 1. Types of junctions investigated.

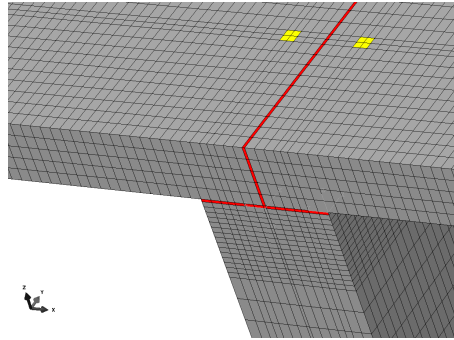


Figure 2. Detail of mesh, glue in red, screws in yellow.

semble the real construction. The plate, the beam and the screws were modeled using solid brick elements `C3D8R` which is an 8-node reduced integration linear brick element with hourglass control. The glue was modeled using the cohesive element `COH3D8` which is an 8-node three-dimensional element. The screws were manifested as square pins going through the plate and into the beam. In figure 2 a detail of the mesh can be seen, the screws are highlighted in yellow and the glue layer is highlighted in red.

The structure was only exposed to small loads and displacements, meaning that all non-linear behavior was neglected and hence allowing us to model the materials as linear elastic. Likewise, a convergence analysis was performed on the constituent parts to decide the element mesh size. The typical element size in the model is 4mm and the number of degrees of freedom in the model is 937530. Having such a fine mesh enables us to resolve higher frequencies with greater accuracy in further studies. In the modal analysis there were no boundary conditions in the model, and in the frequency sweeps the model was fixed in the z-axis in two points towards the short edges on the bottom side of the beam.

The FE-model was first used to perform a modal analysis for the four different structures as discussed above. The model was also used to perform a parameter study on the influence of the structural damping and the stiffness of the glue in the attenuation over the junction when subjected to an impact.

The attenuation was compared over the four points on either side of the beam. To evaluate the attenuation over the discontinuity in the junction, the frequency response function (frf) was calculated for the case of dual plates glued together over the beam using a frequency sweep from 0 to 200 Hz.

Results

Some of the mode shapes for the measured and the simulated cases are shown in Figures 3, 4, 5 and 6. To compare the measured eigenmodes with the simulated ones the modal assurance criteria (MAC) was used. The MAC-value for the i -th eigenmode is defined as

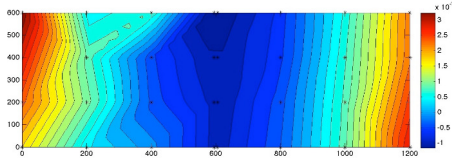


Figure 3. First measured eigenmode

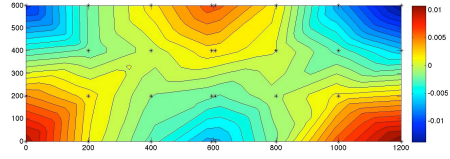


Figure 4. First simulated eigenmode

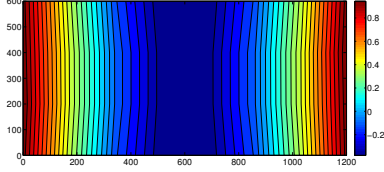


Figure 5. Third measured eigenmode

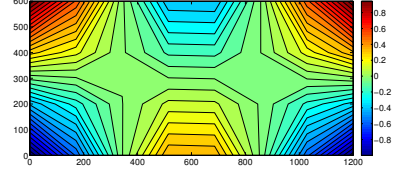


Figure 6. Third simulated eigenmode

$$MAC = \frac{|(\Phi_i^{sim})^T(\Phi_i^{meas})|^2}{(\Phi_i^{sim})^T(\Phi_i^{sim})(\Phi_i^{meas})^T(\Phi_i^{meas})} \quad (1)$$

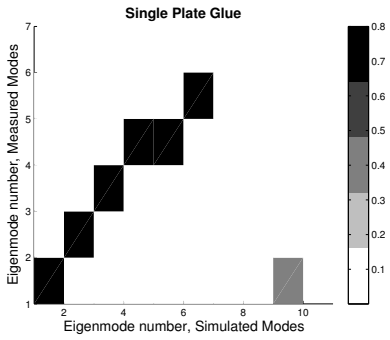


Figure 7. MAC-values single plate glue

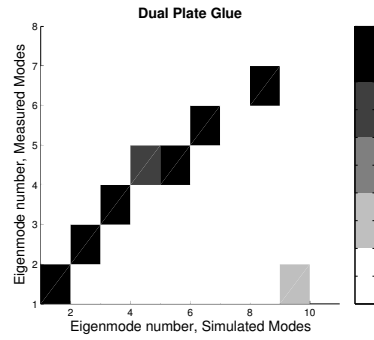


Figure 8. MAC-values dual plate glue

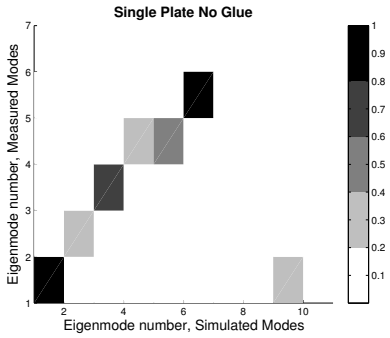


Figure 9. MAC-values single plate no glue

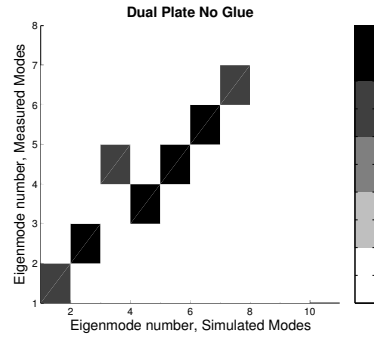


Figure 10. MAC-values dual plate no glue

Equation 1 is the normalized scalar product of the eigenvectors from the measured and the simulated models. The MAC-value is in the range 0-1, where 1 represents total correlation. For a more comprehensive explanation of the MAC see [2] In figure 7, 8, 9 and 10 the MAC-values for the four cases are shown. There is a good correlation in the dual plate cases and in the glued single plate case. The correlation in the unglued single plate case is worse than in the three other cases, a fact that is reflected in the measured and simulated eigenfrequencies.

Conclusions

The parameter study performed in the FE-model indicates that the influence on the attenuation from the stiffness of the glue is the most dominant. The same simulation was performed for the single plate case both with and without glue. The effect of the damping ratio on the attenuation could not be distinguished in the simulations, the only parameter in the study that had any discernible effect in the parameter study was the stiffness in the glue.

In order to compare the two types of junctions, a frequency sweep was performed with a single continuous plate over beam. Both glued and unglued cases were considered. It was noted that the attenuation in the two plate case is much higher than in the single plate case due to the discontinuity in the plate in the two plate case. It was also noted that the influence of the glue on the attenuation is greater in the higher frequencies.

References

- [1] Rosenhouse,G. and Ertel,H. and Mechel,F. P. Theoretical and experimental investigations of structureborne sound transmission through a “T” joint in a finite system. *Journal of the Acoustical Society of America*, 70, 2, 492-499, 1981
- [2] Allemang, R.J. The Modal Assurance Criterion (MAC): Twenty Years of Use and Abuse *Sound and Vibration Magazine*, 37, 8, 14-23, 2003
- [3] R. Oeqvist and F. Ljunggren and A. Aagren, Variations in sound insulation in nominally identical prefabricated lightweight timber constructions, *Building Acoustics*, 17, 91-103, 2010
- [4] K.A. Dickow, and P.G. Domadiya, and L. Andersen and S. Sorokin Influence of Periodic Stiffening on Flanking Noise Transmission, *Proceedings of the International Congress on Noise Control Engineering*, The Institute of Noise Control Engineering of Japan (NCE/J) Proceedings of the 40th International Congress and Exposition on Noise Control Engineering 2011,
- [5] K.A. Dickow, and P.G. Domadiya, and L. Andersen and P.H. Kirkegaard, A Parameter Study of Coupling Properties in Finite Element Models of Single-Stud Double-Plate Panels, *Proceedings of the International Congress on Noise Control Engineering*,The Institute of Noise Control Engineering of Japan (NCE/J), 2011, Proceedings of the 40th International Congress and Exposition on Noise Control Engineering,
- [6] L. Galbrun, Vibration transmission through plate/beam structures typical of lightweight buildings: Applicability and limitations of fundamental theories, *Applied Acoustics*, 71, 587-596, 2010
- [7] J. M. Craik and J. A. Steel, The Effect of Workmanship on Sound Transmission through Buildings: Part 1 Airborne Sound, *Applied Acoustics*, 27, 57-63, 1989
- [8] J. M. Craik and D. I. Evans, Article The Effect of Workmanship on Sound Transmission through Buildings: Part 2 Structure Borne Sound, *Applied Acoustics*, 27, 137-145, 1989
- [9] J. W. Trevathan and J. R. Pearse, Article The Effect of Workmanship on the Transmission of Airborne Sound through Light Framed Walls, *Applied Acoustics*, 69, 127-131, 2008
- [10] J. Negreira and A. Sjöström and D. Bard, Experimental investigation about the influence of the use of glue in joints in lightweight structures, *COMPADYN 2011, Computational Methods in Structural Dynamics and Earthquake Engineering*, Corfu Greece, 2011

Investigating acoustic fatigue using CFD and FEM on a model problem

Johan Nilsson¹, Robert-Zoltán Szász² and Per-Erik Austrell¹

⁽¹⁾Division of Structural Mechanics, Lund University, Box 118, SE-221 00 Lund, Sweden,
Johan.Nilsson@construction.lth.se

⁽²⁾Division of Fluid Mechanics, Lund University

Summary. In order to predict acoustic fatigue is desired to improve the prediction of the spatial distribution of the load that cause these issues. In this work the possibility to simulate the pressure load by CFD is investigated on a model problem. The load is also applied to a FE-model of a panel structure that is exposed to the load to investigate its response.

Key words: CFD, FEM, Acoustic fatigue

Introduction

Acoustic fatigue is an issue concerning both civil and military aircraft. It is caused by high frequency sound excitations with sound pressure level as high as 150-170 dB exciting structural components such as skin panels. This typically occurs in areas near motor installation and adjacent to the propeller wash / jet plume. Also geometrical sources introduced by flaps, cavities or external installations on, or close to, the airframe can also lead to an acoustically excited structure. Acoustic fatigue is often considered in a late stage of the design phase and when it occurs it can cause time consuming and costly experimental investigations. The design methods for acoustic fatigue is often based on design guidelines such as the ESDU [1], however the rms stress predicted by the guidelines can at best be expected to be within a factor 2 from the measured value. The design guidelines assume that the load on the panel structure has a uniform spatial distribution. This is unlikely to be the case in reality and it is thought that this assumption limits the accuracy of the response predictions. Cunningham et al. [2] found that if the spatial distribution of the load is specified to something more realistic the response predictions are dramatically improved.

To improve the knowledge of the spatial distribution of the load without resorting to expensive measurements it is desired to be able to simulate the load instead. In this work the load causing acoustic fatigue is computed with CFD. The simulated load can then be applied to a FE model of the panel structure to obtain the panel response to predict the risks of fatigue. To investigate this method, it has been applied to a model problem from an EURAM-BRITE project called ACOUFAT (Acoustic fatigue and related damage tolerance of advanced composite and metallic structures) [3].

Test case

The case studied in this work was originally investigated in the ACOUFAT program. It consists of a table with a simple flap located upstream of a skin panel structure and the whole setup was placed in a wind tunnel as illustrated by Figure 1. The load on the panel was measured

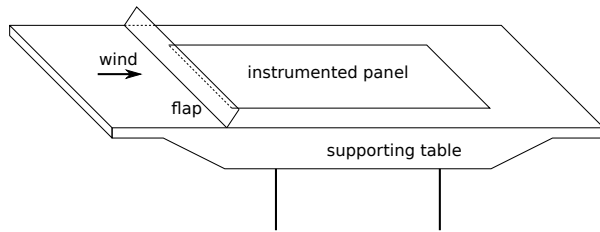


Figure 1. Wind tunnel setup.

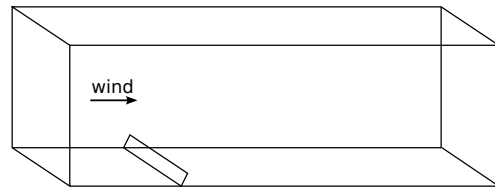


Figure 2. Schematic figure of the CFD domain, not to scale.

using microphones and static pressure sensors and the response of the panel was measured with accelerometers and strain gauges. The measurements used in this work were done at a Mach number of 0.7. As shown in Figure 1 the flap covers the full width of the table, which is 1300 mm, but the panel structure does not (only 736 mm wide). The details of the experiment are reported in [3, 4, 5].

Method

To simulate the load on the panel and the panel response, a two step method has been used. First a CFD simulation to determine the load was performed. This load was then applied to a FE-model of the panel. This means that the system is coupled only one way as it is believed that the effect of the panel on the flow can be neglected. The CFD-simulation is covered in more detail in [6].

CFD simulation

The CFD simulation was made with a compressible solver (`sonicDyMFoam`) from the OpenFOAM package [7]. The turbulence modelling is done by LES (Large Eddy Simulation) with the Smagorinsky model for the subgrid stresses. To reduce the high computational demands in the boundary layer, wall functions were used. From the measurements it seems that the 3D effect of the flow going around the flap rather than over it is small. Therefore it was decided to neglect this effect by letting the flap cover the whole computational domain and symmetry boundary conditions are used at the sides, see Figure 2. This way the flap can be seen in the simulations as infinitely wide. As discussed in [6] it is believed that a significant feature in the load spectra was caused by the shed vortices interacting. This was in turn affected by a likely vibration in the flap. To simulate this a prescribed rigid motion was applied to the flap. The prescribed motion makes the flap vibrate back and forth with the point attached to the table fixed which is a coarse approximation of the first bending mode of the flap.

FEM simulation

The FEM simulation of the panel structure was performed using the inhouse code CALFEM [8]. The outer skin of the panel that is exposed to the flow is simulated using four node plate elements. The pressure field from the CFD simulation was interpolated onto the FE-mesh. Then the pressure load was applied to each element with the assumption that load is constant over each element. Panel response and eigenmodes were investigated.

Results

The flow over the flap and panel is illustrated by the mean flow in Figure 3. The flap deflects the flow and there is a recirculation bubble behind the flap. The reattachment point is close to the downstream end of the panel in the mean flow, but it fluctuates along the downstream half of the panel and the table behind the plate. An instantaneous load extracted on the plate is shown time in Figure 4 and the panel response for the same time instant is given in Figure 5.

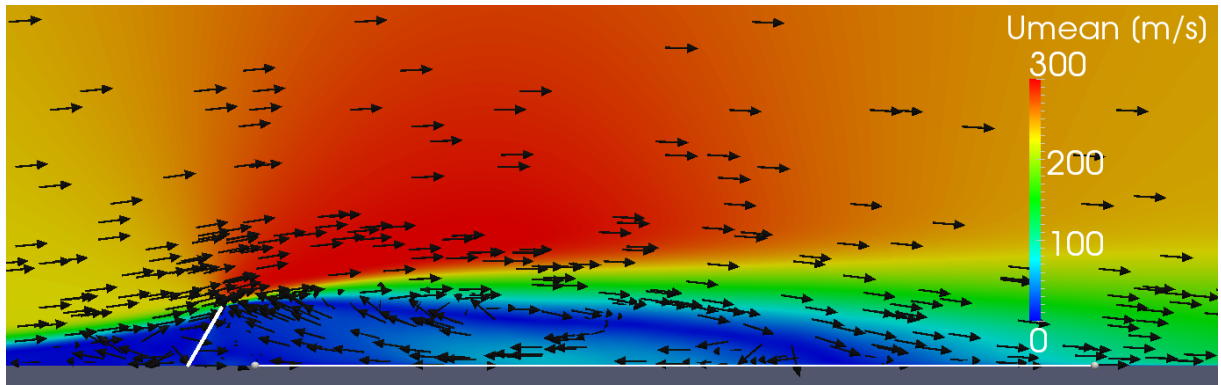


Figure 3. Mean velocities of the flow as seen from the side. The white marker at the bottom marks the location of the instrumented panel as illustrated in Figure 1.

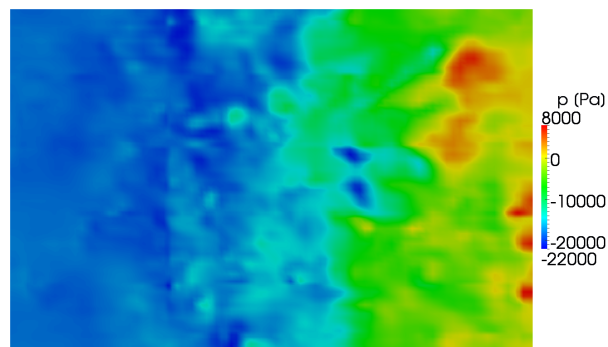


Figure 4. The pressure load on the panel structure after interpolation from the CFD simulation to the FEM mesh for a given moment in time.

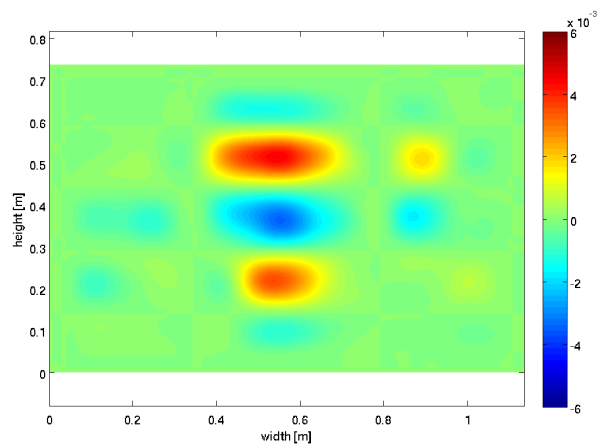


Figure 5. Panel response in terms of displacement for the same instance in time as Figure 4.

Acknowledgements

This work was supported by SAAB and the Swedish Agency for Innovation Systems (VINNOVA). The CFD simulations were performed on resources provided by the Swedish National Infrastructure for Computing (SNIC) at Lunarc, Lund University.

References

- [1] ESDU 72005, *The estimation of r.m.s. stress in stiffened skin panels subjected to random acoustic loading*, ESDU International PLC, London, United Kingdom, 2011
- [2] P.R. Cunningham, R.S. Langley, R.G. White. Dynamic response of doubly curved honeycomb sandwich panels to random acoustic excitation. Part 2: Theoretical study. *Journal of Sound and Vibration*, 264:605-637, 2003.
- [3] D. Tougard, Acoustic Fatigue and Related Damage Tolerance of Advanced Composite and Metallic Structures (ACOUFAT). In: J.M.M. Hernandez (Ed.). *Advances in Acoustics Technology*. Wiley, Chichester, 83-195, 1995.
- [4] A. Bourguine. *Wall pressure fluctuations and induced vibrations on a plane panel downstream a flap in transonic mach number range*. Document AERO 0025-1079 / D16 / 1, Internal report, 1992.
- [5] L.M.B.C. Campos, A. Bourguine, B. Bonomi. Comparison of theory and experiment on aeroacoustic loads and deflections. *Journal of Fluids and Structures*, 13:3-35, 1999.
- [6] J. Nilsson, R.-Z. Szász, P.-E. Austrell. Simulating the loads that causes acoustic fatigue. *In preparation*.
- [7] OpenFOAM. *The Open Source CFD Toolbox User Guide, version 2.1.0*, 2011.
- [8] P.-E. Austrell, O. Dahlblom, J. Lindemann, K.-G. Olsson, K. Persson, H. Petersson, M. Ristinmaa, G. Sandberg, P.-A. Wernberg. *CALFEM - A Finite Element Toolbox version 3.4*. Lund University, The Division of Structural Mechanics, 2004.

Optimisation

Room: Lilla Hörsalen, Thursday 25 October, 16:15 - 17:55



The inverse motion problem for quasi-incompressible electroelasticity

Anna Ask¹, Ralf Denzer², Andreas Menzel^{1,2} and Matti Ristinmaa¹

⁽¹⁾Lund University, Division of Solid Mechanics, P.O. Box 118, SE-221 00 Lund, Sweden.
anna.ask@solid.lth.se,

matti.ristinmaa@solid.lth.se

⁽²⁾Institute of Mechanics, Department of Mechanical Engineering, TU Dortmund, Leonhard-Euler-Str. 5, D-442 27 Dortmund, Germany.

ralf.denzer@tu-dortmund.de, andreas.menzel@udo.edu

Summary. In the inverse motion problem the deformed state of an elastic body for a given set of loads and boundary conditions is specified and the undeformed configuration is found by solving the resulting boundary value problem, e.g. with the finite element method. In this work the inverse motion problem is formulated as a four-field mixed variational problem and solved for quasi-incompressible electroelastic bodies.

Key words: electroelastic, inverse motion, form finding

Introduction

Elastomers exhibiting electromechanically coupled behavior are often denoted electroactive. Technological applications for electroactive elastomers include actuators, sensors and dampers. A typical configuration is a capacitor set-up, with an elastomer film sandwiched between two highly compliant electrodes, and variants of this configuration such as stack actuators or spring-roll actuators. An increase in interest in electroactive elastomers in recent years motivates efforts towards constitutive and numerical modeling of these materials.

Electromagnetic fields give rise to forces and torques on polarizable media and the usual balance equations of continuum mechanics must be altered accordingly. The theoretical framework necessary to do so has long been well established, with early works including those of Brown [3] and Toupin [10], and was further elaborated on by e.g. Eringen [5] and Maugin [7] and more recently Dorfmann and Ogden [4]. Works on the numerical treatment of boundary value problems for electroactive elastomers include e.g. Wissler and Mazza [12] and Vu and Steinmann [11].

The original numerical scheme for solving the inverse motion problem for elastic bodies was introduced by Govindjee and Mihalic [6] and interpreted in the more general framework of configurational mechanics by Steinmann et al. [9]. In this work, a four-field formulation in the spirit of Simo et al. [8] is set up for the inverse motion problem for electroelastostatics. By means of the finite element model, representative boundary value problems are then solved.

Kinematics

Let the initial or reference state of a body be denoted \mathcal{B}_0 and the deformed or current state at time t be denoted \mathcal{B}_t , c.f. Fig 1. Material points in \mathcal{B}_0 have position vectors \mathbf{X} and the same points in \mathcal{B}_t have position vectors \mathbf{x} . In the direct motion problem, the initial configuration

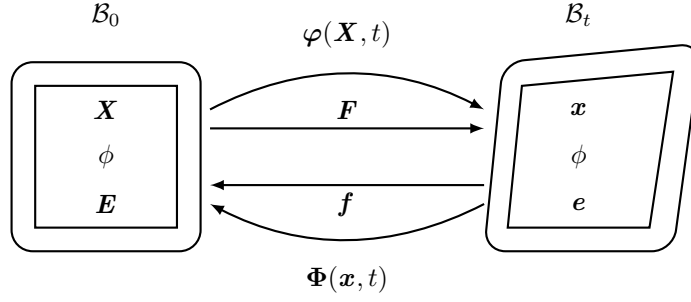


Figure 1. Kinematics of the direct and inverse motion problem

\mathcal{B}_0 of a body is known together with certain loads and boundary conditions and the resulting deformed state of the body is sought. In the inverse motion problem on the other hand, the deformed state \mathcal{B}_t at time t is known beforehand, and for a given set of loads and boundary conditions one seeks the initial configuration \mathcal{B}_0 of the body.

The direct motion is described by the mapping $\mathbf{x} = \varphi(\mathbf{X}, t)$ and the deformation gradient by $\mathbf{F} = \text{Grad } \varphi$, with determinant $\det \mathbf{F} = J$. For the inverse motion problem, the map $\mathbf{X} = \Phi(\mathbf{x}, t)$ is defined together with the inverse deformation gradient $\mathbf{f} = \text{grad } \Phi$ with determinant $\det \mathbf{f} = j$. The composition $\varphi \circ \Phi = \text{id}_{\mathcal{B}_t}$ gives the identity map, and as a consequence, the relation $\Phi = \varphi^{-1}$ holds as well as $\mathbf{f} = \mathbf{F}^{-1}$.

The electric field \mathbf{e} in \mathcal{B}_t is the gradient of the scalar electric potential ϕ , so that $\mathbf{e} = -\text{grad } \phi$, whereas the electric field \mathbf{E} in \mathcal{B}_0 is given by $\mathbf{E} = -\text{Grad } \phi$. It follows that they are related as $\mathbf{E} = \mathbf{e} \cdot \mathbf{F}$.

To account for the incompressibility of the elastomer, a four-field approach as suggested by [8] is adopted. The hydrostatic pressure p and a dilatation variable θ subject to the condition $\theta = J$ in the continuum are therefore introduced in the formulation. This allows for the deformation gradients to be decomposed as $\hat{\mathbf{F}} = \theta^{1/3} \bar{\mathbf{F}}$ and $\hat{\mathbf{f}} = \theta^{-1/3} \bar{\mathbf{f}}$ where $\bar{\mathbf{F}}$ and $\bar{\mathbf{f}}$ are the isochoric parts of the deformations.

Boundary value problem

It is assumed that the material is described by an energy function $\hat{\Omega}_0(\theta, \bar{\mathbf{F}}, \mathbf{E})$ which takes the dilatation variable, the deformation gradient and the material electric field as independent variables. The mechanical and electrical equilibrium equations are then given in integral form as

$$\mathcal{L}_1 = \int_{\mathcal{B}_t} \text{grad } \delta \varphi : \bar{\boldsymbol{\sigma}} \, dv - \int_{\mathcal{B}_t} \delta \varphi \cdot \mathbf{b}_t \, dv - \int_{\partial \mathcal{B}_t} \delta \varphi \cdot \mathbf{t}_t \, ds = 0, \quad (1a)$$

$$\mathcal{L}_2 = \int_{\mathcal{B}_t} \text{grad } \delta \phi \cdot \mathbf{d} \, dv + \int_{\partial \mathcal{B}_t} \delta \phi \, d_t \, ds = 0, \quad (1b)$$

where $\bar{\boldsymbol{\sigma}} = \bar{\boldsymbol{\sigma}}_0 + p \mathbf{i}$ is the stress, with \mathbf{i} being the spatial identity tensor, and \mathbf{d} is the electric displacement. The mechanical boundary conditions are prescribed tractions \mathbf{t}_t and body force \mathbf{b}_t . These are of mechanical origin, whereas the electromagnetic contributions are included via an amended term in the free energy function. For the electric displacement, it must fulfill jump conditions on surfaces of discontinuity given by $[[\mathbf{d}]] = -q$ where q is the surface charge. On the boundary the surface charge may be prescribed so that $q = d_t$.

The problem is solved for the inverse motion by performing a reparameterization so that the stress and electric displacements are considered functions of \mathbf{f} and \mathbf{e} rather than \mathbf{F} and \mathbf{E} . The constitutive relations are given by

$$\bar{\boldsymbol{\sigma}}_0 = 2j \mathbf{f}^{-1} \cdot \frac{\partial \hat{\Omega}_0}{\partial \mathbf{C}} \cdot \mathbf{f}^{-t} \quad \text{and} \quad \mathbf{d} = -j \frac{\partial \hat{\Omega}_0}{\partial \mathbf{E}} \cdot \mathbf{f}^{-t}. \quad (2)$$

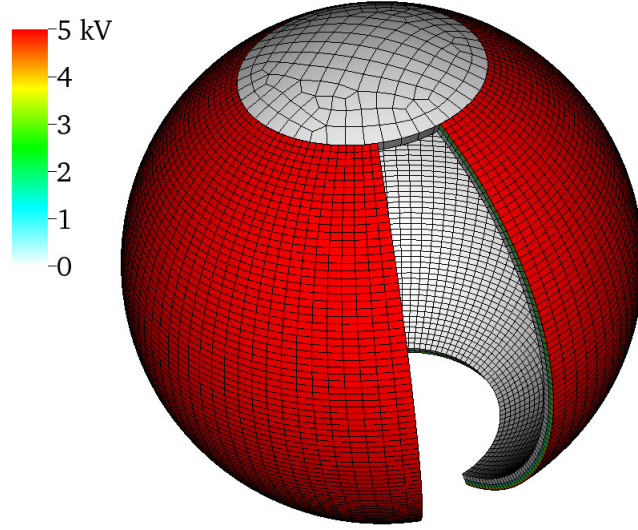


Figure 2. Desired loaded and deformed configuration for the gripper with one arm excluded.

By linearizing the equilibrium equations in terms of \mathbf{f} and \mathbf{e} , and keeping the current configuration \mathbf{x} fixed, the finite element scheme will directly provide the inverse motion Φ . The governing equations for the pressure and the dilatation variable are given by

$$\mathcal{L}_3 = \int_{\mathcal{B}_t} \delta p \left[1 - \frac{\theta}{J} \right] dv = 0, \quad \text{and} \quad \mathcal{L}_4 = \int_{\mathcal{B}_t} \delta \theta \left[\frac{\partial \hat{\Omega}_0}{\partial \theta} - p \right] j dv = 0. \quad (3)$$

In this work a constant-pressure approximation is adopted, where p and θ are assumed constant within each finite element.

Electroactive gripper

The specific material model and material parameters used can be found in [1] and [2]. As a representative boundary value problem, an electroactive gripper is considered. In the loaded state, the gripper is supposed to have a circular shape as seen in Fig. 2. The gripper consists of twelve identical arms, has an outer radius of 20 mm and a thickness of 1 mm. An electric potential difference is applied over half of the thickness, inducing bending deformation. In the loaded state, the potential difference is 5 kV. In Fig. 2, one of the arms is excluded for visualisation purposes.

In Fig. 3, the undeformed configuration, found by solving the inverse motion problem, is shown. This is then the configuration which, if loaded by a total potential difference of 5 kV as specified above, would yield the desired deformed configuration in Fig. 2.

List of references

References

- [1] Ask, A., Menzel, A. and Ristinmaa, M., Phenomenological modeling of viscous electrostrictive polymers. *Int. J. Nonlinear Mech.* 47:156–165, 2012.
- [2] Ask, A., Menzel, A. and Ristinmaa, M. Electrostriction in electro-viscoelastic polymers. *Mech. Mater.* 50:9–21, 2012.

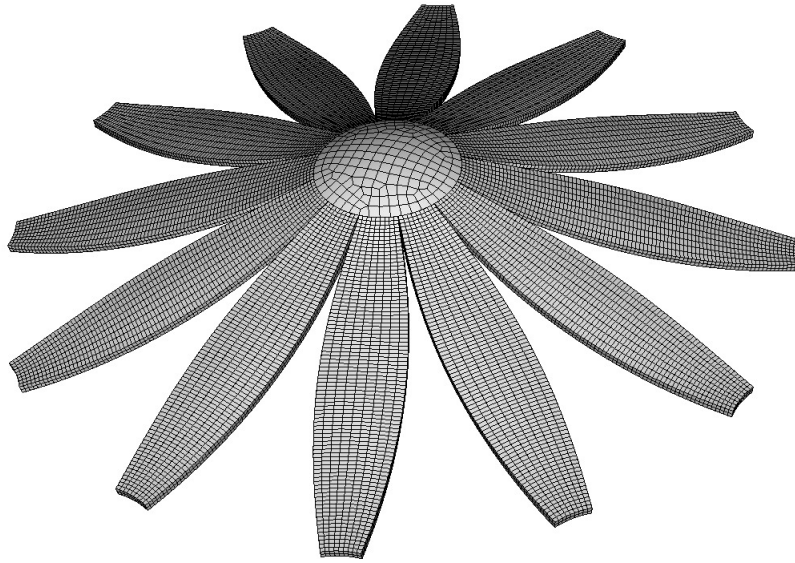


Figure 3. Calculated undeformed configuration for the gripper.

- [3] Brown, W.F., Electric and Magnetic Forces: A Direct Calculation. I. *Am. J. Phys.* 19:290-304, 1951.
- [4] Dorfmann, A. and Ogden, R.W., Nonlinear electroelasticity. *Acta Mech.* 174:167–183, 2005.
- [5] Eringen, A.C., On the foundations of electroelastostatics. *Int. J. Engng. Sci.* 1:127–153, 1963.
- [6] Govindjee, S. and Mihalic, P.A., Computational methods for inverse deformations in quasi-incompressible finite elasticity. *Int. J. Numer. Meth. Eng.* 43:821–838, 1998.
- [7] Maugin, G.A., *Continuum Mechanics of Electromagnetic Solids*. North-Holland, 1988.
- [8] Simo, J.C., Taylor, R.L. and Pister, K.S., Variational and projection methods for the volume constraint in finite deformation elasto-plasticity. *Comput. Method Appl. M.* 51:177–208, 1985.
- [9] Steinmann, P., Scherer, M. and Denzer, R., Secret and joy of configurational mechanics: From foundations in continuum mechanics to applications in computational mechanics. *Z. Angew. Math. Mech.* 89:614–630, 2009.
- [10] Toupin, R.A., The elastic dielectric. *J. Ration. Mech. Anal.* 5:849–915, 1956.
- [11] Vu, D.K. and Steinmann, P., Nonlinear electro- and magneto-elastostatics: Material- and spatial settings. *Int. J. Solids Struct.* 44:7891–7905, 2007.
- [12] Wissler, M. and Mazza, E., Electromechanical coupling in dielectric elastomer actuators. *Sensor Actuat. A-Phys.* 138:384–393, 2007.

Stochastic model reduction applied to inverse problems

Tomasz Garbowski¹ and Maciej Putowski¹

⁽¹⁾Poznan University of Technology, Institute of Structural Engineering, Piotrowo 5, 60-695 Poznan, tomasz.garbowski@put.poznan.pl, maciej.m.putowski@doctorate.put.poznan.pl

Summary. This article describes the use of Gaussian Processes in model reduction techniques with application to inverse problems. Mainly, the work is focused on the proper construction of the model approximation, namely on training process based on minimal number of learning samples, by making use of automatic samples selection through computed standard deviation of model prediction. An example of application of stochastic surrogate model for the paperboard characterization through biaxial tensile test and DIC measurements is also presented.

Key words: Gaussian processes, inverse analysis, model approximation

Introduction

The inverse analysis often uses a numerical model as a counterpart to experiment in order to build the discrepancy function between experimentally measured and numerically computed quantities, such as displacements, reaction forces, strains, accelerations, etc. If the numerical model is complex and/or has to be computed many times, the iterative minimization procedure becomes very expensive, therefore, not attractive from practical point of view especially when the test has to be performed 'in situ' (i.e. without a computer which can handle heavy computations). The alternative is to use a surrogate which approximates the behavior of the numerical model but is much simpler, thus less expensive. The surrogate is usually constructed as a 'black box' where for the approximation the following methods, among others, are commonly used: Radial Basis Functions (RBFs), Polynomials, Proper Orthogonal Decomposition (POD) combined with RBFs, Artificial Neural Networks (ANNs) or Gaussian Processes (GP) [1, 2].

All listed here approximation techniques require the numerically computed responses (i.e. training samples) in order to build a smooth and accurate analytical approximation of the sought solution. It would be best to use a method which needs the smallest possible number of 'training' points and in the same time is precise and robust. The approximation method based on GP satisfies all above-mentioned requirements: it gives very good results when the number of training examples is limited. Another important feature of GP is that it gives not only the approximation of the mean value of sought solution but also its standard deviation. This feature gives a possibility of automatic and systematic improvement of the solution, because the computed standard deviation of the model prediction provides a localization where the approximation is weak (and therefore, it points out where, in the parameter space, the additional experimental or numerical data are necessary to improve the approximation).

The presented stochastic algorithm is formulated within Bayesian framework, thus provides additional information about the magnitude of correlation between state variables (i.e. measurable quantities) and control variables (i.e. parameters). It is very important to know the relevance of input-output correlation because based on it one can exclude from the model the parameters which do not influence the measurable quantities. Such reduction saves the experimental efforts of finding parameters which appear to be irrelevant in particular simulation.

Model reduction through Gaussian Processes

In order to explain how to construct a model approximation by Gaussian Processes, first, a linear regression model should be considered. It is a linear function of model parameters \mathbf{w} and nonlinear function of the input vector \mathbf{x} , and usually is defined as:

$$y(\mathbf{x}, \mathbf{w}) = \sum_{j=1}^M w_j \phi_j(\mathbf{x}), \quad (1)$$

which simply is a linear combination of fixed, nonlinear basis functions $\phi_j(\mathbf{x})$ of the input variables (e.g. polynomial basis functions).

If we now take N given training patterns (\mathbf{x}_n, t_n) , \mathbf{x}_n being the input vector, t_n the response for $n = 1 \dots N$, then the parameters \mathbf{w} of the linear model can be computed by, for example, penalized least squares method:

$$\mathbf{w} = (\Phi^T \Phi + \lambda \mathbf{I})^{-1} \Phi^T \mathbf{t}, \quad (2)$$

where Φ is $N \times M$ design matrix with elements defined as $\phi_m(\mathbf{x}_n)$. The regularization parameter λ is called hyperparameter and can be estimated using validation set or by applying Bayesian inference and maximizing evidence of dataset $p(\mathbf{t}|\lambda)$ w.r.t. λ (details are given in [1]).

Gaussian Process

Gaussian process model can be obtained by reformulation of the linear model in terms of dual representation. In this approach, linear model is trained by minimizing a regularized error, which is defined using $N \times N$ symmetric Gram matrix:

$$\mathbf{K} = \Phi \Phi^T = \phi(\mathbf{x})^T \phi(\mathbf{x}') = k(\mathbf{x}, \mathbf{x}'), \quad (3)$$

where $k(\mathbf{x}, \mathbf{x}')$ is a kernel function. The vector $\mathbf{k}_n = k(\mathbf{x}_n, \mathbf{x})$ represents n -th row or column of \mathbf{K} matrix.

The prediction for a new input \mathbf{x}^* can be computed by the formula:

$$y(\mathbf{x}^*) = \mathbf{k}(\mathbf{x}, \mathbf{x}^*)^T (\mathbf{K} + \lambda \mathbf{I})^{-1} \mathbf{t}, \quad (4)$$

where $k(\mathbf{x}, \mathbf{x}^*)$ is a covariance between a new input \mathbf{x}^* and the other inputs, $\mathbf{t} = (t_1 \dots t_N)^T$ is a vector of training target values.

From the Bayesian point of view the dual representation of linear model leads to the Gaussian process, where the kernel function is interpreted as a covariance function of the GP. Application of such regression model for prediction allows to compute the predictive distribution of the target variable $y(\mathbf{x}^*)$ for a new input vector \mathbf{x}^* . This requires evaluation of conditional distribution $p(y|\mathbf{t})$, which for the Gaussian processes is a Gaussian distribution with mean and covariance respectively given by:

$$m(\mathbf{x}^*) = \mathbf{k}^T \mathbf{C}^{-1} \mathbf{t}, \quad (5)$$

$$\sigma^2(\mathbf{x}^*) = c - \mathbf{k}^T \mathbf{C}^{-1} \mathbf{k}, \quad (6)$$

where \mathbf{C} is the $N \times N$ covariance matrix given by:

$$C(\mathbf{x}, \mathbf{x}') = k(\mathbf{x}, \mathbf{x}') + \beta^{-1} \mathbf{I}, \quad (7)$$

where β is the variance of the target distribution. The covariance function $C(\mathbf{x}, \mathbf{x}')$ defines the property that vectors \mathbf{x}_n and \mathbf{x}_m , which are close in input space, should give rise to highly correlated outputs $y(\mathbf{x}_n)$ and $y(\mathbf{x}_m)$.

Covariance function

The covariance function can be any function that will generate a non-negative definite covariance matrix for any ordered set of (input) vectors ($\mathbf{x}_1, \dots, \mathbf{x}_N$). A stationary, non-isotropic squared exponential covariance function $k(\mathbf{x}, \mathbf{x}')$ is chosen here, and given by:

$$k(\mathbf{x}_n, \mathbf{x}_m) = \nu \exp\left(-\frac{1}{2} \sum_{i=1}^d w_i (x_n^i - x_m^i)^2\right) + b, \quad (8)$$

where the term b represents a bias that controls the vertical offset of the Gaussian process, while ν controls the vertical scale of the process. The w_i parameters allow a different distance measure for each dimension. If w_i is small then the i -th input is downweighted and have little effect on the input.

After defining the covariance function we can make predictions of the new input vectors but it is necessary to learn the hyperparameters. In order to find those parameters one can search for the most probable ones by maximizing the log likelihood function given by:

$$\ln p(\mathbf{t}|\theta) = \frac{1}{2} \ln |\mathbf{C}| - \frac{1}{2} \mathbf{t} \mathbf{C}^{-1} \mathbf{t} - \frac{N}{2} \ln 2\pi, \quad (9)$$

using gradient-based optimization algorithms, such as a first-order batch Levenberg-Marquardt Algorithm (LMA), which provides fast and robust convergence.

Active learning

In order to optimize the training procedure of GP based surrogate model, the active learning criterion, that improve the global model fit, is also utilized here. A new training points are sequentially added in the zones where the model predictions are poor and/or in the vicinity of the minimum of the approximated solution, meaning that the iterative re-training of the surrogate model is performed by adding a new training patterns, sampled in the new locations in the parameter space (selected by the algorithm itself). This approach is very efficient when the number of training samples is limited, so the algorithm starts building approximation with small selection of patterns (randomly or uniformly distributed) and improves the approximation by sampling the parameter space in a clever way (based on its confidence about the quality of the approximation). It stops when the maximum number of training samples is reached.

Application

In the present communication an example of a model characterization is used to show the application of above described model reduction techniques. The examples show the use of GP as numerical model surrogate for characterization of paperboard parameters [3] through biaxial test and DIC measurements techniques combined with inverse analysis. From such test we can identify most of the in-plane parameters of paperboard (for the details see [4]).

In the above examples the GP based approximation serves as a surrogate of numerical model, which in combination with iterative minimization routine (e.g. trust-region algorithm) or evolutionary-based techniques (e.g. particle swarm algorithm) gives very fast and accurate results of model identification. The model reduction approach has the following important advantages w.r.t. the procedure based on evaluation of full numerical model: (1) it's fast (the computational burden is moved to training phase) and (2) it doesn't require to use powerful computers for heavy and repetitive computations of numerical model, so once the model is constructed it can be used 'in situ' on the portable computer.

Summary

The GP approximation model which serves as a numerical model reduction is used here in combination with inverse analysis to solve practical engineering identification problems. The work is mainly focused on the proper construction of the GP model, namely on: (1) training process based on minimal number of training data, by making use of automatic samples selection through computed standard deviation of model prediction and (2) control parameters reduction based on input-output correlation. The successful application of stochastic model reduction techniques for the material model characterization problems is also shown here.

References

- [1] C.M. Bishop. *Pattern Recognition and Machine Learning*. Springer, 2007.
- [2] C.E. Rasmussen, C.K.I. Williams. *Gaussian Processes for Machine Learning*. MIT Pres, 2006.
- [3] Q.S. Xia, M.C. Boyce, D.M. Parks. A constitutive model for the anisotropic elastic-plastic deformation of paper and paperboard. *International Journal of Solids and Structures*, 61:1–48, 2000.
- [4] T. Garbowski, G. Maier, G. Novati. On calibration of orthotropic elastic-plastic constitutive models for paper foils by biaxial tests and inverse analyses. *Structural and Multidisciplinary Optimization*, 46:111–128, 2012.

Numerical modelling and optimization of all plywood sandwich panels with rib-stiffened cores

Edgars Labans¹ and Kaspars Kalnins¹

⁽¹⁾Riga Technical University, Institute of Materials and Structures, Riga, Azenes st. 16/20, edgars.labans@rtu.lv, kaspars.kalnins@sigmanet.lv

Summary. The current paper deals with numerical modelling of all plywood sandwich panels with rib-stiffened core. Commercially available finite elements code ANSYS has been implemented to simulate mechanical behaviour of sandwich panels in bending, according to the EN 789 standard. It has been confirmed that in order to simulate plywood a multilayered panel model with shell type elements could adequately represent the mechanical behaviour of such a structure sufficiently well. Developed parametrical model has been initially validated with experimental results showing less than 10 % scatter among finite element model and physical model. Following this a validated numerical model has been implemented for structural parameter optimization resulting in significant improvement of initial panel design.

Key words: plywood, sandwich panels, ANSYS

Introduction

All plywood sandwich panels with hollow core structure could offer significant weight reduction comparing with conventional plywood boards for applications where the lightweight design could provide cost saving benefits in long term perspective, like freight cargo transport. However in order to develop effective therefore functional product some research effort is required to design a reliable methodology with sole ability to predict mechanical behaviour of such item.

The finite element method (FEM) analysis is well accepted design methodology by all sectors of industry and for sure scientific institutions. For example, numerical modelling of wood based sandwich panels are extensively studied and described in several recent papers [1,2] where good correlations between experimental and numerical results were found.

All plywood sandwich panels with rib-stiffened and corrugated plywood core has been experimentally studied earlier by Zudrags [3] with aim to increase plywood specific stiffness. Kalnins [4] described theoretically optimal cross-sections configurations for sandwich panels with rib-stiffened cores.

The aim of current research is to extend and to improve the numerical model's accuracy for design of sandwich panels with multi angular stiffener orientations: longitudinal, transverse and diagonal direction along panel length. Moreover numerical models are validated with

experimental tests in four point bending mode. Once numerical models has been validated and the convergence approved an optimization procedure with aim to increase stiffness/weight ratio of sandwich panels has been realised.

Materials and methods

Numerical model has been built using 4-node SHELL181 elements with multilayered structure (1.3 mm thin layers) implementing the birch mechanical properties. Panel's geometrical tolerance and loading conditions are kept as close as possible to the experimental set up. Numerical model is made parametrical to be suitable for further optimizations tasks. The FE mesh step of 10 mm has been assigned to sandwich plate (Figure 1). Both deflection at the panel mid-span as well as strains and stresses at various plies have been extracted and applied as constraint for optimisation task.

Four point bending test on static load frame INSTRON 8802 (Figure 1) has been performed according to EN 789 [5] for several types of sandwich panels (Table 1) in order to verify if developed numerical models appropriately represent the mechanical behaviour. The distance between supports is 1000 mm and between loading points 200 mm. The bending deflection of the panels have been measured with LVDT deflectometer at the bottom of the panel's midspan. All sandwich panels were tested in elastic range up to 22 mm (about 1/50 of the span length) to deliver stiffness properties of such structure without reaching the ultimate load. Moreover in structural engineering applications deflection extending 1/150 of the span is restricted by legislation thus experimental results are within the range of good engineering practice

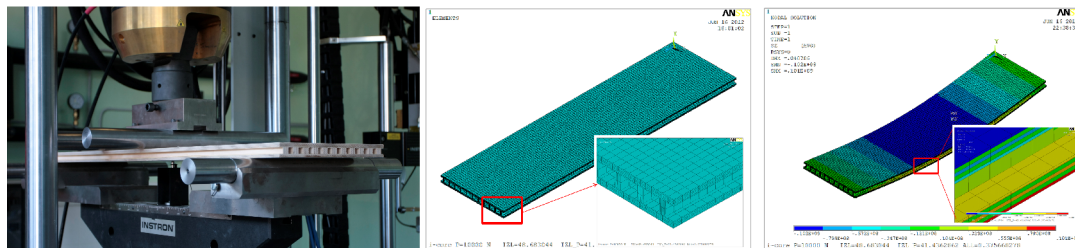


Figure 1. Experimental test set-up in line with level of detail of numerical model of rib-stiffened panel and a stress plot in each ply.

Table 1. Specification of tested panels

Series number	Direction of stiffeners	Average thickness, [mm]	Thickness of stiffener, [mm]	Distance between stiffeners, [mm]	Surface thickness, [mm]	Surface plies orientation
Nr. 1	Diagonal	28.21	14.4	22.0	9.0	/-/-/-/
Nr. 2	Transverse	27.65	14.4	27.0	9.0	-/-/-/-
Nr. 3	Longitudinal	28.42	14.4	22.0	9.0	/-/-/-/

/ fibres direction parallel to panel's longitudinal direction

- fibres direction perpendicular to panel's longitudinal direction

Design parameters considered for the sandwich panel cross-section optimizations are following: the panel height, the thicknesses of separate components – the face sheets and stiffeners, all expressed in odd number of layers. Metamodelling technique has been employed to acquire sensitivity of each parameter and mechanical responses of plywood sandwich panel. The sequential experimental design based on Mean Square Error (MSE) space filling criteria has been elaborated in order to sample the design variables within the domain of interest. The optimization function is to maximise the stiffness/weight ratio.

Results and discussion

In order to compare the experimental and numerical results, the load/deflection and load/strain curves have been compared with numerical results obtained from ANSYS. It is obvious that sandwich structure has fully elastic mechanical behaviour within tested deflection range and linear numerical model describes structure behaviour sufficiently well. The difference between average experimentally obtained deflection at 5 kN load magnitude and one obtained numerical not exceeding 10 % for panels with diagonal, transverse (Figure 2) and longitudinal (Figure 3) orientation of stiffeners

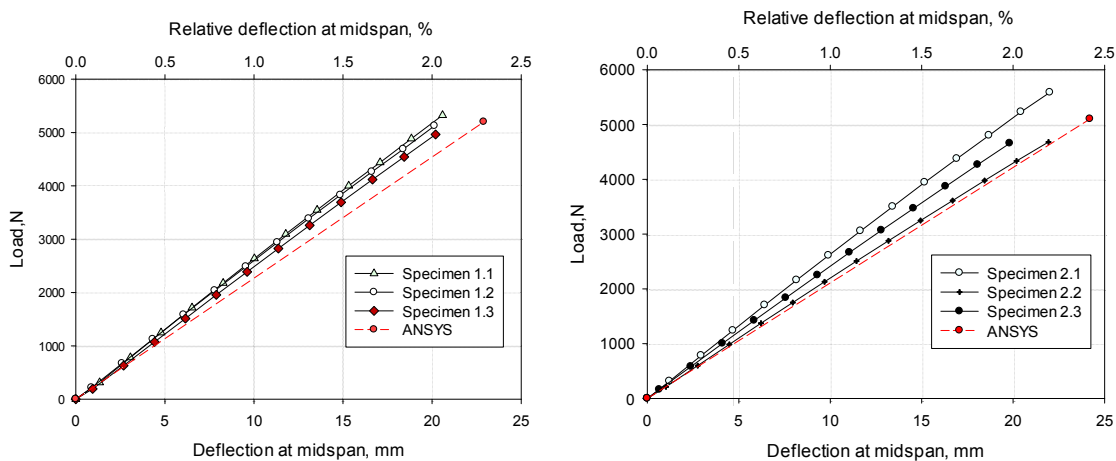


Figure 2. Load/deflection curves for panels with diagonal and transverse orientation of stiffeners

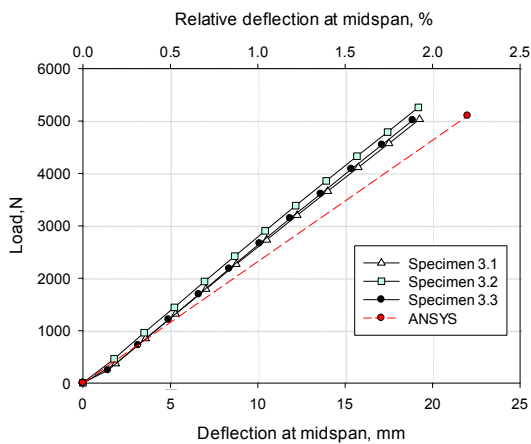


Figure 3. Load/deflection curves for panels with longitudinal orientation of stiffeners

Taking into the consideration a natural wood material property scatter, obtained accuracy of numerical model could be considered as adequate for employing it in further optimisation tasks. An overall efficiency of all plywood sandwich panels have been demonstrated by formulating Pareto optimization problem (Figure 3) where maximization of relative stiffness ΔK is done simultaneously by minimizing the relative volume ΔV of the panel.

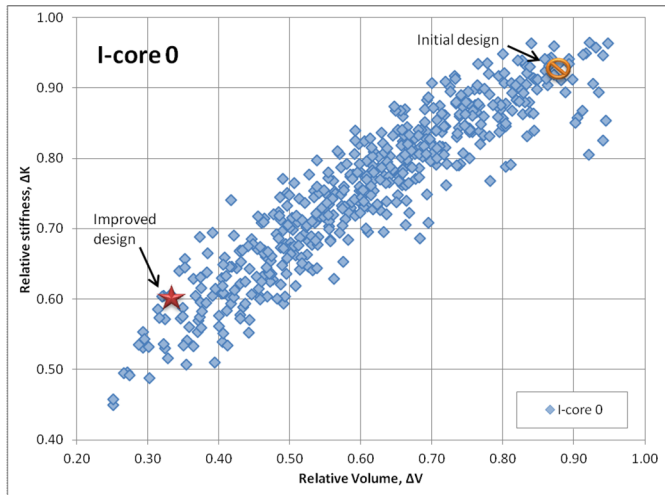


Figure 3. Pareto optimality plot for panels with longitudinal stiffeners direction.

Relative stiffness is acquired dividing numerically calculated conventional plywood board deflection with calculated deflection of sandwich panel with same length and thickness, under the same loading conditions. Relative volume is acquired by dividing sandwich panel volume with full plywood panel volume. Using these plots is possible to select beneficial combination of variables as well as improve initial design of prototype panels. It has been concluded that numerical optimisation task has generated improved design scenarios with up to 80% weight efficiency. A further prototyping will be carried out in order to validate the optimisation results.

References

- [1] J.F. Hunt, 3D Engineered Fiberboard: Finite Element Analysis of a New Building Product. *International ANSYS Conference* [CD-ROM], Pittsburg, PA, May, 24-26, 2004
- [2] C. W. Hudson, J.J. Carruthers, A.M. Robinson, Multiple objective optimisation of composite sandwich structures for rail vehicle floor panels. *Composite Structures* 92, p. 2077–2082, 2010
- [3] K. Zudrags, K. Kalnins, G. Jekabsons, O. Ozolins. Bending properties of plywood I-core sandwich panel. *Proceedings of the 5th Nordic-Baltic Network in Wood Material Science and Engineering*. Meeting, Copenhagen, p. 169-175, 2009
- [4] K. Kalnins, G. Jekabsons, K. Zudrags, R. Beitlers. Metamodels in optimisation of plywood sandwich panels. *Shell Structures: Theory and Applications*, Vol. 2. Pietraszkiewicz W. and Kreja I. (eds.), CRC press /Taylor & Francis Group, London, UK, p. 291-294, 2009
- [5] EN 789: 2004. Timber structures. Test methods. Determination of mechanical properties of wood based panels. European Committee for Standardization (CEN), Brussels

Thickness Optimization of Laminated Composites using the Discrete Material Optimization Method

Søren Nørgaard Sørensen, René Sørensen, and Erik Lund

Department of Mechanical and Manufacturing Engineering, Aalborg University,
Aalborg East, DK-9220, Denmark, {sns, rso, el}@m-tech.aau.dk

Summary. This work concerns a novel large scale multi-material topology optimization method for simultaneous determination of the optimum variable integer thickness and fiber orientation throughout laminated composites with fixed outer geometries while adhering to certain manufacturing constraints. The conceptual combinatorial/integer problem is relaxed to a continuous problem and solved on basis of the so-called Discrete Material Optimization method, explicitly including the manufacturing constraints as linear constraints.

Key words: Laminate design optimization, thickness optimization.

Introduction

Fiber reinforced laminated composites are applied in a variety of high performance structures because the stiffness to weight ratio surpasses e.g., steel and aluminum alloys. The basis of this work is laminated structures where the outer geometry for some reason is fixed which could be the case for e.g., wind turbine blades where aerodynamics may govern the shape of the outer surface. Weight reduction while maintaining sufficient stiffness of such structures implies that the thickness of the laminate must vary inwards in an optimal manner. The individual layers/plies that together constitute the laminate are typically chosen among a finite set of materials with finite sets of fiber angles, e.g., Carbon/Glass Fiber Reinforced Polymer (CFRP/GFRP) with $\{0^\circ, +45^\circ, -45^\circ, 90^\circ\}$ fiber orientation. The task for the designer is simultaneously to determine the optimum variable integer thickness and fiber orientation throughout the laminate structure. The problem is therefore conceptually a combinatorial multi-material topology optimization problem. This short paper presents a novel method that treats this problem. The optimized design is typically subject to certain manufacturing constraints (MC): To accommodate application of predefined fiber mats, large regions/patches within the layers of the total geometry/laminate must be identical (MC1); to prevent failure such as delamination and matrix cracking problems, changes in thickness cannot be too abrupt (MC2); the number of identical contiguous layers should not be too high (MC3), and intermediate void is not allowed (MC4). Explicit inclusion of these manufacturing constraints in the topology optimization problem yields an optimized starting point for detailed post processing before true realization may take place. Stress constraints and failure criteria are not considered explicitly in this work. However, fulfilling MC1-MC4 will implicitly reduce the risk of failure.

Figure 1 illustrates a simplified 1D example, discretized as six Equivalent Single Layer (ESL) shell elements (one ESL shell element per column), each containing three layers (rows).

The example in Figure 1 could represent the solution to an optimization problem subject to the following requirements: Bottom layer is enforced material (i.e. free from void); choose between void and $\{0^\circ, +45^\circ, -45^\circ, 90^\circ\}$ CFRP; maximum allowable mass fraction is 13/18;

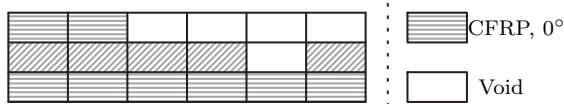


Figure 1: Example of a thickness optimized laminate. The bottom layer is enforced material; free from void.

besides void there must be fiber angle continuity in an entire row/layer (MC1); total allowable thickness change is ± 1 ply thickness between neighbouring ESL shell elements (MC2); only a single contiguous identical layer/ply is allowed (MC3); Intermediate void is not allowed (MC4).

Recent work on simultaneous material distribution and orientation has been summarized in [2]. Although heuristic methods such as genetic algorithms are frequently applied and in principle well suited for combinatorial/integer problems, they do, however, rely on extensive amounts of finite element analyses. Despite the ever-increasing parallelizable computational power, it is unacceptably expensive to apply such methods for large scale optimization problems. In this short paper, the combinatorial/integer thickness optimization problem is relaxed thus allowing application of gradient based state-of-the-art optimizers as e.g., SNOPT [3] that is used in this work. The problem is solved on basis of the so-called Discrete Material Optimization method, see [4]. The manufacturing constraints MC1-MC4 are explicitly included in the optimization problem as a large number of sparse linear constraints.

Problem Formulation

The method to be presented takes basis in multi-phase compliance minimization through the density approach, see [1]. With this approach the constitutive properties of all layers in all ESL shell elements in the discretized domain are functions of the densities (design variables). For example, the effective constitutive matrix \mathbf{E}_{el} is obtained as

$$\mathbf{E}_{el} = \mathbf{E}_0 + \frac{\rho_{el}}{1 + p(1 - \rho_{el})} \sum_{c=1}^{n^c} \frac{x_{elc}}{1 + q(1 - x_{elc})} (\mathbf{E}_c - \mathbf{E}_0) \quad , \quad \forall(e, l) \quad (1)$$

In (1), index e concerns a specific ESL shell element, index l concerns a specific layer, and index c concerns a specific candidate material. \mathbf{E}_c is the constitutive matrix for candidate material c , $\rho_{el} \in [0, 1]$ are topology variables (densities), $x_{elc} \in [0, 1]$ are candidate material variables, p and q are penalization powers for the variables, and n^c is the number of specific candidate materials. \mathbf{E}_0 is massless and significantly more compliant than all \mathbf{E}_c . The parameterization in (1) utilizes the material interpolation scheme RAMP (Rational Approximation of Material Properties), see [5]. A result to the topology optimization problem is satisfactory when: Compliance is reduced; all variables are binary; the mass constraint and the manufacturing constraints (MC1-MC4) are satisfied.

Example and Results

The optimization approach is illustrated by the example defined by Figure 2. A corner hinged 8-layered plate is subjected to a mid-point load, and the plate is discretized by 50×50 square ESL 9-node isoparametric shell elements. A layer has thickness $t = 1mm$.

The problem is solved for three different cases, illustrating how the design variables can be associated both with elements and with larger patches having the same parameterization. In case 1 all elements must have the same fiber angle in a given layer (MC1) and the total allowable thickness change is ± 1 ply thickness between neighbouring ESL shell elements (MC2). Case 2 represents an expansion of the design space in case 1, as the layerwise material selection is

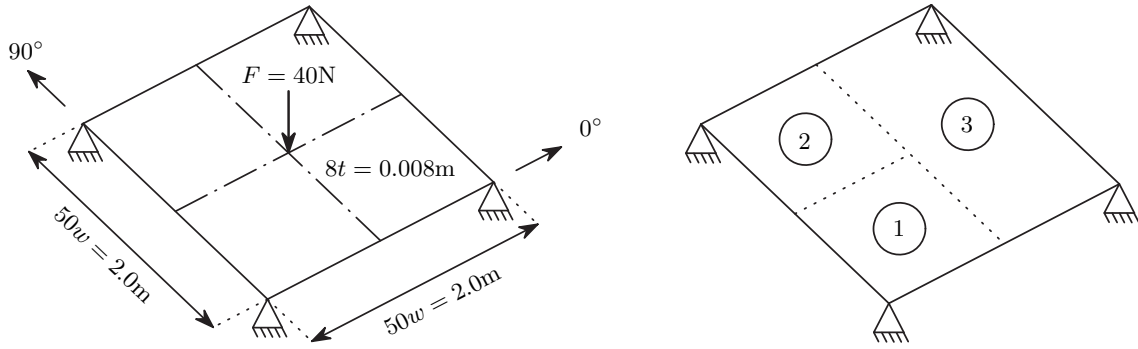


Figure 2: A corner hinged 8-layered plate is subjected to a mid-point load, $F = 10\text{N}$. The square element side length is denoted with w and t denotes the layer thickness. In optimization case 2 and 3 the plate is divided into the three patches illustrated on the right figure.

now performed individually for the three patches. Similarly, in case 3 all elements in each of the three patches must have the same fiber angle (MC1) in a given layer. Furthermore, MC2 is varying, such that thickness may change elementwise in patch 1 and in the two other patches it can only change patchwise. The total allowable thickness change is still ± 1 ply thickness between neighbouring elements. Thus, in case 2 and 3 inplane discontinuities in fiber angles are allowed.

In all three cases the allowable mass fraction is 50%; the bottom layer is enforced to have full density; only four contiguous identical layers are allowed (MC3); intermediate void is not allowed (MC4). A distinct 0/1 solution is obtained nearly everywhere in the design domain for all three cases.

The optimization problems are linearized and solved sequentially, using SNOPT with an adaptive move limit update scheme. Each problem is solved in two consecutive steps. Step 1 converges without penalization. Step 2 continues with constant penalization.

Figures 3-5 illustrate the optimized thickness and fiber angle distributions obtained. Comparing the results between case 1 and case 2, it is clear that the expansion of the design space in case 2 has resulted in a lower compliance (larger stiffness). Notice the influence of MC3 in patch 1 and 2 for case 2 (only four contiguous identical layers are allowed). Finally, case 3 with more restrictions on allowable thickness change results in the largest compliance of the three cases.

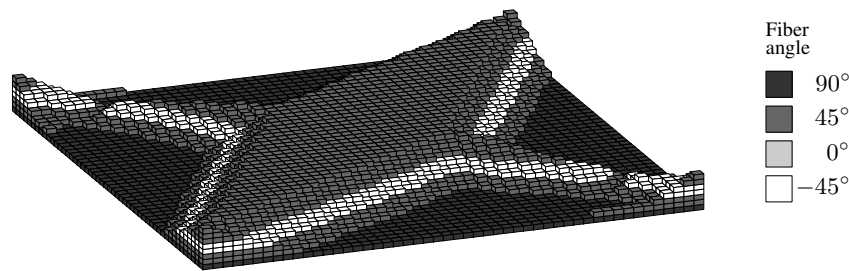


Figure 3: Minimum compliance design for case 1. All elements must have the same fiber angle in a given layer but thickness may change elementwise. Layer thicknesses are scaled by a factor of 20. Compliance is 0.7077.

Concluding Remarks

A novel method for simultaneous determination of optimum variable integer thickness and fiber orientation in a laminated composite subject to certain manufacturing constraints has been

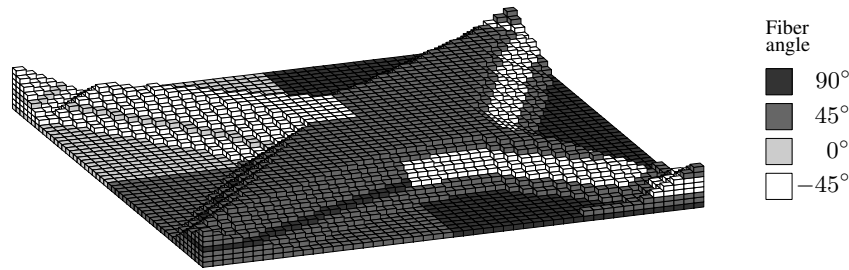


Figure 4: Minimum compliance design for case 2. All elements in each of the three patches must have the same fiber angle in a given layer, but thickness may change elementwise. Layer thicknesses are scaled by a factor of 20. Compliance is 0.6701.

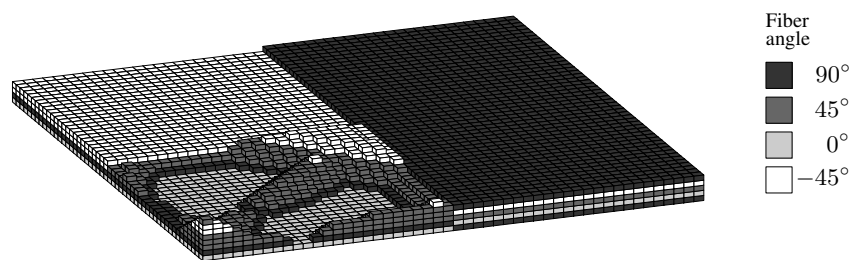


Figure 5: Minimum compliance design for case 3. All elements in each of the three patches must have the same fiber angle in a given layer. Thickness may change elementwise in patch 1 and in the two other patches it can only change patchwise. Layer thicknesses are scaled by a factor of 20. Compliance is 1.922.

presented. The method is applicable for designs of composite structures with a fixed outer geometry but may also be used for structures with a fixed plane of symmetry. The generality of linking material and thickness variables to a given layered structure has been illustrated for three different parameterizations of a corner hinged 8-layered plate. The sequential linear programming strategy with an adaptive move limit update scheme causes large variations in the required number of iterations until convergence, and the non-convexity of the posed optimization problem entails the risk of sub-optimal local minima. Although the presented examples result in a nearly binary design, this is not always the case. Different settings for the adaptive update scheme and alternative solution approaches are elaborated in future work.

References

- [1] Bendsøe M.P., Sigmund O.: *Topology Optimization - Theory, Methods and Applications*. Springer Verlag, Berlin Heidelberg, 2003.
- [2] Ghiasi H., Kazem F., Pasini D., Lessard L.: Optimum stacking sequence design of composite materials part II: Variable stiffness design. *Composite Structures* **93**(1):1–13, 2010.
- [3] Gill P.E., Murray W., Saunders M.A.: SNOPT: An SQP algorithm for large-scale constrained optimization. *SIAM Review* **47**(1):99–131, 2005.
- [4] Stegmann J., Lund E.: Discrete material optimization of general composite shell structures. *International Journal for Numerical Methods in Engineering* **62**(14):2009–2027, 2005.
- [5] Stolpe M., Svanberg K.: An alternative interpolation scheme for minimum compliance topology optimization. *Structural and Multidisciplinary Optimization* **22**(2):116–124, 2001.

Design and Optimization of a Spring-loaded Cable-driven Robotic Exoskeleton

Lelai Zhou, Shaoping Bai, Michael Skipper Andersen, and John Rasmussen

Department of Mechanical and Manufacturing Engineering, Aalborg University
Fibigerstraede 16, 9220 Aalborg, Denmark, {lzh, shb, msa, jr}@m-tech.aau.dk

Summary. An approach of designing a robotic exoskeleton for a partially paralyzed human upper extremity is proposed in this paper. A musculoskeletal arm model is built to simulate the injury symptom in terms of evaluating the muscle activations. The exoskeleton is built with a gravity compensation system. The biomechanical human arm model and the exoskeleton are integrated together to form a bio-robotic system. Design analysis and optimization are conducted in the bio-robotic system to evaluate parameters of the exoskeleton.

Key words: exoskeleton, spring-loaded, cable-driven, biomechanics

Introduction

Exoskeleton robots have attracted more and more research interests, as they have prospective applications in rehabilitation and patient assistance. Effective means of motion assistance, such as weight balancing orthoses, will be studied in this work. Several passive exoskeletons have been developed recently. The X-ArTM exoskeletal arm with passive actuated joints is provided by Equipois to support human arms in the working environment [1]. Wilmington Robotic Exoskeleton (WREX) is a two-segment, 4-DOF (degree of freedom) passive orthoses provided by Nemours [2]. A variable impedance powered elbow exoskeleton named NEUROExos [3] was developed for the rehabilitation task of stroke patients.

In this work, an integrated musculoskeletal-exoskeleton simulation approach is proposed for the optimal design of exoskeletons. An important part of our work is an advanced biomechanical model of the upper extremity, which provides a deep understanding of the elasticity required to support the patient's motion depending on the nature of the disability. The bio-robotic system is built in AnyBody Modeling System, where the design parameters of the exoskeleton are formulated as an optimization problem.

Modeling of the Bio-robotic System

The bio-robotic system is built by integrating a musculoskeletal model and a robotic exoskeleton model.

Biomechanical Modeling

The biomechanical study is conducted with the AnyBody Modeling System, in which the human arm model is built and generated from the system's model repository. The upper body is constrained at the pelvis, and the right arm has seven joints to be activated.

In a musculoskeletal model, the biomechanics of muscles and bones is statically indeterminate. The

muscle recruitment can be formulated as an optimization problem as

$$\begin{aligned} \min \quad & G(\mathbf{f}^{(M)}) \\ \text{s.t.} \quad & \mathbf{C}\mathbf{f} = \mathbf{d} \\ & f_i^{(M)} \geq 0, \quad i \in \{1, \dots, n^{(M)}\} \end{aligned} \quad (1)$$

where $\mathbf{f} = [\mathbf{f}^{(R)}, \mathbf{f}^{(M)}]$ is composed of a n -dimensional vector of joint reaction forces $\mathbf{f}^{(R)}$ and muscle forces $\mathbf{f}^{(M)}$. The vector \mathbf{d} is the external force, and \mathbf{C} is a coefficient matrix generated from the arm anatomy and muscle attachments. The choice of the objective function $G(\mathbf{f}^{(M)})$ depends on the muscle recruitment criterion. The polynomial criterion is adopted as

$$G(\mathbf{f}^{(M)}) = \sum_i \left(\frac{f_i^{(M)}}{N_i} \right)^p \quad (2)$$

where N_i are normalization factors or functions, which take the form of muscle strength in this work. The power p indicates the synergy of muscles. $p = 3$ is recommended as it yields good results for most submaximal muscle efforts. The ratio $f_i^{(M)}/N_i$ refers to the muscle activity. The overall muscle activity can be calculated as

$$H = \sum_i \frac{f_i^{(M)}}{N_i} \quad (3)$$

In order to simulate the muscle condition of a patient, any single piece of muscle can be enabled or disabled. In the model the muscle is disabled by setting its muscle force to zero.

Exoskeleton Modeling

The wearable exoskeleton stores the springs in a box which can be carried on the back (Fig. 2). As shown in Fig. 1, the green lines are the cables for transferring spring forces. In this design, two springs are used to drive the elbow joint and three springs to drive the shoulder joint.

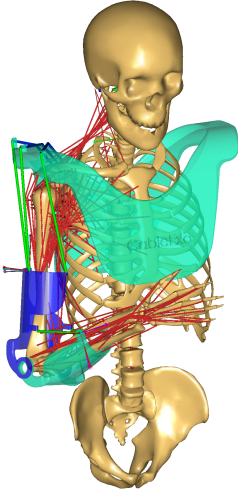


Figure 1. A wearable cable-driven exoskeleton.

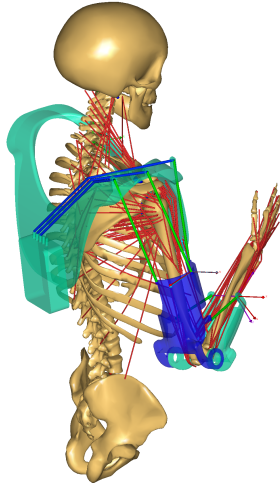


Figure 2. Back view of the wearable exoskeleton.

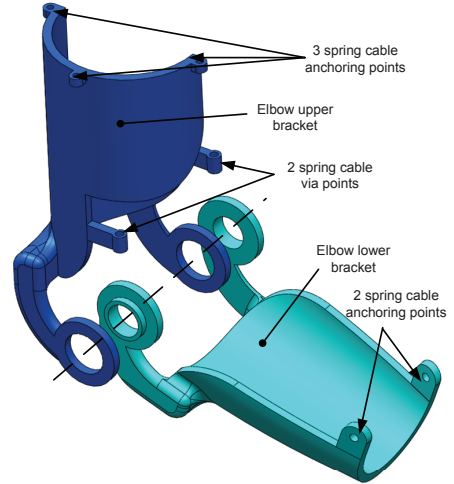


Figure 3. CAD embodiment of the exoskeleton.

At the elbow joint, two anchoring nodes are designed on the elbow lower bracket, as shown in Fig. 3. Two cables linked to two springs from the anchoring point through the two via points on the elbow upper bracket. The force in the spring cable is defined as

$$F_s = F_{pre} + k * \Delta l \quad (4)$$

where F_{pre} denotes pre-load force of the spring. k is the spring stiffness co-efficient and Δl is the variation of the spring length.

A Bio-robotic Model

The bio-robotic is developed through integrating the human arm and the exoskeleton model, as shown in Fig. 1. The exoskeleton model is built in SolidWorks and then exported to AnyBody. All joints need to be defined in AnyBody. The armor part of the exoskeleton is fixed to the trunk of the human model. The elbow lower bracket is connected to the lower arm through a translation-spherical joint. The attachment of the upper bracket to the upper arm is modelled as a revolute joint.

Optimization on the Exoskeleton

In this work, the design of the exoskeleton is formed as an optimization problem through biomechanical simulation. The kinematics and dynamics simulation of the bio-robotic system is conducted in AnyBody Modeling System.

Brachial Plexus Injury

The brachial plexus is a network of nerves that conducts signals from the spinal cord, which is housed in the spinal canal of the vertebral column (or spine), to the shoulder, arm and hand. The branches of the brachial plexus and their associated muscles are listed in Table 1, sorted with respect to their roots.

Table 1. Branches of brachial plexus.

No.	Nerve	Roots	From	Muscles
1	axillary	C5, C6	posterior cord	deltoid, teres minor
2	radial	C5, C6, C7, C8, T1	posterior cord	triceps brachii, supinator, anconeus, the extensor muscles of the forearm, brachioradialis
3	upper subscapular nerve	C5, C6	posterior cord	subscapularis(upper part 1 2)
4	lower subscapular nerve	C5, C6	posterior cord	subscapularis(lower part 3 4 5 6), teres major
5	thoracodorsal nerve	C6, C7, C8	posterior cord	latissimus dorsi
6	lateral pectoral nerve	C5, C6, C7	lateral cord	pectoralis major
7	musculocutaneous nerve	C5, C6, C7	lateral cord	coracobrachialis, brachialis, biceps brachii
8	suprascapular nerve	C5, C6	upper trunk	supraspinatus, infraspinatus
9	long thoracic nerve	C5, C6, C7	root	serratus anterior
10	dorsal scapular nerve	C5	root	rhomboid muscles, levator scapulae

Formulation of Optimization

To simplify the optimization, the three springs for the shoulder joint use the same type of spring which means they have the same stiffness co-efficient defined as k_u . The two springs for the elbow joint also use the same type of spring with the stiffness of k_l . The objective of the exoskeleton is to reduce the maximal muscle activation (MMA). The objective function is defined as

$$\min_{\mathbf{x}} \max f(\mathbf{x}) = \sum_i \frac{f_i^{(M)}}{N_i} \quad (5)$$

$$\mathbf{x} = [\mathbf{F}_{pre}, \mathbf{k}]$$

where $\mathbf{F}_{pre} = [F_1, \dots, F_5]$ and $\mathbf{k} = [k_u, k_l]$, which means there are 7 design variables for the problem. The optimization problem is solved by the Complex method [4].

Results and Discussions

Maximal Muscle Activation

The maximal muscle activation is calculated for different nerve lesion conditions. We categorized the muscles into groups according to the nerve root and origin, as shown in Table 1. The motion of picking

up a mobile and making a call is captured with the duration of 4.6 seconds. The payload is 0.5kg holding at hand. The calculated MMA of different nerve lesion is shown in Fig. 4. Note that the case BASE refers to the motion without any nerve lesion.

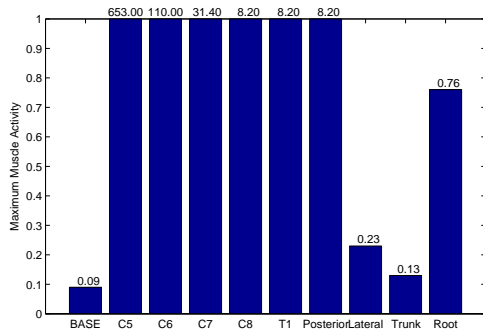


Figure 4. Maximal MMA of different nerve lesion cases.

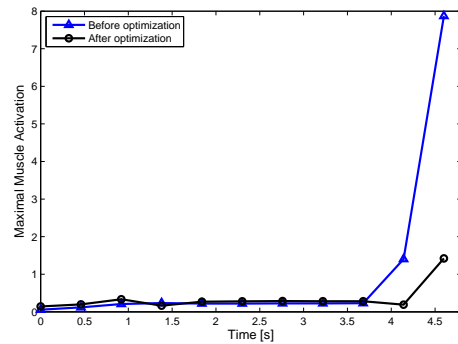


Figure 5. The comparison of the MMA after optimization.

Optimization Results

For the case C8 in the motion of making a phone, we set a population number of 14 to the Complex method for executing optimization. The objective convergence tolerance is 0.001, and the convergence tolerance for the design variables is 0.1. The maximal MMA is reduced from 8.2 to 1.42 after optimization with 269 iterations.

The optimal design variables are obtained as $\mathbf{F}_{pre} = [23.7, 34.9, 3.3, 19.4, 10.5]$, and $\mathbf{k} = [58.8, 20.4]$. The stiffness co-efficient is used to select springs for the exoskeleton. With the optimal parameters, the MMA is calculated for the case without exoskeleton and the one with the optimal design, as plotted in Fig. 5. Wearing the optimal designed exoskeleton, the patient can accomplished the motion of lifting the arm and making a phone call.

Conclusions

A spring-loaded cable-driven exoskeleton was designed in this work. A musculoskeletal human arm model was built to simulate the brachial plexus injury. The cable-driven exoskeleton model was integrated with the musculoskeletal model for dynamics simulation and design optimization of the exoskeleton. Parameters of the exoskeleton were obtained through optimization. A prototype will be built to testify the model and validate its application in patients' daily living.

References

- [1] X-ar skeletal arm. Available from: <http://equipoisinc.com/products/xAr>.
- [2] T. Rahman, W. Sample, S. Jayakumar, M. M. King, J. Y. Wee, R. Seliktar, M. Alexander, M. Scavina, and A. Clark. Passive exoskeletons for assisting limb movement. *Journal of Rehabilitation Research & Development*, 43(5):583–590, 2006.
- [3] T. Lenzi, N. Vitiello, S. M. M. De Rossi, S. Roccella, F. Vecchi, and M. C. Carrozza. NEUROExos: a variable impedance powered elbow exoskeleton. In *Proceedings of IEEE International Conference on Robotics and Automation*, pages 1419–1426, Shanghai, China, 2011.
- [4] M. J. Box. A new method of constrained optimization and a comparison with other methods. *Computer Journal*, (8):42–52, 1965.

Proceedings of the 25TH NORDIC SEMINAR
COMPUTATIONAL MECHANICS, 2012

Constitutive Modelling

Room: Stora Hörsalen, Thursday 25 October, 16:15 - 17:55



Mesoscale modeling of dislocation density gradients and microstructure evolution

Håkan Hallberg, Matti Ristinmaa

Division of Solid Mechanics, Lund University, Box 118, S-221 00 Lund, Sweden
hakan.hallberg@solid.lth.se, matti.ristinmaa@solid.lth.se

Summary. The presence of grain boundaries in the microstructure of metallic materials causes heterogeneous distributions of dislocation density. In the present contribution, the evolution of dislocation density is viewed as a reaction-diffusion system, involving mobile and immobile dislocations. Gradient effects are introduced by making the immobilization of dislocations sensitive to presence of grain boundaries. The model provides a macroscopic yield stress behavior of Hall-Petch type, without explicitly incorporating a yield stress dependence on the grains size. In addition, the model is employed in a cellular automaton algorithm, allowing a polycrystalline microstructure to evolve due to dynamic recrystallization, confirming that the introduced gradients provide important additions to recrystallization modeling.

Key words: Gradient effects, Dislocation density, Grain boundaries, Hall-Petch, Recrystallization, Cellular automata

Introduction

Many important aspects of the macroscopic material behavior in metals are controlled by the microlevel grain structure. Especially the presence of grain boundaries plays an important role as they pose obstacles to slip deformation by preventing dislocation motion, resulting in localized dislocation storage and heterogeneous deformation fields within the grains.

The dislocation storage at grain boundaries increases as the volume fraction of grain boundaries increase, i.e. as the average grain size decreases. This is macroscopically observable as a Hall-Petch effect, cf. [1, 2], suggesting a proportionality between the macroscopic yield stress $\bar{\sigma}_y$ and the inverse of the square root of the average grain size d , i.e.

$$\bar{\sigma}_y = \bar{\sigma}_{y0} + \frac{\bar{k}}{\sqrt{d}} \quad (1)$$

where $\bar{\sigma}_{y0}$ and \bar{k} are parameters.

In the present work, a mesoscale model of microstructure evolution is established where a distinction is made between the densities of mobile and immobile dislocations. The two dislocation species are allowed to evolve through a reaction-diffusion process, driven by macroscopic deformation. Dislocation density gradients are introduced by making the reaction-diffusion system sensitive to the presence of grain boundaries. The model is employed in simulations of dislocation density evolution in single grains and polycrystals and the homogenized macroscopic flow stress exhibits the expected Hall-Petch behavior in both cases.

The polycrystal model is formulated in a combined finite difference/cellular automaton setting and a methodology for treating the dislocation density gradients due to grain boundaries is introduced. This results in an efficient hybrid algorithm for mesoscale modeling of grain microstructures.

Reaction-diffusion modeling of dislocation density evolution and gradients

The dislocation density is assumed to be comprised of the densities of mobile dislocations ρ_m and immobile dislocations ρ_i . The two populations are assumed to evolve in a reaction-diffusion process where the two types of dislocations are allowed to react with each other and each type is allowed to diffuse through the crystal structure. Following [3, 4], the balance equation for each type of dislocation density is given by

$$\begin{aligned}\frac{\partial \rho_m}{\partial t} + \nabla \mathbf{j}_m &= \left(k_1 \frac{\rho_i}{\rho_m} - k_2 \rho_m - k_3 \sqrt{\rho_i} \right) \dot{\varepsilon}_{\text{eff}}^{\text{P}} \\ \frac{\partial \rho_i}{\partial t} + \nabla \mathbf{j}_i &= (k_2 \rho_m + k_3 \sqrt{\rho_i} + -k_4 \rho_i) \dot{\varepsilon}_{\text{eff}}^{\text{P}}\end{aligned}\quad (2)$$

where ∇ is the divergence operator and $\mathbf{j}_{m,i}$ the fluxes of mobile and immobile dislocations, respectively. These fluxes are given by

$$\nabla \mathbf{j}_m = -D_m \nabla \rho_m \quad \text{and} \quad \nabla \mathbf{j}_i = -D_i \nabla \rho_i \quad (3)$$

where $D_{m,i}$ is the diffusion coefficient of each type of dislocations, satisfying $D_m \gg D_i$.

The right-hand sides of eqs. (2) are allowed to depend on the rate of macroscopic effective plastic strain $\dot{\varepsilon}_{\text{eff}}^{\text{P}}$, where a superposed dot denotes differentiation with respect to time t .

In eq. (2), the parameter k_2 controls the decrease of mobile dislocation density due to interaction between mobile dislocations and the parameter k_3 governs the immobilization of mobile dislocations. The density of mobile dislocations is further influenced by a production term k_1 and the density of immobile dislocations evolves under the influence of a dynamic recovery term k_4 .

The total dislocation density, measuring the stored energy in the material, is taken as the sum of the mobile and immobile dislocation densities, i.e. $\rho = \rho_m + \rho_i$.

To introduce dislocation density gradients in the vicinity of grain boundaries the parameter k_3 in eq. (2) is allowed to vary with the distance l to the boundary, i.e.

$$k_3 = k_3(l) \quad (4)$$

With $k_3(l)$ attaining its highest value at the boundary, where $l = 0$, and then gradually fade away for increasing values of l . This represents the physical processes of increased immobilization and storage of dislocations as the grain boundary is approached. Grain boundaries are in the present model assumed to be impenetrable for dislocations by prescribing zero fluxes. Transmission of dislocations across the grain boundaries can, however, be incorporated into the present formulation by prescribing non-zero fluxes.

Model formulation for polycrystals

To investigate the behavior of the reaction-diffusion model in the case of polycrystalline materials, a 2D microstructure is considered, noting that extension to 3D is straight-forward. An explicit finite difference scheme is used for the evolution of the dislocation densities in a RVE described by a fixed two-dimensional grid with dimensions $512 \times 512 \mu\text{m}$ and a total of 1024×1024 grid divisions. Periodic boundary conditions are employed.

As the present dislocation model is also applied to cellular automata modeling of dynamic recrystallization, the notion of each grid point being a ‘‘cell’’ is introduced. To each cell belongs a number of state variables. For the present purpose, the state variables consist of the cell’s density of mobile and immobile dislocations, respectively, and an identifying number stating to which grain the cell belongs.

In eq. (4), the parameter k_3 was made dependent on the distance l to the grain boundary. To keep track of the distance of each cell in a single grain, relative to the grain boundary, a distance

number n_{dist} is assigned to the individual cells. The boundary cells of the grains are identified and are given the distance number 1. All cells within the grain, having a neighbor with distance number 1 are subsequently given the distance number 2 and so on. This is continued until all cells are numbered.

Based on the distance numbers, the distance l from the boundary is identified as an integer number of cells n_l defining the distance from the boundary – where $n_l = 1$ – and the function $k_3(l)$ is assumed to appear as

$$k_3(n_l) = k_{3,\text{max}} - (k_{3,\text{max}} - k_{3,\text{min}})(1 - \exp[-w(n_l - 1)]), \quad n_l \geq 1 \quad (5)$$

In this form, eq. (5) satisfies $k_3 = k_{3,\text{max}}$ at the boundary where $n_l = 1$ and $k_3 = k_{3,\text{min}}$ a distance away from the boundary, indirectly determined by the parameter w .

The homogenized macroscopic yield stress is obtained from the RVE by considering $\sigma_y = \sigma_{y0} + \alpha\mu b\sqrt{\bar{\rho}}$ where $\bar{\rho}$ is the volume-averaged dislocation density. This homogenization procedure is discussed further in [6].

Polycrystal simulations

To examine the grain size influence on the model behavior, a number of microstructures with different grain sizes are generated and employed in simulations.

The different RVE microstructures are used with the present reaction-diffusion model to simulate the evolution of dislocation densities up to a total strain of $\varepsilon_{\text{eff}}^{\text{P}} = 0.5$. Material parameters are set to values typical for steel. Fig. 1a shows the resulting, homogenized, flow stress for some of the grain sizes under consideration when $w = 0.1$. As expected, an increased flow stress can be observed in Fig. 1a as smaller grain sizes are considered.

The variation of the flow stress with grain size at $\varepsilon_{\text{eff}}^{\text{P}} = 0.25$ is shown in Fig. 1b for different values of the parameter w . In Fig. 1b, symbols represent simulation results and the solid lines represent fits of the Hall-Petch relation in eq. (1).

As $w = 0.1$ is employed, grain boundary effects dominate far into the grain interiors. Consequently, the simulation results in Fig. 1b obtained for $w = 0.1$ deviate significantly from a Hall-Petch type of behavior as smaller grain sizes are considered, consistent with experimental observations for small grain sizes.

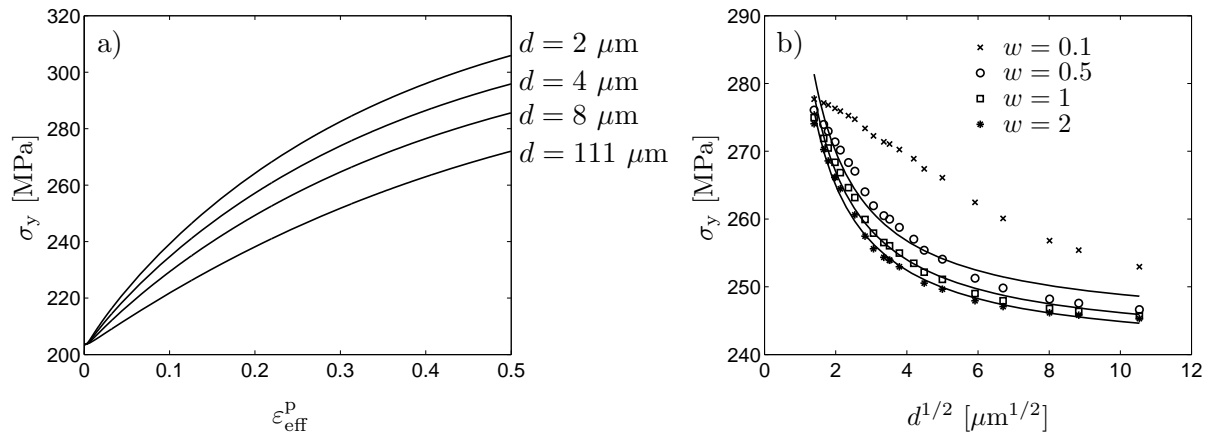


Figure 1. a) Homogenized flow stress obtained from the polycrystal simulations for some different grain sizes and with $w = 0.1$. b) Variation of the flow stress, obtained at $\varepsilon_{\text{eff}}^{\text{P}} = 0.25$, for different grain sizes and for different values of the w -parameter. Symbols represent simulation results and solid lines show least-squares fits of the Hall-Petch relation in eq. (1).

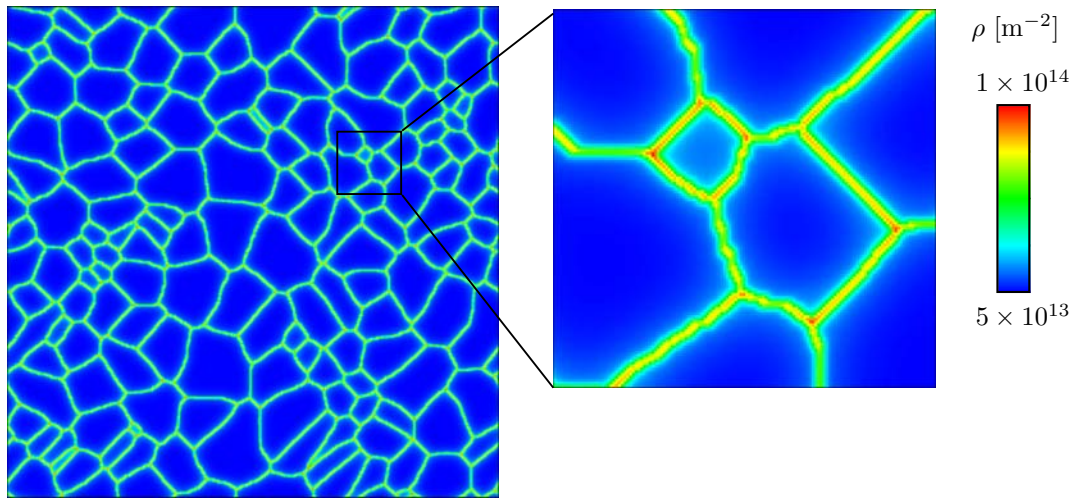


Figure 2. Distribution of total dislocation density at a strain of $\varepsilon_{\text{eff}}^{\text{p}} = 0.5$. The close-up shows how the dislocation is concentrated primarily at triple junctions and secondly along grain boundaries.

Implications on recrystallization modeling

The distribution of total dislocation density at $\varepsilon_{\text{eff}}^{\text{p}} = 0.5$ is shown in Fig. 2. The close-up view shows how the highest levels of dislocation density can be found at triple junctions and to a lesser extent along grain boundaries. The dislocation density gradients gradually decline as one moves away from the grain boundaries and into the grain interiors where the dislocation density is considerably reduced.

The heterogeneous concentrations of dislocation density have important implications in recrystallization modeling. Experiments show that nucleation of new grains occur at sites of high stored energy, i.e. of high dislocation density, which are primarily located at triple junctions and along grain boundaries. The usual approach in simulations of recrystallization is to manually place the recrystallization nuclei at these preferred sites. Using the present approach, with dislocation density gradients, the nucleation sites emerge naturally without manual intervention.

References

- [1] E.O. Hall. The Lüders Deformation of Mild Steel. *Proc. R. Soc., London*, Section B(64):1085–1086, 1951.
- [2] N.J. Petch. The Cleavage Strength of Polycrystals. *J. Iron Steel Inst.*, 174(1):25–28, 1953.
- [3] D. J. Bammann and E. C. Aifantis. On a proposal for a continuum with microstructure. *Acta Mech.*, 45:91–121, 1982.
- [4] E.C. Aifantis. On the dynamical origin of dislocation patterns. *Mater. Sci. Eng.*, 81:563–574, 1986.
- [5] Y. Estrin and L.P. Kubin. Local strain hardening and nonuniformity of plastic deformation. *Acta Metall. Mater.*, 34(12):2455–2464, 1986.
- [6] H. Hallberg, M. Wallin, and M. Ristinmaa. Modeling of discontinuous dynamic recrystallization in pure Cu using a probabilistic cellular automaton. *Comp. Mater. Sci.*, 49(1):25–34, 2010.

Modeling of the cyclic behaviour of Haynes 282, including cyclic softening.

Rebecka Brommesson¹ and Magnus Ekh¹

⁽¹⁾Department of Applied Mechanics, Division of Material and Computational Mechanics, Chalmers University of Technology, Gothenburg, rebecka.brommesson@chalmers.se, magnus.ekh@chalmers.se

Summary. In this paper the mechanical behaviour of the Ni-based superalloy Haynes 282 is studied. Haynes 282 is developed for high-temperature applications in aero and land based gas turbine engines. To capture the cyclic hardening/softening of the material at different temperatures, a plasticity model has been calibrated against LCF experiments. In this contribution special attention is given to the slow cyclic softening that Haynes 282 shows at elevated temperatures. Two approaches to model the cyclic softening are presented. The first approach consists of using negative isotropic hardening while the second approach instead uses a kinematic hardening parameter dependent on the accumulated plastic strain. It is shown that both approaches give good prediction of the cyclic behaviour with respect to experiments.

Key words: constitutive modeling, Ni-based superalloy, cyclic softening

Introduction

Thermomechanical fatigue (TMF) is a challenging problem for structural components in gas turbine industry. The requirements of withstanding high temperatures while keeping efficient and light designs put high demands on engineering with accurate modeling of the material behaviour. Many constitutive models have been proposed to characterize the phenomenological behavior of metals on the macroscale, see e.g. overviews [1], [2], [3]. For superalloys, used in gas turbine applications, the constitutive model should be able to mimic phenomena such as cyclic hardening/softening, the Bauschinger effect, ratchetting, shake down, creep and stress relaxation.

Due to the high and varying temperatures in gas turbine applications, the rate and temperature dependent phenomena are of great importance to give an adequate prediction of the material behaviour. However, in this paper we focus on modeling of the thermal and cyclic plasticity behaviour. As a base-model we choose a rate independent plasticity model that was originally formulated in [4].

The predictions of the plasticity model are compared to experimental results for uniaxial LCF experiments at various elevated temperatures. Special attention is given to the modeling of the cyclic softening and how it is influenced by temperature. Two different approaches are evaluated with respect to experimental results. The first approach is based on isotropic softening (negative hardening) and the second approach is based on a kinematic softening parameter that depends on the accumulated plastic strain.

Material model

In the model framework the stress is partitioned into a volumetric σ_{vol} and a deviatoric part σ_{dev} which are related, by assuming linear isotropic elasticity, to the volumetric and deviatoric

parts of the elastic strain ϵ_e as follows

$$\begin{aligned}\boldsymbol{\sigma} &= \boldsymbol{\sigma}_{\text{dev}} + \frac{1}{3}\sigma_{\text{vol}}\mathbf{I} \\ \boldsymbol{\sigma}_{\text{dev}} &= 2G\boldsymbol{\epsilon}_{e,\text{dev}} \\ \sigma_{\text{vol}} &= 3K_b\epsilon_{\text{vol}}\end{aligned}\tag{1}$$

where G is the shear modulus and K_b is the bulk modulus. The elastic part of the strain ϵ_e is obtained from the total strain ϵ by subtracting the plastic strain ϵ_p and the thermal strain

$$\boldsymbol{\epsilon}_e = \boldsymbol{\epsilon} - \boldsymbol{\epsilon}_p - \alpha\Delta\Theta\mathbf{I}\tag{2}$$

where α is the thermal expansion coefficient and $\Delta\Theta$ is the temperature increase. Furthermore, the plastic yielding is assumed to be governed by the von Mises yield function

$$\Phi = \sqrt{\frac{3}{2}}|\boldsymbol{\sigma}_{\text{dev}} - \mathbf{B}| - (\sigma_y - \kappa)\tag{3}$$

where \mathbf{B} is the back-stress (kinematic hardening), σ_y is the initial yield stress and κ is the drag-stress (isotropic hardening). According to the normality rule, the plastic strain is assumed to evolve in an associative fashion

$$\dot{\boldsymbol{\epsilon}}_p = \dot{\lambda}\frac{\partial\Phi}{\partial\boldsymbol{\sigma}} = \dot{\lambda}\sqrt{\frac{3}{2}}\frac{\boldsymbol{\sigma}_{\text{dev}} - \mathbf{B}}{|\boldsymbol{\sigma}_{\text{dev}} - \mathbf{B}|}\tag{4}$$

Furthermore, the evolution of isotropic and kinematic hardening are assumed to be of Voce and of Armstrong-Frederick type

$$\begin{aligned}\dot{\kappa} &= \dot{\lambda}H_{\text{iso}}\left(1 - \frac{\kappa}{\kappa_{\infty}}\right) \\ \dot{\mathbf{B}} &= \dot{\lambda}H\left(\sqrt{\frac{2}{3}}\frac{\boldsymbol{\sigma}_{\text{dev}} - \mathbf{B}}{|\boldsymbol{\sigma}_{\text{dev}} - \mathbf{B}|} - \frac{\mathbf{B}}{B_{\infty}}\right)\end{aligned}\tag{5}$$

where H_{iso} , κ_{∞} , H and B_{∞} are material parameters. The plastic multiplier $\dot{\lambda}$ describes the amount of plastic strain rate and is, for the case of rate independent inelasticity, determined from the Kuhn-Tucker loading/unloading conditions

$$\Phi\dot{\lambda} = 0, \quad \dot{\lambda} \geq 0, \quad \Phi \leq 0\tag{6}$$

To expand the model to include rate dependence the loading/unloading conditions could easily be replaced by introducing an over-stress function (see e.g. [1]). It is further noted that the parameters G , K_b , α , σ_y , H_{iso} , κ_{∞} , H , and B_{∞} are in general dependent on temperature.

Cyclic softening

The evolution of the cyclic response of the material is modeled by two different approaches. The first approach is based on negative isotropic hardening ($H_{\text{iso}} < 0$). In combination with a negative value for the saturated drag stress ($\kappa_{\infty} < 0$), a nonlinear cyclic softening can be modeled. Saturation of the cyclic softening can then be controlled by the ratio $H_{\text{iso}}/\kappa_{\infty}$.

In the second approach the kinematic hardening parameters are dependent on the amount of accumulated plastic strain via a coupling function

$$\phi(a, v) = a + (1 - a)\exp(-v\bar{\lambda})\tag{7}$$

where a and v are temperature dependent material parameters and $\bar{\lambda}$ is the accumulated plastic strain. Here, the amount of cyclic softening is controlled by parameter a and the saturation of

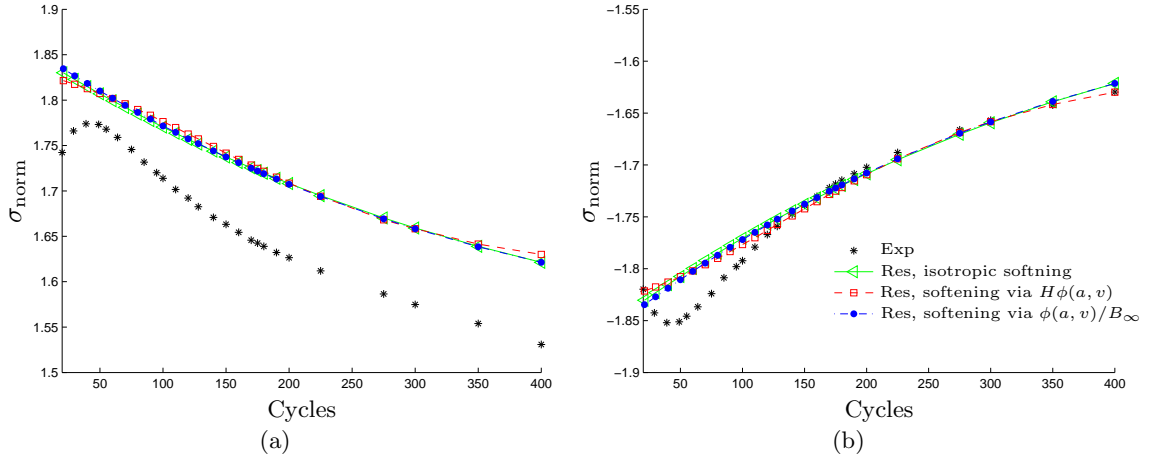


Figure 1. Experimental data and different model predictions showing cyclic softening at 650°C in terms of a) maximum stress and b) minimum stress.

cyclic softening is controlled by the value of parameter v . The function $\phi(a, v)$ can be used to modify the total back-stress evolution multiplicatively

$$\dot{\mathbf{B}} = \dot{\lambda} H \phi(a, v) \left(\sqrt{\frac{2}{3}} \frac{\boldsymbol{\sigma}_{\text{dev}} - \mathbf{B}}{|\boldsymbol{\sigma}_{\text{dev}} - \mathbf{B}|} - \frac{\mathbf{B}}{B_{\infty}} \right), \quad \phi < 1 \quad (8)$$

or it can be used to only modify the saturation term of the back-stress evolution

$$\dot{\mathbf{B}} = \dot{\lambda} H \left(\sqrt{\frac{2}{3}} \frac{\boldsymbol{\sigma}_{\text{dev}} - \mathbf{B}}{|\boldsymbol{\sigma}_{\text{dev}} - \mathbf{B}|} - \phi(a, v) \frac{\mathbf{B}}{B_{\infty}} \right), \quad \phi > 1 \quad (9)$$

Depending on the placement of $\phi(a, v)$ a difference in the model response can be observed in the cyclic behaviour after some softening.

Numerical results

Since the experimental data for Haynes 282 are classified, the numerical values of model response and experimental results cannot be given explicitly. Instead the presented numerical values and results will be normalized by a stress x_{σ} . Identification of the material parameters in the constitutive model will be presented for uniaxial LCF experiments at various temperatures and the dependency on temperature will be discussed. As an example, the model response of the predicted maximum and minimum stress, using the two different approaches of modeling the cyclic softening, is compared to experimental results in figure 1. The cyclic softening can also be observed in figure 2, where the hysteresis loops at 25 and 75 % of the experimental life, N_f , are given. From figure 1 it can be concluded that both approaches of modeling the cyclic softening give good results with respect to LCF experiments for Haynes 282 at 650°C. However, in figure 2 it can be observed that the cyclic model responses at 75% of N_f are different. This will affect the choice of approach for including cyclic softening in the model.

References

- [1] J. Lemaitre and J.L. Chaboche. *Mechanics of solid materials*. Cambridge University Press, Cambridge, 1990.
- [2] D.C. Stouffer and L.T. Dame. *Inelastic deformation of metals : models, mechanical properties, and metallurgy*. Wiley and Sons, Inc., New York, 1996.

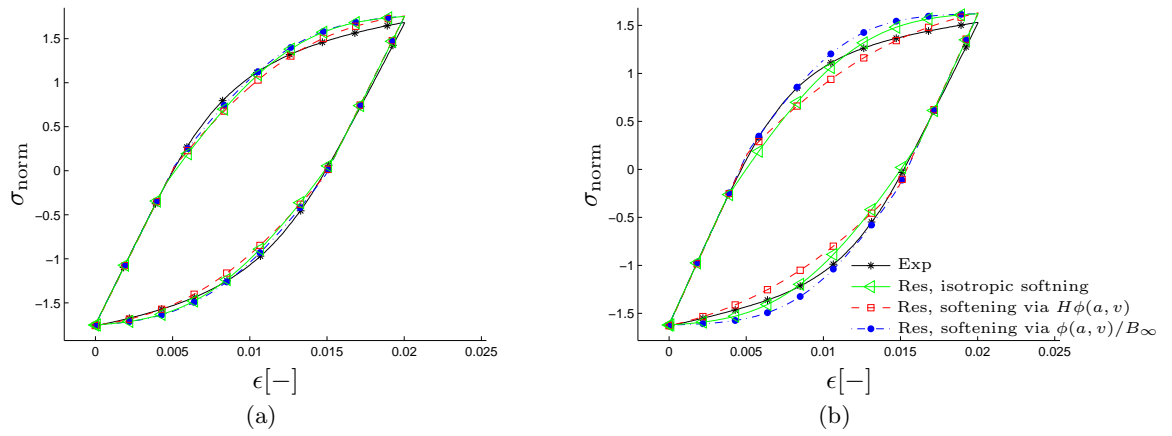


Figure 2. Hysteresis loops from experimental data and model responses at a) 25 % of Nf and b) 75% of Nf.

- [3] J.L. Chaboche. A review of some plasticity and viscoplasticity constitutive theories. *International Journal of Plasticity*, 24:1642 – 1693,2008.
- [4] J.L. Chaboche. Constitutive Equations for Cyclic Plasticity and Cyclic Viscoplasticity. *International Journal of Plasticity*, 5:247 – 302,1989.

Comparison of the BPA model to DIC measurements of polycarbonate

Jonas Engqvist, Mathias Wallin, Stephen Hall and Matti Ristinmaa

Division of Solid Mechanics, Lund University, Box 118, 221 00 Lund, Sweden
 jonas.engqvist@solid.lth.se

Summary. The well known eight chain BPA model for glassy polymers proposed by Boyce *et al.* is reviewed and implemented. To evaluate the model, DIC measurements are performed and the simulated responses are compared to the experimental results.

Key words: Glassy polymers, Constitutive modelling, BPA model, DIC

Introduction

Glassy polymers are commonly used in industrial as well as consumer products. This has created a need for reliable constitutive models that are able predict the mechanical response of the material. A well known constitutive model for capturing the behaviour of glassy polymers during monotonic loading is the BPA model that was proposed by Boyce, Parks and Argon [1].

The BPA model

The eight chain BPA model is based on the assumption that a glassy polymer can be represented by an idealized chain network. The simplified network is assumed to consist of eight chain segments that extend from the center point of a cube to its corners. The driving force for the plasticity in the BPA model is the reduced Cauchy stress, $\tilde{\boldsymbol{\sigma}}$, which is defined as

$$\tilde{\boldsymbol{\sigma}} = \boldsymbol{\sigma} - \mathbf{F}^e \mathbf{B} \mathbf{F}^{eT}, \quad (1)$$

where $\boldsymbol{\sigma}$ is the Cauchy stress and \mathbf{B} is the back stress. The principal components of the back stress, B_α ($\alpha = 1, 2, 3$), are expressed in terms of the principal plastic stretches, λ_α^p , as

$$B_\alpha = \frac{C_R \sqrt{N}}{3\lambda^p} \mathfrak{L}^{-1} \left\{ \frac{\lambda^p}{\sqrt{N}} \right\} \left((\lambda_\alpha^p)^2 - (\lambda^p)^2 \right), \quad \lambda^p = \frac{1}{\sqrt{3}} \sqrt{\sum_\alpha (\lambda_\alpha^p)^2}, \quad (2)$$

where C_R and N are material parameters, λ^p is the plastic stretch on a chain and \mathfrak{L}^{-1} is the inverse Langevin function. The evolution law for the plastic deformation is

$$\dot{\gamma}^p = \dot{\gamma}_0 \exp\left(-\frac{A s_s}{\theta} \left(1 - \left(\frac{\tau}{s_s}\right)^{\frac{5}{6}}\right)\right), \quad s_s = s + \alpha p, \quad (3)$$

where $\dot{\gamma}_0$, A and α are material parameters, $p = -(tr\boldsymbol{\sigma})/3$ is the hydrostatic pressure, τ is the equivalent stress, θ is the absolute temperature and s is the athermal shear stress. The athermal shear stress evolves as

$$\dot{s} = h(1 - s/s_{ss})\dot{\gamma}^p, \quad s(0) = s_0, \quad (4)$$

where s_{ss} is the steady state or “preferred” state value of s . s_0 and h are material parameters.

Experiments

Uniaxial tensile tests on flat, symmetrical notched specimens of polycarbonate (PC) were performed using a custom built test machine. The experimental set-up and the geometry of the specimen is shown in Figure 1. The tests were performed at a constant displacement rate of 2 mm/min of the machine grips. In addition to the axial force and the displacement the deformation fields were measured using an Aramis 3D-surface digital image correlation (DIC) system. The force-displacement curve from an uniaxial tensile test and the corresponding result from the DIC are shown in Figure 2. The DIC results in Figure 2 are showing the largest principle strain at four levels of deformation. The DIC measurements clearly shows an inhomogeneous deformation field which shows a localization of the strain followed by a period of enlargement of the necking zone until an almost uniform strain state is achieved in the neck region.

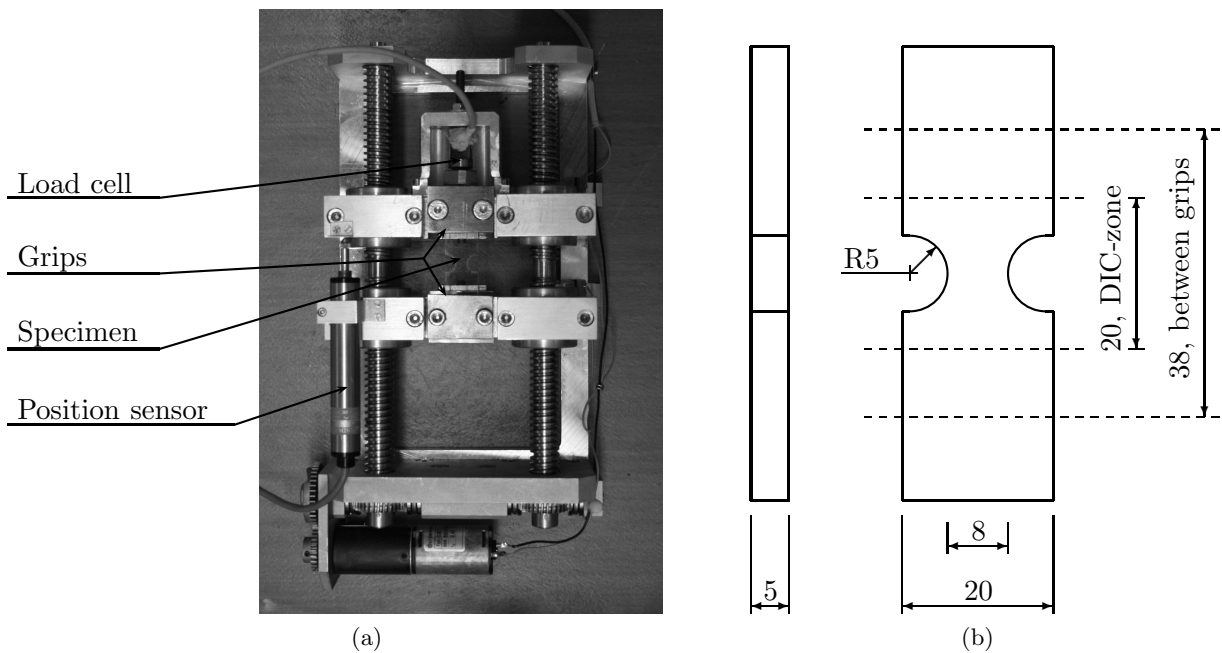


Figure 1: The experimental set-up with the custom built tensile test machine is shown in (a). The geometry of the specimen including the distance between the grips and the DIC measuring zone are shown in (b).

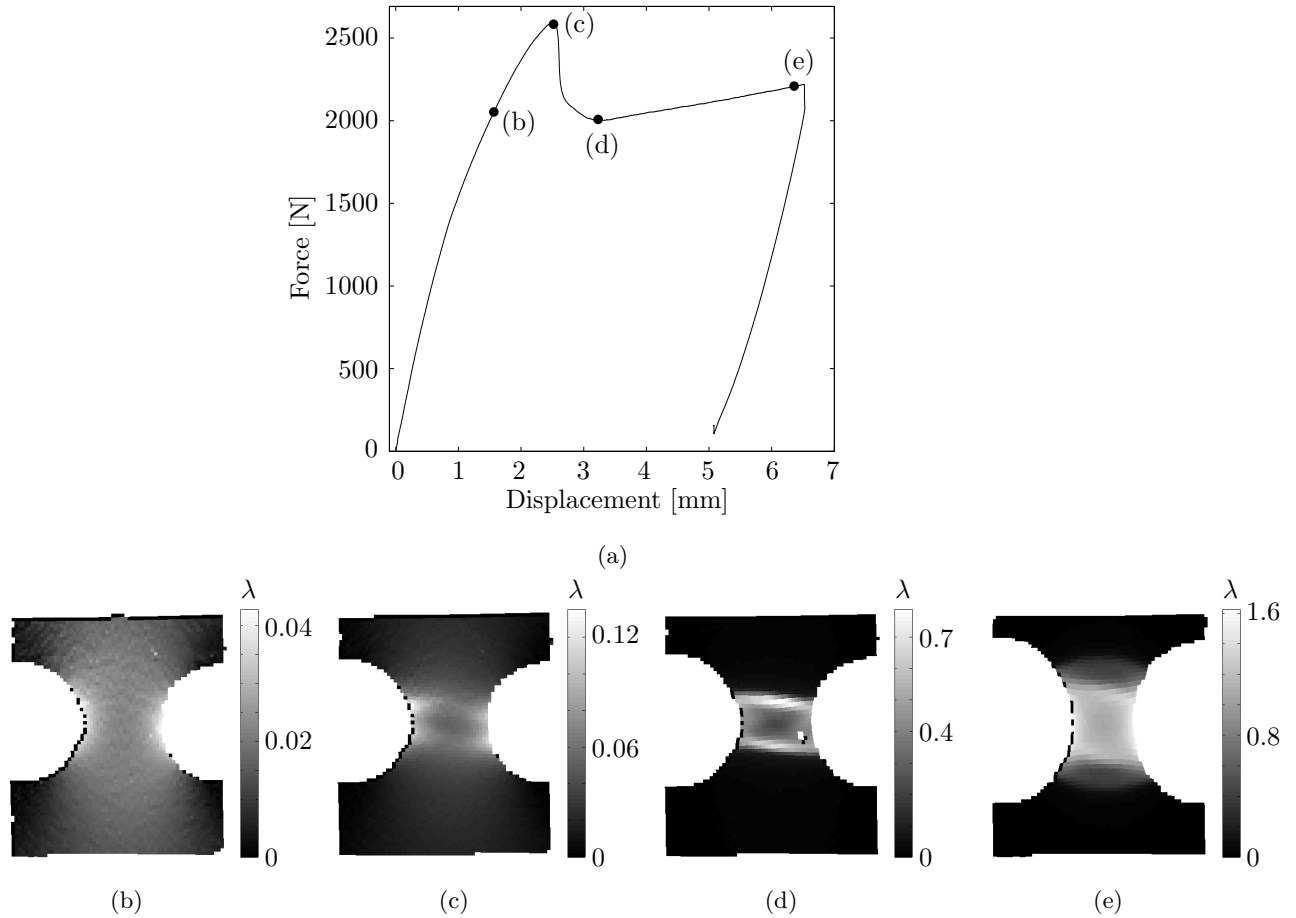


Figure 2: (a) is showing the force-displacement curve from an uniaxial tensile test. (b)-(d) are showing the largest principle strains, λ , calculated from DIC at four levels of deformation.

Future work

The BPA model will be calibrated to the tensile tests based on the standard axial stress and strain measurements. Deformation fields from the model will then be compared with the deformation field obtained by the DIC measurements to further refine the parameters and develop the model. Future modifications of the BPA model will be based on the results from small angle x-ray scattering (SAXS) experiments, made at MAX-lab at Lund University, that will give insight onto polymer chain orientation and alignment.

References

- [1] M. C. Boyce, D. M. Parks and A. S. Argon Large inelastic deformation of glassy polymers. Part I: rate dependent constitutive model. *Mech. of Materials*, 7:15-33, 1988

A constitutive model for the out-of-plane behaviour of paperboard.

Eric Borgqvist, Mathias Wallin, and Matti Ristinmaa

Solid Mechanics Lund University, Box 118, 221 00 Lund Sweden
Eric.Borgqvist@solid.lth.se

Summary. An approach to model the out of plane behaviour of paperboard is presented together with some general experimental characteristics. A scalar damage variable is introduced to take into account the degradation of the material properties. A hyper elastic format is adopted with three different limit surfaces. Simulations in a strain driven have been performed and fitted to experimental curves.

Key words: Paperboard, Constitutive modelling, Orthotropy, Damage

Introduction

Paperboard is made of several layers of wood-fibers and is used as the basis material within the packaging industry. The strive to improve the final product have during the last two decades increased the need of computer simulations. Thus a need for more accurate models is called for. In the present project, we aim to develop a computer model that is suitable for the creasing and folding operations, c.f. Fig.1. In a creasing operation a male die is punched against the paperboard causing the material to be damaged and fibers to debond. During this operation, both delamination and micro cracking occurs. The creasing operation is done in order to preserve the integrity of the package when the paperboard later is folded. It has been shown that the out of plane properties, such as out of plane tension and shearing, are of importance during these operations [1]. These properties have however not yet been entirely satisfactorily characterized.

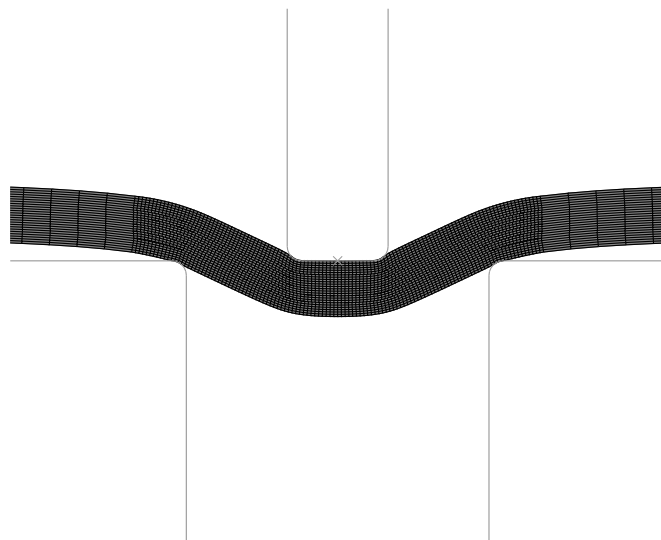


Figure 1. Simulation of creasing operation in Abaqus

Several attempts have been made to establish models for paperboard. An excellent review on the different aspects concerning the paperboard can be found in [2]. Due to the layered structure of the paperboard in the manufacturing process, the paperboard have frequently been modelled using cohesive zone elements (cf. [1],[3],[4]) together with an orthotropic elasto-plastic material model. The modelling of the out of plane behaviour have previously been attributed to these cohesive zones and the material model for the out of plane directions have often been calibrated according to some apriori assumption. But due to the heterogeneous structure of paperboard, it is not entirely obvious that the cohesive zones should be placed between the layers. In the material model proposed herein, the effect of micro cracks is incorporated via the introduction of a scalar damage variable.

Paperboard characteristics

The paperboard has very different behaviour in the different directions, which are denoted as the Machine Direction (MD), Cross Direction (CD) and the out of plane direction (ZD), cf. Fig. 2 below. The failure stress is typically about 2-3 times higher in MD compared to CD and about 100 times higher than ZD.

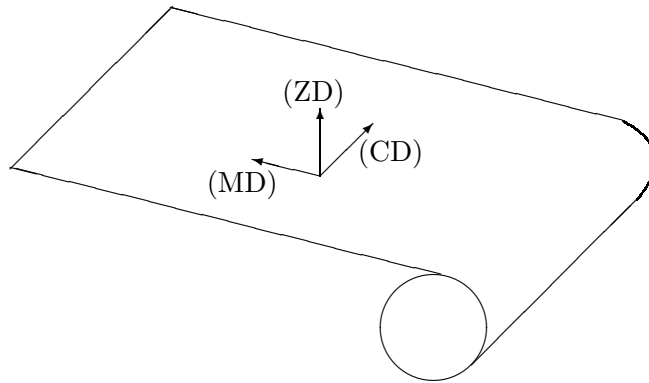


Figure 2. The preferred directions of the paperboard

The Poisson's ratios between the out-of-plane direction and the in-plane direction have some interesting characteristics. It has been shown in [5] that the (ZD) thickness increases initially as the sample is loaded in MD/CD, i.e. the material exhibits a negative Poisson's ratio. However, this effect is usually very small and a good approximation (cf. [6]) is that the Poisson's ratio between the-out-of plane and the in-plane direction is zero.

The material shows a pressure dependency during shearing in the out-of-plane direction([5], [7]). Moreover the shearing behaviour is significantly different when the shearing test is superimposed by a pressure in the ZD-direction. During the creasing operation the paperboard is sheared in the out-of-plane direction, but also compressed in ZD. Therefore this friction like effect needs to be accounted for in the material model.

Modelling

So far, a model based on small strains have been established. This model is currently under development to be extended to large strains. The assumption that there is no coupling between the in-plane and the out-of-plane behaviour is made. A hyperelastic format is proposed where three structural tensors ($\mathbf{N}^{(\alpha)}, \alpha = \{1, 2, 3\}$) are introduced to model the orthotropy together with a scalar damage variable ϕ to model the material degradation. The potential function is assumed to be a function of the following variables

$$\psi = \psi(\boldsymbol{\varepsilon} - \boldsymbol{\varepsilon}^I, \mathbf{N}^{(\alpha)}, \phi, \kappa^d, \kappa^c, \kappa^{ip}) \quad (1)$$

where $\boldsymbol{\varepsilon}^I$ is the inelastic strain and $\kappa^d, \kappa^c, \kappa^{ip}$ are isotropic hardening variables related to different yield surfaces. The inelastic strains are further assumed to additively decomposed into

$$\boldsymbol{\varepsilon}^I = \boldsymbol{\varepsilon}^{ip} + \boldsymbol{\varepsilon}^d + \boldsymbol{\varepsilon}^c \quad (2)$$

where the inelastic strain caused by micro cracks is denoted by $\boldsymbol{\varepsilon}^d$ above, the inelastic strain that arises when the material is compressed in ZD is denoted $\boldsymbol{\varepsilon}^c$ and the in-plane inelastic strain by $\boldsymbol{\varepsilon}^{ip}$. Three different surfaces are introduced for the evolution of the internal variables,

$$f^d = f^d(Y, \boldsymbol{\sigma}, \mathbf{N}^{(3)}, R), \quad f^c = f^c(\boldsymbol{\sigma}, \mathbf{N}^{(3)}, C), \quad f^p = f^p(\boldsymbol{\sigma}, \mathbf{N}^{(1)}, \mathbf{N}^{(2)}, K) \quad (3)$$

where Y is the conjugate damage force and R, C and K are hardening parameters conjugated to κ^d, κ^c and κ^{ip} , respectively.

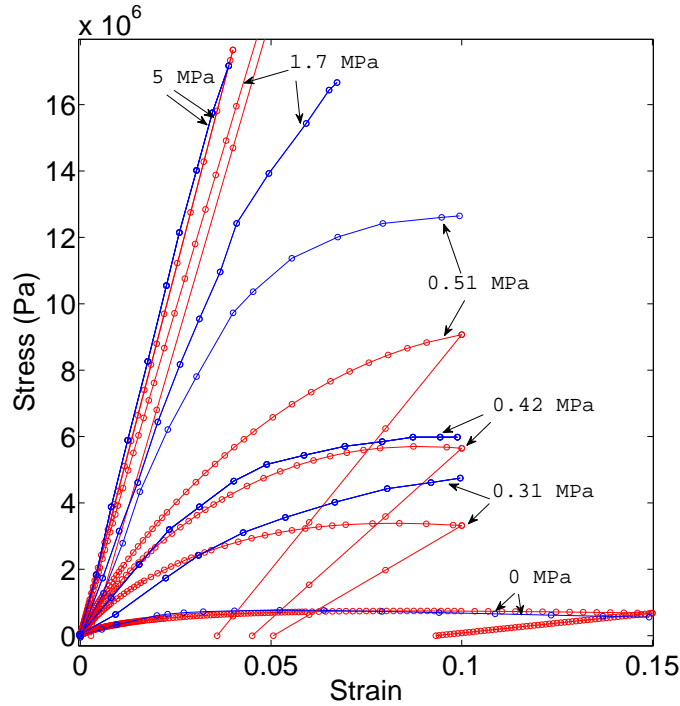


Figure 3. Shearing behaviour at different out of plane pressures (5 MPa, 1.7 MPa, 0.5 MPa, 0.42 MPa, 0.31 MPa and 0 MPa). Experiment curve (blue) and simulation curve (red). Experimental results taken from [7].

Results

The out-of-plane behaviour has been modelled using the model described above. The pressure dependent shearing behaviour has been fitted to the experiment data taken from [7]. The model is able to capture the pressure dependent behaviour qualitatively and there is good agreement between some of the experimental and simulated curves (5 MPa, 0.42 and 0 MPa). However, more experimental data is needed to fully understand this behaviour.

References

- [1] L.A.A. Beex and R.H.J. Peerlings *An experimental and computational study of laminated paperboard creasing and folding*. International Journal of Solids and Structures Vol. 46 (2009) 4192-4207
- [2] Kaarlo Niskanen (Ed), et al. *Mechanics of Paper products* 2012 by Walter de Gruyter GmbH & Co. KG, Berlin/Boston
- [3] Qingxi Steve Xia *Mechanics of inelastic deformation and delamination in paperboard*, 2002, Ph.D. thesis. Massachusetts Institute of Technology, Massachusetts, United States of America
- [4] Nygård, Magnus Just and Johan Tryding *Experimental and numerical studies of creasing of paperboard* International Journal of Solids and Structures Vol. 46 (2009) 2493-2505
- [5] Niclas Stenberg *On the out of plane behaviour Mechanical Behaviour of paper Materials* 2002. Ph. D thesis. Department of Solid Mechanics Royal Institute of Technology, Stockholm, Sweden.
- [6] Hui Huang and Mikael Nygård *A simplified material model for finite element analysis of paperboard creasing* Nordic Pulp and Paper Research Journal Vol. 25 no. 4/2010 505
- [7] Aron Tysen *Testing of paperboard under combined shear and compressive load* B.Sc thesis performed at Innventia.

Physically based plasticity model coupled with precipitate model for IN718

Martin Fisk¹, Lars-Erik Lindgren²

⁽¹⁾Materials Science, Malmö University, Malmö, SE-20506, Sweden, Martin.Fisk@mah.se

⁽²⁾Dept. of Eng. Sci. and Mathematics, Luleå University of Technology, 971 87 Luleå, Sweden

Summary. This talk describes the nucleation, growth and coarsening of γ'' precipitates in Inconel 718 (IN718) during heat treatments. The model can be used in thermo-mechanical simulations of repair welding followed by heat treatment to predict residual stresses and final microstructure in aeroengine components. The interactions between precipitates and dislocations are included in a dislocation density based material model.

Key words: Strengthening mechanisms, Dislocations, Nucleation, Growth, Coarsening

Introduction

The Nickel-based superalloy IN718 is a precipitate hardening alloy commonly used in aircraft engines, power plants and gas turbines. The most important strengthening mechanism is precipitation hardening that results from around 13 vol. % of coherent ordered disk-shaped body-centred tetragonal (BCT) γ'' phase comprising nickel and niobium (Ni_3Nb). There is also a hardening contribution from ordered FCC γ' precipitates (approx. 4 vol. %). It is, however, not the dominant strengthening precipitate. The strengthening of the material depends mainly on the size of the precipitates and the volume fraction. On the other hand, the size of the precipitates depends on the ageing temperature and the time of a heat treatment.

The shape of the γ'' precipitates are disc-shaped (assumed to be oblate-shaped in the following theory) where the aspect ratio of the precipitate changes with the size of the precipitate. Due to the slightly difference in the minor and major axis for small precipitates, nucleation is assumed to follow the theory for spherical precipitates whereas the growth and coarsening follow the theory for a disc-shaped geometry. The interactions between precipitates and dislocations are included in a dislocation density based material model. Compression tests have been performed using solution annealed, fully-aged and half-aged material. Models were calibrated using data for solution annealed and fully-aged material, and validated using data from half-aged material.

Calculation of precipitate radii, nucleation rate and particle size distribution

One can distinguish three stages in a continuous precipitation process: 1) nucleation, 2) growth of the nuclei until the matrix reaches its equilibrium concentration of the solute and 3) Ostwald ripening. At least two processes may occur simultaneously, nucleation and growth or growth and coarsening (Ostwald ripening).

Nucleation and growth

The growth rate of the average precipitate depends on two components: the growth rate of existing particles of mean radius \bar{r}_p and the nucleation rate of new particles of the critical nucleation radius. Thus, we can write:

$$\left. \frac{d\bar{r}_p}{dt} \right|_{n\&g} = \left. \frac{d\bar{r}_p}{dt} \right|_g - \frac{1}{N} \frac{dN}{dt} (\bar{r}_p - r^*) \quad (1)$$

where $d\bar{r}_p/dt|_g$ is the growth rate of the average radius of existing particles, r^* is the critical nucleation radius, J_n is the homogeneous nucleation rate and N is the number of precipitates. If the nucleus is assumed to be spherical, the critical nucleation radius r^* is:

$$r^* = \frac{1}{S} \frac{2\gamma V_{at}}{kT} = \frac{R_0}{S} \quad (2)$$

where γ is the matrix/precipitate interfacial energy, S is the driving force for nucleation and V_{at} is the atomic volume. R_0 is a thermodynamic parameter that has the dimension of length. The nucleation rate depends on the surface area of the nucleus and the rate at which diffusion can occur:

$$J_0 = \frac{dN}{dt} = N_0 Z \beta^* \exp\left(-\frac{\Delta G^*}{kT}\right) \exp\left(-\frac{\tau}{t}\right) \quad (3)$$

where N_0 is the number of atoms per unit volume in the phase, Z is the Zeldovich factor (in the order of 1/20 to 1/40), $\beta^* = (4\pi r^{*2} D C_0)/a^4$ and $\tau = 1/(2\beta^* Z)$ (an incubation time). C_0 is the initial solute mole fraction, a is the lattice parameter and D is the diffusion coefficient of solute atoms in the matrix. ΔG^* is the activation energy barrier for creation of new precipitates.

The rate of change of existing spherical particles assumes to grow as if they were disk-shaped. The expression is [1]:

$$\left. \frac{d\bar{r}_p}{dt} \right|_g = \frac{2qD}{\pi} \frac{C - C_{eq}(r)}{C_p - C_{eq}(r)} \quad (4)$$

where $C_{eq}(r)$ is the equilibrium solute concentration in the matrix next to the phase boundary to a precipitate of radius r and $q = L/h$ is the aspect ratio between the major axis $L = 2r_p$ and the minor axis h of the disk respectively. The equilibrium concentration next to a precipitate of radius r is given by the Gibbs-Thomson equation. C is the current solute balance in the matrix.

Growth and coarsening

In order to achieve transformation from a metastable single-phase state to a stable two-phase state, second phase particles must first nucleate and then grow. Growth will continue until the concentration of solute is in equilibrium with the two phases. Thereafter coarsening occurs; larger precipitates will grow and smaller precipitates will disappear. In order to avoid a singularity between the two states, a linear transition is applied. During coarsening we use the LSW theory applied for disc-shape geometries [1]:

$$\left. \frac{d\bar{r}_p}{dt} \right|_c = \frac{8q}{27\pi} \frac{C_{eq}}{C_p - C_{eq}} \frac{D}{\bar{r}_p} R_0 \quad (5)$$

The corresponding rate of change in precipitate density can be written [2]:

$$\left. \frac{dN}{dt} \right|_c = \frac{1}{\bar{r}_p} \left. \frac{d\bar{r}_p}{dt} \right|_c \left[\frac{R_0 C}{\bar{r}_p (C_p - C)} \left(\frac{q}{2\pi \bar{r}_p^3} - N \right) - 3N \right] \quad (6)$$

Devaux et al. [3] gives the average aspect ratio of the γ'' precipitates, q , as a function of the precipitate radius by comparing four different sources. It is seen that the aspect ratio of the precipitates basically growth linearly where the growth rate, depending on their diameter, can be collected into two groups. The change in growth rate is correlated with the loss of coherency.

Dislocation density model accounting for precipitate hardening

Plastic deformation occurs principally by shearing the atom planes, and is facilitated by the introduction and movement of dislocations in the crystal lattice. The hardening and softening process is associated with the interaction of the material structure, which is the lattice itself, immobile dislocations, solutes, precipitates, defects etc. It is common to assume that they give contributions to the macroscopic flow stress by using expressions similar to:

$$\sigma_y = \sigma_G + \sigma^* + \sigma_p + \dots \quad (7)$$

where σ_y is the flow (yield) stress, σ_G is an athermal stress due to long-range disturbances of the lattice due to immobile dislocations, σ^* is the short-range interaction and is the stress needed to move dislocations past short-range obstacles, σ_p results from the additional stress required to move dislocations around or through precipitate and solutes. The dots tell that there may be other contributions.

The long-range term in Eq. (7) is an athermal stress contribution, which means that it is independent of temperature, i.e. thermal vibrations cannot assist dislocations in overcoming disturbances in the lattice. It is written:

$$\sigma_G = \alpha G b \sqrt{\rho_i} \quad (8)$$

where ρ_i is the effective immobile (forest) dislocation density within the microstructure of the material during deformation, b is the Burgers vector, G is the shear modulus and M is the Taylor factor. The factor α is a proportionality factor measuring the efficiency of dislocation strengthening.

The second term in Eq. (7) is the stress needed to move dislocations past short-range obstacles. It is based on the energy (Gibbs free energy) needed for a particle to overcome an obstacle taking atomic thermal vibrations into account. It can be written as [4]:

$$\sigma^* = \tau_0 G \left(1 - \left(\frac{kT}{\Delta f_0 G b^3} \ln \left(\frac{\dot{\epsilon}_{ref}}{\dot{\epsilon}^p} \right) \right)^{1/q} \right)^{1/p} \quad (9)$$

where the quantity τ_0 is depending on the strength of the obstacle (dimensionless), Δf_0 is a calibration constant, $\dot{\epsilon}_{ref}$ is a reference strain rate and p and q are calibration constants. The conditions for the exponents can be found in Lindgren et al. [4].

The last term in Eq. (7) describes the flow stress contribution due to precipitates. Precipitates, or second-phase particles, commonly act as geometric barriers to dislocation glide. If all the particles are sheared, it is possible to model the strengthening contribution as [2]:

$$\sigma_{shear} \propto \sqrt{f_p} \quad (10)$$

where G is shear modulus and f_p is the particle volume fraction. For large precipitates, it is assumed that dislocations bow around rather than shear through the particles. Ignoring the strain hardening, the stress contribution due to bowing can be modelled as [2]:

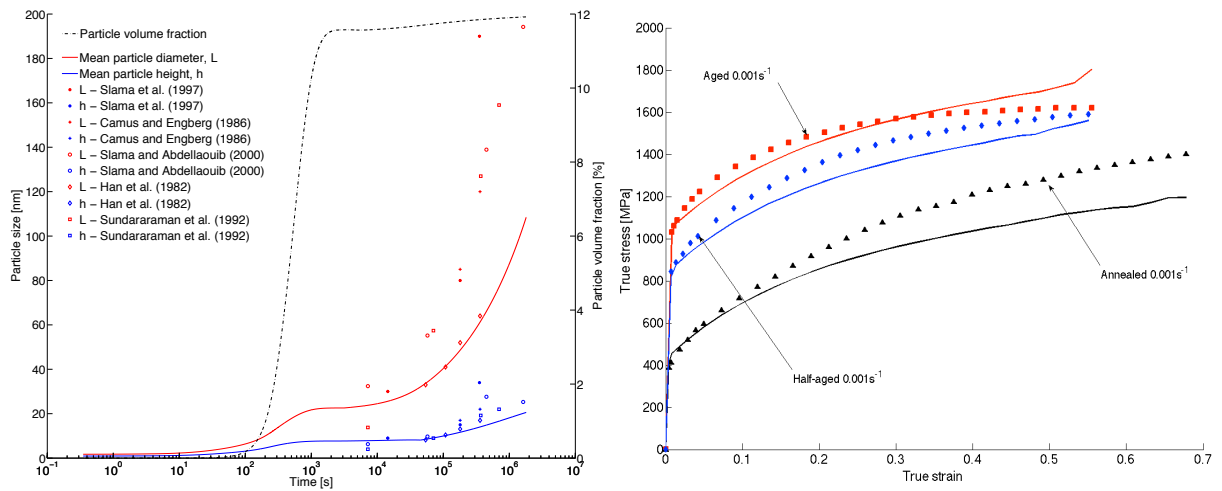
$$\sigma_{bow} \propto \frac{\sqrt{f_p}}{\bar{r}_p} \quad (11)$$

Results

The relation between the precipitate size and the addition of strengthening described earlier makes it possible to calculate the yield stress for different ageing times. This - the dislocation density model accounting for precipitate hardening and the nucleation growth and coarsening - can be applied in an incremental fashion, which is applicable in a finite element code. The

model consists of relations that describe the precipitate evolution needed in the dislocation density model according to the summary given in the previous section. The model is calibrated using compression test data at 400 °C and 600 °C for two strain rates and two states; fully-aged and solution annealed.

Figure a) shows the computational results of the particle diameter, L , height, h , and volume fraction, f_p . The results from the precipitate evolution are compared with experiments taken from journal articles. All experiments are carried out at a temperature of 750 °C. Figure b) shows measured (smoothed) and computed stress strain curves for fully-aged (heat treated for 5 h at 760 °C), half-age (heat treated for 30 min at 760 °C) and solution annealed IN718 material. The line correspond to calculated values and the symbols are measured values.



(a) Evolution of particle diameter, particle height and particle volume fraction. Computational results (full line) are compared with experiments (marks).

(b) Computed stress strain curves at 600 °C.

Conclusions

In this work, it is shown that a dislocation density based flow stress model can account for precipitate hardening. Considering the simplifications that are necessary, the material model shows good agreement with experimental measurements and is expected to be fit for its purpose; thermo-mechanical simulation of the ageing process in IN718.

References

- [1] J. Boyd and R. Nicholson. The coarsening behaviour of θ'' and θ' precipitates in two al-cu alloys. *Acta Metallurgica*, 19(12):1379 – 1391, 1971.
- [2] A. Deschamps and Y. Brechet. Influence of predeformation and ageing of an al-zn-mg alloy- ii. modeling of precipitation kinetics and yield stress. *Acta Materialia*, 47(1):293–305, 1998.
- [3] A. Devaux, L. Nazé, R. Molins, A. Pineau, A. Organista, J. Guédou, J. Uginet, and P. Héritier. Gamma double prime precipitation kinetic in alloy 718. *Materials Science and Engineering: A*, 486(1-2):117 – 122, 2008.
- [4] L.-E. Lindgren, K. Domkin, and S. Hansson. Dislocations, vacancies and solute diffusion in physical based plasticity model for aisi 316l. *Mechanics of Materials*, 40(11):907–919, 2008.

Proceedings of the 25TH NORDIC SEMINAR
COMPUTATIONAL MECHANICS, 2012

Dynamics

Room: 304, Friday 26 October, 10:00 - 12:00



Comparison of vibration suppression of flexible rotors supported by passive and controllable constraint elements during passing their critical speeds

Jaroslav Zapoměl¹, and Petr Ferfecki²

⁽¹⁾VŠB-Technical University of Ostrava, Department of Mechanics, 17.listopadu 15, Ostrava-Poruba, Czech Republic, jaroslav.zapomel@vsb.cz

⁽²⁾VŠB-Technical University of Ostrava, Center of Excellence IT4 Innovations, 17.listopadu 15, Ostrava-Poruba, Czech Republic, petr.ferfecki@vsb.cz

Summary. Lateral vibration of rotating machines can be significantly reduced if damping devices are added to the constraint elements coupling the rotor and its casing. To achieve their optimum performance their damping effect must be controllable. The proposed constraint element is equipped with an electric coil generating magnetic field. It works on the principle of squeezing two concentric films formed by normal and magnetorheological oils. As the flow of the magnetorheological liquid depends on magnetic induction, the change of electric current can be used to control the damping force. The computational simulations proved that the proposed constraint element enabled to minimize the rotor vibration in the whole extent of the running velocities in contrast to application of normal (uncontrollable) squeeze film dampers frequently used to vibration reduction of rotating machines.

Key words: flexible rotors, passing critical speed, magnetorheological damping element

Introduction

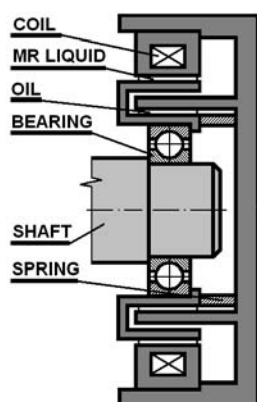


Figure 1.

A common technological solution of reducing lateral vibration of rotors excited by imbalance forces is placing damping devices between the rotor and its casing. To achieve their optimum performance their damping effect must be controllable.

For this purpose a concept of a new damping element has been proposed [1]. In fact, it represents a combination of classical and magnetorheological squeeze film dampers (figure 1). As resistance against the flow of magnetorheological fluid depends on magnetic induction, the change of electric current generating magnetic flux can be used to control the damping force.

Efficiency of the proposed controllable constraint element was evaluated by comparing its performance with those of classical squeeze film dampers which are frequently used for reducing vibrations of rotating machines.

Mathematical model of the proposed constraint element

It is assumed in the developed mathematical model of the proposed constraint element that its geometry and design make it possible to consider it as short and that it is symmetric relative to its middle plane. The pressure distribution in the lubricating layers is governed by Reynolds equations [2], [3]. The one referred to the magnetorheological oil (2) has been modified for Bingham material which was used to represent the magnetorheological lubricant

$$\frac{\partial^2 p_{CO}}{\partial Z^2} = \frac{12\eta}{h_{CO}^3} \dot{h}_{CO}. \quad (1)$$

$$h_{MR}^3 p_{MR}'^3 + 3(h_{MR}^2 \tau_y - 4\eta_B \dot{h}_{MR} Z) p_{MR}'^2 - 4\tau_y^3 = 0 \quad \text{for } Z > 0 \quad (2)$$

h_{CO} , h_{MR} denote the thicknesses of the films of classical and magnetorheological oils [2], p_{CO} denotes the pressure in the layer of the normal oil, η is its dynamic viscosity, p_{MR} , p_{MR}' denote the pressure and the pressure gradient in the axial direction in the layer of magnetorheological fluid, η_B is the Bingham dynamical viscosity, τ_y represents the yield shear stress, Z is the axial coordinate and $(\dot{})$ denotes the first derivative with respect to time. More details on solving equation (2) can be found in [3].

In the simplest design case the magnetorheological part of the proposed constraint element, can be considered as a divided core of an electromagnet. Then the dependence of the yield shear stress on magnetic induction can be approximately expressed

$$\tau_y = k_y \left(\frac{N_C I}{2 h_{MR}} \right)^{n_y}. \quad (3)$$

k_y and n_y are material constants of the magnetorheological liquid, N_C is the number the coil turns and I is the electric current.

In areas in the lubricating films where the pressure drops to a critical level a cavitation occurs. In the developed mathematical model it is assumed that pressure in cavitated regions remains constant and equal to the pressure in the ambient space. Components of the damping force are then calculated by integration of the pressure distributions in both lubricating films around the circumference and along the length of the constraint element.

The classical squeeze film damper produce damping in one lubricating layer formed by normal oil. Its mathematical model and the procedure for determination of the damping force is analogous to those of the proposed constraint element.

Computational simulations

The investigated rotor is flexible with one disc (figure 2). It turns at variable angular speed and is loaded by its weight and by the disc unbalance. The rotor is supported at both its ends: in the first design variant by normal squeeze film dampers, in the second variant by the proposed constraint elements. In both cases the squirrels prings are prestressed to be eliminated their deflection caused by the weight of the rotor.

In the computational model the rotor was represented by a Jeffcott one and the constraint elements by springs and force couplings. The task was to analyse the rotor vibration during its acceleration to study efficiency of the proposed constraint device.

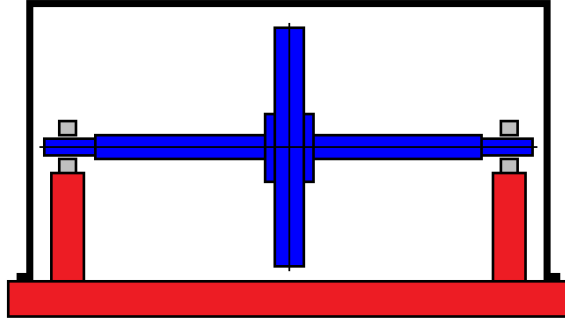


Figure 2.

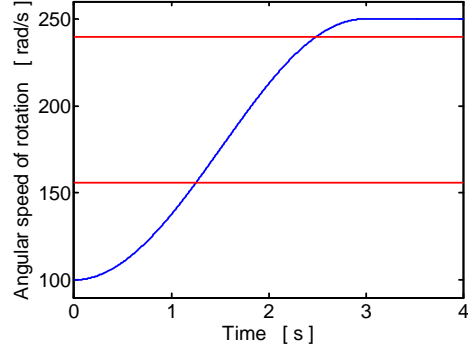


Figure 3.

Vibration of the investigated rotor system is governed by a set of four nonlinear differential equations of the first and second order

$$m\ddot{y} = -b_p\dot{y} - k_S y + k_S y_B + me_T \dot{\vartheta}^2 \cos \vartheta + me_T \ddot{\vartheta} \sin \vartheta \quad (4)$$

$$m\ddot{z} = -b_p\dot{z} - k_S z + k_S z_B + me_T \dot{\vartheta}^2 \sin \vartheta - me_T \ddot{\vartheta} \cos \vartheta - mg \quad (5)$$

$$0 = k_S y - (k_S + 2k_B) y_B + 2F_{dy} \quad (6)$$

$$0 = k_S z - (k_S + 2k_B) z_B + 2F_{dz} \quad (7)$$

m is the disc mass, k_S is stiffness of the shaft, k_B is stiffness of each squirrel spring, b_p is the coefficient of the disc external damping, e_T is eccentricity of the disc centre of gravity, g is the gravity acceleration, y , z , y_B , z_B are displacements of the disc and shaft journal centres in the horizontal and vertical directions, ϑ is the angle of the disc rotation, F_{dy} , F_{dz} are the y and z components of the damping force and $(\ddot{\cdot})$ denotes the second derivative with respect to time.

Time histories of lateral displacements of the disc centre for three constant magnitudes of the applied current are depicted in figure 4. The results show that for lower angular velocities of the rotor rotation higher current arrives at reducing amplitude of the rotor vibration and this reduction is significant especially in the resonance area. But in the interval of higher angular speeds increasing current leads to rising the vibration amplitude. This implies that a suitable control of the applied current according to angular velocity of the rotor rotation makes it possible to minimize amplitude of the rotor vibration in the whole extent of its running speeds. Time history of the disc centre displacement in the horizontal direction drawn in figure 6 correspond to the current control carried out according to the diagram in figure 5.

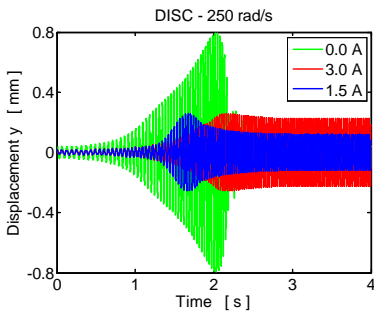


Figure 4.

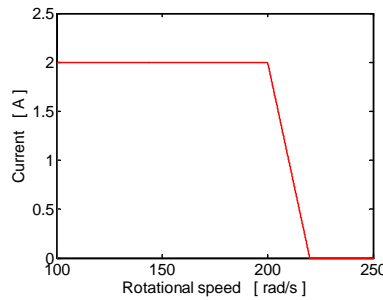


Figure 5.

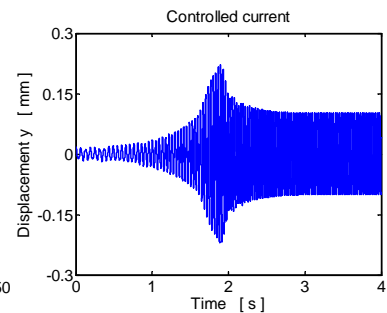


Figure 6.

To study efficiency of the proposed constraint element its performance was compared with performance of three variants of normal squeeze film dampers whose design solution differ in the width of the clearance (100 μm , 200 μm , 300 μm) which determines magnitude of the damping force. The results are summarized in figure 7. It is evident that in all cases the proposed controllable constraint device attenuates the rotor vibration more efficiently and suppresses significantly the resonance peaks.

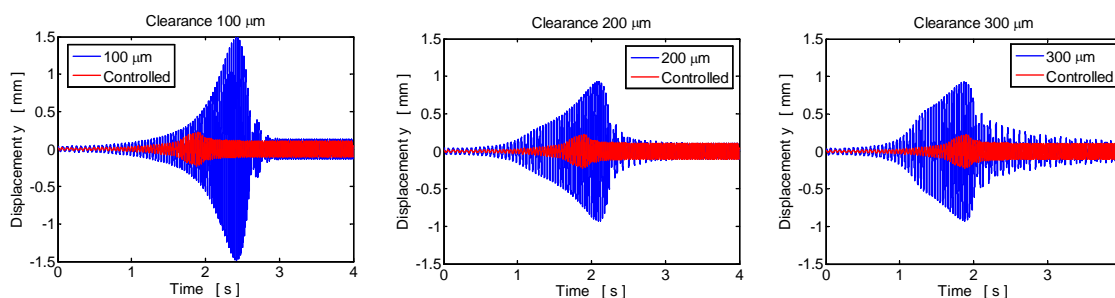


Figure 7.

Conclusions

The proposed constraint element attenuates the rotor lateral vibration due to squeezing the films of normal and magnetorheological oils. It is equipped with an electric coil generating magnetic flux passing through the layer of magnetorheological lubricant and as its flow depends on magnetic induction the change of electric current makes it possible to control the damping force. The carried out computer simulations showed that its properties were strongly nonlinear. They confirmed that if the damping force was suitably adapted to the rotor angular speed its vibration could be minimized in the whole extent of the running velocities in contrast to application of commonly used classical (uncontrollable) squeeze film dampers. Advantage of the proposed constraint element is that it does not require an expensive and complicated control system for its operation. Its magnetorheological part works as an auxiliary damping device which can be switched on only if required by the operating conditions. This enables to simplify the design solution of the proposed constraint element and to reach its lower consumption of magnetorheological oil.

This work was supported by the research projects P101/10/0209 and MSM 6198910027.

References

- [1] J. Zapoměl, P. Ferfecki, Stability investigation of the steady state response of flexibly supported rigid rotors attenuated by a new controllable damping element working on the principle of squeezing thin layers of classical and magnetorheological fluids, *Vibration Problems ICOVP 2011, Springer Proceedings in Physics*, 139: 521-527, 2011.
- [2] E. Krämer, *Dynamics of Rotors and Foundations*, Springer-Verlag, 1993.
- [3] J. Zapoměl, P. Ferfecki, L. Čermák, A computational method for determination of a frequency response characteristic of flexibly supported rigid rotors attenuated by short magnetorheological squeeze film dampers, *Applied and Computational Mechanics*, 5(1): 101-110, 2011.

Optimal Brain Surgeon on Artificial Neural Networks in Nonlinear Structural Dynamics

Niels H. Christiansen^{1,2}, Jonas Hultmann Job³, Katrine Klyver⁴, and Jan Høgsbrg¹

⁽¹⁾Department of Mechanical Engineering, Technical University of Denmark, Kgs. Lyngby, Denmark

⁽²⁾DNV Denmark, Hellerup, Denmark

⁽³⁾Rambøll Danmark - Offshore Wind, Copenhagen, Denmark

⁽⁴⁾NOV Flexibles, Broendby, Denmark

Summary. It is shown how the procedure known as optimal brain surgeon can be used to trim and optimize artificial neural networks in nonlinear structural dynamics. Beside optimizing the neural network, and thereby minimizing computational cost in simulation, the surgery procedure can also serve as a quick input parameter study based on one simulation only.

Key words: Nonlinear structural dynamics, Artificial neural networks, Optimal brain surgeon.

Introduction

Time domain simulation of nonlinear systems using finite element method (FEM) analysis can be computationally very expensive. One method that has shown to be very time saving is the use of artificial neural networks (ANN). In the literature it has been shown on various types of structures how this method can reduce calculation time by up to two orders of magnitude [1, 2]. However, a major problem with this method is the difficulty of developing a robust algorithm that automatically generates an optimized ANN for a given structure. In this paper it is shown how a trained ANN can be further optimized and reduced in size by the procedure known as optimal brain surgeon (OBS). This procedure prunes the least salient network weights in an ANN. Besides trimming the network this operation can be used as a quick ranking of the importance of the various inputs that go into the analysis. Dynamic response of structures often depends on several external loads. By applying the OBS procedure to a trained ANN it is possible to determine which of these external force components that play the least significant role and also evaluate if one or more components can be ignored completely in the analysis. Hence, the OBS procedure can serve as an input parameter study based on one simulation only.

Artificial neural networks and optimal brain surgeon

Artificial neural networks are in principal mathematical models that replicate the human brain's impressive ability to do high speed pattern recognition. They serve as tools which perform nonlinear mapping between a given input and a corresponding output without time consuming equilibrium iterations. There exists vast literature on the fundamentals of neural networks and the philosophy behind. Since the ANN is not the main object in this paper it will be left to the reader to consult e.g. [3] for further information on that topic. Here it will just be mentioned that an ANN with one input layer, one hidden layer with tangent hyperbolic as activation

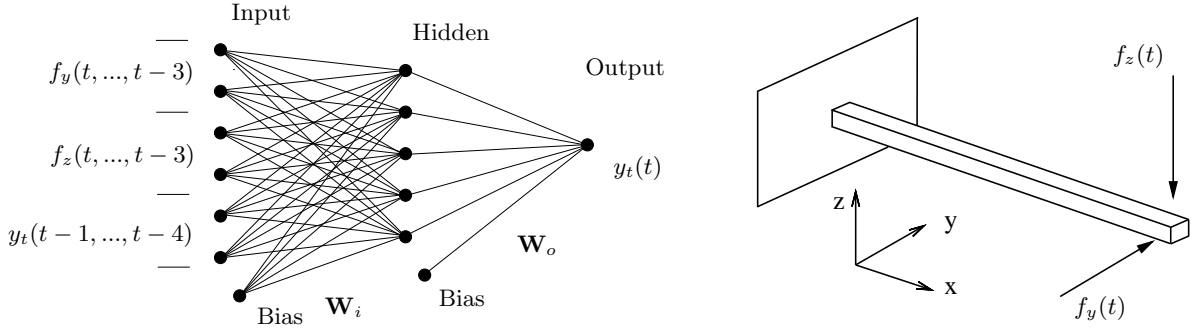


Figure 1. Left: ANN with one hidden layer. Right: Model of cantilevered beam.

function and a linear output layer as sketched in the left part of figure 1 is used in the following study.

OBS is a procedure that prunes the least salient network weights in a trained ANN. When training an ANN the first derivative of the error function is used to find the direction in which to step in weight space in order to minimize the error. The OBS procedure uses the second derivative to find the curvature of the error function in weight space. That information can be used to arrange all network weights and to find out which weight is least salient and thereby 'cheapest' to delete [4]. The saliency of a weight q is calculated by

$$L_q = \frac{1}{2} \frac{w_q^2}{[\mathbf{H}^{-1}]_{qq}}, \quad (1)$$

where \mathbf{H}^{-1} is the inverse of the Hessian matrix ($\mathbf{H} \equiv \partial^2 E / \partial \mathbf{w}^2$) containing all second order derivatives. Having found the least salient weight we can update the rest of the weights using

$$\delta \mathbf{w} = - \frac{w_q}{[\mathbf{H}^{-1}]_{qq}} \mathbf{H}^{-1} \cdot \mathbf{e}_q, \quad (2)$$

where \mathbf{e}_q is the unit vector in weight space. The inverse Hessian is calculated directly using a slightly modified version of the Sherman-Morrison formula (3) and a single sequential pass through the training data $1 \leq m \leq P$.

$$\mathbf{H}_{m+1}^{-1} = \mathbf{H}_m^{-1} - \frac{\mathbf{H}_m^{-1} \mathbf{X}_{m+1} \cdot \mathbf{X}_{m+1}^T \cdot \mathbf{H}_m^{-1}}{P + \mathbf{X}_{m+1}^T \mathbf{H}_m^{-1} \mathbf{X}_{m+1}}, \quad (3)$$

where P is the number of training data sets.

So the procedure is to take a network that has been trained to a local minimum, calculate \mathbf{H}^{-1} using (3), find the network weight that gives the smallest saliency using (1), and determine the adjustment of the network weights (2). This procedure can in principal be repeated until all weights are deleted. However, after each deletion of the cheapest weight one can evaluate the increase in error and see if it exceeds an acceptable level. In that case the procedure must be stopped.

Structural model

To demonstrate the OBS method a 3D FEM model of a cantilevered beam is set up. The beam has the properties listed in table 1 and is shown to the right in figure 1. The model uses the co-rotational beam element formulation as described in [5]. Hence, it is a nonlinear model able to handle large rotations and deflections. The beam model is divided into five elements of equal length and is damped through Rayleigh damping. The beam is subject to two stochastic load histories working in two different directions at the beam tip. The two load histories are

l	E	I_y	I_z	A	ρ
10 m	$1 \cdot 10^5$ MPa	$1 \cdot 10^4$ mm ⁴	$1 \cdot 10^5$ mm ⁴	$1 \cdot 10^5$ mm ²	$1 \cdot 10^5$ kg/m ³

Table 1. Beam properties

different but have equal characteristics in terms of mean value, standard deviation and dominant frequency. The load has a mean of 2.7 kN with a standard deviation of 0.3 kN and a dominating frequency around 0.7 Hz. The response of the beam is calculated by Newmark’s method of direct integration. The Newton-Raphson method is used to achieve force equilibrium in each time step, i.e. to update system matrices in accordance with the procedures described in [5]. Time step size is 0.1 sec. and equilibrium is assumed when force and displacement residuals are below 1×10^{-6} .

Data generated by the FEM is used to train an ANN to predict the horizontal response $y_t(t)$ of the beam tip. A 400 sec. simulated response history is divided into 3 sets. The first set is used for training the ANN, the second set is used for testing and the last set is saved to demonstrate the accuracy of the pruned ANN on new data. The ANN has 40 neurons in the hidden layer and 13 neurons in the input layer. The network input vector consists of the four previous time steps of the tip response and the two loads, as indicated in figure 1. This gives a $[13 \times 40]$ weight matrix \mathbf{W}_i between input and hidden layer and a $[40 \times 1]$ weight matrix \mathbf{W}_o between hidden and output layer.

One step in the OBS procedure is to evaluate the network error each time a network weight is deleted. Depending on the structure and the type of analysis carried out one must decide an error increase tolerance for when to stop the deletion of weights. Figure 2 shows how the network error increases with the number of deleted weights. It is seen that it is possible to delete about half the weights without increasing the network error considerably.

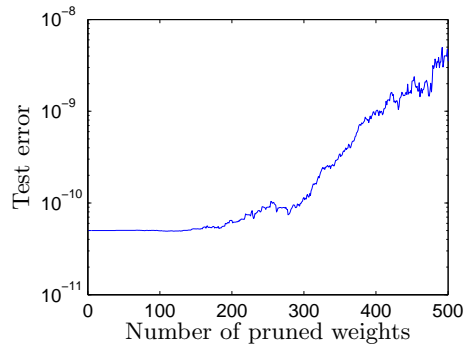


Figure 2. Test error vs. number of pruned weights.

Figure 3 shows response histories calculated by the FEM model and the pruned ANN. It is seen that even though almost half of the network connections have been deleted the ANN still predicts the horizontal deflection very accurately. Note that the ANN in this case simulates about two orders of magnitude faster than the FEM. If we examine the input weight matrix \mathbf{W}_i containing all connection weights between the input layer and the hidden layer it is possible to do some interpretation of the importance of the input variables.

As the procedure deletes the least important weights and since the loads on the beam are arranged in the network input vector it is possible to evaluate the importance of the loads and whether one or more inputs can be neglected. The pruned weight matrix $\mathbf{W}_{i,prune}$ is written below. As actual values of individual weights are unimportant for this evaluation of the pruned matrix positive and negative weights are marked by $+/-$ while deleted weights are denoted 0. It is seen that the load in the z -direction is almost completely ruled out by the OBS and thereby

A SEMI-ANALYTICAL MODEL FOR FREE VIBRATIONS OF OFFSHORE FREE SPANNING PIPELINES

Knut Vedeld¹, Håvar Sollund¹

⁽¹⁾ Mechanics Division Department of mathematics University of Oslo, Molte Moes vei 35, Pb 1053, 0316 Oslo, E-mail: knutved@math.uio.no

Summary.

An exact analytical solution to the Euler-Bernoulli beam on a partial elastic foundation is presented. The solution is based on a Rayleigh-Ritz approach and the displacement assumption is taken as a Fourier sine series. The model evades complex time consuming FE modeling and is more accurate than the simple semi-empirical formulae of Fyrileiv & Mørk [1]. The methodology is easily implemented and determines static and harmonic response with excellent accuracy. Compared to the solution of Fyrileiv & Mørk [1], accuracy is increased and the range of applicability is extended. The solution is validated based on comparisons to detailed FE analyses.

Introduction

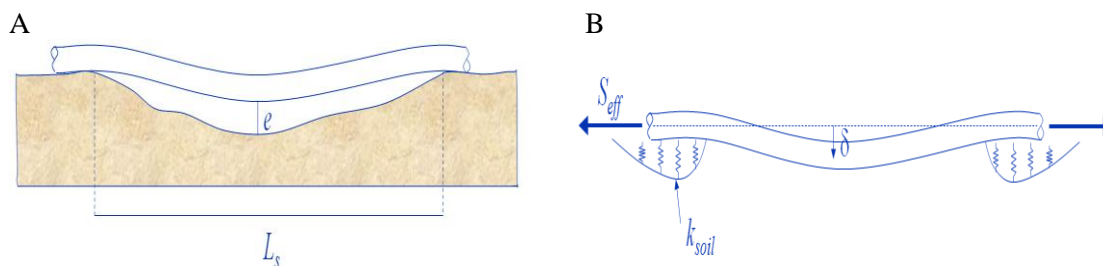


Figure 1 – Panel A: Typical pipeline free span configuration. Panel B: Free span modeling and nomenclature

Fig. 1 displays a typical pipeline free span scenario. In Panel A, the gap e is the distance between bottom of pipe and the seabed. The length is termed L_s . The total effective mass m_e is used for dynamic analyses and taken as the sum of the dry and the added mass. In Panel B, the static vertical displacement δ is the static displacement at mid span due to submerged weight and the effective axial force. For the purpose of this paper, the pipe-soil interaction will be modeled according to DNV-RP-F105 [2], applying linear soil stiffness, given as k_{soil} in Panel B. The effective axial force for an axially constrained pipe $S_{eff,i}$, Ref. [3], is defined as:

$$S_{eff,i} = H_{eff} - \Delta p_i A_i (1 - 2\nu) - A_s E \Delta T \alpha . \quad (1)$$

In Eq (1), H_{eff} is the residual lay tension, Δp_i is the internal pressure difference relative to laying, A_i is the internal area of the pipe cross-section, A_s is the steel cross-sectional area, E is the Young's modulus, ΔT is the temperature difference relative to laying and α is the temperature expansion coefficient.

Methodology

Three solutions are necessary to generate in order to determine the harmonic response of free spans:

1. A solution for the static equilibrium case where the pipe is subject to its submerged weight q and effective axial force S_{eff} .
2. A solution to determine the Eigen-frequencies, later referred to simply as frequencies, and associated Eigen-modes, later referred to as mode shapes, for the linearized harmonic Eigen-value problem in in-line direction subject to pipe effective mass m_e and effective axial force in equilibrium configuration S_{eff} .
3. A solution to determine frequencies and mode shapes for the linearized harmonic Eigen-value problem in cross-flow direction, accounting for the stiffening effect of vertical static displacement, effective mass m_e and effective axial force in equilibrium configuration S_{eff} .

The equilibrium effective axial force is calculated according to Eq. (2) below, where the axial strain caused by static deformation is estimated:

$$S_{eff} = S_{eff,i} + \frac{EA}{L} \left(\int_0^L \sqrt{1 + (v_s')^2} dx - L \right) \approx S_{eff,i} + \frac{EA}{2L} \int_0^L (v_s')^2 dx . \quad (2)$$

In Eq. (2), $S_{eff,i}$ is the initial effective axial force prior to application of static loading and v_s is the vertical static displacement. In a curvilinear coordinate system, the only non-zero strain component is the tangential strain ε_{tt} given by, Ref. Tarnopolskaya [4]:

$$\varepsilon_{tt} = \frac{1}{1 - \kappa y} \left(\frac{\partial u_r}{\partial s} - \kappa u_r \right) = \frac{1}{1 - \kappa y} \left[\frac{\partial u_0}{\partial s} - \kappa v_0 - y \frac{\partial}{\partial s} \left(\frac{\partial v_0}{\partial s} + \kappa u_0 \right) \right] \quad (3)$$

where the unknown displacements u_0 and v_0 are the tangential and the normal displacements, respectively, of a point on the centroidal axis. From Eq. (3) the following differential operator can be determined:

$$\mathbf{d} = \begin{bmatrix} d_{u_0} & d_{v_0} \end{bmatrix} = \frac{1}{1 - \kappa(s)y} \begin{bmatrix} \frac{\partial}{\partial s} - y \frac{\partial}{\partial s} \kappa(s) & -\kappa(s) - y \frac{\partial^2}{\partial s^2} \end{bmatrix} \quad (4)$$

Based on a Fourier sine approximation to u_0 and v_0 , and assumed linear soil stiffness parameters, the expressions for the displacements, stiffness and mass matrices become:

$$\begin{aligned}
\mathbf{u} &= \begin{bmatrix} u_0 \\ v_0 \end{bmatrix} = \begin{bmatrix} \mathbf{N}_u & \mathbf{0} \\ \mathbf{0} & \mathbf{N}_v \end{bmatrix} \begin{bmatrix} \mathbf{D}_u \\ \mathbf{D}_v \end{bmatrix} = \mathbf{ND} \quad \text{where} \quad \mathbf{N}_u = \mathbf{N}_v = \begin{bmatrix} \sin\left(\frac{\pi s}{L}\right) & \sin\left(\frac{2\pi s}{L}\right) & \dots \end{bmatrix} \\
\mathbf{M} &= \int_0^L m_e \mathbf{N}^T \mathbf{N} ds \\
\mathbf{K}_{struc} &= E \int_V (\mathbf{dN})^T (\mathbf{dN}) dV = \begin{bmatrix} \mathbf{K}_{11} & \mathbf{K}_{12} \\ \mathbf{K}_{21} & \mathbf{K}_{22} \end{bmatrix} \\
\mathbf{K}_{11} &= EA \int_0^L \mathbf{N}_{u,s}^T \mathbf{N}_{u,s} ds + EI \left(\int_0^L \kappa^2 \mathbf{N}_{u,s}^T \mathbf{N}_{u,s} ds + \int_0^L \kappa_{,s}^2 \mathbf{N}_u^T \mathbf{N}_u ds + \int_0^L \kappa \kappa_{,s} (\mathbf{N}_{u,s}^T \mathbf{N}_u + \mathbf{N}_u^T \mathbf{N}_{u,s}) ds \right) \\
\mathbf{K}_{12} &= -EA \int_0^L \kappa \mathbf{N}_{u,s}^T \mathbf{N}_v ds + EI \left(\int_0^L \kappa \mathbf{N}_{u,s}^T \mathbf{N}_{v,ss} ds + \int_0^L \kappa_{,s} \mathbf{N}_u^T \mathbf{N}_{v,ss} ds \right) \quad \text{and} \quad \mathbf{K}_{21} = \mathbf{K}_{12}^T \\
\mathbf{K}_{22} &= EA \int_0^L \kappa^2 \mathbf{N}_v^T \mathbf{N}_v ds + EI \int_0^L \mathbf{N}_{v,ss}^T \mathbf{N}_{v,ss} ds \\
\mathbf{K}_{soil} &= \int_0^L \begin{bmatrix} k_{soil,A} \mathbf{N}_u^T \mathbf{N}_u & \mathbf{0} \\ \mathbf{0} & k_{soil} \mathbf{N}_v^T \mathbf{N}_v \end{bmatrix} ds - \int_{L_{shoulder}}^{L_{shoulder}+L} \begin{bmatrix} k_{soil,A} \mathbf{N}_u^T \mathbf{N}_u & \mathbf{0} \\ \mathbf{0} & k_{soil} \mathbf{N}_v^T \mathbf{N}_v \end{bmatrix} ds \\
\mathbf{K}_g &= \int_0^L \begin{bmatrix} \mathbf{0} & \mathbf{0} \\ \mathbf{0} & \mathbf{N}_{v,s}^T \mathbf{N}_{v,s} \end{bmatrix} ds \\
\mathbf{K} &= \mathbf{K}_{struc} + S_{eff} \mathbf{K}_g + \mathbf{K}_{soil}
\end{aligned} \tag{4}$$

Results

20 representative cases were selected and compared between the presented analytical solution and FE modeling using PIPE31 elements in ABAQUS. Static sag, equilibrium effective axial force, modal frequencies for three modes in-line and three modes cross-flow, and corresponding modal stresses were compared for all 20 cases. Relative differences between ABAQUS results and the analytical model presented herein were less than 1% for all compared parameters and all cases. Based on the comparisons to FE-analyses, the semi-analytical model is considered verified and accurate.

Comparing results for the semi-empirical model of Fyrileiv & Mørk [1], comparisons for the fundamental frequency and associated modal stresses are presented for one representative case:

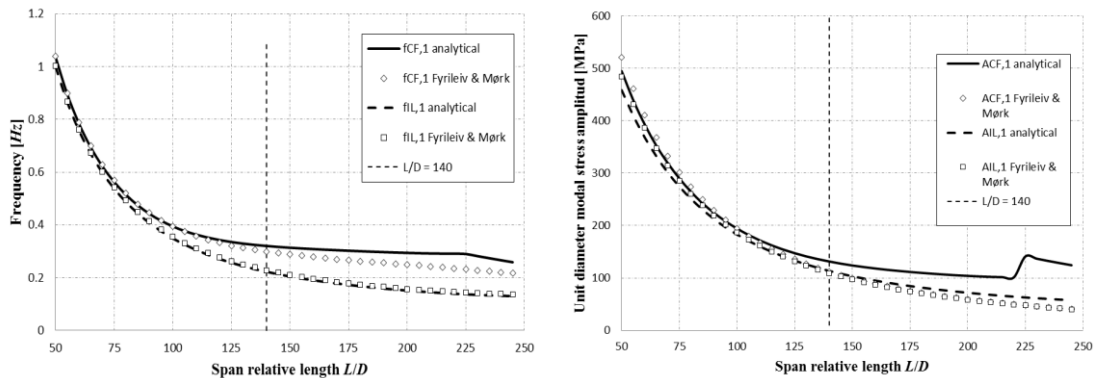


Figure 4 – Comparisons between semi-analytical solutions and the semi-empirical formulae of Fyrileiv & Mørk for fundamental frequencies and associated modal stresses

From Fig. 4 it is observed that the in-line fundamental frequency calculated by the two methodologies constitutes a substantial match. The biggest relative difference between the two methodologies is 4.6%, with relative differences increasing for increasing L/D. Consequently, the semi-empirical model gives excellent predictions for in-line fundamental frequencies also for $L/D > 140$ in the present example. For $L/D < 100$, the semi-empirical model predicts frequencies very accurately but for increasing L/D it underestimates frequencies cross-flow. The largest relative difference between the models is 24.9%, but limited to 7.1% if $L/D < 140$. There are two reasons why the cross-flow frequency is less accurately predicted by the semi-empirical method than the in-line frequency. Firstly, the sag correction in the semi-empirical model is only approximate. The second reason may be observed for relative length 225. For this length, the present example yields a static mid-span deflection of 5D. For large vertical static deflections, the stiffening effect introduced by the static deformation configuration suppresses the first symmetric cross-flow mode, and the first anti-symmetric mode achieves the lower frequency.

The maximum relative differences for unit diameter stress amplitudes in-line and cross-flow, disregarding $L/D > 225$ cross-flow, is 43% in-line and 50.7% cross-flow. If $L/D < 140$, these relative differences decrease to 5.4% in-line and 14.7% cross-flow. Consequently, the analytical model of Fyrileiv & Mørk is more accurate for estimating frequencies compared to modal stresses.

Conclusions

- The semi-analytical methodology developed in this paper is accurate to within 1% deviation compared to detailed FE analyses, regardless of free span lengths, level of effective axial force and static deformation configuration.
- Euler-Bernoulli beam theory is sufficient with regard to pipeline free span modeling, since shear deformation has been shown not to influence the static and dynamic response behavior.
- The semi-analytical model is more than 600 times faster than typical detailed FE analyses with no loss of accuracy.
- Compared to the semi-empirical method developed by Fyrileiv & Mørk, the semi-analytical model developed in this paper has better accuracy, particularly on modal stresses, and no limitations on range of validity.

References

- [1] Fyrileiv, O. & Collberg, L. "Influence of pressure in pipeline design – effective axial force", Proc. of 24th int. conf. on offshore mechanics and arctic engineering. OMAE 2005, Halkidiki, Greece, June 12-17.
- [2] DNV-RP-F105, "Free spanning pipelines", Feb. 2006
- [3] Fyrileiv, O. & Collberg, L. "Influence of pressure in pipeline design – effective axial force", Proc. of 24th int. conf. on offshore mechanics and arctic engineering. OMAE 2005, Halkidiki, Greece, June 12-17.
- [4] Tarnopolskaya, T., De Hoog, F., Fletcher, N.H. & Thwaites, S. "Asymptotic analysis of the free in-plane vibrations of beams with arbitrarily varying curvature and cross-section", Journal of sound and vibration, 1996, Vol. 196, pp. 659-680.

Analytical Stiffness Optimization of High-Precision Hexapods for Large Optical Telescope Applications

Behrouz Afzali Far^{1,2}, Per Lidström¹, Kristina Nilsson¹, and Arne Ardeberg²

(1) Division of Mechanics, Lund University, Lund, Sweden,
Behrouz.Afzali_Far@mek.lth.se, Per.Lidstrom@mek.lth.se,
Kristina.Nilsson@mek.lth.se

(2) Lund Telescope Group AB, Trollebergsvägen 5, Lund, Sweden,
Arne.Ardeberg@ltgab.se

Summary. An analytical stiffness and eigenfrequency model of symmetric parallel 6-6 Stewart platforms (hexapods) is developed based on geometrical design variables to optimize the dynamical performance. The model is based upon Lagrangean dynamics in which the Bryant angles are used for the kinematics formulation. With the analytical eigenfrequency model, optimum stiffness characteristics can be obtained for any industrial application with limited workspace such as optical collimation systems. The actuator length-flexibility dependency is also considered in the analytical model. It is proposed that to increase the actuation bandwidth in six degrees of freedom, an eigenfrequency cost function can be defined and optimized.

Key words: Gough Stewart platform, hexapod, analytical, stiffness, eigenfrequency, telescope

Introduction

Cassegrain-type [1] large optical telescopes for astronomy have two mirrors; the secondary mirror (M2) is the optical element which reflects the light collected by the primary mirror (M1) to the scientific instrument (figure 1). Active collimation of M2 corrects image-quality defects due to structure deformations caused by gravity and thermal variations. Due to the tracking velocity of optical telescopes, the bandwidth required is approximately 0.01 Hz [2]. The image-quality of a stable telescope with a well-figured M1 surface and well-collimated M2 is limited by the atmospheric disturbances. Further improvement of the image-quality requires correction of at least first-order defects due to the atmospheric disturbances as well as errors caused by telescope structural vibrations. Such first-order defects of atmospheric disturbances can be compensated by tilting M2 with a sufficient high bandwidth. In practice, tilting is responsible for a major part of the image degradation caused by the atmosphere. Given the importance of tilting, major improvements of observed image-quality can be achieved through two-axes rotations (tip-tilt), first-order compensatory movements of M2 [3]. Successful operation requires a very stiff yet light-weight system including the active mechanism, M2 and its support structure. The tip-tilt movements are controlled with a bandwidth of at least 10 Hz, in closed-

loop mode via an optical sensor. The corresponding angular range should be several arcsec. The system will, in addition to effects of atmospheric disturbances, correct for image degradation due to structural vibrations caused by wind buffeting. Mainly due to precision and stiffness requirements for the collimation system of M2, high-precision hexapods can be used in large telescopes [4]. For further improvements of image-quality, a stiff high-bandwidth hexapod can provide three additional useful degrees of freedom (decentering in two axes and focusing) compared with only using tip-tilt.

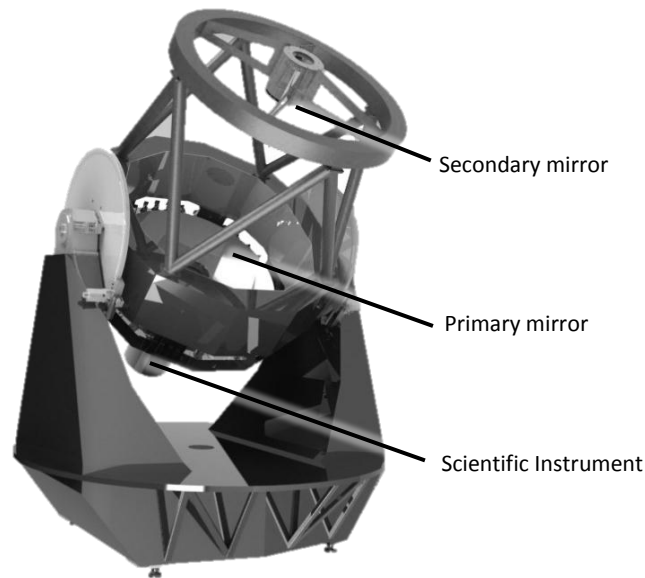


Figure 1. Model of a Cassegrain-type large optical telescope

Hexapods have attracted the attention of researchers and designers since the time it was first introduced by Stewart in 1965. A hexapod is the minimum arrangement of a parallel robot to provide six degrees of freedom. Hexapods are also known as Stewart platforms or Gough-Stewart platforms which have a wide range of precision engineering applications such as in machining technology, astronomical telescopes and surgical robots [5]. Parallel robots in general and hexapods in particular have some advantages over serial robots. Among these advantages, for the large optical telescope application which is the interest of this paper, precision and stiffness are of great importance. Much research has been carried out on the kinematics of hexapods, but few on stiffness [6,7]. The stiffness matrix can be obtained using Jacobian matrix methods or as a product of force and deformation related matrices [8]. The stiffness matrix can also be assembled from the linearization of the equations of motion. There are some studies about the workspace evaluation based on stiffness [9]. H. Jiang [10,11] calculates the eigenfrequencies and studies geometric conditions leading to equal eigenfrequencies, however, the length-flexibility dependency and optimum geometries using an eigenfrequency cost function remain to be evaluated.

This abstract introduces an analytical eigenfrequency model for hexapods, based on the geometrical design variables to optimize the geometry restricted by eigenmodal requirements. Geometrical variables of hexapods are important, especially in the telescope applications where the workspace is quite limited. Therefore, to increase the actuation bandwidth and precision for all six degrees of freedom, which are limited by the eigenfrequencies of any system, optimization of the hexapod geometry is a key objective.

Stiffness and eigenfrequency Modeling

In the present study, formulation of the stiffness model of hexapods starts with solving the reverse kinematics of the system. Reverse kinematics means obtaining the length of each actuator with a given configuration of the platform (figure 2). The kinematics is formulated using a general geometry of symmetric hexapods. There are totally 12 nodes on the planar base (figure 2) and the planar platform where the actuator ends are attached with spherical joints. All the joint nodes of each platform are located on a circle with an arrangement leading to three pairs of actuators with 120 degrees axial symmetry in the neutral configuration. The base and the platform are considered rigid but the actuators are flexible elements without mass. The geometrical design variables are; the ratio of the base and platform radii, the ratio of the height of the hexapod over the base radius, and the angles between the nearest two nodes on each platform.

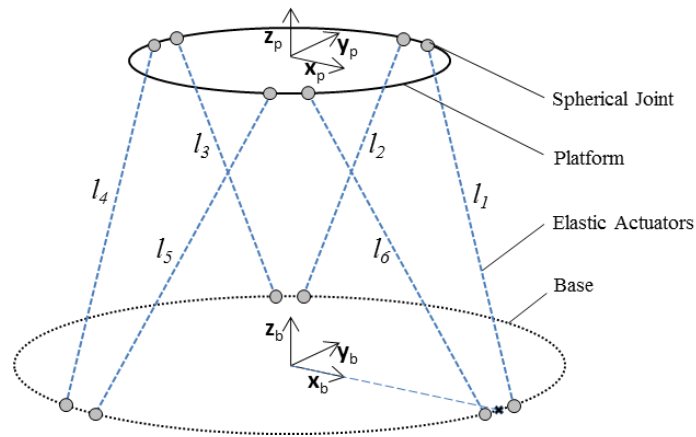


Figure 2. A general symmetric 6-6 Stewart platform

By assuming small angles, which is the case in vibrations, the choice of Bryant angles for the rotation matrix leads to a very simple formulation for the angular velocity and it is shown that these angles are decoupled for all six eigenmodes of symmetric hexapods. In addition to the simplicity of equations, the nonsingularity for small angles is an advantage of the Bryant angles.

The equations of motion of the system are solved with the Lagrangean dynamics approach. Stiffness modeling is based on two generalized coordinate systems, Cartesian and length coordinates. Analytical Stiffness and mass matrices for both coordinate systems are developed. Furthermore, the analytical eigenfrequencies of the system as well as the eigenmodes are formulated based on the geometric design variables.

To avoid optimum results on the boundary of the design variables domain and to consider stiffness practicalities, the flexibility of each actuator is assumed to be proportional to its length in the neutral configuration. This realistic approach leads to analytical optimum values for each design variable based on the requirements of the system dynamical performance.

To reduce the system of six equations for each eigenfrequency, an eigenfrequency cost function is defined which is driven mainly by the minimum eigenfrequency. The method presented is an analytical approach to design an optimal hexapod with the maximum dynamical performance.

Conclusion

In the present work, an analytical eigenfrequency model of a general symmetric hexapod is formulated based on geometrical design variables for optimizing stiffness of limited workspace applications such as in large optical telescopes. High-precision hexapods can be used as an active mechanism for large telescopes to collimate mirrors against gravity and temperature in low bandwidth, and to improve the image-quality by compensating for structural vibrations and atmospheric disturbances in high bandwidth. The stiffness model is based on the equations of motion, using Lagrangean dynamics. To avoid singularity and to have simpler eigenfrequency equations, Bryant angles have been chosen for the generalized kinematic modeling. It is suggested that to increase the actuation bandwidth of such a system, an eigenfrequency cost function can be defined and optimized to avoid resonances in six degrees of freedom. It is also concluded that, considering the actuators length-flexibility dependency, more realistic optimum results can be obtained.

References

- [1] Torben Andersen, Anita Enmark, *Integrated Modeling of Telescopes*, Springer New York, 2011.
- [2] Pierre Y. Bely, *The Design and Construction of Large Optical Telescopes*, Springer, 2003
- [3] Roddier, Francois; Northcott, Malcolm; Graves, J. Elon, A simple low-order adaptive optics system for near-infrared applications, *Astronomical Society of the Pacific*, 103:131-149, 1991.
- [4] P. Schipani, L. Marty, Stewart platform kinematics and secondary mirror aberration control, *Optomechanical Technologies for Astronomy*, 62733B, 2006.
- [5] Y. D. Patel, P. M. George, Parallel Manipulators Applications-A Survey, *Modern Mechanical Engineering*, 1(1): 57-64, 2012.
- [6] Bhaskar Dasguptaa, T.S. Mruthyunjaya, The Stewart platform manipulator: a review, *Mechanism and Machine Theory*, 35:15-40, 2000.
- [7] J. Chen, F. Lan, Instantaneous stiffness analysis and simulation for hexapod machines, *Simulation Modelling Practice and Theory*, 16:419-428, 2008.
- [8] Jokin Aginaga, Isidro Zabalza, Oscar Altuzarra, Jasiel Nájera, Improving static stiffness of the parallel manipulator using inverse singularities, *Robotics and Computer-Integrated Manufacturing*, 28(4):458-471, 2012.
- [9] V.T. Portman, V.S. Chapsky, Y. Shneor, Workspace of parallel kinematics machines with minimum stiffness limits: Collinear stiffness value based approach, *Mechanism and Machine Theory*, 49:67-86, 2012.
- [10] Hong-Zhou Jiang, Jing-Feng He, Zhi-Zhong Tong, Characteristics analysis of joint space inverse mass matrix for the optimal design of a 6-DOF parallel manipulator, *Mechanism and Machine Theory*, 45(5): 722-739, 2010.
- [11] Hong-zhou Jiang, Jing-feng He, Zhi-zhong Tong, Wei Wang, Dynamic isotropic design for modified Gough–Stewart platforms lying on a pair of circular hyperboloids, *Mechanism and Machine Theory*, 46(9):1301-1315, 2011

An analytical approach to solving the rigid sliding rod on the smooth walls

Ali Mohammadi¹, Mohammadhassan Mohammadi²

⁽¹⁾ Young Researchers Club, Shiraz Branch, Islamic Azad University, Shiraz, Iran,
Email: amohammadi@iaushiraz.ac.ir

⁽²⁾ Young Researchers Club, Shiraz Branch, Islamic Azad University, Shiraz, Iran,
Email: mohmoh@kth.se

Summary. This paper applies He's max-min method to solve analytically the nonlinear equations arising the motion of a rigid sliding rod on the smooth walls. Study of a dynamical system with high nonlinearity and under periodic forcing is one of the most important problems of nonlinear science. Therefore, an analytical approach for such problems could be interesting. Max- Min technique as a promising tool for solving nonlinear equations is employed and to show the efficiency and accuracy of the method a comparison is made with numerical solution developed by authors. Finally, it is shown that this method can simply be used in the same way for other problems in nonlinear dynamics and vibration

Key words: Max-Min method, Nonlinear oscillators, Sliding rod

Proceedings of the 25TH NORDIC SEMINAR
COMPUTATIONAL MECHANICS, 2012

Structural Mechanics II

Room: Lilla Hörsalen, Friday 26 October, 10:00 - 12:00



Multi-parametric stability investigations for pressurized thin membranes

Anders Eriksson

KTH Mechanics, Royal Institute of Technology
Osquars backe 18, SE-100 44 Stockholm, Sweden
anderi@kth.se

Summary. Pressurized thin membranes are frequently encountered in engineering and medical contexts. Membranes subjected to pneumatic pressurization respond by changing volume and internal over-pressure, and can exhibit different instability conditions. The response is significantly dependent on parameters for the loading, geometry and material. We used generalized equilibrium path and surface evaluation algorithms to describe and investigate the parameter dependence in different response aspects. We describe the algorithmic setting, but also give some aspects of quasi-static instability for pneumatically pressurized thin membranes. Two examples are used to illustrate the methodology and the obtainable results.

Key words: Thin membranes, Pneumatic pressurization, Multi-parametric setting, Instability

Introduction and formulation

A large variety of thin three dimensional pressurized structures are studied in engineering and medical contexts. In the present work, pneumatically loaded balloon-like structures were considered, with simulations based purely on the membrane behavior. Only quasi-static surface-normal pressure loads were present, demanding that any combination of pressure and volume can be immediately introduced, without dynamic or thermal effects. It was assumed that the pressure came from a compressible medium with negligible density. A hyper-elastic flat triangular membrane element in a total Lagrangian ('TL') reference frame was used for the large displacement analysis. The element is based on the common 'CST' (constant strain triangle), but includes full non-linear strain components, is restricted to local in-plane stresses, and assumes incompressibility. The pressure loading on a deformed geometry demands some consideration of the tangential stiffness matrix, used both in equilibrium iterations and as a quantitative stability indicator of equilibrium states. This tangential stiffness matrix is symmetric for a suitably closed structure, even if the element contributions are non-symmetric.

One main focus of the present work was the detailed phenomenological description of quasi-static structural instabilities. Evaluations of these are useful tools for understanding the behavior of many structures, particularly as they are often the attractors of dynamic response. The simulations demand methods for finding all occurring critical equilibrium states. This is thereby based on the diagonalization of the tangential stiffness matrix of the discretized problem, showing the principal stiffness directions and values.

The instability investigations of any class of optimized structures demand elaborate solution methods. Previous papers have described generalized path-following methods for non-linear quasi-static discretized structural problems. The methods thereby make possible the calculation of more general paths, e.g., the parameter dependence in different aspects of structural response: deflections, stresses, critical loads, et cetera. The term parameter dependence also implies that

these go beyond sensitivity investigations, but rather consider finite length deviations. The generalized equilibrium paths and surfaces allow the evaluation of these parameter dependent aspects in a systematic manner, giving important information on the generic behavior variations of a basic structure. The present work has focused on the dependence of the criticality (maximum and minimum pressures during inflation) on the constitutive constants in the Mooney-Rivlin hyper-elastic material model, on the criticality seen as related to either the pressure or the injected amount of gas, and on the effects of pre-stressing the membrane before pressurization, but also other types of parameterizations are used for illustration purposes.

The present work thereby discusses the numerical treatment of pneumatically pressurized membranes under different internal and ambient conditions. The details of a numerical finite element model are given in [1], and the path-following methods are discussed in [2, 3, 4, and further references therein].

Numerical demonstration

A finite element model of an inflated spherical membrane is used as the main numerical example, with variations of parameters for the membrane itself and the environment as the main objective. The necessary terms are, however, first introduced and described for a pre-stretched circular membrane.

Although essentially a one-dimensional problem, in order to see the behavior of the algorithms in a more general context, a detailed 5120 element model was used for the spherical membrane of radius $r = 10$ mm, thickness $t = 0.1$ mm, and shear modulus $\mu = 0.4225$ MPa. A temperature $T_c = 20$ °C and an ambient pressure $\psi^0 = 100$ kPa was assumed at initial inflation.

Basic tests introduced different ratios $k = c_2/c_1$ for the constitutive coefficients in the Mooney-Rivlin model. Pressure-expansion curves were evaluated for different k , Fig. 1(a), with non-linear response and critical states. Starting from equilibrium solutions B and C on the path for $k = 0.1$, the responses to the same over-pressures were evaluated from generalized equilibrium paths, where the membrane thickness t was varied. The equilibrium solutions were thereby found without complete non-linear response analysis. Also, the dependence of the critical — maximum and minimum — pressure states on the constitutive ratio $k = c_2/c_1$ were studied by following a fold line, with criticality as an augmenting equation. The relation is shown in Fig. 1(c), isolating to very high accuracy the ratio k for which the limit pressure states disappear; for higher k , the expansion is monotonically increasing with pressure. It is noted that simulations where the injected amount of gas is seen as the loading parameter will give other

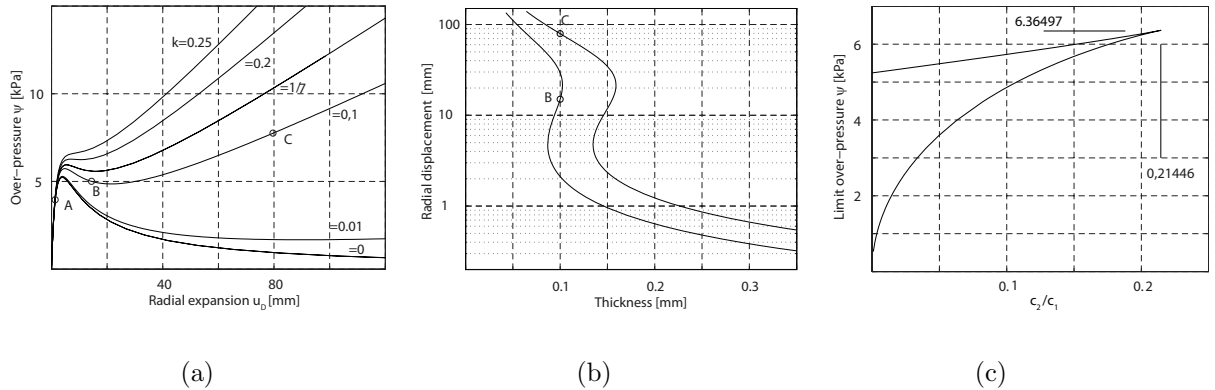


Figure 1. Simulations of inflated spherical membrane. (a) Pressure-expansion for different k , with $t = 0.1$ mm; (b) Expansion for two pressures at different t , with $k = 0.1$; (c) Critical pressures as function of k , with $t = 0.1$ mm.

conclusions regarding the stability of the loading process.

Further simulations of the same basic problem included the ambient pressure and the temperature as variables. Varying these parameters, independently or simultaneously, show how a balloon inflated to a certain state in typical sea-level conditions will behave when subjected to other ambient variables. For instance, a simulated atmospheric variation of both temperature and pressure with height can be introduced, and the response for the balloon evaluated by following one generalized path. The work also shows how a solution surface can be used to give further information on how the response depends on pressure and constitutive constants.

The work has also studied the stability of long cylindrical balloons, with both analytical and numerical methods. These long pressurized closed membranes will have some similarities with the spherical balloons, but will also show some significant differences in instability behavior.

Conclusions

A conclusion from the study is that the generalized equilibrium path and surface calculations can be valuable tools for understanding the qualitative behavior of instability sensitive structures, e.g., thin membranes. In particular, the methods allow the determination on how different parametric regions can lead to qualitatively different responses to loading. The methods can also be efficient in the design of membranes, as variations in parameters can be easily studied without the need for complete non-linear response evaluations.

References

- [1] Anders Eriksson and Arne Nordmark. Instability of thin hyper-elastic space membranes under pressure loads. *Computer Methods in Applied Mechanics and Engineering*, 237:118–129, 2012.
- [2] Anders Eriksson. Equilibrium subsets for multi-parametric structural analysis. *Computer Methods in Applied Mechanics and Engineering*, 140:305–327, 1997.
- [3] Anders Eriksson. Structural instability analyses based on generalised path-following. *Computer Methods in Applied Mechanics and Engineering*, 156:45–74, 1998.
- [4] Anders Eriksson and Costin Pacoste, Solution surfaces and generalised paths in non-linear structural mechanics. *International Journal for Structural Stability and Dynamics*, 1:1–30, 2001.

Approximate buckling model for steel-elastomer sandwich plates

Ole J. Hareide¹, Lars Brubak^{1,2}, Eivind Steen¹ and Jostein Hellesland²

⁽¹⁾Section for Ship Structures and Concepts, Maritime Advisory, Det Norske Veritas AS, Norway.
E-mail: ole.jakob.hareide@dnv.com

⁽²⁾Mechanics Division, Department of Mathematics, University of Oslo, Norway

Summary. This article describes the development of a semi-analytic buckling model for steel-elastomer sandwich plates using the Rayleigh-Ritz method. The model includes transverse shear deformations which are important in this type of plate. The unknowns - the deflections and cross-sectional rotations - are approximated by Fourier series. All combinations of in-plane tensile, compressive and shear loads are allowed. Pre-stressing of the plate and elastic springs on the boundary are also included. The model has been implemented in a FORTRAN programme and the results have been compared with results from the finite element programme ABAQUS.

Key words: Buckling, eigenvalues, Rayleigh-Ritz, sandwich plates

Introduction

In the maritime industry, structures have traditionally been constructed with stiffened steel panels. Recently a type of sandwich plates for heavy construction has been introduced to replace stiffened steel panels in secondary ship structures, such as hatch covers and superstructures. This type of plate is easier to manufacture and maintain and offers an increased stiffness to weight ratio. Consisting of a lightweight polyurethane core bonded on both sides with steel face plates, the sandwich plate can be used for new-building, but also to repair damaged structures. DNV has recently completed a classification note [1] on this type of sandwich plates.

In order to calculate the elastic buckling loads for such plates one must take the transverse shear deformations, or cross-sectional rotations, into account. Because the core material is weak compared to the face material, the two face plates will slide relative to each other in bending deformations. The method presented here is a Rayleigh-Ritz approach used to approximate the eigenvalue solution of the plate differential equation by representing the unknowns by Fourier series. The model includes in-plane tensile, compressive and shear loading in any combination. Elastic springs are included around the plate so that any boundary condition between, and including, simply supported and fully clamped can be modelled. The springs can be activated individually to model a wide range of boundary conditions. The plate can be pre-stressed before the buckling analysis is started. A more thorough description of the model is available in [2].

Eigenvalue model for buckling

The Rayleigh-Ritz method is based on the potential energy of the plate. The method has previously been used by Brubak, Hellesland and Steen [3] for irregularly stiffened plates. For the type of plate considered here, the internal strain energy is not only due to the moments doing work through curvature, but also the transverse shear forces doing work through transverse

shear deformations. The boundary springs will store energy through their rotations. The total potential energy of the plate is $\Pi = U_{plate} + U_{springs} - W$. The strain energy for the plate is

$$U_{plate} = \frac{1}{2} \int_{y=0}^b \int_{x=0}^a \left[D_x \left(\frac{\partial}{\partial x} \left(\frac{\partial w}{\partial x} - \gamma_{xz} \right) \right)^2 + (D_x \nu_{yx} D_y \nu_{xy}) \frac{\partial}{\partial x} \left(\frac{\partial w}{\partial x} - \gamma_{xz} \right) \frac{\partial}{\partial y} \left(\frac{\partial w}{\partial y} - \gamma_{yz} \right) \right. \\ \left. + D_y \left(\frac{\partial}{\partial y} \left(\frac{\partial w}{\partial y} - \gamma_{yz} \right) \right)^2 + \frac{D_{xy}}{2} \left(\frac{\partial}{\partial x} \left(\frac{\partial w}{\partial y} - \gamma_{yz} \right) + \frac{\partial}{\partial y} \left(\frac{\partial w}{\partial x} - \gamma_{xz} \right) \right)^2 \right. \\ \left. + T_x \gamma_{xz} + T_y \gamma_{yz} \right] dx dy \quad (1)$$

The strain energy for the springs is on the form

$$U_{springs} = U_{x=0}^s + U_{x=a}^s + U_{y=0}^s + U_{y=b}^s \quad \text{where all four terms are of the form:} \\ U_{x=0}^s = \frac{1}{2} \int_0^b k_{x0} \left(\left[\frac{\partial w}{\partial x} - \gamma_{xz} \right]_{x=0}^2 \right) dy \quad (2)$$

where k_{x0} is the spring stiffness coefficient for the edge $x = 0$. The potential of external loads is

$$W = \frac{1}{2} \int_{y=0}^b \int_{x=0}^a \left[N_x \left(\frac{\partial w}{\partial x} \right)^2 + 2N_{xy} \left(\frac{\partial w}{\partial x} \right) \left(\frac{\partial w}{\partial y} \right) + N_y \left(\frac{\partial w}{\partial y} \right)^2 \right] \quad (3)$$

Because the plate is considered isotropic in the x-y-plane, the stiffness coefficients found in Zenkert [4] are used:

$$D_x = D_y = \frac{E_f}{4(1 - \nu_f^2)} (t_{f1}(t_c + t_{f1})^2 + t_{f2}(t_c + t_{f2}^2)) + \frac{E_c t_c^3}{12(1 - \nu_c^2)} \quad (4) \\ D_{xy} = \frac{E_f}{4(1 + \nu_f)} (t_{f1}(t_c + t_{f1})^2 + t_{f2}(t_c + t_{f2})^2) + \frac{E_c t_c^3}{12(1 + \nu_c)} S_x = S_y = \frac{G_c}{t_c} (t_{f1}/2 + t_{f2}/2 + t_c)$$

Here E_f and ν_f are the Young's modulus and the Poisson ratio of the face plate material, E_c and ν_c are the same for the core material. The thicknesses of the two face plates are denoted by t_{f1} and t_{f2} and the core thickness is t_c . G_c is the shear modulus of the core material and is defined by $G_c = E_c/(2(1 + \nu_c))$.

The three unknown displacement fields are approximated by the following Fourier series

$$w = \sum_{m=1}^{\infty} \sum_{n=1}^{\infty} A_{mn} \sin \frac{m\pi x}{a} \sin \frac{n\pi y}{b} \quad (5) \\ \gamma_{xz} = \sum_{m=1}^{\infty} \sum_{n=1}^{\infty} B_{mn} \cos \frac{m\pi x}{a} \sin \frac{n\pi y}{b} \quad \gamma_{yz} = \sum_{m=1}^{\infty} \sum_{n=1}^{\infty} C_{mn} \sin \frac{m\pi x}{a} \cos \frac{n\pi y}{b}$$

where a and b are the longitudinal and transverse dimensions of the plate and A_{mn} , B_{mn} and C_{mn} are the amplitudes. When the displacement fields are differentiated with respect to x and y and inserted into the potential energy, the continuous problem described by the differential equation has been converted into a set of algebraic equations with coefficients A_{mn} , B_{mn} and C_{mn} .

The requirement for equilibrium of the system is that the potential energy has a stationary value, this is fulfilled when the bracketed term in Eq. 6 is zero. The eigenvalue problem for a system which in addition to the plate itself also includes elastic springs on the boundary and the effects of pre-stressing the plate before the eigenvalue analysis is defined as

$$[(\mathbf{K}^M + \mathbf{K}^S - \mathbf{K}^{pre}) - \Lambda \mathbf{K}^G] \mathbf{A} = \mathbf{0} \quad (6)$$

where the material stiffness matrix, \mathbf{K}^M , is defined as

$$\mathbf{K}^M = \begin{bmatrix} \mathbf{K}_{AA}^M & \mathbf{K}_{AB}^M & \mathbf{K}_{AC}^M \\ \mathbf{K}_{BA}^M & \mathbf{K}_{BB}^M & \mathbf{K}_{BC}^M \\ \mathbf{K}_{CA}^M & \mathbf{K}_{CB}^M & \mathbf{K}_{CC}^M \end{bmatrix}$$

in which each of the nine sub-matrices is the potential energy twice differentiated with respect to the coefficients A_{mn} , B_{mn} and C_{mn} . The first sub-matrix is

$$\mathbf{K}_{AA}^M = \frac{\partial^2 U}{\partial A_{ij} \partial A_{kl}} = \sum_{i=1}^M \sum_{j=1}^N \left[D_x \left(\frac{i\pi}{a} \right)^4 + (D_x \nu_{yx} + D_y \nu_{xy}) \left(\frac{i\pi}{a} \right)^2 \left(\frac{j\pi}{b} \right)^4 + D_y \left(\frac{j\pi}{b} \right)^4 + 2D_{xy} \left(\frac{i\pi}{a} \right) \left(\frac{j\pi}{b} \right) \right] \frac{ab}{4} \quad (7)$$

and the other nine sub-matrices in the material stiffness matrix, \mathbf{K}^M , are computed in the same way. In the geometric stiffness matrix, however, the only non-zero sub-matrix is \mathbf{K}_{AA}^G . The reason is that the expression for the potential of external loads, W , from which the geometric stiffness matrix is derived (in the same way as the material stiffness matrix was derived from the internal strain energy), is only a function of the single displacement field, w , and hence the coefficients, B_{mn} and C_{mn} , do not enter the expression at all.

The stiffness matrix for the elastic springs, \mathbf{K}^S , is found by twice differentiating Eq. (2). If a clamped boundary condition or an intermediary between simply supported and clamped is wanted, this stiffness matrix should be added to the material stiffness matrix, as indicated by Eq. (6). This will raise the overall stiffness of the system, enabling the plate to carry higher external loads by storing energy in the elastic springs. To account for any existing loads in the plate before doing an eigenvalue analysis a pre-stress matrix, \mathbf{K}^{pre} , is derived in the same way as the geometric stiffness matrix from the potential of external loads and also included. This matrix will reduce the overall stiffness of the plate, as can be seen by the negative sign in the eigenvalue equation (6).

Results and conclusions

The model was implemented in a FORTRAN programme. Fig. 1 shows two plots comparing the current Rayleigh-Ritz model with ABAQUS. The plate considered had in-plane dimensions $a = 4190mm$ and $b = 2800mm$ and thicknesses $t_{f1} = t_{f2} = 4mm$ and $t_c = 25mm$. The face plates were of steel with a Young's modulus of $E_f = 208000MPa$ and Poisson's ratio of $\nu_f = 0.3$. The core had a Young's modulus of $E_c = 750MPa$ and a Poisson's ratio of $\nu_c = 0.3$, giving a core shear modulus of $G_c = 288MPa$. The applied forces are shown in Fig. 1.(d).

Fig. 1(a) shows an interaction curve plot for a simply supported plate with varying combination of normal longitudinal, N_x , and transverse, N_y , loading, with different levels of pre-loading of shear, N_{xy} . Fig. 1(c) shows the same for a clamped plate with a combination of normal longitudinal, N_x , and shear, N_{xy} , with different levels of pre-loading of normal transverse force, N_y . The results show very good agreement between the Rayleigh-Ritz model and ABAQUS. For clamped plates, the results differ somewhat. This is due to the fact that a larger number of terms is needed in the series to achieve convergence of the plate with springs.

Acknowledgments: The authors would like to express their thanks to Philippe Noury, Kristofer Brinchmann and Gabriele Notaro at DNV for their support and contributions.

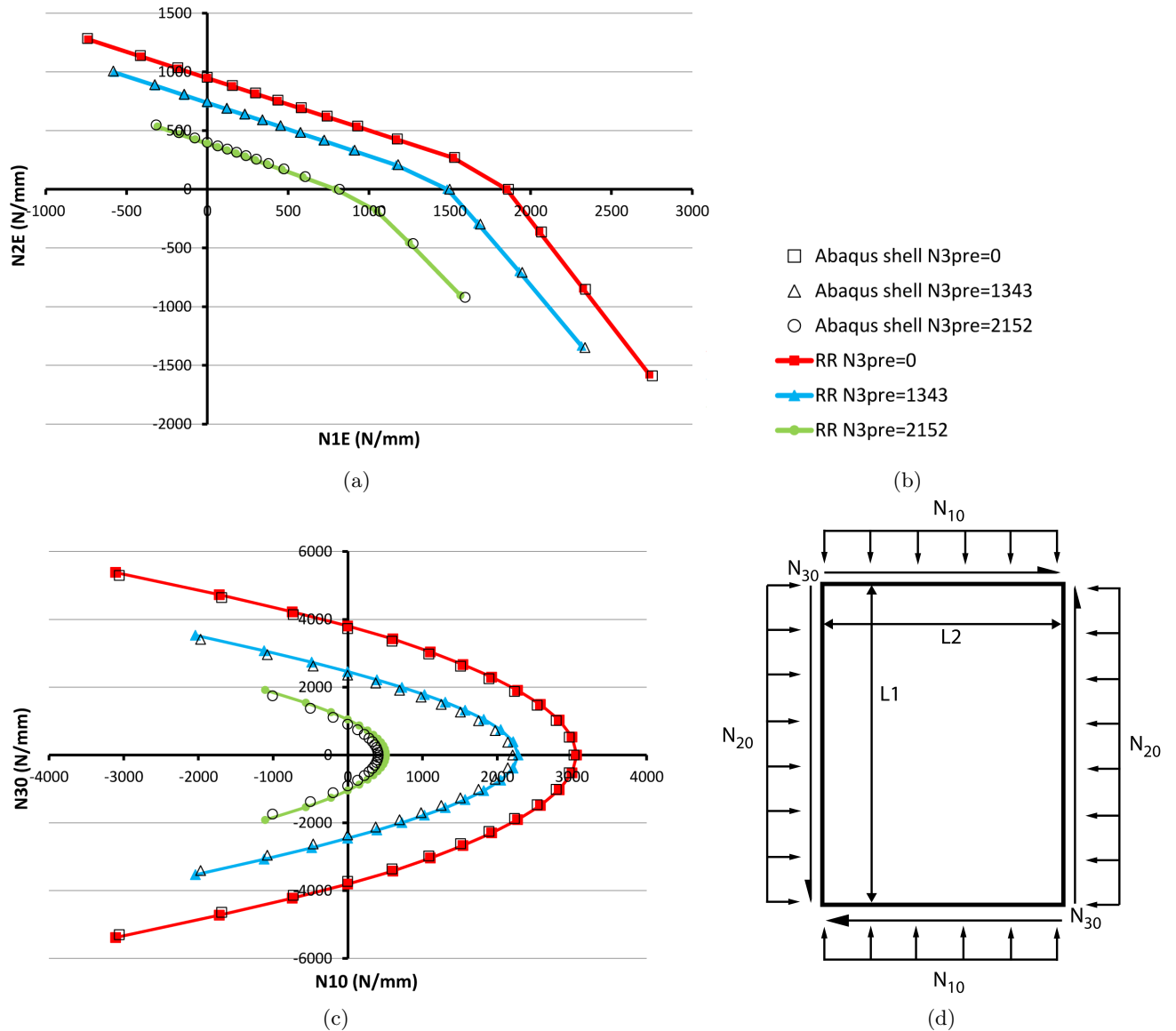


Figure 1: Rayleigh-Ritz results compared to the ABAQUS results (a-c) and the forces acting on the plate (d).

References

- [1] Det Norske Veritas AS. *Classification Note - No. 30.11 - Steel Sandwich Panel Construction*. DNV AS, Høvik, Norway, 2012.
- [2] Ole J. Hareide. *Analytical and semi-analytical methods for buckling and bending of steel-elastomer sandwich plates*. MSc Thesis, Mechanics Division, Department of Mathematics, University of Oslo, 2012.
- [3] Lars Brubak, Jostein Hellesland, and Eivind Steen. *Semi-analytical buckling strength analysis of plates with arbitrary stiffener arrangements*. J. of Construct. Steel Res., Vol. 63, 2007: 532-543.
- [4] Dan Zenkert. *An Introduction to Sandwich Structures - Student Edition*. Dan Zenkert, 2005.

Static redundancy factors in conceptual design

Gunnar Tibert¹ and Lina M. Achi²

⁽¹⁾KTH Mechanics, Osquars backe 18, 100 44 Stockholm, Sweden, tibert@kth.se

⁽²⁾Tyréns AB, Peter Myndes backe 16, 118 46 Stockholm and KTH Architecture, Östermalmsgatan 26, 100 44 Stockholm, Sweden, lina.martinssonachi@tyrens.se

Summary. This paper describes a part of an on-going project with multiple objectives, its main problem being defined as ambiguity of force flow as a result of morphological redundancy. The primary objective is to develop a new method for structural analysis based on graph theory, in order to better understand the impact of morphology on structural behaviour. The approach aims to unlock both the knowledge-generating and the innovative potential of morphology analysis. As a first step, element redundancy factors in trusses are introduced as a way to visualise the structural redundancy in a complex truss, so that non-redundant regions could be distinguished from over-redundant regions.

Key words: conceptual design, structural morphology, static redundancy, redundancy factor

Back to basics

“In practice a great many problems are solved by what is called judgment. The better a man understands how the stresses follow through a member or structure, the better his judgment will be” [1]

The section title *Back to basics* refers to the overall approach of the research that this paper gives a very brief account of, a piece of research prompted by the acknowledgement of what appears to be a gradually weakened knowledge basis of the structural engineering profession. Coupled with the increased usage of ever more advanced tools, this weakening is stifling innovation within the field, since ill-informed creativity may lead to dire consequences [3, 4]. The present research, [2], seeks to activate powerful basics, like basic human skills and first principles, in the strive to improve our understanding of structural morphology via an approach based on graph theory. The proposed methodology seeks to help reconstruct the intuitive understanding of the fundamental characteristics of structural systems, i.e. the relation between structural morphology and force flow, boosting the structural engineer’s knowledge basis that is required in order to successfully tackle the ever more challenging design tasks of today.

Impact of redundancy

“For a structural system to survive unforeseen events or circumstances, with its intended functions intact, it must possess sufficient reserve capacity.” [4]

The necessity as well as difficulty to properly and efficiently account for the relation between structural morphology and force flow becomes acutely felt when confronted with redundant structural systems, especially when redundancy is accompanied by irregularity. Contemporary design proposals are increasingly striving to adopt these two characteristics for aesthetic reasons. However, there are important structural benefits of redundancy, and possibly also irregularity,

the primary one being structural robustness [3]. An approach exploiting morphological redundancy has got the potential to be weight-optimised. It may therefore challenge the current juxtaposition between robustness and optimisation, [4], also enabling for the development of a strategy with an ability to account for multiple, combined loading scenarios in a holistic manner. Following on from the above, ambiguity of force flow as a result of morphological redundancy was identified as an equally imperative and complicated problem to be addressed. Assuming that morphological redundancy may indeed offer a new approach to robustness, this would provide valuable support to the structural engineer, at a time when the building codes greatly emphasise the importance of robustness [4]. Furthermore, the Eurocodes stipulate that “*potential damage shall be avoided or limited by appropriate choice of one or more of the following: selecting a structural form which has low sensitivity to the hazards considered; selecting a structural form and design that can survive adequately the accidental removal of an individual member or a limited part of the structure, or the occurrence of acceptable localised damage; tying the structural members together...*” [5]. It is proposed that developing a better understanding of the relation between structural properties and structural behaviour may inform a new strategy for addressing robustness and for developing appropriate structural forms with a “*low sensitivity to the hazards considered*” that “*can survive adequately the accidental removal of an individual member or a limited part of the structure*”. The difficulty experienced by the structural engineer when attempting to analyse morphologically redundant systems is intimately related to the difficulty to visually assess them. This means that even though one might be able to successfully produce results using a wide selection of readily available commercial packages in order to perform the structural analysis, it is still difficult to make sense of and interpret the results from multiple load cases. Structural morphology is a rather unknown field, which means that its specific characteristics largely remain hidden from us. This in turn means that what might indeed be structurally beneficial characteristics of structural morphology is currently not being appreciated to their fullest extent.

Redundancy factors in trusses

Here, redundancy factors are introduced as a way of visually assess the redundancy of 3D trusses without considering specific load cases and only indirectly the material stiffness, so the focus is only on the topology and geometry.

Degree of static indeterminacy

Consider a 3D pin-jointed truss with j joints and b bars acted upon by external forces at the joints. The framework is restrained in 3D by c kinematic constraints. The number of states of self-stress s and the number of mechanisms m is expressed by the generalised Maxwell’s rule

$$m - s = 3j - b - c \quad (1)$$

Here, we assume that the framework is kinematically determinate, $m = 0$. The set of equilibrium equations for the framework is written as

$$\mathbf{H}\mathbf{t} = \mathbf{f} \quad (2)$$

where \mathbf{H} is the $3j - c \times b$ equilibrium matrix, \mathbf{t} is the internal force vector of length b , and \mathbf{f} is the external force vector of length $3j - c$. The external forces give rise to displacements which must be compatible with the elongations of the bars. The set of linear compatibility equations is

$$\mathbf{C}\mathbf{d} = \mathbf{e} \quad (3)$$

where $\mathbf{C} = \mathbf{H}^T$ is the $b \times 3j - c$ compatibility matrix, \mathbf{d} is the joint displacement vector of length $3j - c$, and \mathbf{e} is the bar elongation vector of length b [7]. The number of states of self-stress or

the degree of static indeterminacy is

$$s = b - \text{rank}(\mathbf{H}) \quad (4)$$

where $\text{rank}(\mathbf{H})$ is found from a singular value decomposition of \mathbf{H} , [7].

Redundancy factors

Assuming linear-elastic material, the element forces \mathbf{t} are related to the bar elongations \mathbf{e} by the elements flexibility matrix Φ as

$$\mathbf{e} = \mathbf{e}_0 + \Phi \mathbf{t}, \quad (5)$$

where \mathbf{e}_0 is the vector of initial bar elongations. The $b \times b$ diagonal elements flexibility matrix Φ has $\phi_i = l_i/A_i E_i$ as its entry of position (i, i) . The inverse of the flexibility matrix is the diagonal elements stiffness matrix

$$\Psi = \Phi^{-1} \quad (6)$$

with $\psi_i = A_i E_i / l_i$ at position (i, i) . Using (6) and (3), (5) can be re-written as

$$\mathbf{t} = \Psi(\mathbf{C}\mathbf{d} - \mathbf{e}_0) \quad (7)$$

Combining (2)–(7) yields

$$\mathbf{t} = \underbrace{\Psi \mathbf{H}^T (\mathbf{H} \Psi \mathbf{H}^T)^{-1} \mathbf{f}}_{\mathbf{t}_f} - \underbrace{\Psi [\mathbf{I} - \mathbf{H}^T (\mathbf{H} \Psi \mathbf{H}^T)^{-1} \mathbf{H} \Psi]}_{\mathbf{t}_{e_0}} \mathbf{e}_0 \quad (8)$$

Hence, the total element force \mathbf{t} may be separated into two parts: \mathbf{t}_f due to the external loads \mathbf{f} and \mathbf{t}_{e_0} due to initial element elongations \mathbf{e}_0 , i.e. imperfections, pretension, temperature effects, etc. The expression for the element forces due to initial elongations is re-written

$$\mathbf{t}_{e_0} = -\Psi \Lambda \mathbf{e}_0 \quad (9)$$

where Λ is a scaling matrix expressing the stiffness of the structure surrounding a specific element. For kinematically determinate frameworks, $m = 0$, it is shown, [6], that the trace of the scaling matrix Λ is equal to the degree of statical indeterminacy

$$\text{Tr}(\Lambda) = s \quad (10)$$

The diagonal element λ_{ii} can thus be interpreted as the contribution of element i to the total degree of static indeterminacy or redundancy s and is therefore denoted *static redundancy factor*.

Redundancy factors in design

Figure 1 shows a 2D truss with the normalised redundancy factor for elements with equal flexibility, l/AE . A normalised redundancy factor of 0% (blue colour) means that the element cannot be removed as its removal will render the framework unstable whereas a factor equal to 100% (red) means that the element is highly redundant. This redundancy analysis is done without considering a specific load case, only the topology, geometry, constraints and element flexibilities are considered. The robustness in terms of redundancy is shown in Fig. 1 as elements are added and removed. The diagonal bracing elements for each square is more redundant than the elements forming the sides of the square, which is obvious since the side elements provide more stiffness than the diagonal elements in the horizontal-vertical plane.

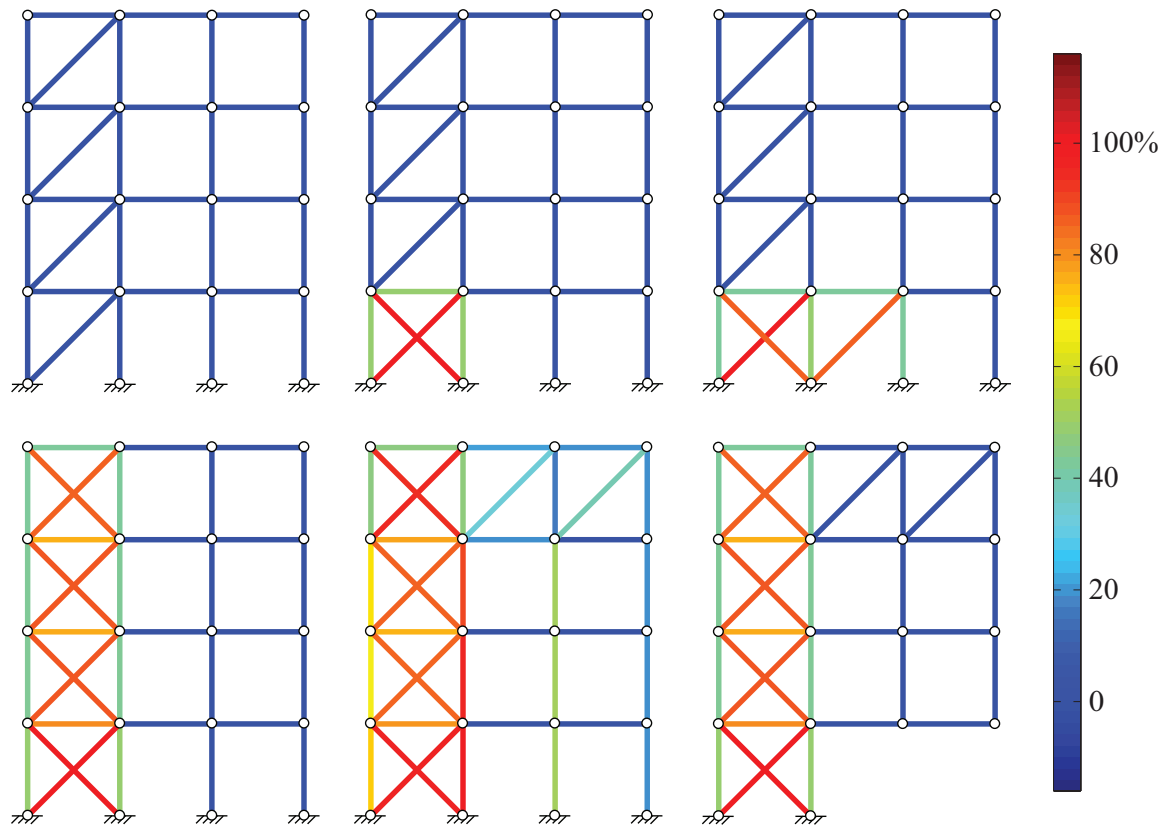


Figure 1. Normalised redundancy factors for a four-floor 2D truss.

Conclusions

This paper seeks to communicate the potent power inherent in a structural analysis approach that is based on engineering basics rather than specifics, with the intention to create order out of chaos. Redundancy factors have the potential to visualise the non-redundant regions in an overall over-redundant complex 3D truss and thus serve as useful tool for the conceptual design of robust structures.

References

- [1] W.S. Wolfe. *Graphical Analysis: A Text Book on Graphic Statics*. Wexford College Press, Palm Springs, USA, 2006.
- [2] L. M. Achi and G. Tibert. A Graph Theoretical Methodology for Conceptual Design. *Proceedings of the 2012 IASS Symposium*, Seoul, Korea, 2012.
- [3] M. Majowiecki. Ethics and Structural Reliability in Free-Form Design (FFD). *Journal of the International Association for Shell and Spatial Structures*, 48(4):29–50, 2007.
- [4] F. Knoll and T. Vogel. *Design for Robustness*. Structural Engineering Documents 11, International Association for Bridge and Structural Engineering, Zurich, 2009.
- [5] EN 1991-7. *Eurocode 1: Actions on Structures: Part 1-7: Accidental Actions*. CEN, 2006.
- [6] D. Ströbel. *Die Anwendung der Ausgleichsrechnung auf elastomechanische Systeme*. PhD thesis, University of Stuttgart, 1997.
- [7] S. Pellegrino. Structural Computations with the Singular Value Decomposition of the Equilibrium Matrix. *International Journal of Solids and Structures*, 30(21):3025–3035, 1993.

Using touch and multi-touch interfaces in structural mechanics software

J. Lindemann¹ and D. Åkesson²

⁽¹⁾Division of Structural Mechanics, PO Box 118, 221 00 Lund, jonas.lindemann@byggmek.lth.se

⁽²⁾Division of Structural Mechanics, PO Box 118, 221 00 Lund, civ04dak@student.lu.se

Summary. Touch and multi-touch user interface has become widely available by the introduction of the iPad and android tablets. These user interfaces are very direct and users often interact with applications in different ways than conventional user interfaces. This paper describes some of the user interfaces that we have developed that take advantage of this new interaction model in structural mechanics software.

Key words: touch, multi-touch, tablets, user interfaces, mechanics software

Introduction

During the last years, the popularity of touch and multi-touch user interfaces has increased with the introduction of the iPhone, iPad and other touch based devices. User interfaces for these devices are often very direct and also use direct-manipulation interfaces. This gives the user the feeling of directly manipulating objects on the screen compared to using an extra device such as a mouse. This direct modeling using touch and multi-touch is well suited for structural mechanics software for increasing the efficiency of previously developed mouse based applications.

At Structural Mechanics in Lund we have a long experience in developing novel user interfaces that support conceptual design and modeling by using direct-manipulation interfaces. The best example of this is the ForcePAD [1, 2] application that can be used for creating conceptual 2D structures by "painting" with stiffness. This application is implemented as a standard window based application using either a mouse or a stylus for input.

This paper, describes how touch and multi-touch can be used to enhance the user experience in existing and new applications developed at Structural Mechanics.

SmartBoard enabled ForcePAD

At the Science Center at LTH [3], they wanted an exhibition where people could experiment with forces and structures. ForcePAD is a good tool for visualizing forces in structures. At exhibition they have installed a so called SmartBoard. A SmartBoard is a combination of a touch-enabled white screen onto which a standard computer project displays its output. This device enables users to use fingers to touch the projected screen and interact with the application. As the white screen is over 100 inches wide it can be used in the same way as a white board in teaching. Several people can also interact with the application at the same time. Figure 1 shows the actual setup in the Science Center.

Using ForcePAD on the SmartBoard required some modification of the user interface. As the exhibition is public and for the casual passers by, the user interface was simplified. The application menu was removed and the window was made fullscreen by default. To enable experimenting with different structures a special floating window was implemented with the



Figure 1. SmartBoard setup in the LTH science center

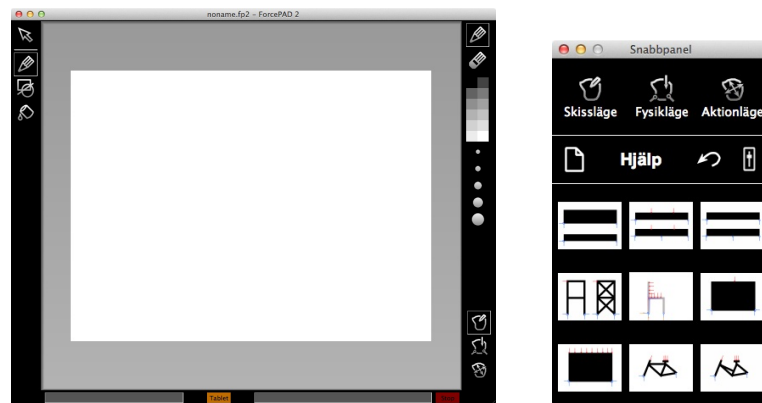


Figure 2. SmartBoard enabled ForcePAD with additional tool window

most used functions displayed. It also contains a grid of 9 standard examples that can be quickly loaded without a file selection dialog. Figure 2 shows the floating tool window.

The exhibition has been used successfully for a couple events in the Science Center. It is very powerful to work with the application at the larger screen sizes that the white screen enables. The touch-screen eliminates the need for a mouse and makes the interaction more direct. It also creates a virtual "white board" that can be used effectively to illustrate phenomena interactively for the audience. However, users still needs some additional instruction for using the application. An interactive instructional video will probably be added to the exhibition, to help users working with the application.

Sketch-a-frame

The iPad and iPhone made multi-touch technologies available for a wide range of users. To investigate the use of multi-touch in structural mechanics application we decided to develop a concept application, Sketch-a-frame. Sketch-a-frame is a very simple finite element application for studying simple 2D frame and truss structures, which builds on and extends concepts from the PointSketch application [5] with multi-touch gestures. The basic idea of the application is to make it completely interactive without any intermediate calculation steps. Moving nodes and forces will automatically update forces and deflections. The application also automatically determines if the structure is stable or a mechanism. Figure 3 shows the user interface of the Sketch-a-frame application.

During the development of the application, it was apparent that many of the normal interaction models for using a mouse were not suitable when using a multi-touch interface. Graphics

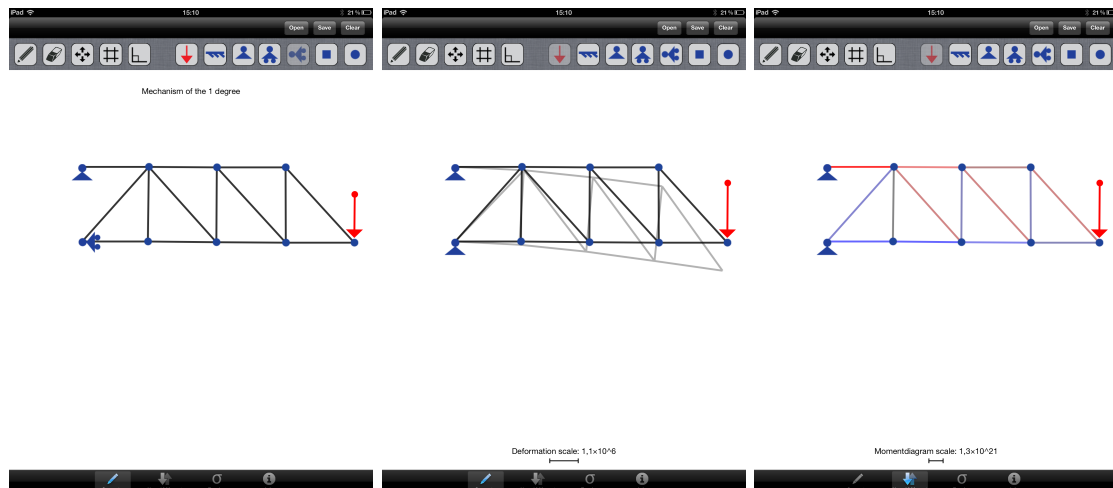


Figure 3. The Sketch-a-frame application

and user interface elements need to be adapted for use with fingers as the precision of using a mouse is lost. Graphics have to be larger and have larger tolerances during selection operations.

Sketch-a-frame, can be seen as a conceptual sketchpad for 2D structure, enabling experimentation with different structural concepts. The direct feedback of the user interface enables the user to get a direct understanding of the structural behavior, which is also enhanced by the touch interface.

Conclusions

Using touch and multi-touch greatly enhances the application experiences by providing a more direct interacting with the application. For structural mechanics application means that the phenomena studied can be visualised more directly and also encourages experimentation in a more direct ways. The SmartBoard device also adds an additional dimension to a touch application by enabling more people to simultaneously using an application. It can effectively used in a educational settings as an interactive "white board" for visualizing structural concepts.

References

- [1] J. Lindemann, G. Sandberg and L. Damkilde, Finite-element software for conceptual design, *Proceedings of the ICE - Engineering and Computational Mechanics*, Volume 163, Issue 1, 01 March 2010, pages 15-22
- [2] J. Lindemann, G. Sandberg, and K. Olsson, An approach to teaching architectural and engineering students utilizing computational mechanics software ForcePAD, *ITcon Special Issue ICT Supported Learning in Architecture and Civil Engineering*, 9:219-228, 2004
- [3] Vattenhallenn Science Center LTH, <http://www.vattenhallen.lth.se/>, 2012
- [4] SMART Board interactive whiteboards, <http://smarttech.com/us/Solutions/Education+Solutions/Products+for+education/Interactive+whiteboards+and+displays/SMART+Board+interactive+whiteboards>, 2012
- [5] P.Olsson, Conceptual studies in structural design : pointSketch - a based approach for use in early stages of the architectural process, *Doktorsavhandlingar vid Chalmers tekniska högskola. Ny serie*, ISSN 0346-718X; nr 2435, 2006

Finite element simulation of an excavation using diaphragm wall

A. Spetz¹, O. Dahlblom¹ and P. Lindh²

⁽¹⁾Department of Construction Sciences, Lund University, Box 118, SE-221 00, Lund, Sweden, E-mail: alex.spetz@construction.lth.se, ola.dahlblom@construction.lth.se

⁽²⁾PEAB Sverige AB, Karbingatan 10, SE-254 67, Helsingborg, Sweden, E-mail: per.lindh@peab.se

Summary. The work presented in this paper has been done to investigate the possibilities of using three dimensional finite element calculations to establish reliable alert and stop limits for excavations using diaphragm walls. A finite element analysis has been performed on the construction of lower parts of Malmö central station where extensive measurements were recorded during the construction.

Key words: Geotechnical engineering, finite element method, soil-structure, NSCM-25

Introduction

When building underground construction in close proximity to sensitive existing buildings the regulations regarding soil deformation can be very strict. Conventional methods of predicting soil behaviour are then often too crude and finite element (FEM) calculations are therefore becoming an increasingly important tool used for predicting soil behaviour.

Malmö central station

The lower parts of Malmö central station, a part of the Citytunnel project creating a faster commute between Sweden and Denmark, was built as a 20 meter deep cut and cover construction. As there were three listed buildings in close proximity of the excavation pit the vertical and horizontal displacements along the most sensitive areas were restricted to 10 mm and 5 mm respectively. To be able to handle these restrictions diaphragm walls were used along the most vulnerable parts of the pit. During the construction measurements were taken to ensure that the allowed deformations were not exceeded.

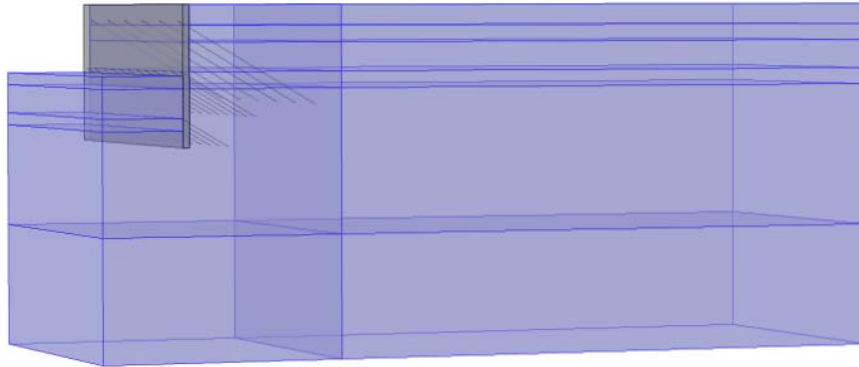


Figure 1. Finite element model used to simulate the excavation down to second anchoring level.

Objective and Method

The work presented in this paper was carried out to investigate the possibilities of establishing reliable alert and stop limits for excavations with diaphragm walls using three dimensional finite element simulations, see Figure 1. An analysis has been performed on the displacements of the soil and diaphragm wall used in the construction of Malmö central station. The finite element simulations were conducted in steps to resemble the actual workflow at the construction site. The measurements taken during construction have been used to validate the finite element model used. The material parameters used have been evaluated from experimental investigations at site.

The influence of surface elasticity on the flexural rigidity of nanowires

Pär A. T. Olsson¹ and Harold S. Park²

⁽¹⁾Materials Science, Malmö University, Malmö, SE-20506, Sweden, Par.Olsson@mah.se

⁽²⁾Mechanical Engineering, Boston University, Boston, MA 02215, USA, ParkHS@bu.edu

Summary. This talk describes a recently derive continuum model for estimating the flexural rigidity of nanowires. The model is linear elastic and includes contributions of surface stiffness as a result of lowered coordination. Predictions of the model are validated by comparison to benchmark molecular dynamics and statics simulations via two examples: resonant properties of top-down nanowires and buckling of nanowires. Overall, the present work demonstrates that continuum mechanics can be utilized to study the elastic and mechanical behavior and properties of ultrasmall nanowires if surface elastic contributions to the flexural rigidity are accounted for.

Key words: surface elasticity, nanowires, molecular dynamics simulations

Introduction

Over the past two decades, dramatic technological progress made in the field of nanotechnology has made it possible not only to visualize but also manipulate, assemble and organize matter with high precision on the atomic scale. This has opened the possibility of fabricating structural nanodevices by piecing basic nanosized building blocks together to form grander, more complex and more elaborate systems; the so-called bottom-up strategy. This has led to a gain in interest from many different branches and disciplines in the scientific community, which has paved the way for the discovery and recognition of many novel physical properties of nanostructures that differ significantly from those of macroscopic structures [1].

However, applications where the mechanical properties are of importance have been plagued with difficulties in predicting the mechanical response accurately. An examples of this is, for instance, nanoscale resonators where the flexural rigidity plays a central role [2]. The flexural rigidity of nanowires is highly affected by surface elastic contributions as a result of the high surface to volume ratio of nanostructures and the lowered coordination of surface atoms.

The purpose of this talk is to discuss a recently derived continuum model for estimating the flexural rigidity of nanowires. The model is linear elastic and includes the surface elastic contributions to the flexural rigidity through the second moment, which accounts for the fact that surfaces are subjected to the greatest amounts of strain in bending. Details of the model can be found in [3].

Continuum model

Based on the seminal work by Dingreville and coworkers [4], it is assumed that the surface energy density, Γ , can be expanded in terms of the surface strains, $\epsilon_{\alpha\beta}^s$,

$$\begin{aligned}\Gamma(\epsilon_{\alpha\beta}^s) &= \Gamma_0 + \frac{\partial\Gamma}{\partial\epsilon_{\alpha\beta}^s}\epsilon_{\alpha\beta}^s + \frac{1}{2}\frac{\partial^2\Gamma}{\partial\epsilon_{\alpha\beta}^s\partial\epsilon_{\gamma\eta}^s}\epsilon_{\alpha\beta}^s\epsilon_{\gamma\eta}^s + \dots = \\ &= \Gamma_0 + \Gamma_{\alpha\beta}^{(1)}\epsilon_{\alpha\beta}^s + \frac{1}{2}\Gamma_{\alpha\beta\gamma\eta}^{(2)}\epsilon_{\alpha\beta}^s\epsilon_{\gamma\eta}^s + \dots\end{aligned}\quad (1)$$

where Γ_0 , $\Gamma_{\alpha\beta}^{(1)}$, and $\Gamma_{\alpha\beta\gamma\eta}^{(2)}$ are the area specific surface energy density, the surface stress, and the surface elastic constants, respectively. Greek indices are 1 and 2 and repeated indices are summed. These surfaces are assumed to be flat and of infinitesimal thickness, which is an approximation as the influence of the surfaces has a finite range. Moreover, it is assumed that the potential energy of the bulk can be expanded in terms of the bulk strains

$$\begin{aligned}\Phi(\epsilon_{ij}) &= \Phi_0 + \frac{\partial\Phi}{\partial\epsilon_{ij}}\epsilon_{ij} + \frac{1}{2}\frac{\partial^2\Phi}{\partial\epsilon_{ij}\partial\epsilon_{kl}}\epsilon_{ij}\epsilon_{kl} + \dots = \\ &= \Phi_0 + \sigma_{ij}\epsilon_{ij} + \frac{1}{2}C_{ijkl}\epsilon_{ij}\epsilon_{kl} + \dots\end{aligned}\quad (2)$$

where Φ_0 , σ_{ij} , and C_{ijkl} are the volume specific energy density, the bulk stress tensor, and the bulk elastic constants, respectively. Roman indices range from 1 to 3 and repeated indices are summed. The surface and bulk contributions add up to the total strain energy

$$U(\epsilon_{ij}) = \int_{V_0} \int_0^{\epsilon_{ij}} \frac{\partial\Phi}{\partial e_{ij}} de_{ij} dV + \int_{A_0} \int_0^{\epsilon_{\alpha\beta}^s} \frac{\partial\Gamma}{\partial e_{\alpha\beta}^s} de_{\alpha\beta}^s dA \quad (3)$$

The surfaces are assumed to be rigidly attached to the bulk, which means that the surface strains can be obtained from the bulk strains simply through an appropriate projection operation. The flexural rigidity can be found from by taking a weighted integral of the elastic properties over the cross section and bounding surface

$$\mu^{(2)} = \int_A E_b z^2 dA + \oint_S E_s z^2 dS \quad (4)$$

where Young's modulus of the bulk and the surfaces are denoted E_b and E_s , respectively. This way the composite character of the elastic properties across the nanowire cross section is accounted for, which gives an improved estimate of the flexural rigidity.

Atomistic simulations

To benchmark the continuum formulation we consider the special cases of slender $\langle 100 \rangle / \{100\}$ and $\langle 100 \rangle / \{110\}$ metallic face centered cubic (fcc) doubly clamped nanowires with square cross sections. Two different boundary value problems have been considered: the fundamental eigenfrequency of top-down nanowires subjected to transverse vibrations, and the critical compressive strain leading to buckling instability. We have obtained benchmark results for both boundary value problems using both classical molecular statics (MS) and molecular dynamics (MD) simulations. The interatomic interaction is modelled through an embedded atom method (EAM) potential fitted to properties for gold [5]. The relevant surface properties are evaluated using the free surface strain meshing technique suggested by Shenoy [6].

Resonant properties

The nanowires are called top-down as they can be considered to have been etched out from a bigger piece of matter while being rigidly constrained at both ends. Because of this, the interplanar distance along the wire axis corresponds to that of the ideal. The atomistic simulations are performed at liquid Helium temperature, e.g. 4.2 K, as described by [5] and the reader is referred to that paper for numerical details.

In Fig. 1 we have compared the fundamental eigenfrequency attained from atomistic simulations of $\langle 100 \rangle / \{100\}$ top-down nanowires with the aspect ratio 12, with predictions of the newly derived continuum model and the those of macroscopic Bernoulli-Euler beam theory for different cross sectional widths. It can be seen that the atomistic results are in great agreement with those derived from the continuum model, while macroscopic continuum beam theory severely underestimates the fundamental eigenfrequency. This discrepancy is attributed to two separate

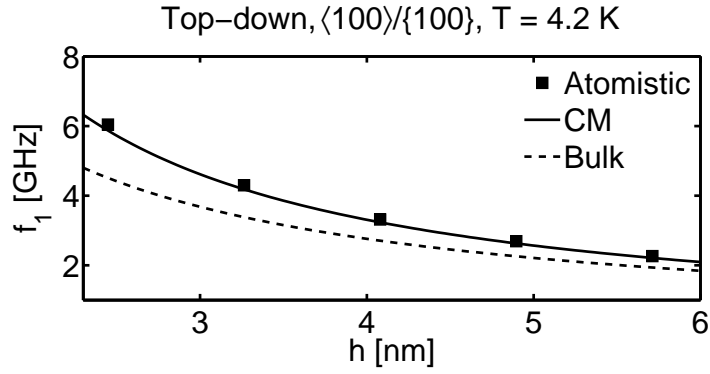


Figure 1. The fundamental eigenfrequency for $\langle 100 \rangle / \{ 100 \}$ top-down nanowires of different cross sectional dimensions. The aspect ratio of all nanowires is 12. The markers correspond to atomistic results, the solid and dashed lines are predictions from the newly derived continuum model and macroscopic beam theory, respectively.

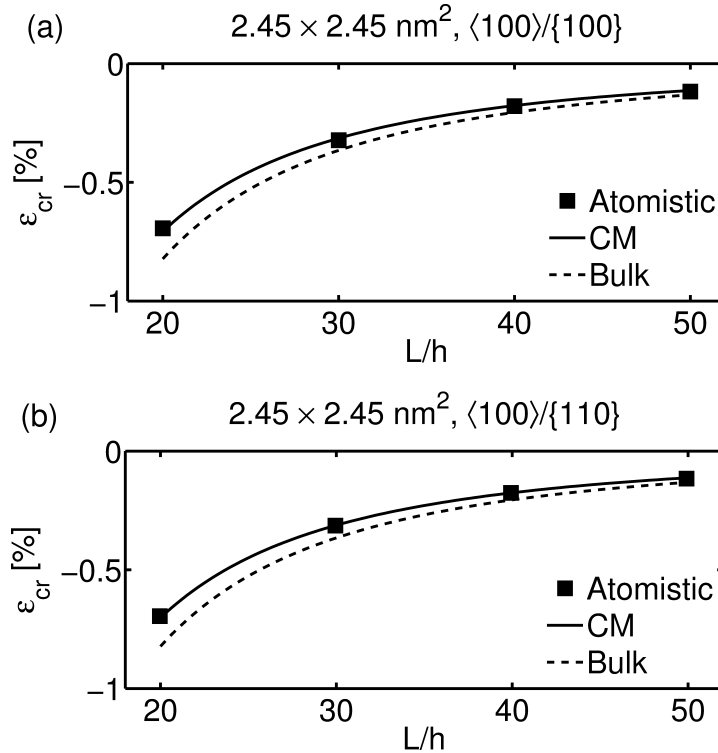


Figure 2. Critical buckling strain for (a) $\langle 100 \rangle / \{ 100 \}$ and (b) $\langle 100 \rangle / \{ 110 \}$ nanowires with $2.45 \times 2.45 \text{ nm}^2$ cross sections for different aspect ratios.

contributions. First, the lack of influence of surface elastic properties on the flexural rigidity. The second and most important mechanism is the lack of surface stress in the macroscopic beam picture. Both of these contributions are accounted for in the newly derived continuum model.

Buckling

The most important test of the new formulation is to evaluate how well buckling can be described by the present formulation. The reason why buckling is of greater interest than the eigenfrequency spectra of nanowires is due to the dependence of each boundary value problem

on the flexural rigidity. The atomistic results are taken from [7] where the numerical details are given.

In Figs. 2(a) and (b) we have compared the critical buckling strain for $\langle 100 \rangle / \{ 100 \}$ and $\langle 100 \rangle / \{ 110 \}$ nanowires with $2.45 \times 2.45 \text{ nm}^2$ cross sections for different aspect ratios, respectively. It can be seen that the bulk predictions overestimate the atomistic results and the newly derived continuum model predicts critical strains that are in excellent agreement with the atomistic results. This is an effect that emanates solely from the heterogeneous description of the cross section when calculating the flexural rigidity.

Conclusions

In this presentation we have described a novel continuum formulation for dealing with the influence of surface effects influence on the mechanical properties of nanowires. The model has been compared with results from atomistic simulations and has been proven to show great accuracy. In addition to the benchmark tests in this abstract a plethora of comparisons have been documented in [3].

References

- [1] H.S. Park, W. Cai, H.D. Espinosa and H. Huang. Mechanics of Crystalline Nanowires. *MRS Bulletin*, 34(3):178-183, 2009.
- [2] S. Cuenot, C. Fretigny, S. Demoustier-Champagne and B. Nysten. Surface tension effect on the mechanical properties of nanomaterials measured by atomic force microscopy. *Physical Review B*, 69(16):165410, 2004.
- [3] P.A.T. Olsson and H.S. Park. On the Importance of Surface Elastic Contributions to the Flexural Rigidity of Nanowires. *Journal of the Mechanics and Physics of Solids*, 60(12):2064-2083, 2012.
- [4] R. Dingreville, J. Qu and M. Cherkaoui. Surface free energy and its effect on the elastic behavior of nano-sized particles, wires and films. *Journal of the Mechanics and Physics of Solids*, 53(8):1827-1854, 2005.
- [5] P.A.T. Olsson. Transverse resonant properties of strained gold nanowires. *Journal of Applied Physics*, 108(3):034318, 2010.
- [6] V. B. Shenoy. Atomistic calculations of elastic properties of metallic fcc crystal surfaces. *Physical Review B*, 71(9):94104, 2005.
- [7] P.A.T. Olsson and H.S. Park. Atomistic study of the buckling of gold nanowires. *Acta Materialia*, 59(10):3883-3894, 2011.

Proceedings of the 25TH NORDIC SEMINAR
COMPUTATIONAL MECHANICS, 2012

Solid Mechanics II

Room: Stora Hörsalen, Friday 26 October, 10:00 - 12:00



Modelling of stress driven material dissolution

Per Ståhle¹ and Eskil Hansen²

⁽¹⁾Div. of Solid Mechanics, Lund University, Sweden, pers@solid.lth.se

⁽²⁾Centre for Mathematical Sci., Lund University, Sweden, eskil.hansen@appl.math.lth.se

Summary. The evolution of surfaces exposed to an aggressive environment and mechanical load is studied. The evolution is the initial part of a stress corrosion process that leads to pitting, crack initiation and growing cracks. In conventional fracture analyses requires a known or a postulated crack. A serious drawback is that a large part of the lifetime of a crack or a surface flaw is spent during the initiation of the crack. The knowledge of the mechanisms leading from a pit, flaw, scratch, etc. to a crack is very limited. One reason is the complication caused by the less definite defined original geometry. The motivation for the present study is to increase the understanding of the transition from stress induced pitting to growing cracks.

Key words: Surface morphology, pitting, crack initiation, phase field model

Introduction

A strained body exposed to an aggressive environment may suffer from continuous material dissolution during corrosion. The result is a progressive roughening of its surfaces. After roughening pitting occurs and eventually cracks will form and grow into the body. Apart from an aggressive environment and a mechanical stress the material needs to have an inherent sensitivity or to be sensitized to the environment. This can be due to local heating, plastic deformation, fatigue damage, etc. The aggressive environment can be a bulk aqueous environment surrounding the body or a micro environment, such as moist in pits, crevices, under deposits and not seldom very local environments created by microbial colonies established on the body surface.

The focus here is on the evolving surface morphology and initiation of cracks caused by the corrosion. The mechanism is the mass transportation resulting after dissolution and diffusion of matter into the environment or surface diffusion. The strain energy and the chemical energy provide driving forces for dissolution and transport of molecules. The observation an evolving surface waviness that was explained theoretically by [1,2]. The spectrum of the waves depends on the strain energy of the body surface and the surface energy. Experimental results by Kim et al. [3] show that the typical wavelength in, e.g., aluminium is on the scale of a few hundred nanometres when the stress is large and comparable to the yield stress. Several non-linear analyses show that the indents grow markedly faster and the peaks of the surface grow slower. This sharpens the indents and leads to a formation of pits. Thereafter, growth continues in the form of a blunted crack or, in a strict sense a deep notch with a relatively sharp tip. The crack tip always preserves a finite radius that may depend on the crack tip driving force and the thermodynamic chemical and mechanical properties of the surface. Further, the crack frequently branches and the crack width becomes slightly larger as the crack gets longer.

Phase field modeling of the evolving surface morphology

For a virtually sharp surface, treated as a discontinuity, specific chemical and mechanical properties may be ascribed to the surface. This simplifies the analysis and has normally no significant

influence on the thermodynamical behaviour of the body. However, when the distance between structural inhomogeneities or other characteristic distances are of the same order of magnitude as the thickness of the surface, e.g., as at a rough surface, at the tip of a crack or during emission of dislocations etc., the thickness of the surface may play a role and the negligence thereof may lead to unrealistic predictions. As opposed to this, a diffuse surface model assumes a continuous variation of composition, structure and other properties within the modelled region (cf. Landau and Lifshitz [4,5]). This includes the body, the diffuse surface and the surrounding environment. Here, the total free energy of the continuous body is formulated as a function of the material composition. The width of the surface layer is not assumed given, but instead the model predicts surface layers with a finite width and the associated surface energy is a result of the thermodynamical state of the material composition of the surface.

The total free energy of the system is formulated as a function of the phase fields and the variation of the free energy with respect to the fields act as driving forces for the evolution over time. In the proposed study an order parameter is used to distinguish empty space from the solid and to model the properties of the surface of the body. Phase field models formulated with phenomenological order parameters have been utilized as a numerical technique to avoid moving boundary tracking in describing the evolving body geometry.

The governing equations constitute a system of nonlinear elliptic-parabolic equations. Solutions for given initial conditions and boundary conditions is obtained by combining splitting methods with a semi-implicit time stepping scheme using finite differences. The calculations are performed in a moving coordinate system where the known solution for a straight corroding edge is subtracted from the sought solution.

Conclusions

Stress corrosion can be modelled as a moving boundary problem. Phase field modelling simplifies the analysis and the tracking of the moving boundary. The instability of a flat surface subjected to mechanical load is in agreement with results from traditional analyses. Formation cracks and crack growth are captured.

References

- [1] Asaro, R.J. and Tiller, W.A.: Metall. Trans. 3:1789, 1972.
- [2] Grinfeld, M.A.: Sov. Phys. Dokl. 31(831):1986; J. Nonlinear Sci. 3(35), 1993.
- [3] Kim, K.S. Hurtado, JA., and Tan, H.: Evolution of a Surface-Roughness Spectrum Caused by Stress in Nanometer-Scale Chemical Etching, Physical Rev. Letters, 83(19), 1999.
- [4] Landau L, Lifshitz E.: Phys Zeit Sowjetunion 8:153, 1935.
- [5] Ginzburg, VL. and Landau, LD.: Zh. Eksp. Teor. Fiz. 20, 1064, 1950.

Mixed methods for viscoelastic solids with weak symmetry elements

Douglas N. Arnold¹, Jeonghun J. Lee²

⁽¹⁾School of mathematics, University of Minnesota, Minnesota, USA, arnold@math.umn.edu

⁽²⁾Department of mathematics and systems analysis, Aalto University, Espoo, Finland, jeonghun.lee@aalto.fi

Summary. We consider mixed finite element methods for the standard linear solid model of viscoelastic materials. We use mixed finite elements for elasticity with weak symmetry of stress and show the a priori error analysis.

Key words: viscoelasticity, mixed methods, weak symmetry, error analysis

Introduction

A material is called *viscoelastic* when it shows kinematic features of both solids and fluids. It is involved in applications of various areas including geophysics, chemical and biomedical engineering. Depending on the manner that the features of solids and fluids are combined, there are numerous different viscoelastic materials. In this paper, we study numerical algorithms for linear viscoelastic solids using mixed finite elements for elasticity with weak symmetry. We are particularly interested in the standard linear solid model, or the Zener model in some literatures, of viscoelastic materials.

Governing equations

Let $\Omega \subset \mathbb{R}^n$ with $n = 2, 3$. The standard linear solid model can be described as in Figure ?? as a mechanical model. The stresses from the Maxwell component and from the other spring unit,

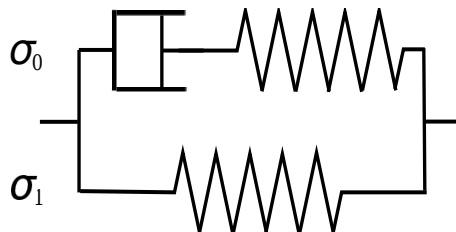


Figure 1. A mechanical model of the standard linear solids.

are denoted by σ_0 and σ_1 . Then the total stress is $\sigma = \sigma_0 + \sigma_1$. By splitting the displacement \vec{u} into $\vec{u} = \vec{u}_0 + \vec{u}_1$ where \vec{u}_0, \vec{u}_1 are the displacement parts involved in the spring and dashpot of the Maxwell component. By the generalized Hooke's law, $\sigma_1 = C_1 \epsilon(\vec{u})$ for the spring unit where ϵ is the symmetric gradient. In the Maxwell component, $\sigma_0 = C_0 \epsilon(\vec{u}_0) = C'_0 \partial_t \epsilon(\vec{u}_1)$ where C_0, C'_0 are the stiffness tensor given by the spring and dashpot units. Using A_0, A'_0, A_1 for the inverses of C_0, C'_0, C_1 , we have $A_1 \sigma_1 = \epsilon(\vec{u})$, $A_0 \partial_t \sigma_0 = \partial_t \epsilon(\vec{u}_0)$, and $A'_0 \sigma_0 = \partial_t \epsilon(\vec{u}_1)$. From the

addition of the second and third equations with $\vec{u} = \vec{u}_0 + \vec{u}_1$, from the first equation, and from the balance of linear momentum, we have

$$A_0 \partial_t \boldsymbol{\sigma}_0 + A'_0 \boldsymbol{\sigma}_0 = \partial_t \epsilon(\vec{u}), \quad A_1 \boldsymbol{\sigma}_1 = \epsilon(\vec{u}), \quad \rho \partial_t^2 \vec{u} - \operatorname{div}(\boldsymbol{\sigma}_0 + \boldsymbol{\sigma}_1) = \vec{f},$$

where \vec{f} is an external body force and ρ is the mass density. By introducing $\vec{v} = \partial_t \vec{u}$, the equations are

$$A_0 \partial_t \boldsymbol{\sigma}_0 + A'_0 \boldsymbol{\sigma}_0 = \epsilon(\vec{v}), \quad A_1 \partial_t \boldsymbol{\sigma}_1 = \epsilon(\vec{v}), \quad \rho \partial_t \vec{v} - \operatorname{div}(\boldsymbol{\sigma}_0 + \boldsymbol{\sigma}_1) = \vec{f}.$$

A weak formulation with weak symmetry

For a weak symmetry approach we use $\boldsymbol{\gamma} = \operatorname{skw} \operatorname{grad} \vec{u}$, the skew-symmetric part of $\operatorname{grad} \vec{u}$, as a Lagrange multiplier for the symmetry of stress. Our mixed method is based on the finite element spaces

$$\mathbf{M}_h \times \mathbf{M}_h \times V_h \times \mathbf{K}_h \subset H(\operatorname{div}, \Omega; \mathbb{R}^{n \times n}) \times H(\operatorname{div}, \Omega; \mathbb{R}^{n \times n}) \times L^2(\Omega; \mathbb{R}^n) \times L^2(\Omega; \mathbb{R}_{\operatorname{skw}}^{n \times n}),$$

where $(\mathbf{M}_h, V_h, \mathbf{K}_h)$ is a triple of the elements in [?, ?, ?, ?, ?], which are stable mixed finite elements for elasticity with weak symmetry.

We extend the tensors A_0, A'_0 and A_1 , which are defined only for symmetric tensors, to be defined for all tensors. For time discretizations, we use the Crank–Nicolson method. Let $k > 0$ be the time step interval. For simplicity, we define

$$\bar{\partial}_t g^{i+\frac{1}{2}} = \frac{g^{i+1} - g^i}{k}, \quad \hat{g}^{i+\frac{1}{2}} = \frac{g^i + g^{i+1}}{2}. \quad (1)$$

For the homogeneous Dirichlet boundary condition, $\vec{u} \equiv 0$, a weak formulation is to seek $(\boldsymbol{\sigma}_{0,h}^i, \boldsymbol{\sigma}_{1,h}^i, \vec{v}_h^i, \boldsymbol{\gamma}_h^i)$ such that

$$\begin{aligned} \left(A_0 \bar{\partial}_t \boldsymbol{\sigma}_{0,h}^{i+\frac{1}{2}}, \boldsymbol{\tau}_0 \right) + \left(A'_0 \hat{\boldsymbol{\sigma}}_{0,h}^{i+\frac{1}{2}}, \boldsymbol{\tau}_0 \right) + \left(\operatorname{div} \boldsymbol{\tau}_0, \hat{\vec{v}}_h^{i+\frac{1}{2}} \right) + \left(\bar{\partial}_t \boldsymbol{\gamma}_h^{i+\frac{1}{2}}, \boldsymbol{\tau}_0 \right) &= 0, & \boldsymbol{\tau}_0 \in \mathbf{M}_h, \\ \left(A_1 \bar{\partial}_t \boldsymbol{\sigma}_{1,h}^{i+\frac{1}{2}}, \boldsymbol{\tau}_1 \right) + \left(\operatorname{div} \boldsymbol{\tau}_1, \hat{\vec{v}}_h^{i+\frac{1}{2}} \right) + \left(\bar{\partial}_t \boldsymbol{\gamma}_h^{i+\frac{1}{2}}, \boldsymbol{\tau}_1 \right) &= 0 & \boldsymbol{\tau}_1 \in \mathbf{M}_h, \\ \left(\rho \bar{\partial}_t \vec{v}_h^{i+\frac{1}{2}}, \vec{w} \right) - \left(\operatorname{div}(\hat{\boldsymbol{\sigma}}_{0,h}^{i+\frac{1}{2}} + \hat{\boldsymbol{\sigma}}_{1,h}^{i+\frac{1}{2}}), \vec{w} \right) &= (\hat{\vec{f}}^{i+\frac{1}{2}}, \vec{w}), & \vec{w} \in V_h, \\ \left(\bar{\partial}_t \boldsymbol{\sigma}_{0,h}^{i+\frac{1}{2}} + \bar{\partial}_t \boldsymbol{\sigma}_{1,h}^{i+\frac{1}{2}}, \boldsymbol{\eta} \right) &= 0, & \boldsymbol{\eta} \in \mathbf{K}_h. \end{aligned}$$

When an initial displacement \vec{u}_h^0 is given, a numerical solution for the displacement vector is obtained by

$$\vec{u}_h^i = \vec{u}_h^0 + k \sum_{j=0}^{i-1} \hat{\vec{v}}_h^{j+\frac{1}{2}},$$

using the trapezoidal rule.

A weakly symmetric elliptic projection for error analysis

Let \mathbf{M}_h be the finite element space for stress in [?, ?, ?, ?, ?]. For $\boldsymbol{\sigma} \in H^1(\Omega; \mathbb{R}^{n \times n})$, there exists a projection $\tilde{\Pi}_h : H^1(\Omega; \mathbb{R}^{n \times n}) \rightarrow \mathbf{M}_h$ such that $\|\tilde{\Pi}_h \boldsymbol{\sigma}\|_0 \leq c \|\boldsymbol{\sigma}\|_1$ with $c > 0$ which is uniformly bounded in h . Furthermore,

$$\|\boldsymbol{\sigma} - \tilde{\Pi}_h \boldsymbol{\sigma}\|_0 \leq c \|\boldsymbol{\sigma} - \Pi_h \boldsymbol{\sigma}\|_0, \quad (2)$$

$$\operatorname{div} \tilde{\Pi}_h \boldsymbol{\sigma} = P_h \operatorname{div} \boldsymbol{\sigma}, \quad (\tilde{\Pi}_h \boldsymbol{\sigma}, \boldsymbol{\eta}) = (\boldsymbol{\sigma}, \boldsymbol{\eta}), \quad \boldsymbol{\eta} \in \mathbf{K}_h, \quad (3)$$

where P_h is the orthogonal L^2 projection onto V_h . Note that $\tilde{\Pi}_h$ maps a symmetric tensor to a weakly symmetry one and it plays an important role in the error analysis.

Postprocessing

When the elements in [?, ?, ?] are used and the mass density is piecewise Lipschitz adapted to triangulations, a postprocessing is eligible for numerical solutions of displacement vector. For the postprocessing, we use V_h^* , the space of piecewise polynomials of one degree higher than V_h , and define \tilde{V}_h as the orthogonal complement of V_h in V_h^* . A new numerical solution $\tilde{u}_h^{i,*} \in V_h^*$ is defined by

$$\begin{aligned} (\text{grad}_h \tilde{u}_h^{i,*}, \text{grad}_h \vec{w}) &= (A_1 \boldsymbol{\sigma}_{1,h}^i + \boldsymbol{\gamma}_h^i, \text{grad}_h \vec{w}), & \vec{w} \in \tilde{V}_h, \\ (\tilde{u}_h^{i,*}, \vec{w}) &= (\tilde{u}_h^i, \vec{w}), & \vec{w} \in V_h, \end{aligned}$$

where grad_h is the piecewise gradient operator adapted to triangulations. Since the space V_h^* consists of discontinuous piecewise polynomials, this postprocessing process is done element-wise, so its computational cost is small. Note also that this postprocessing does not need postprocessings of the previous time steps.

Numerical results

For numerical simulations we use the Arnold–Falk–Winther elements in [?] of degree 2. All numerical examples are implemented using the Dolfin Python module of FEniCS project [?].

We assume that the medium is homogeneous with the mass density $\rho = 1$, and compliance tensors A_0, A'_0, A_1 are given as the compliance tensors of homogeneous isotropic materials with parameters $\mu_0, \lambda_0, \mu'_0, \lambda'_0, \mu_1, \lambda_1$. For simplicity, we put $\mu_0 = \lambda_0 = 1, \mu'_0 = \lambda'_0 = 5$, and $\mu_1 = \lambda_1 = 10$. Let the displacement field be

$$\vec{u}(t, x, y) = \begin{pmatrix} (1-x)x^2 \sin(\pi y) \cos t \\ (1+t) \sin(\pi x) \sin(\pi y) \end{pmatrix}, \quad (4)$$

and $\boldsymbol{\sigma}_0(0) = 0$. The numerical result for (??) is in Table ??.

Table 1. Order of convergence for the exact solution with the displacement as in (??) and $\boldsymbol{\sigma}_0(0) = 0$ ($\mu_0 = \lambda_0 = 1, \mu'_0 = \lambda'_0 = 5, \mu_1 = \lambda_1 = 10, h = k$ and errors are evaluated at $T_0 = 1$).

$\frac{1}{h}$	$\ \boldsymbol{\sigma}_0 - \boldsymbol{\sigma}_{0,h}\ _0$		$\ \boldsymbol{\sigma}_1 - \boldsymbol{\sigma}_{1,h}\ _0$		$\ \vec{v} - \vec{v}_h\ _0$		$\ \boldsymbol{\gamma} - \boldsymbol{\gamma}_h\ _0$	
	error	order	error	order	error	order	error	order
4	2.37e-01	–	1.08e+00	–	1.96e-02	–	5.77e-02	–
8	3.15e-02	2.91	1.83e-01	2.55	4.88e-03	2.01	1.46e-02	1.99
16	4.81e-03	2.71	3.82e-02	2.26	1.22e-03	2.00	3.64e-03	2.00
32	9.11e-04	2.40	8.93e-03	2.10	3.05e-04	2.00	9.09e-04	2.00
64	2.05e-04	2.15	2.18e-03	2.03	7.62e-05	2.00	2.27e-04	2.00

For another numerical example, we consider wave propagation in domains consisting of subdomains with different material parameters. Purely elastic materials are simply described in our model by assuming $A'_0 \equiv 0$. The diagrams of domains for model problems are drawn in Figure ?. For reflected waves we observe a damping effect of viscoelastic materials in Figure ?.

Conclusions

We propose a mixed method for the standard linear solid model of viscoelasticity and carry out the a priori error analysis. In our approach, the problem is described as a differential equation and no numerical time integration is needed. It also provides a unified numerical framework for a composition of elastic and viscoelastic solids.

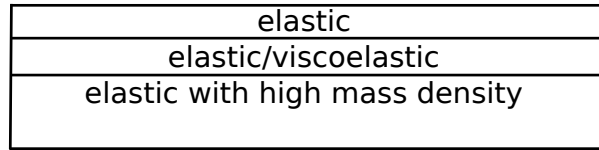


Figure 2. The diagram of domains with different material features.

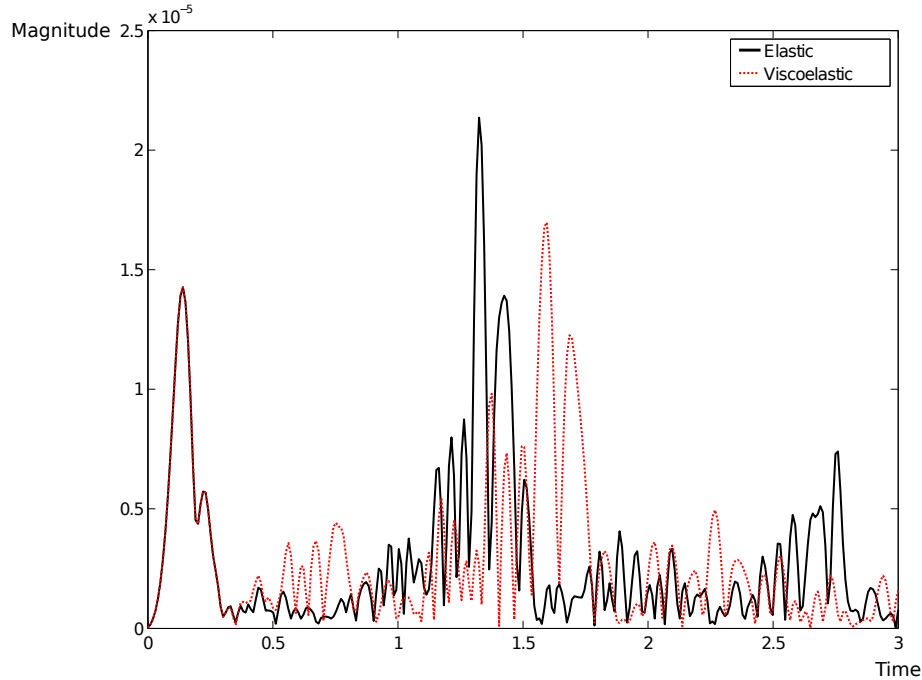


Figure 3. Reflected waves for domains with purely elastic materials and a composition of elastic/viscoelastic materials.

References

- [1] D. N. Arnold and R. S. Falk and R. Winther. Mixed finite element methods for linear elasticity with weakly imposed symmetry. *Math. Comp.*, 76(260):1699–1723, 2007.
- [2] G. Awanou. Rectangular mixed elements for elasticity with weakly imposed symmetry condition. *Adv. Comp. Math.*, To appear.
- [3] B. Cockburn and J. Gopalakrishnan and J. Guzmán. A new elasticity element made for enforcing weak stress symmetry. *Math. Comp.*, 79(271):1331–1349, 2010.
- [4] J. Gopalakrishnan and J. Guzmán. A second elasticity element using the matrix bubble. *IMA J. Numer. Anal.*, 32(1):357–372, 2012.
- [5] M. Rognes and R. Winther. Mixed finite element methods for linear viscoelasticity using weak symmetry. *Math. Models Methods Appl. Sci.*, 20(6):955–985, 2010.
- [6] R. Stenberg. A family of mixed finite elements for the elasticity problem. *Numer. Math.*, 53(5):513–538, 1988.
- [7] A. Logg and K.-A. Mardal and G. N. Wells. (Eds.) *Automated Solution of Differential Equations by the Finite Element Method, Lecture Notes in Computational Science and Engineering, Vol.84*. Springer, 2012.

Debonding analyses in anisotropic materials with strain-gradient effects

Brian Nyvang Legarth¹

⁽¹⁾ Department of Mechanical Engineering, Technical University of Denmark, Kgs. Lyngby, 2800, Denmark

Summary. A unit cell approach is adopted to numerically analyze the effect of plastic anisotropy on damage evolution in a micro-reinforced composite. The matrix material exhibit size effects and a visco-plastic anisotropic strain gradient plasticity model accounting for such size effects is adopted. A conventional cohesive law is extended such that both the average as well as the jump in plastic strain across the fiber-matrix interface are accounted for. Results are shown for both conventional isotropic and anisotropic materials as well as for higher order isotropic and anisotropic materials with and without debonding. Generally, the strain gradient enhanced material exhibits higher load carry capacity compared to the corresponding conventional material. A sudden stress drop occurs in the macroscopic stress-strain response curve due to fiber-matrix debonding and the results show that a change in yield stress, which is caused by plastic anisotropy, affects the overall composite failure strain.

Key words: Debonding, Plastic Anisotropy, Strain-Gradient Plasticity

Introduction

For a composite reinforced at the micron scale, two competing mechanisms affect the overall behavior: (I) interfacial failure reduces the strength and (II) strain-gradient effects enhance the strength. When analyzing such composites in general a full 3D analysis is required in order to fully represent the geometry, the loading and the boundary conditions. Such analyses are complicated and the computations become very time consuming when anisotropic plasticity and progressive debonding is to be accounted for. Thus, assuming a periodical distribution of the reinforcement allows for greatly simplified approaches. Here, a composite material having a periodical distribution of reinforcement is analyzed using a plane strain unit cell approach. Thus, the results presented in this study approximate a composite of rather long, almost aligned, stiff reinforcement which is subjected to a fixed stress state that is acting mainly in the transverse direction of the reinforcement. Fig. 1(a) shows the distribution of fibers and Fig. 1(b) shows the unit cell adopted here. The orthonormal basis, \mathbf{n}_i , of the principal axes of plastic anisotropy, \hat{x}_i , is defined by the angle θ , from from the global Cartesian coordinate system, x_i . The displacements Δ_1 and Δ_2 are prescribed such that ratio, κ , of the average stress at the cell edges remains constant. Fig. 1(c) shows an example of the finite element mesh adopted. The element type is 8-node elements.

Material models

Higher order elasto-plastic constitutive model

The fibers are assumed to be purely elastic with a stiffness much larger than the elasto-plastic matrix material, which is assumed to obey the strain gradient model proposed by Fleck and Hutchinson [1]. In addition, plastic anisotropy is accounted for using the anisotropic version of the Fleck and Hutchinson model suggested by Legarth [2]. Thus, the effective plastic strain, \dot{E}^p ,

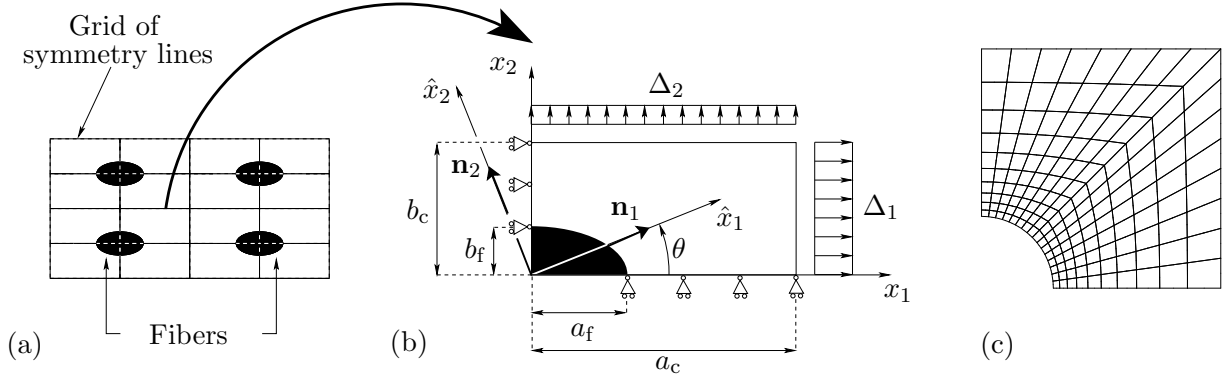


Figure 1. The plane strain cell model for the composite. (a) Periodically distributed fibers. (b) The cell used for modeling with initial dimensions, loads, supports and coordinate systems. (c) Example of finite element mesh using adopted, $\frac{a_f}{b_f} = \frac{a_c}{b_c} = 1$.

is enriched by the gradients of the conventional effective plastic strain, ϵ^p , and a material length scale parameter, l_* , as

$$\dot{E}^p = \sqrt{\frac{2}{3}\dot{\epsilon}_{ij}^p \dot{\epsilon}_{ij}^p + l_*^2 \dot{\epsilon}_{,i}^p \dot{\epsilon}_{,i}^p} \quad ; \quad \dot{\epsilon}_{ij}^p = \dot{\epsilon}^p \frac{\partial \Gamma}{\partial \sigma_{ij}} \quad ; \quad \dot{\epsilon}^p = \sqrt{\frac{2}{3}\dot{\epsilon}_{ij}^p \dot{\epsilon}_{ij}^p} \quad (1)$$

The work-conjugate effective stress is denoted σ_c and is given in table 1. Plastic anisotropy is accounted for by the classical anisotropic Hill yield surface. For the case of plane strain conditions with $\sigma_{13} = \sigma_{23} = 0$ the yield surface is

$$\Gamma = \sqrt{\frac{3}{2(F+G+H)} [F(\hat{\sigma}_{22} - \hat{\sigma}_{33})^2 + G(\hat{\sigma}_{33} - \hat{\sigma}_{11})^2 + H(\hat{\sigma}_{11} - \hat{\sigma}_{22})^2 + 2N\hat{\sigma}_{12}^2]} \quad (2)$$

where the Cauchy stresses, $\hat{\sigma}_{ij}$, refer to the principal axes of plastic anisotropy. For $F = G = H = 1$ and $N = L = M = 3$, Eq. (2) equals the isotropic Mises yield surface, σ_e . A higher-order stress measure is also introduced as ρ_i .

	Conventional materials ($l_* = 0, \rho_i = 0$)	Higher order materials ($l_* \neq 0, \rho_i \neq 0$)
Isotropic ($\Gamma = \sigma_e$)	$\rho_{i,i} = 0$ $\sigma_c = \sigma_e$	$\rho_{i,i} = q - \sigma_e$ $\sigma_c = \sqrt{(\sigma_e + \rho_{i,i})^2 + l_*^{-2} \rho_i \rho_i}$
Anisotropic	$\rho_{i,i} = 0$ $\sigma_c = \Gamma$	$\rho_{i,i} = q - \Gamma$ $\sigma_c = \sqrt{(\Gamma + \rho_{i,i})^2 + l_*^{-2} \rho_i \rho_i}$

Table 1. Summary of the effective stress, σ_c , for different materials.

Higher-order cohesive model

The bi-axial loading on the unit cell, Fig. 1, will tend to cause both normal and tangential interfacial separation, u_n and u_t , respectively, at the fiber-matrix interface. The cohesive zone model proposed by Tvergaard [3] takes both types of separation into account and therefore this model may seem suitable for the present study. However, due to the existence of the higher order stress, ρ_i and corresponding higher order tractions, $\rho_i n_i$ additional terms need to be included in order to have a conventional as well as higher order stress-free surface after debonding failure. Hence, a non-dimensional damage parameter is introduced as [4]

$$\lambda = \sqrt{\left(\frac{u_n}{\delta_n}\right)^2 + \left(\frac{u_t}{\delta_t}\right)^2 + l_*^2 \left[\left(\frac{\langle \epsilon^p \rangle}{l_A}\right)^2 + \left(\frac{[\epsilon^p]}{l_J}\right)^2 \right]} \quad (3)$$

where $\langle \epsilon^p \rangle$ is the average (subscript A) and $[\epsilon^p]$ is the *half* jump (subscript J) in plastic strain across the interface, respectively, whereas l_A and l_J are corresponding critical interfacial length scale parameters. For $\lambda \geq 1$ total separation have occurred. It is noted, that since the fiber is taken to be purely elastic, $\langle \epsilon^p \rangle = [\epsilon^p]$. The corresponding tractions are

$$T_n = \frac{u_n}{\delta_n} F(\lambda) \quad ; \quad T_t = \alpha \frac{u_t}{\delta_t} F(\lambda) \quad ; \quad T_A = l_*^2 \frac{\delta_n}{l_A^2} F(\lambda) \langle \epsilon^p \rangle \quad ; \quad T_J = l_*^2 \frac{\delta_n}{l_J^2} F(\lambda) [\epsilon^p] \quad (4)$$

with $\alpha = \delta_n / \delta_t$ and $F(\lambda) = \frac{27}{4} \sigma_{max} (1 - 2\lambda + \lambda^2)$ for $0 \leq \lambda \leq 1$. The maximum interfacial stress is denoted σ_{max} .

Results

Fig. 2 shows results for a load case with $\kappa = \frac{\sigma_2}{\sigma_1} = 0.5$ corresponding to bi-axial plane strain tension. The fiber volume fraction is $V_f = \frac{\pi a_f b_f}{4 a_c b_c}$, with $\frac{a_f}{b_f} = \frac{a_c}{b_c} = 1$. The initial yield stress is $\sigma_0 / E = 0.003$, where E is Young's modulus. The coefficients of anisotropy are $F = 0.7, G = 3.33, H = 1$ and $N = 9.6$ with $\theta = 0^\circ$ and $\sigma_{max} = 3\sigma_0$.

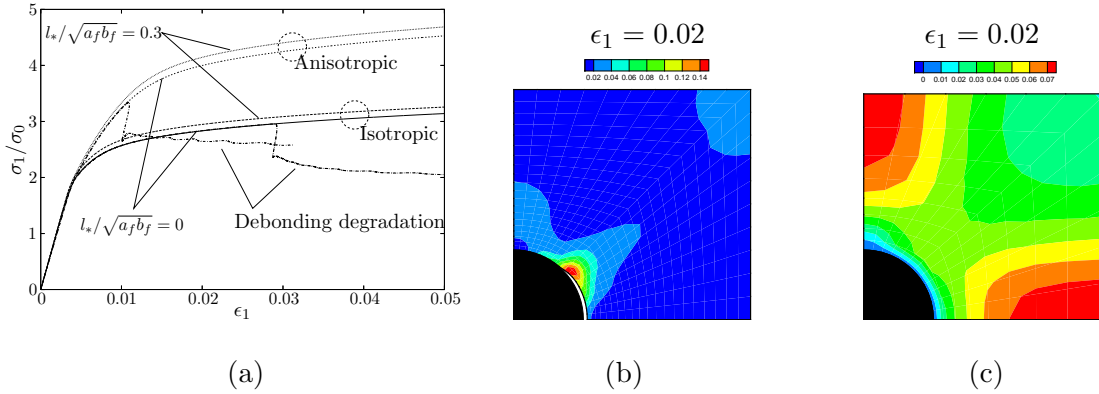


Figure 2. Bi-axial tension results, $\kappa = 0.5$. (a) Average stress-strain curves (b) Contours of effective plastic strain for a conventional anisotropic material with debonding (c) Contours of effective plastic strain for a higher order anisotropic material without debonding.

For both isotropic and anisotropic behavior the effect of the material length scale parameter, l_* , is an increased load carrying capacity, Fig. 2(a). A sudden stress drop occurs due to debonding, Fig. 2(a), and in Fig. 2(b) the corresponding void at the fiber-matrix interface is shown. Fig. 2(c) illustrates, that at the fiber-matrix interface the plastic strain is suppressed and the strain is smaller compared to the conventional case with severe plastic deformations at the tip of the void, Fig. 2(b).

The failure strain is depicted in Fig. 3 as function of the new cohesive length scale parameter, L_J , normalized against the matrix material length scale parameter, l_* . Both isotropic results as well as anisotropic results are shown. In addition to the yield function of Hill, Eq. (2), results using the anisotropic yield function of Barlat *et al.* are shown [5]. The coefficients of anisotropy in the two yield functions are chosen such that an identical 0° uniaxial stress strain curve in the x_1 -directions is reproduced. It is seen that the cohesive length scale parameter, L_J , greatly affect the failure strain as it becomes smaller and smaller. On the other hand, for increasing larger L_J -values the plastic behaviour of the cohesive law is suppressed and conventional results are obtained as shown by the asymptotic lines. For the Hill material the effect is very small, as debonding failure occurs at a rather small plastic strain, see Fig. 2. Thus, the influence of plasticity in the cohesive law is limited.

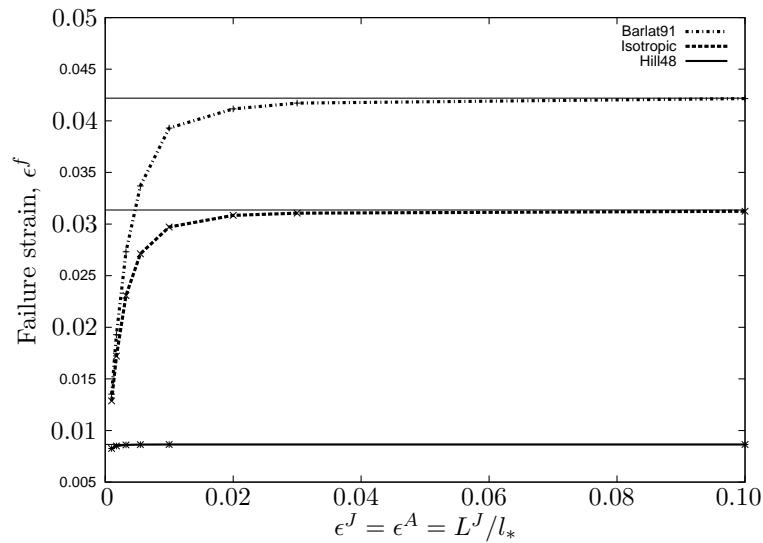


Figure 3. The failure strain as function of the new cohesive length scale parameter, L_J , normalized against the matrix material length scale parameter, l_* . Isotropic as well as anisotropic results are shown for $\kappa = 0.5$.

Conclusion

In conclusion, this study analyzes numerically the combined effects of plastic anisotropy, size-effects and debonding in a composite material. Debonding is seen as a sudden stress drop and plastic anisotropy highly affects the failure strain, while the size-effect is observed as an increased load carrying capacity. The material length scale of the cohesive law tends to reduce the failure strain of the composite, but as the parameter becomes sufficient large conventional results are predicted. This holds for both isotropic as well as anisotropic materials.

References

- [1] Fleck, N. A., Hutchinson, J. W.: A reformulation of strain gradient plasticity. *J. of the Mech. and Phys. of Solids*. **49**, 2245–2271, 2001.
- [2] Legartha, B. N.: Strain-gradient effects in anisotropic materials. *Model. and Sim. in Mater. Sci. and Eng.* **15**, S71–S81, 2007.
- [3] Tvergaard, V.: Effect of fibre debonding in a whisker-reinforced metal. *Mater. Sci. & Eng.* **A125**, 203–213, 1990.
- [4] Niordson, C. F.: Cohesive element for Fleck & Hutchinson 2001. *Technical report*, Technical University of Denmark, 2010.
- [5] Barlat, F., Lege, D.J. and Brem, J.C.: A six-component yield function for anisotropic materials. *Int. J. Plast.* **7**, 693–712, 1991.

Acknowledgment

This work was supported by the Danish Center for Composite Structures and Materials for Wind turbine (DCCSM), supported by The Danish Council for Strategic Research grant no: 09-067212.

A non-affine micro-sphere formulation for electroactive polymers

Sara Thylander¹, Andreas Menzel^{1,2}, and Matti Ristinmaa¹

⁽¹⁾Division of Solid Mechanics, Lund University, P.O. Box 118, SE-221 00 Lund, Sweden. sara.thylander@solid.lth.se, andreas.menzel@solid.lth.se, matti.ristinmaa@solid.lth.se

⁽²⁾Institute of Mechanics, Department of Mechanical Engineering, TU Dortmund, Leonhard-Euler-Strasse 5, D-44227 Dortmund, Germany. andreas.menzel@udo.edu

Summary. The need for reliable modelling and predictive simulation techniques continue to increase as the industrial applications of electroactive polymers continue to grow. The so-called micro-sphere framework enables the transformation of physics-based models for individual polymer chains as well as chain networks to the three-dimensional continuum level. In this contribution a previously established electromechanically coupled micro-sphere formulation is extended to include non-affine kinematics in combination with tube-type constraints on the movements of the chains in a polymer network. A numerical example is discussed which shows that the formulation proposed produces physically sound results.

Key words: non-linear electroelasticity, electroactive polymers, smart materials, coupled micro-sphere framework

Introduction

With the capability to convert electrical energy into mechanical energy, electroactive polymers (EAP) continuously keep generating and finding new and advanced applications. Their ability to considerably change in size and shape together with low cost and weight makes them suitable for technological applications in robotics and biomimetics as actuators and sensors.

Advanced modelling of EAP in combination with predictive simulation methods constitutes an active area of interdisciplinary research; see the finite-element formulation in [1] and the constitutive models for viscous EAP in [2, 3] as well as references cited therein. In view of physics-based modelling of polymers, so-called chain models have been established. Such statistics-based one-dimensional models can be extended to the three-dimensional continuum level by means of the so-called micro-sphere framework as established in [4, 5, 6]. As this work proceeds, the electromechanically coupled micro-sphere formulation proposed in [7] is now further extended by adopting the non-affine and tube-constrained kinematic framework introduced in [4]. The formulation will be restricted to isotropic material behaviour. In view of the incorporation of anisotropic elasticity, the reader is referred to [8], whereas formulations and applications of deformation-induced anisotropy evolution are discussed in, for example, [9, 10].

Basic equations

In this section the basic equations of electroelasticity are briefly reviewed together with the constitutive framework used. For detailed background information the reader is referred to [11].

Local balance equations

Adopting standard notation, placements of position vectors in a reference configuration are denoted by \mathbf{X} and their spatial counterpart by $\mathbf{x} = \boldsymbol{\varphi}(\mathbf{X}, t)$, with t representing time. The so-called deformation gradient is denoted by $\mathbf{F} = \nabla_{\mathbf{X}}\boldsymbol{\varphi}$ with $J = \det(\mathbf{F}) > 0$ and $\text{cof}(\mathbf{F}) = J\mathbf{F}^{-t}$ as well as $\bar{\mathbf{F}} = J^{-1/3}\mathbf{F}$.

In the absence of magnetic fields, the electric displacement \mathbf{d} and electric field \mathbf{e} in the current configuration are governed by the following equations in local form,

$$\nabla_{\mathbf{x}} \cdot \mathbf{d} = 0 \quad \text{and} \quad \nabla_{\mathbf{x}}^t \times \mathbf{e} = \mathbf{0}. \quad (1)$$

In consequence, the electric field \mathbf{e} can be represented as the gradient of a scalar potential, in this case the electric potential $\phi(\mathbf{X}, t)$, such that $\mathbf{e} = -\nabla_{\mathbf{x}}\phi = \mathbf{E} \cdot \mathbf{F}^{-1}$, where \mathbf{E} is the referential counterpart to \mathbf{e} . The polarisation \mathbf{p} , the electric field \mathbf{e} and the electric displacement \mathbf{d} are related through $\mathbf{d} = \varepsilon_0 \mathbf{e} + \mathbf{p} = \mathbf{D} \cdot \text{cof}(\mathbf{F}^{-1})$, where ε_0 is the vacuum electric permittivity and \mathbf{D} represents the referential counterpart of \mathbf{d} .

In view of a representation of the quasi-static local form of the balance of linear momentum in the presence of electric fields, the electric-field-related volume forces $\nabla_{\mathbf{x}}\mathbf{e} \cdot \mathbf{p}$ are transferred to the stresses. This renders the total spatial stresses, present in the local balance of linear momentum relation

$$\nabla_{\mathbf{x}} \cdot \boldsymbol{\tau} + \mathbf{f}_t^{\text{mec}} = \mathbf{0}, \quad (2)$$

to be symmetric. Note that $\mathbf{f}_t^{\text{mec}}$ collects purely mechanical volume forces. Alternatively, eq.(2) can be referred to the reference configuration, i.e. $\nabla_{\mathbf{X}} \cdot \mathbf{T} + \mathbf{f}_0^{\text{mec}} = \mathbf{0}$, with the Piola-type total stresses $\mathbf{T} = \boldsymbol{\tau} \cdot \text{cof}(\mathbf{F})$ and $\mathbf{f}_0^{\text{mec}} = J\mathbf{f}_t^{\text{mec}}$.

Constitutive equations

The subsequently elaborated constitutive model makes use of the introduction of a free amended energy function Ω as introduced in [12]. This energy function is split into the following contributions

$$\Omega(\mathbf{F}, \mathbf{E}) = \Omega^{\text{vol}}(J) + \Omega^{\text{iso}}(\bar{\mathbf{F}}) + \Omega^{\text{mel}}(\bar{\mathbf{F}}, \mathbf{E}) + \Omega^{\text{ele}}(\mathbf{E}) + \frac{1}{2}\varepsilon_0 J \mathbf{e} \cdot \mathbf{F}^{-1} \cdot \mathbf{F}^{-t} \cdot \mathbf{e}. \quad (3)$$

Micro-sphere formulation

The micro-sphere approach and kinematic framework established in [4] is adopted as this work proceeds. The non-affine micro-sphere stretch is introduced as a p-root average of the affine micro-sphere stretches. Moreover, the tube-related constraint on the chain deformation is adopted. In view of the electromechanical coupling, the extension established in [7] is used, here in combination with the non-affine and tube-related deformation measures. From a conceptual point of view, the energy function, the electromechanical flux terms, and related tangent operators, are evaluated by numerical integration over the unit-sphere \mathbb{U}^2 . To give an example, let \bullet denote a scalar-valued quantity so that numerical integration over \mathbb{U}^2 results in

$$\int_{\mathbb{U}^2} \bullet \, dA \approx \sum_{i=1}^m \bullet_i w_i, \quad (4)$$

where the index i refers to a referential integration direction $\mathbf{r}_i \in \mathbb{U}^2$ so that \bullet_i is the value of \bullet in the direction of \mathbf{r}_i . The non-negative integration weights and directions are constrained by $\sum_{i=1}^m w_i = 1$ and $\sum_{i=1}^m \mathbf{r}_i \otimes \mathbf{r}_i w_i = \frac{1}{3} \mathbf{I}$, with \mathbf{I} as the second-order identity tensor.

As basic scalar-valued isochoric deformation measures referred to the individual integration directions, we adopt the affine quantities

$$\bar{\lambda}_i = \|\bar{\mathbf{F}} \cdot \mathbf{r}_i\| \quad \text{and} \quad \bar{\nu}_i = \|\mathbf{r}_i \cdot \text{cof}(\bar{\mathbf{F}})\| = \|\bar{\mathbf{F}}^{-1} \cdot \mathbf{r}_i\|. \quad (5)$$

The affine stretch $\bar{\lambda}_i$ is transformed to the non-affine stretch measure via

$$\bar{\lambda} = \left[\sum_{i=1}^m \bar{\lambda}_i^p \omega_i \right]^{1/p}, \quad (6)$$

see [4]. In view of the contribution of the electric field on the micro-sphere level, the projection

$$E_i = \mathbf{E} \cdot \mathbf{r}_i. \quad (7)$$

is introduced, cf. [7].

With these quantities in hand and by splitting the elastic isochoric energy contribution Ω^{iso} additively into a non-affine stretch part $\Omega^{\text{iso},s}$ and a tube part $\Omega^{\text{iso},t}$, the free energy function Ω is approximated in the context of the micro-sphere formulation as

$$\Omega(\mathbf{F}, \mathbf{E}) \approx \Omega^{\text{vol}}(J) + \sum_{i=1}^m \left[\Omega_i^{\text{iso},s}(\bar{\lambda}) + \Omega_i^{\text{iso},t}(\bar{\nu}_i) + \Omega_i^{\text{mel}}(\bar{\lambda}_i, E_i) + \Omega_i^{\text{ele}}(E_i) \right] w_i \quad (8)$$

with the free space contribution including the parameter ε_0 being neglected. Note that different forms and representations of, for example Ω_i^{mel} , can be chosen. Hyper-elastic-type forms then render the electromechanical flux terms represented in, for instance, referential form so that

$$\mathbf{D} = - \frac{\partial \Omega}{\partial \mathbf{E}} \approx - \sum_{i=1}^m \frac{\partial [\Omega_i^{\text{mel}} + \Omega_i^{\text{ele}}]}{\partial \mathbf{E}} w_i, \quad (9)$$

and

$$\mathbf{T} = \frac{\partial \Omega}{\partial \mathbf{F}} \approx \frac{\partial \Omega^{\text{vol}}}{\partial J} \text{cof}(\mathbf{F}) + \sum_{i=1}^m \frac{\partial [\Omega_i^{\text{iso},s} + \Omega_i^{\text{iso},t} + \Omega_i^{\text{mel}}]}{\partial \mathbf{F}} w_i. \quad (10)$$

Numerical example

To show that the chosen form of energy function together with the electromechanically coupled micro-sphere framework captures the essential behaviour of non-linear electroelasticity, a numerical example of a homogeneous deformation is discussed. A cube of initial dimensions $L \times W \times W$ is put under a difference in electric potential at the boundaries so that a homogeneous electric field is produced. The electrical loading is applied in the x -direction with related initial length L . The specific form of the respective contributions to the energy function Ω as well as the in-

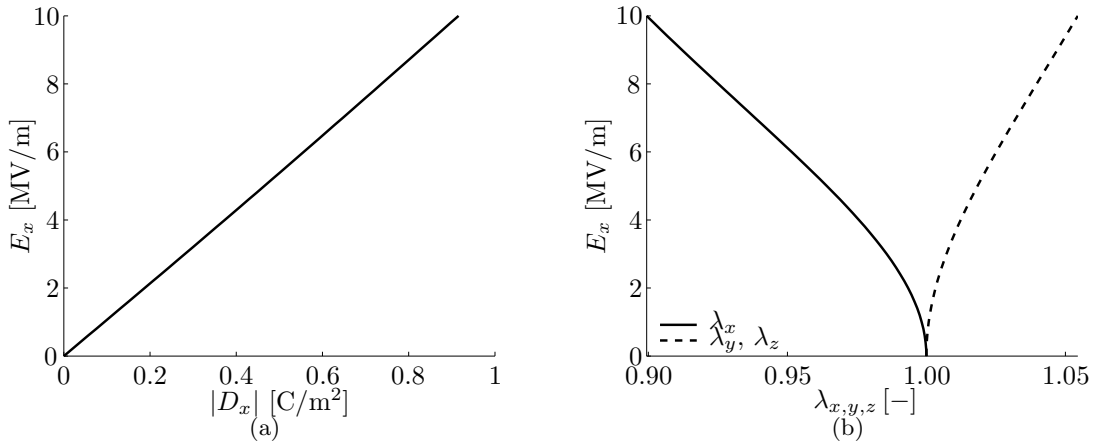


Figure 1. Homogeneous deformation under tension: (a) longitudinal electric field E_x plotted vs. absolute value of longitudinal electric displacement D_x ; (b) longitudinal electric field E_x plotted vs. longitudinal stretch λ_x and transverse stretches λ_y and λ_z .

corporated material parameters adopted are not summarised here; instead the reader is referred to [4] and [7] for more details.

Figure 1(a) shows the expected linear relation between the electric field \mathbf{E} and the electric displacements \mathbf{D} in the reference configuration, both in the direction of the applied electrical loading. In figure 1(b) the nonlinear relationship between the electric field \mathbf{E} and the stretches $\lambda_x = l/L$, $\lambda_y = w/W$ and $\lambda_z = w/W$ is clearly shown. Note that the deformation is not prescribed so that the results in figure 1(b) are calculated within an iterative scheme.

Acknowledgement

This work was made possible due to financial support from the Swedish Research Council (VR) under grant 2011-5428 which is gratefully acknowledged.

References

- [1] D.K. Vu, P. Steinmann, and G. Possart. Numerical modelling of non-linear electroelasticity, *Int. J. Numer. Methods Eng.*, 70:685-704, 2007.
- [2] A. Ask, A. Menzel, and M. Ristinmaa. Phenomenological modeling of viscous electrostrictive polymers, *Int. J. Non-lin. Mech.*, 47(2):156-165, 2012.
- [3] A. Ask, A. Menzel, and M. Ristinmaa. Electrostriction in electro-viscoelastic polymers, *Mech. Mat.*, 50:9-21, 2012.
- [4] C. Miehe, S. Göktepe, and F. Lulei. A micro-macro approach to rubber-like materials. Part I: the non-affine micro-sphere model of rubber elasticity, *J. Mech. Phys. Solids*, 52:2617-2660, 2004.
- [5] C. Miehe and Göktepe. A micro-macro approach to rubber-like materials. Part II: the micro-sphere model of rubber viscoelasticity, *J. Mech. Phys. Solids*, 53:2231-2258, 2005.
- [6] S. Göktepe and C. Miehe. A micro-macro approach to rubber-like materials. Part III: The micro-sphere model of anisotropic Mullins-type damage *J. Mech. Phys. Solids*, 53:2259-2283, 2005.
- [7] S. Thylander, A. Menzel, and M. Ristinmaa. An electromechanically coupled micro-sphere framework: application to the finite element analysis of electrostrictive polymers, *Smart Mater. Struct.*, 21:094008, 2012.
- [8] V. Alastrue, M.A. Martinez, M. Doblare, and A. Menzel. Anisotropic micro-sphere-based finite elasticity applied to blood vessel modelling, *J. Mech. Phys. Solids*, 57:178-203, 2009.
- [9] R. Ostwald, T. Bartel, and A. Menzel, A computational micro-sphere model applied to the micromechanical simulation of phase-transformations, *ZAMM*, 90(7-8):605-622, 2010.
- [10] T. Waffenschmidt and A. Menzel. Application of an anisotropic growth and remodelling formulation to computational structural design, *Mech. Res. Commun.*, 42:77-86, 2012.
- [11] G.A. Maugin. *Continuum Mechanics of Electromagnetic Solids*, North-Holland, 1988.
- [12] A. Dorfmann and R.W. Ogden. Nonlinear electroelasticity, *Acta Mech.*, 174:167-183, 200.

Ductile dynamic fracture modeling using embedded strong discontinuities in CGI machining simulations

Goran Ljustina¹, Ragnar Larsson¹, and Martin Fagerström¹

⁽¹⁾Division of Material and Computational Mechanics, Department of Applied Mechanics
Chalmers University of Technology, SE-412 96 Göteborg, Sweden
goran.ljustina@chalmers.se, ragnar@chalmers.se, martin.fagerstrom@chalmers.se

Summary. In order to model the material behavior in machining simulations it is proposed to use a continuum damage approach on the basis of the Johnson-Cook (JC) plasticity model for the ductile continuous behavior up to the critical stress-strain states where discontinuous bifurcation may occur. Whenever a critical state has been diagnosed, a Cohesive Zone (CZ) is established so that the actual critical stress state is located right at the onset of stress degradation in the CZ. Both pre-peak continuum damage and post-peak CZ damage are considered in the formulation. The localized cohesive zone damage is kinematically realized as an element embedded discontinuity, cf. [2], which is introduced elementwise, thereby facilitating the model developments in standard FE-packages.

Key words: Enhanced strain approach, Strong discontinuity, Finite strain, Dynamic, Ductile fracture

Pathological mesh dependence

A major driving force for the industry to simulate various manufacturing processes is the incorporation of new design materials to promote lightweight design. Machining is one of the operations where this may be efficiently achieved based on computational mechanics based modeling. In the current contribution we are concerned with the modeling of Compacted Graphite Iron (CGI) with respect to orthogonal machining simulations. The orthogonal machining simulations show that the used standard continuum damage model exhibit a pathological mesh size dependence, cf. Fig. 1.

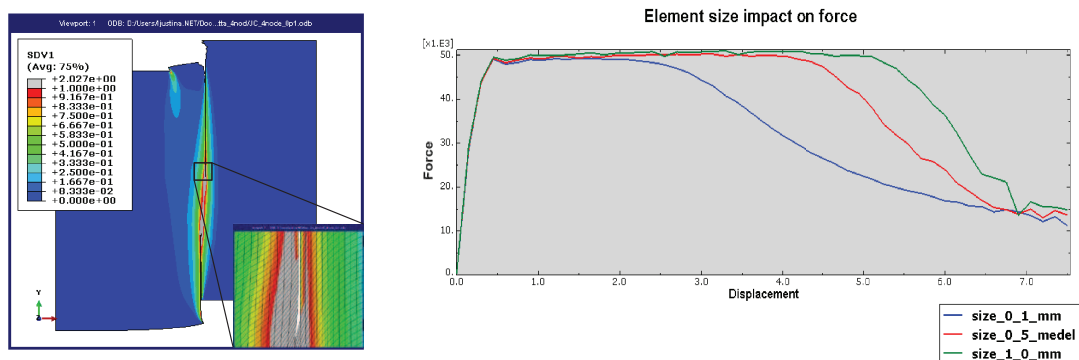


Figure 1. Pathological mesh sensitivity pertinent to standard damage visco-inelastic response of a dynamically loaded plate in shear. Three different mesh sizes are considered.

Ductile fracture using embedded discontinuities

A continuum damage approach is adopted on the basis of the Johnson-Cook (JC) plasticity model for the ductile continuous behavior up to the critical stress–strain states where discontinuous bifurcation may occur. Whenever a critical state has been diagnosed, a Cohesive Zone (CZ) is established so that the actual critical stress state is located right at the onset of stress degradation in the CZ. Both pre–peak continuum damage and post–peak CZ damage are considered in the formulation. The localized cohesive zone damage is kinematically realized as an element embedded discontinuity, cf. [2], which is introduced elementwise, thereby facilitating the model developments in standard FE–packages. In particular, due to the adopted structure of the enhanced strain field involving the embedded band, cf. Fig. 2, the *elementwise* projection problem corresponds to the generalized *traction continuity problem*

$$-\frac{1}{l} \int_{B_{0e}} \bar{\mathbf{d}} \cdot \mathbf{t}_1 dB + \int_{\Gamma_{S_{0e}}} \bar{\mathbf{d}} \cdot \mathbf{t}_1 d\Gamma = 0 \quad (1)$$

where $\mathbf{t}_1 = \Sigma_1^t \cdot \mathbf{N}$ nominal traction vector \mathbf{t}_1 . To formulate a cohesive zone model representing the post–peak response of the ductile fracture behaviour of the pearlite phase of the CGI, we follow the developments in [1] and consider the fracture process as a damage–plasticity process, where the energy dissipation is confined to the development of a propagating cohesive zone. To formulate the CZ with $\mathbf{t}_1 = \mathbf{t}_1[\mathbf{d}, \phi]$, let us introduce the material Mandel traction vector \mathbf{Q} defined as

$$\mathbf{Q} = \mathbf{T} \cdot \mathbf{N} = (1 - \phi)\bar{\mathbf{Q}} \quad (2)$$

where $\mathbf{T} = \mathbf{F}_c^t \cdot \Sigma_1^t$ (\mathbf{F}_c is the compatible part of the deformation gradient) is the material Mandel stress tensor and $0 \leq \phi \leq 1$ is the scalar damage variable of the embedded band. It follows that the transformation between the effective traction vectors $\bar{\mathbf{t}}_1$ and $\bar{\mathbf{Q}}$ are obtained as $\bar{\mathbf{t}}_1 = \mathbf{F}_c^{-t} \cdot \bar{\mathbf{Q}}$. As to the cohesive zone law, we thus propose to formulate effective stress $\bar{\mathbf{Q}}$ vector in terms of the material jump $\mathbf{J} = \mathbf{F}_c^{-1} \cdot \mathbf{d}$, and we formulate the condition for fracture initiation defined as

$$F = \sigma_f \left(\frac{\bar{Q}_t}{\gamma \sigma_f} \right)^2 + \frac{\sigma_f}{\gamma} (\gamma - 2\mu) \left(\frac{\langle \bar{Q}_n \rangle}{\sigma_f} \right)^2 - \frac{1}{\gamma} (\gamma \sigma_f - 2\mu \bar{Q}_n) \quad (3)$$

where σ_f is the failure stress in simple tension and the parameter $\gamma = \tau_f/\sigma_f$ defines the ratio between failure stress in simple shear and simple tension. Let us next define the evolution of the internal variables $\dot{\mathbf{J}} \approx \dot{\mathbf{J}}^p$ and $\dot{\phi}$ as

$$\dot{\mathbf{J}}^p = \dot{\lambda} \frac{\partial F}{\partial \mathbf{Q}}, \quad \dot{\phi} = \frac{\dot{\lambda}}{S(1 - \phi)} \quad \text{with } F \leq 0, \dot{\lambda} \geq 0, F\dot{\lambda} = 0 \quad (4)$$

Preliminary results

Preliminary results from simulations, cf. Fig. 3 show that when the adopted element embedded discontinuity approach (where the cohesive zone enhancement of the model is added) the pathological mesh dependence is removed. The modeling framework allows for the representation of the ductile fracture in terms of dissipated fracture energy in the post–localized response.

References

- [1] M. Fagerström and R. Larsson Theory and numerics for finite deformation fracture modelling using strong discontinuities. *Int. J. Num. Meth. in Engng.*, 66 (2006), 911–948.
- [2] R. Larsson, P. Steinmann and K. Runesson. Finite element embedded localization band for finite strain plasticity based on a regularized strong discontinuity. *Mech. Cohes.-Frict. Mater.*, 4 (1998), 171–194.

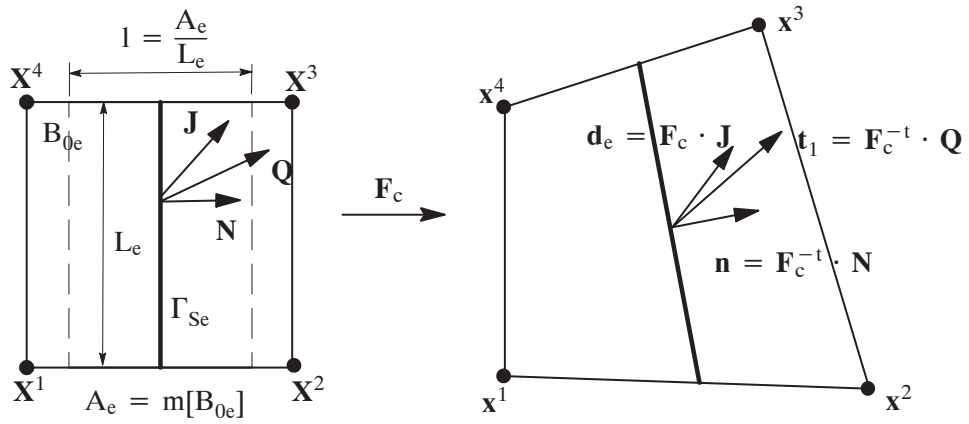


Figure 2. Bi-linear element enhanced with embedded strong discontinuity d .

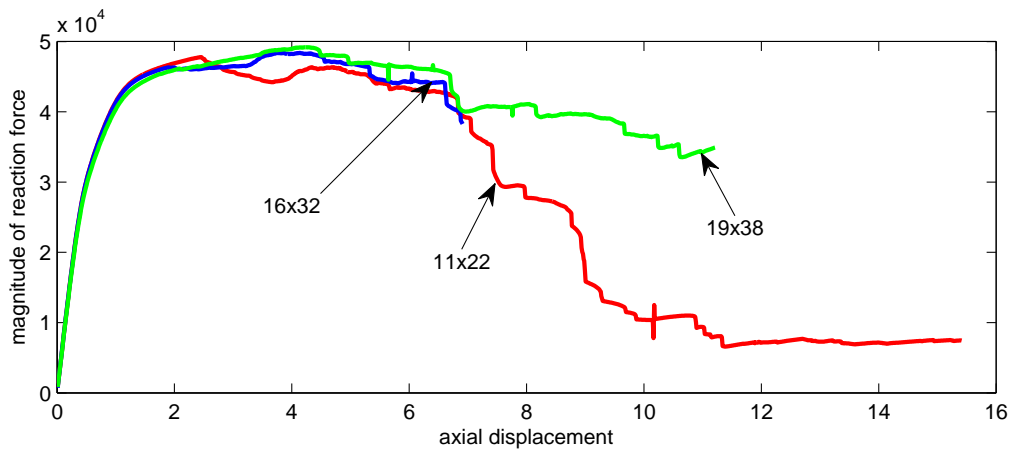


Figure 3. Force–displacement curves for element embedded discontinuity approach. Three different mesh sizes are considered. d .

Composite manufacturing modeling using porous media theory

Mohammad Rouhi^{1,2}, Maciej Wysocki^{1,2}, Ragnar Larsson¹

⁽¹⁾ Department of Applied Mechanics, Chalmers University of Technology, SE-412 96 Gothenburg, Sweden

⁽²⁾ Swerea Sicomp, Box 104, SE-43122 Mölndal, Sweden

Summary. We recently developed a simulation tool to simulate a quite wide class of composites manufacturing processes based on a compressible porous media theory formulation involving three constituents, solid, fluid and pore gas embedded in the voids. The aim of this tool is: firstly to model the highly deformable preform and its interaction with external loading and the intrinsic fluid pressure as well as the resulting changes in permeability, compaction and level of saturation. Secondly, the aim is to track the resin flow front during the infusion process using the continuum formulation itself, thereby avoiding methods like level set, etc. [1].

Keywords: liquid resin infusion, phase compressible continuum, free surface migration

Introduction

Darcy law is commonly used to model the resin flow in composite processing. This model describes the fluid flow in porous media and it typically relates the flow rate Q to the pressure difference over the specimen ($\Delta p/L$) defined as

$$Q = K \frac{A \Delta p}{\mu L}, \quad (1)$$

where μ is the viscosity and K the permeability. Since both the mechanical and the fluid flow properties (i.e. the permeability) of composites are to a large extent determined by fiber volume fraction, it is common to study the permeability variation with fiber volume fraction, as proposed by Carman [2]. However, in case of unidirectional reinforcement, where the transverse flow is much more constrained as compared to flow along the fibers, isotropic predictions of permeability are false. In this context, a permeability model of an idealized unidirectional reinforcement consisting of regularly ordered, parallel fibers was derived both for flow along and perpendicular to the fibers by Gebart [3]. In the present work we approach the problem similar to Gebart; however, here we consider the partially impregnated layers of prepregs, the so called EvaC prepregs [4]. In such a prepreg the fiber bed is kept dry and the matrix cover both sides of the preform. Therefore, we assume that during the manufacturing processes two kinds of flow will develop; (i) the macroscopic flow between the layers and (ii) the infiltration flow

into the dry fiber bed. In summary, the flow is restricted perpendicular to the plies and fairly unrestricted parallel to the plies.

The goal of this paper is to combine the theory of porous media with respect to the liquid resin infusion problem, as developed in [1], with the constitutive relation for anisotropic permeability introduced in following section.

A homogenized theory of porous media

The fiber bed during infusion is considered as a porous material which its pores are either partially filled by liquid resin or contains unfilled void space. The macroscopic volume fractions for the solid and the fluid phases n^s and n^f , respectively, are defined as

$$n^s = \frac{V^s}{V}, \quad n^f = \frac{V^f}{V} \quad \text{with} \quad n^s + n^f = 1 \quad (2)$$

where V^s is the volume portion of the solid relative to a representative volume with volume V , and V^f is the compressible fluid volume portion of the pore space. The volume fractions are connected via the saturation constraint [1].

The fluid phase mixture may be further described upon introducing the degree of liquid saturation $0 \leq \xi[x, t] \leq 1$, where $\xi = 0$ corresponds to gas-filled pores and $\xi = 1$ corresponds to the situation of complete liquid saturation.

Governing and Constitutive equations

To formulate the coupled problem of partially fluid saturated solid, mass balance and momentum balance is used

$$\rho^f \nabla \cdot \mathbf{v} - n^f \dot{\rho}^f = -\nabla \cdot (\rho^f \mathbf{v}^d), \quad (3)$$

$$\bar{\boldsymbol{\sigma}} \cdot \nabla + \hat{\rho} \mathbf{g} = \mathbf{0} \quad \forall \mathbf{x} \in B, \quad (4)$$

where \mathbf{v}^d is the Darcian velocity defined as $\mathbf{v}^d = n^f \mathbf{v}^r$ and $\bar{\boldsymbol{\sigma}} = \boldsymbol{\sigma}^s + \boldsymbol{\sigma}^f$ is the total Cauchy stress. In turn, $\bar{\boldsymbol{\sigma}}$ is related to the effective (constitutive) stress $\boldsymbol{\sigma}$ and the fluid pressure p via the Terzaghi effective stress principle as $\bar{\boldsymbol{\sigma}} = \boldsymbol{\sigma} - p\mathbf{1}$.

Assuming hyper-elasticity for the effective stress response for a Neo-Hookean elastic material we obtain the free energy $\psi[\mathbf{C}]$ for the solid phase which correspond constitutive state equations as

$$\mathbf{S} = 2\hat{\rho}_0^s \frac{\partial \psi}{\partial \mathbf{C}}, \quad (5)$$

$$p = (\rho^f)^2 \frac{\partial \psi^f}{\partial \epsilon}, \quad (6)$$

where $\mathbf{S} = \bar{\mathbf{S}} - J\mathbf{C}^{-1}p$ is the consequent effective second Piola Kirchhoff stress due to the Terzaghi effective stress principle.

In order to assess the pressure dependence in the fluid density, it is assumed that the same pressure prevails in the liquid and gas constituents and that the highly compressible gas constituent is pressure dependent in the spirit of the ideal gas law. It should be noted that the rate behavior of the fluid density may be characterized in terms of the compression modulus of the liquid-gas mixture.

$$\rho^f = \xi \rho^l + (1 - \xi) \rho^g \quad (7)$$

$$\dot{\rho}^f = \frac{1}{K^f} \dot{p} + (\rho^l - \rho^g) \dot{\xi} \quad \text{with} \quad K^f = \frac{1}{(1 - \xi)k^g} \quad (8)$$

Indeed, the value of K^f increases for increased saturation and decreased gas-compliance k^g . For continued saturation towards $\xi = 1$, we obtain that $K^f \rightarrow \infty$ and $\xi = 0$ leading to fluid incompressibility, i.e. $\rho^f \rightarrow \rho^l$. c.f. Larsson et. al. [1] for further details.

Solid-fluid interaction

A key feature of the present contribution is the solid-fluid interaction model, where it is assumed that two types of flow will develop during the composites processing; (i) the macroscopic flow between the layers and (ii) the infiltration flow into the dry fiber bed.

$$\mathbf{v}^d = -\frac{1}{\nu(1-\phi^p)} \left((K_{fB}(1-\phi_l) + K_{Ch}\phi_l)(\mathbf{1} - \mathbf{M}) + K_{fB}\mathbf{M} \right) \cdot \mathbf{h}_e^f, \quad (9)$$

where K_{fB} is the permeability through the fiber, K_{Ch} is the permeability through the channel, ϕ_l is liquid volume fraction, structural tensor $\mathbf{M} = \mathbf{T} \otimes \mathbf{T} \in B_0$, where \mathbf{T} is a unit vector transverse to the fibre bed.

The permeability through the fiber bed K_{fB} is represented using the Gebart equation as in (10). The permeability through the channel may be approximated considering the resistance to viscous flow within a rectangular channel, [5]

$$K_{fB} = \frac{16r^2}{9\pi\sqrt{2}} \left[\sqrt{\frac{\pi}{2\left(\frac{\phi_0}{J}\right)\sqrt{3}}} - 1 \right]^{\frac{5}{2}}, \quad (10)$$

$$K_{Ch} = \frac{(h^f)^2}{12}, \quad (11)$$

where h^f is the channel height.

A smooth free surface problem

The key idea of paper is to consider the motion of flow front in terms of the evolution of the fluid saturation field $\xi = \xi[\mathbf{x}, t]$. Clearly, at the initiation of a wetting process the initial condition is that $\xi[\mathbf{x}, t] = 0$ in order to define the one phase non-wet region, whereas the fully saturated region is defined by $\xi[\mathbf{x}, t] = 1$. We thereby replace the strictly discontinuous free surface problem by a smooth transition of the liquid front in terms of the evolution of the fluid saturation field $\xi = \xi[\mathbf{x}, t]$. We can recall the saturation evolution [1] along with the Darcian flow model which is to be satisfied locally according to

$$n^f \dot{\xi} + \frac{J}{J} \xi + \nabla \cdot \mathbf{v}^d = 0 \quad (12)$$

whereby the saturation degree variable may be regarded as a local field variable $\xi = \xi[\mathbf{x}, t]$ or, simply, as an internal variable governed by equation (12).

Numerical results and concluding remarks

A simulation of liquid resin infusion with a flexible fiber bed based on hyper elastic material model is considered using the same boundary conditions and material parameter as in Larsson et. al. [1]. The goal is to assess the permeability model developed in this paper invoked to the infusion simulation algorithm.

As to the assessment of the global saturation degree for the numerical solution, we simply consider $\bar{\xi}$ as the average value of the saturation degree in the elements, i.e. $\bar{\xi} = \langle \xi \rangle$.

In Figure 1, the deformation of the preform is shown along with the distribution of ξ . A non-uniform compaction of the preform is induced by the vacuum pressure and so is the temporal evolution of the diffusive flow front. During the infusion, as the fluid pressure increases, some of the deformation will be balanced off, leading to a difference in deformation in the saturated and in the non-saturated regions. Preform deformation has a direct influence on the permeability, porosity and the Darcian liquid flow advancement. Figure 1 also shows the resulting fluid pressure distribution, which is the key mechanism driving the resin infusion via

the anisotropic permeability. As time passes, the Darcian velocity decreases due to the decrease in the pressure gradient, and the process is significantly slowed down, as shown in Figure 2. The convergence of the solution upon mesh refinements is also shown in Figure 2 and it can be noted that the total infusion time is around $T \approx 60$ minutes.

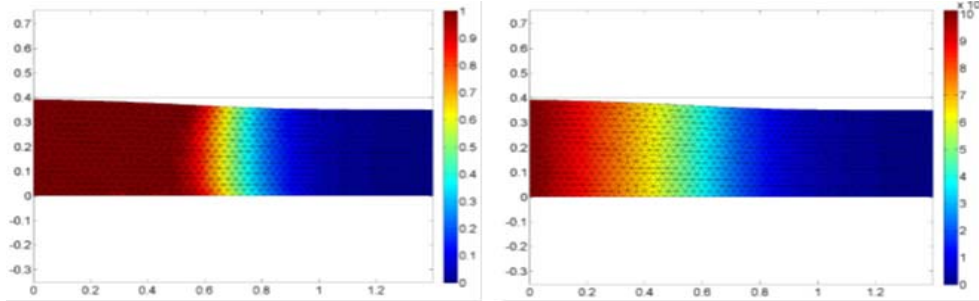


Figure 1. Preform deformation during infusion process along with current state of saturation and pressure

In the present paper we have framed the liquid resin infusion of composites (and other related processes) into a free surface formulation based on two-phase porous media theory while the driving flow is modeled by Darcy law with an anisotropic permeability model. As compared to other methods available in the literature for these types of problems, typically restricted to simplified 1D approximations with isotropic assumption for the flow, the approach is quite general in the sense that it provides the coupling between the preform deformation and the free surface migration in one and the same formulation considering flow properties different in different directions.

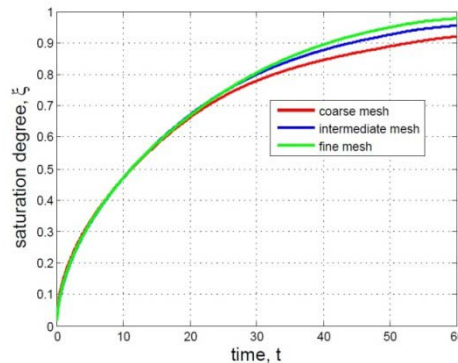


Figure 2. Global saturation degree versus time, mesh sensitivity analysis

References

- [1] Larsson, R., Rouhi, M., Wysocki, M., "Free surface flow and preform deformation in composites manufacturing based on porous media theory", *European Journal of Mechanics A/Solids* 31 (2012) 1-12
- [2] Carman, P. C. 1937, Fluid flow through granular Bed, *Transaction institution of chemical engineering*, 15:150-166.
- [3] Gebart, B. R., Permeability of unidirectional reinforcement for RTM, *Journal of composite materials*, v 26, No. 8/1992, p1100-1133
- [4] Thomas, S., Bongiovanni, C., Nutt, S.R., In situ estimation of through-thickness resin flow using ultrasound, 2008, *Composites Science and Technology* 68 (15-16), pp. 3093-3098
- [5] *Dynamics of Fluids in Porous Media*, Jacob Bear, Dover Civil and Mechanical Engineering, 1988